



HAL
open science

The organoid revolution to assess mycobacterial pulmonary infections

Stephen Adonai Leon Icaza

► **To cite this version:**

Stephen Adonai Leon Icaza. The organoid revolution to assess mycobacterial pulmonary infections. Human health and pathology. Université Paul Sabatier - Toulouse III, 2022. English. NNT : 2022TOU30168 . tel-03969087

HAL Id: tel-03969087

<https://theses.hal.science/tel-03969087v1>

Submitted on 2 Feb 2023

HAL is a multi-disciplinary open access archive for the deposit and dissemination of scientific research documents, whether they are published or not. The documents may come from teaching and research institutions in France or abroad, or from public or private research centers.

L'archive ouverte pluridisciplinaire **HAL**, est destinée au dépôt et à la diffusion de documents scientifiques de niveau recherche, publiés ou non, émanant des établissements d'enseignement et de recherche français ou étrangers, des laboratoires publics ou privés.

Université Fédérale



Toulouse Midi-Pyrénées

THÈSE

En vue de l'obtention du
DOCTORAT DE L'UNIVERSITÉ DE TOULOUSE

Délivré par l'Université Toulouse 3 - Paul Sabatier

Présentée et soutenue par
STEPHEN ADONAI LEON ICAZA

Le 29 septembre 2022

**La révolution des organoïdes pour étudier et cibler les infections
pulmonaires médiées par les mycobactéries**

Ecole doctorale : **BSB - Biologie, Santé, Biotechnologies**

Spécialité : **BIOLOGIE CELLULAIRE**

Unité de recherche :

IPBS - Institut de Pharmacologie et Biologie Structurale

Thèse dirigée par
Céline COUGOULE

Jury

Mme Fabienne ARCHER, Rapporteur

Mme Claire ANDREJAK, Rapporteur

M. Jean-François CAVALIER, Examineur

Mme Céline COUGOULE, Directrice de thèse

M. Matthieu ARLAT, Président

Dedicado a mi padre, hermanos y a mi novia. Gracias por apoyarme en todo momento. Los amo con todo mi corazón.....

Acknowledgments

Thanks to the jury

Thank all the members of the jury. Especially my thesis reviewers, Fabienne Archer and Claire Andrejak. Thank you for all the advice and suggestions you gave me to improve my thesis manuscript.

Thanks to the lab

Céline: Thank you so much for allowing me to come to France and for your help with everything I needed to finish my doctorate. After four years of hard work, successes, and failures, I can say that you have taught me to be a better scientist and a better human being.

Etienne: Thank you for all the advice and suggestions you gave me during my thesis. You are a great scientist and a great person. I will be forever grateful for all the support you gave me during the pandemic.

PJ, Audrey, David, Romain, Elif and Rémi: Thank you very much for all the help you gave me during the design and performance of my experiments, as well as for every advice given during the lab meetings. I wish you all the best.

Thanks to my friends

Karin y Miriam: Muchas gracias a las dos por cada risa y momento divertido en el lab. Ustedes hicieron que no extrañara tanto mi casa con su cariño español. Estoy seguro que ambas serán muy buenas científicas, les deseo lo mejor.

Estefanía: Fanny, gracias por siempre estar al pendiente de mí y por todos los días que pasamos hablando por horas durante el almuerzo. Sin lugar a dudas eres mi venezolana favorita y espero que sigamos siendo muy buenos amigos por muchos años y sin importar dónde nos encontremos viviendo. Te quiero mucho.

Salimata: My dear friend, my brother. What can I say to you? You know that you were a fundamental part of my adaptation to France. You know that I consider you one of the best scientists I have ever met, and I am sure you will have a successful career. Thank you very much for every personal or scientific talk we had, you made me grow as a person and as a researcher. Thank you for your friendship and love.

Marseille Friends: Micaela, Karen, Hiba, Maria, Mike, David, Scarlett. Even though we are all from different parts of the world, I would like to thank you for your friendship, and all the trips and fun moments we have had together. With you, I feel that no matter what country I visit, I will always have a place to stay.

Thanks to my family

Familia Regia: Juan, Florencia, Alex, Frecia, Aide. Amigos míos, los quiero mucho. Gracias por siempre apoyar sin importar la distancia ni la hora. Ustedes son esa familia que uno elige pero son igual de importante que la de sangre. Saben que siempre estoy aquí para usted y los apoyo tanto en sus éxitos como en sus fracasos. Ésta tesis también va dedicada hasta el cielo para tu papá Flor y para tu mamá Frecia.

Familia Rangel Sosa: Ustedes son un gran pilar en mi vida, gracias por apoyarme siempre. Los quiero con todo mi corazón. Muchas gracias por siempre creer en Montse y en mi.

Mi familia (familia León): Papá, Chris, Kevinn. Los amo mucho. Siento el no haber podido estar con usted en los momentos complicados y en los felices, no obstante, tengan por seguro que todo lo que hago es pensando en ustedes. Gracias por siempre esforzarse, motivarme y creer en mi.

Mi pequeña familia (Montse Rangel): Mi compañera de vida, palabras me faltan para agradecerte a ti. Gracias por aguantar mis locuras, mis necesidades, mis ideas. Gracias por apoyarme y motivarme a cada momento. Espero podamos seguir por siempre haciendo locuras y conociendo gente y lugares nuevos. Eres mi persona favorita. Te amo con todo mi corazón.

¡Life is pain..... pain au chocolat!

Abstract

Respiratory infections including tuberculosis (TB) and nontuberculous mycobacterial pulmonary diseases (NTM-PD) are a major global health concern. Chronic respiratory infections due to mycobacteria are causing high rates of morbidity and mortality worldwide. According to the World Health Organization Global Tuberculosis Report 2021, in 2020, *Mycobacterium tuberculosis* (Mtb) affected 10 million people globally with an estimated 1.5 million deaths. On the other hand, the incidence and prevalence of non-tuberculous mycobacteria (NTM) infections, such as *Mycobacterium abscessus* (Mabs), are increasing due to rise of immunocompromised and vulnerable individuals, including cystic fibrosis (CF) patients. Nonetheless, our understanding and models to address the very early steps of Mtb infection and the host and bacterial determinants driving Mabs pathology in CF patients are at the best, rudimentary. Recent advances in stem cell biology have allowed the growth of human tissues *in vitro* that resemble organs *in vivo*. Organoids enables the generation and maintenance of complex epithelia *in vitro* derived from human adult stem cells. Of most importance, organoids recapitulate the general architecture and functional aspects of the original epithelium while remaining genetically stable for years. The organoid system is much more representative of *in vivo* physiology than single-cell models, providing unique opportunities for the study of human diseases and complementing animal models (1, 2). Thus, organoids could be consider as a connection between *in vitro* and *in vivo* models. Here, we evaluated whether the human airway organoid (AO) technology from healthy tissue and CF patients is appropriate for modelling Mtb and Mabs infection and treatment efficacy.

We show in healthy AOs that Mtb and Mabs reside primarily as extracellular bacteria and infect epithelial cells with relatively low efficiency. While the AOs microenvironment was able to control, but not eliminate Mtb, Mabs thrives. We demonstrate that AOs responded to infection by modulating the expression of cytokines, antimicrobial peptides, mucin and antioxidant genes.

Our findings indicate that organoids derived from CF patients have a thicker epithelium, accumulate mucus, and undergo oxidative stress and increased lipid peroxidation, and cell death, key features of CF. Mabs rough (R) and smooth (S) morphotypes replicate more efficiently in CF patient organoids and CF-induced organoids (Healthy organoids + CFTR inhibitors) compared to healthy organoids, while S Mabs forms biofilms, R Mabs forms cords and display a higher virulence, further validating the relevance of CF organoids as a model for the study of Mabs pathogenesis. Finally, we prove that Mabs take advantage of the oxidative microenvironment in the CF airways to thrive, and that pharmacological activation of antioxidant pathways resulted in better control of Mabs growth.

In conclusion, we have established AOs as a suitable human system to decipher very early events of mycobacteria infection and the mechanisms of CF-enhanced respiratory infection by Mabs, thus offering new avenues for fundamental and therapeutic research.

Résumé

Les infections respiratoires, y compris la tuberculose (TB) et les maladies pulmonaires à mycobactéries non tuberculeuses (NTM-PD), constituent un problème majeur de santé mondiale. Les infections respiratoires chroniques dues aux mycobactéries entraînent des taux élevés de morbidité et de mortalité dans le monde. Selon le Rapport mondial sur la tuberculose 2021 de l'Organisation mondiale de la santé, en 2020, *Mycobacterium tuberculosis* (Mtb) a touché 10 millions de personnes dans le monde, avec un nombre de décès estimé à 1,5 million. D'autre part, l'incidence et la prévalence des infections à mycobactéries non tuberculeuses (NTM), telles que *Mycobacterium abscessus* (Mabs), augmentent en raison de l'accroissement de la population des personnes immunodéprimées et vulnérables, tels que les patients atteints de mucoviscidose. Cependant, notre compréhension et les modèles permettant d'aborder les premières étapes de l'infection par Mtb et les déterminants de l'hôte et de la bactérie à l'origine de la pathologie de Mabs chez les patients atteints de la mucoviscidose (CF) sont, au mieux, rudimentaires. Les récentes avancées dans le domaine de la biologie des cellules souches ont permis la croissance de tissus humains *in vitro* qui ressemblent aux organes *in vivo*. Les organoïdes permettent de générer et de maintenir *in vitro* des épithéliums complexes dérivés de cellules souches adultes humaines. Le plus important est que les organoïdes récapitulent l'architecture générale et les aspects fonctionnels de l'épithélium d'origine tout en restant génétiquement stables pendant des années. Le système organoïde est beaucoup plus représentatif de la physiologie *in vivo* que les modèles unicellulaires. Il offre des possibilités uniques pour l'étude

des maladies humaines et complète les modèles animaux. Ainsi, les organoïdes ont contribué à combler le fossé entre les modèles *in vitro* et *in vivo*. Nous avons évalué ici si la technologie des organoïdes des voies respiratoires (AO) provenant de tissus sains et de patients atteints de CF est appropriée pour modéliser l'infection par Mtb et Mabs et l'efficacité du traitement.

Nous montrons dans des AOs sains que Mtb et Mabs résident principalement en tant que bactéries extracellulaires et infectent les cellules épithéliales avec une efficacité relativement faible. Alors que le microenvironnement de l'AO est capable de contrôler, mais pas d'éliminer Mtb, Mabs prospère. Nous démontrons que les AOs répondent à l'infection en modulant l'expression des cytokines, des peptides antimicrobiens, des mucines et des gènes antioxydants.

Nos résultats indiquent que les organoïdes dérivés de patients atteints de CF ont un épithélium plus épais, accumulent du mucus et subissent un stress oxydatif, une peroxydation lipidique accrue et une mort cellulaire, caractéristiques clés de la CF. Les morphotypes rugueux (R) et lisses (S) de Mabs se répliquent plus efficacement dans les organoïdes de patients atteints de CF par rapport aux organoïdes sains, tandis que les Mabs S forment des biofilms, les Mabs R forment des cordons et affichent une virulence plus élevée, ce qui valide davantage la pertinence des organoïdes de CF comme modèle pour l'étude de la pathogenèse de Mabs. Enfin, nous prouvons que Mabs profite du microenvironnement oxydatif des voies respiratoires des patients atteints de CF pour se développer, et que l'activation

pharmacologique des voies antioxydantes permet de mieux contrôler la croissance bactérienne.

En conclusion, nous avons établi que les AO constituent un système *in vitro* humain approprié pour déchiffrer les événements précoces de l'infection par les mycobactéries et les mécanismes de l'infection respiratoire aggravés par la CF, offrant ainsi de nouvelles voies pour la recherche fondamentale et thérapeutique.

Table of content

ABSTRACT	1
RÉSUMÉ	3
TABLE OF CONTENT	6
ABBREVIATIONS.....	10
TABLES AND FIGURES INDEX	12
CHAPTER I: INTRODUCTION	14
1.1 The respiratory tract	15
1.1.1 Airway epithelial mechanisms in host defense against infection.....	17
1.1.1.1 Mucus	17
1.1.1.2 Mucociliary clearance.....	18
1.1.1.3 Antimicrobial peptides	19
1.1.1.4 Reactive oxygen and nitrogen species.....	20
1.2 Respiratory infections	21
1.3 <i>Mycobacterium</i>, a genus in constant evolution	22
1.4 <i>Mycobacterium tuberculosis</i>	24
1.4.1 Overview	24
1.4.2 Epidemiology and transmission	25
1.4.3 Pathogenesis	27

1.4.3.1 Role of the airway epithelial cells during Mtb infection.....	27
1.4.3.1.1 Sensing of Mtb by Airway epithelial cells: an early warning system for the immune cells .	28
1.4.3.1.2 Airway epithelial cells infection by Mtb.....	29
1.4.3.1.3 Airway epithelial cells crosstalk with immune cells during Mtb infection.....	30
1.4.3.2 Interaction of Mtb at the alveoli	30
1.4.3.3 Primary infection	31
1.4.3.4 Latent infection: Granuloma	32
1.4.3.5 Progression to active infection.....	34
1.4.4 Treatment	35
1.5 <i>Mycobacterium abscessus</i>.....	37
1.5.1 Overview	37
1.5.2 Epidemiology and transmission	38
1.5.3 Pathogenesis	40
1.5.3.1 Colonization of airways by Mabs.....	43
1.5.3.1.1 Cystic fibrosis as a risk factor for Mabs infection	43
1.5.3.1.2 Mabs interaction with airway epithelial cells	46
1.5.3.2 Crosstalk between the host innate immune system and Mabs	48
1.5.3.3 Granuloma.....	48
1.5.4 Treatment	50
1.5.5 Models used to study Mabs infection	53
1.5.5.1 Cellular models.....	54
1.5.5.2 Non-mammalian models	55
1.5.5.3 Mammalian models.....	56
1.6 The organoid revolution.....	58
1.6.1 Overview	58
1.6.2 Classification of organoids	60

1.6.2.1 Organoids Derived from Pluripotent Stem Cells.....	61
1.6.2.2 Organoids Derived from Adult Stem Cells	62
1.6.3 Human lung organoids	63
1.6.3.1 Types of human lung organoids	64
1.6.3.1.1 Proximal lung organoids	65
1.6.3.1.2 Intermediate lung organoids	67
1.6.3.1.3 Distal lung organoids	68
1.6.3.1.4 Other lung organoid models.....	70
1.6.4 Disease modelling in human organoids	71
1.6.4.1 Cystic fibrosis.....	71
1.6.4.2 Infectious diseases.....	73
 CHAPTER II: OBJECTIVES.....	 76
 CHAPTER III: RESULTS	 77
 3.1 Mycobacteria-host interactions in human bronchiolar airway organoids	 77
3.1.1 Paper summary	77
3.1.2 Article	79
 3.2 Human bronchial organoids unveil druggable pathways against <i>Mycobacterium abscessus</i> infection in cystic fibrosis	 92
3.2.1 Paper summary	92
3.2.2 Article	94
 CHAPTER IV: DISCUSSION AND PERSPECTIVES	 143
 REFERENCES.....	 154

ANNEXES	181
I. Antiviral and anti-inflammatory activities of Fluoxetine in a SARS-CoV-2 infection mouse model.....	182
II. Efficacy and Mode of Action of a Direct Inhibitor of <i>Mycobacterium abscessus</i> InhA.....	212
III. Human NLRP1 is a sensor of pathogenic coronavirus 3CL proteases in lung epithelial cells.....	239
IV. Nigraline as dual inhibitor of necroptosis and ferroptosis regulated cell death	278
V. Host phospholipid peroxidation fuels ExoU-dependent cell necrosis and supports <i>Pseudomonas</i> <i>aeruginosa</i> -driven pathology	289
VI. A Pulmonary <i>Lactobacillus murinus</i> Strain Induces Th17 and ROR γ t + Regulatory T Cells and Reduces Lung Inflammation in Tuberculosis	322

Abbreviations

2D	Two-dimensional	ECM	Extracellular matrix
3D	Three-dimensional	EGF	Epidermal growth factor
aa	Arachidonic acid	ENaC	Epithelial sodium channel
AEC	Alveolar epithelial cells	ESCs	Embryonic stem cells
AEC1	Type 1 alveolar cells	ESX-4	Type VII secretion system
AEC2	Type 2 alveolar cells	ETZ	Electron transparent zone
ALF	Alveolar lining fluid	FGF	Fibroblast growth factor
ALI	Air-liquid interface	GDND	Glycosyl-diacylated-nondecyl-diols
AM	Alveolar macrophages	GPLs	Glycopeptidolipids
AMPs	Antimicrobial peptides	H-AO	Healthy airway organoid
AO	Airway organoid	HBHA	Heparin-binding haemagglutinin
ASCs	Adult stem cells	HGF	Hepatocyte growth factor
ASL	Airway surface liquid	HNE	Human nasal epithelial organoids
BCG	Bacillus Calmette–Guérin	IGF	Insulin-like growth factor
BMP	Bone morphogenetic protein	IMC	Inner cell mass
CF	Cystic fibrosis	iPSC	Induced pluripotent stem cells
CF-AO	CF airway organoid	LAM	Lipoarabinomannan
CFTR	CF transmembrane conductance regulator	LM	Lipomannan
COPD	Chronic obstructive pulmonary disease	Lrp	Leucine-responsive regulatory protein
DC	Dendritic cells	LTBI	Latent tuberculosis infection
DM	Type 2 diabetes mellitus	Mabs	<i>Mycobacterium abscessus</i>
DS-TB	Drug-susceptible Tuberculosis	MAC	<i>Mycobacterium avium</i> complex
EBs	Embryoid bodies	ManLAM	Mannose-capped lipoarabinomannan
EC	Epithelial cells	MDR-TB	Multidrug-resistant tuberculosis

MHC-II	Class II major histocompatibility complex molecules	S	Mabs smooth
Mtb	<i>Mycobacterium tuberculosis</i>	SARS-CoV-2	Severe acute respiratory syndrome coronavirus 2
NETs	Neutrophil extracellular traps	SGM	Slowly growing mycobacteria
NHBE	Normal human bronchial epithelial	TB	Tuberculosis
NOD	Nucleotide-binding oligomerization domain	TDM	Trehalose dimycolate
NOS	Nitric oxide synthases	TDR-TB	Totally drug resistant tuberculosis
NTM	Non-tuberculous mycobacteria	TGF	Transforming growth factor
NTM-PD	Non-tuberculous mycobacterial pulmonary diseases	Th	Lymphocytes T helper
PAMP	Pathogen-associated molecular patterns	TLR	Toll-like receptor
PCL	Periciliary liquid layer	TMM	Trehalose monomycolate
PDX	Patient-derived xenografts	TPP	Trehalose polyphosphate
PEC	Primary epithelial cells	VEGF	Vascular endothelial growth factor
PIM	Phosphatidyl inositol mannosides	WHO	World Health Organization
PL	Phospholipid	XDR-TB	Extensively drug resistant tuberculosis
PRR	Pattern recognition receptor		
PSCs	Pluripotent stem cells		
R	Mabs rough		
RGM	Rapidly growing mycobacteria		
RNS	Reactive nitrogen species		
ROCK	RHO-associated protein kinase		
ROS	Reactive oxygen species		
RTI	Respiratory tract infections		

Tables and figures index

FIGURE 1. ORGANIZATION AND CELLULAR COMPOSITION OF HUMAN AIRWAYS.	16
FIGURE 2. BACTERIA CAUSING LOW RESPIRATORY TRACT INFECTIONS.....	21
FIGURE 3. CLASSIFICATION OF MYCOBACTERIA AFFECTING HUMANS.	22
FIGURE 4. TOP CAUSES OF DEATH WORLDWIDE IN 2019.....	25
FIGURE 5. MTB LATENT INFECTION.	33
FIGURE 6. MTB ACTIVE INFECTION.	34
FIGURE 7. DRUG RESISTANCE MECHANISMS IN MTB.....	36
FIGURE 8. FACTORS PREDISPOSING TO NTM DISEASE.....	39
FIGURE 9. MABS CELL ENVELOPE.....	41
FIGURE 10. MABS INFECTION CYCLE.....	42
FIGURE 11. CLASSES OF CFTR MUTATIONS.....	45
FIGURE 12. PHAGOCYTOSIS AND PROCESSING OF MABS BY MACROPHAGES.	50
FIGURE 13. RESISTANCE MECHANISMS EXHIBITED BY MABS.....	51
FIGURE 14. RECOMMENDED APPROACH TO TREATMENT OF MABS.	52
TABLE 1. NON-MAMMALIAN MODELS USED TO STUDY MABS INFECTION.....	55
TABLE 2. SOME MOUSE MODELS TO STUDY MABS INFECTION.....	57
FIGURE 15. BIOLOGICAL MODEL SYSTEMS.	58
FIGURE 16. COMPARISON OF ORGANOID WITH OTHER MODEL SYSTEMS.	60
FIGURE 17. ESTABLISHMENT OF PSCS-DERIVED ORGANOID.	62
FIGURE 18. ESTABLISHMENT OF ASCS-DERIVED ORGANOID.	63
FIGURE 19. TYPES OF LUNG ORGANOID.	65
FIGURE 20. HUMAN TRACHEOSPHERE COMPOSITION.....	66
FIGURE 21. AIRWAY ORGANOID COMPOSITION.....	68
FIGURE 22. ALVEOLAR ORGANOID COMPOSITION.....	69

TABLE 3. SUMMARY OF THE KEY FINDINGS OF THE MOLECULAR BASIS OF INFECTIOUS DISEASE USING THE ORGANOID MODEL.....	74
FIGURE 23. ASC-DERIVED ALVEOLAR ORGANOID INFECTED WITH GFP-EXPRESSING MABS S.	148
FIGURE 24. CF-AOS SENSITIVITY TO FERROPTOSIS.	152

Chapter I: Introduction

Respiratory infections including tuberculosis (TB) and non-tuberculous mycobacterial pulmonary diseases (NTM-PD) are a major global health concern. Chronic respiratory infections due to mycobacteria are causing high rates of morbidity and mortality worldwide (3). According to the World Health Organization (WHO) Global Tuberculosis Report 2021, in 2020, *Mycobacterium tuberculosis* (Mtb) affected 10 million people globally with an estimated 1.5 million deaths (4). This is the first yearly increase in TB deaths since 2005. It was primarily caused by delays in the supply of and access to crucial tuberculosis testing and treatment services during the COVID-19 pandemic, overturning years of progress made by the WHO end-TB plan. On the other hand, non-tuberculous mycobacteria (NTM) infections incidence and prevalence are increasing owing to a growing population of immunocompromised and vulnerable individuals, however, the true global burden of pulmonary and extrapulmonary disease is unknown (5, 6). Incidence rates of NTM-PD in Europe range from 0.2 to 2.9/100,000 persons. The diagnosis and treatment of mycobacterial infections, so far until today are challenging and complex, frequently requiring long-duration treatments with antibiotics, which lead in the most the cases to poor patient outcomes (7). Therefore, the following introduction will aim to describe the epidemiology, pathogenesis, and treatment of Mtb and NTM, as well as the description of the organoid model as a new tool, to better understand the host-pathogen interaction in the airways and identify new therapeutic targets.

1.1 The respiratory tract

The respiratory tract is an incredibly complicated system composed of semi-rigid conducting airway tubes that branch from the trachea, fork at the bronchi, and taper at the bronchioles, leading to alveoli where breathing gases are exchanged (8).

The respiratory tract has evolved along the proximal-distal axis in a zoned manner, where a unique and diverse cellular composition characterizes each region (9). In a reductionist way, the normal human tracheal and bronchial epithelium is a pseudostratified epithelium predominantly comprised of basal, ciliated, goblet and serous cells. More distally, the intrapulmonary bronchiolar area is a more simplified columnar epithelium, mainly composed of ciliated cells, secretory club cells, and relatively few basal cells and goblet cells. The conducting airways of the human lung finish in a transitional zone of respiratory epithelium, referred to as the respiratory bronchiole. Respiratory bronchioles are principally composed of the club and ciliated cells (Figure 1) (10). Each one of the cells of the conducting airways play a functionally distinct role. The basal cells are considered the stem cells of the respiratory epithelium, so they play an essential role in its regeneration. The club cells secrete the surfactant liquid, which has immunomodulatory functions. Goblet cells generate mucus where pollutants and pathogens are trapped, while the ciliated cells are responsible for removing them through mucociliary clearance (11).

The conducting airways lead to an alveolar region, which is covered by alveolar type 1 (AEC1) and type 2 epithelial cells (AEC2) (also known as alveolar epithelial cells (AEC) or pneumocytes) (Figure 1). AEC1 cells are flattened and squamous. These

cells are responsible for the gas exchange in the lung and are associated with the endothelial capillary plexus to form the thin gas-diffusible interface. AEC2 are cuboidal and prevent the collapse of the alveolus during respiration by generating surfactant liquid and help preserve the integrity of the tissue after any damage because they are considered progenitors of the AEC1 (12).

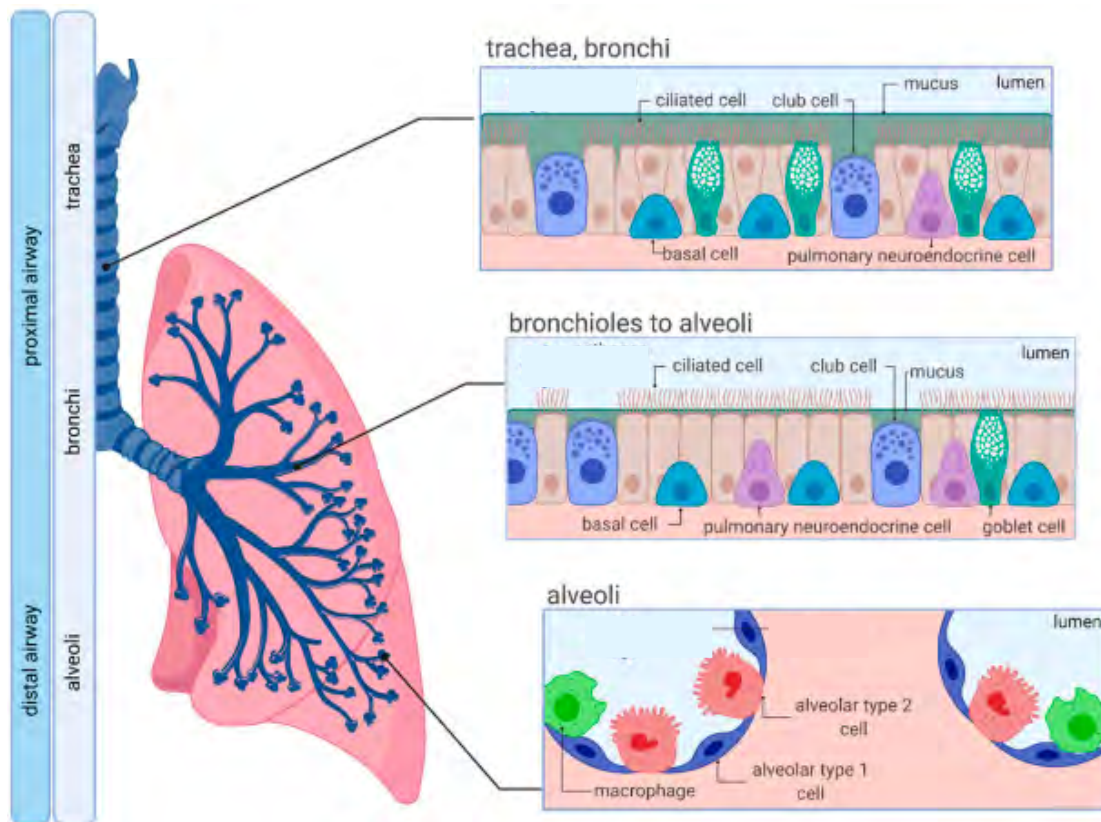


Figure 1. Organization and cellular composition of human airways (adapted from (13)).

Apart from participating in gas exchange, the cells that form the respiratory tract also play an essential role as the first line of defense against pathogens and pollutants we breathe (14).

1.1.1 Airway epithelial mechanisms in host defense against infection

Among the principal defense mechanisms of the airway epithelium against pathogens are the barrier function, the mucus, the mucociliary clearance, and the activation of cell autonomous immune functions which include the production of antimicrobial peptides (AMPs) and proteins, reactive nitrogen and oxygen species (RNS and ROS, respectively), and a variety of growth factors, cytokines, and chemokines. These together result in an increased leukocyte recruitment and communication with mesenchymal cells (including lymphatics, endothelial cells, smooth muscle cells, myofibroblasts, cartilage-forming cells, mesothelial cells, and mesenchymal stem cells) in the airway wall, allowing the airway epithelium to contribute directly to the host defense and lung repair (15–17).

1.1.1.1 Mucus

The mucus is an extracellular gel composed of water, mucins, and associated molecules. It is considered as a key component for mucociliary clearance. Among the principal cells responsible for generating mucins are goblet, club, serous and glandular mucous cells (15). Mucins are large glycoproteins that carry multiple O-glycans clustered in central domains of tandem repeats rich in serine and threonine (18). Several factors can trigger mucin gene expression, including inflammatory

cytokines and inhaled toxins or microorganisms. Following their production, they are stored in condensed granules until a stimuli such as calcium, ATP or other mechanisms activate their release (15). The secreted airway mucins (MUC5B, MUC5AC and MUC2) form a mucous gel that disrupts bacterial aggregation, binds microbial pathogens, and prevents them from adhering to cell surfaces, enhancing their clearance (19).

1.1.1.2 Mucociliary clearance

Mucociliary clearance is a complex process that takes place in the airway surface liquid (ASL), formed by the periciliary liquid layer (PCL) (media for ciliary beating), cilia, and mucus. After being trapped in the ASL mucus, which prevents them from reaching the distal part of the respiratory tract, contaminants and pathogens are removed thanks to the coordinated regulation of ciliary movement. ASL is also composed of many antimicrobial proteins (e.g., defensin, cathelicidin, lactoferrin, lysozyme), which help limit bacterial proliferation and orchestrate mucociliary clearance in the absence of an exacerbated inflammatory response. (10, 20, 21).

In some pathological context, the incapacity to clear certain pathogens and their inflammatory mediators can lead to tissue inflammation, infection, and even destruction. In CF, the dysfunction of cystic fibrosis transmembrane conductance regulator (CFTR) reduces ASL pH, impairs liquid secretion, and causes that strands of mucus remain attached to submucosal gland ducts, impeding proper mucociliary transport and thus, making impossible a proper host defense program (15).

1.1.1.3 Antimicrobial peptides

Antimicrobial peptides are a class of small peptides (~10–50 amino acids) that constitute a crucial part of the innate immune system of complex organisms. AMPs present extensive inhibitory effects against microorganisms like bacteria, fungi, parasites and viruses (22). Airway epithelial cells (EC) produce antimicrobial peptides including members of the β -defensin and cathelicidin families, as well as lactoferrin and lysozyme; each one of them mediates pathogen killing through different mechanisms (11).

Defensins are a family of small (2–5 kDa) cationic host defense peptides. Their structure is composed by a β -sheet core with three conserved intramolecular disulfide bonds to stabilize the peptide structure (23). Human β -defensin 1, 2, 3 and 4 are mainly expressed in EC, synthesized as precursors and secreted after cleavage. However, while human β -defensin-1 is constitutively secreted, the other defensins seem to be inducible. They are produced in response to proinflammatory cytokines or Toll-like receptors (TLRs) and nuclear factor- κ B pathways (15). Defensins can efficiently eliminate bacteria via membrane depolarization and premature activation of cell wall lytic enzymes (11). Besides their well-known antimicrobial function, it has been shown that β -defensins are able to activate dendritic cells and chemoattract immune cells (15).

Another important AMP generated by ECs is cathelicidins. These are stored as preformed granules and are characterized by showing two hydrophobic α -helix domains. Upon stimulation of the ECs, the preformed granules are cleaved at their

N-terminal domain resulting in the active form of the peptide known as LL-37. So far, LL-37 cathelicidin has been reported to be the only cathelicidin generated and secreted by human lung epithelial cells (24). The antimicrobial effects of LL-37 depend on their capacity to generate pores in the cell wall of the mycobacteria and their role in attracting monocytes, neutrophils, and CD4⁺ T cells and activating mast cells (11, 25, 26).

The AMPs lysozyme and lactoferrin participate in maintaining lung homeostasis by controlling infections by gram-positive and gram-negative bacteria, respectively, through the degradation of their membranes. In addition, because lactoferrin is an iron chelator, it creates a hostile environment for bacterial growth (11).

1.1.1.4 Reactive oxygen and nitrogen species

Reactive oxygen species are well-known signaling molecules. Moreover, in the last years more evidence acknowledge their function as direct antimicrobial effectors through at least 2 mechanisms: disruption of lipid peroxidation at microbial membranes and DNA damage (27). Both mechanisms depend on ROS production by ECs through NADPH oxidases such as DUOX 1 and DUOX2 (15). This ROS contributes directly to bacterial control in ASL and serves as a precursor for the generation of antimicrobial molecules such as hypothiocyanite (28). EC produce RNS in addition to ROS by the activity of nitric oxide synthases (NOS) enzymes. The resulting nitric oxide has a range of functions in immunological regulation and host defense against infection. The NOS-1 and NOS-2 enzymes, produce nitric oxide in the lung epithelium (29, 30).

1.2 Respiratory infections

Respiratory tract infections (RTI) are a prominent cause of morbidity and mortality in children and adults worldwide, accounting for roughly 3 to 5 million deaths each year, with a considerable impact on public health, society, and economy. The RTIs include viral, bacterial or fungi infections in both, the upper respiratory tract (rhinitis, sinusitis, pharyngitis, or tracheitis) and/or lower respiratory tract (mainly bronchitis and pneumonia) (31). The microbes causing low respiratory tract infections, such as tuberculosis, cystic fibrosis-related infections, and pneumonia/bronchitis-related infections, reside deep inside the respiratory tract, embedded in a combination of thick mucus and biofilm. In consequence, their treatment is one of the most difficult healthcare challenges (Figure 2) (32).

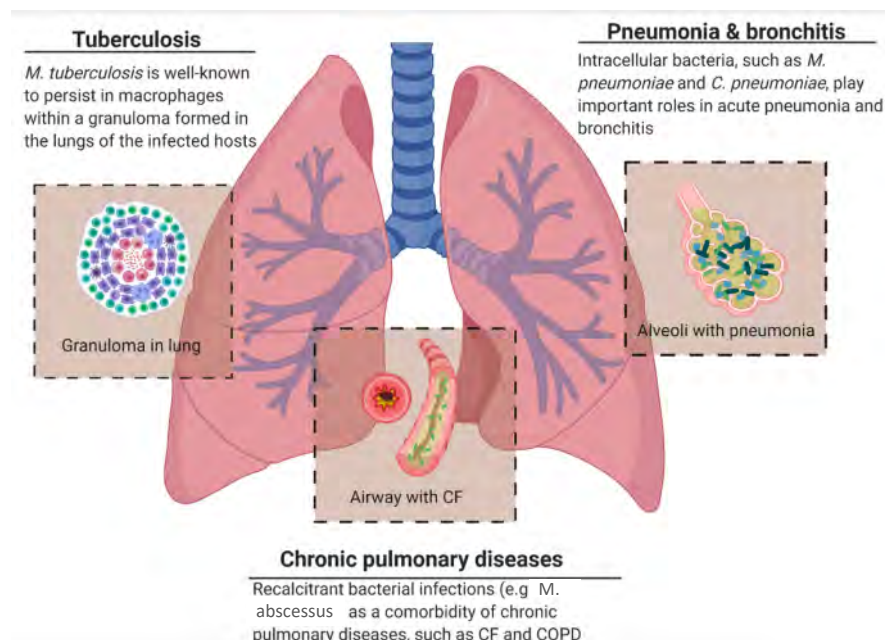


Figure 2. Bacteria causing low respiratory tract infections (adapted from (32)).

1.3 *Mycobacterium*, a genus in constant evolution

In 1986, Lehmann and Neumann classified Mycobacteria inside of the genus *Mycobacterium*, which belongs to the family of *Mycobacteriaceae*, in the order *Actinomycetales*. This order includes diverse microorganisms, but mycobacteria and allied taxa are easily distinguished on the basis of the ability to synthesize mycolic acids (33).

Mycobacteria are non-motile acid-fast bacilli with a high GC content (57-73%) and complex long chain mycolic acids (60-90 carbons); they can be straight or slightly curved and range from aerobic to microaerophilic (34). Due to this extreme diversity, in 1959, Ernest Runyon classified mycobacteria affecting humans into two extensive categories: tuberculosis-causing mycobacteria and non-tuberculous mycobacteria. Mycobacteria can be further classified according to their growth rate in slowly growing mycobacteria (SGM) and rapidly growing mycobacteria (RGM) (Figure 3). This phenotype is defined on the basis of growth (from a diluted inoculum) occurring either before or after 7 days (34).

Non-tuberculous mycobacteria		
Rapidly growing mycobacteria	Slowly growing mycobacteria	
<i>M. chelonae-abscessus</i> complex • <i>M. abscessus</i> subsp. <i>abscessus</i> • <i>M. abscessus</i> subsp. <i>bolletii</i> • <i>M. abscessus</i> subsp. <i>massiliense</i> • <i>M. chelonae</i> <i>M. fortuitum</i>	<i>M. marinum</i> <i>M. ulcerans</i>	<i>M. tuberculosis</i> complex <i>M. leprae</i>
<i>M. smegmatis</i> <i>M. vaccae</i>	<i>M. avium</i> complex • <i>M. avium</i> • <i>M. intracellulare</i> • <i>M. chimaera</i> <i>M. haemophilum</i> <i>M. xenopi</i> <i>M. kansasii</i> <i>M. simiae</i>	
	<i>M. terrae</i> complex <i>M. goodii</i>	

 True pathogens
 Opportunistic pathogens
 Saprophytes*

Figure 3. Classification of mycobacteria affecting humans (from (35)).

Currently, the genus contains over 190 named species, including strict pathogens such as *Mtb* and *Mycobacterium leprae*, as well as NTM, many of which are major opportunistic pathogens such as *Mycobacterium abscessus* (Mabs) and *Mycobacterium avium* (36). Among the NTM species identified to date, 95% are environmental bacteria, the majority of them being saprophytes or non-pathogenic to humans and animals, contrastingly, strict pathogenic mycobacteria have no environmental reservoir and are spread exclusively from host-to-host (35).

Although *Mtb* and *Mycobacterium leprae* are the most notable mycobacterial human pathogens, *Mycobacterium bovis* and *Mycobacterium avium* are, as well, responsible of severe diseases in humans and a broad range of other animal species, including cattle, sheep, goats, deer, possums, badgers, elephants, dogs, cats, birds, amphibians, and fish. Moreover, species such as *M. bovis* represent serious zoonotic pathogens and have become important agents at the interface of humans, domestic livestock, and wildlife (37).

Over the years, the taxonomic classification has been reinforced by molecular techniques such as 16S sequencing and phylogenomic analyses (36). Because of this, the diagnosis of mycobacterial infection has improved in recent years, helping to progress in their detection and identification. However, more research is still needed it.

1.4 *Mycobacterium tuberculosis*

1.4.1 Overview

Mycobacterium tuberculosis complex was described as the causative agent of tuberculosis by Robert Koch in 1882. This disease was described as an airborne infectious disease (38). Mtb has evolved to become the perfect example of an obligate pathogen adapted to humans (39).

Although Mtb is primarily a pulmonary pathogen, it can cause disease throughout the body. Clinically, infections in patients are classified as latent tuberculosis infection (LTBI), an asymptomatic and non-transmissible state where granulomas are generated to isolate the bacteria; or active tuberculosis lung disease, a contagious state where patients exhibit symptoms like cough, fever, night sweats, and weight loss (40). About a quarter of the world's population is infected with Mtb in its latent form, and are usually adults who develops the active disease, presenting higher incidence men than women (41).

The standard treatment for TB usually requires a prolonged course of multiple antimicrobials. The Bacillus Calmette–Guérin (BCG) vaccine is used worldwide to prevent life-threatening TB in infants and young children, unfortunately, it has been incapable to controlling the global TB epidemic (42). Consequently, TB continues to be one of the top causes of death worldwide. Until the COVID-19 pandemic, TB was the leading cause of death from a single infectious agent, ranking above HIV/AIDS (Figure 4) (41).

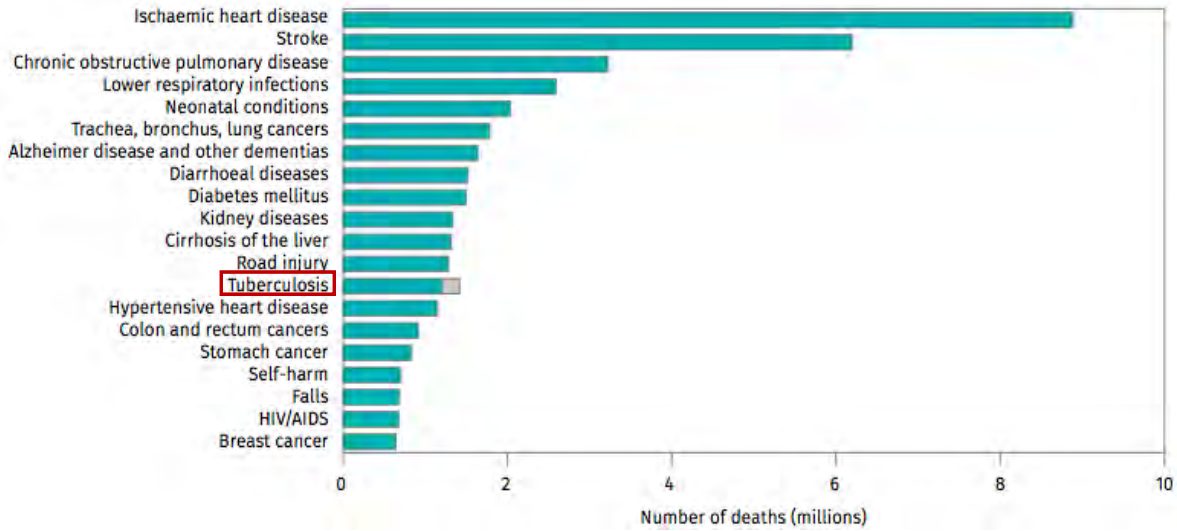


Figure 4. Top causes of death worldwide in 2019 (adapted from (41)).

1.4.2 Epidemiology and transmission

The WHO estimates that in 2020, 10 million people fell ill with TB worldwide (5.6 million men, 3.3 million women and 1.1 million children), of whom 1.5 million died. TB is heterogeneously distributed in all countries and age groups, nevertheless, two-thirds of the total burden are comprised in just eight countries: India, China, Indonesia, the Philippines, Pakistan, Nigeria, Bangladesh and South Africa, in order of prevalence (41, 43).

Although TB is curable and preventable, many new cases of TB are attributable to five risk factors: undernutrition, HIV infection, alcohol use disorders, smoking (especially among men) and diabetes (41). A co-infection between TB and HIV is the major known risk factor, registering 214 000 deaths among TB/HIV-positive people in 2020 (41, 44). The risk of developing TB is 26 times higher in people with HIV infection, compared to the non-HIV population. This increased risk is due to the

weakening of the immune system by HIV infection. The risk of developing TB is about 7% to 10% each year among HIV-positive individuals (3). Other important risk factor for TB is type 2 diabetes mellitus (DM). DM patients triple the risk of developing active TB, have a faster disease progression following Mtb infection, and they respond poorly to treatment (45, 46). Therefore, addressing these social and behavioral determinants could help improve current TB control.

The transmission of Mtb occurs person-to-person almost exclusively by aerosolized particles. People with active pulmonary or laryngeal TB generate droplet nuclei (dried mucous droplets) that contain few viable Mtb through coughing, singing, shouting, sneezing, or any other forceful expiratory maneuver that shears respiratory secretions from the airways, with coughing being the most efficient at generating infectious aerosols (47). The size of infectious droplets from Mtb infected patients ranges from 0.65 (small) to >7.0 μm (medium–large). While small Mtb aerosol particles remain in air for 2–40 hours and are expected to transit past the nasopharyngeal or tracheobronchial region to be deposited in the distal airways, larger particles can be trapped in the upper airway, being less effective in transmission and generally falling to the ground by gravity (48, 49). Mtb transmission occurs more efficiently indoors where dilution is limited and occupants are concentrated. All indoor environments are potential sites of transmission, most importantly, homes and congregate settings such as hospitals, clinics, refugee camps, factories, homeless shelters, prisons, and many more, including most modes of transportation (50). Once Mtb is transmitted, 5-15% of people will develop the

active TB disease within months or few years, nevertheless the rest of the individuals could develop the active disease throughout their lifetime (42).

1.4.3 Pathogenesis

After being inhaled and throughout the infection process, Mtb encounters different pulmonary microenvironments in the host. These environments can be extracellular (at the beginning of the infection, after escaping from immune cells, or in the cavities after reactivation) or intracellular (after being phagocytosed by alveolar macrophages (AM) in the primary infection or the granulomas in the latency state) (51).

1.4.3.1 Role of the airway epithelial cells during Mtb infection

Our understanding of early events during Mtb infection in humans is currently very limited (42). Recent findings suggest that the AM are the main target of Mtb infection, however, the airway epithelium, which is the first protective barrier in defense against respiratory/mucosal pathogens, can be infected too (49, 52).

The airway epithelium is pseudostratified and mostly consists of multiciliated cells, goblet cells and club cells, interspersed with neuroendocrine cells and basal cells (11). EC are one of the host cells that encounter Mtb in the respiratory tract and play an important role in its sensing, since they will further interact with innate and adaptive immune cells to contribute to the immune response against the bacteria (53).

1.4.3.1.1 Sensing of Mtb by Airway epithelial cells: an early warning system for the immune cells

The pattern recognition receptors (PRRs) (including membrane-bound TLRs, C-type lectins, cytosolic nucleotide-binding oligomerization domain (NOD)-like receptors and nucleic acid sensors) are expressed by airway epithelial cells to recognize microorganisms (53). EC recognition of Mtb by TLR2, TLR4, TLR9, NOD2, and Dectin-1 activates diverse signaling pathways triggering the production of cytokines (e.g., TNF- α , IFN- γ , GM-CSF, IL-6, IL-10) and chemokines (e.g., IL-8, IP-10, IL-27, MCP-1) (54–56). The early release of these immune mediators will initiate recruitment and activation of monocytes, lymphocytes, phagocytes, and polymorphonuclear leukocytes to the lung (57). For instance, stimulation of EC by *Mycobacterium bovis* BCG induced IL-8 and IL-6 secretion and neutrophil recruitment towards infected epithelia, which rises the presence of CD4⁺ T cell-associated type 1 helper (Th1) and Th17 cells to fight pulmonary TB (58). Interestingly, in primary EC (PEC), type-1 and type-2 cytokines have been demonstrated to control the expression of several TLRs (59). Additionally, in response to BCG infection, PEC cultures produced the anti-inflammatory cytokines IL-10 and IL-22 (53). Thus, EC may play a critical role in regulating the inflammatory/anti-inflammatory balance throughout mycobacterial infections.

In response to Mtb infection, EC were shown to produce AMPs such as β -defensin-2, cathelicidin LL-37, and hepcidin (57). Human β -defensin-2 and cathelicidin LL-37 control Mtb growth and have chemotactic activity. β -defensin-2 chemoattracts

memory lymphocytes and immature dendritic cells (DC), meanwhile LL-37 chemoattracts neutrophils (53, 60, 61). Hepcidin modulates the pool of extracellular iron, a crucial micronutrient for Mtb growth and survival (62–64). In consequence, being the airway epithelium the first site of exposure against Mtb, it has an essential role to initiate and guide the following immune response, having an active participation in disease progression and outcome (57).

1.4.3.1.2 Airway epithelial cells infection by Mtb

In addition to pathogen detection and defense barrier, EC can also be directly infected by mycobacteria, as have shown *in vitro* in bronchial, and airway epithelial cells (53, 65).

Airway epithelial cells are non-professional phagocytes and seemed relatively insensitive to infection with Mtb *in vitro* (52). Nevertheless, some mechanisms of mycobacterial uptake by EC have been described. For example, it is known that some epithelial transmembrane receptors such as integrins and Dectin-1 interact with Mtb cell surface effector molecules, including the adhesins malate synthase, ESAT-6, and heparin-binding haemagglutinin (HBHA), which favors its uptake (66, 67). Once inside the epithelial cells, Mtb is localized in non-acidify late endosomes, which in the most of the cases, allow the bacteria to thrive (68).

1.4.3.1.3 Airway epithelial cells crosstalk with immune cells during Mtb infection

On some occasions, the early response generated by the ECs that comprise the airways is not sufficient to eliminate the pathogens that invade it (53). In line with this, EC have developed a range of mechanisms that allow them to interact and respond to infected cells, as well as to alert other cells of the immune system after succumbing to infection. It was shown that PEC, after activation by Mtb-infected AM and monocytes, generate antimycobacterial peptides, defensins and S100-family members that were not induce during the direct infection of the PEC (52).

Importantly, it was shown *in vitro* that airway EC express the major histocompatibility complex class II (MHC-II) molecules and the co-stimulatory molecule CD86 on their surface (69). This MHC-II appears to be functional and can stimulate T cells (70).

1.4.3.2 Interaction of Mtb at the alveoli

Once Mtb leave behind the first mechanical defense barriers in nose, sinuses, tracheobronchial tree and bronchioles, the bacteria will ultimately reach the alveoli (49). The alveoli is a sac-like structure composed of a large thin layer of AEC1 responsible for gas exchange and cuboidal AEC2 responsible for the surfactant liquid production (53). Inside the alveolar space we can find AM, which are the dominant cell type that Mtb infects (42), meanwhile the interstitial space surrounding the alveoli contains macrophages, DC, neutrophils, and T cells, among other host cells (51). At this alveolar level, Mtb bacilli interact rapidly with host soluble innate

molecules present in the alveolar lining fluid (ALF), where surfactant proteins, the complement system and hydrolases can cleave and modify the Mtb cell envelope, reducing the amount of virulence factors, such as Mannose-capped lipoarabinomannan (ManLAM) and Trehalose dimycolate (TDM) (49). The changes generated by the ALF to the cell envelope of Mtb allow a better control of this by professional phagocytes increasing the fusion between the phagosome and the lysosome (71), by neutrophils increasing local oxidative response and the production of inflammatory cytokines (72) and by alveolar epithelial cells secreting cytokines, antimicrobial peptides, nitric oxide, and surfactant proteins into the ALF (73).

The outcome of these initial interactions at the alveoli will determine the Mtb clearance or the establishment of the primary or latent infection.

1.4.3.3 Primary infection

After Mtb's initial interaction with the AECs, AM proceed to the recognition of Pathogen-associated molecular patterns (PAMP) present in Mtb envelope, such as lipoproteins, glycolipoproteins, lipomannan and ManLAM (74). Mtb components are recognized through an array of PRRs, as TLRs, c-type lectin receptors and scavenger receptors, among others (75). Upon recognition of Mtb, the phagocytosis mechanism begins, which triggers a wide range of cellular processes, such as ROS production, secretion of inflammatory mediators, maturation of Mtb-containing phagosomes, antigen processing, and presentation, as well as cell death (autophagy and apoptosis). All these processes are essential to prevent and control Mtb infection (51, 76).

Nevertheless, Mtb has learned to circumvent host defenses prior or after being phagocytosed. For example, Mtb is able to produce cell envelope glycolipids that are antagonists of TLR2, thus preventing its phagocytosis (77, 78). Another example is the leucine-responsive regulatory protein (Lrp) of Mtb envelope, which shown to dampen TLR signaling by interfering with the assembly of the MyD88, thereby inhibiting proinflammatory cytokine production (79).

Once Mtb is internalized by macrophages, it activates mechanisms that ensure their survival, such as blocking phagolysosome formation or direct disruption of the phagosome by the ESX-1 secretion system. These mechanisms not only allow Mtb to escape but also promote the secretion of some bacterial components (mycobacterial DNA) into the cytoplasm of macrophages, which activates a type I IFN response and generates a more permissive environment for Mtb growth (42, 76).

At the end, the balance between macrophage capacity to control intracellular replication and Mtb ability to escape macrophage killing may dictate the outcome of the infection (51).

1.4.3.4 Latent infection: Granuloma

After infecting AM in the alveoli, the Mtb infection process continues to progress at the level of the interstitial space of the lungs. As the primary infection is established, both DC and infected macrophages migrate to lymph nodes, presenting Mtb

antigens to T cells for activation. This event allows the recruitment of more immune cells to the site of infection and favors granuloma formation (Figure 5) (42).

Granulomas are a structure formed by innate host immune cells (e.g., macrophages, neutrophils, DCs, multinucleated giant cells, epitheloid cells), surrounded by T and B lymphocytes (Figure 5) (49). Granulomas are involved in the control of the replication and dissemination of Mtb. Interestingly, the immune response in the granuloma is diverse, being pro-inflammatory at the center of this and anti-inflammatory at its periphery (80). It has been reported that the granuloma microenvironment (low in oxygen, pH, and nutrients) is highly adverse to the bacillus, which has been persistently found in this environment in a non-replicative and metabolically adapted state. At this stage, Mtb does not induce substantial tissue pathology, then the person has LTBI (51).

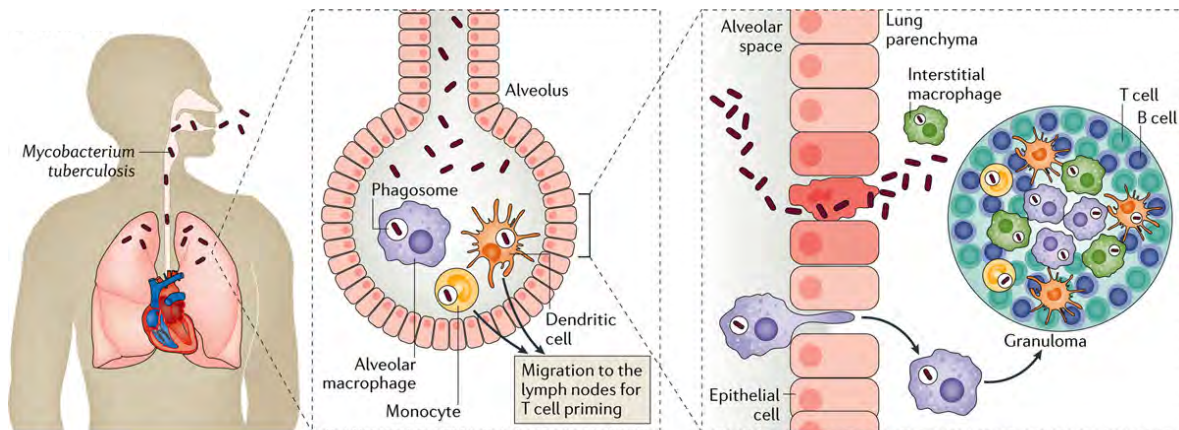


Figure 5. Mtb latent infection (adapted from (42)).

1.4.3.5 Progression to active infection

In the majority of people with LTBI, the presence of immune cell such as T cells, macrophages and DC is enough to maintain an asymptomatic infection for decades (42). However, sometimes when the host's immune system declines drastically due to factors such as TNF blockade treatments, malnutrition, HIV, DM, aging/immune-senescence, among others (81); granulomas grow in size and fail to contain Mtb. In this stage, the latent infection is reactivated (active TB disease), resulting in the generation of necrotic granulomas, extracellular growth of Mtb, destruction of lung tissue, and subsequent dissemination of Mtb (lung cavitation stage of TB) (Figure 6) (51). People in a severe state of cavitary pulmonary TB have so much bacteria in their respiratory tract that it is easily expelled in small droplets generated by coughing or sneezing, thus restarting the cycle of pathogen transmission (49).

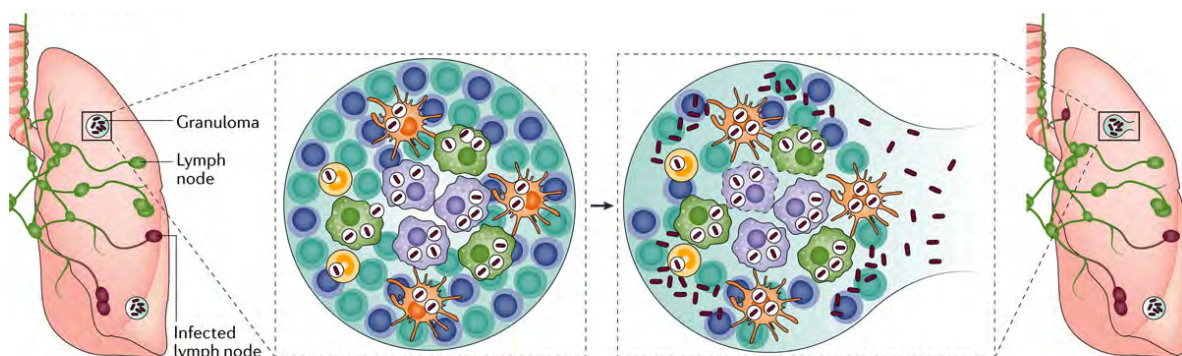


Figure 6. Mtb active infection (adapted from (42)).

1.4.4 Treatment

Since TB is a common malignancy worldwide, different strategies have been developed to cure it. Currently standardized treatments against drug-susceptible TB (DS-TB) patients require the 6-9 months regimen with a combination of four first-line anti-TB drugs (rifampicin, isoniazid, pyrazinamide, and ethambutol) (82). Successful treatment of DS-TB has been reported in 85% of patients (83), and usually less than 5% of patients face a relapse. Unfortunately, at the early 1990s, a multidrug-resistant tuberculosis (MDR-TB) that is not affected for both rifampicin and isoniazid, emerged (84). Actually, MDR-TB can be cured but its treatment is usually longer, for 18 months or more and consists of selected first-line drugs along with different combinations of second-line drugs (such as fluoroquinolone and an injectable aminoglycoside), which are more expensive and toxic. WHO has reported a global success rate of 55% for MDR-TB treatment (82). Therefore, even if some successful therapies are available, the use of inappropriate drugs and regimens allowed *Mtb* to gain resistance to the most important anti-TB drugs (85).

Since 2006, it has been recognized the presence of even more resistant strains of *Mtb* labelled as extensively drug resistant (XDR-TB) (86). Treatments against XDR-TB have just 39% of success, they are resistant to rifampicin and isoniazid, in combination with fluoroquinolone, and to at least one of the three injectable second-line drugs (amikacin, kanamycin, or capreomycin) (51). More strikingly, totally drug-resistant *Mtb* (TDR-TB) strains have been described recently, which, as its name

stands, is resistant to all available antibiotics (86). Infections with TDR Mtb strains are essentially incurable by the current anti-TB drugs (87).

Treatment of TB has been a therapeutic challenge because of not only the naturally/intrinsic high resistance level of Mtb to antibiotics but also the newly acquired mutations that confer further resistance (Figure 7). For example, the principal natural resistance mechanism against macrolides and hydrophilic antibiotics is the low cell wall permeability of Mtb. On the other hand, acquired antibiotic resistance may occur in bacteria through either mutations or horizontal gene transfer mediated by phages, plasmids, or transposon elements. In Mtb, horizontal transfer of drug resistance genes has not been reported; but resistance mostly arises from chromosomal mutations under the selective pressure of antibiotic use (e.g., alteration of drug target, efflux pumps overexpression, drug inactivation). Hence, the development of new anti-TB drugs is urgent (87, 88).

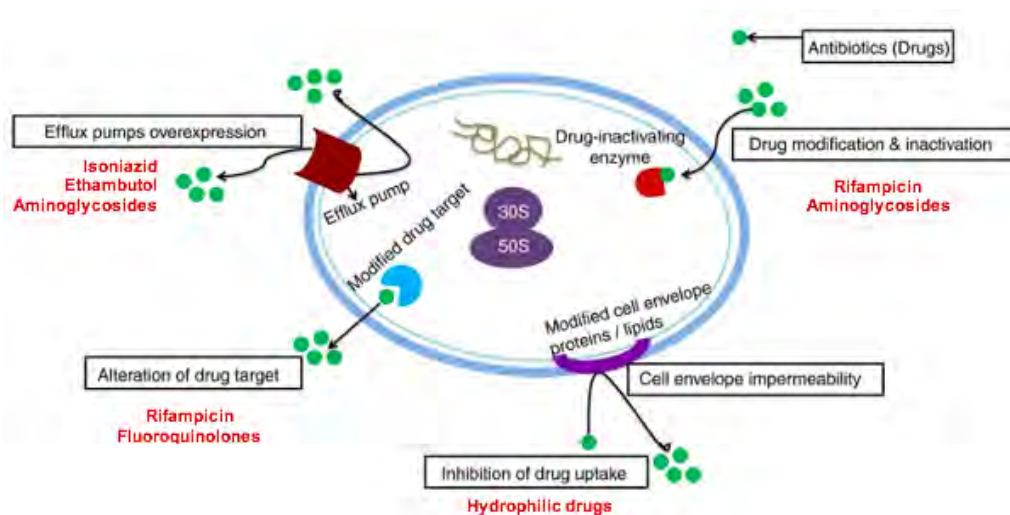


Figure 7. Drug resistance mechanisms in Mtb (adapted from (82)).

1.5 *Mycobacterium abscessus*

1.5.1 Overview

Pulmonary infections caused by NTM are also spread worldwide. Although over 170 different species of NTM have been described, pulmonary diseases in humans are mostly caused by species of *Mycobacterium avium* complex (MAC), *Mycobacterium kansasii*, and *Mycobacterium abscessus* complex (3). *Mycobacterium abscessus* complex comprises three distinct subspecies: *Mycobacterium abscessus* subspecies *abscessus* or *Mabs*, *Mycobacterium abscessus* subspecies *bolletii* or *Mycobacterium bolletii*, and *Mycobacterium abscessus* subspecies *massiliense* or *Mycobacterium massiliense* (89).

Mycobacterium abscessus is a rod-shaped acid-fast bacillus, and a facultative intracellular bacterium (90). This opportunistic mycobacterium was first isolated in 1953 by Moore and Frerichs from a 63-year-old woman's knee abscess (91). *Mabs* can cause a wide range of clinical diseases, including lung infections in people with chronic lung conditions such as cystic fibrosis, as well as skin and soft tissue infections, including infections in cartilage, tendons, and the fat and muscle layers beneath the skin (92).

Mycobacterium abscessus is a fast growth NTM and it is the third most common cause of lung disease (93), with an average treatment success rate of only 45.6%. *Mabs* is one of the most resistant microorganisms to chemotherapeutic therapy, and its main threat as a human pathogen is its high multidrug resistance. *Mabs* is also

associated with biofilm formation, resistance to germicides, high temperatures and acidic environments (94).

1.5.2 Epidemiology and transmission

Different to TB, it is difficult to calculate NTM-PD prevalence. because their diagnosis is criteria-based and the physicians are not obliged to notify infected patients (6). However, NTM-PD is increasing in North America, Europe and Asia (95, 96), having the highest prevalence in USA (23-37/100,000) and Japan (33-65/100,000) (6). In Europe, it is estimated that the annual prevalence rate of diagnosed NTM-PD cases is in the range of 3–6/100,000 (97). Importantly, in contrast to TB, pulmonary NTM infections are more prevalent in women (59%) and the elderly (median age 66) than younger men (98).

The NTM infections are acquired by complex interactions between the host, the pathogen, environmental determinants and risk factors. The main risk factors include genetic and acquired structural lung diseases such as CF, chronic obstructive pulmonary disease (COPD), non-CF bronchiectasis, alpha-1 antitrypsin deficiency, previous pulmonary tuberculosis, lung cancer and primary ciliary dyskinesia (99, 100). Between 6-13% of patients with CF present NTM-PD, particularly due to *Mabs* infection (ranging from 16% to 68%), which appears to be remarkably well adapted to the CF lung (101). There, *Mabs* is able to cause severe pulmonary infections, making this pathogen an important cause of morbidity and mortality in CF patients (102).

Another high-risk group for NTM disease are patients under immunosuppressant medications, including oral corticosteroids, biological therapy against TNF- α , and biological drugs blocking innate cytokines that promote Th17 differentiation (6, 103). Finally, the presence of IFN- γ autoantibodies in adults and low CD4⁺ T cell counts in patients with advanced HIV were strongly associated with disseminated Mabs infection (104, 105). However, NTM-PD also occurs in immunocompetent patients without underlying respiratory disorders (Figure 8) (7, 106).

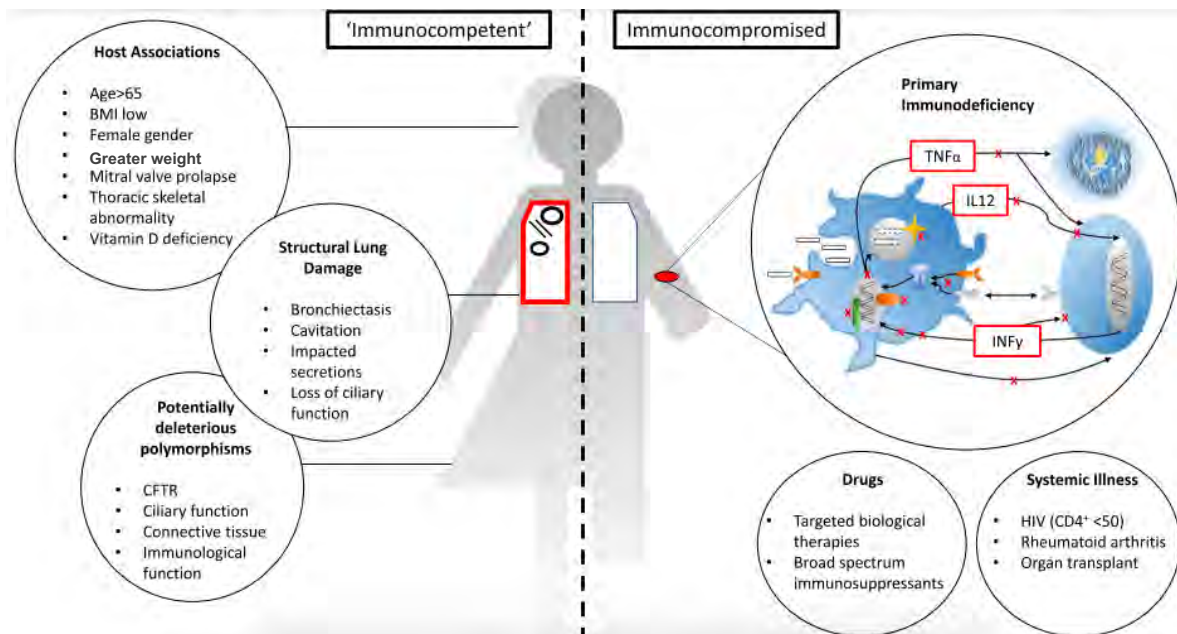


Figure 8. Factors predisposing to NTM disease (from (106)).

Non-tuberculous mycobacteria are widely distributed throughout the environment, which is believed to represent the reservoir of human infection (107). NTM is frequently acquired through inhalation (aerosol, showers) or inoculation (trauma, plastic surgery, acupuncture) (108), and it can be isolated from water (e.g. swimming

pool, showers, tap water) and soils (e.g. garden, mine, construction) (109). *Mabs* was originally thought to only be independently acquired from the environment, but cases of infection occurring at the same location suggest a common source (probably long-lived infectious aerosols or fomites) (110, 111). Whole genome sequencing of *Mabs* isolated in global CF centers has revealed the presence of dominant circulating clones with diverse geographical distribution (112). Recent hospital data have shown that transmission of macrolide-resistant strains of *Mabs* is possible among CF patients (110, 111, 113). Therefore, hospitals were advised to enhance infection control measures around CF patients. Interestingly, the *Mabs* dominant circulating clones can also infect non-CF individuals (114, 115).

1.5.3 Pathogenesis

The infection process of *Mabs* shares remarkable similarities with that of *Mtb* infection. However, *Mabs* show essential differences in the morphotypes of the colonies that generate on a solid medium compared to *Mtb*, which provides clear pathogenesis differences between the two infections (35).

Mycobacterium abscessus displays two distinct morphotypes: a smooth (S) variant, non-cording but motile and biofilm-forming, and a rough (R) variant, cording but non-motile and non or hyperaggregative/stiffer biofilm-forming. The major difference between these two variants resides in the decrease number of surface-associated glycopeptidolipids (GPLs) in the R form (116–118). GPLs are a family of glycolipids found in several pathogenic and nonpathogenic NTM species, their main function is to mask phosphatidyl inositol mannosides (PIM), lipoproteins and lipids at the

bacterial surface, therefore avoiding their recognition through TLR2 receptors located at the macrophages and ECs membranes (Figure 9) (119, 120). Importantly, Mabs colonization of lung begins with S strains, whilst the hypervirulent R variant appears to arise only during severe infections as observed in CF patients (112, 121). The Mabs S to R transition is caused by the modulation of the expression of a cluster of genes that control the biosynthesis (mps genes) or transport (mmpL4a or mmpL4b genes) of GPLs (Figure 9) (90, 120).

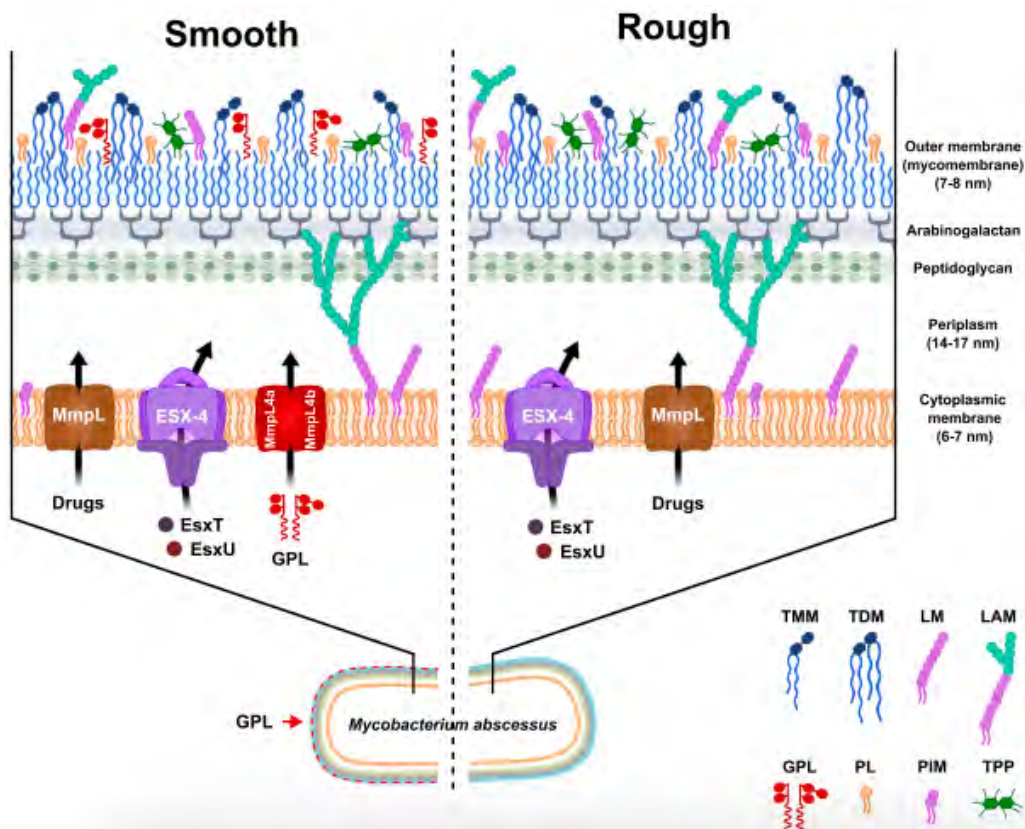


Figure 9. Mabs cell envelope (from (90)). Abbreviations: LAM, lipoarabinomannan; LM, lipomannan; PIM, phosphatidyl-inositol mannoside; PL, phospholipid; TDM, trehalose dimycolate; TPP, trehalose polyphleate; TMM, trehalose monomycolate; ESX-4, type VII secretion system.

The cycle of Mabs pulmonary infection comprises three steps. First, inhalation of bacteria into the airways, leading to its colonization (108). Second, recruitment of macrophages, neutrophils and DC to the site of infection and phagocytose of Mabs in an attempt to destroy the invading pathogen (35). Third, the infected macrophages and DC migrate to the lymph nodes to present the mycobacterial antigen to naive T cells, which activates the polarization of effector T cells and the production of T-cell-derived cytokines to the recruitment of adaptive immune cells and containment of the infection in a granuloma (35, 122). However, granuloma formation is not always sufficient to restrict Mabs infection. Under certain unknown conditions, Mabs S switch to R morphotype, which induces macrophage cell death and release of extracellular bacteria, which form large serpentine cords that avoid phagocytosis and resist immune defense (Figure 10) (123, 124).

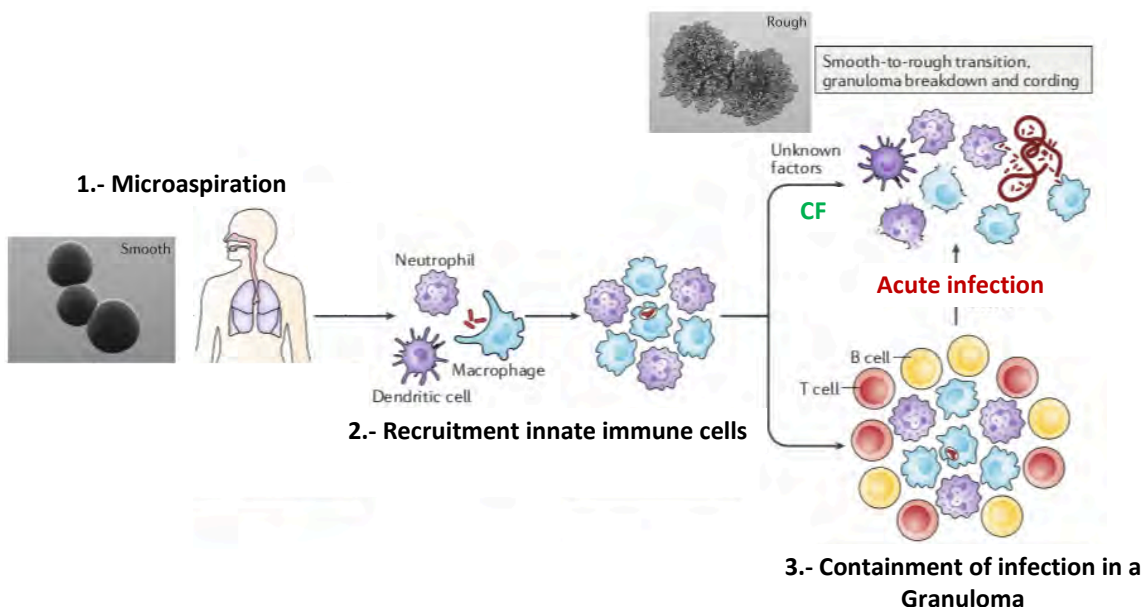


Figure 10. Mabs infection cycle (adapted from (35)).

1.5.3.1 Colonization of airways by Mabs

Water is the most significant environmental reservoir of mycobacteria that causes human disease. Humans are exposed to mycobacteria in water by drinking, swimming, and bathing. Furthermore, aerosol particles produced during these activities can be inhaled, potentially resulting in disease (125). Mabs pulmonary infection is uncommon in immunocompetent people with normal lung airways. On the other hand, individuals with abnormal lung airways, such as CF patients, develop a progressive, severe, intractable pulmonary infection (126, 127).

1.5.3.1.1 Cystic fibrosis as a risk factor for Mabs infection

Currently, cystic fibrosis is a disease affecting more than 90,000 people worldwide. France is one of the top 10 countries with the highest records of CF patients, showing in 2019 an estimated prevalence of 7-10 patients per 100,000 habitants (128). CF is a recessive autosomal disease caused by mutations in the cystic fibrosis transmembrane conductance regulator gene. Around 2,000 mutations in this gene have been described to date (129). The CFTR gene is located in the chromosome 7, spans 250 kb, and is composed of 27 exons. The gene is transcribed into a 6.5 kb messenger RNA that encodes a 1,480 amino acid protein (130). CFTR encodes an anion channel, activated by cAMP-dependent phosphorylation, whose primary function is the transport of chloride and bicarbonate. Furthermore, the CFTR controls water secretion and absorption through the apical plasma membrane of epithelial cells. CFTR can also regulates other ion channels activity, including the epithelial sodium channel (ENaC) (128, 131).

Mutations in the CFTR gene may impact mRNA and protein expression, function, stability, or a combination of these (132, 133). All mutations that cause CF can be grouped according to their functional defect into seven classes (Figure 11). Class I mutations are due to premature truncation or nonsense alleles, thus often causing degradation of mRNA and affecting protein production. Class II mutations lead to misfolding of the protein, which is retained at the endoplasmic reticulum followed by premature degradation by proteosomes. This group includes the most common CFTR mutation, which is termed $\Delta F508$ and is present in 70% of defective CFTR alleles and in 80% of patients with CF in Europe (134, 135). Class III mutations lead to full-length CFTR channel incorporated into the cell membrane, but with impaired gating. Class IV mutations cause a decrease in chloride and bicarbonate conductance (136, 137). Class V mutations result in the decreased presence of CFTR at the cell surface, often because of alternative splicing, promoter or missense mutations. Class VI mutations destabilize CFTR at the cell surface, which results in increased endocytosis and degradation by lysosomes, and decreasing its recycling back to the cell surface. Finally, class VII mutations or un-rescuable pharmacological mutations. It is the most severe class due to the total absence of mRNA transcription (128, 135, 138).

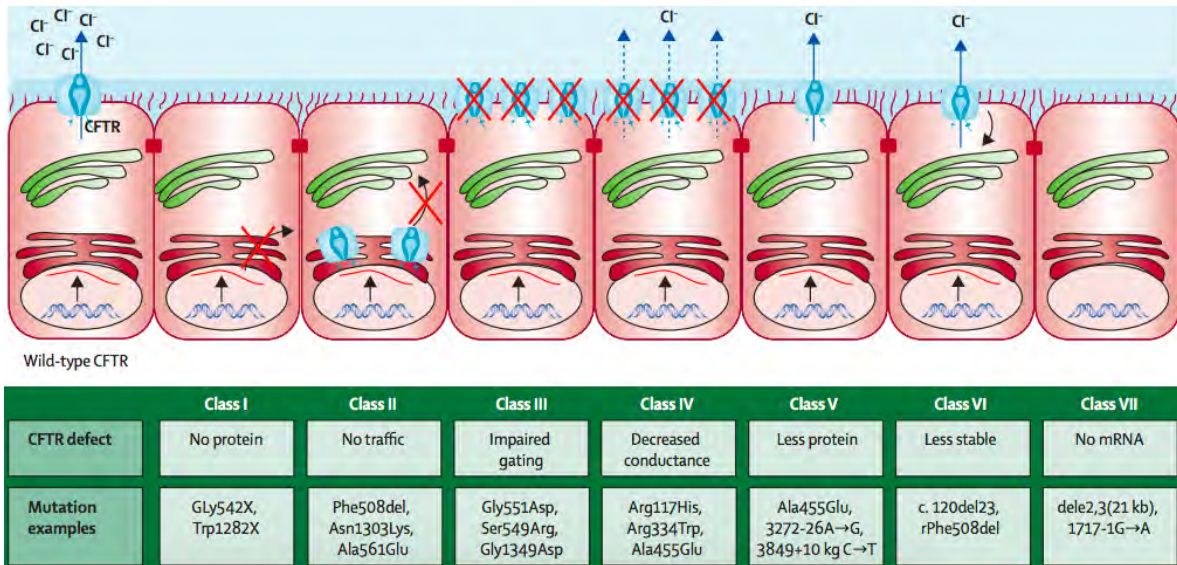


Figure 11. Classes of CFTR mutations (adapted from (135)).

The defective CFTR affects different systems, such as the gastrointestinal, glandular, reproductive and mainly, the respiratory (133). In the latter one, the absence or dysfunction of the CFTR causes increased production of sticky mucus, impaired mucociliary clearance, inflammation, high levels of ROS, overproduction of cytokines and chemokines (IL-8, GM-CSF), increased recruitment of neutrophils and macrophages and impaired phagocytosis, leading to chronic bacterial infection and colonization by opportunistic pathogens, such as Mabs (102, 139–142).

Treatments against CF are designed to target all different aspects of the disease. Antibiotics are given for the infections, mucolytics to decrease the viscousness and stickiness of mucus, and physiotherapy is recommended to finish to detach and expectorate sputum from airways. Nowadays, etiologic therapies (targeting directly

defects present in the CFTR) called CFTR correctors and potentiators are being implemented (143).

In the last years, more evidence allowed to conclude that CF patients are more susceptible to *Mabs* infections compared to other NTM (144). Prospective and multicenter investigations have shown that CF is a major risk factor for NTM infections, with *Mabs* being the most prevalent (145, 146). *Mabs* infection has been linked to decreased lung function in CF patients, thus more likely to require a transplant. However, CF patients with pre-transplant *Mabs* infection could develop post-transplant invasive *Mab* disease. Consequently, *Mabs* is considered a relevant cause of morbidity and mortality in CF patients (147). Furthermore, in an age-related prevalence study, *Mabs* was isolated from airway secretions in all ages, in contrast to *MAC*, which was only observed in patients over the age of 15 (92). Although it is well accepted that CF predisposes to *Mabs* infection, it is still unclear why. Recently, some studies have shown that CF patients are especially susceptible to colonization by biofilm-forming bacteria due to their altered pulmonary physiology. Under these conditions, *Mab S* strains expressing GPL may be favored (121). However, further research is still needed.

1.5.3.1.2 *Mabs* interaction with airway epithelial cells

Mycobacterium abscessus is the most virulent RGM. However, the specific pathways in the colonization of the airways and the establishment of infection are not well understood. So far, there is only evidence that colonization of the lungs is primarily due to the role of GPLs during biofilm formation (144). GPL-expressing *S*

variants have been shown to be able to establish biofilm in the lungs of patients with abnormal airways and decreased mucociliary clearance (148). GPLs not only play a role during the biofilm formation, but are also important for the sensing of Mabs by the EC. GPLs are immunologically inert and can mask bioactive molecules from the bacterial cell wall. Nevertheless, the loss of GPLs unmasks underlying Mabs cell wall molecules such as PIM, which are recognized by TLR2 on EC, leading to their activation and release of IL-8 and human β -defensin-2 (108, 149).

Since the S morphotype is the one reported to be found in the environment, it is also the predominant one in the early stages of infection, which allows Mabs to evade recognition by the innate immune system (121). Interestingly, despite having GPLs on its cell wall, Mabs S showed interaction with normal human bronchial epithelial (NHBE) cells, resulting in the overexpression of genes such as DUOX2, an enzyme involved in ROS production, and IL-32, a cytokine associated with epithelial cell apoptosis (150). It is worth noting that Mabs S was able to lower the percentage of ciliated cells *in vitro* as well as the ciliary beat frequency. However, the slight increase expression of some genes, overall, denote a low responsiveness of lung epithelial cells to the bacterial challenge (150, 151). In contrast to Mabs S, NHBE cells overexpressed IFN-I proteins (OAS1, Mx1, ISG15) and upregulated pro-inflammatory (IL-36) and chemoattractant (CCL5, CCL22) genes after being exposed to Mabs R cell wall microparticles (152). Lastly, Mabs S revealed low internalization and survival in A549 cells (153).

1.5.3.2 Crosstalk between the host innate immune system and Mabs

Following colonization, immune cells such as neutrophils, DC and macrophages are recruited to the site of infection. *In vitro*, human neutrophils are able to phagocytose Mabs S, which triggers a modest increase of intracellular ROS and release of neutrophil extracellular traps (NETs). However, Mabs takes advantage of neutrophils by eliciting a limited and dysregulated immune response, as well as accelerating biofilm formation, which may promote the persistence of the infection (154, 155). Besides, Mabs induces *in vitro* murine DC maturation via TLR4 and production of pro-inflammatory cytokines, such as IL-6, TNF- α , IL-1 β , and IL-12p70. Additionally, Mabs can polarize naive T cells towards CD4 or CD8 cells. After being activated, T cells produce several cytokines, such as IFN- γ , IL-17, and IL-22. These subsequently activate macrophages, thus enhancing the elimination of Mabs (122, 156). Finally, *in vitro*, human and murine macrophages recognize and internalize Mabs through the C-type lectin receptor Dectin-1 (157–159). Macrophages uptake Mabs S as individual bacteria in loner phagosomes, where they are processed and maintained in a tightly apposed phagosomal membrane, forming an electron translucent/transparent zone (ETZ), which play an important role in the scape of Mabs from macrophages and evasion of the granuloma control (116).

1.5.3.3 Granuloma

Smooth variants can persist for a long time within macrophages, which induce the production of inflammatory cytokines such as TNF to restrict intramacrophage bacterial growth and promote the production and release of IL-8 to recruit nearby

neutrophils and T cells to start the granuloma formation (124, 160, 161). At this stage, the innate immune response is sufficient to restrain Mabs. However, Mabs can elude phagosomal defense mechanisms. The ETZ formed after phagocytosis of Mabs S, prevents maturation of the phagosomes, apoptosis-mediated pathways and activation of autophagy (35, 116). Phagosomal escape is mediated in part by the secretion system ESX-4 and by MmpL8. ESX-4 limits the acidification of the phagosome; meanwhile, MmpL8 produces glycosyl-diacylated-nondecyl-diols (GDND), a new glycolipid employed by the bacterium to facilitate its attachment to macrophages and induce phagosome disruption (Figure 12) (112).

Mycobacterium abscessus has a unique course of infection in that it can irreversibly switch from the S to the R variety during persistent infections. The precise biological and environmental mechanisms that cause this transformation are still unclear. Macrophages and neutrophils are unable to phagocytose the large cords of Mabs R (123). Instead, small clusters of rough bacilli are effectively detected via PIM-TLR2 interaction, and consequently engulfed by macrophages, leading to the formation of social phagosomes, which contain several bacteria (35, 162). The social phagosome rapidly melds with the lysosome, causing the acidification of the phagosome, autophagy activation, and apoptosis, which leads to the release of the bacilli into the extracellular milieu, where they freely replicate and form cords, resulting in granuloma breakdown, strong inflammation and extensive tissue destruction (Figure 12) (144).

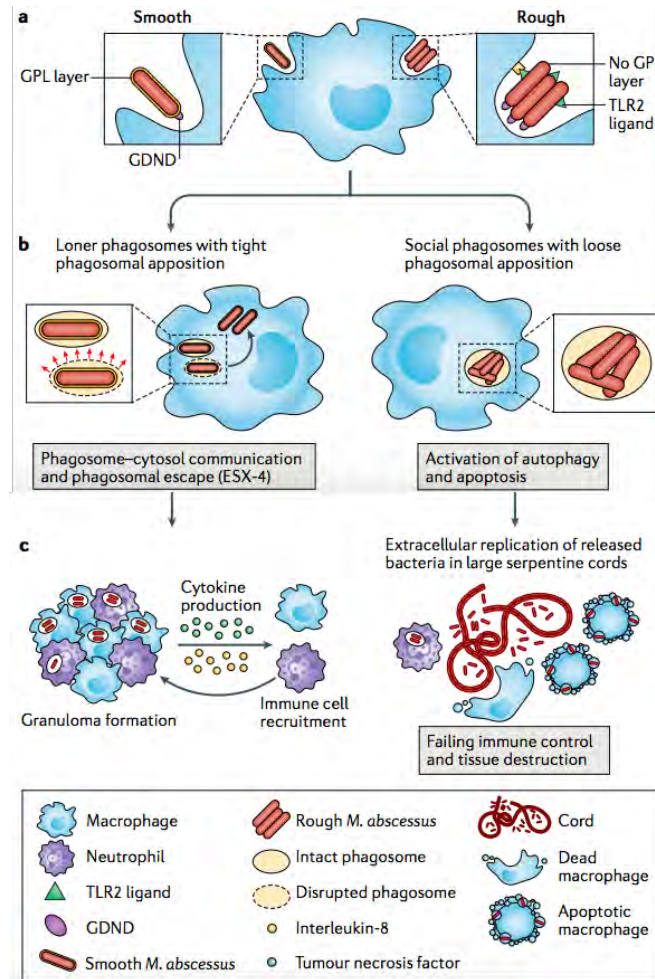


Figure 12. Phagocytosis and processing of Mabs by macrophages (from (35)).

1.5.4 Treatment

Mycobacterium abscessus is one of the most resistant NTM, being uniformly resistant to standard antituberculous drugs and most antimicrobial agents (163), so the cure rate of pulmonary disease is low, ranging from 30% to 50% (164). Antimicrobial treatment for Mabs infection is particularly difficult owing to intrinsic, adaptive and acquired resistance to the majority of routinely used antibiotics (165). Among its most important resistance mechanisms are a waxy and impermeable cell

wall, drug export systems, antibiotic modifying/inactivating enzymes and genetic polymorphism of target genes (Figure 13) (91).

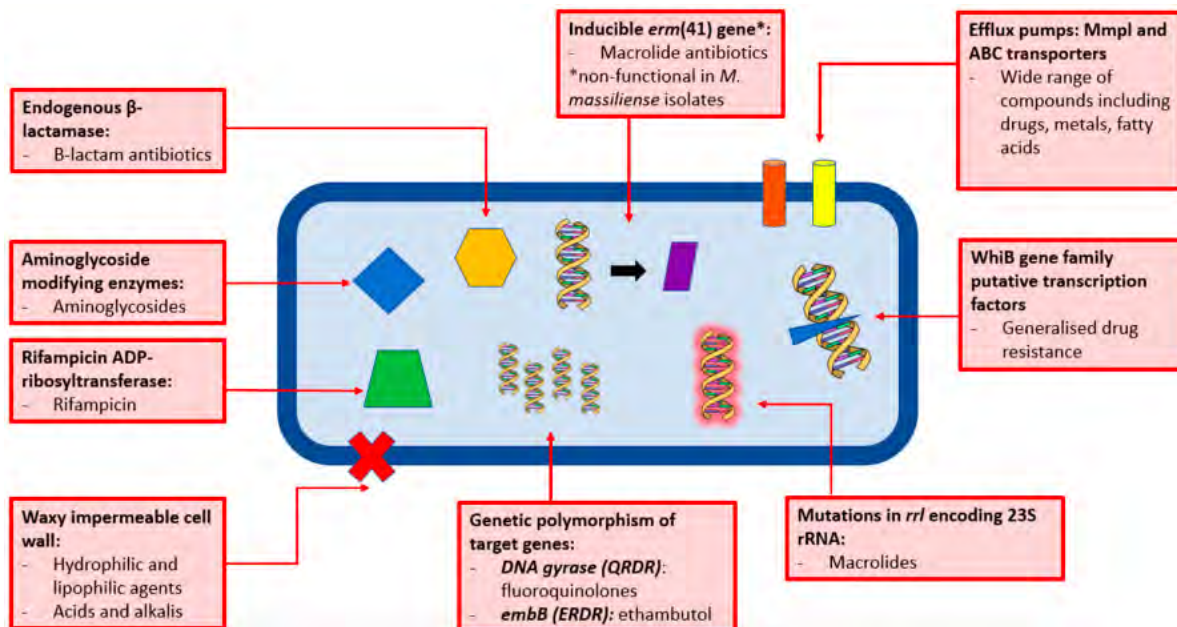


Figure 13. Resistance mechanisms exhibited by Mabs (from (91)).

Before to start the treatment and due to all the antibiotic resistance mechanisms developed by Mabs, recently, the Clinical and Laboratory Standards Institute recommended testing Mabs susceptibility to macrolides, aminoglycosides, fluoroquinolones, imipenem, doxycycline, tigecycline, cefoxitin, cotrimoxazole and linezolid by microdilution for 14 days to rule out resistance (166, 167). After susceptibility testing, the current treatment regimens for Mabs requires 18 months of multidrug therapy. Multidrug regimen includes oral macrolides (azithromycin or clarithromycin) based combination therapy with two parenteral agents for the initial phase (2-4 months) (110, 168). Recently, The British Thoracic Society recommend

that the first 4 weeks of treatment comprise intravenous aminoglycosides (amikacin), tigecycline, beta-lactams (cefoxitin or imipenem), and oral clarithromycin (168, 169). This was followed by a continuation phase (10-14 months) composed of nebulized amikacin and an oral macrolide in combination with additional antibiotics such as linezolid, clofazimine, minocycline cotrimoxazole, and moxifloxacin (Figure 14) (170). In all cases the patients should receive a minimum of 12 months of treatment (171), unfortunately, the side effects caused by this drugs often discourage patients to finish the treatment (172).

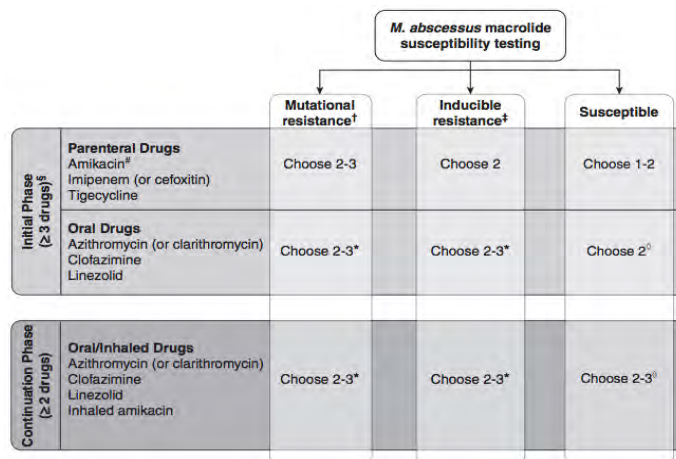


Figure 14. Recommended approach to treatment of Mabs (from (173)).

Importantly, Mabs infection in CF patients is notoriously difficult to treat, not only because the bacteria form biofilms and exhibit a natural resistance to a wide range of antibiotics, but also because CF patients often suffer from malnutrition, gastrointestinal problems, and have low body mass. Consequently, they show significant failure and recurrence rates despite adequate treatment (174–176).

When antibiotics are ineffective, surgery should be considered in specific individuals with localized structural lung disease and good pulmonary functions without having an impaired gas exchange (171, 177). Mabs treatment is longer than the one for TB, more likely to fail and more likely to cause toxicity, thus new or repurposed treatments are being explored *in vitro*, in animal models and in clinical trials, including novel beta-lactamase inhibitor/lactam combinations, dual-lactam combinations, efflux pump inhibitors, novel antimicrobials, inhaled clofazimine suspension and bacteriophages (178).

1.5.5 Models used to study Mabs infection

A major reason for the poor advances in Mabs research has been a lack of adequate experimental animal models leading to delayed progress in the effective evaluation of potentially active antibiotics. Indeed, Mabs has shown a decreased capacity to induce a sustained progressive infection in classical immunocompetent mouse models, which leads to transient colonization of them (179). Therefore, there is an urgent need to develop new models that allow us to deeply characterize Mabs infection, making possible the generation of host-directed therapies and therapeutic vaccines (180). However, in the past few years, the development of multiple cellular, non-mammalian and mammalian models has helped to study the chronology and the pathology of Mabs infection (179, 180).

1.5.5.1 Cellular models

Regarding the cellular models, several studies have used murine and human primary macrophages, as well as cell lines (THP-1, A549). The study of the interactions between Mabs and eukaryotic cells has significantly contributed to delineate the basis of the early interaction and survival strategies between the pathogen in its human host (179). For example, macrophage PRRs (TLR2 and Dectin-1) interact with Mabs surface lipids, promoting their phagocytosis (158). Also, these models established that Mabs R is more aggressive in cells and tends to aggregate in social phagosomes, which is associated with increased cell mortality (116, 181, 182). Meanwhile, Mabs S showed intramacrophage survival and resistance mechanisms, such as phago-lysosomal fusion blockade and resistance to apoptosis and autophagy (116). Curiously, murine bone-marrow macrophages provided evidence of the ability of Mabs to assimilate host lipids, which may represent an important source of long-term energy supply (183). Interestingly, the cellular models have helped to elucidate one of the most important milestones in Mabs pathogenesis, the transition from S to R phenotype due to the loss of GPLs (184). In addition, in recent years, the Mabs research focused on neutrophils. However, they have shown a limited and sometimes ineffective response against Mabs (154, 155). Despite the great advances made with cellular models, they still lack the multicellular environment that Mabs face when infecting humans.

1.5.5.2 Non-mammalian models

Non-mammalian models are also used to study Mabs infection. Among these models, we can find amoebas (*Dictyostelium discoideum*, *Ancathamoeba castellanii*), *Drosophila melanogaster*, *Galleria mellonella* larvae, Silkworm, and zebrafish (Table 1). Non-mammalian models are valuable for screening anti-mycobacterial drugs and imaging host–pathogen interactions at a cellular level due to their relative transparency combined with the development of recombinant bacterial strains that express fluorescent proteins (180).

Table 1. Non-mammalian models used to study Mabs infection (adapted from (180)).

Type of Model	Model	Nature	Advantages	Drawbacks
Nonmammalian models	Amoebas (<i>Dictyostelium discoideum</i>)	<ul style="list-style-type: none"> - Environmental phagocyte organisms - Natural hosts of NTM organisms 	<ul style="list-style-type: none"> - Model for host-pathogen interaction - Used for screening anti-mycobacterial drugs - Relative transparency 	<ul style="list-style-type: none"> - Maximal survival temperature is 27 °C which may affect bacterial growth - Inability to mimic chronic infection
	<i>Drosophila melanogaster</i>	<ul style="list-style-type: none"> - Adult ages 5 to 7 days are used as models for <i>M. abscessus</i> infection 	<ul style="list-style-type: none"> - Host for <i>M. abscessus</i> infection - Used for screening anti-mycobacterial drugs 	<ul style="list-style-type: none"> - Minimal pathogenicity after <i>M. abscessus</i> infection
	<i>Galleria mellonella</i> larvae	<ul style="list-style-type: none"> - Larvae are used as models for studying the innate immune system 	<ul style="list-style-type: none"> - Physiologic temperatures (up to 37 °C) suitable for bacterial growth - Relative transparent - Used for screening anti-mycobacterial drugs 	<ul style="list-style-type: none"> - Drug-exposure response doesn't emulate mammalian host 1. Inability to mimic chronic infection
	Zebrafish	<ul style="list-style-type: none"> - Model for early innate immunity given by macrophages and neutrophils - Mycobacteria-infected zebrafish mimics granuloma-like lesions 	<ul style="list-style-type: none"> - Used for screening anti-mycobacterial drugs - Relative transparent 	<ul style="list-style-type: none"> - Susceptibility profiles to different mycobacterial organisms are different
	Silk worm	<ul style="list-style-type: none"> - Larvae are used as models for studying bacterial infections 	<ul style="list-style-type: none"> - Used for screening anti-mycobacterial drugs 	<ul style="list-style-type: none"> - Rapid growing NTM are detrimental for larvae

Amoebas are environmental phagocytic organisms and are considered natural hosts of NTM (185). Co-cultures of Mabs with amoebas have demonstrated the induction of virulence factor expression by Mabs (e.g., phospholipase C) when the bacterium is inside the amoeba (186). Despite the failure to isolate Mabs from environmental sources, these studies support the view that amoebas contribute to shaping the virulence of Mabs (186). On the other hand, in recent years, zebrafish have been widely exploited to understand the role of innate and adaptive immunity against Mabs. Zebrafish embryos allow visualizing, by non-invasive imaging, the progression, and fate of Mabs infection, as well as host-pathogen interactions in a live animal at a high-resolution level (179). In general, work using zebrafish as a model has identified the role of TNF in the development and maintenance of granulomas (124), the importance of a functional CFTR in innate immunity against Mabs (187), as well as the differential control of Mabs S and R by T cells during chronic infections (161). However, despite their unique features, the major disadvantage of non-mammalian models over mammalian models resides in their anatomical differences, such as gills instead of lungs (179).

1.5.5.3 Mammalian models

The mouse model has been more extensively utilized than any other preclinical model for drug discovery and vaccine research. As previously mentioned, the use of an immunocompetent mouse model in Mabs infection is not considered an adequate model due to the rapid clearance of this bacteria. Notwithstanding, further research

has led to establishment of mouse models with deficits in innate or acquired immunity, resulting in high levels of Mabs progressive infection (Table 2) (180).

Table 2. Some mouse models to study Mabs infection (adapted from (180)).

Type of Model	Model	Nature	Advantages	Drawbacks
Mammalian models	Nude Mice	- Compromised B cells, T cells and natural killer cells	- Similar progressive infection with human <i>M. abscessus</i> lung disease	- Can't be used for studying the efficacy of either prophylactic or therapeutic vaccines
	GKO Mice	- Ifny knock out	- Similar progressive infection with human <i>M. abscessus</i> lung disease	- Can't be used for studying the efficacy of either prophylactic or therapeutic vaccines
	Beige Mice	- Mutation of a lysosomal trafficking regulator protein leading to impaired phagocytosis	- Extreme susceptibility to MAC - Can be used for studying the efficacy of vaccines	- Less studied mouse model for <i>M. abscessus</i> infection
	C57BL/6 Mice	- Susceptible to NTM infection	- Can be used for studying the efficacy of vaccines	- Rapid clearance of the <i>M. abscessus</i>
	BALB/c	- Susceptible to NTM infection	- Can be used for studying the efficacy of vaccines	- Rapid clearance of the <i>M. abscessus</i>

However, initial studies established that immunocompromised mice, such as Beige (dominant Th-2 immunity), *iNOS*^{-/-}, *Cybb*^{-/-} (devoid of super-oxide generating enzyme), and *TNFαR*^{-/-} were still able to clear Mabs. By contrary, C3HeB/FeJ, GKO, and *MyD88*^{-/-} mice sustained diminished amounts of Mabs after 40 days, whereas nude and *GM-CSF*^{-/-} mice infected intravenously with Mabs showed progressive Mabs burden. Although certain genetically manipulated immunocompromised strains were able to maintain bacterial burden (179). This is a compromise in favor of perpetuating the infection, but at a loss of immune cells and inflammatory markers (NOS, ROS, TNF, IFN γ , and MyD88) normally observed in response to infection. Therefore, as mice are unable to mount an immune response, this precludes evaluation of critical aspects of host-pathogen interactions and pathology

development that may impact efficacy of antibiotic treatments (188). Therefore, there is still an imperative need to develop new models to study Mabs infection.

1.6 The organoid revolution

1.6.1 Overview

Human diseases are challenging to study due to the complexity of biological processes. For this reason, scientists resort to model systems, which range in complexity and scale from single cells to model animals. While animal models are valuable for understanding physiology and pathophysiology *in vivo* and assisting in the pre-clinical development of treatments, they are expensive, difficult to interrogate, and suffer inter-specie differences with human biology. As a result, three-dimensional (3D) cell cultures, such as organoids, have emerged as attractive model systems that incorporate fundamental characteristics of *in vivo* tissues and organ complexity while being more experimentally tractable than model organisms (Figure 15) (189).

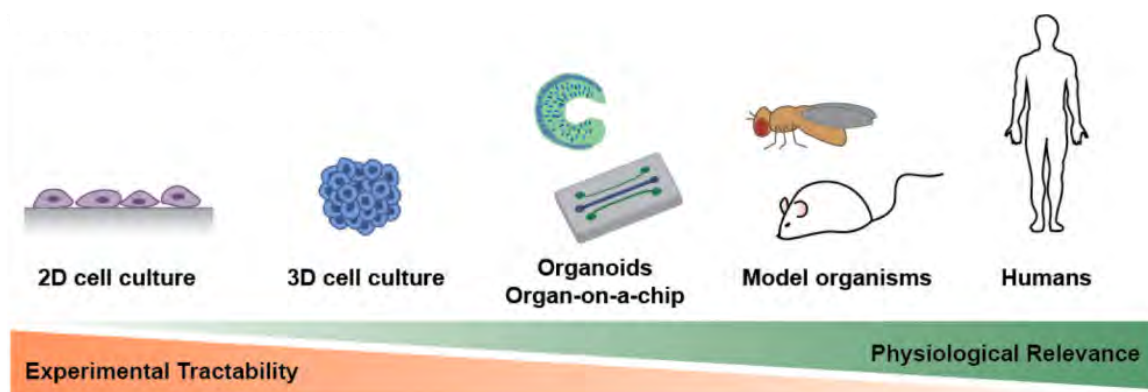


Figure 15. Biological model systems (from (189)).

One of the major breakthroughs by the stem cell field in the past decade consists in the development of “organs” in a dish, also known as organoids (190). Organoids are defined as 3D cell clusters formed from pluripotent or adult stem cells that spontaneously organize into organ-like or tissue-like structures that are enriched for the cell types typically present in the tissue of origin and recapitulate at least one function of the organ (190–192). Once in culture, the stem cell differentiation will be promoted by conditioned medium; regarding their self-organization, they will use hydrogels as scaffolds, which resembles the presence of an extracellular matrix, (ECM). The most commonly used ECM is called Matrigel, a ECM rich in laminine secreted by the Engelbreth Holm-Swarm tumor line (193, 194). Organoids recapitulate the general architecture and functional aspects of the original tissue while remaining genetically stable for years (195, 196). Importantly, the same analytical techniques employed with single cell cultures can be applied to organoids, making them a useful model in basic research, disease modeling, with great promises for regenerative medicine (197, 198). Moreover, organoid biobanking holds potential for future drug screening and personalized medicine. Even though organoids partially recapitulate organ complexity (no vasculature, no innervation, no immune cells) (199), drug regulatory agencies, such as the Food and Drug Administration, consider organoids for pre-clinical and clinical phases of drug development by filtering out the toxic compounds (191, 200, 201). In summary, the organoids resemble in a better way cells and conditions that can be found in the human body, making them an important improvement in the model systems field.

(Figure 16). Organoids combine the best of two worlds, *in vitro* and *in vivo* models (1, 2).

	2D cell culture	C.elegans	D. melanogaster	D. rerio	M. musculus	PDX	Human organoids
Ease of establishing system	✓/✗	✓	✓	✓	✓	✓	✓
Ease of maintenance	✓	✓	✓	✓	✓	✓	✓
Recapitulation of developmental biology	✗	✓	✓	✓	✓	✗	✓
Duration of experiments	✓	✓	✓	✓	✓	✓	✓
Genetic manipulation	✓	✓	✓	✓	✓	✗	✓
Genome-wide screening	✓	✓	✓	✓	✗	✗	✓
Physiological complexity	✗	✓	✓	✓	✓	✓	✓
Relative cost	✓	✓	✓	✓	✓	✓	✓
Recapitulation of human physiology	✓	✓	✓	✓	✓	✓	✓

✓ Best ✓ Good ✓ Partly suitable ✗ Not suitable

Figure 16. Comparison of organoids with other model systems (from (2)). Abbreviation: PDX, Patient-derived xenografts.

1.6.2 Classification of organoids

Organoids can be derived from two main types of stem cells. The first is derived from pluripotent stem cells (PSCs) that include both embryonic stem cells (ESCs) and induced pluripotent stem cells (iPSCs), and the second type is derived from organ-restricted adult stem cells (ASCs). Both approaches exploit the seemingly infinite expansion potential of normal stem cells in culture. For PSCs, this potential has been a necessary requirement for their discovery. In contrast, ASCs were long thought to be incapable of proliferate outside of the body. Nonetheless, growth factor mixtures that replicate the numerous organ stem cell niches have been rapidly developed in recent years (202).

1.6.2.1 Organoids Derived from Pluripotent Stem Cells

All organs evolve from primitive tissues that form early in embryogenesis. Once the egg cells are fertilized, two compartments will be formed: extraembryonic tissue that will differentiate to placenta and amniotic sac to support the fetus, and the inner cell mass (ICM) that will give rise to the embryo. The human PSCs resemble ICM stem cells, and actually, when human ESCs samples are collected, they are taken from the ICM of the human blastocyst. After gastrulation, the ICM will form the embryonic disc, that will later generate the three germ layers: endoderm, mesoderm and ectoderm (203). The acquisition of ESCs was first reported in 1998, with the expectation that they would be valuable for scientific research in different biological and medical fields. However, since their use implicate the sacrifice of human embryos, they gave rise to massive and serious ethical concerns (2, 204). The generation of the human iPSCs in 2007, which allowed the conversion of differentiated skin or blood cells from an adult human into pluripotent cells, effectively circumvented the controversy about human ESCs. The cell reprogramming into a pluripotent state is achieved by the forced expression of a specific set of transcription factors, and once this state is reached, these cells can be differentiated into specific cell types (2). Surprisingly, human PSCs can be induced to spontaneously undergo differentiation and morphogenetic behaviors that mimic the embryonic germ layers formation, especially when they are forced to form 3D aggregates called embryoid bodies (EBs). By applying specific growth factors, the EBs are able to generate the different germ layers which are positive to well-described molecular markers (Figure 17). Therefore, the PSCs can be used as a starting point to produce 3D organoids

that recapitulate, *in vitro*, the human developmental process and tissue organogenesis (203).

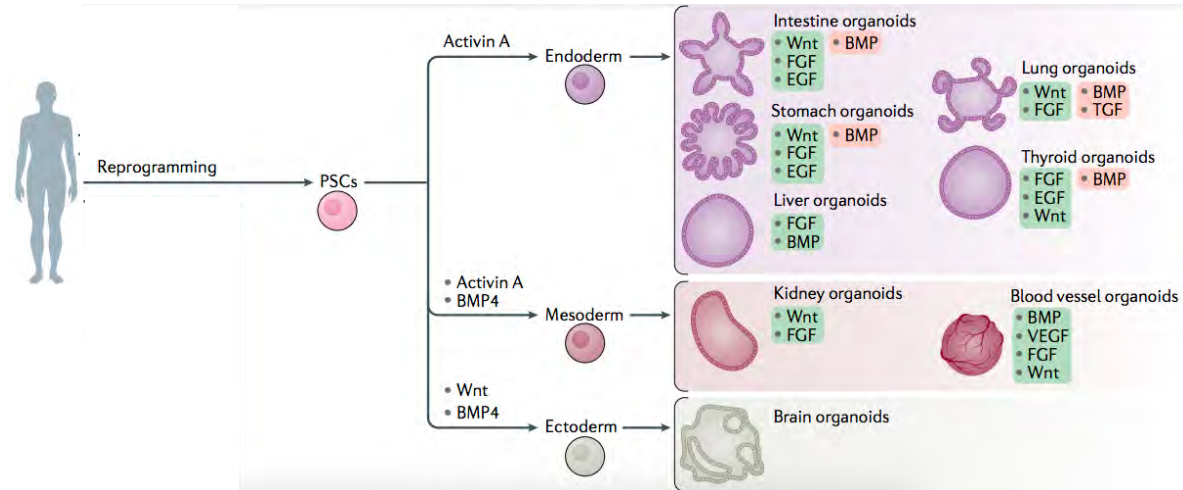


Figure 17. Establishment of PSCs-derived organoids (adapted from (2)). Green background molecules: activated signaling pathways; Red background molecules: inhibited signaling pathways. Abbreviations: BMP, bone morphogenetic protein; EGF, epidermal growth factor; FGF, fibroblast growth factors; TGF, transforming growth factor; VEGF, vascular endothelial growth factor.

1.6.2.2 Organoids Derived from Adult Stem Cells

The human body contains multiple different tissue-specific ASCs. These ASCs have the ability to self-renew, thereby playing a key role in tissue homeostasis and/or repair (205). ASCs have been found in several tissues, including lung, brain, bone marrow, liver, adipose tissue, intestine, and skin. With aging, the number, regenerative ability, and growth of these cells decrease. While ESCs are pluripotent and can generate all cell types, ASCs are multipotent or unipotent, meaning they can only yield distinct cell types (206). The ASC-derived organoids are generated using adult tissues (or postnatal) containing ASCs cultured with a cocktail of growth

factors that recapitulate the different signaling pathways found in normal tissue homeostasis (Figure 18) (207).

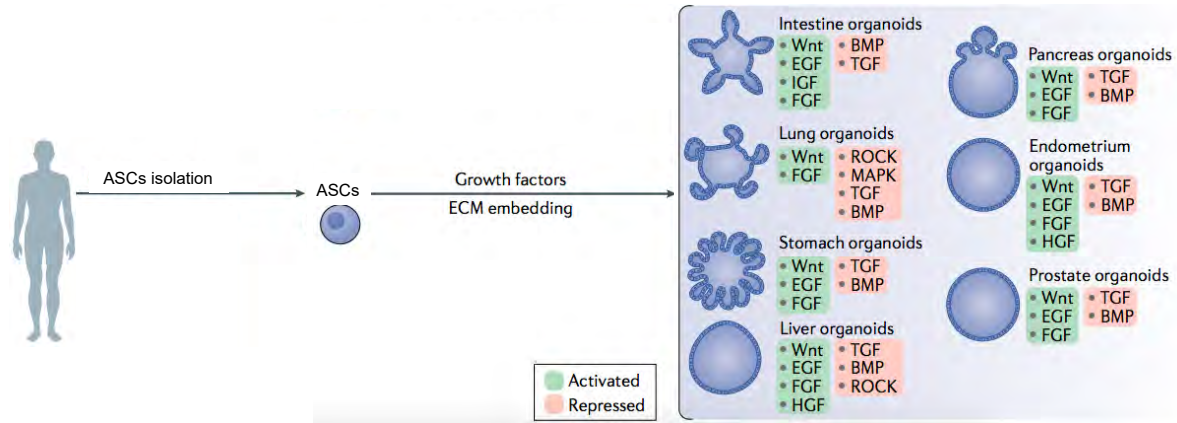


Figure 18. Establishment of ASCs-derived organoids (adapted from (2)). Green background molecules: activated signaling pathways; Red background molecules: inhibited signaling pathways. Abbreviations: HGF, hepatocyte growth factor; IGF, insulin-like growth factor; ROCK, RHO-associated protein kinase.

1.6.3 Human lung organoids

The lung organoids, as other kind of organoids, can derive from stem cells or organ-specific progenitors through a self-organization process. The lung organoids can simulate the developmental process of the lung, as well as recapitulate the 3D organizational structure (such as alveoli, airways, and lung buds) and some functions (such as ciliary beating and mucus production) of the lung *in vitro* (196, 208, 209). They are commonly used to study a variety of inflammatory conditions and progressive diseases (210, 211), including idiopathic pulmonary fibrosis (212, 213), asthma (214), COPD (215, 216), primary dyskinesia (217), cystic fibrosis (196), and respiratory infections (218–220). Human models are preferable to mice models

when studying the pathogenesis of respiratory infectious diseases (221). The composition of epithelial cells varies between similar regions of human and mice (222–224), and pathogens often have a narrow species or tissue tropism, meaning that they infect only certain species or even just certain cell types (221). Lung organoids are particularly well-suited as a model for the study of infectious diseases because they are mainly composed by epithelial cells that can grow *in vitro*, plus, they can be coculture with pathogens, allowing the study of cell-pathogen interaction as in a human infection (225). To date, lung organoids have been used in studies of a number of viruses that cause respiratory diseases, including influenza and parainfluenza viruses, respiratory syncytial virus and coronaviruses (220). On the contrary, further research on bacteria is needed; so far, there are only a couple of studies, one with *Pseudomonas aeruginosa* and another with *Streptococcus pneumoniae* (226, 227).

1.6.3.1 Types of human lung organoids

The human lungs are an incredibly complex organ that consists of several regions or compartments. In general, it is composed of thin tubes, branching and transporting air to the most distal part where the alveoli are located for gas exchange. Each compartment is populated by various epithelial cell types (228). Accordingly, lung organoids can be broadly classified as proximal lung organoids that feature cells mimicking the conducting airway, intermediate lung organoids which correspond to the transitional respiratory airway, and distal lung organoids that recapitulate the alveoli (Figure 19) (228, 229). Most of the conducting airways are formed by

pseudostratified columnar epithelium, which contains specific lineages of stem cells that maintain lung tissue homeostasis by participating in its regeneration after damage (230). Because organoids are derived from cells with progenitor potential, lung organoids may be created from epithelial stem/progenitor cell populations found in the adult lung, qualifying three categories of cells. In the proximal and middle airways, basal cells and secretory club cells (formerly known as Clara cells), meanwhile in the distal airways AEC2 (231).

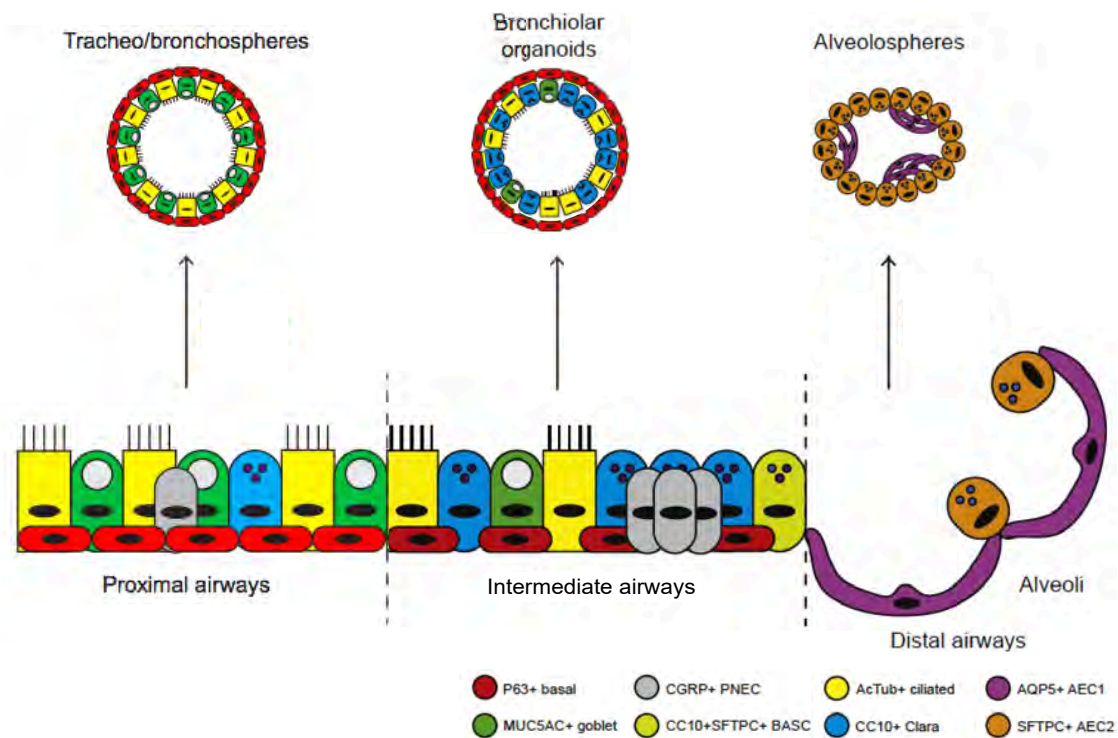


Figure 19. Types of lung organoids (adapted from (232)).

1.6.3.1.1 Proximal lung organoids

The proximal lung organoids are comprised of the tracheospheres or bronchospheres. In 2009, a study demonstrated that basal cells harvested from

mouse and human lungs can self-organize into organoids when cultured in a 3D air-liquid interface (ALI) (232). These organoids could be passaged at least twice, and they are formed of an outer layer of basal cells and ciliated cells facing their lumen (Figure 20) (196, 229).

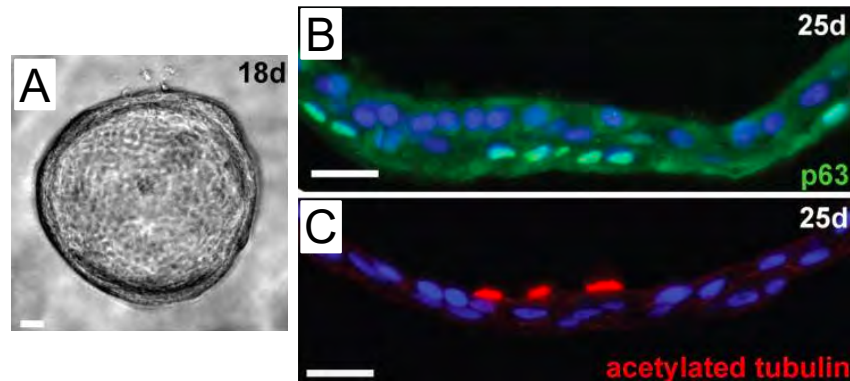


Figure 20. Human tracheosphere composition (adapted from (233)). (A) Light micrograph of human spheres at 18 days of culture. (B) Human spheres at 25 days stained for p63 (green, basal cells) and (C) acetylated tubulin (red, cilia). (Scale bars 25 μ m).

However, these organoids still lacked certain cells that form the conductive airways. In 2015, using human bronchospheres, a study discovered that the Notch signaling pathway plays an essential role in basal cell differentiation. This study showed that blocking the Notch1 receptor increases basal cell markers, whereas blocking the Notch2 receptor increases ciliated markers at the expense of goblet ones (234). This advancement enabled another group of researchers to propose a methodology for the production of mature bronchospheres from primary human airway basal cells in 2016. Mature bronchospheres were composed of ciliated functional cells, mucin-producing cells, and basal cells (196, 235).

At this point, organoids had shown to be a promising alternative in developing more relevant models for the study of diseases. However, they still lacked certain cells, could not be maintained in culture for long periods, and did not present a natural 3D configuration (192).

1.6.3.1.2 Intermediate lung organoids

The intermediate organoids are constituted by the bronchiolar organoids, also known as airway organoids. In 2017, Emma Rawlins and co-workers were the first who identified signaling pathways that allow long-term self-renewal of murine primary fetal lung tip progenitors as differentiation-competent organoids (209). However, it was not until 2019 that Hans Clevers and co-workers reported long-term culture conditions for adult human lung tissue-derived airway organoids (196). In this study, primary human lung tissue was digested and seeded in a growth factor cocktail and 3D Matrigel. The growth factor cocktail comprised differentiation molecules, including FGF7 and FGF10, and inhibition of the BMP and TGF- β pathways, which allow the maintenance of the basal cell population for long-term culture (192). The airway organoids form approximately after 21-28 days in culture. These organoids are fully differentiated and are composed of a polarized, pseudostratified airway epithelium containing secretory club cells, multiciliated cells, mucus-producing goblet cells, and basal (stem) cells (Figure 21). Importantly, both the secretory cells and the cilia were functional, as evidenced by the beating of the cilia and the presence of mucus in the lumen of the organoids. It is worth noting that human airway organoids can not only be developed from "healthy" tissue but can also be

generated from lung cancer or cystic fibrosis patient tissue, under the same culture conditions (196).

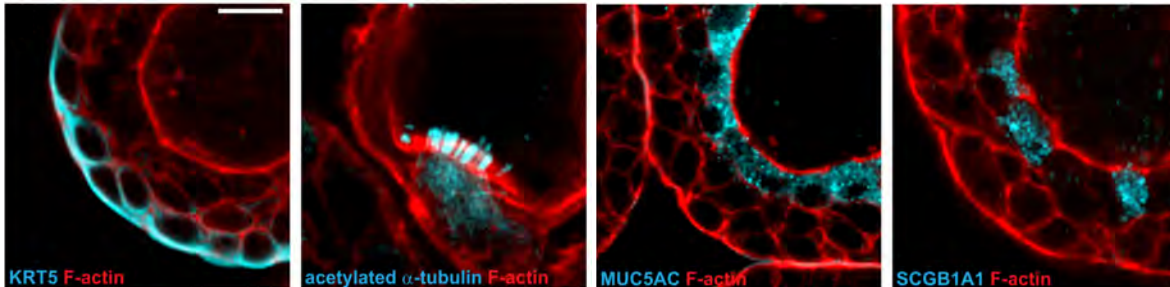


Figure 21. Airway organoid composition (adapted from (196)). Immunofluorescent sections of AOs showing markers for basal cells (KRT5), cilia (acetylated α -tubulin), secretory cells (MUC5AC), and club cells (SCGB1A1). KRT5 is present exclusively in basally localized cells, while cilia, MUC5AC, and SCGB1A1 localize luminally. Counterstained is the actin cytoskeleton (red). Scale bar equals 10 μ m.

So far, these are the most widely used lung organoids to study diseases such as CF, lung cancer and infections (236).

1.6.3.1.3 Distal lung organoids

As part of this group, we find the alveolar organoids. The alveoli are covered by AEC1 and AEC2 (228). The cuboidal AEC2 constitute 90% of the alveolar epithelial cells and function as tissue stem cells secreting pulmonary surfactant, while the flattened AEC1 comprise the majority of the alveolar surface, directly contributing to gas exchange (237). AEC2 isolated from mice were first accounted to generate alveolar organoids. FACS-enriched AEC2 cultured in Matrigel system along with primary PDGFR α -positive lung fibroblasts, MLg cell lines, lung mesenchymal cells or lung endothelial cells were shown to form 3D spherical structures termed

“alveolospheres” comprising SFTPC-positive AEC2 and cells positive for AEC1 markers such as AQP5 and HOPX (229, 237). To date, fibroblast-free cultures of single adult human AEC2 or KRT5 positive basal cells are developed by utilizing fibroblast-expressed ligands and small molecule inhibitors (221, 238). Currently, fibroblast-free human alveolar organoid cultures have been developed. This was achieved by the magnetic bead-based selection of AEC2 cells using the apical surface marker HTII-280 (215, 239, 240). The human AEC2 resist in a feeder-free 3D culture system providing in the medium factors implicated in lung development and in the grow of human embryonic lung tip cells. Being, the activation of the WNT pathway with the molecule CHIR99021 the essential factor for clonal expansion of AEC2 (241, 242). The alveolar organoids form in approximately 14 days with AEC2 on the exterior and AEC1s inside the lumen (Figure 22). These organoids can be sustained long-term (243).

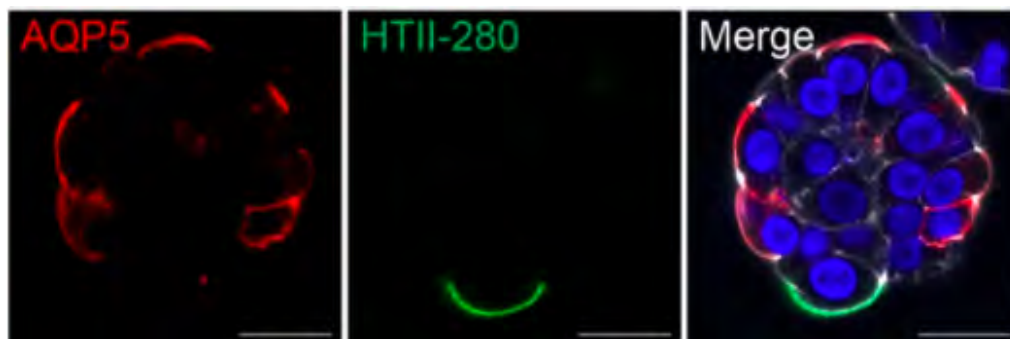


Figure 22. Alveolar organoid composition (adapted from (244)). Alveolar organoids immunofluorescence staining showing markers for AEC1 (AQP5, red) and AEC2 (HTII-280, green). Nuclei and actin filaments were counterstained with DAPI (blue) and Phalloidin-647 (white), respectively. Scale bar, 20 μ m.

Alveolar organoids generated from primary sources have shown tremendous promise in mimicking disease pathology and addressing the scarcity of physiologically appropriate *in vitro* systems for therapeutic testing (13, 229). A recent example of this was the use of lung organoids as a model for severe acute respiratory syndrome coronavirus 2 (SARS-CoV-2) infection (241, 243–245).

1.6.3.1.4 Other lung organoid models

Organoid models are a constantly evolving technology. Therefore, other lung organoid models have been created, which have not yet been fully characterized but are worth mentioning. That is the case with the human nasal epithelial (HNE) organoids. HNE organoids are derived directly from patient nasal brushing samples, which circumvents the problem of obtaining tissue biopsies (246). These organoids grow after 21 days of culture in Matrigel and are composed of basal cells, secretory club cells, goblet cells, and ciliated cells (247). However, more studies are needed to know the percentage of each cell type forming the HNE organoid and if this is similar to the cellular composition of the bronchiolar organoids. Until now, HNE organoids have been applied to study therapeutic responses in CF and respiratory virus pathogenesis (246–248).

Finally, during the COVID-19 pandemic in 2021, researchers generated a complete lung organoid model (also known as the bronchioalveolar model) derived from adult stem cells. This organoid model was generated from lung biopsies obtained from the healthy regions of lung lobes surgically resected for lung cancer. After digestion of the tissue, the cells were seeded in Matrigel and 10 days cultured in a growth factor

cocktail supplemented with the conditioned media from L-WRN cells that express Wnt3, R-spondin, and Noggin. The complete adult lung organoid was scalable, propagable, personalized, and cost-effective. The complete lung organoid showed both proximal (basal, ciliated, club, and goblet cells) and distal (AEC1 and AEC2) airway epithelia. This model demonstrated that proximal airway cells are critical for sustained SARS-CoV-2 infection, whereas distal airway cells contribute to fatal disease by generating an exacerbated immune response (245, 249–251).

In summary, lung organoids represent state-of-the-art platforms that recapitulate the main architecture and functions of the lung. Therefore, they are promising powerful tools for the modeling of human lung diseases and drug screening (210).

1.6.4 Disease modelling in human organoids

Human organoids have had a variety of applications since their creation. They can be used to model from rare inherited diseases to cancer or infections. One of their main advantages are the diversity of approaches they can be used for, including genotype-phenotype testing, drug screening, and even the generation of biobank for future personalized treatments, including cell therapies (203, 206).

1.6.4.1 Cystic fibrosis

The first human condition that was modelled in organoids was CF in an intestinal organoid system context. In 2013, Dekkers and colleagues generated CF-patient-derived intestinal organoids that could closely recapitulate the disease features *in*

vitro. They developed a swelling assay in which wild-type organoids respond to cAMP stimulation (forskolin–cAMP signalling-induced CFTR channel activity) by importing fluid into the lumen and swelling, but CF organoids do not respond (203). This relatively simple *in vitro* assay made possible to identify which CF patients would respond to, and could therefore be treated with, existing CFTR modulator therapies (2, 252). Consequently, in 2015, a Dutch boy named Fabian became the first person to receive successful treatment (Kalydeco) for CF based on organoid drug screening (253). To date, several studies have indicated that patient-specific intestinal organoid swelling responses correlate with clinical outcomes following CFTR modulator therapy. Correlations with clinical indicators, such as the forced expiratory volume in one second and sweat chloride concentrations, imply that organoid swelling may be utilized to predict individual therapy results (252, 254, 255). Currently, the HIT-CF project (an acronym for (Drug) Hits for Cystic Fibrosis) was created in Europe. An initiative aimed at improving treatment and quality of life for people with CF and unusual mutations. In the program, drug candidates from various companies are evaluated in patient-derived intestinal organoids, then clinical trials with the top candidates are conducted (256, 257). Finally, Geurts and collaborators recently demonstrated that CRISPR/Cas9 technology successfully corrects some CFTR mutations (e.g., CFTR-F508del) in intestinal organoids, which was confirmed by the forskolin swelling assay. This result raises a new set of possibilities for the treatment of patients (258).

In addition to the intestinal organoids, other organoid models have been created for the CF study, such as the AOs and the HNE organoids. The AOs can be generated

from CF patients' tissue resections or broncho-alveolar lavage fluid. Interestingly, AOs from F508del CF individuals exhibit secondary phenotypes such as mucus buildup, in addition to faulty CFTR mediated swelling, as initially described in rectal organoids, allowing us to consider them a more faithful model of CF lung disease. Additionally, CFTR modulators can partially rescue the defective swelling of forskolin stimulated AOs, same that was reported for rectal organoids (196). On the other hand, CF HNE organoids were generated relatively easily from nasal brushings. These organoids showed less luminal area and forskolin induced swelling in compared to non-CF controls. Organoids swelling in F508del CF HNE organoids can be rescued with CF modulators (246, 259, 260). Overall, the organoids are an excellent tool for testing the reaction of modulators on patients.

1.6.4.2 Infectious diseases

The emergence of new pathogens and increased resistance to most current antibiotic treatments have resulted in infectious diseases remaining a severe health problem today. Therefore, a better understanding of infectious processes is necessary (219). Given that organoids have established as a reliable model representing different tissues *in vivo* (such as the brain, lung, stomach, intestine, liver, kidney, heart, and reproductive tract) (261), they have been exploited for modeling infectious diseases and monitoring how these behave in the hosts (219). In addition, organoids are a model with a high predictive value for patient response to drugs. As a result, they have served as platforms for developing new treatments and evaluating their efficacy and toxicity (262).

However, the study of pathogen-host interactions remains challenging to date due to the cystic nature of organoids (263). To circumvent this limitation, scientists have developed several techniques, such as the generation of apical out organoids, microinjection devices, and monolayer cultures (264).

Currently, organoids are used to model viral, bacterial, and parasitic infections, making them an essential tool in the fight against infectious diseases (Table 3) (220).

Table 3. Summary of the key findings of the molecular basis of infectious disease using the organoid model (adapted from (261)).

Organ Modelled by Organoid	Infectious Pathogen	Molecular Basis				
		Mechanism of Entry	Tissue Tropism	Replication/Propagati	Immune Response	Disease State
Brain	Prion	✓	✓	✓	✓	
	SARS-CoV-2	✓	✓	✓	✓	✓
	Zika Virus				✓	✓
Respiratory Tract	<i>Mycobacterium</i> species		✓	✓	✓	
	Influenza Virus		✓	✓		
	SARS-CoV-2	✓	✓	✓	✓	
Stomach	<i>Helicobacter pylori</i>	✓	✓	✓		
Intestines	<i>Cryptosporidium</i>		✓	✓		
	Human Noroviruses	✓		✓		
	Human Rotaviruses				✓	
Liver	SARS-CoV-2	✓	✓		✓	
	Hepatitis B	✓			✓	
	Hepatitis C	✓		✓		
Heart	Malaria (<i>Plasmodium</i> species)		✓	✓		
	SARS-CoV-2				✓	
Reproductive Tract	<i>Chlamydia trachomatis</i>		✓	✓		
	Human Papillomavirus					✓
Skin	SARS-CoV-2		✓			
	<i>Trichophyton rubrum</i>				✓	✓

In conclusion, organoid studies have identified specific important points during infections, host factors that influence disease outcomes, and clarified patient-specific responses to treatments (219). The organoid future as models of infection will be

associated with improvements in system complexity, including abilities to model tissue structure, a dynamic microenvironment, and co-infection (220).

Chapter II: Objectives

As stated in the introduction, our understanding regarding the mycobacterial interactions with the human airway epithelium, as well as the models to study the early steps during the establishment of the infections, and the efficacy of their treatment are at the best rudimentary. Consequently, **my Ph.D. thesis project aims to further adapt 3D human lung organoid technology to model mycobacterial pulmonary infections and evaluate treatment efficacy.** During my Ph.D., I addressed four objectives:

- 1.- The development and characterization of healthy and cystic fibrosis airway organoids.
- 2.- Describe the influence of airway organoids on mycobacteria infectivity.
- 3.- Define the airway organoid response against mycobacteria infection.
- 4.- Evaluate the efficacy of a novel strategy for the treatment of mycobacterial infections using airway organoids.

Chapter III: Results

3.1 Mycobacteria-host interactions in human bronchiolar airway organoids

3.1.1 Paper summary

Mycobacterial pulmonary diseases cause significant morbidity and mortality in humans (3). In addition to TB, caused by *Mtb*, recent epidemiological studies have shown that the prevalence of pulmonary infections caused by NTM has increased over the past three decades, being *Mabs* one of the most common (110, 265). While TB is transmitted by inhalation of aerosol droplets containing *Mtb* produced by persons with active disease, NTM is spread primarily through aerosols originated from the environment (49, 266). After inhalation, only the smallest droplets containing mycobacteria reach the alveolar space, where macrophages try to control the infection by several well-described mechanisms (116, 267, 268). However, it is still unknown how the epithelial cells that comprise the trachea, bronchi, and bronchioles interact and contribute to mycobacteria pathogenesis during the early infection.
















The study of early stages of mycobacterial infections *in vivo* is complicated; the lung is not easily accessible and the patients are often diagnosed at later stages of the infection. In addition, some animal models, including mice, vary in epithelial cell composition between similar regions of the lungs when compared to humans (53). Though, recent advances in cell culture technologies have offered the opportunity to model the lung microenvironment more closely (269).

In this study, for the first time, we implemented the ASC-derived airway organoid technology to study specific early stages of mycobacterial infection. We showed that mycobacteria occupied mainly the lumen of the organoids as extracellular bacteria; regardless, the NTM Mabs S was able to thrive. On the opposite, Mtb was controlled by the organoid microenvironment through the overexpression of cytokines and AMPs. Interestingly, both bacteria down-regulated the mucins expression by AOs during the infection. Finally, we demonstrated that macrophages can interact with mycobacteria-infected AOs. In conclusion, this paper brought the AO technology as a really valuable model to study the first interactions of mycobacteria with the airway epithelium.

In this article, in which I am sharing the first author position with Nino Iakobachvili. I contributed by maintaining the organoid culture, preparing the mycobacterial culture for microinjections, designing/performing and analyzing all qPCR experiments, as well as I participated in the writing of the article.

Web link to access the supplementary movies of the paper:
<https://www.ncbi.nlm.nih.gov/pmc/articles/PMC9298242/>

Mycobacteria–host interactions in human bronchiolar airway organoids

Nino Iakobachvili ¹ | Stephen Adonai Leon-Icaza ² | Kèvin Knoop ¹ | Norman Sachs ³ | Serge Mazères ² | Roxane Simeone ⁴ | Antonio Peixoto ² | Célia Bernard² | Marlène Murriss-Espin⁵ | Julien Mazières ⁵ | Kaymeuang Cam² | Christian Chalut ² | Christophe Guilhot² | Carmen López-Iglesias¹ | Raimond B. G. Ravelli ¹ | Olivier Neyrolles ^{2,6,7} | Etienne Meunier² | Geanncarlo Lugo-Villarino ^{2,6,7} | Hans Clevers ³ | Céline Cougoule ^{2,6,7} | Peter J. Peters ¹

¹M4i Nanoscopy Division, Maastricht University, Maastricht, The Netherlands

²Institut de Pharmacologie et Biologie Structurale (IPBS), Université de Toulouse, CNRS, UPS, Toulouse, France

³Oncode Institute, Hubrecht Institute, Royal Netherlands Academy of Arts and Sciences and University Medical Center, Utrecht, The Netherlands

⁴Institut Pasteur, Unit for Integrated Mycobacterial Pathogenomics, CNRS UMR3525, Paris, France

⁵Service de Pneumologie, Hôpital Larrey, CHU de Toulouse, Toulouse, France

⁶International Associated Laboratory (LIA) CNRS “IM-TB/HIV” (1167), Toulouse, France

⁷International Associated Laboratory (LIA) CNRS “IM-TB/HIV” (1167), Buenos Aires, Argentina

Correspondence

Céline Cougoule, Institut de Pharmacologie et Biologie Structurale (IPBS), Université de Toulouse, CNRS, UPS, Toulouse, France.
Email: Celine.Cougoule@ipbs.fr
Peter J. Peters, M4i Nanoscopy Division, Maastricht University, Maastricht, The Netherlands.
Email: pj.peters@maastrichtuniversity.nl

Funding information

FRM “Amorçage Jeunes Equipes”, Grant/Award Number: AJE20151034460; ZonMw,

Abstract

Respiratory infections remain a major global health concern. Tuberculosis is one of the top 10 causes of death worldwide, while infections with Non-Tuberculous Mycobacteria are rising globally. Recent advances in human tissue modeling offer a unique opportunity to grow different human “organs” in vitro, including the human airway, that faithfully recapitulates lung architecture and function. Here, we have explored the potential of human airway organoids (AOs) as a novel system in which to assess the very early steps of mycobacterial infection. We reveal that *Mycobacterium tuberculosis* (Mtb) and *Mycobacterium abscessus* (Mabs) mainly reside as extracellular bacteria and infect epithelial cells with very low efficiency. While the AO microenvironment was able to control, but not eliminate Mtb, Mabs thrives. We demonstrate that AOs responded to infection by modulating cytokine, antimicrobial peptide, and mucin gene expression. Given the importance of myeloid cells in mycobacterial infection, we co-cultured infected AOs with human monocyte-derived macrophages and found that these cells interact with the organoid epithelium. We conclude that adult stem cell (ASC)-derived AOs can be used to decipher very early events of mycobacteria infection in human settings thus offering new avenues for fundamental and therapeutic research.

KEYWORDS

airways, infection, mycobacteria, organoids, tuberculosis

Nino Iakobachvili and Stephen Adonai Leon-Icaza are shared the first authorship.

Céline Cougoule and Peter J. Peters are shared the last authorship.

This is an open access article under the terms of the Creative Commons Attribution-NonCommercial License, which permits use, distribution and reproduction in any medium, provided the original work is properly cited and is not used for commercial purposes.

© 2021 The Authors. *Molecular Microbiology* published by John Wiley & Sons Ltd.

Grant/Award Number: 3R's 114021005; Campus France PHC Van Gogh, Grant/Award Number: 40577ZE; Nuffic Van Gogh Programme, Grant/Award Number: VGP.17/10; Agence Nationale de la Recherche, Grant/Award Number: ANR-15-CE15-0012; LINK program; H2020 European Research Council, Grant/Award Number: INFLAME 804249

1 | INTRODUCTION

Pulmonary diseases due to mycobacteria cause significant morbidity and mortality to human health. Although the global burden of tuberculosis (TB) has declined over the last decades, *Mycobacterium tuberculosis* is still one of the deadliest infectious agent worldwide with an estimated 10 million disease cases and 1.4 million deaths in 2019 (World Health Organization, 2020). By contrast, Nontuberculous Mycobacteria (NTM) infections are rising globally, especially in developed countries, causing opportunistic pulmonary infections affecting individuals who are immunocompromised and who have underlying health conditions (Ratnatunga et al., 2020; To et al., 2020). Among them, *Mycobacterium abscessus* is considered one of the most antibiotic-resistant mycobacteria and is associated with pulmonary disease such as cystic fibrosis (Johansen et al., 2020).

The lung is the main entry port for mycobacteria and the main site of disease. Bacteria-containing droplets or aerosols first navigate through the respiratory tract interacting with airway epithelium functions in order for mycobacteria to reach the alveolar space and thrive in alveolar macrophages (Corleis & Dorhoi, 2020; Leiva-Juárez et al., 2018; Torrelles & Schlesinger, 2017). However, how mycobacteria interact with the airway to establish a successful primary infection remains poorly understood. One of the challenges to address remains the complexity of host–pathogen interactions, particularly within human multicellular tissue.

Conventional 2D cell cultures of epithelial and immune cells, in vitro human-based 3D granuloma, and animal models have contributed to deciphering key host–pathogen mechanisms at play during mycobacterial infection (Bermudez et al., 2002; Bernut et al., 2014, 2015; Bielecka et al., 2017; Cohen et al., 2018; Elkington et al., 2019; Fonseca et al., 2017; Parasa et al., 2014; Puissegur et al., 2007; Rampacci et al., 2020; Silva-Miranda et al., 2015). More recently, in vitro lung models have been developed based on organ-on-chip and organoid technologies to mimic the structural and biological properties of the in vivo human lung environment to better replicate human disease and drug profiles (Cidem et al., 2020; Dutta & Clevers, 2017; Rossi et al., 2018). Lung-on-chip technology reconstructs the alveolar epithelium/endothelium interface and has deciphered the crucial role of surfactant in controlling Mtb replication (Thacker et al., 2020). We, and others, have applied organoid technology for respiratory infection modeling, including *Cryptosporidium* (Heo et al., 2018), RSV (Sachs et al., 2019), influenza viruses (Hui et al., 2018; Zhou et al., 2018), SARS-CoV-2 (Lamers et al., 2020,

2021), and *Pseudomonas aeruginosa* (Bagayoko et al., 2021) to decipher pathogen fitness, cell tropism, and host responses.

While the ongoing COVID-19 pandemic has very recently fueled the development of new human lung organoid models (Salahudeen et al., 2020; Youk et al., 2020), the first human lung organoid model described was derived from lung adult stem cells (ASC's) and composed of a polarized, pseudostratified airway epithelium containing basal, secretory, and multi-ciliated cells, thus reproducing the bronchiolar part of the airway (Sachs et al., 2019). AOs display functional mucus secretion and ciliate beating (Sachs et al., 2019), therefore, constituting a human 3D system in which to model host–mycobacteria interactions (Iakobachvili & Peters, 2017).

Here, we have set out to use AOs as a model in which to study mycobacteria interaction with airway epithelial cells. Our data demonstrate that mycobacteria can be readily found in the lumen of AOs with some internalization by airway epithelial cells. While Mtb growth was overall controlled, Mabs readily replicated in the lumen of AOs. In response to Mtb infection, we showed that AOs induced the secretion of cytokines and antimicrobial peptides. Interestingly, both Mabs and Mtb inhibited the expression of mucins which function in pathogen clearance. The option to model innate cell recruitment by co-culturing human macrophages with bacteria-injected AOs was demonstrated in this work.

2 | RESULTS AND DISCUSSION

First of all, we evaluated the morphology and cell composition of AOs. As shown in Figure S1, AOs displayed a cystic structure (Figure S1a) and are composed of basal cells lined with ciliated and goblet cells on the lumen facing side (Figure S1b and Movie S1). AOs presented functional ciliate beating (Movies S2 and S3) and evident from the live-cell imaging is the functional mucociliary system where cilia beat secreted mucus and cell debris around the lumen (Movie S4).

Due to the innate cystic structure of AOs, where the pathogen-sensing apical side faces the lumen, DsRed-expressing H37Rv Mtb or dTomato-expressing Mabs were microinjected via a BSL-3- or a BSL-2-approved custom-made micro-injection system (Figure 1a). Mycobacteria could be found in the lumen of AOs and occasionally making contact with epithelial cells but without causing obvious alterations to organoid architecture and ultrastructure (Figures 1b,c, S2 and Movie S5–S7). We evaluated whether mycobacteria infection could trigger cell death and found neither Mtb nor Mabs infection

triggered additional cell death compared to uninfected AOs, which undergo regular cell turnover (Figure 1d).

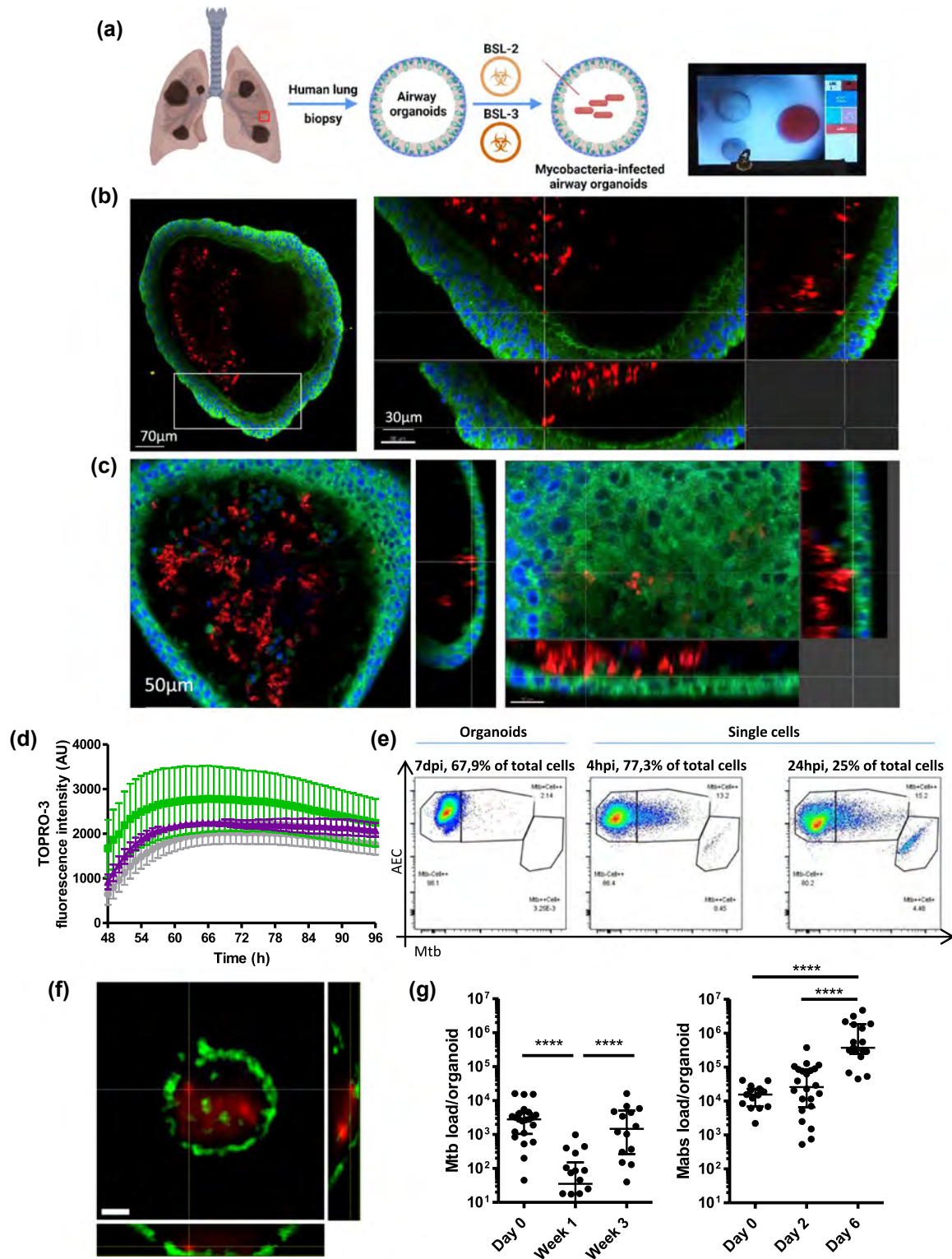
Mtb is known to infect bronchial epithelial cells in 2D conditions (Reuschl et al., 2017), and pneumocytes in vitro (Ryndak et al., 2015) and in vivo (Cohen et al., 2018), but with low efficiency. To determine whether Mtb could infect airway epithelial cells, Mtb-infected AOs were dissociated and analyzed by flow cytometry to quantify cells positive for Mtb in an unbiased manner. Only 2% of the cells composing the organoid were positive for Mtb (Figure 1e). As mucociliary movement could minimize bacteria interaction with epithelial cells, to favor optimal contact between epithelial cells and bacteria, AOs were dissociated, and single cells were infected with Mtb and analyzed by flow cytometry. Approximately 13% and 15% of epithelial cells were found associated with bacteria after 4 and 24 hr of infection, respectively (Figure 1e), confirming that Mtb has a low tropism for epithelial cells as already described with primary bronchial cells (Reuschl et al., 2017). To evaluate bacterial internalization by epithelial cells, double positive cells sorted after flow cytometry were imaged by confocal microscopy. As shown in Figure 1f, epithelial cells containing Mtb could be found, suggesting cell invasion by a yet unknown mechanism and confirming that the majority of mycobacteria are extracellular in the lumen of AOs. The functioning mucociliary system within AOs is likely responsible for preventing mycobacterial contact with, and internalization by, epithelial cells (Leiva-Juárez et al., 2018; Whitsett & Alenghat, 2015).

We next investigated mycobacterial survival in AOs. Bacteria-infected AOs were collected individually, lysed and analyzed for bacterial load by CFU assay. Mtb demonstrated a bi-phasic curve, with a significant decrease of bacterial load after 7 days followed by an increase at 21 days post-infection back to the initial load, without affecting AO viability (Figure 1d). This suggests an early stage of Mtb control by the AO microenvironment followed by bacterial adaptation and proliferation, with cell debris present in the lumen which could foster bacterial replication, as already shown in macrophages (Mahamed et al., 2017). By contrast, Mabs growth displayed a 2-day lag phase followed by significant bacterial replication and an increase in bacterial burden over 6 days (Figure 1g). These results also confirm that the airway constitutes a hospitable microenvironment for Mabs to thrive, compared to Mtb that establishes its replicative niche in alveolar macrophages (Corleis & Dorhoi, 2020; Johansen et al., 2020).

Next, we determined whether AOs mounted an inflammatory/antimicrobial response to mycobacteria infection. Mtb- or Mabs-infected AOs were collected and subjected to RT-qPCR analysis to evaluate cytokine, antimicrobial peptide, and mucin gene expression (Figure 2a). Mtb induced significant gene expression of IL-8 (Figure 2b), a immune cell chemoattractant (Baggiolini & Clark-Lewis, 1992), while IL-8 secretion did not reach significance (Figure 2c). Non-significant expression of IP-10, GM-CSF, and CCL5, cytokines mediating the accumulation of neutrophils and macrophages for optimal granuloma formation and control of Mtb (Domingo-Gonzalez et al., 2016) was observed. The antimicrobial peptides β -defensin-1 and 2, lactoferrin, hepcidin, and RNase7 were enhanced upon Mtb infection, being significant for only β -defensin-1 (Figure 2b). β -Defensin-1 and RNase7 may participate in Mtb restriction during early infection, promoting pore formation on the bacteria cell membrane (Arranz-Trullén et al., 2017; Torres-Juarez et al., 2018), while β -defensin-2 improves the chemoattraction of macrophages (Rivas-Santiago et al., 2005; Semple & Dorin, 2012). Interestingly, β -defensin-3 and 4, which are related to long-term control of mycobacterial infection (Dong et al., 2016) were downregulated. The upregulation of Hepcidin and Lactoferrin could contribute to decrease the transmembrane transport of iron (Sow et al., 2007, 2009) and modulate its extracellular pool by hijacking it (Schaible et al., 2002), making the airway microenvironment more hostile for Mtb survival (Boelaert et al., 2007).

By contrast, Mabs infection did not enhance the expression of cytokines and antimicrobial peptides (Figure 2a). This could be due to the presence of glycopeptidolipids on the surface of its cell wall (Johansen et al., 2020), which mask other lipids and prevent the interaction of Mabs with pattern recognition receptors expressed by host cells (Rhoades et al., 2009), resulting in overall low responsiveness of lung epithelial cells to bacterial challenge (Matsuyama et al., 2018). Surprisingly, both Mabs and Mtb significantly downregulated the expression of mucins, including MUC5B and MUC4 (Figure 2b). Mucin expression and secretion are normally enhanced in response to inflammatory challenge and form part of an efficient clearance system for pathogen removal from the airway (Leiva-Juárez et al., 2018; Ridley & Thornton, 2018; Whitsett & Alenghat, 2015). Our data also showed that mycobacterial infection is associated with downregulation of NF κ B-regulated genes such as IL-1b and IL-6 (Figure 2a), which could participate in mucin expression impairment as IL-1b is a powerful inducer of mucin expression in the airway (Chen

FIGURE 1 Human airway organoids (AOs) infected with Mtb and Mabs. (a) Experimental scheme and bright-field image of the microinjection procedure. Created with Biorender.com. (b) Confocal microscopy of DsRed-expressing H37Rv inside AOs, 4 days post-infection. Nuclei are labeled with DAPI (blue); cellular membranes with CellMask green (green). (c) Confocal microscopy of dTomato-expressing Mabs inside AOs, 4 days post-infection. Nuclei are labeled with DAPI (blue); cellular membranes with CellMask green (green). (d) AOs were injected with PBS (grey), H37Rv Mtb (green), or *Mycobacterium abscessus* (purple), stained with ToPRO3 and imaged hourly for four consecutive days after embedding in matrigel. Fluorescence intensity from ToPRO3 incorporation, and therefore epithelial cell death, was quantified using Fiji and plotted for each condition. The experiment was performed three times independently. (e) Representative flow cytometry dot plots of cells associated with H37Rv after 4 (left) or 24 hr (middle) incubation with AOs-derived single cells or 7 days incubation in whole organoids (right). (f) Representative image of a sorted epithelial cell with intracellular DsRed-expressing Mtb, scale bars = 5 μ m. (g) Colony-forming unit (CFU) counts from individual organoids on the day of microinjection (day 0), 7 and 21 days post-infection. Each dot represents one organoid. Lines indicate median CFU counts. The experiment was performed at least three times independently. *** $p < .001$ by a two-tailed Mann-Whitney test



et al., 2019). Pathogens such as *Helicobacter pylori* have been shown to downregulate the expression of mucin genes to promote stomach tissue colonization (Cooke et al., 2009). How downregulation of mucin expression by mycobacteria might interfere with mucociliary function and infection outcome remains to be elucidated.

Upon Mtb infection, macrophages mount an inflammatory response that modulates the lung microenvironment (Fonseca et al.,

2017; Lastrucci et al., 2015). AOs were stimulated with the supernatant of Mtb-infected human macrophages (cmMTB) and analyzed for gene expression compared to stimulation with the supernatant of non-infected macrophages (cmCTR). As shown in Figure 2d, the expression of IL-8 and GM-CSF, major cytokines for macrophage control of Mtb infection, were significantly enhanced in cmMTB-stimulated AOs compared to those treated with cmCTR which

mimics the paracrine macrophage-epithelial signaling naturally occurring during lung Mtb infection (Reuschl et al., 2017).

Finally, due to the essentiality of macrophages in TB disease (Cadena et al., 2016; Corleis & Dorhoi, 2020), we co-cultured human monocyte-derived macrophages, alongside mycobacteria-injected organoids, and observed hourly by confocal microscopy over the course of 4 days. Due to the complex nature of this experiment, it was optimized and set up under BSL-2 conditions using *Mycobacterium bovis* BCG. Human macrophages were found to migrate within the collagen matrix and in some instances, moved towards organoids containing mycobacteria (Movie S8). While we found no evidence of macrophages being able to traverse the basal side and enter the organoid lumen to clear mycobacteria, we did observe macrophages migrating to and interacting with the basal edge of the AO, capturing and ingesting bacteria (Movie S8). This resembles the natural process of peri-bronchiolar macrophage migration to the site of infection and phagocytosis of pathogenic material (Cambier et al., 2014).

Using AOs as a human 3D system to study the early steps of mycobacterial infection, we have shown that Mtb remains viable for up to 21 days within the lumen of AOs, while Mabs actively replicated over 7 days (Figure 1g). During this timeframe, while AO integrity remained uncompromised (Figures 1b,c, S2 and Movies S5 and S6), molecular interactions began as early as 48 hr after injection with the modulation of cytokines and antimicrobial peptides, and the inhibition of mucin expression (Figure 2b–d). Within 72 hr, innate immune cells can be recruited to the surface of infected AOs (Movie S8). Together, these data indicate that AOs offer a valuable 3D system to assess early interactions of mycobacteria with the human airway.

The ability to model these early timeframes in a responsive, multicellular and functionally similar system to the human airway, but without the complications, monetary and ethical restrictions of animal research, constitutes a major advance for the field. Organoid technology provides a complementary strategy to model in vitro human tissues, and infection by human-related pathogens. Organoids based on lung ASC's are advantageous as they generate AOs via a one-step proliferation and differentiation protocol and naturally self-organize in 3D to recapitulate the complexity of the lung epithelium. The resulting epithelium comprises all the different cell types and related secreted products (mucus, surfactant proteins), thus providing a reductionist system to assess host–pathogen interactions at the tissue level. Due to the self-renewal of ASC's, one of the most important advantages of organoids is that they are a genetically stable during long-term culture, allowing for their cryopreservation in biobanks.

One of the main limitations of the organoid system comes from the absence of air-liquid-mucosa interface due to their closed, cystic structure. Very recent advances in bioprinting and microfluidic approaches allowed intestinal organoid-based tissue engineering to create tube-shaped epithelia and a continuous lumen (Nikolaev et al., 2020), with the potential of extending such an approach to airway models. Lung-on-a-chip technology also constitutes an alternative approach to reproduce the air-liquid-mucosa interface and model mycobacterial infection

(Huh et al., 2013; Thacker et al., 2020). However, lung-on-chips are generally developed using induced Pluripotent Stem Cells (iPSC) or epithelial cell lines, require complex expertise in both iPSC cultures based on long stepwise differentiation protocols, and in nano-micro fabrication for chip devices. Therefore, organoids and on-chip organs are complementary approaches that provide alternatives to animal experimentation thus complying with the “3R's”—Replacement, Reduction, Refinement—which call for in vitro or a alternatives to model functional organs and pathologies (Gkatzis et al., 2018).

As mycobacteria, especially Mtb, establish their replicative niche in the alveolar part of the lung, another limitation comes from the absence of pneumocytes in the AO model. Recent advances in modeling the human alveolar part of the human lung as organoids (Salahudeen et al., 2020; Youk et al., 2020) will allow further modeling of the mycobacterial replicative niche. Finally, the ability to introduce human macrophages allows functional modeling of a key cell type and its cellular network, overcoming another limitation of organoid systems. Extension of the BALO technology, combining connected airway with alveoli and engraftment of macrophages (Vazquez-Armendariz et al., 2020), to human stem cells could open new venues for mycobacterial infection modeling. We believe that this work forms a starting point for modeling a wide range of human respiratory pathogens using lung organoids, as exemplified with SARS-CoV-2, (Lamers et al., 2020, 2021; Salahudeen et al., 2020; Si et al., 2021; Thacker et al., 2021), but also respiratory infections driven by host disorders such as cystic fibrosis.

3 | METHODS

3.1 | Ethic statements

The collection of patient data and tissue for AO generation was performed according to the guidelines of the European Network of Research Ethics Committees following European and national law. In the Netherlands and France, the responsible accredited ethical committees reviewed and approved this study in accordance with the Medical Research Involving Human Subjects Act. Human lung tissue was provided by the Primary Lung Culture Facility (PLUC) at MUMC+, Maastricht, The Netherlands. Collection, storage, use of tissue and patient data were performed in agreement with the “Code for Proper Secondary Use of Human Tissue in the Netherlands” (<http://www.fmwv.nl>). The scientific board of the Maastricht Pathology Tissue Collection approved the use of materials for this study under MPTC2010-019 and formal permission was obtained from the local Medical Ethical Committee (code 2017-087). The CHU of Toulouse and CNRS approved protocol CHU 19 244 C and Ref CNRS 205782. All patients participating in this study consented to scientific use of their material; patients can withdraw their consent at any time, leading to the prompt disposal of their tissue and any derived material.

Human buffy coats were obtained from volunteers with informed consent via Sanquin (NVT0355.01) or établissement français du sang (Agreement 21PLER2017-0035AV02).

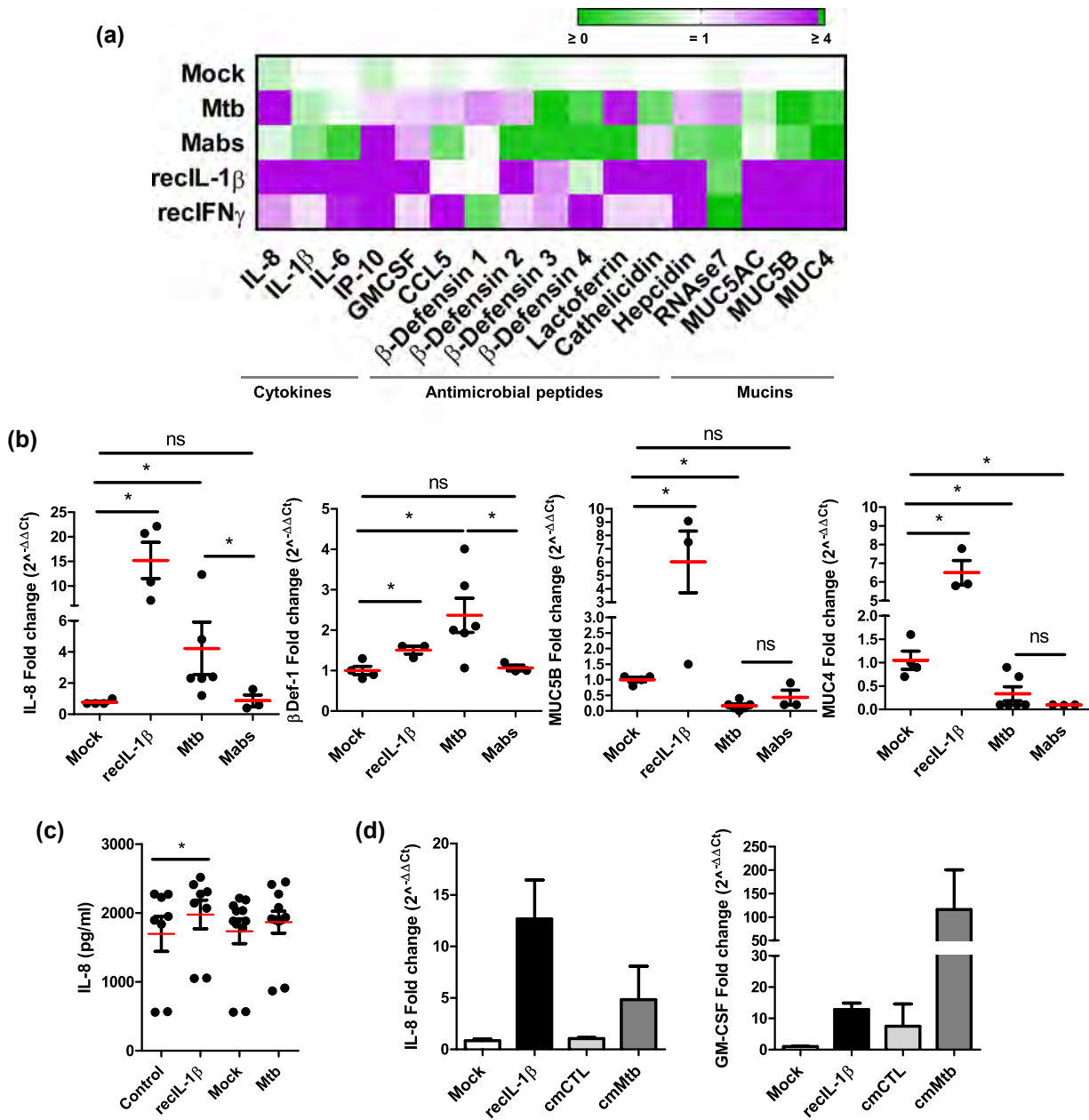


FIGURE 2 Mycobacteria-induced host responses in AOs. (a) Heat map displaying modulation of cytokines, antimicrobial peptides, and mucins in AOs in response to Mtb H37Rv or Mabs injection compared to mock-injected organoids. As positive controls, AOs were treated with recombinant IL-1 β and IFN β . The experiment was performed four times independently. (b) Statistically significant expression changes of IL-8, β -defensin-1, MUC5B, and MUC4 as determined by RT-qPCR at 48 hr post-infection. * $p < .05$ by a two-tailed Mann-Whitney test. (c) ELISA quantification of IL-8 secretion by H37Rv-infected AOs at 48 hr post-infection. IL-8 secretion in H37Rv-infected AOs was almost significantly ($p = .053$ by two-tailed Wilcoxon matched-pairs signed-rank test), recIL-1 β -treated AOs (recIL-1 β) was used as positive control. The experiment was performed three times independently. (d) Expression changes of IL-8 and GM-CSF as determined by RT-qPCR at 72 hr after conditioning with cmCTR and cmMTB, defined as conditioned media from non-infected and Mtb-infected macrophages, respectively. The experiments were performed two times independently with pooled conditioned medium from three independent donors

3.2 | Organoid culture

Healthy tissue from five independent donors receiving surgical treatment for lung cancer were used to derive organoids. AOs were characterized as described (Sachs et al., 2019).

3.3 | Bacterial culture and microinjection

DsRed-WT H37Rv Mtb strains were obtained by complementation with the pMRF plasmid containing a DsRed cassette, and were cultured in the continuous presence of 20 μ g/ml of the selective

antibiotic hygromycin under BSL-3 conditions (Simeone et al., 2015). Mtb strains (BSL-3) and GFP expressing *M. bovis* BCG (BSL-2) were grown under the selection of 20 µg/ml Kanamycin in BSL-2 conditions. *M. abscessus sensu stricto* (Mabs) strain CIP104536T (ATCC19977T) morphotype Smooth (S) carrying pASTA3 plasmid (Addgene, plasmid 24,657) that express red fluorescent protein (tdTomato), was cultured in presence of 500 µg/ml of the antibiotic hygromycin B as previously described (Bernut et al., 2014). All the bacteria were prepared for microinjection as described (Lastrucci et al., 2015). Bacterial density was adjusted to $OD_{600} = 1$, and phenol red was added at 0.005% to visualize successful microinjection (Bartfeld & Clevers, 2015). Pulled borosilicate capillaries (1.2 mm diameter, Harvard Apparatus Ltd.) were backfilled with the bacterial suspension using Microloader Tips (Eppendorf) and the tapered end broken off using tweezers until the smallest size droplet could be injected using a Femtojet microinjector (Eppendorf). We determined the CFU of these droplets that were destined for organoids by injecting them into 100 µl media and plating directly onto agar for enumeration. This was a reproducible way to quantify the initial bacterial load at the start of our experiments. An in-house custom-made Raspberry Pi-controlled digital camera was used to observe organoids and the capillary. The capillary was attached to a TransferMan micro-manipulator (Eppendorf) to facilitate semi-automated injection. Injected organoids were allowed to recover for 2 hr at 37°C, individually collected, washed to remove extracellular bacteria and re-seeded into fresh matrix for subsequent analysis.

3.4 | Microscopy

For time-lapse imaging, injected organoids were seeded in IBIDI 4 well chambers (IBIDI) and stained with CellMask™ Green Plasma Membrane Stain (1/1000, Molecular Probes) for 30 min at 37°C. Organoids were washed and fresh medium containing TOPRO-3 Iodide (1/1000, Molecular Probes) was added. Organoids were imaged using a FEI CorrSight at Maastricht University (BSL-2) or Andor/Olympus Spinning Disk Confocal CSU-X1 (10× Air 0,4 NA, 3,1 mm WD) at IPBS (BSL-3). Z-stacks were acquired every hour for the duration of experiments and data analyzed using Fiji/Image J and IMARIS. The fluorescent labels used in this work are summarized in Table 2.

For transmission electron microscopy (TEM), injected AOs were fixed in 4% PFA for a minimum of 3 hr at RT prior to removal from the containment lab and embedding in epon blocks as described in (Bartfeld & Clevers, 2015; Lamers et al., 2020). TEM data was collected autonomously as virtual nanoscopy slides on a 120 kV FEI Tecnai Spirit T12 Electron Microscope equipped with an Eagle CCD camera.

3.5 | Colony-forming unit (CFU) assay

Four to six Mtb or Mabs-injected organoids were collected manually using a 200 µl pipette, washed in PBS, seeded into 24-well

TABLE 1 List of primers used for RT-qPCR experiments on airway organoids

Gene	Primers 5'-3'	Reference
<i>Cytokines and chemokines</i>		
CCL5 (NM_002985)	F- CCTCATTGCTACTGCCCTCT R- CGGGTGACAAAGACGACTGC	In-house
GM-CSF (NM_000758)	F- CCTGAACCTGAGTAGAGACACT R- CCTTGAGCTTGTTGAGGCTG	In-house
IL-1β (NM_000576)	F- AGCTACGAATCTCCGACCAC R- GGGAAAGAAGGTGCTCAGGTC	In-house
IL-6 (NM_000600.5)	F: ACTCACCTTTCAGAACGAATTG R: CCATCTTTGGAAGTTTCAGGTTG	PrimerBank
IL-8 (NM_000584)	F- TACTCCAAACCTTTCCACCCC R- CTTCTCCACAACCTCTGCA	In-house
IP-10 (NM_001565)	F- GTGGCATTCAAGGAGTACCTC R- GATTCCAGACATCTTCTCACCC	In-house
<i>Antimicrobial peptides</i>		
β-Defensin 1 (NM_005218)	F- ATGGCCTCAGGTGGTAACTTTC R- GGTCACCTCCAGCTCACTTG	In-house
β-Defensin 2 (NM_004942)	F-ATAGGCGATCCTGTTACCTGC R-CCTCCTCATGGCTTTTTCAG	In-house
β-Defensin 3 (NM_018661)	F- TGGGGTGAAGCCTAGCAG R- ACTTGCCGATCTGTTCTCC	In-house
<i>β-Defensin 4</i>		
(NM_080389.3)	F: TGCCGAAGAAATGTGCGA R: CGACTCTAGGGACCAGCAC	In-house
Cathelicidin LL37 (NM_004345)	F- ATGCTAACCTCTACCGCTCC R- TCACCAGCCCGTCTTCTTG	In-house
Hepcidin (NM_021175)	F- GTTTTCCACAACAGACGGG R- AGATGGGGAAGTGGGTGTC	In-house
Lactoferrin (NM_002343)	F- CCCCTACAACTGCGACCTG R- CAGACCTTGCGATTCGTTCCAG	In-house
RNAse 7 (NM_032572)	F- GGAGTCACAGCACGAAGACCA R- GGCTTGGCACTGACTGGGATC	In-house
<i>Mucins</i>		
MUC4 (NM_018406.7)	F: CTCAGTACCGCTCCAGCAG R: CCGCCGTCTTCATGGTCCAG	In-house
MUC5AC (NM_001304359.2)	F: CCAGTCTGCCTTTGTACGG R: GACCCTCTCTCAATGGTGC	In-house
MUC5B (NM_002458.3)	F: GCCCACATCTCCACCTATGAT R: GCAGTCTCGTTGTCCGTCA	PrimerBank
<i>Housekeeping</i>		
GAPDH (NM_002046)	F-CTCCAAAATCAAGTGGGGCGATG R-GGCATTGCTGATGATCTTGAGGC	In-house

plates, and cultured in complete AO medium for 2–21 days. At the relevant timepoint, organoids were lysed in 100 µl of 10% Triton X100 in water, serial dilutions were plated on 7H11 agar plates for Mtb or LB agar plates for Mabs and cultured for 3 weeks or 6 days respectively at 37°C.

TABLE 2 Summary of fluorescent markers used for flow cytometry and microscopy

Dye	Concentration/ Dilution	Marker of	Flow cytometry or microscopy
DAPI	1 µg/ml	Nuclei	Microscopy
CellMask deep red	1/30000	Cell membranes	Microscopy and Flow Cytometry
CellMask Green	1/1000	Cell membranes	Microscopy
TOPRO-3 iodide	1/1000	Dead cells	Microscopy
CellTracker CMAC blue	20 µM	Cell cytosol	Microscopy

3.6 | RT-qPCR

Uninfected control and Mtb- or Mabs-infected AOs (15 per condition) were collected at 48 hr post-infection, lysed in 1 ml of TRIzol Reagent (Invitrogen) and stored at -80°C for 2 days. As positive controls, AOs were stimulated with 0.02 µg/ml of human IL-1 β (Invivogen) or 0.1 µg/ml of IFN γ (PeproTech) for 48 hr. Total RNA was extracted using the RNeasy mini kit (Qiagen) and retrotranscribed (150 ng) using the Verso cDNA Synthesis Kit (Thermo Scientific). mRNA expression was assessed with an ABI 7,500 real-time PCR system (Applied Biosystems) and the SYBR™ Select Master Mix (ThermoScientific). Relative quantification was determined using the $2^{-\Delta\Delta\text{Ct}}$ method and normalized to GAPDH. Primer sequences are provided in Table 1.

3.7 | Enzyme-linked immunosorbent assay

Between 20 and 30 organoids were embedded in fresh BME Cultrex and cultured with 800 µl complete media. After 48 hr, the supernatant was collected, sterilized through double 0.22 µm filters and stored at -80°C until analysis. IL-8 ELISA was performed according to manufacturer instructions (Qiagen).

3.8 | Flow cytometry and cell sorting

Organoids were washed out of Matrigel and dissociated into single cells using TrypLE for 5 min at 37°C . A minimum of 5×10^5 cells/ml were incubated with dsRED expressing Mtb at an MOI of 10 in complete organoid media. After 4 or 24 hr for single cells, or 7 days for whole intact organoids, samples were washed with PBS, stained with CellMask Deep Red (1:30,000) to highlight all cells composing the organoid and fixed in 4% paraformaldehyde overnight at 4°C . Cells were pelleted and resuspended in PBS supplemented with 2% FCS. Samples were filtered just before analysis and sorted using a BD FACS ARIA Fusion. Cells were selected on their FSC-A/SSC-A profile, doublets were excluded on FSC-W/FSC-H and SSC-W/SSC-H parameters. Finally, double positive cells were gated based on Cell Mask Deep Red staining and DsRED-expressing Mtb. The population of cells from P5 (positive for GFP/bacteria and APC/ organoid cells) was pooled and imaged by confocal microscopy to determine if bacteria was intracellular. The fluorescent dyes used are summarized in Table 2.

3.9 | CmMTB preparation and macrophage co-cultures

Peripheral blood mononuclear cells were enriched from buffy coat using RosetteSep human monocyte enrichment cocktail according to the manufacturer's instructions (Stem Cell Technologies). Monocytes were purified by density gradient centrifugation using Lymphoprep (Stem Cell Technologies) according to the manufacturer's protocol. Monocytes were differentiated into macrophages by addition of 5 ng/ml macrophage colony-stimulating factor (Sigma Aldrich) for 6 days. cmCTR and cmMTB were prepared and used as previously described (Lastrucci et al., 2015). Organoids were stained with CellMask Deep Red plasma membrane dye as previously described, and macrophages stained with 20 µM CellTracker Blue CMAC dye (ThermoFisher Scientific) for 1 hr in serum-free media. Microinjected organoids and macrophages were resuspended in freshly prepared Rat Tail Collagen type 1 (ThermoFisher, 1 mg/ml) and polymerized in a 4-well, glass-bottom µ-slide (Ibidi) at 37°C for 30 min and imaged for 96 hr under a FEI CorrSight microscope.

ACKNOWLEDGMENTS

Authors acknowledge C. Kuo (Stanford University, USA) for the stable expressing Rsp01-Fc cell line, and the Hubrecht Institute for the stable expressing Noggin cell line; Genotoul TRI-IPBS core facility for flow cytometry and imaging, in particular E. Näser and E. Vega; IPBS BSL-3 facilities, in particular C. Verollet for technical support. Authors also acknowledge the Microscopy CORE lab and PLUC facility at Maastricht University. This work was supported by grants from Campus France PHC Van Gogh (40577ZE to GL-V), the Agence Nationale de la Recherche (ANR-15-CE15-0012 (MMI-TB)) to GL-V, FRM "Amorçage Jeunes Equipes" (AJE20151034460 to EM), ERC StG 693 (INFLAME 804249 to EM), ATIP to EM, ZonMW 3R's (114021005) to PJP, the Nuffic Van Gogh Programme (VGP.17/10 to NI), and by the LINK program from the Province of Limburg, the Netherlands.

CONFLICT OF INTEREST

Hans Clevers and Norman Sachs are inventors on patents related to organoid technology. Other authors declare no conflict of interest.


AUTHOR CONTRIBUTIONS

NI, CC, and PJP designed the experiments with the help of CLI, ON, EM, and GLV. NI, SALI, and CC performed the experiments with the contribution of KK, RBGR, SM, AP, CCh, KC, and CG. SR generated

the fluorescent Mtb strains. MME and JM provided the lung biopsies. HC and NS developed the lung organoid technology. NI, CC, SALI, and PJP wrote the manuscript.

ORCID

Nino Iakobachvili  <https://orcid.org/0000-0003-0797-2665>

Stephen Adonai Leon-Icaza  <https://orcid.org/0000-0002-7546-8228>

Kévin Knoops  <https://orcid.org/0000-0002-7539-1160>

Norman Sachs  <https://orcid.org/0000-0002-5467-7151>

Serge Mazères  <https://orcid.org/0000-0002-0263-634X>

Roxane Simeone  <https://orcid.org/0000-0002-7082-7842>

Antonio Peixoto  <https://orcid.org/0000-0001-9493-1954>

Julien Mazières  <https://orcid.org/0000-0002-5921-7613>

Christian Chalut  <https://orcid.org/0000-0002-4849-1369>

Raimond B. G. Ravelli  <https://orcid.org/0000-0001-6056-5888>

Olivier Neyrolles  <https://orcid.org/0000-0003-0047-5885>

Geanncarlo Lugo-Villarino  <https://orcid.org/0000-0003-4620-8491>

Hans Clevers  <https://orcid.org/0000-0002-3077-5582>

Céline Cougoule  <https://orcid.org/0000-0002-6795-5448>

Peter J. Peters  <https://orcid.org/0000-0002-2964-5684>

REFERENCES

- Arranz-Trullén, J., Lu, L., Pulido, D., Bhakta, S. & Boix, E. (2017) Host antimicrobial peptides: the promise of new treatment strategies against tuberculosis. *Frontiers in Immunology*, 8, 1.
- Bagayoko, S., Leon-Icaza, S.A., Pinilla, M., Hessel, A., Santoni, K., Péricat, D. et al. (2021, February 17) Host phospholipid peroxidation fuels ExoU-dependent cell necrosis and supports *Pseudomonas aeruginosa*-driven pathology. *bioRxiv*, 17(9), e1009927. <https://doi.org/10.1371/journal.ppat.1009927>
- Baggiolini, M. & Clark-Lewis, I. (1992) Interleukin-8, a chemotactic and inflammatory cytokine. *FEBS Letters*, 307, 97–101.
- Bartfeld, S. & Clevers, H. (2015) Organoids as model for infectious diseases: Culture of human and murine stomach organoids and microinjection of *Helicobacter pylori*. *Journal of Visualized Experiments*, 2015, 53359.
- Bermudez, L.E., Sangari, F.J., Kolonoski, P., Petrofsky, M. & Goodman, J. (2002) The efficiency of the translocation of *Mycobacterium tuberculosis* across a bilayer of epithelial and endothelial cells as a model of the alveolar wall is a consequence of transport within mononuclear phagocytes and invasion of alveolar epithelial cells. *Infection and Immunity*, 70, 140.
- Bernut, A., Dupont, C., Sahuquet, A., Herrmann, J.-L., Lutfalla, G. & Kremer, L. (2015) Deciphering and imaging pathogenesis and cording of *Mycobacterium abscessus* in zebrafish embryos. *Journal of Visualized Experiments*, 2015, 53130.
- Bernut, A., Herrmann, J.-L., Kissa, K., Dubremetz, J.-F., Gaillard, J.-L., Lutfalla, G. et al. (2014) *Mycobacterium abscessus* cording prevents phagocytosis and promotes abscess formation. *Proceedings of the National Academy of Sciences*, 111, E943–E952.
- Bielecka, M.K., Tezera, L.B., Zmijan, R., Drobniowski, F., Zhang, X., Jayasinghe, S. et al. (2017) A Bioengineered three-dimensional cell culture platform integrated with microfluidics to address antimicrobial resistance in tuberculosis. *mBio*, 8(1), e02073-16. <https://doi.org/10.1128/mBio.02073-16>
- Boelaert, J.R., Vandecasteele, S.J., Appelberg, R. & Gordeuk, V.R. (2007) The effect of the host's iron status on tuberculosis. *Journal of Infectious Diseases*, 195, 1745–1753.
- Cadena, A.M., Flynn, J.L. & Fortune, S.M. (2016) The importance of first impressions: Early events in *Mycobacterium tuberculosis* infection influence outcome. *mbio*, 7(2), e00342-16. <https://doi.org/10.1128/mBio.00342-16>
- Cambier, C.J., Takaki, K.K., Larson, R.P., Hernandez, R.E., Tobin, D.M., Urdahl, K.B. et al. (2014) Mycobacteria manipulate macrophage recruitment through coordinated use of membrane lipids. *Nature*, 505, 218–222.
- Chen, G., Sun, L., Kato, T., Okuda, K., Martino, M.B., Abzhanova, A. et al. (2019) IL-1 β dominates the promucin secretory cytokine profile in cystic fibrosis. *Journal of Clinical Investigation*, 129, 4433.
- Cidem, A., Bradbury, P., Traini, D. & Ong, H.X. (2020) Modifying and integrating in vitro and ex vivo respiratory models for inhalation drug screening. *Front Bioeng Biotechnol*, 8, 581995.
- Cohen, S.B., Gern, B.H., Delahaye, J.L., Adams, K.N., Plumlee, C.R., Winkler, J. et al. (2018) Alveolar macrophages provide an early *Mycobacterium tuberculosis* niche and initiate dissemination. *Cell Host & Microbe*, 24, 439.
- Cooke, C.L., An, H.J., Kim, J., Canfield, D.R., Torres, J., Lebrilla, C.B. et al. (2009) Modification of gastric mucin oligosaccharide expression in rhesus macaques after infection with *Helicobacter pylori*. *Gastroenterology*, 137, 1061–1071.e8.
- Corleis, B. & Dorhoi, A. (2020) Early dynamics of innate immunity during pulmonary tuberculosis. *Immunology Letters*, 221, 56–60.
- Domingo-Gonzalez, R., Prince, O., Cooper, A. & Khader, S.A. (2016) Cytokines and chemokines in *Mycobacterium tuberculosis* infection. *Microbiology Spectrum*, 4(5). <https://doi.org/10.1128/microbiolspec.TB2-0018-2016>
- Dong, H., Lv, Y., Zhao, D., Barrow, P. & Zhou, X. (2016) Defensins: the case for their use against mycobacterial infections. *Journal of Immunology Research*, 2016, 7515687. <https://doi.org/10.1155/2016/7515687>
- Dutta, D. & Clevers, H. (2017) Organoid culture systems to study host-pathogen interactions. *Current Opinion in Immunology*, 48, 15.
- Elkington, P., Lerm, M., Kapoor, N., Mahon, R., Pienaar, E., Huh, D. et al. (2019) In vitro granuloma models of tuberculosis: potential and challenges. *Journal of Infectious Diseases*, 219, 1858.
- Fonseca, K.L., Rodrigues, P.N.S., Olsson, I.A.S. & Saraiva, M. (2017) Experimental study of tuberculosis: from animal models to complex cell systems and organoids. *PLoS Pathogens*, 13(8), e1006421. <https://doi.org/10.1371/journal.ppat.1006421>
- Gkatzis, K., Taghizadeh, S., Huh, D., Stainier, D.Y.R. & Bellusci, S. (2018) Use of three-dimensional organoids and lung-on-a-chip methods to study lung development, regeneration and disease. *European Respiratory Journal*, 52, 1800876.
- Heo, I., Dutta, D., Schaefer, D.A., Iakobachvili, N., Artegiani, B., Sachs, N. et al. (2018) Modeling cryptosporidium infection in human small intestinal and lung organoids. *Nature Microbiology*, 3, 814.
- Huh, D., Kim, H.J., Fraser, J.P., Shea, D.E., Khan, M., Bahinski, A. et al. (2013) Microfabrication of human organs-on-chips. *Nature Protocols*, 8(11), 2135–2157.
- Hui, K.P.Y., Ching, R.H.H., Chan, S.K.H., Nicholls, J.M., Sachs, N., Clevers, H. et al. (2018) Tropism, replication competence, and innate immune responses of influenza virus: an analysis of human airway organoids and ex-vivo bronchus cultures. *The Lancet Respiratory Medicine*, 6, 846–854.
- Iakobachvili, N. & Peters, P.J. (2017) Humans in a dish: the potential of organoids in modeling immunity and infectious diseases. *Frontiers in Microbiology*, 8, 2402.
- Johansen, M.D., Herrmann, J.-L. & Kremer, L. (2020) (2020) Non-tuberculous mycobacteria and the rise of *Mycobacterium abscessus*. *Nature Reviews Microbiology*, 18(18), 392–407.
- Lamers, M.M., Beumer, J., van der Vaart, J., Knoops, K., Puschhof, J., Breugem, T.I. et al. (2020) SARS-CoV-2 productively infects human gut enterocytes. *Science* (80-), 369, 50–54.

- Lamers, M.M., van der Vaart, J., Knoops, K., Riesebosch, S., Breugem, T.I., Mykytyn, A.Z. et al. (2021) An organoid-derived bronchioalveolar model for SARS-CoV-2 infection of human alveolar type II-like cells. *EMBO Journal*, 40(5), e105912. <https://doi.org/10.15252/embj.2020105912>
- Lastrucci, C., Bénard, A., Balboa, L., Pingris, K., Souriant, S., Poincloux, R. et al. (2015) Tuberculosis is associated with expansion of a motile, permissive and immunomodulatory CD16⁺ monocyte population via the IL-10/STAT3 axis. *Cell Research*, 25, 1333.
- Leiva-Juárez, M.M., Kolls, J.K. & Evans, S.E. (2018) Lung epithelial cells: therapeutically inducible effectors of antimicrobial defense. *Mucosal Immunology*, 11, 21.
- Mahamed, D., Boulle, M., Ganga, Y., Arthur, C.M., Skroch, S., Oom, L. et al. (2017) Intracellular growth of *Mycobacterium tuberculosis* after macrophage cell death leads to serial killing of host cells. *Elife*, 6, e22028. <https://doi.org/10.7554/eLife.22028>
- Matsuyama, M., Martins, A.J., Shallom, S., Kamenyeva, O., Kashyap, A., Sampaio, E.P. et al. (2018) Transcriptional response of respiratory epithelium to nontuberculous mycobacteria. *American Journal of Respiratory Cell and Molecular Biology*, 58, 241.
- Nikolaev, M., Mitrofanova, O., Broguiere, N., Geraldo, S., Dutta, D., Tabata, Y. et al. (2020) Homeostatic mini-intestines through scaffold-guided organoid morphogenesis. *Nature*, 585(7826), 574–578.
- Parasa, V.R., Rahman, M.J., Hoang, A.T.N., Svensson, M., Brighenti, S. & Lerm, M. (2014) Modeling *Mycobacterium tuberculosis* early granuloma formation in experimental human lung tissue. *Disease Models & Mechanisms*, 7, 281.
- Puissegur, M.-P., Lay, G., Gilleron, M., Botella, L., Nigou, J., Marrakchi, H. et al. (2007) Mycobacterial lipomannan induces granuloma macrophage fusion via a TLR2-dependent, ADAM9- and β 1 integrin-mediated pathway. *The Journal of Immunology*, 178, 3161–3169.
- Rampacci, E., Stefanetti, V., Passamonti, F. & Henao-Tamayo, M. (2020) Preclinical models of nontuberculous mycobacteria infection for early drug discovery and vaccine research. *Pathogens*, 9, 1–24.
- Ratnatunga, C.N., Lutzky, V.P., Kupz, A., Doolan, D.L., Reid, D.W., Field, M. et al. (2020) The rise of non-tuberculosis mycobacterial lung disease. *Frontiers in Immunology*, 11, 303.
- Reuschl, A.-K., Edwards, M.R., Parker, R., Connell, D.W., Hoang, L., Halliday, A. et al. (2017) Innate activation of human primary epithelial cells broadens the host response to *Mycobacterium tuberculosis* in the airways. *PLoS Pathogens*, 13(9), e1006577. <https://doi.org/10.1371/journal.ppat.1006577>
- Rhoades, E.R., Archambault, A.S., Greendyke, R., Hsu, F.-F., Streeter, C. & Byrd, T.F. (2009) *Mycobacterium abscessus* glycopeptidolipids mask underlying cell wall phosphatidyl-myo-Inositol mannosides blocking induction of human macrophage TNF- α by preventing interaction with TLR2. *The Journal of Immunology*, 183, 1997–2007.
- Ridley, C. & Thornton, D.J. (2018) Mucins: the frontline defence of the lung. *Biochemical Society Transactions*, 46, 1099.
- Rivas-Santiago, B., Schwander, S.K., Sarabia, C., Diamond, G., Klein-Patel, M.E., Hernandez-Pando, R. et al. (2005) Human β -defensin 2 is expressed and associated with *Mycobacterium tuberculosis* during infection of human alveolar epithelial cells. *Infection and Immunity*, 73, 4505.
- Rossi, G., Manfrin, A. & Lutolf, M.P. (2018) Progress and potential in organoid research. *Nature Reviews Genetics*, 19(11), 671–687.
- Ryndak, M.B., Singh, K.K., Peng, Z. & Laal, S. (2015) Transcriptional profile of *Mycobacterium tuberculosis* replicating in type II alveolar epithelial cells. *PLoS One*, 5, 112–114. <https://doi.org/10.1016/j.gdata.2015.05.026>
- Sachs, N., Pappaspyropoulos, A., Ommen, D.D.Z., Heo, I., Böttinger, L., Klay, D. et al. (2019) Long-term expanding human airway organoids for disease modeling. *EMBO Journal*, 38(4), e100300. <https://doi.org/10.15252/embj.2018100300>
- Salahudeen, A.A., Choi, S.S., Rustagi, A., Zhu, J., van Unen, V. & Sean, M. et al. (2020) Progenitor identification and SARS-CoV-2 infection in human distal lung organoids. *Nature* 588(7839), 670–675.
- Schaible, U.E., Collins, H.L., Priem, F. & Kaufmann, S.H.E. (2002) Correction of the iron overload defect in β -2-microglobulin knockout mice by lactoferrin abolishes their increased susceptibility to tuberculosis. *Journal of Experimental Medicine*, 196, 1507.
- Semple, F. & Dorin, J.R. (2012) β -Defensins: multifunctional modulators of infection, inflammation and more? *Journal of Innate Immunity*, 4, 337.
- Si, L., Bai, H., Rodas, M., Cao, W., Oh, C.Y., Jiang, A. et al. (2021) A human-airway-on-a-chip for the rapid identification of candidate antiviral therapeutics and prophylactics. *Nature Biomedical Engineering*, 2021, 1–15.
- Silva-Miranda, M., Ekaza, E., Breiman, A., Asehounne, K., Barros-Aguirre, D., Pethe, K. et al. (2015) High-content screening technology combined with a human granuloma model as a new approach to evaluate the activities of drugs against *Mycobacterium tuberculosis*. *Antimicrobial Agents and Chemotherapy*, 59, 693.
- Simeone, R., Sayes, F., Song, O., Gröschel, M.I., Brodin, P., Brosch, R. et al. (2015) Cytosolic access of *Mycobacterium tuberculosis*: critical impact of phagosomal acidification control and demonstration of occurrence in vivo. *PLoS Pathogens*, 11(2), e1004650. <https://doi.org/10.1371/journal.ppat.1004650>
- Sow, F.B., Alvarez, G.R., Gross, R.P., Satoskar, A.R., Schlesinger, L.S., Zwilling, B.S. et al. (2009) Role of STAT1, NF- κ B, and C/EBP β in the macrophage transcriptional regulation of hepcidin by mycobacterial infection and IFN- γ . *Journal of Leukocyte Biology*, 86, 1247–1258.
- Sow, F.B., Florence, W.C., Satoskar, A.R., Schlesinger, L.S., Zwilling, B.S. & Lafuse, W.P. (2007) Expression and localization of hepcidin in macrophages: a role in host defense against tuberculosis. *Journal of Leukocyte Biology*, 82, 934–945.
- Thacker, V.V., Dhar, N., Sharma, K., Barrile, R., Karalis, K. & McKinney, J.D. (2020) A lung-on-chip model of early *Mycobacterium tuberculosis* infection reveals an essential role for alveolar epithelial cells in controlling bacterial growth. *Elife*, 9, 1–73.
- Thacker, V.V., Sharma, K., Dhar, N., Mancini, G., Sordet-Dessimoz, J., & McKinney, J.D. (2021) Rapid endotheliitis and vascular damage characterize SARS-CoV-2 infection in a human lung-on-chip model. *EMBO Reports*, 22(6), e52744. <https://doi.org/10.15252/embr.202152744>
- To, K., Cao, R., Yegiazaryan, A., Owens, J. & Venketaraman, V. (2020) General overview of nontuberculous mycobacteria opportunistic pathogens: *Mycobacterium avium* and *Mycobacterium abscessus*. *Journal of Clinical Medicine*, 9, 2541.
- Torrelles, J.B. & Schlesinger, L.S. (2017) Integrating lung physiology, immunology and tuberculosis. *Trends in Microbiology*, 25, 688.
- Torres-Juarez, F., Touqui, L., Leon-Contreras, J., Rivas-Santiago, C., Enciso-Moreno, J.A., Hernández-Pando, R. et al. (2018) RNase 7 but not psoriasin nor sPLA2-IIA associates with *Mycobacterium tuberculosis* during airway epithelial cell infection. *Pathogens and Disease*, 76(2). <https://doi.org/10.1093/femspd/fty005>
- Vazquez-Armendariz, A.I., Heiner, M., Agha, E.E., Salwig, I., Hoek, A., Hessler, M.C. et al. (2020) Multilineage murine stem cells generate complex organoids to model distal lung development and disease. *EMBO Journal*, 39(21), e103476. <https://doi.org/10.15252/embj.2019103476>
- Whitsett, J.A. & Alenghat, T. (2015) Respiratory epithelial cells orchestrate pulmonary innate immunity. *Nature Immunology*, 16(1), 27–35. <https://doi.org/10.1038/ni.3045>
- World Health Organization. (2020) *Tuberculosis*. Accessed August 5, 2021, <https://www.who.int/teams/global-tuberculosis-programme/data>
- Youk, J., Kim, T., Evans, K.V., Jeong, Y.-I., Hur, Y., Hong, S.P. et al. (2020) Three-dimensional human alveolar stem cell culture models reveal infection response to SARS-CoV-2. *Cell Stem Cell*, 27, 905.

Zhou, J., Li, C., Sachs, N., Chiu, M.C., Wong, B.-H.-Y., Chu, H. et al. (2018) Differentiated human airway organoids to assess infectivity of emerging influenza virus. *Proceedings of the National Academy of Sciences of the United States of America*, 115, 6822.

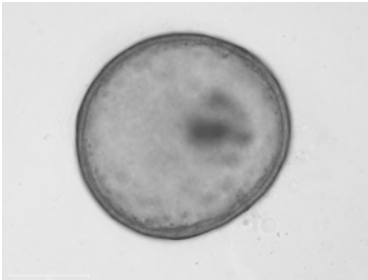
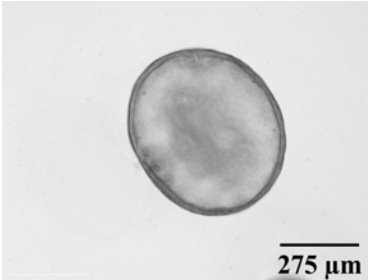
SUPPORTING INFORMATION

Additional supporting information may be found in the online version of the article at the publisher's website.

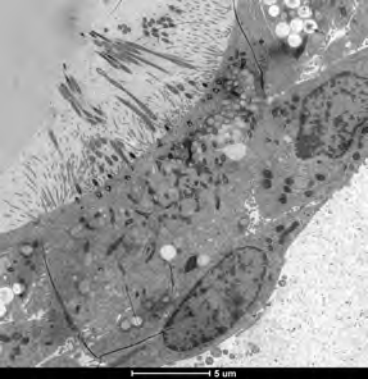
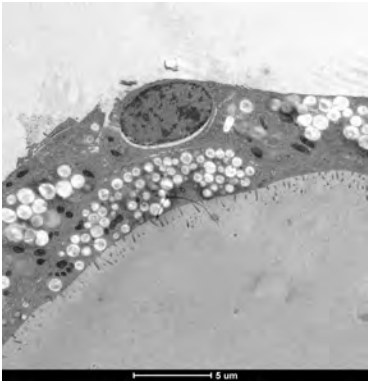
How to cite this article: Iakobachvili, N., Leon-Icaza, S.A., Knoop, K., Sachs, N., Mazères, S., Simeone, R., et al (2022) Mycobacteria–host interactions in human bronchiolar airway organoids. *Molecular Microbiology*, 117, 682–692. <https://doi.org/10.1111/mmi.14824>

Iakobachvili et al. Supp Figure 1

A

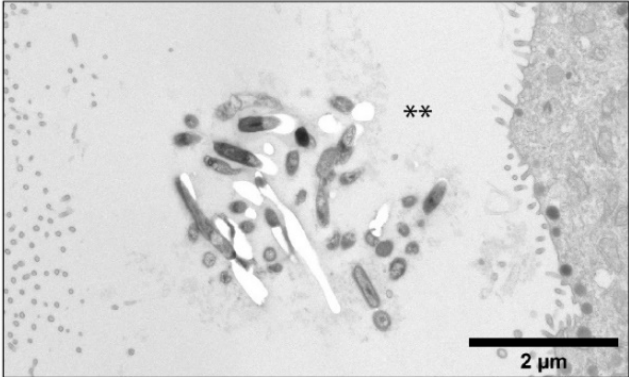
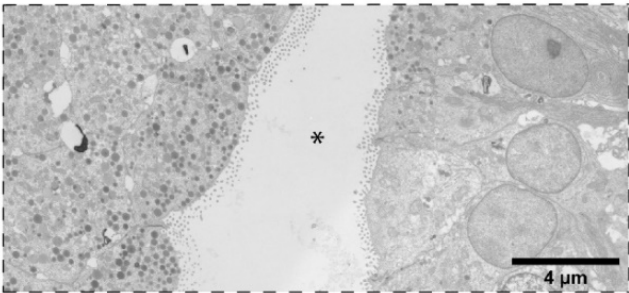
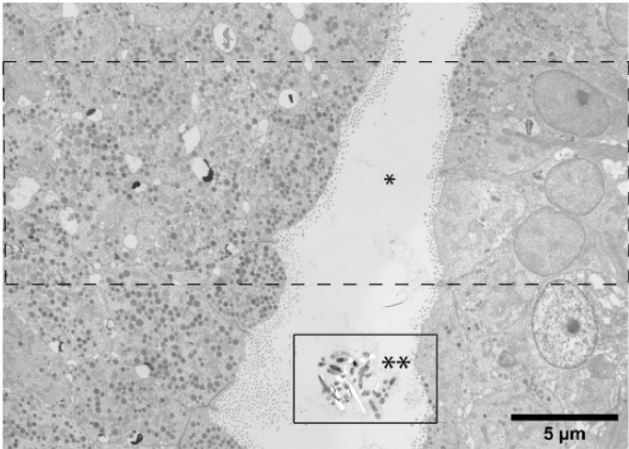


B



Iakobachvili et al. Supp Figure 2

A



3.2 Human bronchial organoids unveil druggable pathways against *Mycobacterium abscessus* infection in cystic fibrosis

3.2.1 Paper summary

Non-tuberculous mycobacteria are increasingly being identified in the sputum of adults and children with CF, both in America and in Europe (174). To date, *Mabs* is one of the most NTM isolated from individuals with CF (270). *Mabs* is an opportunistic pathogen of increasing clinical importance (271). In CF patients, *Mabs* is associated with rapidly worsening disease, is difficult to treat and requires antibiotic regimens with substantial side effects. Since NTM can infect transplanted lungs causing high mortality, this procedure is often contraindicated (121, 272). The underlying mechanisms that allow *Mabs* to preferentially colonize the lungs of the CF patients, remain largely unknown.

A major reason for the poor advances in *Mabs* research has been a lack of adequate models that resembles human CF manifestations (zebrafish, mice), like the severe muco-obstructive phenotype (126, 179, 273).

In the present study, for the first time, we applied the human airway organoid technology to model *Mabs* infection in a CF environment. We showed that CF-derived airway organoids have a thicker epithelium, accumulate mucus, undergo oxidative stress, and increased lipid peroxidation and cell death, all of them key features of CF. Both, *Mabs* S and R replicated more efficiently in CF patient organoids and CF-induced organoids (treated with CFTR inhibitors) compared to the

healthy ones. Remarkably, while Mabs S forms biofilms, Mabs R forms cords and display a higher virulence, further validating the relevance of CF organoids as a model for the study of Mabs pathogenesis. Finally, we exhibited that direct activation of antioxidant pathways, mitigates oxidative stress in CF AOs and synergizes with cefoxitin to control Mabs growth. In conclusion, we demonstrate that the oxidative microenvironment of the CF airway epithelium plays a fundamental role during Mabs colonization.

In this article, of which I am the first author. I performed and/or was involved in all the experiments, as well as in the writing of the manuscript.

This article is under review in Embo Molecular Medicine.

Web link to access the supplementary movies of the paper:
<https://www.biorxiv.org/content/10.1101/2022.01.03.474765v1.supplementary-material>

Main Manuscript for

Human bronchial organoids unveil druggable pathways against *Mycobacterium abscessus* infection in cystic fibrosis

Stephen Adonai Leon-Icaza¹, Salimata Bagayoko¹, Nino Iakobachvili², Chloé Ferrand¹, Talip Aydogan³, Celia Bernard¹, Angelique Sanchez Dafun¹, Marlène Murriss-Espin⁴, Julien Mazières⁴, Pierre Jean Bordignon¹, Serge Mazères¹, Pascale Bernes-Lasserre⁵, Victoria Ramé⁵, Jean-Michel Lagarde⁵, Julien Marcoux¹, Marie Pierre Bousquet¹, Christian Chalut¹, Christophe Guilhot¹, Hans Clevers⁶, Peter J. Peters², Virginie Molle³, Geanncarlo Lugo-Villarino¹, Kaymeuang Cam¹, Laurence Berry³, Etienne Meunier¹, Céline Cougoule^{1*}

¹Institut de Pharmacologie et de Biologie Structurale (IPBS), Université de Toulouse, CNRS, UPS, Toulouse, France

²M4i Nanoscopy Division, Maastricht University, Maastricht, Netherlands

³Laboratory of Pathogen Host Interactions (LPHI), Université Montpellier, CNRS, Montpellier, France

⁴Service de Pneumologie, Hôpital Larrey, CHU de Toulouse, Toulouse, France

⁵Imactiv-3D SAS, 1 Place Pierre POTIER, 31100 Toulouse, France

⁶Oncode Institute, Hubrecht Institute, Royal Netherlands Academy of Arts and Sciences and University Medical Center, Utrecht, Netherlands

*Céline Cougoule, Institut de Pharmacologie et Biologie Structurale (IPBS), Université de Toulouse, CNRS, UPS, Toulouse, France. Email: Celine.Cougoule@ipbs.fr

Author Contributions: Conceptualization and methodology: SALI, SB, NI, CF, TA, M. M-E, JM, P-J.B, CB, ASD, PBL, VR, JML, JM, MPB, CCh, CG, HC, P-J P, G.L-V, VM, KC, LB, EM and CCo; Investigation: SALI, SB, NI, CF, TA, P-J.B, CB, CCh, KC, LB, and CCo. Resources: CG, HC, M. M-E, JM, J-M L., HC, P-J P, VM, LB, EM and CCo; Funding acquisition: P-J P., G L-V, VM, LB, EM and CCo;

Competing Interest Statement:

Stephen Adonai Leon-Icaza has nothing to disclose.

Salimata Bagayoko has nothing to disclose.

Nino Iakobachvili has nothing to disclose.

Chloé Ferrand has nothing to disclose.

Talip Aydogan has nothing to disclose.

Celia Bernard has nothing to disclose.

Angelique Sanchez Dafun has nothing to disclose.

Marlène Murriss-Espin has nothing to disclose.

Julien Mazières reports grants or contracts from Astra Zeneca, Roche and Pierre Fabre; and payment or honoraria for board and expertise (personal and institution) from Merck, Astra Zeneca, BMS, MSD, Roche, Novartis, Daiichi, and Pfizer; outside the submitted work.

Pierre Jean Bordignon has nothing to disclose.

Serge Mazères has nothing to disclose.

Pascale Bernes-Lasserre has nothing to disclose.

Victoria Ramé has nothing to disclose.

Jean-Michel Lagarde has nothing to disclose.

Julien Marcoux has nothing to disclose.

Marie Pierre Bousquet has nothing to disclose.

Christian Chalut has nothing to disclose.

Christophe Guilhot has nothing to disclose.

Hans Clevers reports invention on patents related to organoid research. His full disclosure: [www.uu.nl/staff/JCClevers/Additional function](http://www.uu.nl/staff/JCClevers/Additional%20function).

Peter J. Peters has nothing to disclose.

Virginie Molle has nothing to disclose.

Geanncarlo Lugo-Villarino has nothing to disclose.

Kaymeuang Cam has nothing to disclose.

Laurence Berry has nothing to disclose.

Etienne Meunier has nothing to disclose.

Céline Cougoule has nothing to disclose.

Classification:

Major classification : BIOLOGICAL SCIENCES

Minor classification : Systems Biology

Keywords: Organoids, Lung, Non Tuberculous Mycobacteria, Cystic Fibrosis,

This PDF file includes:

Main Text

Figures 1 to 5

Grant support

This project has been funded by grants from “Vaincre La Mucoviscidose” and “Grégory Lemarchal” foundations (N°RF20210502852/1/1/48) to CC, from the “Fondation pour la Recherche Médicale” (“Amorçage Jeunes Equipes”, AJE20151034460), CNRS ATIP avenir and ERC StG (INFLAME 804249) to EM. SALI was funded by “Vaincre La Mucoviscidose” PhD fellowship (N°RF20210502852/1/1/48). SB was funded by “Fondation pour la Recherche Médicale” PhD fellowship (FDT202106012794). This work was also supported by grants from CNRS (IEA 300134) to CC, Campus France PHC Van Gogh (40577ZE) to GL-V, ZonMW 3R’s (114021005) to PJP, the Nuffic Van Gogh Programme (VGP.17/10 to NI), and by the LINK program from the Province of Limburg, the Netherlands. TA, VM and LB were funded by "La Région Languedoc-Roussillon" (N° DRTE/RSS - ESR_R&S_DF-000061-2018-003268).

Funders had no interference in the conduct of the project.

Abstract

Mycobacterium abscessus (Mabs) drives life-shortening mortality in cystic fibrosis (CF) patients, primarily because of its resistance to chemotherapeutic agents. Both our knowledge on and models to investigate the host and bacterial determinants that drive Mabs pathology in CF patients remain rudimentary. Here, we evaluated whether the lung organoid technology is appropriate for modelling Mabs infection and whether antioxidant treatment is a candidate therapeutic approach in the context of CF disease. We derived airway organoids (AOs) from lung biopsy and microinjected smooth (S-) or rough (R-)Mabs in the lumen of AOs to evaluate its fitness, responses of AOs to infection, and treatment efficacy. We show that S Mabs formed biofilm, R Mabs formed cord serpentine and displayed a higher virulence. While Mabs infection triggers enhanced oxidative stress in AOs, pharmacological activation of antioxidant pathways resulted in better control of Mabs growth. Using CF-patient derived AOs and pharmacological inhibition of the CFTR, we show that S and R Mabs replicated more efficiently and display higher virulence in CF context. Finally, pharmacological activation of antioxidant pathways inhibited Mabs growth and synergized with cefoxitin, a first line antibiotic. In conclusion, we have established AOs as a suitable human system to decipher mechanisms of CF-enhanced respiratory infection by Mabs and confirmed antioxidant approaches as a potential host-directed strategy to improve Mabs infection control.

Significance Statement

This study provided evidence for the relevance of airway organoids as a human 3D system to model cystic fibrosis (CF)-driven infection, the first cause of CF patient lung function failure and death. Our data show that *Mycobacterium abscessus* exhibits both variant phenotype, and thrives in an oxidative stress-dependent manner, enhanced by the CF microenvironment. Our data support the

use of antioxidant to better control Mabs infection and to synergize with current antibiotic treatments.

Introduction

Cystic Fibrosis (CF) is due to mutations in the CF transmembrane conductance regulator (CFTR) gene (1), which regulates ion transport, that impair lung mucociliary clearance and result in pathological triad hallmarks of CF, i.e., chronic airway mucus build-up, sustained inflammation, and microbe trapping leading to parenchyma epithelial cell destruction. The major reason CF patients succumbing to this disease is respiratory failure resulting from chronic lung infection (2).

CF Patients have a greater risk of infection by Non-Tuberculous Mycobacteria (NTM), mainly by the most virulent and drug-resistant NTM *Mycobacterium abscessus* (Mabs) (3, 4). Mabs display two distinct morphotypes based on the presence or absence of glycopeptidolipids (GPL) in their cell wall (5). The smooth (S) GPL-expressing variant forms biofilm and is associated with environmental isolates. The Rough (R) variant does not express GPL, forms cording and induces more aggressive and invasive pulmonary disease, particularly in CF patients (5–7). In CF patients, Mabs colonization is initiated by the infection with the S variant that, over time, switches to the R morphotype by losing or down-regulating surface GPL (8, 9). Although animal models like immunocompromised mice (10), zebrafish (11–13) and *Xenopus laevis* (14) contributed to a significant advance in the understanding of Mabs infection (15), their tissue architecture and cell composition are different from that of humans and do not recapitulate the hallmarks of CF (16–18). Models with anatomical and functional relevance to the human airway and displaying CFTR gene mutations would complement other *in vivo* models.

Recent advances in stem cell biology have allowed the growth of human tissues *in vitro* that resemble organs *in vivo* (19–21). Human airway organoids (AOs) are derived from adult stem cells

present in lung tissues (22), are self-organized 3D structures and share important characteristics with adult bronchiolar part of the human lung (22, 23). Of particular interest, organoids derived from CF patients constitute a unique system to model natural mutations of CFTR and its dysfunctions, thus recapitulating critical aspects of CF in human (22, 24, 25) that are not achievable with other cellular or animal models. AOs have also been adapted for modelling infectious diseases with bacteria, such as *Pseudomonas aeruginosa* (26), with viruses, such as RSV (22) and SARS-CoV-2 (27–29), and with parasites (30). We previously showed that *M. abscessus* thrives in AOs (31) demonstrating that AOs constitute a suitable human system to model mycobacteria infection. Here, we report that both Mabs S and R infect and replicate within AOs and display their specific features, such as forming biofilm and cording, respectively. Moreover, enhanced reactive oxygen species (ROS) production by Mabs infection or the CF context favours Mabs growth, which is reversed by antioxidant treatments, synergizing with antibiotics.

Results

Bronchial airway organoids support S- and R-Mabs replication and phenotype

To investigate whether bronchial airway organoids (AOs) can be used for modelling Mabs infection *in vitro*, we infected AOs with S- and R- Mabs variants as previously described (31). We first quantified bacterial load in AOs overtime by colony forming unit (CFU) (Figure 1A). After a latency phase of 2 days, both Mabs S and R propagated over 12 days. Based on these data, we decided to perform experiments at 4 days post-infection, corresponding to bacteria exponential growth phase. When analysed microscopically, we observed that bacteria mainly reside in the lumen of AOs and did not detect obvious alteration of the architecture of Mabs-infected AOs compared to mock injected AOs (Figure 1B-C, supp fig 1, supp movies 1 & 2). Interestingly, we observed that S bacteria formed aggregates in the lumen of the organoids whereas R variant formed the characteristic

serpentine cords (Figure 1B-C) observed *in vitro* and *in vivo* (32). To further characterize the interaction of Mabs with airway epithelial cells S- and R-Mabs-infected AOs were analysed by SEM and then TEM (Figure 1D). As previously described (22), the organoid epithelium is composed of basal, ciliated and goblet cells (Figure 1D, 1st row). As expected, Mabs S bacilli occupied the organoid lumen, formed chaotically scattered aggregates (Figure 1D, 2nd row) (33). Mabs S preferentially localised in close contact with the apical side of the epithelial cells (Figure 1D, 4), particularly in the presence of cilia (Figure 1D, 3). More importantly, the same samples observed by TEM revealed that S bacteria in the lumen were surrounded by what could be an extracellular polymeric substance (34) (Figure 1D, 5), suggesting that S variant Mabs might form biofilm in the organoid lumen. We convincingly identified Mabs R forming serpentine cords, characterized by aligned bacteria, in the organoid lumen (Figure 1D, 6-8). Importantly, electron microscopy confirmed no significant internalization of Mabs by epithelial cells (31). Finally, we evaluated the virulence of S- and R-Mabs by assessing epithelial cell death. As shown in Figures 1E-F, AOs infected with the R variant exhibited enhanced cell death compared to those infected with the S variant, reflecting R bacteria hypervirulence.

Altogether, our results showed that S and R Mabs variants thrived in AOs and displayed respective features observed in *in vivo* models and in the lung of CF patients.

ROS production contributes to *Mycobacterium abscessus* growth

ROS production is an important antimicrobial process and is enhanced in the CF context (35, 36), we thus evaluated whether oxidative stress played a role in Mabs fitness in AOs. We first evaluated the expression of genes related to the production and detoxification of ROS upon Mabs infection and observed increased expression of oxidases NOX1 and DUOX1, suggesting enhanced ROS production upon Mabs infection. Moreover, we observed overexpression of not only the transcription factor Nrf-2 and the Nrf-2-induced gene NQO-1, denoting Nrf-2 activation, but also detoxifying enzymes

such as superoxide dismutases, PDRX1, and catalase, suggesting activation of cell protective antioxidant pathways (Figure 2A).

To confirm ROS production upon Mabs infection, Mabs-infected AOs were microscopically analysed after incubation with either MitoSOX or H₂DCFDA to detect mitochondrial ROS and H₂O₂ production, respectively. Both S- and R-Mabs infections enhanced the incorporation of MitoSOX and H₂DCFDA (Figures 2B-D), in agreement with the induction of ROS production. Interestingly, productions of mitochondrial ROS and H₂O₂ were higher with the R variant, further confirming R-Mabs hypervirulence compared to S-Mabs in AO.

The contribution of cell protective antioxidant pathways during mycobacterial infection remains poorly understood (37, 38). We then determined the consequence of boosting antioxidant pathways for Mabs fitness. First, we used the anti-oxidant N-acetyl cysteine (NAC) known to exhibit potent anti-mycobacterial effects both through suppression of the host oxidative response and direct antimicrobial activity (39). We found that NAC inhibited Mabs growth both in vitro and in AOs (Supp fig 2A-C). To directly assess the role of host-derived oxidative stress, Mabs-infected AOs were treated with either resveratrol or the Nrf-2 agonist sulforaphane, which reduced S and R variant growth in AOs, without affecting Mabs growth in vitro (Figures 2E-H, Supp fig 2D).

Altogether, the results showed that, independent of the immune system, epithelial cells mounted an oxidative response upon Mabs infection, which contributed to Mabs growth in the human airway microenvironment.

AOs recapitulate hallmarks of cystic fibrosis, and display enhanced oxidative stress

In order to evaluate CF lung context on Mabs infection, we derived AOs from a CF patient who underwent lung transplantation. Characterization of CF versus healthy AOs showed that CF AOs displayed a thicker epithelium (Sup figures 3A-B), abolished swelling in the forskolin assay (Sup figure 3C) denoting CFTR channel malfunction, even stronger than pharmacological inhibition of the

CFTR. Mass spectrometry analysis of CF vs healthy AOs revealed enhanced abundance of mucins MUC5AC and MUC5B (Figure 3A) that was confirmed at the mRNA level and by exacerbated accumulation of mucus in the CF AO lumen (Figures 3B-D, sup Fig. 3D). A gene ontology enrichment study revealed the upregulation of the cellular oxidant detoxification pathway in CF AOs (fold-change 11.6; p-value 3.55e-2; Figure 3E). To further evaluate the oxidative status in the CF context, healthy and CF AOs were stained with MitoSOX or H2DCFDA. The ROS production was enhanced in CF AOs compared to healthy ones (Figures 3F-H), which was further exacerbated after treatment with the oxidative stress inducer tert-Butyl hydroperoxide (tBHP) (40) (Sup fig. 3E). Because high ROS levels induce lipid peroxidation leading to cell death (41–43), we examined and quantified these processes by microscopy using BODIPY (measuring lipid peroxidation) or propidium iodide (measuring cell death) and found that levels of peroxidized lipids (Figures 3I-J) and cell death (Figure 3K, sup Fig. 3F) were higher in CF AOs than in healthy AOs.

Altogether, these results showed that organoids derived from CF lung tissue exhibited not only CFTR dysfunction and exacerbated mucus accumulation but also an increased oxidative stress, therefore representing a suitable *ex vivo* model to investigate how the lung CF context drives Mabs infections.

***Mycobacterium abscessus* takes advantage of CF-driven oxidative stress to thrive**

As oxidative stress is enhanced in CF AOs, we hypothesised that the CF context could favour Mabs growth. To test this hypothesis, we infected CF-AOs with S- or R-Mabs variant and quantified Mabs proliferation. As shown in Figure 4A, the S variant formed aggregates whereas the R variant formed cords in CF AOs. At four days post-infection, we observed an enhanced replication of Mabs in CF-AO compared to in H-AOs (Figure 4B-C), indicating that the CF environment favours Mabs fitness. To support these results, we next used CFTR inhibitors. CFTR inhibitors by themselves did not alter Mabs growth *in vitro* (Supp Fig. 4A). We treated AOs with CFTR inhibitors then infected them with S- and R-Mabs variants and measured bacterial load 4 days post-infection. Treatment of AOs with

CFTR inhibitors enhanced Mabs proliferation compared with untreated organoids (Figure 4D-F), confirming that alteration of CFTR function promoted Mabs growth. Interestingly, Mabs-infected CF-AOs exhibited more epithelial cell death than Mabs-infected H-AOs indicating that CF AOs exhibited higher susceptibility to Mabs infection (Figure 4G-H, sup Fig. 4B).

As oxidative stress favoured Mabs growth and CF-AOs displayed increased ROS production, we next evaluated whether antioxidants inhibited Mabs growth. CF-AOs treated with sulforaphane expressed higher NQO-1, confirming Nrf-2 activation (Supp figure 5A), exhibited mitigated oxidative environment (Figure 5A-B), reduced bacterial load (Figures 5C-D), and epithelial cell death (Figure 5E-F), indicating that CF-driven oxidative stress stimulated Mabs growth and tissue damage.

Finally, we evaluated the potential synergy between cefoxitin, a first line antibiotic to treat Mabs-infected patients, and anti-oxidant. While both cefoxitin and sulforaphane alone significantly inhibited Mabs growth in CF-AOs, combination of both compounds was much more efficient to reduce bacterial load (Figure 5G).

Altogether, these results confirmed that, exuberant oxidative stress, enhanced in the CF context, favoured Mabs fitness, which could be pharmacologically targeted to complement current antibiotic therapies.

Discussion

In this study, we evaluate the pertinence of human AOs to model Mabs infection in the context of CF. We show that both S- and R-morphotypes of *M. abscessus* proliferate and exhibit infection hallmarks in AOs. Moreover, AOs derived from a CF patient recapitulate key features of CF disease. Finally, we demonstrate that antioxidant pathway boosting as a potential complementary therapeutic strategy to current antibiotic treatment to better control *Mabs* infection in CF patients.

Therefore, AOs are suitable to model both CF disease and Mabs infection, opening new venues for deciphering critical relevant host pathways and identifying new potential therapeutic intervention. We and others have already applied the organoid technology to model host-pathogen interactions (22, 26, 30, 31, 44, 45). Here, we have reproduced Mabs infection hallmarks in AOs. Specifically, we show that both S- and R-Mabs replicate in AOs, that S variants are surrounded by an extracellular substance resembling a biofilm, and that the R variant forms serpentine cords associated with higher virulence, in agreement with reported *in vivo* Mabs R hypervirulence compared to Mabs S (5–7). Although Mabs R form characteristic cords *in vitro* and *in vivo* (32, 46), visualizing bacterial biofilm remains a challenge, especially in *ex vivo* and *in vivo* settings. The formation of biofilm plays a crucial role in establishing an infection and at protecting bacilli from immune response and antimicrobial agents, leading to treatment failure (47, 48). Therefore, the detection of biofilm in Mabs S-infected AOs opens new venues to not only testing potential anti-biofilm compounds but also further investigating how the CF lung context favours biofilm formation (47, 49).

ROS production is a part of host antimicrobial defence but requires a fine-tuned balance to prevent tissue damage. Indeed, during Mabs infection, the production of ROS is essential to control infection, as knock-down of NOX2, expressed in immune cells, resulted in uncontrolled bacteria proliferation in zebrafish and mouse models (12, 50). Here, we show that Mabs infection of AOs triggers ROS production through enhanced expression of host ROS production genes NOX1 and DUOX1 concomitantly to enhanced expression of the Nrf2-mediated antioxidant pathway. In alveolar macrophages, Nrf2 deficiency results in a better control of Mtb infection (37), indicating that early activation of cell protective pathways impairs the control of mycobacteria. By contrast, an oxidative environment has been shown to favour Mabs growth in macrophages (51, 52). Moreover, activation of Nrf2 reduces the bacterial burden both *in vitro* and *in vivo* (38, 53–55). Finally, apart from its direct antimicrobial effect, the antioxidant N-acetyl cysteine has been shown

to inhibit Mtb growth in macrophages and in infected mice (39). Consistently, we show here that treatment of Mabs-infected AOs with resveratrol or sulforaphane results in a better control of bacteria growth. Because resveratrol and sulforaphane do not inhibit Mabs growth *in vitro*, our results indicate that ROS production by epithelial cells is sufficient to generate a permissive environment for Mabs proliferation. Even in the absence of immune cells and low bacteria internalization by epithelial cells (31), AOs recapitulate the contribution of host oxidative stress in bacteria fitness in the airway.

The organoid technology has demonstrated its usefulness in developing potential therapies for treating CF (56, 57). CF patient-derived organoids bear natural CFTR mutations, thus allowing to recapitulate *ex vivo* the spectrum of CFTR dysfunctions and CF disease severities (24, 58). Extended to the airway, CF patient-derived AOs have been shown to display epithelium hyperplasia, luminal mucus accumulation and abrogated response to forskolin-induced swelling, thus recapitulating CFTR dysfunction and consequences on the airway homeostasis (22). Here, we derived an AO line from a CF patient carrying class I mutations, which lead to the most severe manifestation of CF disease (59). These CF AOs reproduce the expected epithelium hyperplasia, mucus accumulation and defective response to forskolin-induced swelling. Moreover, these CF AOs display enhanced oxidative stress and lipid peroxidation, as previously measured in CF patients (35, 36) or *in vitro* in CFTR mutated cell lines (60), as well as enhanced cell death recapitulating CF-driven tissue damage. Therefore, AOs derived from CF patients also recapitulate the CF-driven imbalance in oxidant/antioxidant status observed in patients and, importantly, demonstrate that CFTR dysfunction in epithelial cells is sufficient to cause the oxidative status imbalance in the airway epithelium, independent of immune cells.

Finally, using both AOs derived from a CF patient and CFTR pharmacological inhibition, we show that CF microenvironment favours the multiplication of Mabs associated with enhanced cell death,

recapitulating the higher susceptibility of CF patients to NTM infection (61, 62). Cumulative oxidative stress due to both the CF context and Mabs infection might result in a permissive environment for bacteria growth and the establishment of chronic infection in the lung of CF patients. Interestingly, CF is associated with a defective Nrf2 expression, which contributes to the excessive oxidative stress and lung tissue damage, whereas CFTR modulators rescue Nrf2 function and therefore improve tissue oxidative status (63), which might contribute to a better control of bacterial infection. Indeed, CF AOs treated with sulforaphane have reduced oxidative stress, tissue damage, and better control of Mabs growth, indicating that activation of Nrf2 can constitute a complementary therapeutic strategy to improve tissue redox homeostasis and better infection control by synergizing with current antibiotic treatment as we observed here with cefoxitin. Further investigation are required to integrate ROS production by immune cells. Interestingly, treating R Mabs-infected zebrafishes with resveratrol improves fish survival and reduces bacterial load (54), indicating that modulating the global host redox status improves Mabs infection control.

A limitation of our study is that only one CF patient-derived organoid line has been used. This CF AO line bears class I mutations that lead to the most severe form of CF disease. As a complementary approach, we also observe better bacteria growth by using CFTR inhibitors to partially alter the CFTR function indicating that this phenotype can also be observed with partially impaired CFTR function as seen with other classes of CFTR mutations. Nevertheless, establishing CF AO lines carrying a wide range of CFTR mutations might be facilitated by emerging protocols (64) and would constitute precious tools to further model the full spectrum of CF disease severity, susceptibility to infection and potential of host-directed therapies targeting oxidative stress on tissue damage (26) and bacteria fitness.

In conclusion, we have established AOs as a pertinent model of both CF airway dysfunction and susceptibility to NTM infection. Moreover, we have identified the cell protective Nrf2 pathway as a

potential therapeutic target to restore CF tissue redox homeostasis and improve the control of bacteria growth, opening promising venues to further decipher CF airway dysfunction and susceptibility to infection.

Materials and Methods

Detailed protocols are provided in the supplement.

Ethic statements: The collection of patient data and tissue for AO generation was performed according to the guidelines of the European Network of Research Ethics Committees following European and national law. The accredited ethical committee reviewed and approved the study in accordance with the Medical Research Involving Human Subjects Act. Human lung tissue was provided by the CHU of Toulouse under protocol agreement (CHU 19 244 C and Ref CNRS 205782). All patients participating in this study consented to scientific use of their material; patients can withdraw their consent at any time, leading to the prompt disposal of their tissue and any derived material.

Airway organoid culture and maintenance

Healthy adjacent tissue from donors with lung cancer, and lung biopsy of a cystic fibrosis heterozygous patient (G542X/1811+1.6kbA-->G) were used to derive organoids as previously described with minor changes (22, 31). To prevent risk of culture contamination, airway organoid complete media was supplemented with 10 $\mu\text{g ml}^{-1}$ Normocure (InvivoGen) and 2.5 $\mu\text{g ml}^{-1}$ Fungin (InvivoGen) during the first 4 weeks of the cystic fibrosis airway organoid culture.

Bacteria culture and organoid infection

Mycobacterium abscessus sensu stricto strain CIP104536T (ATCC19977T) morphotype S and R were grown as previously described (32). Before infection, AO were pretreated or no with 10 μM of Resveratrol (Sigma-Aldrich) or Sulforaphane (Selleck Chemicals, Houston, TX, USA) for 1hr or 6hr

respectively. Bacteria were prepared for microinjection as described (31, 65) and bacterial density was adjusted to $OD_{600} = 0.1-0.4$. Injected organoids were individually collected, washed in PBS 1x and embedded into fresh matrix. Injected organoids were cultured for 3-4 day if not stated otherwise. Both antioxidants were maintained throughout the experiment and refreshed every two days. Where indicated, 20 μ g/ml of cefoxitin (Sigma-Aldrich) was added with or without sulforaphane.

RT-qPCR and Colony forming unit assay

Organoids were collected at day 4 post-infection or stimulation and processed as reported (31). Primer sequences are provided in supplementary Table S1.

Microscopy

Assessing CFTR function was performed by forskolin-induced organoid swelling assay as described (66). Live imaging was performed to quantify mucus accumulation with Zinpyr-1 (Santa Cruz Biotechnology), ROS levels by H2DCFDA (Invitrogen) or MitoSOX (Thermo Scientific), lipid peroxidation by BODIPY (Thermo Scientific) and cell death with Propidium Iodide (Thermo Scientific) in non-infected and Mabs-infected organoids. Images were acquired under an EVOS M7000 Imaging System and analyzed post-acquisition with Fiji/ImageJ.

For scanning electron microscopy (SEM) and transmission electron microscopy (TEM), organoids were fixed in 2% paraformaldehyde (EMS, Hatfield, PA, USA), 2.5% glutaraldehyde (EMS) and 0.1 M Sodium Cacodylate (EMS). Samples were embedding in Durcupan ACM resin (Sigma-Aldrich) then, semi-thin (300nm) serial sections were made using an UC7 ultramicrotome (Leica, Wetzlar, Germany) and collected on silicon wafers (Ted Pella, Redding, CA, USA). Sections were imaged on a Quanta FEG 250 SEM microscope in BSE mode. Ultrathin sections were also collected on copper grids formvar coated for TEM analysis on a JEOL 1200 EXE II microscope.

For Lightsheet imaging, fixed (overnight in 4% paraformaldehyde) airway organoids were stained with propidium iodide (6µg/ml in PBS) for 30 minutes at room temperature then rinsed in PBS.

Organoids were then embedded in 1% low-melting agarose inside glass capillaries and imaged in PBS using a light-sheet fluorescence microscope (Zeiss Lightsheet Z.1). The 3D reconstructions were performed with Amira software (v2020.2).

Statistics

Statistical analyses were performed using Prism 8 and 5 (GraphPad Software). Data were compared by Mann-Whitney or unpaired T test and results reported as mean with SD. Data statistically significant was represented by *P<0.05; **P<0.01; ***P<0.001 and **** P<0.0001.

Acknowledgments

We thank Nicole Schieber (EMBL Heidelberg, Germany) for sharing with us the embedding protocol.

We thank Veronique Richard and Franck Godiard from the “Microscopie Electronique et Analytique” service of the University of Montpellier for assistance in ultramicrotomy and TEM, respectively. We

thank Bruno Payre from the “Centre de Microscopie Electronique pour la Biologie” of the University of Toulouse 3 for his assistance in SEM. This manuscript was edited at Life Science Editors.

References

1. M. C. Dehecchi, A. Tamanini, G. Cabrini, Molecular basis of cystic fibrosis: from bench to bedside. *Ann. Transl. Med.* **6**, 334–334 (2018).
2. M. Lopes-Pacheco, CFTR Modulators: The Changing Face of Cystic Fibrosis in the Era of Precision Medicine. *Front. Pharmacol.* **10**, 1662 (2020).
3. R. C. Lopeman, J. Harrison, M. Desai, J. A. G. Cox, Mycobacterium abscessus: Environmental bacterium turned clinical nightmare. *Microorganisms* **7** (2019).

4. W. J. Koh, J. E. Stout, W. W. Yew, Advances in the management of pulmonary disease due to Mycobacterium abscessus complex. *Int. J. Tuberc. Lung Dis.* **18**, 1141–1148 (2014).
5. M. D. Johansen, J.-L. Herrmann, L. Kremer, Non-tuberculous mycobacteria and the rise of Mycobacterium abscessus. *Nat. Rev. Microbiol.* **2020** *187* **18**, 392–407 (2020).
6. G. Clary, *et al.*, Mycobacterium abscessus smooth and rough morphotypes form antimicrobial-tolerant biofilm phenotypes but are killed by acetic acid. *Antimicrob. Agents Chemother.* **62** (2018).
7. A. V. Gutiérrez, A. Viljoen, E. Ghigo, J.-L. Herrmann, L. Kremer, Glycopeptidolipids, a Double-Edged Sword of the Mycobacterium abscessus Complex. *Front. Microbiol.* **9**, 1145 (2018).
8. K. To, R. Cao, A. Yegiazaryan, J. Owens, V. Venketaraman, General Overview of Nontuberculous Mycobacteria Opportunistic Pathogens: Mycobacterium avium and Mycobacterium abscessus. *J. Clin. Med.* **9**, 1–24 (2020).
9. B. E. Jönsson, *et al.*, Molecular Epidemiology of Mycobacterium abscessus, with Focus on Cystic Fibrosis. *J. Clin. Microbiol.* **45**, 1497 (2007).
10. V. Le Moigne, *et al.*, Efficacy of bedaquiline, alone or in combination with imipenem, against Mycobacterium abscessus in C3HeB/FeJ mice. *Antimicrob. Agents Chemother.* (2020) <https://doi.org/10.1128/AAC.00114-20>.
11. A. Bernut, *et al.*, In Vivo assessment of drug efficacy against Mycobacterium abscessus using the embryonic zebrafish test system. *Antimicrob. Agents Chemother.* **58**, 4054–4063 (2014).
12. A. Bernut, *et al.*, CFTR Protects against Mycobacterium abscessus Infection by Fine-Tuning Host Oxidative Defenses. *Cell Rep.* **26**, 1828-1840.e4 (2019).
13. A. L. Lefebvre, *et al.*, Inhibition of the β -lactamase BlaMab by avibactam improves the in vitro and in vivo efficacy of imipenem against Mycobacterium abscessus. *Antimicrob. Agents Chemother.* **61** (2017).

14. A. Lopez, *et al.*, Developing tadpole xenopus laevis as a comparative animal model to study Mycobacterium abscessus pathogenicity. *Int. J. Mol. Sci.* **22**, 1–12 (2021).
15. A. Bernut, J.-L. Herrmann, D. Ordway, L. Kremer, The Diverse Cellular and Animal Models to Decipher the Physiopathological Traits of Mycobacterium abscessus Infection. *Front. Cell. Infect. Microbiol.* **7**, 100 (2017).
16. A. McCarron, D. Parsons, M. Donnelley, Animal and Cell Culture Models for Cystic Fibrosis: Which Model Is Right for Your Application? *Am. J. Pathol.* **191**, 228–242 (2021).
17. A. McCarron, M. Donnelley, D. Parsons, Airway disease phenotypes in animal models of cystic fibrosis. *Respir. Res.* **19**, 1–12 (2018).
18. A. Semaniakou, R. P. Croll, V. Chappe, Animal Models in the Pathophysiology of Cystic Fibrosis. *Front. Pharmacol.* **9** (2018).
19. F. Schutgens, H. Clevers, Human Organoids: Tools for Understanding Biology and Treating Diseases. *Annu. Rev. Pathol.* **15**, 211–234 (2020).
20. J. Kim, B. K. Koo, J. A. Knoblich, Human organoids: model systems for human biology and medicine. *Nat. Rev. Mol. Cell Biol.* **2020 2110** **21**, 571–584 (2020).
21. H. Clevers, Modeling Development and Disease with Organoids. *Cell* **165**, 1586–1597 (2016).
22. N. Sachs, *et al.*, Long-term expanding human airway organoids for disease modeling. *EMBO J.* **38** (2019).
23. N. Iakobachvili, P. J. Peters, Humans in a dish: The potential of organoids in modeling immunity and infectious diseases. *Front. Microbiol.* **8** (2017).
24. K. M. de Winter – de Groot, *et al.*, Forskolin-induced swelling of intestinal organoids correlates with disease severity in adults with cystic fibrosis and homozygous F508del mutations. *J. Cyst. Fibros.* **19**, 614–619 (2020).
25. J. F. Dekkers, *et al.*, Characterizing responses to CFTR-modulating drugs using rectal

- organoids derived from subjects with cystic fibrosis. *Sci. Transl. Med.* **8**, 344ra84-344ra84 (2016).
26. S. Bagayoko, *et al.*, Host phospholipid peroxidation fuels ExoU-dependent cell necrosis and supports *Pseudomonas aeruginosa*-driven pathology. *PLoS Pathog.* **17** (2021).
 27. G. S. Kronemberger, F. A. Carneiro, D. F. Rezende, L. S. Baptista, Spheroids and organoids as humanized 3D scaffold-free engineered tissues for SARS-CoV-2 viral infection and drug screening. *Artif. Organs* (2021) <https://doi.org/10.1111/aor.13880>.
 28. A. Z. Mykytyn, *et al.*, Sars-cov-2 entry into human airway organoids is serine protease-mediated and facilitated by the multibasic cleavage site. *Elife* **10**, 1–23 (2021).
 29. Y. Han, *et al.*, Identification of SARS-CoV-2 inhibitors using lung and colonic organoids. *Nature* **589**, 270–275 (2021).
 30. I. Heo, *et al.*, Modelling *Cryptosporidium* infection in human small intestinal and lung organoids. *Nat. Microbiol.* **3**, 814–823 (2018).
 31. N. Iakobachvili, *et al.*, Mycobacteria-host interactions in human bronchiolar airway organoids. *Mol. Microbiol.* **00**, 1–11 (2021).
 32. A. Bernut, *et al.*, Mycobacterium abscessus cording prevents phagocytosis and promotes abscess formation. *Proc. Natl. Acad. Sci. U. S. A.* **111**, E943–E952 (2014).
 33. L. B. Davidson, R. Nessar, P. Kempaiah, D. J. Perkins, T. F. Byrd, Mycobacterium abscessus Glycopeptidolipid Prevents Respiratory Epithelial TLR2 Signaling as Measured by H β D2 Gene Expression and IL-8 Release. *PLoS One* **6**, e29148 (2011).
 34. J. McCutcheon, G. Southam, Advanced biofilm staining techniques for TEM and SEM in geomicrobiology: Implications for visualizing EPS architecture, mineral nucleation, and microfossil generation. *Chem. Geol.* **498**, 115–127 (2018).
 35. B. M. Winkelhofer-Roob, Oxygen free radicals and antioxidants in cystic fibrosis: the concept

- of an oxidant-antioxidant imbalance. *Acta Paediatr. Suppl.* **83**, 49–57 (1994).
36. A. J. Causer, *et al.*, Circulating biomarkers of antioxidant status and oxidative stress in people with cystic fibrosis: A systematic review and meta-analysis. *Redox Biol.* **32** (2020).
 37. A. C. Rothchild, *et al.*, Alveolar macrophages generate a noncanonical NRF2-driven transcriptional response to *Mycobacterium tuberculosis* in vivo. *Sci. Immunol.* **4** (2019).
 38. M. Nakajima, *et al.*, Nrf2 regulates granuloma formation and macrophage activation during *mycobacterium avium* infection via mediating nramp1 and ho-1 expressions. *MBio* **12**, 1–17 (2021).
 39. E. P. Amaral, *et al.*, N-acetyl-cysteine exhibits potent anti-mycobacterial activity in addition to its known anti-oxidative functions. *BMC Microbiol.* **16**, 1–10 (2016).
 40. R. E. Koch, G. E. Hill, An assessment of techniques to manipulate oxidative stress in animals. *Funct. Ecol.* **31**, 9–21 (2017).
 41. H. Benabdeslam, *et al.*, Lipid peroxidation and antioxidant defenses in cystic fibrosis patients. *Clin. Chem. Lab. Med.* **37**, 511–516 (1999).
 42. L. J. Su, *et al.*, Reactive Oxygen Species-Induced Lipid Peroxidation in Apoptosis, Autophagy, and Ferroptosis. *Oxid. Med. Cell. Longev.* **2019** (2019).
 43. C. A. Juan, J. M. P. de la Lastra, F. J. Plou, E. Pérez-Lebeña, The Chemistry of Reactive Oxygen Species (ROS) Revisited: Outlining Their Role in Biological Macromolecules (DNA, Lipids and Proteins) and Induced Pathologies. *Int. J. Mol. Sci.* **22**, 4642 (2021).
 44. M. M. Lamers, *et al.*, An organoid-derived bronchioalveolar model for SARS-CoV-2 infection of human alveolar type II-like cells. *EMBO J.* **40**, e105912 (2021).
 45. J. Zhou, *et al.*, Differentiated human airway organoids to assess infectivity of emerging influenza virus. *Proc. Natl. Acad. Sci. U. S. A.* **115**, 6822–6827 (2018).
 46. A. L. Roux, *et al.*, The distinct fate of smooth and rough *Mycobacterium abscessus* variants

inside macrophages. *Open Biol.* **6** (2016).

47. P. Chakraborty, S. Bajeli, D. Kaushal, B. D. Radotra, A. Kumar, Biofilm formation in the lung contributes to virulence and drug tolerance of *Mycobacterium tuberculosis*. *Nat. Commun.* **12** (2021).
48. J. Esteban, M. García-Coca, *Mycobacterium* Biofilms. *Front. Microbiol.* **8** (2018).
49. T. Bjarnsholt, The role of bacterial biofilms in chronic infections. *APMIS. Suppl.*, 1–51 (2013).
50. W. C. Chao, *et al.*, *Mycobacterial* infection induces higher interleukin-1 β and dysregulated lung inflammation in mice with defective leukocyte NADPH oxidase. *PLoS One* **12** (2017).
51. B. R. Kim, B. J. Kim, Y. H. Kook, B. J. Kim, *Mycobacterium* abscessus infection leads to enhanced production of type 1 interferon and NLRP3 inflammasome activation in murine macrophages via mitochondrial oxidative stress. *PLoS Pathog.* **16** (2020).
52. R. E. Oberley-Deegan, *et al.*, An oxidative environment promotes growth of *Mycobacterium abscessus*. *Free Radic. Biol. Med.* **49**, 1666–1673 (2010).
53. M. Bonay, *et al.*, Caspase-independent apoptosis in infected macrophages triggered by sulforaphane via Nrf2/p38 signaling pathways. *Cell Death Discov.* **1**, 1 (2015).
54. Y. J. Kim, *et al.*, Sirtuin 3 is essential for host defense against *Mycobacterium abscessus* infection through regulation of mitochondrial homeostasis. *Virulence* **11**, 1225–1239 (2020).
55. Q. Sun, X. Shen, J. Ma, H. Lou, Q. Zhang, Activation of Nrf2 signaling by oltipraz inhibits death of human macrophages with *Mycobacterium tuberculosis* infection. *Biochem. Biophys. Res. Commun.* **531**, 312–319 (2020).
56. S. Y. Graeber, *et al.*, Comparison of Organoid Swelling and In Vivo Biomarkers of CFTR Function to Determine Effects of Lumacaftor-Ivacaftor in Patients with Cystic Fibrosis Homozygous for the F508del Mutation. *Am. J. Respir. Crit. Care Med.* **202**, 1589–1592 (2020).
57. J. D. Anderson, Z. Liu, L. V. Odom, L. Kersh, J. S. Guimbellot, CFTR function and clinical

- response to modulators parallel nasal epithelial organoid swelling. *Am. J. Physiol. Lung Cell. Mol. Physiol.* **321**, L119–L129 (2021).
58. K. M. de Winter-De Groot, *et al.*, Stratifying infants with cystic fibrosis for disease severity using intestinal organoid swelling as a biomarker of CFTR function. *Eur. Respir. J.* **52** (2018).
59. M. P. Reboul, *et al.*, Splice mutation 1811+1.6kbA>G causes severe cystic fibrosis with pancreatic insufficiency: report of 11 compound heterozygous and two homozygous patients. *J. Med. Genet.* **39** (2002).
60. L. de Bari, *et al.*, Aberrant GSH reductase and NOX activities concur with defective CFTR to pro-oxidative imbalance in cystic fibrosis airways. *J. Bioenerg. Biomembr.* **50**, 117–129 (2018).
61. B. S. Furukawa, P. A. Flume, Nontuberculous Mycobacteria in Cystic Fibrosis. *Semin. Respir. Crit. Care Med.* **39**, 383–391 (2018).
62. T. Qvist, *et al.*, Comparing the harmful effects of nontuberculous mycobacteria and Gram negative bacteria on lung function in patients with cystic fibrosis. *J. Cyst. Fibros.* **15**, 380–385 (2016).
63. D. C. Borchering, *et al.*, Clinically approved CFTR modulators rescue Nrf2 dysfunction in cystic fibrosis airway epithelia. *J. Clin. Invest.* **129**, 3448–3463 (2019).
64. J. van der Vaart, *et al.*, Modelling of primary ciliary dyskinesia using patient-derived airway organoids. *EMBO Rep.* **22** (2021).
65. C. Lastrucci, *et al.*, Tuberculosis is associated with expansion of a motile, permissive and immunomodulatory CD16(+) monocyte population via the IL-10/STAT3 axis. *Cell Res.* **25**, 1333–1351 (2015).
66. S. F. Boj, *et al.*, Forskolin-induced Swelling in Intestinal Organoids: An In Vitro Assay for Assessing Drug Response in Cystic Fibrosis Patients. *J. Vis. Exp.* **2017** (2017).

Figures

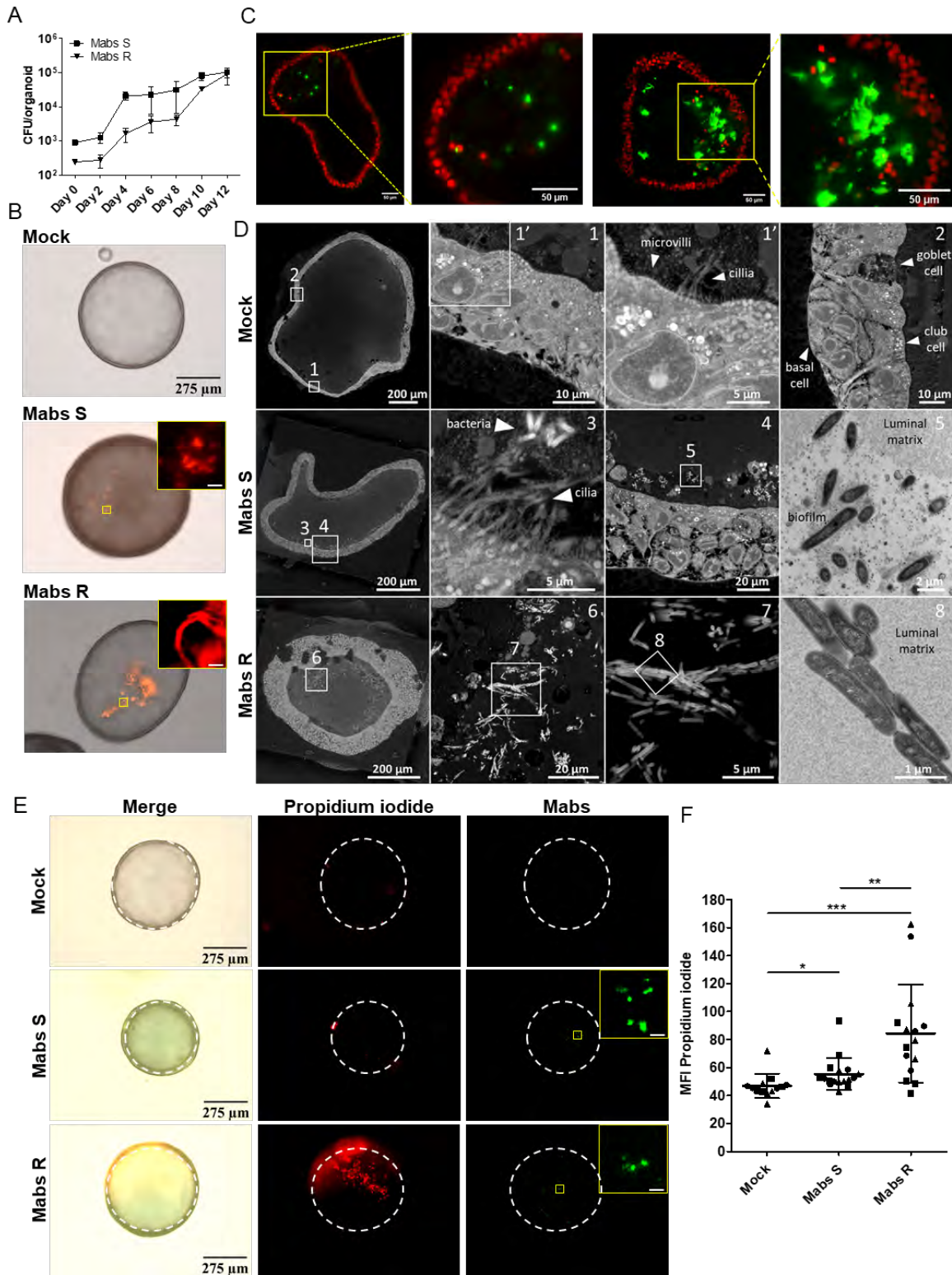


Figure 1. Mabs infection in airway organoids. (A) Kinetics of Mabs S and R growth in AOs. Graph shows three pooled independent experiments. (B) Representative images of a mock (PBS) infected AO or AOs infected with tdTomato-expressing Mabs S or R. (C) Light-sheet fluorescence microscopy of a XY plane at the $z=120\mu\text{m}$ (left two images) or $z=80\mu\text{m}$ (right two images) positions of a AO infected with Mabs S and R, respectively; Zoom-in image of the yellow square zone. (D) Electron micrographs obtained with a FEI Quanta200 scanning electron microscope set up in back-scattered mode. Resin blocks were sectioned and imaged at different magnifications showing normal AO organization and the different cell types typical of lung epithelium (top row), the biofilm formed by Mabs S on the luminal face of the epithelial cells (middle row), and the bacterial aggregates typical of the cording in the lumen of Mabs R infected AOs (bottom row). Targeted ultrathin sections were made and observed by transmission electron microscopy (images 5 and 8). (E, F) Representative images (E) and MFI quantification (F) of propidium iodide incorporation in mock infected AOs ($n=13$) or AOs infected with Wasabi-expressing Mabs S ($n=17$) or R ($n=15$) for 4 days. The dotted lines delimit the organoids circumference. Graph represents means \pm SD from three independent experiments, indicated by different symbols. Each dot represents one organoid. * $P<0.05$; ** $P<0.01$; *** $P<0.001$ by Mann-Whitney test.

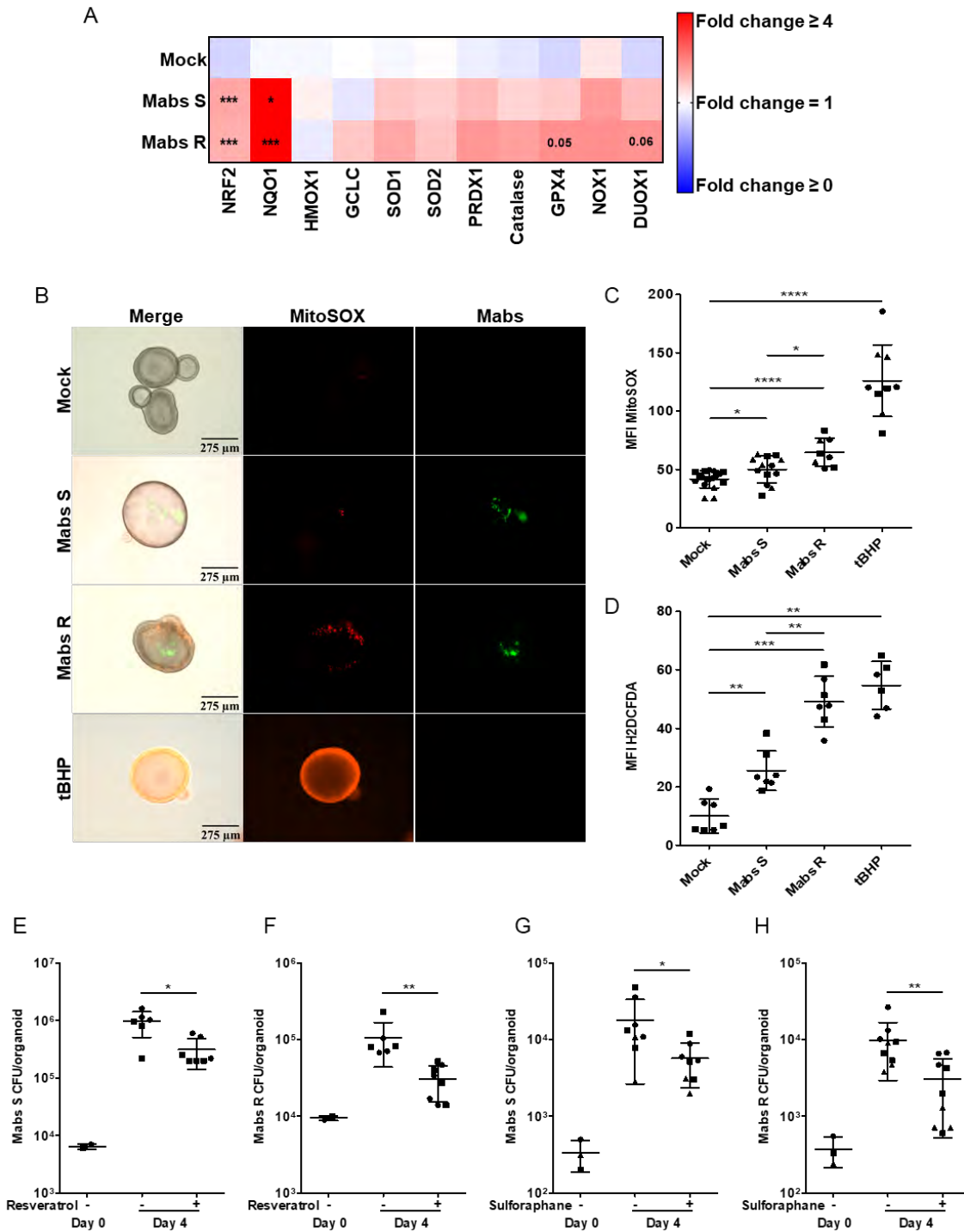


Figure 2. Mabs promote an oxidative environment in airway organoids. (A) Heatmap depicting ROS-related genes in mock-infected H-AO or H-AO infected with Mabs S or R for 4 days. Heatmap represents means from three independent experiments, performed in triplicates. * $P < 0.05$;

P<0.001 by unpaired T test. (B, C) Representative images (B) and MFI quantification (C) of mitochondrial ROS production (MitoSOX) in mock-infected H-AOs (n=17) or H-AO infected with Wasabi-labelled Mabs S (n=13) or R (n=8) for 3 days. (D) MFI quantification of H₂O₂ production (H2DCFDA) in mock-infected AOs (n=7) or AO infected with tdTomato-labelled Mabs S (n=7) or R (n=7) for 3 days. (E, F) Bacterial load by CFU assay of AOs pre-treated with (+) or without (-) resveratrol for 1hr before infection with Mabs S (E) (n+= 7; n-=6) or R (F) (n+= 8; n-=6) for 4 days. (G, H) Bacterial load by CFU assay of H-AO pre-treated with (+) or without (-) sulforaphane for 6hr before infection with Mabs S (G) (n+= 8; n-=8) or R (H) (n+= 9; n-=9) for 4 days. Except otherwise stated, graphs represent means ± SD from at least two independent experiments, indicated by different symbols. Each dot represents one organoid. *P<0.05; **P<0.01; ***P<0.001, * P<0.0001 by Mann-Whitney test.

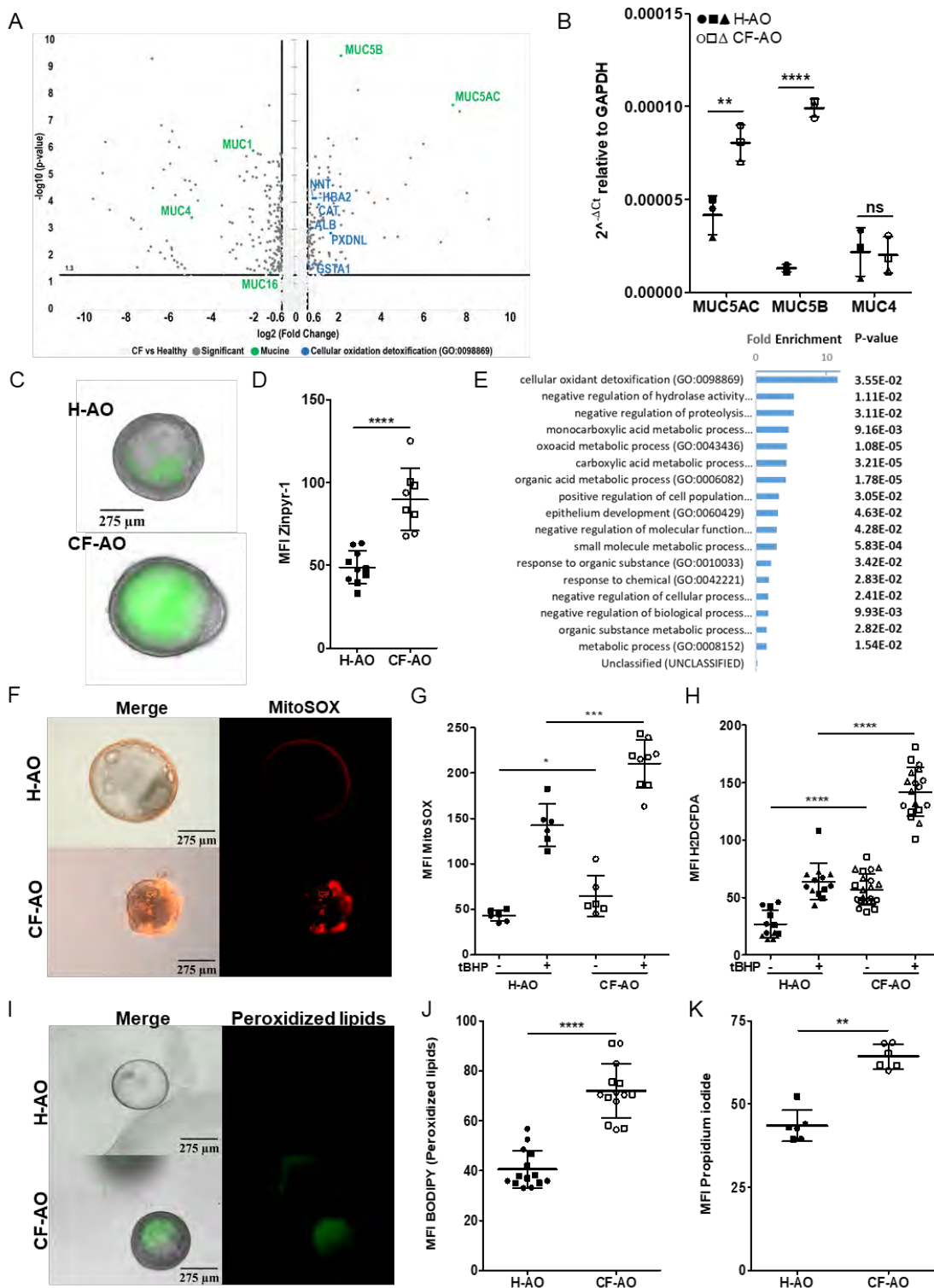


Figure 3. Patient-derived airway organoids recapitulate Cystic fibrosis-driven oxidative stress. (A)

The volcano plot showing the fold-change (x-axis) versus the significance (y-axis) of the proteins

identified by LC–MS/MS in CF-AOs vs in H-AOs. The significance (non-adjusted p-value) and the fold-change are converted to $-\text{Log}_{10}(\text{p-value})$ and $\text{Log}_2(\text{fold-change})$, respectively. (B) Basal expression of mucin genes in H-AO and CF-AO. Graph represents means from three pooled independent experiments, performed in triplicates. ** $P < 0.01$; **** $P < 0.0001$; ns= not significant by unpaired T test. (C, D) Representative images (C) and Mean Fluorescence Intensity (MFI) quantification (D) of mucus staining (Zinpyr-1) in H-AO (n=10) and CF-AO (n=8). (E) Gene Ontology enrichment analysis showing the most enriched Biological Processes and their associated p-values (calculated using the Bonferroni correction for multiple testing) related to the list of up-regulated proteins in CF patients compared to healthy ones. (F, G) Representative images (F) and MFI quantification (G) of basal mitochondrial ROS production (MitoSOX) in H-AO (n=6) and CF-AO (n=6). (H) MFI quantification of basal H_2O_2 production (H2DCFDA) in H-AO (n=12) and CF-AO (n=22). (I, J) Representative images (I) and MFI quantification (J) of peroxidized lipids (BODIPY) in H-AO (n=14) and CF-AO (n=14). (K) MFI quantification of the basal plasma membrane permeabilization (propidium iodide incorporation) in H-AO (n=6) and CF-AO (n=6). Except otherwise noted, graphs represent means \pm SD from at least two independent experiments indicated by different symbols. Each dot represents one organoid. * $P < 0.05$; ** $P < 0.01$; *** $P < 0.001$, **** $P < 0.0001$ by Mann-Whitney test.

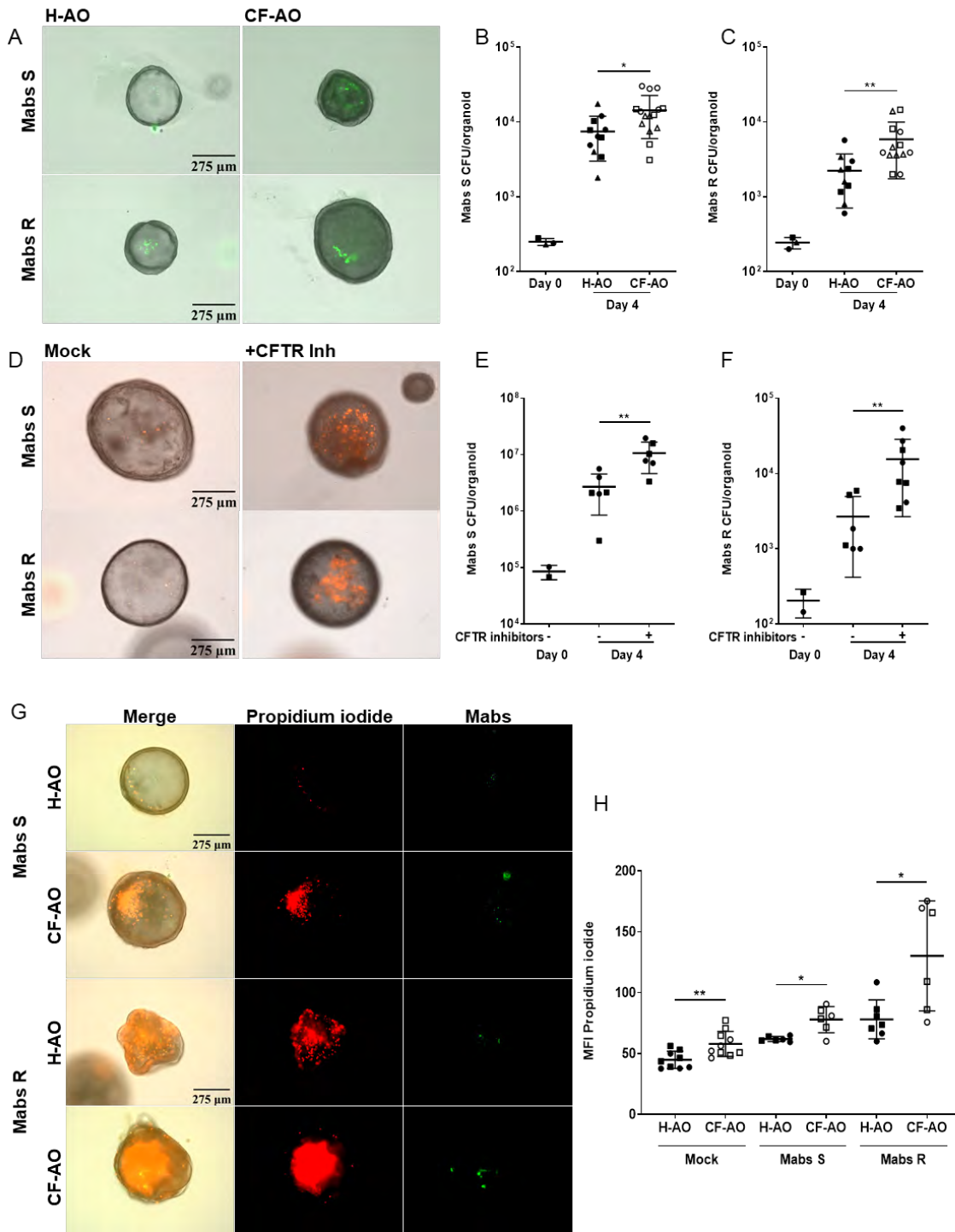


Figure 4. Oxidative stress in cystic fibrosis benefits Mabs growth. (A) Representative images of Wasabi-labelled Mabs S or R 4 days-infected H-AO and CF-AO. (B, C) Bacterial load by CFU assay of H-AO and CF-AO infected for 4 days with Mabs S (B) (n healthy=11; n cystic fibrosis=15) or R (C) (n

healthy=10; n cystic fibrosis=13). (D) Representative images of Mabs S or R (tdTomato) 4 days-infected H-AO. Before infection, H-AO were pre-treated or not for 2 days with CFTR inhibitors (CFTRinh-172 and GlyH 101). (E, F) H-AO were pre-treated (+) or not (-) for 2 days with CFTR inhibitors before infection with (E) Mabs S (n+=6; n-=6) or (F) Mabs R (n+=8; n-=6). After 4 days, bacterial load per organoid was assessed by CFU assay. (G, H) Representative images (G) and MFI quantification (H) of propidium iodide incorporation in Mock-infected H-AO and CF-AO (n healthy= 9; n cystic fibrosis= 10) or H-AO and CF-AO infected with Wasabi-labelled Mabs S (n healthy= 6; n cystic fibrosis= 6) or Mabs R (n healthy= 7; n cystic fibrosis= 6) for 4 days. Except otherwise stated, graphs represent means \pm SD from at least two independent experiments indicated by different symbols. Each dot represents one organoid. *P<0.05; **P<0.01 by Mann-Whitney test.

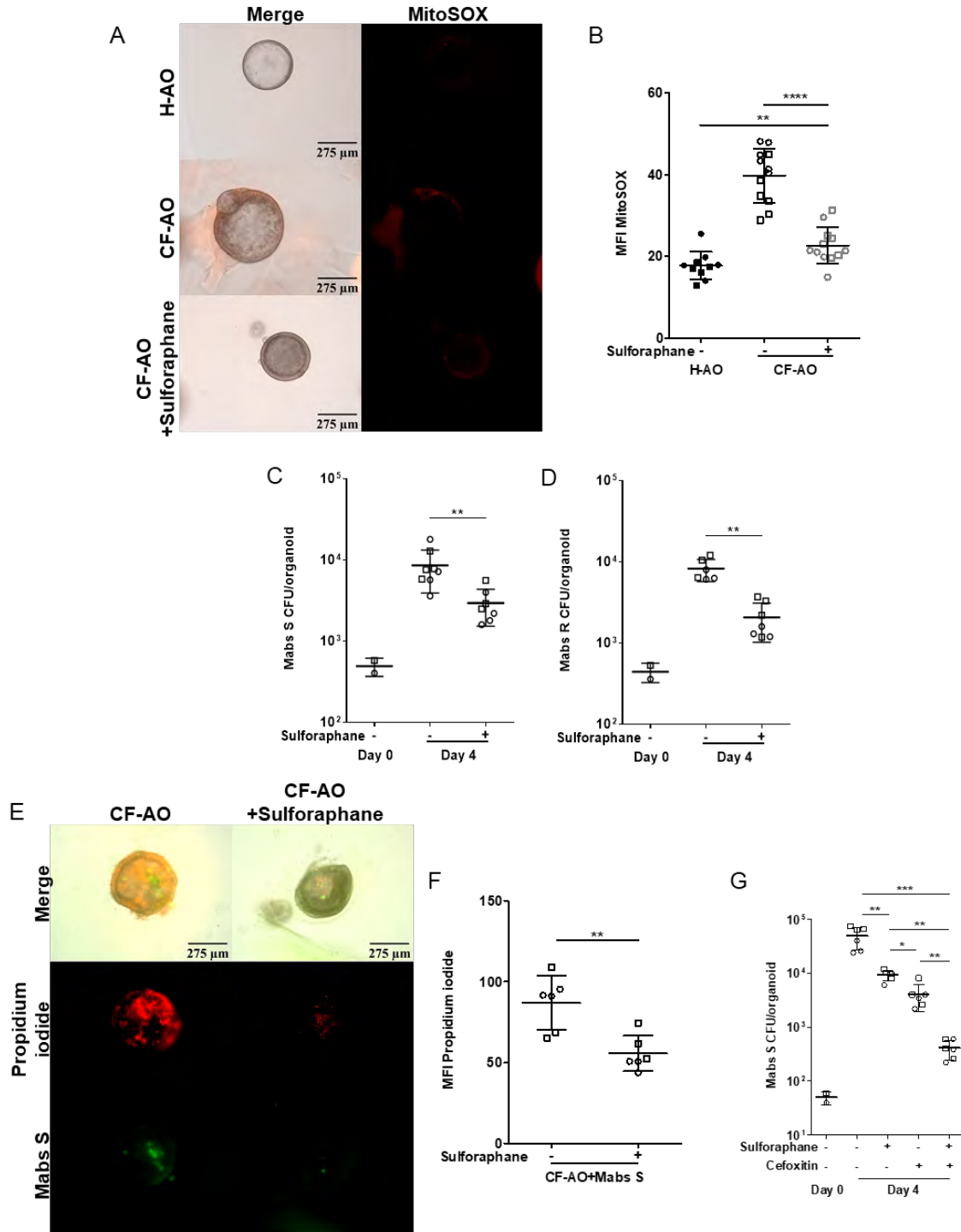


Figure 5. Sulforaphane mitigates oxidative stress in CF-AOs and synergizes with cefoxitin to inhibit Mabs growth. (A, B) Representative images (A) and MFI quantification (B) of mitochondrial ROS production (MitoSOX) in H-AO (n=10) and CF-AO (n+=12; n=12) after 4 days of being treated with

(+) or without (-) sulforaphane. (C, D) Bacterial load by CFU assay of CF-AO pre-treated with (+) or without (-) sulforaphane for 6 hr before infection with Mabs S (C) (n+= 7; n-=8) or Mabs R (D) (n+= 7; n-=6) for 4 days. (E, F) Representative images (E) and MFI quantification (F) of propidium iodide incorporation in CF-AO pre-treated with (+) or without (-) sulforaphane for 6 hr before infection with Wasabi-labelled Mabs S (n+=6; n-=6) for 4 days. (G) Bacterial load by CFU assay of CF-AO pre-treated with (+) or without (-) sulforaphane for 6 hr before infection with Mabs S for 4 days in presence or absence of cefoxitin. Except otherwise stated, graphs represent means \pm SD from at least two independent experiments, indicate them by different symbols. Each dot represents one organoid. **P<0.01; **** P<0.0001 by Mann-Whitney test.

Supplementary Information for

Human bronchial organoids unveil druggable pathways against *Mycobacterium abscessus* infection in cystic fibrosis

Stephen Adonai Leon-Icaza, Salimata Bagayoko, Nino Iakobachvili, Chloé Ferrand, Talip Aydogan, Celia Bernard, Angélique Sanchez Dafun, Marlène Murriss-Espin, Julien Mazières, Pierre Jean Bordignon, Serge Mazères, Pascale Bernes-Lasserre, Victoria Ramé, Jean-Michel Lagarde, Julien Marcoux, Marie Pierre Bousquet, Christian Chalut, Christophe Guilhot, Hans Clevers, Peter J. Peters, Virginie Molle, Geanncarlo Lugo-Villarino, Kaymeuang Cam, Laurence Berry, Etienne Meunier, Céline Cougoule*

*Céline Cougoule, Institut de Pharmacologie et Biologie Structurale (IPBS), Université de Toulouse, CNRS, UPS, Toulouse, France. Email: Celine.Cougoule@ipbs.fr

This PDF file includes:

- Supplementary Materials and Methods
- Figures S1 to S5
- Table S1
- Legends for Datasets S1 to S5
- SI References

Supplementary Information Text

Materials and Methods

Airway organoid culture and maintenance

Healthy and cystic fibrosis airway organoids were derived from lung biopsies as described (1). Briefly, biopsies (1 mm³) of normal lung tissue adjacent to the tumour obtained from donors who underwent lung resection due to Non-small cell lung carcinoma (NSCLC), and a biopsy of cystic fibrosis lung tissue of a heterozygous patient (G542X/1811+1.6kbA-->G) undergoing lung transplantation, were minced and digested with 2 mg ml⁻¹ collagenase (Sigma-Aldrich) on an orbital shaker at 37°C for 1h. The digested tissue suspension was sheared using flamed glass Pasteur pipettes and strained over a 100-µm cell strainer (Corning, NY, USA). The resultant single cell suspensions were treated with Red Blood Cell Lysis Buffer for 5min. and washed before being embedded in 10 mg ml⁻¹ of Cultrex growth factor reduced BME type 2 (R & D Systems, Minneapolis, MN, USA). 40µl drops were seeded on 24-well plates (Nunclon Delta surface, Thermo Scientific). Following polymerization, 500µl of airway organoid complete media (Advanced DMEM/F12 (Invitrogen) supplemented with 1x L-Glutamine (Fisher Scientific), 10mM Hepes (Fisher Scientific), 100 U ml⁻¹ / 100 µg ml⁻¹ Penicillin / Streptomycin (Fisher Scientific), 50 µg ml⁻¹ Primocin (InvivoGen, San Diego, CA, USA), 10% Noggin (homemade), 10% Rspol (homemade), 1x B27 (Gibco, Thermo Scientific), 1.25mM N-Acetylcysteine (Sigma-Aldrich), 10mM Nicotinamide (Sigma-Aldrich), 5µM Y-27632 (Cayman Chemical, Ann Arbor, MI, USA), 500nM A83-01 (Tocris Bioscience, Bristol, UK), 1µM SB 202190 (Sigma-Aldrich), 25 ng ml⁻¹ FGF-7 (PeproTech), 100 ng ml⁻¹ FGF-10 (PeproTech)) was added to each well for healthy and cystic fibrosis airway organoid maintenance. To prevent risk of culture contamination, airway organoid complete media was supplemented with 10 µg ml⁻¹ Normocure (InvivoGen) and 2.5 µg ml⁻¹ Fungin (InvivoGen) during the first 4 weeks of the cystic fibrosis airway organoid culture. Plates were transferred to humidified incubator at 37°C with 5%

CO₂ and the organoids were passaged every 4 weeks. After the first passage, the cystic fibrosis airway organoids were maintained only with the airway organoid complete media.

Epithelium thickness

Healthy and cystic fibrosis airway organoids were passaged after 4 weeks. After passage, 10 thousand cells were embedded in Cultrex, seeded and cultured on Nunclon Delta surface 24-well plates (Thermo Scientific) with airway organoid complete media for 5 weeks at 37°C with 5% CO₂. At the end of the 5 weeks, bright field images of each well were acquired using an EVOS M7000 microscope, and epithelium thickness measured with Image J software.

CFTR inhibition

Healthy airway organoids were seeded on Nunclon Delta surface 35x10mm Dish (Thermo Scientific) and 2ml of airway organoid complete media without N-Acetylcysteine and without antibiotics was added to each plate. Two days prior infection, the organoids were treated with 25µM CFTRinh-172 (Selleck Chemicals) and 25µM GlyH 101 (Tocris Bioscience). Every 48hr the culture media with inhibitors was refreshed until the end of the experiment.

Mucus staining

Healthy and cystic fibrosis airway organoids were seeded on Nunclon Delta surface 24-well plates (Thermo Scientific). 500µl of airway organoid complete media was added to each well. Organoids were stained with 10µM Zinpyr-1 (Santa Cruz Biotechnology) over night at 37°C. The next day, each well was washed (1hr between wash) 3 times with PBS 1x. After the last wash, airway organoid complete media was added to each well and images were acquired using an EVOS M7000 microscope. GFP brightness threshold was kept equal for all the independent experiments. MFI was analyzed using Fiji/ImageJ.

Measurement of ROS, lipid peroxidation and cell death

Mabs-infected organoids and/or uninfected controls (PBS 1x injected organoids) were seeded on Nunclon Delta surface 24-well plates and cultured for 3-4 days. 500µl of airway organoid complete media without N-Acetylcysteine and without antibiotics was added to each well. At day 3-4, the culture media was replaced and ROS levels, lipid peroxidation and cell death were measured by live imaging. As positive control for ROS, 20mM tert-Butyl hydroperoxide (tBHP) (Sigma-Aldrich) was added to 1-2 wells of uninfected organoids for 1hr at 37°C. After an hour, the culture media was replaced. For ROS, at day 3 organoids were stained with 10µM H₂DCFDA (Invitrogen) or with 5µM MitoSOX (Thermo Scientific) for 30 minutes at 37°C, while for lipid peroxidation and cell death, at day 4 organoids were stained with 2µM BODIPY (Thermo Scientific) for 30 minutes at 37°C or 50 µg ml⁻¹ propidium iodide (Thermo Scientific), respectively. At the end of the staining, each well was wash 3 times with PBS 1x and images were acquired using an EVOS M7000 microscope. RFP and GFP brightness threshold were kept equal for all the independent experiments. MFI was analyzed using Fiji/ImageJ.

Bottom-up mass spectrometry analysis of airway organoids:

Organoid pellets (washed three times with PBS) were lysed with 5% SDS in 50 mM ammonium bicarbonate, pH 7.55. Sonication with Bioruptor (15 cycles, 45 sec ON and 15 sec OFF) was done followed by ultracentrifugation at 4°C and 16,000 g for 45 min to obtain the clear lysate. A volume corresponding to 50 µg of total protein in the lysate was reduced with 100 mM tris(2-carboxyethyl) phosphine (Sigma) and alkylated with 400 mM 2-chloroacetamide (Sigma) at 95 °C for 5 min. Each sample was loaded on an S-trap Micro spin column (Protifi, USA), according to the manufacturer's instructions and digested with trypsin (Promega) overnight at 37°C.

Digested peptide extracts were analysed by online nanoLC using an UltiMate 3000 RSLCnano LC system (ThermoScientific) coupled with an Orbitrap Fusion Tribrid mass spectrometer (Thermo

Scientific) operating in positive mode. Five μL of each sample (2.5 μg , analysed by Pierce quantitative fluorometric peptide assay) were loaded onto a 300 mm ID 5 mm PepMap C18 pre-column (Thermo Scientific) at 20 ml/min in 2% (v/v) acetonitrile, 0.05% (v/v) trifluoroacetic acid. After 5 min of desalting, peptides were on-line separated on a 75 mm ID 50 cm C18 column (in-house packed with Reprosil C18-AQ Pur 3 mm resin, Dr. Maisch; Proxeon Biosystems) equilibrated in 95 % buffer A (0.2% [v/v] formic acid), with a gradient increased to 25% buffer B (80% [v/v] acetonitrile, 0.2% [v/v] formic acid) for 75 min, then to 50% B for 30 min and then to 98% B for 10 min, held for 15 min before returning to starting conditions for 25 min, totaling an entire run time of 160 min at a flow rate of 300 nL/min.

The instrument was operated in data-dependent acquisition mode using a top-speed approach (cycle time of 3 s). Survey scans MS were acquired in the Orbitrap over 400–1500 m/z with a resolution of 120,000, and a maximum injection time (IT) of 50 ms. The most intense ions (2+ to 7+) were selected at 1.6 m/z with quadrupole and fragmented by Higher Energy Collisional Dissociation (HCD). The monoisotopic precursor selection was turned on, the intensity threshold for fragmentation was set to 50,000, and the normalized collision energy (NCE) was set to 35%. The resulting fragments were analysed in the Orbitrap with a resolution of 30,000. Dynamic exclusion was used within 60 s with a 10 ppm tolerance. The ion at 445.12003 m/z was used as the lock mass. The Mascot (Mascot server v2.8.1; <http://www.matrixscience.com>) database search engine was used for peptide and protein identification. Mass tolerance for MS and MS/MS was set at 10 ppm and 20 mmu, respectively. The enzyme selectivity was set to full trypsin with two missed cleavages allowed. Protein modifications were fixed carbamidomethylation of cysteines, variable oxidation of methionines, variable phosphorylation of serine, threonine and tyrosine, and variable acetylation of protein N-terminus. Uniprot proteome for both human and mouse was used as the database. The result files were then imported into Proline (doi:10.1093/bioinformatics/btaa118) for validation

with false discovery rate (FDR) of $\leq 1.0\%$. Label-free quantitation was also performed in Proline to compare the two conditions (Healthy vs Cystic Fibrosis). Iterative alignment computation was applied using peptide identity with three as the maximum number of iterations. Alignment smoothing was done with landmark range with 50 landmarks and 50% sliding window overlap. For the master map creation, the mapping tolerances were 5 ppm and 60 sec for the m/z and time, respectively. For the statistics parameters, the T-test p-value of 0.01 was applied on both peptide and protein profile significant analysis. Only specific peptides were used and the median ratio fitting was chosen as the abundance summarizer method. Normalization, missing values inference (Gaussian model), t-test and z-test were also applied. For the R-analysis and reporting, rows with at least two number of values identified by MS/MS (in whole experiment) and with at least 50% of defined values (in one condition) were filtered. LIMMA test was performed with two-sided hypothesis and equal variance assumption. Volcano plot was based on the cut-off: p-value of 5% and log2 ratio of 0.6. The mass spectrometry proteomics data have been deposited to the ProteomeXchange Consortium via the PRIDE (2) partner repository with the dataset identifier PXD030104".

Bacteria culture

Mycobacterium abscessus sensu stricto strain CIP104536T (ATCC19977T) morphotype S and R carrying pTEC15 (Addgene, plasmid 30174) that express green fluorescent protein (Wasabi, kindly provided by Ph.D. Laurent Kremer (Research Institute of Infectious Diseases, Montpellier, France)) or carrying pASTA3 (Addgene, plasmid 24657) that express red fluorescent protein (tdTomato), respectively, were grown as previously described (3) by three days pre-culture and a later on three extra days culture at 37°C without agitation until reach log phase in 7H9 liquid medium (BD Difco™) supplemented with 10% oleic acid–dextrose–catalase (OADC) (BD Difco™), 0.05% Tween-80 (Sigma-Aldrich) and 500 $\mu\text{g ml}^{-1}$ Hygromycin B (Euromedex, Souffelweyersheim, France).

Organoid infections

Before infection, 25µl drops of Matrigel (Fisher Scientific) containing healthy or cystic fibrosis airway organoids were seeded on 35x10mm Dish (Nunclon Delta surface, Thermo Scientific) and 2ml of airway organoid complete media without N-Acetylcysteine and without antibiotics was added to each plate. Depending on the indicated conditions, airway organoids were pretreated or no with 10µM of Resveratrol (Sigma-Aldrich) or with 10µM of Sulforaphane (Selleck Chemicals) for 1hr or 6hr respectively before infection. Both antioxidants were maintained throughout the experiment. At day two of infection, the media with the indicated antioxidant was refresh. The day of the infection, the bacterial pellets of the Mabs S and R cultures were harvested and resuspended in PBS 1x. Bacterial clumps were disaggregated with a 1ml syringe (Terumo™) with blunt needle (Bio-Rad, Hercules, CA, USA) and bacterial density was adjusted to $OD_{600} = 0.1-0.4$. Phenol red (Sigma-Aldrich) was added at 0.05% to allow tracking of injected organoids (4). Injected organoids with Mabs or PBS 1x were individually collected, washed in PBS 1x and embedded into fresh Cultrex (R & D Systems) and 40µl drops were seeded on Nunclon Delta surface 24 or 6-well plates. Injected organoids were cultured for 3-4 day if not stated otherwise.

Electron microscopy

For SEM and TEM, injected organoids were seeded on Nunclon Delta surface 6-well plates (Thermo Scientific) and cultured for 4 days. Airway organoid complete media without N-Acetylcysteine and without antibiotics was added to each well. At day 4, injected organoids were individually collected and fixed in 2% paraformaldehyde (EMS), 2.5% glutaraldehyde (EMS) and 0.1 M Sodium Cacodylate (EMS) over night at room temperature. After fixation, injected organoids were stored at 4°C for subsequent processing. Samples were post-fixed with 2% osmium tetroxide(OsO_4) (EMS), followed by 2,5% K-ferrocyanide (EMS) without washing and 1% thiocarbohydrazide (EMS) at 40 °C, prior 2% OsO_4 for second time and followed by overnight in 1% uranyl acetate (EMS) at 4°C. Next day, the

samples were heated at 40°C, followed incubation in lead aspartate (EMS) at 50°C. Dehydration was performed with growing concentrations of acetonitrile (EMS). Sample were then impregnated in Durcupan ACM resin (Sigma-Aldrich), and polymerized 48h at 60°C. All the procedure except the overnight incubation in uranylyl acetate were performed using a Pelco Biowave® PRO+ Microwave processing systems (TED Pella).

Semi-thin (300 nm) serial sections were made using an UC7 ultramicrotome (Leica) equipped with a Jumbo Histo diamond knife (Diatome) and an ASH2 (RMC Boeckler) and collected on silicon wafers (Ted Pella). Sections were imaged on a Quanta FEG 250 SEM microscope in BSE mode, set up at 15kV, spot 4.0, working distance 6.8 mm, dwell time 300 ms. Ultrathin sections were also collected on copper grids formvar coated for TEM analysis on a JEOL 1200 EXE II Microscope at 100kV.

Lightsheet imaging of AO

Fixed airway organoids were stained with propidium iodide (6µg/ml in PBS) for 30 minutes at room temperature then rinsed three times in PBS.

Organoids were then embedded in 1% low-melting agarose inside glass capillaries and imaged in PBS using a light-sheet fluorescence microscope (Zeiss Lightsheet Z.1) with a 20x/1.0 detection objective combined with a 0.5 zoom (10x final magnification) and dual illumination with 488nm and 561nm lasers (exposure times were 49-99 ms). The voxel size is 0.4645 x 0.4645 x 1 µm.

For image processing, images were processed with Fiji software (5). The 3D reconstructions were performed with Amira software (v2020.2).

Effect of N-Acetylcysteine, Resveratrol and CFTR inhibitors on *Mabs* growth

Mabs S and R were grown as previously described until reach $OD_{600} = 1$. Bacterial density was adjusted to $OD_{600} = 0.1$ with 7H9 liquid medium (supplemented as before) without Hygromycin B. N-Acetylcysteine (10µM), Resveratrol (10µM) or CFTR inhibitors (25µM) were added to the bacterial cultures as appropriate. N-Acetylcysteine, Resveratrol and CFTR inhibitors were refreshed after 48

hours. The cultures were maintained at 37°C without agitation and each 24 hours the OD₆₀₀ was measured.

SI Figures and legends

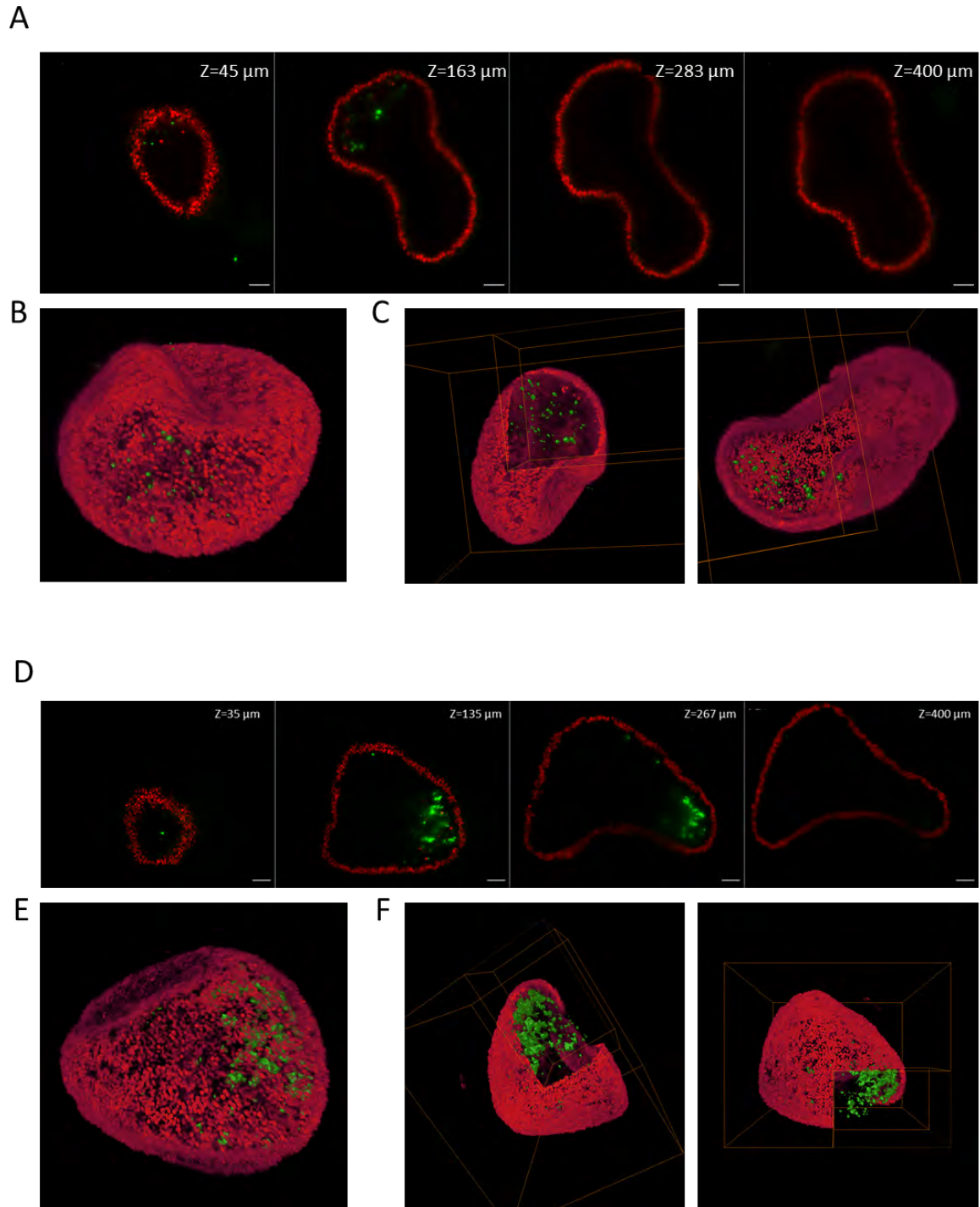


Fig S1. Supplementary to figure 1. 3D light-sheet imaging of airway organoids infected with wasabi (green) Mabs S or R. H-AOs were fixed then stained with propidium iodide to visualize cell nuclei

(red) before imaging using Zeiss Lightsheet 1 microscope. (A) XY planes at the indicated z positions of the 400 μm z-stack of an H-AO after infection with MAbs S shown in Supplementary movie 1 (10X objective). (B) 3D visualization using AMIRA software of the z-stack of AO after infection with Mabs S. (C) Corner cut from two different angles using AMIRA software through a volume rendering of the nuclei while keeping the Mabs S fluorescent signal. Scale bar: 50 μm . (D) XY planes at the indicated z positions of the 400 μm z-stack of a patient-derived AO after infection with MAbs R shown in Supplementary movie 2 (10X objective). (E) 3D visualization using AMIRA software of the z-stack of AO after infection with Mabs R. (F) Corner cut from two different angles using AMIRA software through a volume rendering of the nuclei while keeping the Mabs R fluorescent signal. Scale bar: 50 μm .

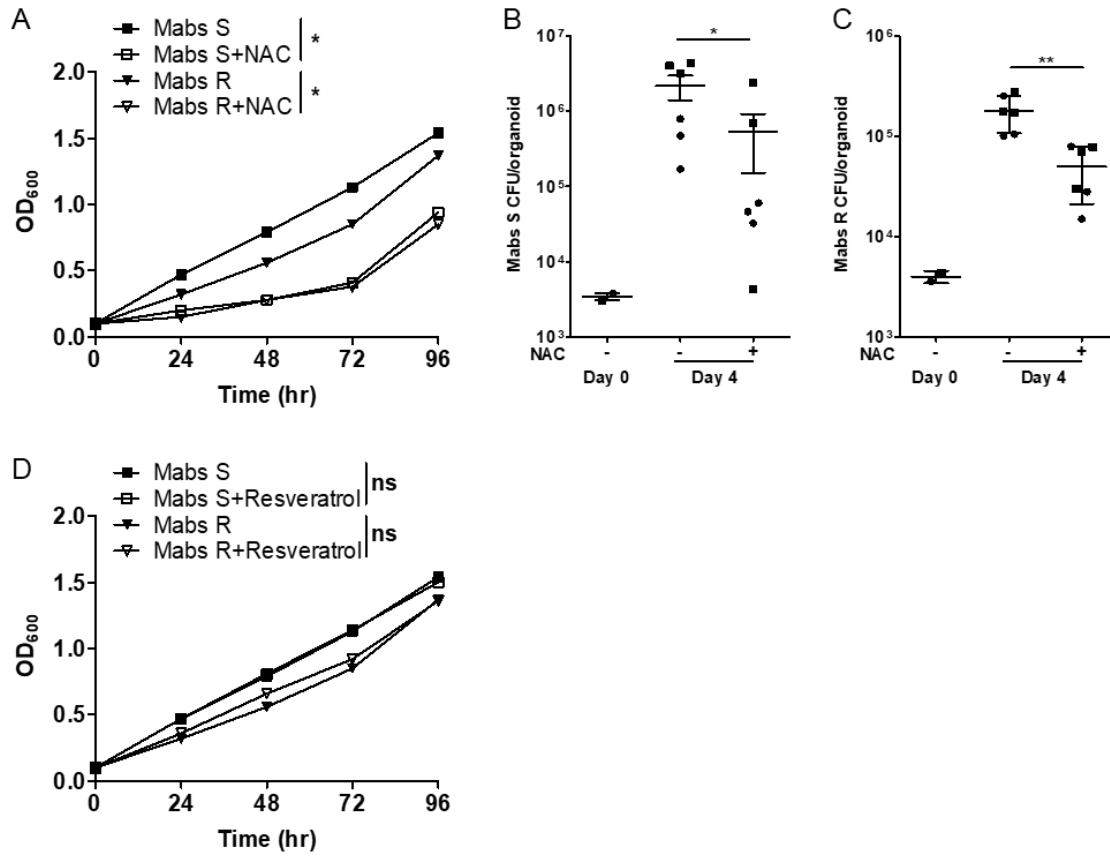


Fig S2. Supplementary to figure 2. (A) Kinetics of *in vitro* Mabs S and R growth in absence or presence of 10 μ M N-Acetylcysteine (NAC). Graph represents means from one experiment performed in triplicates. *P<0.05 by Mann-Whitney test. (B, C) Bacterial load by CFU assay of AOs pre-treated with (+) or without (-) NAC for 1hr before infection with Mabs S (B) (n+= 6; n-=6) or R (C) (n+= 6; n-=6) for 4 days. Graphs represent means \pm SEM from two independent experiments, indicated by different symbols. Each dot represents one organoid. *P<0.05; **P<0.01 by Mann-Whitney test. (D) Kinetics of *in vitro* Mabs S and R growth in absence or presence of resveratrol. Graph represents means from one experiment performed in triplicates. ns= not significant by Mann-Whitney test.

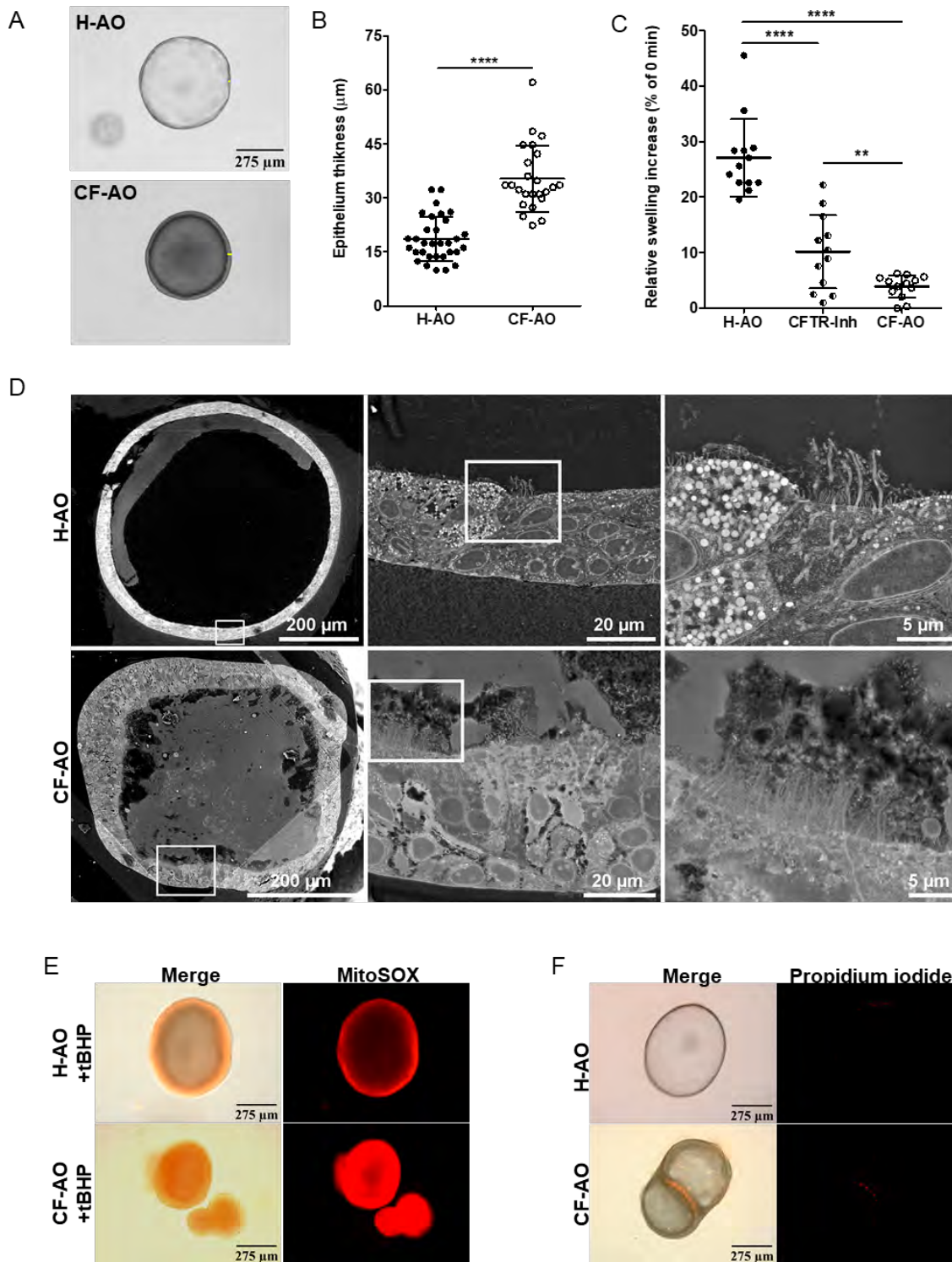


Fig S3. Supplementary to figure 3. (A, B) Representative bright-field images (A) and quantification (B) of epithelium thickness in healthy AOs (H-AO, n=32) and cystic fibrosis AOs (CF-AO, n=24). Data from three independent wells per donor. (C) Percentage of area increase of H-AO (n=13), H-AO pre-

treated with CFTR inhibitors for 4 days (CFTR-Inh, n=13), and CF-AO (n=13) after 2hr stimulation with 5 μ M forskolin. Data from two independent wells per donor. (D) Electron micrographs of H-AO and CF-AO revealing mucus accumulation in the lumen and longer cilia in the CF ones. (E) Representative images of mitochondrial ROS production (MitoSOX) in H-AO and CF-AO after 1hr treatment with tBHP. (F) Representative images of the basal propidium iodide incorporation in H-AO and CF-AO.

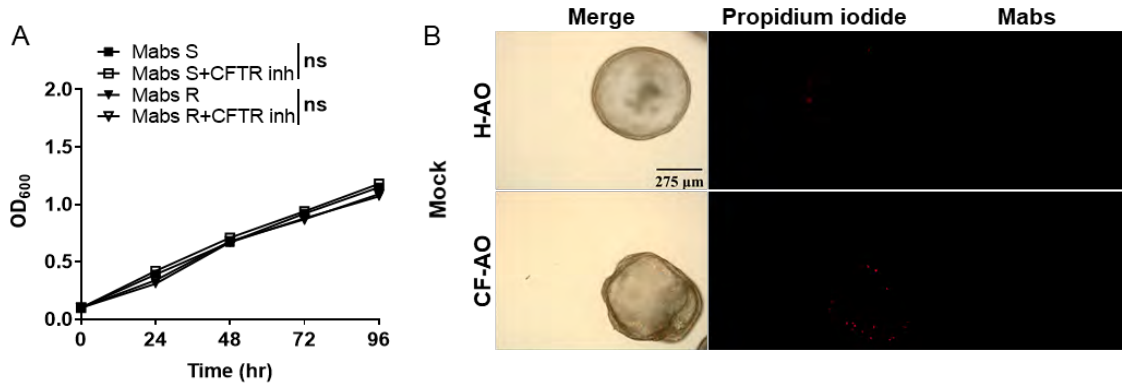


Fig S4. Supplementary to figure 4. (A) Kinetics of Mabs S and R growth in absence or presence of CFTR inhibitors. Data from one experiment performed in triplicates. (B) Representative images of basal level of propidium iodide incorporation in H-AO and CF-AO upon Mabs infection.

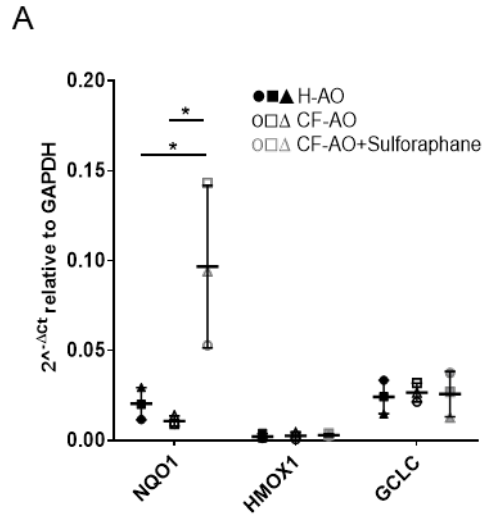


Fig S5. Supplementary to figure 5. (A) Expression of Nrf-2-regulated genes in H-AO and CF-AO after 4 days of being treated with or without sulforaphane. Graph represents means from three pooled independent experiments, performed in triplicates. *P<0.05 by unpaired T test.

SI Table

Table S1. List of primers used for RT-qPCR

Gene	Primers 5'-3'	Reference
GAPDH (NM_002046)	F: CTCCAAAATCAAGTGGGGCGATG R: GGCATTGCTGATGATCTTGAGGC	(4)
NRF2 (NM_006164.5)	F: TCAGCGACGGAAAGAGTATGA R: CCACTGGTTTCTGACTGGATGT	PrimerBank
NQO1 (NM_000903.3)	F: CAGACGCCCCGAATTCAAATC R: AGGCTGCTTGGAGCAAATACA	(6)
HMOX1 (NM_002133.3)	F: TCCGATGGGTCCTTACACTC R: TAAGGAAGCCAGCCAAGAGA	(6)
GCLC (NM_001498.4)	F: GGAGGAAACCAAGCGCCAT R: CTTGACGGCGTGGTAGATGT	PrimerBank
SOD1 (NM_000454.5)	F: ACAAAGATGGTGTGGCCGAT R: TGGGCGATCCCAATTACACC	(7)
SOD2 (NM_000636.4)	F: TTTCAATAAGGAACGGGGACAC R: GTGCTCCCACACATCAATCC	PrimerBank
PRDX1 (NM_002574.4)	F: CATTCTTTGGTATCAGACCCG R: CCCTGAACGAGATGCCTTCAT	PrimerBank
Catalase (NM_001752.4)	F: TGGGATCTCGTTGGAAATAACAC R: TCAGGACGTAGGCTCCAGAAG	PrimerBank
GPX4 (NM_002085.5)	F: GAGGCAAGACCGAAGTAACTAC R: CCGAACTGGTTACACGGGAA	PrimerBank
NOX1 (NM_007052.5)	F: TTGTTTGGTTAGGGCTGAATGT R: GCCAATGTTGACCCAAGGATTTT	PrimerBank
DUOX1 (NM_017434.5)	F: TTCACGCAGCTCTGTGTCAA R: AGGGACAGATCATATCCTGGCT	(8)
MUC5B (NM_002458.3)	F: GCCCACATCTCCACCTATGAT R: GCAGTTCTCGTTGTCCGTCA	PrimerBank
MUC4 (NM_018406.7)	F: CTCAGTACCGCTCCAGCAG R: CCGCCGTCTTCATGGTCAG	(4)
MUC5AC (NM_001304359.2)	F: GGAAGTGTGGGGACAGCTCTT R: GTCACATTCCTCAGCGAGGTC	(9)

SI References

1. N. Sachs, *et al.*, Long-term expanding human airway organoids for disease modeling. *EMBO J.* **38** (2019).
2. Y. Perez-Riverol, *et al.*, The PRIDE database and related tools and resources in 2019: improving support for quantification data. *Nucleic Acids Res.* **47**, D442–D450 (2019).
3. A. Bernut, *et al.*, Mycobacterium abscessus cording prevents phagocytosis and promotes abscess formation. *Proc. Natl. Acad. Sci. U. S. A.* **111**, E943–E952 (2014).
4. N. Iakobachvili, *et al.*, Mycobacteria-host interactions in human bronchiolar airway organoids. *Mol. Microbiol.* **00**, 1–11 (2021).
5. J. Schindelin, *et al.*, Fiji: an open-source platform for biological-image analysis. *Nat. Methods* **2012 97 9**, 676–682 (2012).
6. M. Bonay, *et al.*, Caspase-independent apoptosis in infected macrophages triggered by sulforaphane via Nrf2/p38 signaling pathways. *Cell Death Discov.* **1**, 1 (2015).
7. C. W. Pyo, N. Shin, K. Il Jung, J. H. Choi, S. Y. Choi, Alteration of copper-zinc superoxide dismutase 1 expression by influenza A virus is correlated with virus replication. *Biochem. Biophys. Res. Commun.* **450**, 711–716 (2014).
8. R. W. Harper, *et al.*, Differential regulation of dual NADPH oxidases/peroxidases, Duox1 and Duox2, by Th1 and Th2 cytokines in respiratory tract epithelium. *FEBS Lett.* **579**, 4911–4917 (2005).
9. T. Fujisawa, *et al.*, Regulation of airway MUC5AC expression by IL-1beta and IL-17A; the NF-kappaB paradigm. *J. Immunol.* **183**, 6236–6243 (2009).

Chapter IV: Discussion and perspectives

The airway tract is the main port of entry of allergens, pollutants and microorganisms into the human body. It is mainly composed of specialized epithelial cells, which act as the first line of defense against the inhaled challenges, playing a fundamental role in either their clearing or establishment (274). However, due to pulmonary differences in terms of physiology and cellular composition between animal models and humans, the knowledge we have about the early interactions between respiratory pathogens and host airways is still limited (275). To tackle these issues, for the first time, I exploited in this thesis the ASC-derived airway organoid technology to study the early stages of mycobacterial infections, a major cause of human pulmonary disease.

In my first article: “**Mycobacteria–host interactions in human bronchiolar airway organoids**”, I generated organoids from biopsies of adjacent healthy tissue of lung cancer patients. Electron microscopy and live-cell imaging revealed that these organoids were composed of basal, goblet, club, and ciliated cells, as previously reported (196). This cell composition corresponds to the bronchiolar part of the respiratory tract (276). However, a limitation of this study is that we did not have access to the demographic and clinical data (except for the diagnosis of non-small cell lung carcinoma) of the patients from whom the biopsies were taken, which could affect the kinetics of proliferation and differentiation of basal cells from the different donors, as well as the reproducibility and homogeneity of the data generated due to the interindividual variability of each culture (277). Nevertheless, we tried to

overcome inter-donor variability by establishing a strict protocol to take only biopsies (1 mm³) of normal lung tissue adjacent to the tumor from donors undergoing lung resection for non-small cell lung carcinoma, thus avoiding differences in organoid cultures due to sampling from different regions of the lung (277). It is worth mentioning that all organoid cultures used in this study did not show major differences in terms of proliferation and differentiation.

The human healthy airway organoids (H-AO) presented a classic cystic structure with the apical part of the cells towards the lumen and exhibited functional secretory and ciliated cells (278). Because of the polarization of the organoids, we set up a system to microinject the mycobacteria into their lumen. After microinjection of Mtb or the NTM Mabs S, both bacteria resided mainly at the lumen of the AOs. However, on some occasions, the bacteria were found interacting with the epithelial cells at the surface of the organoids. The transient interactions observed between mycobacteria and epithelium may be due to the proper functioning of the mucociliary clearance mechanism in the AOs. The mucociliary clearance constitutes an innate lung defense mechanism primarily driven by ciliated cells. Respiratory mucus traps pathogens entering the airways, and lung cilia propel them outward via their coordinated directional motion (279). However, since the AOs are a closed system, the bacteria cannot be expelled from them. Instead, the bacteria remain in their lumen with mucus and cellular debris. It should be noted that after 4 days of infection, the epithelial cells forming the organoids showed neither cell death nor massive internalization of the bacteria. These further confirm the previously observed slight response of the NHBE cells to Mtb and Mabs S (52, 150).

Airway organoids revealed no significant changes in architecture following infection, as denoted by confocal microscopy. Despite this, as a perspective, further confirmation of the integrity of the tight junctions should be done by staining of E-cadherin and zonula occludens 1 or by the dextran diffusion barrier integrity assay, as reported before in intestinal organoids (280, 281). The organoids respond differently to Mtb or Mabs S challenge. They appear to control Mtb by increasing the production of AMPs such as β -defensin 1 and 2, lactoferrin, hepcidin, and RNase7. Lactoferrin and hepcidin regulate iron availability (282–285), creating a more hostile environment for Mtb survival (286). Meanwhile, β -defensin 1 and 2, and RNase7 are well known to promote pore formation and disruption of the Mtb cell wall (287–289). Additionally, β -defensin 2 has been shown to have chemoattractant effects on immune cells (290). Besides AMPs, the AO infected with Mtb or stimulated with conditioned media from Mtb-infected human macrophages overexpressed IL-8 and GM-CSF. These cytokines are involved in the recruitment of neutrophils (291) and control of the infection by the macrophages (292, 293), respectively.

Notably, the GM-CSF expression was higher when the organoids were stimulated with conditioned media than when they were infected, thus, reinforcing the fact that a crosstalk between ECs and alveolar macrophages exists (52). We confirmed this, after observing human macrophages interacting with Mtb-infected AOs in co-culture.

Contrary to Mtb, the response of AOs to Mabs S was generally low. It could be explained by the presence of GPLs on the cell wall surface of Mabs S (294). The GPLs mask lipids and other molecules, preventing their recognition by epithelial cells

through TLR2 (149). Surprisingly, both Mtb and Mabs S showed down-regulation of mucins expression. Maybe this is a common mechanism used by mycobacteria to avoid the mucociliary clearance and directly encounter macrophages at the alveoli (49). So far, just *Helicobacter pylori* and *Pseudomonas aeruginosa* have shown to be able to regulate mucins expression to favor the colonization of the stomach tissue and the airways, respectively (295, 296). However, further studies are needed to determine whether or not down-regulation of mucin expression provides an advantage for mycobacterial colonization of the respiratory tract.

Airway organoids are an advantageous model for studying respiratory infections compared to 2D cultures and animal models. AOs are sophisticated multicellular systems that mimic the architecture and essential functions of the human lung. Also, they can be cryopreserved in biobanks and remain stable for years (297, 298). Despite their numerous benefits, organoids have certain limitations, including a lack of vascularization and immune cells and the absence of an air-liquid interface due to their cystic form (2, 210). Nevertheless, the organoid field is evolving all the time. Recent advances such as bioprinting to generate scaffolds (299), the ALI cultures (300), the lung on a chip technology (301), and the improvement of co-culture protocols, as we showed previously in my first article (302), between organoids and immune cells are helping to sort the system limitations (303). Air-liquid interface cultures can be generated from organoids (300). These cultures have an accessible polarized pseudostratified epithelium (196), which allowed them to be broadly used during the Sars-Cov-2 pandemic (13). However, their establishment is highly dependent on the use of a tissue culture plate insert, which is composed of a

permeable membrane and has limited scalability (304). On the other hand, lung on a chip technology comprises microfluidic devices on microchips, which consist of a 3D cell culture system separated by a porous membrane, which contains channels that allow continuous perfusion to mimic circulation in the body and vacuum chambers to mimic breathing in human lungs. Organs on a chip can recapitulate *in vivo*-like environments and allow for the comparison of biological responses under normal and disease conditions. However, lungs on chips are generally developed using iPSCs or epithelial cell lines, requiring complex expertise in iPSC differentiation protocols and nano-micro fabrication for on-chip devices (305). Therefore, all these models are complementary approaches.

In particular, in this work, the main limitation was that the replicative niche of Mtb is the alveoli and not the bronchiolar part of the airways. However, my laboratory and others have already established the appropriate conditions to generate alveolar organoids derived from ASCs (243), thus, we will be able to compare the response of bronchiolar and alveolar organoids to Mtb and Mabs infection in the near future (Figure 23). This will provide us with a comprehensive view of how ECs behave in the presence of Mtb and Mabs.

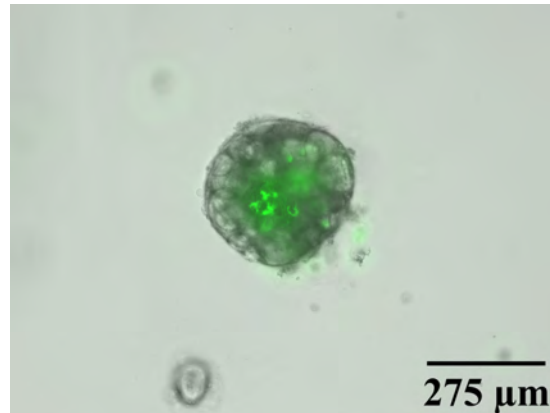


Figure 23. ASC-derived alveolar organoid infected with GFP-expressing Mabs S (unpublished data from Romain Verge and Stephen Leon).

In conclusion, this paper showed that AOs are a suitable and reliable technology that can be applied to understand early events during mycobacterial infections. Furthermore, it opened new questions to be addressed, including the regulation of mucins by mycobacteria.

Due to the validation of AOs as a good model for the study of mycobacterial infections performed in my first article, I had the opportunity to carry out a second research work.

In my second article: "Human bronchial organoids unveil druggable pathways against *Mycobacterium abscessus* infection in cystic fibrosis". I generated AOs from lung biopsies of CF patients to model disease-associated infections and decipher the factors that allow opportunistic pathogens to colonize these airways. It is important to highlight that this is the first paper applying CF AOs to model infections.

Until now, organoids from CF patients have been used successfully to determine the response of CF patients to the CFTR modulator treatment (143, 248, 260, 306, 307).

This research was focused on Mabs, the most common NTM infecting CF patients (308). As stated in the introduction, Mabs displays either S (GPL+) or R (GPL-) morphotypes. S variants are more hydrophilic, enabling increased sliding motility and biofilm formation, while the aggregative R variants have a high propensity to produce large hypervirulent bacterial serpentine cords (90). In AOs both morphotypes resided mainly at the lumen, with the S variant forming biofilm, and the R one, virulent cords. Mabs S was also found directly interacting with ciliated cells at the surface of the organoids. As a result, Mabs retained their fundamental characteristics within the organoids, thus making them an appropriate model to study this bacterial infection. It is worth noting that biofilm visualization remains a challenge, especially in *ex vivo* and *in vivo* settings (309), therefore the AOs seems to be a promising tool to study biofilm formation and its contribution to mycobacterial resistance to antibiotics (118, 310). Interestingly, both Mabs morphotypes grow around death epithelial cells and cellular debris found at the organoid lumen. Probably, this process favors the growth of the bacteria but also the biofilm formation by Mabs S, as demonstrated before *in vitro* in a synthetic cystic fibrosis medium in the presence of host cell DNA (311).

After, I generated and characterized CF-AO derived from a patient with a Class I mutation, leading to the absence of the CFTR protein. Compared to H-AOs, CF-AOs showed a thicker epithelium denoting cell hyperplasia, increased mucus production, and no residual function of the CFTR channel. All these features are in agreement

with previous reports (196). To further characterize CF-AO, we performed a proteomic gene ontology enrichment study, which revealed a positive regulation of the cellular oxidant detoxification pathway. Subsequently, we confirmed that CF-AO produced high levels of ROS, leading to lipid peroxidation and cell death, as previously measured in CF patients (312) and ECs (313, 314). Due to the high basal ROS production and the overrepresentation in the proteomics analysis of oxidation and detoxification pathways by CF-AOs, we hypothesized that the oxidative stress environment of CF might play a role in the growth of Mabs. To validate this hypothesis, we infected healthy and CF AOs with S or R-Mabs and quantified Mabs proliferation and organoid cell death. Mabs growth was higher in CF-AOs, concomitant with an increase in epithelial damage. This was reversed by activating NRF2, the master antioxidant regulator. So far, the role of ROS in Mabs infection remains contradictory. In agreement with our findings, it has been shown that an oxidative environment favors Mabs growth in macrophages (315, 316). Moreover, activation of NRF2 decreases the bacterial proliferation *in vitro* and *in vivo* (317, 318). Curiously, one study reported that treatment of CF NHBE cells with CFTR modulators rescues NRF2 function and improves tissue oxidative stress (319), which might contribute to the control of bacterial infection. In contrast, in a zebrafish model, it was observed that aberrant CFTR function or anti-inflammatory effects of roscovitine lead to deficient ROS production by NADPH oxidases NOX2 and DUOX2, which decreases neutrophil recruitment and promotes uncontrolled growth of intracellular Mabs in macrophages (187, 320).

Although, to combat pathogens, ROS are considered as deadly weapons used by phagocytes and other cell types including lung epithelial cells, there is increasing evidence supporting that in certain particular infections or conditions, antioxidants decrease and prooxidants increase pathogen burden (321). In the particular case of Mabs, the exacerbated oxidative environment in the airway epithelium of CF patients, in the absence of immune cells, seems to provide the right conditions for the establishment of this bacterial infection. However, the exact mechanism by which Mabs take advantage of ECs-generated ROS is still unknown. In this regard, complementary data generated in our laboratory demonstrate that CF-AOs are more sensitive to dye by ferroptosis (Figure 24), an iron- and lipid peroxidation-dependent cell necrosis (322, 323), than the H-AO; this in accordance to what has been described before in CF ECs (314). Apparently, the main peroxidized lipid in the CF-AOs is the arachidonic acid (aa); this was shown by a decreased cell death of the CF-AOs when they were pre-treated with an inhibitor of the enzymes (FADS1 and 2) in charge of aa synthesis, prior ferroptosis induction by cumene (Figure 24). Interestingly, a previous report unraveled that increased bio-availability of aa promotes mycobacterial growth (324). In conclusion, all these complementary data indicate that the ROS effect in Mabs growth could be indirect, by promoting ferroptosis and the bio-availability of aa in the airways of CF patients. Nevertheless, more studies are necessary to confirm this hypothesis.

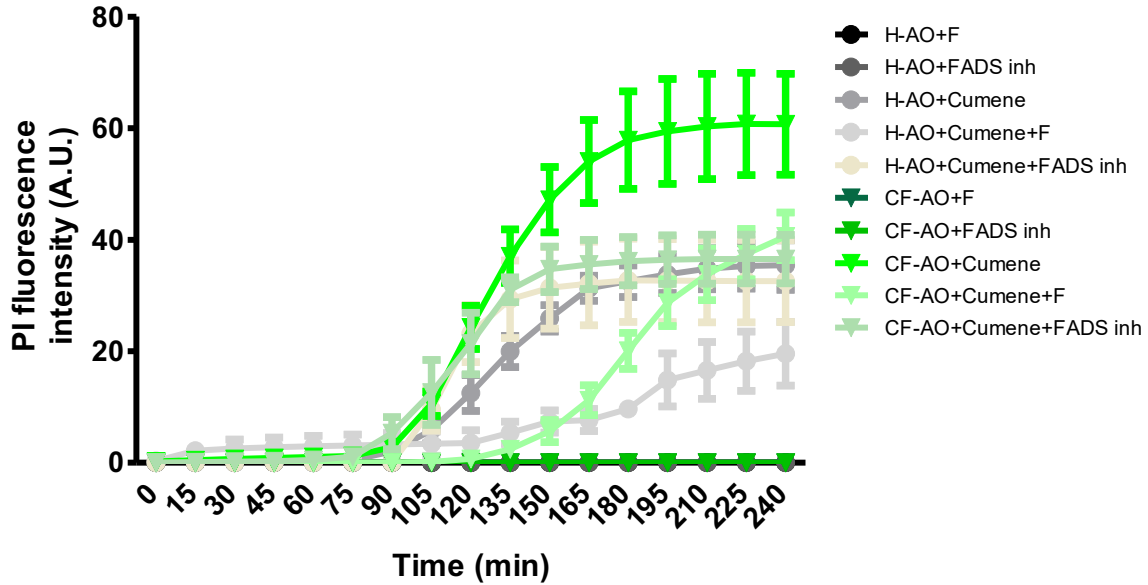


Figure 24. CF-AOs sensitivity to ferroptosis (unpublished data). Time-lapse microscopy of the measure of plasma membrane permeabilization using propidium iodide incorporation in CF-AO. Abbreviations: F, Ferrostatin-1; inh, inhibitor.

Finally, Mabs S-infected CF-AOs were treated with a mixture of the antibiotic cefoxitin and the NRF2 activator sulforaphane. We found that this combination worked together to limit Mabs growth. This synergic effect might be attributed to the antioxidant treatment's reduction of ROS. In recent years, oxidative stress has emerged as one of the primary factors that induces a microorganism to transition from a planktonic to a biofilm state (325). Antibiofilm molecules, such as the antioxidant N-acetylcysteine, can be used to increase the antimicrobial effect of molecules against NTM biofilms (326).

The weakness of this study, is that just one CF patient-derived organoid line was employed. This constraint stems from the difficulty to obtain lung samples from CF patients. However, in the laboratory we have already generated two more CF-AO

lines from biopsies, which will soon be ready for testing. In addition, our team and others have established the proper conditions for producing organoids from CF patients' nasal brushes (246, 248, 260). This strategy will allow us to increase the number of CF donors in order to compare Mabs behavior across organoids with various CFTR mutations, especially the most frequent F508del.

In conclusion, we identified AOs as a relevant model of CF airway dysfunction and vulnerability to NTM infection. Furthermore, we identified the cell-protective Nrf2 pathway as a possible therapeutic target to restore CF tissue redox balance and improve bacterial growth control.

In addition to my two publications as the first author, I had the opportunity to participate during my Ph.D. in six other studies, where I primarily contributed my experience and knowledge of organoids and host-pathogen interactions. These studies are in the annexes section.

References

1. X. Yin, *et al.*, Stem Cell Organoid Engineering. *Cell Stem Cell* **18**, 25 (2016).
2. J. Kim, B. K. Koo, J. A. Knoblich, Human organoids: model systems for human biology and medicine. *Nat. Rev. Mol. Cell Biol.* **21**, 571–584 (2020).
3. R. Gopaldaswamy, S. Shanmugam, R. Mondal, S. Subbian, Of tuberculosis and non-tuberculous mycobacterial infections – a comparative analysis of epidemiology, diagnosis and treatment. *J. Biomed. Sci. 2020 271* **27**, 1–17 (2020).
4. WHO, Global Tuberculosis Report 2021 (2021) (August 10, 2022).
5. I. Ahmed, *et al.*, Non-tuberculous mycobacterial infections—A neglected and emerging problem. *Int. J. Infect. Dis.* **92**, S46–S50 (2020).
6. S. Cowman, J. Van Ingen, D. E. Griffith, M. R. Loebinger, Non-tuberculous mycobacterial pulmonary disease. *Eur. Respir. J.* **54** (2019).
7. H. J. F. Salzer, *et al.*, Personalized Medicine for Chronic Respiratory Infectious Diseases: Tuberculosis, Nontuberculous Mycobacterial Pulmonary Diseases, and Chronic Pulmonary Aspergillosis. *Respiration.* **92**, 199–214 (2016).
8. J. A. Whitsett, T. V. Kalin, Y. Xu, V. V. Kalinichenko, Building and Regenerating the Lung Cell by Cell. *Physiol. Rev.* **99**, 513 (2019).
9. K. J. Travaglini, *et al.*, A molecular cell atlas of the human lung from single-cell RNA sequencing. *Nat. 2020 5877835* **587**, 619–625 (2020).
10. J. C. Snyder, R. M. Teisanu, B. R. Stripp, Endogenous lung stem cells and contribution to disease. *J. Pathol.* **217**, 254–264 (2009).
11. J. D. Davis, T. P. Wypych, Cellular and functional heterogeneity of the airway epithelium. *Mucosal Immunol. 2021 145* **14**, 978–990 (2021).
12. J. A. Zepp, E. E. Morrissey, Cellular crosstalk in the development and regeneration of the respiratory system. *Nat. Rev. Mol. Cell Biol.* **20**, 551–566 (2019).
13. N. Heinen, M. Klöhn, E. Steinmann, S. Pfaender, In Vitro Lung Models and

Their Application to Study SARS-CoV-2 Pathogenesis and Disease. *Viruses* 2021, Vol. 13, Page 792 **13**, 792 (2021).

14. R. J. Hewitt, C. M. Lloyd, Regulation of immune responses by the airway epithelial cell landscape. *Nat. Rev. Immunol.* 2021 216 **21**, 347–362 (2021).
15. P. S. Hiemstra, P. B. McCray, R. Bals, The innate immune function of airway epithelial cells in inflammatory lung disease. *Eur. Respir. J.* **45**, 1150–1162 (2015).
16. R. Bals, P. S. Hiemstra, Innate immunity in the lung: How epithelial cells fight against respiratory pathogens. *Eur. Respir. J.* **23**, 327–333 (2004).
17. S. Fang, *et al.*, The role of pulmonary mesenchymal cells in airway epithelium regeneration during injury repair. *Stem Cell Res. Ther.* **10**, 1–12 (2019).
18. A. Guzman-Aranguez, P. Argüeso, Structure and Biological Roles of Mucin-type O-glycans at the Ocular Surface. *Ocul. Surf.* **8**, 8 (2010).
19. J. A. Whitsett, T. Alenghat, Respiratory epithelial cells orchestrate pulmonary innate immunity. *Nat. Immunol.* **16**, 27 (2014).
20. E. P. Lillehoj, K. Kato, W. Lu, K. C. Kim, Cellular and Molecular Biology of Airway Mucins. *Int. Rev. Cell Mol. Biol.* **303**, 139 (2013).
21. M. R. Knowles, R. C. Boucher, Mucus clearance as a primary innate defense mechanism for mammalian airways. *J. Clin. Invest.* **109**, 571–577 (2002).
22. Y. Huan, Q. Kong, H. Mou, H. Yi, Antimicrobial Peptides: Classification, Design, Application and Research Progress in Multiple Fields. *Front. Microbiol.* **11**, 2559 (2020).
23. D. Xu, W. Lu, Defensins: A Double-Edged Sword in Host Immunity. *Front. Immunol.* **11**, 764 (2020).
24. L. Sharma, J. Feng, C. J. Britto, C. S. Dela Cruz, Mechanisms of Epithelial Immunity Evasion by Respiratory Bacterial Pathogens. *Front. Immunol.* **11**, 91 (2020).
25. K. E. Ridyard, J. Overhage, The Potential of Human Peptide LL-37 as an Antimicrobial and Anti-Biofilm Agent. *Antibiotics* **10** (2021).
26. X. Zhou, Cathelicidin LL37: Defense Roles in the Early Stages of

- Mycobacterium Tuberculosis Infection. *Biomed. J. Sci. Tech. Res.* **10**, 001–003 (2018).
27. M. M. Leiva-Juárez, J. K. Kolls, S. E. Evans, Lung epithelial cells: Therapeutically inducible effectors of antimicrobial defense. *Mucosal Immunol.* **11**, 21–34 (2018).
 28. D. Sarr, E. Tóth, A. Gingerich, B. Rada, Antimicrobial actions of dual oxidases and lactoperoxidase. *J. Microbiol.* **56**, 373 (2018).
 29. M. Varelle, E. Kieninger, M. R. Edwards, N. Regamey, The Airway Epithelium: Soldier in the Fight against Respiratory Viruses. *Clin. Microbiol. Rev.* **24**, 210 (2011).
 30. J. T. Mattila, A. C. Thomas, Nitric Oxide Synthase: Non-Canonical Expression Patterns. *Front. Immunol.* **5** (2014).
 31. J. Oliva, O. Terrier, Viral and Bacterial Co-Infections in the Lungs: Dangerous Liaisons. *Viruses* **13** (2021).
 32. Z. Huang, S. N. Kłodzińska, F. Wan, H. M. Nielsen, Nanoparticle-mediated pulmonary drug delivery: state of the art towards efficient treatment of recalcitrant respiratory tract bacterial infections. *Drug Deliv. Transl. Res.* **2021** *114* **11**, 1634–1654 (2021).
 33. N. Rastogi, E. Legrand, C. Sola, The mycobacteria: an introduction to nomenclature and pathogenesis. *Rev. Sci. Tech.* **20**, 21–54 (2001).
 34. C. Y. Turenne, Nontuberculous mycobacteria: Insights on taxonomy and evolution. *Infect. Genet. Evol.* **72**, 159–168 (2019).
 35. M. D. Johansen, J. L. Herrmann, L. Kremer, Non-tuberculous mycobacteria and the rise of *Mycobacterium abscessus*. *Nat. Rev. Microbiol.*, 1–16 (2020).
 36. C. J. Meehan, R. A. Barco, Y. H. E. Loh, S. Cogneau, L. Rigouts, Reconstituting the genus mycobacterium. *Int. J. Syst. Evol. Microbiol.* **71**, 004922 (2021).
 37. M. V. Palmer, M. D. Welsh, J. M. Hostetter, Mycobacterial Diseases of Animals. *Vet. Med. Int.* **2011** (2011).
 38. I. Barberis, N. L. Bragazzi, L. Galluzzo, M. Martini, The history of tuberculosis: from the first historical records to the isolation of Koch's bacillus. *J. Prev. Med.*

Hyg. **58**, E9 (2017).

39. J. W. Saelens, G. Viswanathan, D. M. Tobin, Mycobacterial Evolution Intersects With Host Tolerance. *Front. Immunol.* **10** (2019).
40. R. Bandaru, D. Sahoo, R. Naik, P. Kesharwani, R. Dandela, Pathogenesis, biology, and immunology of tuberculosis. *Nanotechnol. Based Approaches Tuberc. Treat.*, 1–25 (2020).
41. WHO, Global tuberculosis report 2021 (April 21, 2022).
42. M. Pai, *et al.*, Tuberculosis. *Nat. Rev. Dis. Prim.* 2016 **21** **2**, 1–23 (2016).
43. W. R. O. for E. European Centre for Disease Prevention and Control, Tuberculosis surveillance and monitoring in Europe 2022 –2020 data (April 22, 2022).
44. R. Fukunaga, *et al.*, Epidemiology of Tuberculosis and Progress Toward Meeting Global Targets — Worldwide, 2019. *Morb. Mortal. Wkly. Rep.* **70**, 427 (2021).
45. B. I. Restrepo, Diabetes and tuberculosis. *Microbiol. Spectr.* **4** (2016).
46. M. D. Ngo, S. Bartlett, K. Ronacher, Diabetes-Associated Susceptibility to Tuberculosis: Contribution of Hyperglycemia vs. Dyslipidemia. *Microorg. 2021, Vol. 9, Page 2282* **9**, 2282 (2021).
47. G. Churchyard, *et al.*, What We Know About Tuberculosis Transmission: An Overview. *J. Infect. Dis.* **216**, S629 (2017).
48. M. U. Shiloh, Mechanisms of mycobacterial transmission: how does *Mycobacterium tuberculosis* enter and escape from the human host. *Future Microbiol.* **11**, 1503 (2016).
49. J. B. Torrelles, L. S. Schlesinger, Integrating Lung Physiology, Immunology and Tuberculosis. *Trends Microbiol.* **25**, 688 (2017).
50. E. A. Nardell, Transmission and Institutional Infection Control of Tuberculosis. *Cold Spring Harb. Perspect. Med.* **6** (2016).
51. A. Allué-Guardia, J. I. García, J. B. Torrelles, Evolution of Drug-Resistant *Mycobacterium tuberculosis* Strains and Their Adaptation to the Human Lung Environment. *Front. Microbiol.* **12**, 137 (2021).

52. A.-K. Reuschl, *et al.*, Innate activation of human primary epithelial cells broadens the host response to Mycobacterium tuberculosis in the airways. *PLOS Pathog.* **13**, e1006577 (2017).
53. A. M. de Waal, P. S. Hiemstra, T. H. Ottenhoff, S. A. Joosten, A. M. van der Does, Lung epithelial cells interact with immune cells and bacteria to shape the microenvironment in tuberculosis. *Thorax* **77**, 408 (2022).
54. H. M. Lee, J. M. Yuk, D. M. Shin, E. K. Jo, Dectin-1 is inducible and plays an essential role for mycobacteria-induced innate immune responses in airway epithelial cells. *J. Clin. Immunol.* **29**, 795–805 (2009).
55. R. Van Crevel, J. Kleinnijenhuis, M. Oosting, L. A. B. Joosten, M. G. Netea, Innate Immune Recognition of Mycobacterium tuberculosis. *Clin. Dev. Immunol.* **2011**, 12 (2011).
56. A. A. Dias, *et al.*, TLR-9 Plays a Role in Mycobacterium leprae-Induced Innate Immune Activation of A549 Alveolar Epithelial Cells. *Front. Immunol.* **12**, 3238 (2021).
57. N. Gupta, R. Kumar, B. Agrawal, New players in immunity to tuberculosis: The host microbiome, lung epithelium, and innate immune cells. *Front. Immunol.* **9**, 709 (2018).
58. E. Tenland, *et al.*, Innate Immune Responses after Airway Epithelial Stimulation with Mycobacterium bovis Bacille-Calmette Guérin. *PLoS One* **11**, e0164431 (2016).
59. M. Ritter, D. Mennerich, A. Weith, P. Seither, Characterization of Toll-like receptors in primary lung epithelial cells: Strong impact of the TLR3 ligand poly(I:C) on the regulation of Toll-like receptors, adaptor proteins and inflammatory response. *J. Inflamm.* **2**, 1–15 (2005).
60. B. De Yang, *et al.*, LL-37, the neutrophil granule- and epithelial cell-derived cathelicidin, utilizes formyl peptide receptor-like 1 (FPRL1) as a receptor to chemoattract human peripheral blood neutrophils, monocytes, and T cells. *J. Exp. Med.* **192**, 1069–1074 (2000).
61. B. Rivas-Santiago, *et al.*, Expression of cathelicidin LL-37 during Mycobacterium tuberculosis infection in human alveolar macrophages, monocytes, neutrophils, and epithelial cells. *Infect. Immun.* **76**, 935–941 (2008).
62. S. Silva-Gomes, S. Vale-Costa, R. Appelberg, M. S. Gomes, Iron in

- intracellular infection: To provide or to deprive? *Front. Cell. Infect. Microbiol.* **3**, 96 (2013).
63. J. R. Boelaert, S. J. Vandecasteele, R. Appelberg, V. R. Gordeuk, The effect of the host's iron status on tuberculosis. *J. Infect. Dis.* **195**, 1745–1753 (2007).
 64. R. Abreu, L. Essler, A. Loy, F. Quinn, P. Giri, Heparin inhibits intracellular *Mycobacterium tuberculosis* bacterial replication by reducing iron levels in human macrophages. *Sci. Reports 2018 81* **8**, 1–12 (2018).
 65. Y. Li, Y. Wang, X. Liu, The role of airway epithelial cells in response to mycobacteria infection. *Clin. Dev. Immunol.* **2012** (2012).
 66. M. B. Ryndak, D. Chandra, S. Laal, Understanding dissemination of *Mycobacterium tuberculosis* from the lungs during primary infection. *J. Med. Microbiol.* **65**, 362–369 (2016).
 67. M. Bertuzzi, G. E. Hayes, E. M. Bignell, Microbial uptake by the respiratory epithelium: outcomes for host and pathogen. *FEMS Microbiol. Rev.* **43**, 145–161 (2019).
 68. M. J. Harriff, *et al.*, Human Lung Epithelial Cells Contain *Mycobacterium tuberculosis* in a Late Endosomal Vacuole and Are Efficiently Recognized by CD8+ T Cells. *PLoS One* **9**, e97515 (2014).
 69. J. E. Wosen, D. Mukhopadhyay, C. MacAubas, E. D. Mellins, Epithelial MHC class II expression and its role in antigen presentation in the gastrointestinal and respiratory tracts. *Front. Immunol.* **9**, 2144 (2018).
 70. T. H. Kalb, M. T. Chuang, Z. Marom, L. Mayer, Evidence for accessory cell function by class II MHC antigen-expressing airway epithelial cells. *Am. J. Respir. Cell Mol. Biol.* **4**, 320–329 (1991).
 71. J. Arcos, *et al.*, *Mycobacterium tuberculosis* cell wall released fragments by the action of the human lung mucosa modulate macrophages to control infection in an IL-10-dependent manner. *Mucosal Immunol.* **2016 105** **10**, 1248–1258 (2016).
 72. J. M. Scordo, *et al.*, *Mycobacterium tuberculosis* cell wall fragments released upon bacterial contact with the human lung mucosa alter the neutrophil response to infection. *Front. Immunol.* **8**, 307 (2017).
 73. J. M. Scordo, D. L. Knoell, J. B. Torrelles, Alveolar Epithelial Cells in

Mycobacterium tuberculosis Infection: Active Players or Innocent Bystanders? *J. Innate Immun.* **8**, 3 (2016).

74. S. Ahmad, Pathogenesis, immunology, and diagnosis of latent Mycobacterium tuberculosis infection. *Clin. Dev. Immunol.* **2011** (2011).
75. C. E. Stamm, A. C. Collins, M. U. Shiloh, Sensing of Mycobacterium tuberculosis and consequences to both host and bacillus. *Immunol. Rev.* **264**, 204–219 (2015).
76. S. B. Cohen, *et al.*, Alveolar Macrophages Provide an Early Mycobacterium tuberculosis Niche and Initiate Dissemination. *Cell Host Microbe* **24**, 439-446.e4 (2018).
77. L. Blanc, *et al.*, Mycobacterium tuberculosis inhibits human innate immune responses via the production of TLR2 antagonist glycolipids. *Proc. Natl. Acad. Sci. U. S. A.* **114**, 11205–11210 (2017).
78. A. Arbués, *et al.*, Trisaccharides of Phenolic Glycolipids Confer Advantages to Pathogenic Mycobacteria through Manipulation of Host-Cell Pattern-Recognition Receptors. *ACS Chem. Biol.* **11**, 2865–2875 (2016).
79. Y. Liu, J. Y. Li, S. T. Chen, H. R. Huang, H. Cai, The rLrp of Mycobacterium tuberculosis inhibits proinflammatory cytokine production and downregulates APC function in mouse macrophages via a TLR2-mediated PI3K/Akt pathway activation-dependent mechanism. *Cell. Mol. Immunol.* **13**, 729–746 (2016).
80. M. J. Marakalala, *et al.*, Inflammatory signaling in human Tuberculosis granulomas is spatially organized. *Nat. Med.* **22**, 531 (2016).
81. A. V. Veatch, D. Kaushal, Opening Pandora's Box: Mechanisms of Mycobacterium tuberculosis Resuscitation. *Trends Microbiol.* **26**, 145–157 (2018).
82. R. Singh, *et al.*, Recent updates on drug resistance in Mycobacterium tuberculosis. *J. Appl. Microbiol.* **128**, 1547–1567 (2020).
83. C. M. Gill, L. Dolan, L. M. Piggott, A. M. McLaughlin, New developments in tuberculosis diagnosis and treatment. *Breathe* **18** (2022).
84. Q. Zhang, *et al.*, Uncovering the Resistance Mechanism of Mycobacterium tuberculosis to Rifampicin Due to RNA Polymerase H451D/Y/R Mutations From Computational Perspective. *Front. Chem.* **7**, 819 (2019).

85. M. J. Nasiri, *et al.*, New insights in to the intrinsic and acquired drug resistance mechanisms in mycobacteria. *Front. Microbiol.* **8**, 681 (2017).
86. J. C. Palomino, A. Martin, Drug Resistance Mechanisms in Mycobacterium tuberculosis. *Antibiotics* **3**, 317 (2014).
87. L. Nguyen, Antibiotic resistance mechanisms in M. tuberculosis: an update. *Arch. Toxicol.* **90**, 1585 (2016).
88. S. S. Swain, D. Sharma, T. Hussain, S. Pati, Molecular mechanisms of underlying genetic factors and associated mutations for drug resistance in Mycobacterium tuberculosis. *Emerg. Microbes Infect.* **9**, 1651 (2020).
89. D. Horne, S. Skerrett, Recent advances in nontuberculous mycobacterial lung infections. *F1000Research* **8** (2019).
90. Y. M. Boudehen, L. Kremer, Mycobacterium abscessus. *Trends Microbiol.* **29**, 951–952 (2021).
91. R. C. Lopeman, J. Harrison, M. Desai, J. A. G. Cox, Mycobacterium abscessus: Environmental Bacterium Turned Clinical Nightmare. *Microorganisms* **7** (2019).
92. B. Petrini, Mycobacterium abscessus: an emerging rapid-growing potential pathogen. *APMIS* **114**, 319–328 (2006).
93. M. M. Johnson, J. A. Odell, Nontuberculous mycobacterial pulmonary infections. *J. Thorac. Dis.* **6**, 210–220 (2014).
94. D. G. Lee, *et al.*, 10-DEBC Hydrochloride as a Promising New Agent against Infection of Mycobacterium abscessus. *Int. J. Mol. Sci.* **23** (2022).
95. M. J. Van der Werf, *et al.*, Inventory study of non-tuberculous mycobacteria in the European Union. *BMC Infect. Dis.* **14** (2014).
96. S. K. Brode, C. L. Daley, T. K. Marras, The epidemiologic relationship between tuberculosis and nontuberculous mycobacterial disease: A systematic review. *Int. J. Tuberc. Lung Dis.* **18**, 1370–1377 (2014).
97. N. Veziris, *et al.*, Non-tuberculous mycobacterial pulmonary diseases in France: an 8 years nationwide study. *BMC Infect. Dis.* **21**, 1–10 (2021).
98. K. L. Winthrop, *et al.*, Pulmonary nontuberculous mycobacterial disease

- prevalence and clinical features: an emerging public health disease. *Am. J. Respir. Crit. Care Med.* **182**, 977–982 (2010).
99. C. N. Ratnatunga, *et al.*, The Rise of Non-Tuberculosis Mycobacterial Lung Disease. *Front. Immunol.* **11**, 303 (2020).
 100. C. D. M. Wijers, J. F. Chmiel, B. M. Gaston, Bacterial infections in patients with primary ciliary dyskinesia: Comparison with cystic fibrosis. *Chron. Respir. Dis.* **14**, 392 (2017).
 101. S. L. Martiniano, J. A. Nick, C. L. Daley, Nontuberculous Mycobacterial Infections in Cystic Fibrosis. *Clin. Chest Med.* **37**, 83–96 (2016).
 102. N. Poerio, *et al.*, Combined Host- and Pathogen-Directed Therapy for the Control of Mycobacterium abscessus Infection. *Microbiol. Spectr.* **10** (2022).
 103. K. L. Becker, *et al.*, Deficient interleukin-17 production in response to Mycobacterium abscessus in cystic fibrosis. *Eur. Respir. J.* **47**, 990–993 (2016).
 104. P. Phoompoung, *et al.*, Factors associated with acquired Anti IFN- γ autoantibody in patients with nontuberculous mycobacterial infection. *PLoS One* **12**, e0176342 (2017).
 105. C. K. Tan, *et al.*, Mycobacterial bacteraemia in patients infected and not infected with human immunodeficiency virus, Taiwan. *Clin. Microbiol. Infect.* **16**, 627–630 (2010).
 106. M. A. Lake, L. R. Ambrose, M. C. I. Lipman, D. M. Lowe, '“Why me, why now?” Using clinical immunology and epidemiology to explain who gets nontuberculous mycobacterial infection. *BMC Med.* **14** (2016).
 107. J. O. Falkinham, Ecology of nontuberculous mycobacteria-where do human infections come from? *Semin. Respir. Crit. Care Med.* **34**, 95–102 (2013).
 108. K. Ryan, T. F. Byrd, Mycobacterium abscessus: Shapeshifter of the mycobacterial world. *Front. Microbiol.* **9** (2018).
 109. P. Faverio, *et al.*, Nontuberculous mycobacterial pulmonary disease: an integrated approach beyond antibiotics. *ERJ Open Res.* **7**, 00574–02020 (2021).
 110. L. Victoria, A. Gupta, J. L. Gómez, J. Robledo, Mycobacterium abscessus

complex: A Review of Recent Developments in an Emerging Pathogen. *Front. Cell. Infect. Microbiol.* **11**, 338 (2021).

111. C. Ruis, *et al.*, Dissemination of *Mycobacterium abscessus* via global transmission networks. *Nat. Microbiol.* **2021** 610 **6**, 1279–1288 (2021).
112. K. C. Ferrell, M. D. Johansen, J. A. Triccas, C. Counoupas, Virulence Mechanisms of *Mycobacterium abscessus*: Current Knowledge and Implications for Vaccine Design. *Front. Microbiol.* **13**, 557 (2022).
113. J. M. Bryant, *et al.*, Population-level genomics identifies the emergence and global spread of a human transmissible multidrug-resistant nontuberculous mycobacterium. *Science* **354**, 751 (2016).
114. R. M. Davidson, A Closer Look at the Genomic Variation of Geographically Diverse *Mycobacterium abscessus* Clones That Cause Human Infection and Disease. *Front. Microbiol.* **9** (2018).
115. R. M. Davidson, *et al.*, Genome sequencing of *Mycobacterium abscessus* isolates from patients in the united states and comparisons to globally diverse clinical strains. *J. Clin. Microbiol.* **52**, 3573–3582 (2014).
116. A.-L. Roux, *et al.*, The distinct fate of smooth and rough *Mycobacterium abscessus* variants inside macrophages. *Open Biol.* **6**, 160185 (2016).
117. E. S. Gloag, D. J. Wozniak, P. Stoodley, L. Hall-Stoodley, *Mycobacterium abscessus* biofilms have viscoelastic properties which may contribute to their recalcitrance in chronic pulmonary infections. *Sci. Rep.* **11**, 5020 (2021).
118. G. Clary, *et al.*, *Mycobacterium abscessus* smooth and rough morphotypes form antimicrobial-tolerant biofilm phenotypes but are killed by acetic acid. *Antimicrob. Agents Chemother.* **62** (2018).
119. E. J. Park, P. Silwal, E. K. Jo, Host-Pathogen Interactions Operative during *Mycobacteroides abscessus* Infection. *Immune Netw.* **21** (2021).
120. A. Viljoen, F. Viela, L. Kremer, Y. F. Dufrêne, Fast chemical force microscopy demonstrates that glycopeptidolipids define nanodomains of varying hydrophobicity on mycobacteria. *Nanoscale Horizons* **5**, 944–953 (2020).
121. G. Degiacomi, *et al.*, *Mycobacterium abscessus*, an Emerging and Worrisome Pathogen among Cystic Fibrosis Patients. *Int. J. Mol. Sci.* **20** (2019).

122. M. M. F. Schuurbijs, *et al.*, Immune defects in patients with pulmonary Mycobacterium abscessus disease without cystic fibrosis. *ERJ Open Res.* **6**, 00590–02020 (2020).
123. A. Bernut, *et al.*, Mycobacterium abscessus cording prevents phagocytosis and promotes abscess formation. *Proc. Natl. Acad. Sci. U. S. A.* **111**, E943–E952 (2014).
124. A. Bernut, *et al.*, Mycobacterium abscessus-Induced Granuloma Formation Is Strictly Dependent on TNF Signaling and Neutrophil Trafficking. *PLOS Pathog.* **12**, e1005986 (2016).
125. R. Thomson, C. Tolson, H. Sidjabat, F. Huygens, M. Hargreaves, Mycobacterium abscessus isolated from municipal water - a potential source of human infection. *BMC Infect. Dis.* **13**, 1–7 (2013).
126. T. F. Byrd, E. D. Chan, Editorial: Mycobacterium abscessus; The Paradox of Low Pathogenicity and High Virulence. *Front. Microbiol.* **0**, 2202 (2022).
127. Y. W. Weng, *et al.*, Treatment for Mycobacterium abscessus complex–lung disease. *J. Formos. Med. Assoc.* **119**, S58–S66 (2020).
128. M. Lopes-Pacheco, CFTR Modulators: The Changing Face of Cystic Fibrosis in the Era of Precision Medicine. *Front. Pharmacol.* **10**, 1662 (2020).
129. F. Ratjen, *et al.*, Cystic fibrosis. *Nat. Rev. Dis. Prim.* **1**, 15010 (2015).
130. R. L. Gibson, J. L. Burns, B. W. Ramsey, Pathophysiology and Management of Pulmonary Infections in Cystic Fibrosis. <https://doi.org/10.1164/rccm.200304-505SO> **168**, 918–951 (2012).
131. V. Saint-Criq, M. A. Gray, Role of CFTR in epithelial physiology. *Cell. Mol. Life Sci.* **2016 741 74**, 93–115 (2016).
132. M. J. Welsh, A. E. Smith, Molecular mechanisms of CFTR chloride channel dysfunction in cystic fibrosis. *Cell* **73**, 1251–1254 (1993).
133. M. Lopes-Pacheco, CFTR modulators: Shedding light on precision medicine for cystic fibrosis. *Front. Pharmacol.* **7**, 275 (2016).
134. K. De Boeck, A. Zolin, H. Cuppens, H. V. Olesen, L. Viviani, The relative frequency of CFTR mutation classes in European patients with cystic fibrosis. *J. Cyst. Fibros.* **13**, 403–409 (2014).

135. K. De Boeck, M. D. Amaral, Progress in therapies for cystic fibrosis. *Lancet Respir. Med.* **4**, 662–674 (2016).
136. E. Vallières, J. S. Elborn, Cystic fibrosis gene mutations: evaluation and assessment of disease severity. *Adv. Genomics Genet.* **4**, 161–172 (2014).
137. S. M. Rowe, S. Miller, E. J. Sorscher, Cystic fibrosis. *N. Engl. J. Med.* **352**, 1992–2001 (2005).
138. F. A. L. Marson, C. S. Bertuzzo, J. D. Ribeiro, Classification of CFTR mutation classes. *Lancet Respir. Med.* **4**, e37–e38 (2016).
139. L. E. Donnelly, P. J. Barnes, Defective phagocytosis in airways disease. *Chest* **141**, 1055–1062 (2012).
140. D. Hartl, *et al.*, Innate immunity in cystic fibrosis lung disease. *J. Cyst. Fibros.* **11**, 363–382 (2012).
141. T. S. Cohen, A. Prince, Cystic fibrosis: a mucosal immunodeficiency syndrome. *Nat. Med.* **18**, 509 (2012).
142. J. F. Chmiel, P. B. Davis, State of the Art: Why do the lungs of patients with cystic fibrosis become infected and why can't they clear the infection? *Respir. Res.* **4**, 8 (2003).
143. O. Laselva, M. Conese, Three-Dimensional Airway Spheroids and Organoids for Cystic Fibrosis Research. *J. Respir. 2021, Vol. 1, Pages 229-247* **1**, 229–247 (2021).
144. K. To, R. Cao, A. Yegiazaryan, J. Owens, V. Venketaraman, General Overview of Nontuberculous Mycobacteria Opportunistic Pathogens: Mycobacterium avium and Mycobacterium abscessus. *J. Clin. Med.* **9**, 2541 (2020).
145. I. Sermet-Gaudelus, *et al.*, Mycobacterium abscessus and Children with Cystic Fibrosis. *Emerg. Infect. Dis.* **9**, 1587 (2003).
146. K. N. Olivier, *et al.*, Nontuberculous mycobacteria. I: multicenter prevalence study in cystic fibrosis. *Am. J. Respir. Crit. Care Med.* **167**, 828–834 (2003).
147. B. Fauroux, *et al.*, Mycobacterial lung disease in cystic fibrosis: a prospective study. *Pediatr. Infect. Dis. J.* **16**, 354–358 (1997).

148. T. Qvist, *et al.*, Chronic pulmonary disease with Mycobacterium abscessus complex is a biofilm infection. *Eur. Respir. J.* **46**, 1823–1826 (2015).
149. L. B. Davidson, R. Nessar, P. Kempaiah, D. J. Perkins, T. F. Byrd, Mycobacterium abscessus Glycopeptidolipid Prevents Respiratory Epithelial TLR2 Signaling as Measured by H β D2 Gene Expression and IL-8 Release. *PLoS One* **6**, e29148 (2011).
150. M. Matsuyama, *et al.*, Transcriptional response of respiratory epithelium to nontuberculous mycobacteria. *Am. J. Respir. Cell Mol. Biol.* **58**, 241–252 (2018).
151. C. J. Fowler, *et al.*, Abnormal nasal nitric oxide production, ciliary beat frequency, and toll-like receptor response in pulmonary nontuberculous mycobacterial disease epithelium. *Am. J. Respir. Crit. Care Med.* **187**, 1374–1381 (2013).
152. C. Zhang, *et al.*, Mycobacterium abscessus—Bronchial Epithelial Cells Cross-Talk Through Type I Interferon Signaling. *Front. Immunol.* **10** (2019).
153. G. M. Ribeiro, *et al.*, Increased survival and proliferation of the epidemic strain Mycobacterium abscessus subsp. massiliense CRM0019 in alveolar epithelial cells. *BMC Microbiol.* **17**, 195 (2017).
154. K. C. Malcolm, *et al.*, Neutrophil killing of Mycobacterium abscessus by intra- and extracellular mechanisms. *PLoS One* **13**, e0196120 (2018).
155. K. C. Malcolm, *et al.*, Mycobacterium abscessus Induces a Limited Pattern of Neutrophil Activation That Promotes Pathogen Survival. *PLoS One* **8** (2013).
156. S. J. Lee, *et al.*, Mycobacterium abscessus MAB2560 induces maturation of dendritic cells via Toll-like receptor 4 and drives Th1 immune response. *BMB Rep.* **47**, 512 (2014).
157. K. E. Killick, *et al.*, Receptor-mediated recognition of mycobacterial pathogens. *Cell. Microbiol.* **15**, 1484–1495 (2013).
158. D. M. Shin, *et al.*, Mycobacterium abscessus activates the macrophage innate immune response via a physical and functional interaction between TLR2 and dectin-1. *Cell. Microbiol.* **10**, 1608–1621 (2008).
159. H. M. Lee, *et al.*, Mycobacterium abscessus activates the NLRP3 inflammasome via Dectin-1–Syk and p62/SQSTM1. *Immunol. Cell Biol.* **90**,

601 (2012).

160. M. Cruz-Aguilar, A. I. Castillo-Rodal, R. Arredondo-Hernández, Y. López-Vidal, Non-tuberculous mycobacteria immunopathogenesis: Closer than they appear. a prime of innate immunity trade-off and NTM ways into virulence. *Scand. J. Immunol.* **94**, e13035 (2021).
161. J. Y. Kam, *et al.*, Rough and smooth variants of *Mycobacterium abscessus* are differentially controlled by host immunity during chronic infection of adult zebrafish. *Nat. Commun.* 2022 131 **13**, 1–11 (2022).
162. E. R. Rhoades, *et al.*, *Mycobacterium abscessus* Glycopeptidolipids mask underlying cell wall phosphatidyl-myo-inositol mannosides blocking induction of human macrophage TNF-alpha by preventing interaction with TLR2. *J. Immunol.* **183**, 1997–2007 (2009).
163. R. Nessar, E. Cambau, J. M. Reyrat, A. Murray, B. Gicquel, *Mycobacterium abscessus*: A new antibiotic nightmare. *J. Antimicrob. Chemother.* **67**, 810–818 (2012).
164. W. Nie, *et al.*, Species identification of *Mycobacterium abscessus* subsp. *abscessus* and *Mycobacterium abscessus* subsp. *bolletii* using *rpoB* and *hsp65*, and susceptibility testing to eight antibiotics. *Int. J. Infect. Dis.* **25**, 170–174 (2014).
165. M. Illouz, M. Alcaraz, F. Roquet-Banères, L. Kremer, *Mycobacterium abscessus*, un modèle de résistance aux différentes classes d'antibiotiques. *médecine/sciences* **37**, 993–1001 (2021).
166. A. Somoskovi, M. Salfinger, Nontuberculous mycobacteria in respiratory infections: advances in diagnosis and identification. *Clin. Lab. Med.* **34**, 271–295 (2014).
167. M. R. Lee, *et al.*, *Mycobacterium abscessus* complex infections in humans. *Emerg. Infect. Dis.* **21**, 1638–1646 (2015).
168. M. Gorzynski, T. Week, T. Jaramillo, E. Dzalamidze, L. Danelishvili, *Mycobacterium abscessus* genetic determinants associated with the intrinsic resistance to antibiotics. *Microorganisms* **9** (2021).
169. C. S. Haworth, *et al.*, British Thoracic Society guidelines for the management of non-tuberculous mycobacterial pulmonary disease (NTM-PD). *Thorax* **72**, ii1–ii64 (2017).

170. J. Chen, *et al.*, Clinical efficacy and adverse effects of antibiotics used to treat mycobacterium abscessus pulmonary disease. *Front. Microbiol.* **10**, 1977 (2019).
171. S. Sharma, V. Upadhyay, Epidemiology, diagnosis & treatment of non-tuberculous mycobacterial diseases. *Indian J. Med. Res.* **152**, 185–226 (2020).
172. S. A. Novosad, S. E. Beekmann, P. M. Polgreen, K. Mackey, K. L. Winthrop, Treatment of Mycobacterium abscessus Infection. *Emerg. Infect. Dis.* **22**, 511 (2016).
173. S. G. Kurz, *et al.*, Summary for clinicians: 2020 clinical practice guideline summary for the treatment of nontuberculous mycobacterial pulmonary disease. *Ann. Am. Thorac. Soc.* **17**, 1033–1039 (2020).
174. R. A. Floto, *et al.*, US Cystic Fibrosis Foundation and European Cystic Fibrosis Society consensus recommendations for the management of non-tuberculous mycobacteria in individuals with cystic fibrosis: Executive summary. *Thorax* **71** (2016).
175. S. L. Martiniano, *et al.*, Challenging scenarios in nontuberculous mycobacterial infection in cystic fibrosis. *Pediatr. Pulmonol.* **55**, 521 (2020).
176. P. Allen, J. Borick, J. Borick, Acute and Chronic Infection Management in CF. *Cyst. Fibros. Prim. Care* , 69 (2020).
177. F. Mougari, *et al.*, Infections caused by Mycobacterium abscessus: epidemiology, diagnostic tools and treatment. *Expert Rev. Anti. Infect. Ther.* **14**, 1139–1154 (2016).
178. L. I. Gill, C. Dominic, S. Tiberi, Atypical mycobacterial infections - management and when to treat. *Curr. Opin. Pulm. Med.* **27**, 216–223 (2021).
179. A. Bernut, J.-L. Herrmann, D. Ordway, L. Kremer, The Diverse Cellular and Animal Models to Decipher the Physiopathological Traits of Mycobacterium abscessus Infection. *Front. Cell. Infect. Microbiol.* **7**, 100 (2017).
180. H. F. M. Abdelaal, E. D. Chan, L. Young, S. L. Baldwin, R. N. Coler, Mycobacterium abscessus: It's Complex. *Microorganisms* **10**, 1454 (2022).
181. T. F. Byrd, C. R. Lyons, Preliminary characterization of a Mycobacterium abscessus mutant in human and murine models of infection. *Infect. Immun.*

- 67, 4700–4707 (1999).
182. C. Brambilla, *et al.*, Mycobacteria Clumping Increase Their Capacity to Damage Macrophages. *Front. Microbiol.* **7** (2016).
 183. A. Viljoen, M. Blaise, C. de Chastellier, L. Kremer, MAB_3551c encodes the primary triacylglycerol synthase involved in lipid accumulation in *Mycobacterium abscessus*. *Mol. Microbiol.* **102**, 611–627 (2016).
 184. A. L. Roux, *et al.*, Overexpression of proinflammatory TLR-2-signalling lipoproteins in hypervirulent mycobacterial variants. *Cell. Microbiol.* **13**, 692–704 (2011).
 185. M. Drancourt, Looking in amoebae as a source of mycobacteria. *Microb. Pathog.* **77**, 119–124 (2014).
 186. J. C. B. N’Goma, *et al.*, *Mycobacterium abscessus* phospholipase C expression is induced during coculture within amoebae and enhances *M. abscessus* virulence in mice. *Infect. Immun.* **83**, 780–791 (2015).
 187. A. Bernut, *et al.*, CFTR Protects against *Mycobacterium abscessus* Infection by Fine-Tuning Host Oxidative Defenses. *Cell Rep.* **26**, 1828-1840.e4 (2019).
 188. E. C. Maggioncalda, *et al.*, A mouse model of pulmonary *Mycobacteroides abscessus* infection. *Sci. Reports 2020 101* **10**, 1–8 (2020).
 189. E. L. Jackson, H. Lu, Three-dimensional models for studying development and disease: moving on from organisms to organs-on-a-chip and organoids. *Integr. Biol. (Camb).* **8**, 672 (2016).
 190. F. Schutgens, H. Clevers, Annual Review of Pathology: Mechanisms of Disease Human Organoids: Tools for Understanding Biology and Treating Diseases. *Rev. Adv. first* (2019) <https://doi.org/10.1146/annurev-pathmechdis>.
 191. G. Rossi, A. Manfrin, M. P. Lutolf, Progress and potential in organoid research. *Nat. Rev. Genet.* **19**, 671–687 (2018).
 192. J. van der Vaart, H. Clevers, Airway organoids as models of human disease. *J. Intern. Med.* **289**, 604–613 (2021).
 193. M. A. Lancaster, J. A. Knoblich, Organogenesis in a dish: Modeling development and disease using organoid technologies. *Science (80-.).* **345** (2014).

194. A. Banadka, A. Panwar, H. Bhagwanani, P. Saha, Organoids: inception and utilization of 3D organ models. *Eur. J. Biol. Res.* (2021) <https://doi.org/10.5281/ZENODO.4362214>.
195. T. Sato, *et al.*, Single Lgr5 stem cells build crypt-villus structures in vitro without a mesenchymal niche. *Nat.* 2009 4597244 **459**, 262–265 (2009).
196. N. Sachs, *et al.*, Long-term expanding human airway organoids for disease modeling. *EMBO J.* **38** (2019).
197. D. Dutta, I. Heo, H. Clevers, Disease Modeling in Stem Cell-Derived 3D Organoid Systems. *Trends Mol. Med.* **23**, 393–410 (2017).
198. D. Dutta, H. Clevers, Organoid culture systems to study host-pathogen interactions. *Curr. Opin. Immunol.* **48**, 15–22 (2017).
199. P. Wörsdörfer, T. I, I. Asahina, Y. Sumita, S. Ergün, Do not keep it simple: recent advances in the generation of complex organoids. *J. Neural Transm.* **127**, 1569 (2020).
200. Y. Li, P. Tang, S. Cai, J. Peng, G. Hua, Organoid based personalized medicine: from bench to bedside. *Cell Regen.* 2020 91 **9**, 1–33 (2020).
201. G. Botti, M. Di Bonito, M. Cantile, Organoid biobanks as a new tool for pre-clinical validation of candidate drug efficacy and safety. *Int. J. Physiol. Pathophysiol. Pharmacol.* **13**, 17 (2021).
202. H. Clevers, Modeling Development and Disease with Organoids. *Cell* **165**, 1586–1597 (2016).
203. M. A. Lancaster, M. Huch, Disease modelling in human organoids. *DMM Dis. Model. Mech.* **12** (2019).
204. G. De Wert, C. Mummery, Human embryonic stem cells: research, ethics and policy. *Hum. Reprod.* **18**, 672–682 (2003).
205. J. Drost, H. Clevers, Translational applications of adult stem cell-derived organoids. *Development* **144**, 968–975 (2017).
206. J. Azar, *et al.*, The Use of Stem Cell-Derived Organoids in Disease Modeling: An Update. *Int. J. Mol. Sci.* 2021, Vol. 22, Page 7667 **22**, 7667 (2021).
207. C. Corrà, L. Novellasdemunt, V. S. W. Li, A brief history of organoids. *Am. J.*

Physiol. - Cell Physiol. **319**, C151–C165 (2020).

208. J. Kong, *et al.*, Lung organoids, useful tools for investigating epithelial repair after lung injury. *Stem Cell Res. Ther.* 2021 121 **12**, 1–13 (2021).
209. M. Z. Nikolić, *et al.*, Human embryonic lung epithelial tips are multipotent progenitors that can be expanded in vitro as long-term self-renewing organoids. *Elife* **6** (2017).
210. Z. Heydari, *et al.*, Organoids: a novel modality in disease modeling. *Bio-Design Manuf.* 2021 44 **4**, 689–716 (2021).
211. N. Iakobachvili, P. J. Peters, Humans in a dish: The potential of organoids in modeling immunity and infectious diseases. *Front. Microbiol.* **8** (2017).
212. T. Suezawa, *et al.*, Disease modeling of pulmonary fibrosis using human pluripotent stem cell-derived alveolar organoids. *Stem Cell Reports* **16**, 2973–2987 (2021).
213. J. H. Kim, *et al.*, Human pluripotent stem cell-derived alveolar organoids for modeling pulmonary fibrosis and drug testing. *Cell Death Discov.* 2021 71 **7**, 1–12 (2021).
214. S. P. Sajuthi, *et al.*, Nasal airway transcriptome-wide association study of asthma reveals genetically driven mucus pathobiology. *Nat. Commun.* 2022 131 **13**, 1–17 (2022).
215. S. Van Riet, *et al.*, Organoid-based expansion of patient-derived primary alveolar type 2 cells for establishment of alveolus epithelial Lung-Chip cultures. *Am. J. Physiol. Lung Cell. Mol. Physiol.* **322**, L526–L538 (2022).
216. S. Song, *et al.*, D-dopachrome tautomerase contributes to lung epithelial repair via atypical chemokine receptor 3-dependent Akt signaling. *EBioMedicine* **68** (2021).
217. J. van der Vaart, *et al.*, Modelling of primary ciliary dyskinesia using patient-derived airway organoids. *EMBO Rep.* **22** (2021).
218. Y. Li, Q. Wu, X. Sun, J. Shen, H. Chen, Organoids as a Powerful Model for Respiratory Diseases. *Stem Cells Int.* **2020** (2020).
219. C. Aguilar, *et al.*, Organoids as host models for infection biology – a review of methods. *Exp. Mol. Med.* 2021 5310 **53**, 1471–1482 (2021).

220. A. Shpichka, *et al.*, Organoids in modelling infectious diseases. *Drug Discov. Today* **27**, 223–233 (2022).
221. F. Archer, A. Bobet-Erny, M. Gomes, State of the art on lung organoids in mammals. *Vet. Res.* **52**, 1–10 (2021).
222. K. V. Evans, J. H. Lee, Alveolar wars: The rise of in vitro models to understand human lung alveolar maintenance, regeneration, and disease. *Stem Cells Transl. Med.* **9**, 867–881 (2020).
223. M. C. Basil, *et al.*, Human distal airways contain a multipotent secretory cell that can regenerate alveoli. *Nat. 2022 6047904* **604**, 120–126 (2022).
224. M. C. Basil, *et al.*, The Cellular and Physiological Basis for Lung Repair and Regeneration: Past, Present, and Future. *Cell Stem Cell* **26**, 482 (2020).
225. N. S. Rozich, A. B. Blair, R. A. Burkhart, Organoids: a model for precision medicine. *Precis. Med. Investig. Pract. Provid.*, 123–129 (2020).
226. S. Bagayoko, *et al.*, Host phospholipid peroxidation fuels ExoU-dependent cell necrosis and supports *Pseudomonas aeruginosa*-driven pathology. *PLoS Pathog.* **17** (2021).
227. J. Sempere, *et al.*, Minilungs from Human Embryonic Stem Cells to Study the Interaction of *Streptococcus pneumoniae* with the Respiratory Tract. *Microbiol. Spectr.* (2022) <https://doi.org/10.1128/SPECTRUM.00453-22>.
228. K. G. Chen, K. Park, J. R. Spence, Studying SARS-CoV-2 infectivity and therapeutic responses with complex organoids. *Nat. Cell Biol.* **23**, 822–833 (2021).
229. B. Varghese, Z. Ling, X. Ren, Reconstructing the pulmonary niche with stem cells: a lung story. *Stem Cell Res. Ther.* **13**, 1–12 (2022).
230. N. Kia'i, T. Bajaj, Histology, Respiratory Epithelium. *StatPearls* (2022).
231. B. Cunniff, J. E. Druso, J. L. van der Velden, Lung organoids: advances in generation and 3D-visualization. *Histochem. Cell Biol.* **155**, 301–308 (2021).
232. R. R. Nadkarni, S. Abed, J. S. Draper, Organoids as a model system for studying human lung development and disease. *Biochem. Biophys. Res. Commun.* **473**, 675–682 (2016).

233. J. R. Rock, *et al.*, Basal cells as stem cells of the mouse trachea and human airway epithelium. *Proc. Natl. Acad. Sci. U. S. A.* **106**, 12771 (2009).
234. H. Danahay, *et al.*, Notch2 is required for inflammatory cytokine-driven goblet cell metaplasia in the lung. *Cell Rep.* **10**, 239–252 (2015).
235. M. Hild, A. B. Jaffe, Production of 3-D Airway Organoids From Primary Human Airway Basal Cells and Their Use in High-Throughput Screening. *Curr. Protoc. Stem Cell Biol.* **37**, IE.9.1-IE.9.15 (2016).
236. M. Elbadawi, T. Efferth, Organoids of human airways to study infectivity and cytopathy of SARS-CoV-2. *Lancet Respir. Med.* **8**, e55–e56 (2020).
237. Y. Yamamoto, Y. Korogi, T. Hirai, S. Gotoh, A method of generating alveolar organoids using human pluripotent stem cells. *Methods Cell Biol.* **159**, 115–141 (2020).
238. T. Lu, Y. Cao, P. Zhao, S. Shen, Y. Xi, Organoid: a powerful tool to study lung regeneration and disease. *Cell Regen.* **10**, 1–10 (2021).
239. S. Konishi, A. Tata, P. R. Tata, Defined conditions for long-term expansion of murine and human alveolar epithelial stem cells in three-dimensional cultures. *STAR Protoc.* **3**, 101447 (2022).
240. R. F. Gonzalez, L. Allen, L. Gonzales, P. L. Ballard, L. G. Dobbs, HTII-280, a biomarker specific to the apical plasma membrane of human lung alveolar type II cells. *J. Histochem. Cytochem.* **58**, 891–901 (2010).
241. J. Youk, *et al.*, Three-Dimensional Human Alveolar Stem Cell Culture Models Reveal Infection Response to SARS-CoV-2. *Cell Stem Cell* **27**, 905-919.e10 (2020).
242. D. Liao, H. Li, Dissecting the Niche for Alveolar Type II Cells With Alveolar Organoids. *Front. Cell Dev. Biol.* **8**, 419 (2020).
243. C. T. Ekanger, *et al.*, Human Organotypic Airway and Lung Organoid Cells of Bronchiolar and Alveolar Differentiation Are Permissive to Infection by Influenza and SARS-CoV-2 Respiratory Virus. *Front. Cell. Infect. Microbiol.* **12**, 208 (2022).
244. M. C. Chiu, *et al.*, A bipotential organoid model of respiratory epithelium recapitulates high infectivity of SARS-CoV-2 Omicron variant. *Cell Discov.* **2022 81 8**, 1–15 (2022).

245. A. A. Salahudeen, *et al.*, Progenitor identification and SARS-CoV-2 infection in human distal lung organoids. *Nat. 2020 5887839* **588**, 670–675 (2020).
246. Z. Liu, *et al.*, Human Nasal Epithelial Organoids for Therapeutic Development in Cystic Fibrosis. *Genes (Basel)*. **11**, 1–17 (2020).
247. A. Rajan, *et al.*, The Human Nose Organoid Respiratory Virus Model: an Ex Vivo Human Challenge Model To Study Respiratory Syncytial Virus (RSV) and Severe Acute Respiratory Syndrome Coronavirus 2 (SARS-CoV-2) Pathogenesis and Evaluate Therapeutics. *MBio* **13** (2022).
248. G. D. Amatngalim, *et al.*, Measuring cystic fibrosis drug responses in organoids derived from 2D differentiated nasal epithelia. *bioRxiv*, 2021.07.20.453105 (2021).
249. C. Tindle, *et al.*, Adult stem cell-derived complete lung organoid models emulate lung disease in COVID-19. *Elife* **10** (2021).
250. M. M. Lamers, *et al.*, An organoid-derived bronchioalveolar model for SARS-CoV-2 infection of human alveolar type II-like cells. *EMBO J.* **40** (2021).
251. A. I. Vazquez-Armendariz, *et al.*, Multilineage murine stem cells generate complex organoids to model distal lung development and disease. *EMBO J.* **39** (2020).
252. G. Berkers, *et al.*, Rectal Organoids Enable Personalized Treatment of Cystic Fibrosis. *Cell Rep.* **26**, 1701-1708.e3 (2019).
253. A. Saini, Cystic Fibrosis Patients Benefit from Mini Guts. *Cell Stem Cell* **19**, 425–427 (2016).
254. K. M. de Winter – de Groot, *et al.*, Forskolin-induced swelling of intestinal organoids correlates with disease severity in adults with cystic fibrosis and homozygous F508del mutations. *J. Cyst. Fibros.* **19**, 614–619 (2020).
255. J. F. Dekkers, *et al.*, Characterizing responses to CFTR-modulating drugs using rectal organoids derived from subjects with cystic fibrosis. *Sci. Transl. Med.* **8**, 344ra84-344ra84 (2016).
256. M. A. Lensink, *et al.*, Organoids for personalized treatment of Cystic Fibrosis: Professional perspectives on the ethics and governance of organoid biobanking. *J. Cyst. Fibros.* **20**, 443–451 (2021).

257. , What is HIT-CF Europe? - HIT CF (July 13, 2022).
258. M. H. Geurts, *et al.*, Evaluating CRISPR-based prime editing for cancer modeling and CFTR repair in organoids. *Life Sci. alliance* **4** (2021).
259. M. P. Dumas, S. Xia, C. E. Bear, F. Ratjen, Perspectives on the translation of in-vitro studies to precision medicine in Cystic Fibrosis. *EBioMedicine* **73**, 103660 (2021).
260. J. D. Anderson, Z. Liu, L. V. Odom, L. Kersh, J. S. Guimbellot, CFTR function and clinical response to modulators parallel nasal epithelial organoid swelling. *Am. J. Physiol. - Lung Cell. Mol. Physiol.* **321**, L119–L129 (2021).
261. S. Pei, *et al.*, 3D Human Organoids: The Next “Viral” Model for the Molecular Basis of Infectious Diseases. *Biomed. 2022, Vol. 10, Page 1541* **10**, 1541 (2022).
262. H. Xu, *et al.*, Organoid technology in disease modelling, drug development, personalized treatment and regeneration medicine. *Exp. Hematol. Oncol.* **7**, 1–12 (2018).
263. S. E. Blutt, M. K. Estes, Organoid Models for Infectious Disease. *Annu. Rev. Med.* **73**, 167 (2022).
264. M. B. Kim, S. Hwangbo, S. Jang, Y. K. Jo, Bioengineered Co-culture of organoids to recapitulate host-microbe interactions. *Mater. Today Bio* **16**, 100345 (2022).
265. N. Kwak, *et al.*, Mycobacterium abscessus pulmonary disease: individual patient data meta-analysis. *Eur. Respir. J.* **54** (2019).
266. J. R. Honda, R. Viridi, E. D. Chan, Global Environmental Nontuberculous Mycobacteria and Their Contemporaneous Man-Made and Natural Niches. *Front. Microbiol.* **9** (2018).
267. R. E. Maphasa, M. Meyer, A. Dube, The Macrophage Response to Mycobacterium tuberculosis and Opportunities for Autophagy Inducing Nanomedicines for Tuberculosis Therapy. *Front. Cell. Infect. Microbiol.* **10**, 915 (2021).
268. S. Upadhyay, E. Mittal, J. A. Philips, Tuberculosis and the art of macrophage manipulation. *Pathog. Dis.* **76**, 37 (2018).

269. K. L. Fonseca, P. N. S. Rodrigues, I. A. S. Olsson, M. Saraiva, Experimental study of tuberculosis: From animal models to complex cell systems and organoids. *PLoS Pathog.* **13** (2017).
270. K. Skolnik, G. Kirkpatrick, B. S. Quon, Nontuberculous Mycobacteria in Cystic Fibrosis. *Curr. Treat. Options Infect. Dis.* **8**, 259–274 (2016).
271. R. A. Bronson, *et al.*, Global phylogenomic analyses of *Mycobacterium abscessus* provide context for non cystic fibrosis infections and the evolution of antibiotic resistance. *Nat. Commun.* **2021 121 12**, 1–10 (2021).
272. R. Brugha, H. Spencer, *Mycobacterium abscessus* in cystic fibrosis. *Science* (80-.). **372**, 465–466 (2021).
273. A. McCarron, D. Parsons, M. Donnelley, Animal and Cell Culture Models for Cystic Fibrosis: Which Model Is Right for Your Application? *Am. J. Pathol.* **191**, 228–242 (2021).
274. S. Ganesan, A. T. Comstock, U. S. Sajjan, Barrier function of airway tract epithelium. *Tissue Barriers* **1**, e24997 (2013).
275. A. J. Miller, J. R. Spence, In Vitro Models to Study Human Lung Development, Disease and Homeostasis. *Physiology* **32**, 246 (2017).
276. K. Brown, D. T. Lynch, Histology, Lung. *StatPearls* (2022).
277. C. E. Barkauskas, *et al.*, Lung organoids: current uses and future promise. *Development* **144**, 986 (2017).
278. J. Zhou, *et al.*, Differentiated human airway organoids to assess infectivity of emerging influenza virus. *Proc. Natl. Acad. Sci. U. S. A.* **115**, 6822–6827 (2018).
279. Adivitiya, M. S. Kaushik, S. Chakraborty, S. Veleri, S. Kateriya, Mucociliary Respiratory Epithelium Integrity in Molecular Defense and Susceptibility to Pulmonary Viral Infections. *Biology (Basel)*. **10**, 1–37 (2021).
280. S. C. Pearce, *et al.*, Marked differences in tight junction composition and macromolecular permeability among different intestinal cell types. *BMC Biol.* **16** (2018).
281. J. Y. Co, *et al.*, Controlling Epithelial Polarity: A Human Enteroid Model for Host-Pathogen Interactions. *Cell Rep.* **26**, 2509-2520.e4 (2019).

282. J. K. Actor, Lactoferrin: A Modulator for Immunity against Tuberculosis Related Granulomatous Pathology. *Mediators Inflamm.* **2015** (2015).
283. K. J. Welsh, *et al.*, Influence of Oral Lactoferrin on Mycobacterium tuberculosis induced immunopathology. *Tuberculosis (Edinb)*. **91S1**, S105 (2011).
284. M. Javaheri-Kermani, T. Farazmandfar, A. Ajami, Y. Yazdani, Impact of hepcidin antimicrobial peptide on iron overload in tuberculosis patients. *Scand. J. Infect. Dis.* **46**, 693–696 (2014).
285. F. B. Sow, S. B. Sable, B. B. Plikaytis, W. P. Lafuse, T. M. Shinnick, Role of Hepcidin in the Innate Immune Response to Mycobacterium tuberculosis. *FASEB J.* **22**, 556–556 (2008).
286. R. Tanner, *et al.*, The influence of haemoglobin and iron on in vitro mycobacterial growth inhibition assays. *Sci. Rep.* **7** (2017).
287. R. Sharma, U. N. Saikia, S. Sharma, I. Verma, Activity of human beta defensin-1 and its motif against active and dormant Mycobacterium tuberculosis. *Appl. Microbiol. Biotechnol.* **101**, 7239–7248 (2017).
288. B. Rivas-Santiago, *et al.*, Human β -Defensin 2 Is Expressed and Associated with Mycobacterium tuberculosis during Infection of Human Alveolar Epithelial Cells. *Infect. Immun.* **73**, 4505 (2005).
289. F. Torres-Juarez, *et al.*, RNase 7 but not psoriasin nor sPLA2-IIA associates with Mycobacterium tuberculosis during airway epithelial cell infection. *Pathog. Dis.* **76** (2018).
290. D. Yang, *et al.*, Beta-defensins: linking innate and adaptive immunity through dendritic and T cell CCR6. *Science* **286**, 525–528 (1999).
291. A. Krupa, *et al.*, Binding of CXCL8/IL-8 to Mycobacterium tuberculosis Modulates the Innate Immune Response. *Mediators Inflamm.* **2015** (2015).
292. S. Benmerzoug, *et al.*, GM-CSF targeted immunomodulation affects host response to M. tuberculosis infection. *Sci. Rep.* **8** (2018).
293. B. D. Bryson, *et al.*, Heterogeneous GM-CSF signaling in macrophages is associated with control of Mycobacterium tuberculosis. *Nat. Commun.* **2019** *10*, 1–11 (2019).
294. A. V. Gutiérrez, A. Viljoen, E. Ghigo, J. L. Herrmann, L. Kremer,

- Glycopeptidolipids, a double-edged sword of the *Mycobacterium abscessus* complex. *Front. Microbiol.* **9** (2018).
295. C. L. Cooke, *et al.*, Modification of gastric mucin oligosaccharide expression in rhesus macaques after infection with *Helicobacter pylori*. *Gastroenterology* **137** (2009).
 296. K. Agaronyan, *et al.*, Tissue remodeling by an opportunistic pathogen triggers allergic inflammation. *Immunity* **55**, 895-911.e10 (2022).
 297. Y. Huang, *et al.*, Research Progress, Challenges, and Breakthroughs of Organoids as Disease Models. *Front. Cell Dev. Biol.* **9**, 3259 (2021).
 298. A. Shankaran, K. Prasad, S. Chaudhari, A. Brand, K. Satyamoorthy, Advances in development and application of human organoids. *3 Biotech 2021 116* **11**, 1–22 (2021).
 299. P. Rawal, D. M. Tripathi, S. Ramakrishna, S. Kaur, Prospects for 3D bioprinting of organoids. *Bio-Design Manuf. 2021 43* **4**, 627–640 (2021).
 300. P. S. Hiemstra, *et al.*, Disease modelling following organoid-based expansion of airway epithelial cells. *Eur. Respir. J.* **56**, 4322 (2020).
 301. V. V. Thacker, *et al.*, A lung-on-chip model of early *Mycobacterium tuberculosis* infection reveals an essential role for alveolar epithelial cells in controlling bacterial growth. *Elife* **9**, 1–73 (2020).
 302. N. Iakobachvili, *et al.*, *Mycobacteria*–host interactions in human bronchiolar airway organoids. *Mol. Microbiol.* **117**, 682–692 (2022).
 303. E. Fiorini, L. Veghini, V. Corbo, Modeling Cell Communication in Cancer With Organoids: Making the Complex Simple. *Front. Cell Dev. Biol.* **8**, 166 (2020).
 304. G. Stroulios, *et al.*, Apical-out airway organoids as a platform for studying viral infections and screening for antiviral drugs. *Sci. Reports 2022 121* **12**, 1–14 (2022).
 305. K. Y. G. Choi, B. C. Wu, A. H. Y. Lee, B. Baquir, R. E. W. Hancock, Utilizing Organoid and Air-Liquid Interface Models as a Screening Method in the Development of New Host Defense Peptides. *Front. Cell. Infect. Microbiol.* **10**, 228 (2020).
 306. A. S. Ramalho, *et al.*, Correction of CFTR function in intestinal organoids to

guide treatment of cystic fibrosis. *Eur. Respir. J.* **57** (2021).

307. S. Y. Graeber, *et al.*, Comparison of Organoid Swelling and In Vivo Biomarkers of CFTR Function to Determine Effects of Lumacaftor-Ivacaftor in Patients with Cystic Fibrosis Homozygous for the F508del Mutation. *Am. J. Respir. Crit. Care Med.* **202**, 1589–1592 (2020).
308. H. D. M. Coutinho, V. S. Falcão-Silva, G. F. Gonçalves, Pulmonary bacterial pathogens in cystic fibrosis patients and antibiotic therapy: a tool for the health workers. *Int. Arch. Med.* **1**, 24 (2008).
309. D. Lebeaux, A. Chauhan, O. Rendueles, C. Beloin, From in vitro to in vivo Models of Bacterial Biofilm-Related Infections. *Pathog. (Basel, Switzerland)* **2**, 288–356 (2013).
310. J. Esteban, M. García-Coca, Mycobacterium Biofilms. *Front. Microbiol.* **8** (2018).
311. B. F. Keefe, L. E. Bermudez, Environment in the lung of cystic fibrosis patients stimulates the expression of biofilm phenotype in Mycobacterium abscessus. *J. Med. Microbiol.* **71** (2022).
312. B. M. Winklhofer-Roob, Oxygen free radicals and antioxidants in cystic fibrosis: the concept of an oxidant-antioxidant imbalance. *Acta Paediatr. Suppl.* **83**, 49–57 (1994).
313. J. Chen, *et al.*, Dysfunction of Nrf-2 in CF epithelia leads to excess intracellular H₂O₂ and inflammatory cytokine production. *PLoS One* **3** (2008).
314. P. Maniam, *et al.*, Increased susceptibility of cystic fibrosis airway epithelial cells to ferroptosis. *Biol. Res.* **54**, 1–13 (2021).
315. B.-R. Kim, B.-J. Kim, Y.-H. Kook, B.-J. Kim, Mycobacterium abscessus infection leads to enhanced production of type 1 interferon and NLRP3 inflammasome activation in murine macrophages via mitochondrial oxidative stress. *PLOS Pathog.* **16**, e1008294 (2020).
316. R. E. Oberley-Deegan, *et al.*, An oxidative environment promotes growth of Mycobacterium abscessus. *Free Radic. Biol. Med.* **49**, 1666–1673 (2010).
317. M. Bonay, *et al.*, Caspase-independent apoptosis in infected macrophages triggered by sulforaphane via Nrf2/p38 signaling pathways. *Cell Death Discov.* **1**, 1 (2015).

318. Y. J. Kim, *et al.*, Sirtuin 3 is essential for host defense against Mycobacterium abscessus infection through regulation of mitochondrial homeostasis. *Virulence* **11**, 1225–1239 (2020).
319. D. C. Borchering, *et al.*, Clinically approved CFTR modulators rescue Nrf2 dysfunction in cystic fibrosis airway epithelia. *J. Clin. Invest.* **129**, 3448–3463 (2019).
320. V. Le Moigne, *et al.*, Roscovitine Worsens Mycobacterium abscessus Infection by Reducing DUOX2-mediated Neutrophil Response. *Am. J. Respir. Cell Mol. Biol.* **66**, 439–451 (2022).
321. C. N. Paiva, M. T. Bozza, Are Reactive Oxygen Species Always Detrimental to Pathogens? *Antioxid. Redox Signal.* **20**, 1000 (2014).
322. S. Bagayoko, E. Meunier, Emerging roles of ferroptosis in infectious diseases. *FEBS J.* (2021) <https://doi.org/10.1111/FEBS.16244>.
323. X. Jiang, B. R. Stockwell, M. Conrad, Ferroptosis: mechanisms, biology and role in disease. *Nat. Rev. Mol. Cell Biol.* 2021 224 **22**, 266–282 (2021).
324. T. Laval, *et al.*, De novo synthesized polyunsaturated fatty acids operate as both host immunomodulators and nutrients for mycobacterium tuberculosis. *Elife* **10** (2021).
325. K. S. Ong, C. I. Mawang, D. Daniel-Jambun, Y. Y. Lim, S. M. Lee, Current anti-biofilm strategies and potential of antioxidants in biofilm control. <https://doi.org/10.1080/14787210.2018.1535898> **16**, 855–864 (2018).
326. A. C. Pereira, B. Ramos, A. C. Reis, M. V. Cunha, Non-Tuberculous Mycobacteria: Molecular and Physiological Bases of Virulence and Adaptation to Ecological Niches. *Microorganisms* **8**, 1–49 (2020).

Annexes

I. Antiviral and anti-inflammatory activities of Fluoxetine in a SARS-CoV-2 infection mouse model

II. Efficacy and Mode of Action of a Direct Inhibitor of *Mycobacterium abscessus* InhA

III. Human NLRP1 is a sensor of pathogenic coronavirus 3CL proteases in lung epithelial cells

IV. Nigратine as dual inhibitor of necroptosis and ferroptosis regulated cell death

V. Host phospholipid peroxidation fuels ExoU-dependent cell necrosis and supports *Pseudomonas aeruginosa*-driven pathology

VI. A Pulmonary *Lactobacillus murinus* Strain Induces Th17 and ROR γ t + Regulatory T Cells and Reduces Lung Inflammation in Tuberculosis

I. Antiviral and anti-inflammatory activities of Fluoxetine in a SARS-CoV-2 infection mouse model

Authors: David Pericat*, **Stephen Adonai Leon-Icaza***, Marina Sanchez Rico, Christiane Mühle, Iulia Zoicas, Fabian Schumacher, Rémi Planès, Raoul Mazars, Germain Gros, Alexander Carpinteiro, Katrin Anne Becker, Jacques Izopet, Nathalie Strub-Wourgaft, Peter Sjö, Olivier Neyrolles, Burkhard Kleuser, Frédéric Limosin, Erich Gulbins, Johannes Kornhuber, Etienne Meunier, Nicolas Hoertel, Céline Cougoule.

*These authors contributed equally.

Contribution: I designed and performed all the qPCRs to determine viral loads as well as cytokines and chemokines expression for Figure 1 of the article. I also participated in the writing of the article.

This article was published in the International Journal of Molecular Sciences.



Article

Antiviral and Anti-Inflammatory Activities of Fluoxetine in a SARS-CoV-2 Infection Mouse Model

David Péricat ^{1,†}, Stephen Adonai Leon-Icaza ^{1,†} , Marina Sanchez Rico ^{2,3,4}, Christiane Mühle ⁵ , Iulia Zoicas ⁵ , Fabian Schumacher ⁶ , Rémi Planès ¹ , Raoul Mazars ¹, Germain Gros ¹, Alexander Carpinteiro ⁷, Katrin Anne Becker ⁷ , Jacques Izopet ^{8,9} , Nathalie Strub-Wourgaft ¹⁰, Peter Sjö ¹⁰ , Olivier Neyrolles ¹, Burkhard Kleuser ⁶ , Frédéric Limosin ^{2,3,4}, Erich Gulbins ⁷, Johannes Kornhuber ⁵ , Etienne Meunier ¹, Nicolas Hoertel ^{2,3,4,*} and Céline Cougoule ^{1,*}

- ¹ Institute of Pharmacology and Structural Biology (IPBS), University of Toulouse, CNRS, 31000 Toulouse, France
 - ² Faculté de Santé, Université Paris Cité, 75006 Paris, France
 - ³ Département de Psychiatrie et d'Addictologie de l'Adulte et du Sujet Agé, Assistance Publique-Hôpitaux de Paris (AP-HP), DMU Psychiatrie et Addictologie, Hôpital Corentin-Celton, 92130 Issy-les-Moulineaux, France
 - ⁴ INSERM, Institut de Psychiatrie et Neurosciences de Paris (IPNP), UMR_S1266, 75014 Paris, France
 - ⁵ Department of Psychiatry and Psychotherapy, University Hospital, Friedrich-Alexander-University of Erlangen-Nuremberg, 91054 Erlangen, Germany
 - ⁶ Institute of Pharmacy, Freie Universität Berlin, Königin-Luise-Str. 2-4, 14195 Berlin, Germany
 - ⁷ Institute for Molecular Biology, University Medicine Essen, University of Duisburg-Essen, 47057 Essen, Germany
 - ⁸ Toulouse Institute for Infectious and Inflammatory Diseases (INFINITY), Université Toulouse, CNRS, INSERM, UPS, 31300 Toulouse, France
 - ⁹ Laboratoire de Virologie, CHU Toulouse, Hôpital Purpan, 31300 Toulouse, France
 - ¹⁰ Drugs for Neglected Diseases Initiative, 1202 Geneva, Switzerland
- * Correspondence: nicolas.hoertel@aphp.fr (N.H.); celine.cougoule@ipbs.fr (C.C.); Tel.: +33-(0)1-58-00-44-21 (N.H.); +33-(0)5-61-17-54-61 (C.C.)
- † These authors contributed equally to this work.



Citation: Péricat, D.; Leon-Icaza, S.A.; Sanchez Rico, M.; Mühle, C.; Zoicas, I.; Schumacher, F.; Planès, R.; Mazars, R.; Gros, G.; Carpinteiro, A.; et al. Antiviral and Anti-Inflammatory Activities of Fluoxetine in a SARS-CoV-2 Infection Mouse Model. *Int. J. Mol. Sci.* **2022**, *23*, 13623. <https://doi.org/10.3390/ijms232113623>

Academic Editor: James K. Bashkin

Received: 7 August 2022

Accepted: 26 October 2022

Published: 7 November 2022

Publisher's Note: MDPI stays neutral with regard to jurisdictional claims in published maps and institutional affiliations.



Copyright: © 2022 by the authors. Licensee MDPI, Basel, Switzerland. This article is an open access article distributed under the terms and conditions of the Creative Commons Attribution (CC BY) license (<https://creativecommons.org/licenses/by/4.0/>).

Abstract: The coronavirus disease 2019 (COVID-19) pandemic continues to cause significant morbidity and mortality worldwide. Since a large portion of the world's population is currently unvaccinated or incompletely vaccinated and has limited access to approved treatments against COVID-19, there is an urgent need to continue research on treatment options, especially those at low cost and which are immediately available to patients, particularly in low- and middle-income countries. Prior in vitro and observational studies have shown that fluoxetine, possibly through its inhibitory effect on the acid sphingomyelinase/ceramide system, could be a promising antiviral and anti-inflammatory treatment against COVID-19. In this report, we evaluated the potential antiviral and anti-inflammatory activities of fluoxetine in a K18-hACE2 mouse model of SARS-CoV-2 infection, and against variants of concern in vitro, i.e., SARS-CoV-2 ancestral strain, Alpha B.1.1.7, Gamma P1, Delta B1.617 and Omicron BA.5. Fluoxetine, administrated after SARS-CoV-2 infection, significantly reduced lung tissue viral titres and expression of several inflammatory markers (i.e., IL-6, TNF α , CCL2 and CXCL10). It also inhibited the replication of all variants of concern in vitro. A modulation of the ceramide system in the lung tissues, as reflected by the increase in the ratio HexCer 16:0/Cer 16:0 in fluoxetine-treated mice, may contribute to explain these effects. Our findings demonstrate the antiviral and anti-inflammatory properties of fluoxetine in a K18-hACE2 mouse model of SARS-CoV-2 infection, and its in vitro antiviral activity against variants of concern, establishing fluoxetine as a very promising candidate for the prevention and treatment of SARS-CoV-2 infection and disease pathogenesis.

Keywords: COVID-19; SARS-CoV-2; mouse model; fluoxetine; anti-depressant; inflammation

1. Introduction

The SARS-CoV-2 pandemic has created an economic and health crisis worldwide [1–4]. Since a large proportion of the world's population is currently unvaccinated, or incompletely vaccinated, the availability of outpatient treatment options for COVID-19, such as nirmatrelvir-ritonavir (Paxlovid[®]), neutralizing monoclonal antibodies, remdesivir, and molnupiravir, has raised hopes for reducing COVID-19-related morbidity and mortality. However, the use of these treatments may be held back due to either their medical indications (e.g., within 5 days of symptom onset for nirmatrelvir-ritonavir, specific variants for sotrovimab), contraindications (e.g., concomitant use of drugs that are potent CYP3A inducers, severe hepatic impairment or severe renal impairment for nirmatrelvir-ritonavir [5]), the need of intravenous therapy (for neutralizing monoclonal antibodies and remdesivir), limited supplies, and substantial cost [6]. This supports the urgent need for research on other outpatient treatment options, especially those at lower cost and which are immediately available to allow their use, particularly in low- and middle-income countries with limited access to vaccines and approved treatments against COVID-19 [7–9].

Prior research suggests that certain selective serotonin reuptake inhibitor (SSRI) antidepressants, particularly fluoxetine and fluvoxamine, could be beneficial against COVID-19 [6,10,11], and thus may be a potential means of reaching this goal. First, several preclinical studies demonstrated the *in vitro* efficacy of fluoxetine against different variants of SARS-CoV-2 in human and non-human (i.e., Vero E6, Calu-1, Calu-3, HEK293T-ACE2-TMPRSS2) cells [12–19]. Second, five retrospective observational cohort studies [20–24] of patients with COVID-19 in the acute-care setting reported reduced death or mechanical ventilation in those prescribed with SSRIs prior to hospitalization—particularly fluoxetine. Another observational study [25] also found that exposure to antidepressants, especially those with functional inhibition of acid sphingomyelinase (FIASMA) properties such as fluoxetine, was associated with reduced incidence of emergency department visitation or hospital admission among SARS-CoV-2 positive outpatients, in a dose-dependent manner and from daily doses of at least 20 mg fluoxetine equivalents. Moreover, a retrospective cohort study conducted in an adult psychiatric facility suggested a significant negative association of prior antidepressant use—particularly fluoxetine—with laboratory-detectable SARS-CoV-2 infection [26], a finding that has been recently replicated in another observational study [24]. Third, in the ambulatory setting, two prospective randomized, placebo-controlled trials [27–29] and one non-randomized open-label clinical study [30], as well as a meta-analysis [31], found a significant association between the short-term use (10–15 days) of fluvoxamine prescribed at a dose between 100 and 300 mg/d within 7 days of symptom onset and reduced risk of clinical deterioration. Contrariwise, an RCT of low-dose fluvoxamine [32,32] (i.e., 100 mg/d) among overweight or obese outpatients with COVID-19 showed no significant benefit on emergency department visits, hospitalizations or death. Finally, a prospective cohort study [33] of patients admitted to intensive care unit for COVID-19 reported a significant association between the 15-day use of fluvoxamine prescribed at 300 mg/d and reduced mortality. Taken together, these findings support that certain antidepressants, and particularly fluoxetine or fluvoxamine, could be efficient when prescribed at doses of at least 20–40 mg fluoxetine equivalents [24,25] in limiting clinical deterioration of patients infected with SARS-CoV-2 in both ambulatory and acute-care settings.

Although the mechanisms underlying this potential therapeutic effect of fluoxetine and fluvoxamine against COVID-19 are likely to be multiple and interrelated, several studies support that the interaction with the acid sphingomyelinase (ASM)/ceramide system, resulting in both antiviral and anti-inflammatory effects, may be a prominent one [13]. First, these SSRI antidepressants belong to the group of functional inhibitors of acid sphingomyelinase (FIASMA) [13,34]. *In vitro* and *in vivo*, these pharmacological compounds inhibit ASM, an enzyme that catalyses the hydrolysis of sphingomyelin to ceramide and phosphorylcholine, by detaching it from the lysosomal membrane and thereby triggering its degradation [34]. Preclinical data indicate that SARS-CoV-2 activates

the ASM/ceramide system, resulting in the formation of ceramide-enriched membrane domains, which facilitate viral entry and infection by clustering ACE2, the cellular receptor of SARS-CoV-2, and the release of pro-inflammatory cytokines [12,13,35]. Importantly, the reconstitution of ceramides in cells treated with FIASMA antidepressants restored the infection [12]. In healthy volunteers, oral use of the FIASMA antidepressant amitriptyline prevented infection of freshly isolated nasal epithelial cells, which is also restored after the reconstitution of ceramides in these cells [12]. In observational retrospective studies, the use of a FIASMA medication upon hospital admission was significantly associated with reduced mortality or mechanical ventilation [36]. Finally, plasma levels of certain sphingolipids, including increased levels of ceramides, decreased levels of their derivatives hexosylceramides, and decreased hexosylceramide/ceramide ratio, were found to correlate with clinical disease severity and inflammation markers [37–39] in patients with COVID-19. Altogether, these data support the central role of the ASM/ceramide system in SARS-CoV-2 infection and the potential of FIASMA antidepressants in prevention and treatment of COVID-19.

Among SSRIs, the magnitude of the *in vitro* inhibition of ASM appears to correlate with the magnitude of the *in vitro* antiviral effect against SARS-CoV-2 [13,15,40] (e.g., amitriptyline > fluoxetine > paroxetine > fluvoxamine > citalopram). While amitriptyline exhibits potential toxicity issues in elderly, fluoxetine displays the highest FIASMA activity. In addition, fluoxetine shows anti-inflammatory properties in lipopolysaccharide (LPS)-challenged mouse models [41,42], which may be of interest in patients infected with SARS-CoV-2, as increased levels of proinflammatory cytokines in serum (e.g., IL1B, IL6, IFN γ , CXCL10, and CCL2) are associated with pulmonary inflammation and extensive lung damage [43].

While observational and *in vitro* data on fluoxetine are promising, experiments examining its effect against SARS-CoV-2 infection in an animal model are lacking. Mice are not naturally permissive to SARS-CoV-2 infection, due to the low affinity of the S protein receptor binding domain for mouse ACE2. Previously, a transgenic mouse expressing the human ACE2 gene under the control of the cytokeratin 18 (K18) promoter (the K18-hACE2 mouse) was generated to study SARS-CoV pathogenesis [44]. Recent studies have demonstrated that K18-hACE2 mice support SARS-CoV-2 infection and develop a lethal respiratory illness with weight loss and inflammation [45–47].

In this report, we tested the potential antiviral and anti-inflammatory activities of fluoxetine against SARS-CoV-2 in a K18-hACE2 mouse model of infection, and against several variants of concern *in vitro*, and tested the hypothesis of the implication of ceramides and/or their derivatives hexosylceramides.

2. Results

2.1. Antiviral Activity

Viral loads were evaluated from 44 K18-hACE2 mice euthanized at day 2 and day 6 post-infection. As shown in Figure 1B, fluoxetine treatment significantly reduced the viral load in the lung of SARS-CoV-2 infected mice at both day 2 (\log_{10} TCID₅₀/mL 6.19 (± 0.14) vs. 4.04 (± 0.44); Mann-Whitney test $p = 0.0012$) and day 6 (\log_{10} TCID₅₀/mL 4.22 (± 0.19) vs. 3.28 (± 0.17); $p = 0.0048$). Moreover, viral RNA in lung homogenates was significantly reduced at day 2 post-infection in fluoxetine-treated mice compared to vehicle-treated mice (9.91×10^4 ($\pm 4.15 \times 10^4$) vs. 1.04×10^6 ($\pm 6.60 \times 10^5$); $p = 0.0310$) (Figure 1C). Viral RNA in lung homogenates was still significantly reduced at day 2 post-infection in fluoxetine-treated mice compared to vehicle-treated mice when excluding the 2 outliers in the saline-treated group (3.85×10^4 ($\pm 2.50 \times 10^4$) vs. 3.85×10^5 ($\pm 1.22 \times 10^5$); $p = 0.0295$) (Supplemental Figure S5A). These results show that fluoxetine displays a significant and substantial antiviral activity against SARS-CoV-2 in mice.

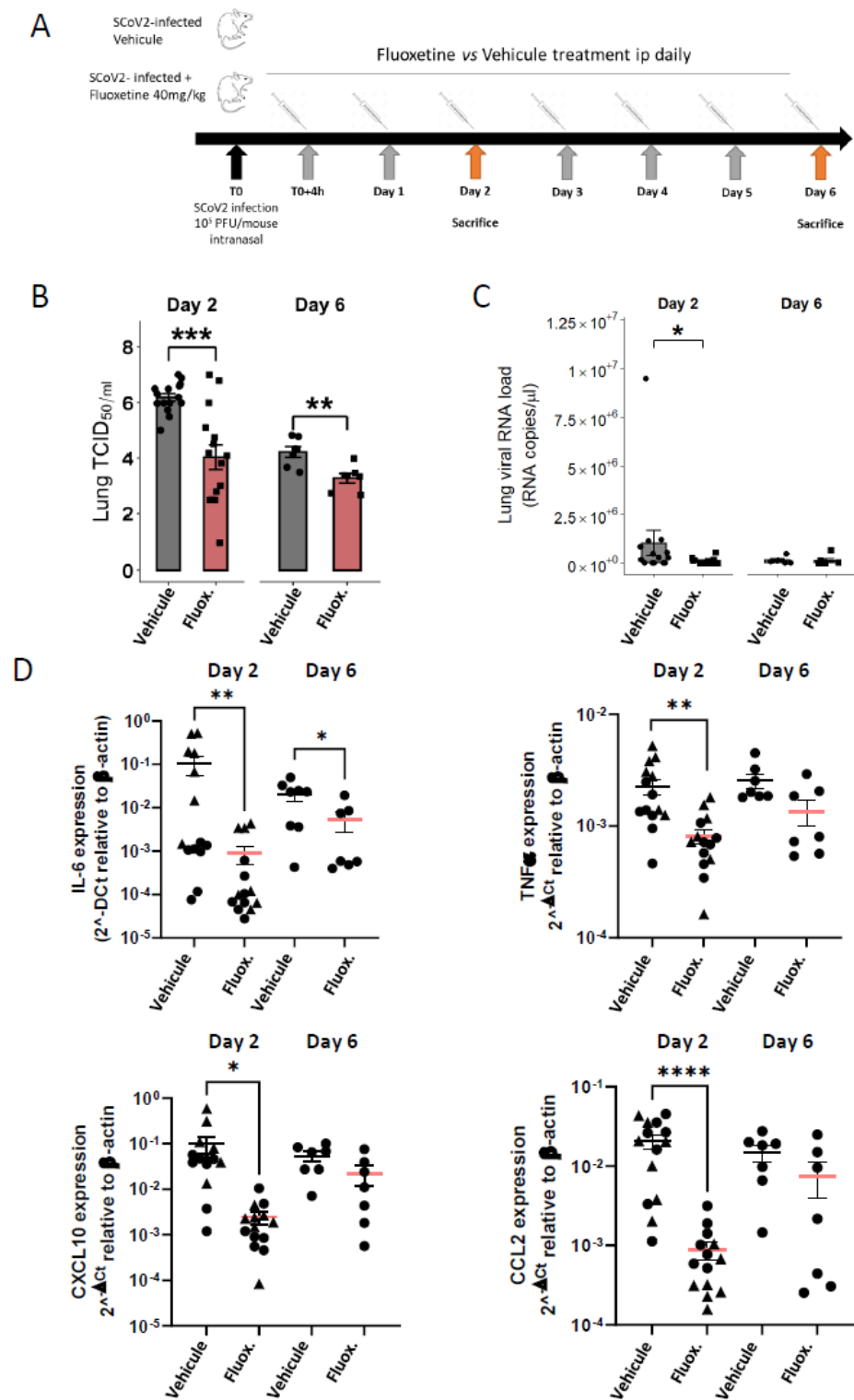


Figure 1. Fluoxetine reduced viral load and inflammatory response in K18-hACE2 mice infected with SARS-CoV-2. (A) Experimental design of the study; (B) infectious viral loads in the lungs of vehicle- and fluoxetine-treated mice infected with SARS-CoV-2 at day 2 and 6 post-infection expressed as log₁₀ TCID₅₀/mL; (C) viral RNA levels in the lungs of vehicle- and fluoxetine-treated mice infected with SARS-CoV-2 at day 2 and 6 post-infection expressed as Lung SARS-CoV-2 RNA load (RNA copies/μL). (D) Cytokine and chemokine transcripts in lung tissue at day 2 and 6 post-infection of SARS-CoV-2-infected mice, treated with vehicle or with fluoxetine. *, *p* < 0.05; **, *p* < 0.01; ***, *p* < 0.001; ****, *p* < 0.0001.

As shown in Figure 1D, fluoxetine significantly reduced expression of IL-6 in the lung tissues at both day 2 (IL-6 8.97×10^{-4} ($\pm 4.09 \times 10^{-4}$) vs. IL-6 1.06×10^{-1} ($\pm 4.88 \times 10^{-2}$); $p = 0.0017$) and day 6 post-infection (IL-6 3.01×10^{-3} ($\pm 1.58 \times 10^{-3}$) vs. IL-6 2.31×10^{-3} ($\pm 6.11 \times 10^{-3}$); $p = 0.0140$), and other pro-inflammatory cytokines at day 2 post-infection, including TNF α (8.07×10^{-4} ($\pm 1.21 \times 10^{-4}$) vs. 2.24×10^{-3} ($\pm 3.70 \times 10^{-4}$); $p = 0.0004$), CXCL10 (2.44×10^{-3} ($\pm 7.17 \times 10^{-4}$) vs. 9.99×10^{-2} ($\pm 4.14 \times 10^{-2}$); $p < 0.0001$) and CCL2 (8.83×10^{-4} ($\pm 1.21 \times 10^{-4}$) vs. 2.24×10^{-3} ($\pm 3.70 \times 10^{-4}$); $p < 0.0001$). A reduction in pro-inflammatory cytokine expression did not appear to be solely related to reduced viral load in fluoxetine-treated mice. Indeed, the difference in levels of IL-6 and TNF α between fluoxetine-treated and vehicle-treated mice was still significant after adjusting successively for viral load and viral RNA at both day 2 and day 6 (Supplemental Table S2). In addition, IL-6 expression level did not correlate with lung viral load or RNA load in both fluoxetine-treated (lung viral load, $r = -0.11$, $p = 0.7131$; lung viral RNA load, $r = -0.18$, $p = 0.5403$) and vehicle-treated mice (lung viral load, $r = -0.14$, $p = 0.6222$; lung viral RNA load, $r = -0.22$, $p = 0.4508$) (Supplemental Figure S2). These results were maintained when excluding three outliers (one fluoxetine- and one vehicle-treated mouse at day 2, and one fluoxetine-treated mouse at day 6) from the analyses (Supplemental Figure S5). To evaluate the immunomodulatory property of fluoxetine, independently of the viral load, we used the A549-DualTM cells consisting in a human NF- κ B-SEAP & IRF-Luc Reporter lung carcinoma cell line. Upon cell stimulation with PolyI:C or TNF α , fluoxetine inhibited NF- κ B activation, while IRF pathway was not affected (Supplemental Figure S3D), indicating that fluoxetine displays, as previously described [41], an immunomodulatory function on the NF- κ B pathway. Altogether, these findings suggest that fluoxetine dampens inflammation during SARS-CoV-2 infection, independently of its antiviral properties.

2.2. Body Weight and Temperature

While fluoxetine at 40 mg/kg is well tolerated over a period of 15 days [48], it induces body weight loss in the first 24 h of treatment [49]. We showed that fluoxetine induced a significant body weight loss after the first 24 h in K18-hACE2 mice, while the body weight was constant in vehicle-treated mice (Supplemental Figure S3). Moreover, we confirmed that vehicle-treated K18-hACE2 mice started to lose weight 2 days post-infection [46], while the body weight was stable longer in fluoxetine-treated mice (Supplemental Figure S3). Further comparison of body weight between groups was biased due to the initial body weight loss in fluoxetine-treated mice, and did not show an overall significant difference (Supplemental Figure S3). While body temperature was reduced at day 6 in vehicle-treated K18-hACE2 mice (compared to non-infected mice (37 ± 0.3 °C, $n = 4$)) as a sign of critical illness [50], we measured a significantly improved body temperature in fluoxetine-treated mice (33.3 ± 1.00 °C vs. 28.6 ± 0.94 °C; $p = 0.0052$) (Supplemental Figure S3).

2.3. Fluoxetine Modulates the Ceramide System

We evaluated whether fluoxetine could modulate the ceramide system in the lung tissues of mice infected with SARS-CoV-2. As shown in Figure 2B,C, fluoxetine treatment significantly increased levels of hexosylceramides 16:0 (166.93 (± 22.4) vs. 101.65 (± 11.0); $p = 0.0186$) and the ratio HexCer 16:0/Cer 16:0 (0.40 (± 0.05) vs. 0.28 (± 0.03); $p = 0.0408$). There were no significant between-group differences in ceramides 16:0 and sphingomyelin 16:0 levels (Figure 2A,D). The between-group differences in ceramides 16:0 and sphingomyelin 16:0 remained non-significant when excluding outliers from the analyses (one fluoxetine-treated mouse in ceramides 16:0, and one fluoxetine- and one saline-treated mouse in sphingomyelin 16:0) (Supplemental Figure S5).

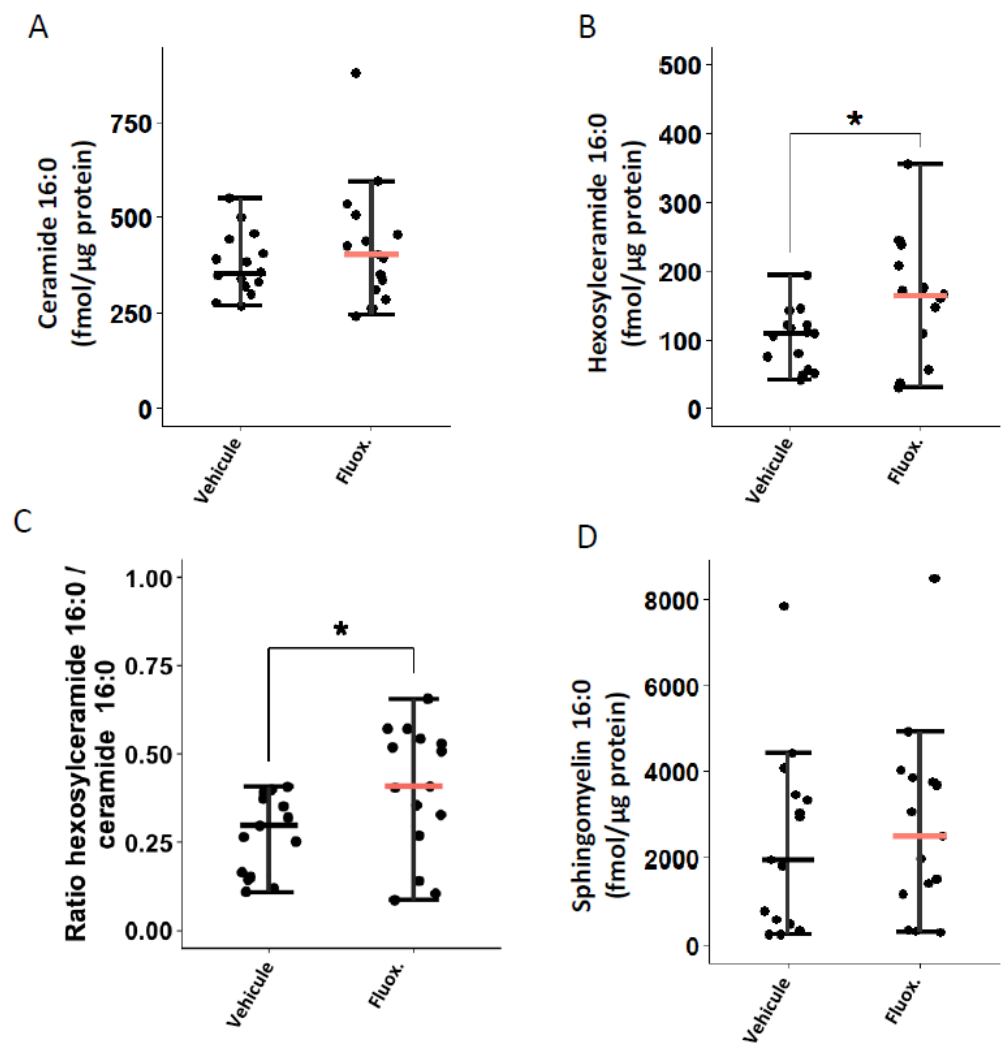


Figure 2. Fluoxetine effect on lung levels of (A) ceramide 16:0, (B) hexosylceramide 16:0, (C) hexosylceramide 16:0 / ceramide 16:0 ratio, and (D) sphingomyelin 16:0, at day 2 post-infection. *, $p < 0.05$.

2.4. Anti-Viral Activity of Fluoxetine In Vitro against Variants of Concern

Vero E6 cells were successively infected with Alpha B.1.1.7, Gamma P1, Delta B1.617 and Omicron BA.5 variants of concern, and viral cytopathic effect and replication were measured. As shown in Figure 3A, fluoxetine, at the non-cytotoxic dose of 12.5 μM (Supplemental Figure S4) inhibited replication of all the variants of concern tested. Finally, we evaluated fluoxetine effectiveness in the human A549 lung carcinoma cells stably overexpressing the SARS-CoV-2 receptor ACE2, and the protease TMPRSS2 to increase their permissiveness to SARS-CoV-2 infection [51]. A549-hACE2-TMPRSS2 cells were permissive to infection by all variants of concern (Figure 3B). A549-hACE2-TMPRSS2 cells infected with SARS-CoV-2 ancestral strain, Alpha B.1.1.7, Gamma P1, Delta B1.617 and Omicron BA.5 variants of concern, and treated with fluoxetine (12.5 μM) showed reduced amount of infectious virus and restored cell viability (Figure 3B). Altogether, these results show that fluoxetine is efficient at inhibiting replication across several SARS-CoV-2 variants of concern.

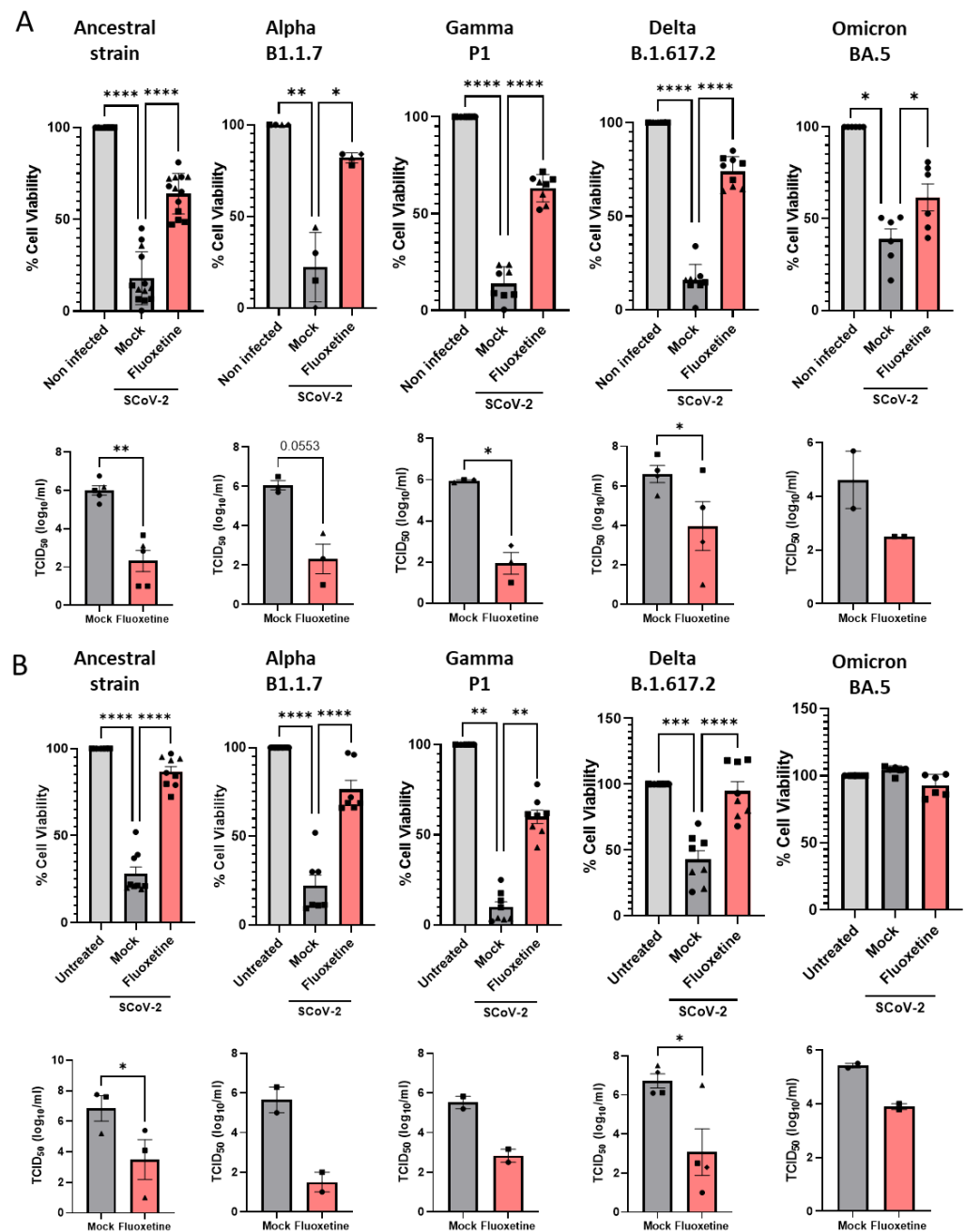


Figure 3. Fluoxetine activity on SARS-CoV-2 variants in vitro. (A) Activity of fluoxetine (12.5 μ M) or mock (water) in Vero E6 cells infected with SARS-CoV-2 (Pasteur, B.1), B.1.1.7 (UK), P1, B.1.617 (Delta) and BA.5 (Omicron) variants measured by assessing cell viability and viral load. (B) Antiviral activity of fluoxetine (12.5 μ M) measured in A549 cells expressing hACE2-TMPRSS2 infected with SARS-CoV-2 (Pasteur, B.1), B.1.1.7 (UK), P1, B.1.617 (Delta) and BA.5 (Omicron) variants measured by cell viability and viral load. Representative of two to seven independent experiments, data are expressed as mean \pm SEM. *, $p < 0.05$; **, $p < 0.01$; ***, $p < 0.001$; ****, $p < 0.0001$.

2.5. Anti-Viral Activity of Fluoxetine Ex Vivo on Human Primary Airway Epithelial Cells

Human airway organoid-derived epithelia cultured in 2D were infected with SARS-CoV-2 as previously described [52], and the percentage of infection was microscopically quantified (Figure 4A). We confirmed that SARS-CoV-2 mainly infects ciliated cells revealed by the ActUB staining. As shown in Figure 4B, fluoxetine significantly inhibited infection of human primary airway epithelial cells in a dose-dependent manner.

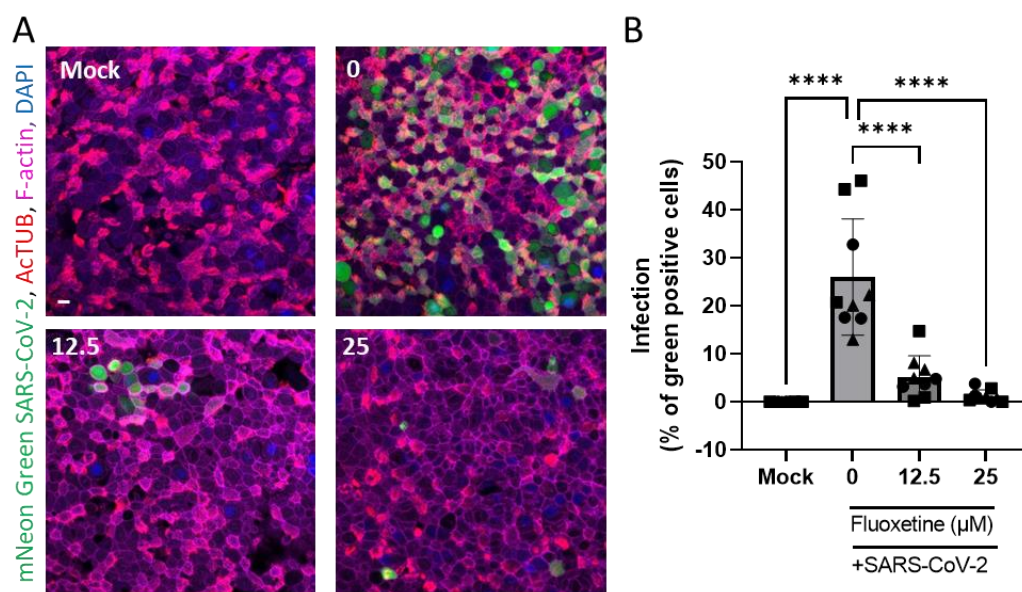


Figure 4. Fluoxetine inhibits SARS-CoV-2 infection of 2D human airway cells. (A) Representative images of immunofluorescent stainings of mNeon Green SARS-CoV-2 infected airway cultures. Acetylated tubulin (ActTUB, red) stains cell ciliates, phalloidin-coupled Alexa Fluor 647 stains F-actin (purple) and DAPI stains nuclei (blue). Scale bar = 10 μm. (B) Live virus titre measured on apical washes 72 h after infection with mNeon Green SARS-CoV-2. Data from three independent experiments on two independent donors, expressed as mean ± SEM, **** $p < 0.0001$.

3. Discussion

In this report, we show that fluoxetine has both significant anti-viral and anti-inflammatory effects in a K18-hACE2 mouse model of SARS-CoV-2 infection, both mechanisms appearing to be potentially, at least partly, independent to each other. We also show that fluoxetine efficiently inhibits the replication of different SARS-CoV-2 variants of concern, including the SARS-CoV-2 ancestral strain, Alpha B.1.1.7, Gamma P1, Delta B.1.617 and Omicron BA.5.

These findings support prior preclinical studies that showed an in vitro efficacy of fluoxetine against SARS-CoV-2 in different host cells (i.e., Vero E6, Calu-1, Calu-3, HEK293T-ACE2-TMPRSS2 cells) and human lung epithelial cells [12,17,18]. They are also in line with results of observational studies showing significant associations between fluoxetine use and reduced COVID-19-related mortality or mechanical ventilation [20,22,24,25] and laboratory-detectable SARS-CoV-2 infection [24,26], and extend them by indicating that fluoxetine effects could be observed quickly when administrated after the start of the infection. Furthermore, they are consistent with results from animal models of septic shock and allergic asthma showing that fluoxetine markedly reduces the inflammatory reaction [42]. Finally, these results are in line with clinical studies conducted among individuals with major depressive disorder, showing that several antidepressants, including fluoxetine, significantly decrease peripheral levels of IL-6, TNF- α , IL-10, and CCL-2 [53], which have been shown to increase in severe COVID-19 patients [54].

By showing a significant increase in lung levels of hexosylceramides 16:0 and in the ratio HexCer 16:0/Cer 16:0 in fluoxetine versus vehicle-treated mice, our results suggest that the ceramide system might be implied in the observed antiviral and/or anti-inflammatory effects. Further analysis is now required to evaluate overtime, in comparison to baseline levels, those lipids dynamics during SARS-CoV-2 infection. Nevertheless, these findings are consistent with preclinical data indicating that the inhibition of the ASM/ceramide system by fluoxetine prevents infection of Vero E6 cells with pp-VSV-SARSCoV-2 spike [12] and that the reconstitution of ceramides in cells treated with fluoxetine restores the infection [12]. They are also in line with observational study results suggesting the utility of medications with high FIASMA activity against COVID-19 disease progression [23,24,36]. The modifica-

tion of the metabolic ratio hexosylceramide/ceramide by fluoxetine is a novel finding of this study that might explain its observed antiviral and anti-inflammatory effects, as this ratio has been shown to correlate with clinical disease severity and inflammation markers in patients with COVID-19 [55]. This result is compatible with either increased activity of glucosylceramidases/galactosylceramidases (leading to the hydrolysis of hexosylceramides to ceramides) or decreased activity of glucosylceramide synthase/galactosylceramide synthase (converting ceramides to hexosylceramides) upon SARS-CoV-2 infection. Further research is required to delineate the explicative weight of these different hypotheses [55–58]. Altogether, these data suggest that the ceramide system could be a relevant treatment target in COVID-19, especially because via its mode of action, fluoxetine maintains activity against SARS-CoV-2 variants.

Importantly, because the blood half-life of fluoxetine is about 2 to 4 days in humans and experimental data showed a human fluoxetine concentration lung:plasma split of 60:1 [59], fluoxetine may lead to subsequent potential antiviral and anti-inflammatory effects in the lungs quickly after its dispensation. This assertion is supported by a population pharmacokinetic modelling study [60] predicting that most patients would reach the antiviral EC₉₀ target, obtained from Calu-3 cells, in the lung tissues by day 1 at 40 mg/d and by day 3 at 20 mg/d. It is also supported by an experiment conducted in healthy volunteers showing that oral use of another FIASMA antidepressant, amitriptyline, whose blood half-life is about 20 h, prevents infection of freshly isolated nasal epithelial cells several hours after having taken the treatment, which is restored after the reconstitution of ceramides in these cells [12].

Fluoxetine is a prescription medication with a number of potential side effects and drug interactions, which are detailed in the Summary of Product Characteristic (SmPC) [61] and should be considered by the treating physician prior to use. Particularly, consistent with the medical contraindications, fluoxetine should not be used in combination with irreversible nonselective monoamine oxidase inhibitors or metoprolol. Fluoxetine is included in the World Health Organization's Model (WHO) List of Essential Medicines [62]. When selecting essential medicines, their safety is also considered. Fluoxetine is the best tolerated antidepressant in the treatment of patients with depression; discontinuation rates are even lower than with placebo treatment [63]. In the U.S., over 10% of the adult population has taken an antidepressant in the past 30 days [64], with fluoxetine being one of the most commonly prescribed antidepressants [65]. This means that fluoxetine is used very widely without major problems.

To the best of our knowledge, this study is the first to identify fluoxetine as a potential anti-SARS-CoV-2 medication in an animal model, through mechanisms that result in both antiviral and anti-inflammatory properties. Since fluoxetine is easy to use as a once-a-day pill, shows high safety margins and good tolerability, is widely available at low cost, and has, among SSRIs, both the greatest in vitro inhibition effect on the ceramide system and antiviral effect [13,15,34], this molecule should be prioritized in large-scale clinical trials at different stages of the disease [6,10], either alone or in combination with other medications. Given the promising results of the FIASMA antidepressant fluvoxamine in four clinical trials [27,28,30,33], fluoxetine, if proven effective in clinical trials, would enrich the current therapeutic arsenal with an inexpensive, well-tolerated, and easily administered medication in the global fight against COVID-19.

4. Materials and Methods

4.1. Safety Procedures

All described experiments involving SARS-CoV-2 infections have been entirely performed and processed in a Biosafety Level 3 (BSL-3) facility. Prior samples from infected cells being taken out of the BSL-3 for subsequent analysis, and all SARS-CoV-2 inactivation procedures were validated and approved by Institute of Pharmacology and Structural Biology (IPBS) biosecurity committee.

4.2. SARS-CoV-2 Virus Production

Virus productions were performed as previously described [51]. Briefly, SARS-CoV-2 isolates were amplified by infecting Vero E6 cells (ATCC CRL-1586) (MOI 0.005) in DMEM (Gibco™, Thermo Fisher Scientific, Waltham, MA, USA) supplemented with 10 mM HEPES and 1% penicillin-streptomycin (Gibco™, Thermo Fisher Scientific, Waltham, MA, USA). The supernatant was harvested at 48 h post-infection when cytopathic effects were observed, cell debris were removed by centrifugation, and aliquots were frozen at -80°C . Viral stocks were titrated by TCID₅₀ assays in Vero E6 cells (see Supplementary Information).

4.3. Virus Titration by TCID₅₀ Calculation

The day prior to infection, 50,000 VeroE6 cells per well were seeded in 96-well tissue culture plates using 10% FBS DMEM, and then incubated overnight at 37°C in a humidified, 5% CO₂ atmosphere-enriched chamber. Serial 2.5-fold dilutions (from 10^{-1} to $10^{-6.5}$) of the samples were prepared in DMEM and used to infect Vero E6 cells; each dilution was tested in four replicates. The plates were incubated for at least 96 h and observed to monitor the development of cytopathic effect using an EVOS Flويد microscope (Invitrogen). Viral titres, expressed as median tissue culture infectious dose (TCID₅₀/mL), were calculated according to both Reed and Muench and Karber methods based on three or four replicates for dilution [66].

4.4. Cell Infection and Treatment with Fluoxetine

For in vitro experiments, fluoxetine hydrochloride (Tocris Bio-Techne, Noyal Châtillon sur Seiche, France; CAS Number: 56296-78-7) was dissolved in H₂O₂ at 10 mM concentration and stored at -20°C until use. The day prior to infection, 50,000 Vero E6 or A549-ACE2-TMPRSS2 cells were seeded in 96-well tissue culture plates in 10% FBS DMEM supplemented with 10 mM HEPES (Gibco™) and 1% penicillin-streptomycin (Gibco™), and then incubated overnight at 37°C in a humidified, 5% CO₂ atmosphere-enriched chamber. One day later, cells were treated with fluoxetine (12.5 μM) for 2 h prior infection, and then infected with SARS-CoV-2 strains at indicated MOI in 90 μL DMEM supplemented with 10 mM HEPES, 1% penicillin-streptomycin and 1% L-Glutamine for 1 h at 37°C . Then, culture medium was completed with 90 μL of culture medium containing fluoxetine at 25 μM .

4.5. Air Liquid Interface (ALI) Cultures

Air-liquid interface cultures were established as previously described [52]. Briefly, to obtain ALI cultures, human airway organoids, derived as previously described [67,68], were dissociated into single cells using TrypLE express. Cells were seeded at a density of $\sim 50,000$ cells per transwell on human placenta collagen I-coated Transwell® permeable supports (6.5 mm diameter; 0.4 μm pore size; Corning) and cultured with organoid medium [67,68]. The medium was replaced 48 h after seeding, and once the cells reached confluence (~ 3 days after seeding), the medium was removed from the apical side of the transwell and replaced by differentiation media (STEMCELL Technologies, Saint Égrève, France; PneumaCult™-ALI Medium (Catalog #05001)). The medium was refreshed every 3 days and mucus removed with warm PBS every week. After 3–4 weeks of differentiation, ALI were used for SARS-CoV-2 infection. Prior to infection, the apical side of ALI were washed with PBS to remove excess of mucus and then pre-treated with fluoxetine on apical (100 μL) and basolateral (500 μL) sides for 2 h at the indicated concentrations. Then ALI were infected with 10 μL of SARS-CoV-2 (5×10^5 PFU/ALI) on the apical side for 4 h, washed with 150 μL of warmed PBS and then incubated for 72 h while maintaining fluoxetine on the basolateral side. Apical side of each ALI was washed with 150 μL of warm PBS to assess live viral load by TCID₅₀ assay on Vero E6 cells. ALI were fixed with 4% paraformaldehyde overnight before being taken out of the BSL-3. For staining, cells were permeabilized with 0.2% Triton X-100, then membranes were excised in 2 mL Eppendorf tubes containing blocking buffer (PBS 3% BSA) and incubated for 20 min at room tempera-

ture. Primary antibodies were incubated overnight at 4 °C (Supplementary Table S3). After three washes with 0.2% Triton X-100 in PBS, secondary antibodies were incubated for 1 h at room temperature in the dark. Three washes were performed and following staining with DAPI. Slides were mounted in Vectafield Antifade Mounting Medium with coverslips on membranes. Images were acquired with an Olympus FV100 inverted confocal microscope.

4.6. Cell Death and Viability

Cell death and viability were measured 72 h after infection, as previously described [51] (see Supplementary Information).

4.7. Pharmacokinetics of Fluoxetine in Mice

Pharmacokinetic studies were approved by the Committee on the Ethics of Animal Experiments of the Government of Unterfranken, Germany (License 55.2-2532.1-27/11) and Landesamt für Natur, Umwelt und Verbraucherschutz Nordrhein-Westfalen, Germany (License 81-02.04.2021.A112) and performed according to the European Union animal protection directive (Directive 2010/63/EU).

C57BL/6 male mice (Charles River, Sulzfeld, Germany) received 5 mg/kg fluoxetine (fluoxetine hydrochloride; Sigma Aldrich, Darmstadt, Germany) orally and serum levels of fluoxetine and its active metabolite desmethylfluoxetine were measured over time as indicated (Supplemental Figure S1). To determine the appropriate dose of fluoxetine that efficiently reduces the activity of ASM in the lung, mice were injected intraperitoneally (i.p.) with saline (0.9% NaCl solution) or different doses of fluoxetine as indicated. Blood and lung tissue were collected 6 h later. As shown in Supplemental Figure S1, serum level of fluoxetine and its metabolite peaked at 6 h and showed a half-life around 20 h. Similar serum levels were obtained by i.p. administration of fluoxetine. ASM activity in lung lysates was assessed as previously described [69], and revealed that a dose of 40 mg/kg i.p. is required to significantly inhibit lysosomal ASM activity in the lung of fluoxetine-treated C57BL/6 mice (Supplemental Figure S1). Therefore, we evaluated the efficacy of 40 mg/kg i.p. fluoxetine on SARS-CoV-2 infection in K18-hACE2.

4.8. Mouse Infection

Mouse infection studies were approved by local and national ethic committees (License APAFIS#27729-2020101616517580 v3, Minister of Research, France) and performed according to local guidelines (French ethical laws) and the European Union animal protection directive (Directive 2010/63/EU).

K18-hACE2 mice (Jackson Laboratory-USA, female, weight between 18 and 20 g, 8 (day 6) to 16 (day 2) per group and time point) were infected under a short anaesthesia (isoflurane 4%), by the intranasal route with 10^5 PFU of SARS-CoV-2 (strain Beta-CoV/France/IDF0372/2020). Thereafter, 4 h post-infection and then once daily, the first group received the vehicle (saline) treatment and the second group received fluoxetine (40 mg/kg i.p.) (Figure 1). During the 6 days of infection, mice were monitored daily for body weight as a measure of disease progression. At day 2 and 6 post-infection, after a terminal anaesthesia (ketamine 100 mg/kg + xylazine 10 mg/kg i.p.), the lung tissues were harvested and homogenated in gentleMACS™ M Tubes (Miltenyi Biotec, Paris, France) containing 3 mL of DPBS (Gibco™) using a gentleMACS™ Dissociator (Miltenyi Biotec, Paris, France). At day 6, body temperature was recorded using a lubricated rectal probe before mouse euthanasia.

4.9. Quantitative Real-Time PCR Analysis of Viral RNA and Inflammatory Genes

For each mouse, 150 µL of lung tissue homogenate was mixed with 1 mL TRIzol Reagent (Invitrogen) and stored at −80 °C at least 48 h before being taken out the BSL-3 facility. Total RNA was extracted, reverse-transcribed and gene expression levels of cytokines and chemokines were assessed as previously described [67]. Viral loads were performed as previously described [70,71]. Briefly, viral load quantifications were carried

out by linear regression employing a standard curve of six known quantities of plasmids containing the RdRp sequence (10^7 to 100 copies) and qPCRs were performed in TaqMan Universal PCR Master Mix (Thermo Fisher Scientific). qPCRs for gene expression and viral load were performed in triplicate and assessed with an ABI 7500 real-time PCR system (Applied Biosystems, Thermo Fisher Scientific, Waltham, MA, USA). Primers and probe sequences are provided in Supplemental Table S1.

4.10. Sphingolipid Quantification by Liquid Chromatography Tandem-Mass Spectrometry (LC-MS/MS)

Sphingolipids were extracted from lung tissue homogenates (20 μ L) as previously described [72]. To this end 1.5 mL methanol/chloroform (2:1, *v:v*) containing the internal standards 17:0 ceramide (d18:1/17:0), d₃₁-16:0 sphingomyelin (d18:1/16:0-d₃₁) and 17:0 glucosyl(β) ceramide (d18:1/17:0) (all Avanti Polar Lipids, Alabaster, AL, USA) were added. Extraction was facilitated by incubation at 48 °C with gentle shaking (120 rpm) overnight. To reduce interference from glycerolipids, samples were saponified with 150 μ L 1 M methanolic KOH for 2 h at 37 °C with gentle shaking (120 rpm) followed by neutralization with 12 μ L glacial acetic acid. After centrifugation at 2200 g for 10 min at 4 °C, organic supernatants were evaporated to dryness using a Savant SpeedVac concentrator (Thermo Fisher Scientific, Dreieich, Germany). Dried residues were reconstituted in 200 μ L acetonitrile/methanol/water (47.5:47.5:5 (*v:v:v*), 0.1% formic acid) and subjected to LC-MS/MS sphingolipid quantification applying the multiple reaction monitoring (MRM) approach. Chromatographic separation was achieved on a 1290 Infinity II HPLC (Agilent Technologies, Waldbronn, Germany) equipped with a Poroshell 120 EC-C8 column (3.0 \times 150 mm, 2.7 μ m; Agilent Technologies) guarded by a pre-column (3.0 \times 5 mm, 2.7 μ m) of identical material. MS/MS analyses were carried out using a 6495 triple-quadrupole mass spectrometer (Agilent Technologies) operating in the positive electrospray ionization mode (ESI+). Chromatographic conditions and settings of the ESI source and MS/MS detector have been published elsewhere [73]. Peak areas of Cer 16:0 (*m/z* 520.5 \rightarrow 264.3), SM 16:0 (*m/z* 703.6 \rightarrow 184.1), and HexCer 16:0 (*m/z* 700.6 \rightarrow 264.3) subspecies, as determined with MassHunter software (version 10.1, Agilent Technologies), were normalized to those of their internal standards. Quantification was performed with MassHunter Software (version 10.1, Agilent Technologies). Further, the determined Cer, SM and HexCer amounts were normalized to the actual protein content of the tissue homogenate used for extraction determined by the Coomassie (Bradford) Protein Assay (Thermo Fisher Scientific, Waltham, MA, USA).

4.11. Dual A549 Cell Stimulation

To investigate whether fluoxetine modulates NF- κ B and interferon pathways, we used A549–Dual cells carrying both an NF- κ B-driven secreted phosphatase alkaline (SEAP) gene and an IRF-driven Luciferase reporter genes (InvivoGen, Toulouse, France). Cells were plated in 96-well plates at 5×10^4 cells per well and incubated at 37 °C. The following day, cells were pre-incubated with or without fluoxetine (12.5–25 μ M) for 1 h before treatment with various activators of the NF- κ B and/or IRF pathways including TNF- α (10–0.1 ng/mL), IFN- α (10–0.1 ng/mL), and poly I:C (10–0.1 μ g/mL, InvivoGen, Toulouse, France). After 24 h of incubation, supernatant was collected and the presence of SEAP and Lucia reporting respectively for NF- κ B and IRF activation was quantified following incubation with SEAP and Lucia enzyme substrates Quanti-blue and Quanti-luc, respectively, according to the manufacturer's instructions (InvivoGen, Toulouse, France).

4.12. Statistical Analysis

All data in the text and figures are expressed as mean (\pm SEM). All means were compared using *t*-tests or Mann-Whitney tests when assumptions were not met. For all associations, we performed residual analyses to assess the fit of the data, checked assumptions, and examined the potential influence of outliers. Outliers were defined as having values outside the 1.5 interquartile range (IQR). Analyses were carried out with

GraphPad Prism 9 and R Software, version 4.1.3. Statistical significance was considered when two-sided $p < 0.05$.

Supplementary Materials: The supporting information can be downloaded at: <https://www.mdpi.com/article/10.3390/ijms232113623/s1>. References [70,71,74,75] are cited in the supplementary materials.

Author Contributions: Conceptualization, N.H., C.C., D.P., A.C., K.A.B., E.G., J.K., C.M., N.S.-W. and P.S.; methodology, D.P., S.A.L.-I., C.C., M.S.R., R.P., C.M., I.Z., F.S., R.M., G.G. and A.C.; formal analysis, C.C., N.H., M.S.R., S.A.L.-I. and C.C.; resources, J.I., O.N., F.L., E.M. and B.K.; writing—original draft preparation, N.H. and C.C.; writing—review and editing, S.A.L.-I., M.S.R., C.M., I.Z., F.S., G.G., A.C., K.A.B., J.I., N.S.-W., P.S., O.N., B.K., E.G., J.K. and E.M.; supervision, N.H. and C.C.; funding acquisition, N.H., C.C., J.K., F.L. and E.M. All authors have read and agreed to the published version of the manuscript.

Funding: This project has been funded by grants from the ANR RA-COVID-19 (ANR-20-COV8-0008-20), Toulouse Tech Transfer (OrganoCOVID) to CC, from the “Fondation pour la Recherche Médicale” (FRM) and ERC StG (INFLAME) to EM, from ERC StG (ANTIViR) to CG. SALI is funded by “Vaincre La Mucoviscidose” PhD fellowship (N RF20210502852/1/1/48). This study was further funded by the DFG research training group 2581 to BK. The BSL-3 structure is supported by LABEX, Investissement d’Avenir and foundation Bettencourt grants to ON. P.S. and N.S.-W acknowledges funding support from the Federal Ministry of Education and Research (BMBF) through KfW, Germany.

Institutional Review Board Statement: The study was conducted according to the guidelines of the Declaration of Helsinki, and approved by the Institutional Review Ethics Committees of the Government of Unterfranken, Germany (License 55.2-2532.1-27/11) and Landesamt für Natur, Umwelt und Verbraucherschutz Nordrhein-Westfalen, Germany (License 81-02.04.2021.A112) and performed according to the European Union animal protection directive (Directive 2010/63/EU) for pharmacokinetics experiments, and by local and national ethic committees (License APAFIS#27729 - 2020101616517580 v3, Minister of Research, France) and performed according to local guidelines (French ethical laws) and the European Union animal protection directive (Directive 2010/63/EU) for SARS-CoV-2 infection experiments.

Informed Consent Statement: Informed consent was obtained from all subjects involved in the study.

Data Availability Statement: Data available in a publicly accessible repository. The data presented in this study are openly available in FigShare at doi:10.6084/m9.figshare.21460026.

Acknowledgments: The authors warmly acknowledge Olivier Moncorgé and Caroline Goujon (IRIM, CNRS, Montpellier, France) for precious advice and technical assistance with SARS-CoV-2 handling, the ANEXPLO Animal Facility Level 3 of the IPBS institute for their extraordinary help regarding all operating and technical procedures this project required, Camille Pujot for technical assistance with ALI cultures, Eve Pitot from IPBS TRI facility for technical assistance with ALI imaging, and Christian Bréchet, MD PhD (Global Virus Network, Baltimore, USA) for critical reading of the manuscript. The authors acknowledge BEI resources for SARS-CoV-2 material transfer, including SARS-CoV-2 variants. We are further thankful to Daniel Herrmann for excellent technical assistance with the LC-MS/MS analyses. Funders had no interference in the conduct of the project, and InvivoGen for support with performing the A549–Dual cells assays.

Conflicts of Interest: The authors declare no conflict of interest.

References

1. Hoertel, N.; Blachier, M.; Blanco, C.; Olfson, M.; Massetti, M.; Rico, M.S.; Limosin, F.; Leleu, H. A Stochastic Agent-Based Model of the SARS-CoV-2 Epidemic in France. *Nat. Med.* **2020**, *26*, 1417–1421. [[CrossRef](#)] [[PubMed](#)]
2. Hoertel, N.; Blachier, M.; Sánchez-Rico, M.; Limosin, F.; Leleu, H. Impact of the Timing and Adherence to Face Mask Use on the Course of the COVID-19 Epidemic in France. *J. Travel Med.* **2021**, *28*, taab016. [[CrossRef](#)] [[PubMed](#)]
3. Matta, J.; Wiernik, E.; Robineau, O.; Carrat, F.; Touvier, M.; Severi, G.; de Lamballerie, X.; Blanché, H.; Deleuze, J.-F.; Gouraud, C.; et al. Association of Self-Reported COVID-19 Infection and SARS-CoV-2 Serology Test Results With Persistent Physical Symptoms Among French Adults During the COVID-19 Pandemic. *JAMA Intern. Med.* **2021**, *182*, 19. [[CrossRef](#)]
4. Chevance, A.; Gourion, D.; Hoertel, N.; Llorca, P.-M.; Thomas, P.; Bocher, R.; Moro, M.-R.; Laprévotte, V.; Benyamina, A.; Fossati, P.; et al. Ensuring mental health care during the SARS-CoV-2 epidemic in France: A narrative review. *L’Encephale* **2020**, *46*, 193–201. [[CrossRef](#)]

5. Lim, S.; Tignanelli, C.J.; Hoertel, N.; Boulware, D.R.; Usher, M.G. Prevalence of Medical Contraindications to Niraparitin/Ritonavir in a Cohort of Hospitalized and Nonhospitalized Patients With COVID-19. *Open Forum. Infect. Dis.* **2022**, *9*, ofac389. [[CrossRef](#)] [[PubMed](#)]
6. Hoertel, N. Do the Selective Serotonin Reuptake Inhibitor Antidepressants Fluoxetine and Fluvoxamine Reduce Mortality Among Patients With COVID-19? *JAMA Netw. Open* **2021**, *4*, e2136510. [[CrossRef](#)] [[PubMed](#)]
7. The Lancet Infectious Diseases Unmet Need for COVID-19 Therapies in Community Settings. *Lancet Infect. Dis.* **2021**, *21*, 1471. [[CrossRef](#)]
8. Venkatesan, P. Repurposing Drugs for Treatment of COVID-19. *Lancet Respir. Med.* **2021**, *9*, e63. [[CrossRef](#)]
9. National Institutes of Health. COVID-19 Treatment Guidelines. The COVID-19 Treatment Guidelines Panel's Statement on the Use of Tocilizumab for the Treatment of COVID-19. Available online: <https://www.covid19treatmentguidelines.nih.gov/statement-on-tocilizumab/> (accessed on 5 March 2021).
10. Hoertel, N.; Sánchez-Rico, M.; Cougoule, C.; Gulbins, E.; Kornhuber, J.; Carpinteiro, A.; Becker, K.A.; Reiersen, A.M.; Lenze, E.J.; Seftel, D.; et al. Repurposing Antidepressants Inhibiting the Sphingomyelinase Acid/Ceramide System against COVID-19: Current Evidence and Potential Mechanisms. *Mol. Psychiatry* **2021**, *26*, 7098–7099. [[CrossRef](#)]
11. Hoertel, N.; Sánchez-Rico, M.; de la Muela, P.; Abellán, M.; Blanco, C.; Leboyer, M.; Cougoule, C.; Gulbins, E.; Kornhuber, J.; Carpinteiro, A.; et al. Risk of Death in Individuals Hospitalized for COVID-19 with and without Psychiatric Disorders: An Observational Multicenter Study in France. *Biol. Psychiatry Glob. Open Sci.* **2022**, *110*, 1498–1511. [[CrossRef](#)]
12. Carpinteiro, A.; Edwards, M.J.; Hoffmann, M.; Kochs, G.; Gripp, B.; Weigang, S.; Adams, C.; Carpinteiro, E.; Gulbins, A.; Keitsch, S.; et al. Pharmacological Inhibition of Acid Sphingomyelinase Prevents Uptake of SARS-CoV-2 by Epithelial Cells. *Cell Rep. Med.* **2020**, *1*, 100142. [[CrossRef](#)] [[PubMed](#)]
13. Kornhuber, J.; Hoertel, N.; Gulbins, E. The Acid Sphingomyelinase/Ceramide System in COVID-19. *Mol. Psychiatry* **2022**, *27*, 307–314. [[CrossRef](#)] [[PubMed](#)]
14. Brunotte, L.; Zheng, S.; Mecate-Zambrano, A.; Tang, J.; Ludwig, S.; Rescher, U.; Schloer, S. Combination Therapy with Fluoxetine and the Nucleoside Analog GS-441524 Exerts Synergistic Antiviral Effects against Different SARS-CoV-2 Variants In Vitro. *Pharmaceutics* **2021**, *13*, 1400. [[CrossRef](#)]
15. Fred, S.M.; Kuivanen, S.; Ugurlu, H.; Casarotto, P.C.; Levanov, L.; Saksela, K.; Vapalahti, O.; Castrén, E. Antidepressant and Antipsychotic Drugs Reduce Viral Infection by SARS-CoV-2 and Fluoxetine Shows Antiviral Activity Against the Novel Variants in Vitro. *Front. Pharmacol.* **2022**, *12*, 755600. [[CrossRef](#)]
16. Dechaumes, A.; Nekoua, M.P.; Belouzard, S.; Sane, F.; Engelmann, I.; Dubuisson, J.; Alidjinou, E.K.; Hober, D. Fluoxetine Can Inhibit SARS-CoV-2 In Vitro. *Microorganisms* **2021**, *9*, 339. [[CrossRef](#)] [[PubMed](#)]
17. Schloer, S.; Brunotte, L.; Mecate-Zambrano, A.; Zheng, S.; Tang, J.; Ludwig, S.; Rescher, U. Drug Synergy of Combinatory Treatment with Remdesivir and the Repurposed Drugs Fluoxetine and Itraconazole Effectively Impairs SARS-CoV-2 Infection in Vitro. *Br. J. Pharm.* **2021**, *178*, 2339–2350. [[CrossRef](#)] [[PubMed](#)]
18. Schloer, S.; Brunotte, L.; Goretzko, J.; Mecate-Zambrano, A.; Korthals, N.; Gerke, V.; Ludwig, S.; Rescher, U. Targeting the Endolysosomal Host-SARS-CoV-2 Interface by Clinically Licensed Functional Inhibitors of Acid Sphingomyelinase (FIASMA) Including the Antidepressant Fluoxetine. *Emerg. Microbes Infect.* **2020**, *9*, 2245–2255. [[CrossRef](#)]
19. Zimniak, M.; Kirschner, L.; Hilpert, H.; Geiger, N.; Danov, O.; Oberwinkler, H.; Steinke, M.; Sewald, K.; Seibel, J.; Bodem, J. The Serotonin Reuptake Inhibitor Fluoxetine Inhibits SARS-CoV-2 in Human Lung Tissue. *Sci. Rep.* **2021**, *11*, 5890. [[CrossRef](#)]
20. Hoertel, N.; Sánchez-Rico, M.; Vernet, R.; Beeker, N.; Jannot, A.-S.; Neuraz, A.; Salamanca, E.; Paris, N.; Daniel, C.; Gramfort, A.; et al. Association between Antidepressant Use and Reduced Risk of Intubation or Death in Hospitalized Patients with COVID-19: Results from an Observational Study. *Mol. Psychiatry* **2021**, *26*, 5199–5212. [[CrossRef](#)]
21. Németh, Z.K.; Szűcs, A.; Vitrai, J.; Juhász, D.; Németh, J.P.; Holló, A. Fluoxetine Use Is Associated with Improved Survival of Patients with COVID-19 Pneumonia: A Retrospective Case-Control Study. *Ideggyogy Sz* **2021**, *74*, 389–396. [[CrossRef](#)]
22. Oskotsky, T.; Marić, I.; Tang, A.; Oskotsky, B.; Wong, R.J.; Aghaepour, N.; Sirota, M.; Stevenson, D.K. Mortality Risk Among Patients With COVID-19 Prescribed Selective Serotonin Reuptake Inhibitor Antidepressants. *JAMA Netw. Open* **2021**, *4*, e2133090. [[CrossRef](#)] [[PubMed](#)]
23. Hoertel, N.; Sánchez-Rico, M.; Gulbins, E.; Kornhuber, J.; Carpinteiro, A.; Abellán, M.; de la Muela, P.; Vernet, R.; Beeker, N.; Neuraz, A.; et al. Association between FIASMA Psychotropic Medications and Reduced Risk of Intubation or Death in Individuals with Psychiatric Disorders Hospitalized for Severe COVID-19: An Observational Multicenter Study. *Transl. Psychiatry* **2022**, *12*, 90. [[CrossRef](#)] [[PubMed](#)]
24. Hoertel, N.; Sánchez-Rico, M.; Kornhuber, J.; Gulbins, E.; Reiersen, A.M.; Lenze, E.J.; Fritz, B.A.; Jalali, F.; Mills, E.J.; Cougoule, C.; et al. Antidepressant Use and Its Association with 28-Day Mortality in Inpatients with SARS-CoV-2: Support for the FIASMA Model against COVID-19. *J. Clin. Med.* **2022**, *11*, 5882. [[CrossRef](#)] [[PubMed](#)]
25. Fritz, B.A.; Hoertel, N.; Lenze, E.J.; Jalali, F.; Reiersen, A.M. Association between Antidepressant Use and ED or Hospital Visits in Outpatients with SARS-CoV-2. *Transl. Psychiatry* **2022**, *12*, 341. [[CrossRef](#)] [[PubMed](#)]
26. Clelland, C.L.; Ramiah, K.; Steinberg, L.; Clelland, J.D. Analysis of the Impact of Antidepressants and Other Medications on COVID-19 Infection Risk in a Chronic Psychiatric in-Patient Cohort. *BJPsych. Open* **2021**, *8*, e6. [[CrossRef](#)] [[PubMed](#)]
27. Reis, G.; dos Santos Moreira-Silva, E.A.; Silva, D.C.M.; Thabane, L.; Milagres, A.C.; Ferreira, T.S.; dos Santos, C.V.Q.; de Souza Campos, V.H.; Nogueira, A.M.R.; de Almeida, A.P.F.G.; et al. Effect of Early Treatment with Fluvoxamine on Risk of Emergency

- Care and Hospitalisation among Patients with COVID-19: The TOGETHER Randomised, Platform Clinical Trial. *Lancet Glob. Health* **2021**, *10*, e42–e51. [[CrossRef](#)]
28. Lenze, E.J.; Mattar, C.; Zorumski, C.F.; Stevens, A.; Schweiger, J.; Nicol, G.E.; Miller, J.P.; Yang, L.; Yingling, M.; Avidan, M.S.; et al. Fluvoxamine vs Placebo and Clinical Deterioration in Outpatients With Symptomatic COVID-19: A Randomized Clinical Trial. *JAMA* **2020**, *324*, 2292–2300. [[CrossRef](#)]
29. Reis, G.; Mills, E. Fluvoxamine for the Treatment of COVID-19—Author’s Reply. *Lancet Glob. Health* **2022**, *10*, e333. [[CrossRef](#)]
30. Seftel, D.; Boulware, D.R. Prospective Cohort of Fluvoxamine for Early Treatment of Coronavirus Disease 19. *Open Forum. Infect. Dis.* **2021**, *8*, ofab050. [[CrossRef](#)]
31. Lee, T.C.; Vigod, S.; Bortolussi-Courval, É.; Hanula, R.; Boulware, D.R.; Lenze, E.J.; Reiersen, A.M.; McDonald, E.G. Fluvoxamine for Outpatient Management of COVID-19 to Prevent Hospitalization: A Systematic Review and Meta-Analysis. *JAMA Netw. Open* **2022**, *5*, e226269. [[CrossRef](#)]
32. Bramante, C.T.; Huling, J.D.; Tignanelli, C.J.; Buse, J.B.; Liebovitz, D.M.; Nicklas, J.M.; Cohen, K.; Puskarich, M.A.; Belani, H.K.; Proper, J.L.; et al. Randomized Trial of Metformin, Ivermectin, and Fluvoxamine for Covid-19. *N. Engl. J. Med.* **2022**, *387*, 599–610. [[CrossRef](#)] [[PubMed](#)]
33. Calusic, M.; Marcec, R.; Luksa, L.; Jurkovic, I.; Kovac, N.; Mihaljevic, S.; Likic, R. Safety and Efficacy of Fluvoxamine in COVID-19 ICU Patients: An Open Label, Prospective Cohort Trial with Matched Controls. *Br. J. Clin. Pharm.* **2021**, *88*, 2065–2073. [[CrossRef](#)] [[PubMed](#)]
34. Kornhuber, J.; Tripal, P.; Reichel, M.; Mühle, C.; Rhein, C.; Muehlbacher, M.; Groemer, T.W.; Gulbins, E. Functional Inhibitors of Acid Sphingomyelinase (FIASMA): A Novel Pharmacological Group of Drugs with Broad Clinical Applications. *Cell Physiol. Biochem* **2010**, *26*, 9–20. [[CrossRef](#)] [[PubMed](#)]
35. Carpinteiro, A.; Gripp, B.; Hoffmann, M.; Pöhlmann, S.; Hoertel, N.; Edwards, M.J.; Kamler, M.; Kornhuber, J.; Becker, K.A.; Gulbins, E. Inhibition of Acid Sphingomyelinase by Ambroxol Prevents SARS-CoV-2 Entry into Epithelial Cells. *J. Biol. Chem.* **2021**, *296*, 100701. [[CrossRef](#)] [[PubMed](#)]
36. Hoertel, N.; Sánchez-Rico, M.; Gulbins, E.; Kornhuber, J.; Carpinteiro, A.; Lenze, E.J.; Reiersen, A.M.; Abellán, M.; Muela, P.; Vernet, R.; et al. Association between FIASMA and Reduced Risk of Intubation or Death in Individuals Hospitalized for Severe COVID-19: An Observational Multicenter Study. *Clin. Pharm. Ther.* **2021**, *110*, 1498–1511. [[CrossRef](#)] [[PubMed](#)]
37. Torretta, E.; Garziano, M.; Polisenio, M.; Capitano, D.; Biasin, M.; Santantonio, T.A.; Clerici, M.; Lo Caputo, S.; Trabattoni, D.; Gelfi, C. Severity of COVID-19 Patients Predicted by Serum Sphingolipids Signature. *IJMS* **2021**, *22*, 10198. [[CrossRef](#)]
38. Abusukhun, M.; Winkler, M.S.; Pöhlmann, S.; Moerer, O.; Meissner, K.; Tampe, B.; Hofmann-Winkler, H.; Bauer, M.; Gräler, M.H.; Claus, R.A. Activation of Sphingomyelinase-Ceramide-Pathway in COVID-19 Purposes Its Inhibition for Therapeutic Strategies. *Front. Immunol.* **2021**, *12*, 784989. [[CrossRef](#)]
39. Mühle, C.; Kremer, A.; Vetter, M.; Schmid, J.; Achenbach, S.; Schumacher, F.; Lenz, B.; Cougoule, C.; Hoertel, N.; Carpinteiro, A.; et al. COVID-19 and Its Clinical Severity Are Associated with Alterations of Plasma Sphingolipids and Enzyme Activities of Sphingomyelinase and Ceramidase. *MedRxiv* **2022**. [[CrossRef](#)]
40. Kornhuber, J.; Muehlbacher, M.; Trapp, S.; Pechmann, S.; Friedl, A.; Reichel, M.; Mühle, C.; Terfloth, L.; Groemer, T.W.; Spitzer, G.M.; et al. Identification of Novel Functional Inhibitors of Acid Sphingomyelinase. *PLoS ONE* **2011**, *6*, e23852. [[CrossRef](#)]
41. Duda, W.; Kubera, M.; Kreiner, G.; Curzytek, K.; Detka, J.; Głombik, K.; Ślusarczyk, J.; Basta-Kaim, A.; Budziszewska, B.; Lasoń, W.; et al. Suppression of Pro-Inflammatory Cytokine Expression and Lack of Anti-Depressant-like Effect of Fluoxetine in Lipopolysaccharide-Treated Old Female Mice. *Int. Immunopharmacol.* **2017**, *48*, 35–42. [[CrossRef](#)]
42. Roumestan, C.; Michel, A.; Bichon, F.; Portet, K.; Detoc, M.; Henriquet, C.; Jaffuel, D.; Mathieu, M. Anti-Inflammatory Properties of Desipramine and Fluoxetine. *Respir. Res.* **2007**, *8*, 35. [[CrossRef](#)] [[PubMed](#)]
43. Huang, C.; Wang, Y.; Li, X.; Ren, L.; Zhao, J.; Hu, Y.; Zhang, L.; Fan, G.; Xu, J.; Gu, X.; et al. Clinical Features of Patients Infected with 2019 Novel Coronavirus in Wuhan, China. *Lancet* **2020**, *395*, 497–506. [[CrossRef](#)]
44. McCray, P.B.; Pewe, L.; Wohlford-Lenane, C.; Hickey, M.; Manzel, L.; Shi, L.; Netland, J.; Jia, H.P.; Halabi, C.; Sigmund, C.D.; et al. Lethal Infection of K18-HACE Mice Infected with Severe Acute Respiratory Syndrome Coronavirus. *J. Virol.* **2007**, *81*, 813–821. [[CrossRef](#)] [[PubMed](#)]
45. Golden, J.W.; Cline, C.R.; Zeng, X.; Garrison, A.R.; Carey, B.D.; Mucker, E.M.; White, L.E.; Shamblin, J.D.; Brocato, R.L.; Liu, J.; et al. Human Angiotensin-Converting Enzyme 2 Transgenic Mice Infected with SARS-CoV-2 Develop Severe and Fatal Respiratory Disease. *JCI Insight* **2020**, *5*, e142032. [[CrossRef](#)] [[PubMed](#)]
46. Zheng, J.; Wong, L.-Y.R.; Li, K.; Verma, A.K.; Ortiz, M.E.; Wohlford-Lenane, C.; Leidinger, M.R.; Knudson, C.M.; Meyerholz, D.K.; McCray, P.B.; et al. COVID-19 Treatments and Pathogenesis Including Anosmia in K18-HACE2 Mice. *Nature* **2021**, *589*, 603–607. [[CrossRef](#)] [[PubMed](#)]
47. Winkler, E.S.; Bailey, A.L.; Kafai, N.M.; Nair, S.; McCune, B.T.; Yu, J.; Fox, J.M.; Chen, R.E.; Earnest, J.T.; Keeler, S.P.; et al. SARS-CoV-2 Infection of Human ACE2-Transgenic Mice Causes Severe Lung Inflammation and Impaired Function. *Nat. Immunol.* **2020**, *21*, 1327–1335. [[CrossRef](#)]
48. Gomes, K.S.; de Carvalho-Netto, E.F.; Monte, K.C.D.S.; Acco, B.; Nogueira, P.J.d.C.; Nunes-de-Souza, R.L. Contrasting Effects of Acute and Chronic Treatment with Imipramine and Fluoxetine on Inhibitory Avoidance and Escape Responses in Mice Exposed to the Elevated T-Maze. *Brain Res. Bull.* **2009**, *78*, 323–327. [[CrossRef](#)]

49. Flores-Ramirez, F.J.; Garcia-Carachure, I.; Sanchez, D.O.; Gonzalez, C.; Castillo, S.A.; Arenivar, M.A.; Themann, A.; Lira, O.; Rodriguez, M.; Preciado-Piña, J.; et al. Fluoxetine Exposure in Adolescent and Adult Female Mice Decreases Cocaine and Sucrose Preference Later in Life. *J. Psychopharmacol.* **2019**, *33*, 145–153. [CrossRef]
50. Sulzbacher, M.M.; Sulzbacher, L.M.; Passos, F.R.; Bilibio, B.L.E.; Althaus, W.F.; Weizenmann, L.; de Oliveira, K.; Frizzo, M.N.; Ludwig, M.S.; Heck, T.G. A Single Dose of EHSP72 Attenuates Sepsis Severity in Mice. *Sci. Rep.* **2020**, *10*, 9198. [CrossRef]
51. Planès, R.; Pinilla, M.; Santoni, K.; Hessel, A.; Passemar, C.; Lay, K.; Paillette, P.; Valadao, A.-L.; Robinson, K.S.; Bastard, P.; et al. Human NLRP1 Is a Sensor of Pathogenic Coronavirus 3CL Proteases in Lung Epithelial Cells. *SSRN J.* **2022**, *82*, 2385–2400.e9. [CrossRef]
52. Lamers, M.M.; Beumer, J.; van der Vaart, J.; Knoops, K.; Puschhof, J.; Breugem, T.I.; Ravelli, R.B.G.; Paul van Schayck, J.; Mykytyn, A.Z.; Duimel, H.Q.; et al. SARS-CoV-2 Productively Infects Human Gut Enterocytes. *Science* **2020**, *369*, 50–54. [CrossRef] [PubMed]
53. Köhler, C.A.; Freitas, T.H.; Stubbs, B.; Maes, M.; Solmi, M.; Veronese, N.; de Andrade, N.Q.; Morris, G.; Fernandes, B.S.; Brunoni, A.R. Peripheral Alterations in Cytokine and Chemokine Levels after Antidepressant Drug Treatment for Major Depressive Disorder: Systematic Review and Meta-Analysis. *Mol. Neurobiol.* **2018**, *55*, 4195–4206. [CrossRef] [PubMed]
54. Venkataraman, A.; Kumar, N.P.; Hanna, L.E.; Putlibai, S.; Karthick, M.; Rajamanikam, A.; Sadasivam, K.; Sundaram, B.; Babu, S. Plasma Biomarker Profiling of PIMS-TS, COVID-19 and SARS-CoV2 Seropositive Children—A Cross-Sectional Observational Study from Southern India. *EBioMedicine* **2021**, *66*, 103317. [CrossRef] [PubMed]
55. Marín-Corral, J.; Rodríguez-Morató, J.; Gomez-Gomez, A.; Pascual-Guardia, S.; Muñoz-Bermúdez, R.; Salazar-Degracia, A.; Pérez-Terán, P.; Restrepo, M.I.; Khymenets, O.; Haro, N.; et al. Metabolic Signatures Associated with Severity in Hospitalized COVID-19 Patients. *IJMS* **2021**, *22*, 4794. [CrossRef]
56. Prakash, H.; Upadhyay, D.; Bandapalli, O.R.; Jain, A.; Kleuser, B. Host Sphingolipids: Perspective Immune Adjuvant for Controlling SARS-CoV-2 Infection for Managing COVID-19 Disease. *Prostaglandins Other Lipid Mediat.* **2021**, *152*, 106504. [CrossRef]
57. Havulinna, A.S.; Sysi-Aho, M.; Hilvo, M.; Kauhanen, D.; Hurme, R.; Ekroos, K.; Salomaa, V.; Laaksonen, R. Circulating Ceramides Predict Cardiovascular Outcomes in the Population-Based FINRISK 2002 Cohort. *ATVB* **2016**, *36*, 2424–2430. [CrossRef]
58. Lopes-Virella, M.F.; Baker, N.L.; Hunt, K.J.; Hammad, S.M.; Arthur, J.; Virella, G.; Klein, R.L. Glycosylated Sphingolipids and Progression to Kidney Dysfunction in Type 1 Diabetes. *J. Clin. Lipidol.* **2019**, *13*, 481–491.e1. [CrossRef]
59. Johnson, R.D.; Lewis, R.J.; Angier, M.K. The Distribution of Fluoxetine in Human Fluids and Tissues. *J. Anal. Toxicol.* **2007**, *31*, 409–414. [CrossRef]
60. Eugene, A.R. Fluoxetine Pharmacokinetics and Tissue Distribution Suggest a Possible Role in Reducing SARS-CoV-2 Titers. *F1000Res* **2021**, *10*, 477. [CrossRef]
61. EMEA Overall Summary of the Scientific Evaluation of Prozac and Associated Names. Available online: https://www.ema.europa.eu/en/documents/referral/prozac-article-6-12-referral-annex-i-ii-iii_en.pdf (accessed on 1 September 2022).
62. World Health Organization WHO Model Lists of Essential Medicines. Available online: <https://www.who.int/groups/expert-committee-on-selection-and-use-of-essential-medicines/essential-medicines-lists> (accessed on 1 September 2022).
63. Cipriani, A.; Furukawa, T.A.; Salanti, G.; Chaimani, A.; Atkinson, L.Z.; Ogawa, Y.; Leucht, S.; Ruhe, H.G.; Turner, E.H.; Higgins, J.P.T.; et al. Comparative Efficacy and Acceptability of 21 Antidepressant Drugs for the Acute Treatment of Adults with Major Depressive Disorder: A Systematic Review and Network Meta-Analysis. *Lancet* **2018**, *391*, 1357–1366. [CrossRef]
64. National Center for Health Statistics Antidepressant Use Among Adults: United States, 2015–2018. Available online: <https://www.cdc.gov/nchs/products/databriefs/db377.htm> (accessed on 1 September 2022).
65. SDI's Vector One®: National 2010 Top 200 Generic Drugs by Total Prescriptions. Available online: <https://web.archive.org/web/20121215070930/http://drugtopics.modernmedicine.com/drugtopics/data/articlestandard//drugtopics/252011/727243/article.pdf> (accessed on 1 September 2022).
66. Reed, L.J.; Muench, H. A Simple Method of Estimating Fifty per Cent Endpoints. *Am. J. Epidemiol.* **1938**, *27*, 493–497. [CrossRef]
67. Iakobachvili, N.; Leon-Icaza, S.A.; Knoops, K.; Sachs, N.; Mazères, S.; Simeone, R.; Peixoto, A.; Bernard, C.; Murriss-Espin, M.; Mazières, J.; et al. Mycobacteria–Host Interactions in Human Bronchiolar Airway Organoids. *Mol. Microbiol.* **2022**, *117*, 682–692. [CrossRef] [PubMed]
68. Goldenberg, D.L. Fibromyalgia and Other Chronic Fatigue Syndromes: Is There Evidence for Chronic Viral Disease? *Semin. Arthritis Rheum.* **1988**, *18*, 111–120. [CrossRef]
69. Mühle, C.; Kornhuber, J. Assay to Measure Sphingomyelinase and Ceramidase Activities Efficiently and Safely. *J. Chromatogr. A* **2017**, *1481*, 137–144. [CrossRef] [PubMed]
70. Corman, V.M.; Landt, O.; Kaiser, M.; Molenkamp, R.; Meijer, A.; Chu, D.K.; Bleicker, T.; Brünink, S.; Schneider, J.; Schmidt, M.L.; et al. Detection of 2019 Novel Coronavirus (2019-nCoV) by Real-Time RT-PCR. *Eurosurveillance* **2020**, *25*, 2000045. [CrossRef]
71. Rebendenne, A.; Chaves Valadao, A.L.; Tauziet, M.; Maarifi, G.; Bonaventure, B.; McKellar, J.; Planès, R.; Nisole, S.; Arnaud-Arnould, M.; Moncorgé, O.; et al. SARS-CoV-2 Triggers an MDA-5-Dependent Interferon Response Which Is Unable To Control Replication in Lung Epithelial Cells. *J. Virol.* **2021**, *95*, e02415-20. [CrossRef]

72. Gulbins, A.; Schumacher, F.; Becker, K.A.; Wilker, B.; Soddemann, M.; Boldrin, F.; Müller, C.P.; Edwards, M.J.; Goodman, M.; Caldwell, C.C.; et al. Antidepressants Act by Inducing Autophagy Controlled by Sphingomyelin–Ceramide. *Mol. Psychiatry* **2018**, *23*, 2324–2346. [[CrossRef](#)]
73. Naser, E.; Kadow, S.; Schumacher, F.; Mohamed, Z.H.; Kappe, C.; Hessler, G.; Pollmeier, B.; Kleuser, B.; Arenz, C.; Becker, K.A.; et al. Characterization of the Small Molecule ARC39, a Direct and Specific Inhibitor of Acid Sphingomyelinase in vitro. *J. Lipid Res.* **2020**, *61*, 896–910. [[CrossRef](#)]
74. Shimizu, K.; Asakura, M.; Fujii, S.I. Prolonged antitumor NK cell reactivity elicited by CXCL10-expressing dendritic cells licensed by CD40L+ CD4+ memory T cells. *J. Immunol.* **2011**, *186*, 5927–5937. [[CrossRef](#)]
75. Koblansky, A.A.; Jankovic, D.; Oh, H.; Hieny, S.; Sungnak, W.; Mathur, R.; Hayden, M.S.; Akira, S.; Sher, A.; Ghosh, S. Recognition of profilin by Toll-like receptor 12 is critical for host resistance to *Toxoplasma gondii*. *Immunity* **2013**, *38*, 119–130. [[CrossRef](#)]

Supplemental information for

Antiviral and anti-inflammatory activities of Fluoxetine in a SARS-CoV-2 infection mouse model

Running title: Fluoxetine in a SARS-CoV-2 infection mouse model

David Péricat^{1*}, Stephen Adonai Leon-Icaza^{1*}, Marina Sanchez Rico^{2,3,4}, Christiane Mühle⁵, Iulia Zoicas⁵, Fabian Schumacher⁶, Rémi Planès¹, Raoul Mazars¹, Germain Gros¹, Alexander Carpinteiro⁷, Katrin Anne Becker⁷, Jacques Izopet^{8,9}, Olivier Neyrolles¹, Burkhard Kleuser⁶, Frédéric Limosin^{2,3,4}, Erich Gulbins⁷, Johannes Kornhuber⁵, Etienne Meunier¹, Nicolas Hoertel^{2,3,4,*}, Céline Cougoule^{1,*#}

¹ Institute of Pharmacology and Structural Biology (IPBS), University of Toulouse, CNRS, Toulouse; France

² Université de Paris Cité, Paris, France.

³ Assistance Publique-Hôpitaux de Paris (AP-HP), Hôpital Corentin-Celton, DMU Psychiatrie et Addictologie, Hôpital Corentin-Celton, Département de Psychiatrie et d'Addictologie de l'adulte et du sujet âgé, Issy-les-Moulineaux, 92130, France.

⁴ INSERM, Institut de Psychiatrie et Neurosciences de Paris (IPNP), UMR_S1266, Paris, France.

⁵ Department of Psychiatry and Psychotherapy, University Hospital, Friedrich-Alexander-University of Erlangen-Nuremberg, Erlangen, Germany.

⁶ Freie Universität Berlin, Institute of Pharmacy, Königin-Luise-Str. 2+4, 14195 Berlin, Germany

⁷ Institute for Molecular Biology, University Medicine Essen, University of Duisburg-Essen, Essen, Germany.

⁸ Infinity, Université Toulouse, CNRS, INSERM, UPS, 31300 Toulouse, France.

⁹ Laboratoire de Virologie, CHU Toulouse, Hôpital Purpan, 31300 Toulouse, France.

* these authors contributed equally

Corresponding author#

Céline Cougoule, Ph.D., H.D.R.,

IPBS-Toulouse, CNRS-Université Toulouse III 205 Route de Narbonne - 31077 Toulouse cedex 4, France

Phone: +33-(0)5 61 17 54 61

Email: celine.cougoule@ipbs.fr

Supplementary Materials and Methods

Ethic statements: The collection of patient data and tissue for human airway organoid generation was performed according to the guidelines of the European Network of Research Ethics Committees following European and national law. The responsible accredited ethical committees reviewed and approved this study in accordance with the Medical Research Involving Human Subjects Act. The CHU of Toulouse and CNRS approved protocol CHU 19 244 C and Ref CNRS 205782. All patients participating in this study consented to scientific use of their material; patients can withdraw their consent at any time, leading to the prompt disposal of their tissue and any derived material. Non-tumor lung tissue from two independent donors receiving surgical treatment for lung cancer were used to derive human airway organoids.

SARS-CoV-2 virus production

The BetaCoV/France/IDF0372/2020 isolate was supplied by Sylvie van der Werf and the National Reference Centre for Respiratory Viruses hosted by Institute Pasteur (Paris, France). The mNeonGreen (mNG) reporter SARS-CoV-2 were based on 2019-nCoV/USA_WA1/2020 isolated from the first reported SARS-CoV-2 case in the USA, and provided through the World Reference Center for Emerging Viruses and Arboviruses (WRCEVA), and UTMB investigator, Dr. Pei Yong Shi. The following reagents were deposited by Centers for Disease Control and Prevention and obtained through BEI Resources, NIAID, NIH: SARS-Related Coronavirus 2, Isolate USA/CA_CDC_5574/2020, NR-54011, SARS-Related Coronavirus 2, Isolate hCoV-19/Japan/TY7-503/2021 (Brazil P.1), NR-54982, contributed by National Institute of Infectious Diseases. SARS-CoV-2 Delta and Omicron BA-5 variants were isolated and provided by Pr. J. Izopet from the Toulouse hospital, France. SARS-CoV-2 isolates were amplified by infecting Vero E6 cells (ATCC CRL-1586) (MOI 0.005) in DMEM (Gibco) supplemented with 10mM HEPES and 1% penicillin-streptomycin (Gibco). The supernatant was harvested at 48 h post-infection when cytopathic effects were observed, cell debris were removed by centrifugation,

and aliquots were frozen at -80°C . Viral stocks were titrated by TCID₅₀ assays in Vero E6 cells. Typical titers were 5 to 10×10^6 PFU/ml.

Cell death and viability

Cell death was measured by quantification of the lactate dehydrogenase (LDH) release into the cell supernatant using LDH Cytotoxicity Detection Kit (Takara). Briefly, 50 μL cell supernatant were incubated with 50 μL LDH substrate and incubated for 15 min. The enzymatic reaction was stopped by adding 50 μL of stop solution. Maximal cell death was determined with whole cell lysates from unstimulated cells incubated with 1% Triton X-100. Cell viability was measured by quantification of intracellular ATP using CellTiter-Glo® One Solution Assay (Promega) according to manufacturer's instructions.

Mice

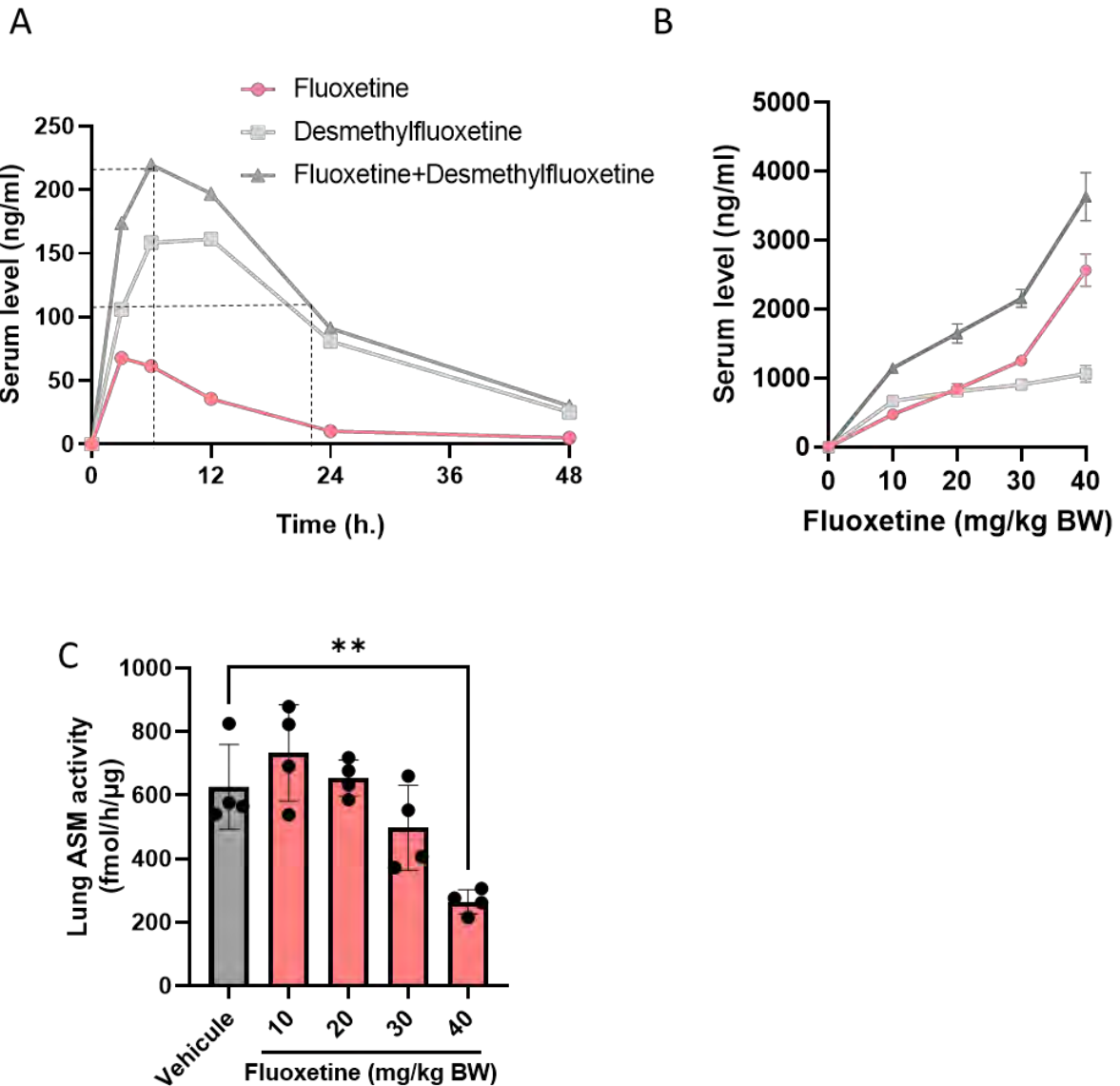
C57BL/6 mice (Charles River, Sulzfeld, Germany; 22 - 26g) and 32 K18-hACE2 mice (Jackson Laboratory-USA, 18 - 20g) were housed in individually ventilated cages under standard laboratory conditions (12:12 light:dark cycle, lights on at 07:00 h, 22 $^{\circ}\text{C}$, 60% humidity, food and water ad libitum) in groups of 4 mice per cage.

Quantitative real-time PCR analysis of viral RNA and inflammatory genes

Lung tissue was first homogenized in 3 ml PBS in an M tube using a GentleMACS dissociator (Miltenyi biotec). For each mouse, 150 μl of lung tissue homogenate were mixed with 1 mL TRIzol Reagent (Invitrogen) and stored at -80°C at least 48 h before to be taken out the BSL-3 facility. Total RNA was extracted using the RNeasy mini kit (Qiagen) and reverse-transcribed (150ng) with the High-Capacity cDNA Reverse Transcription Kit (Thermo Fisher Scientific). Gene expression levels of cytokines and chemokines were assessed with the SYBR Select Master Mix (Thermo Scientific) and relative quantifications were determined using the $2^{-\text{Ct}}$ method with β -actin as reference. Viral loads were performed as previously described.^{41,42} Briefly, viral load quantifications were carried out by linear regression employing a standard

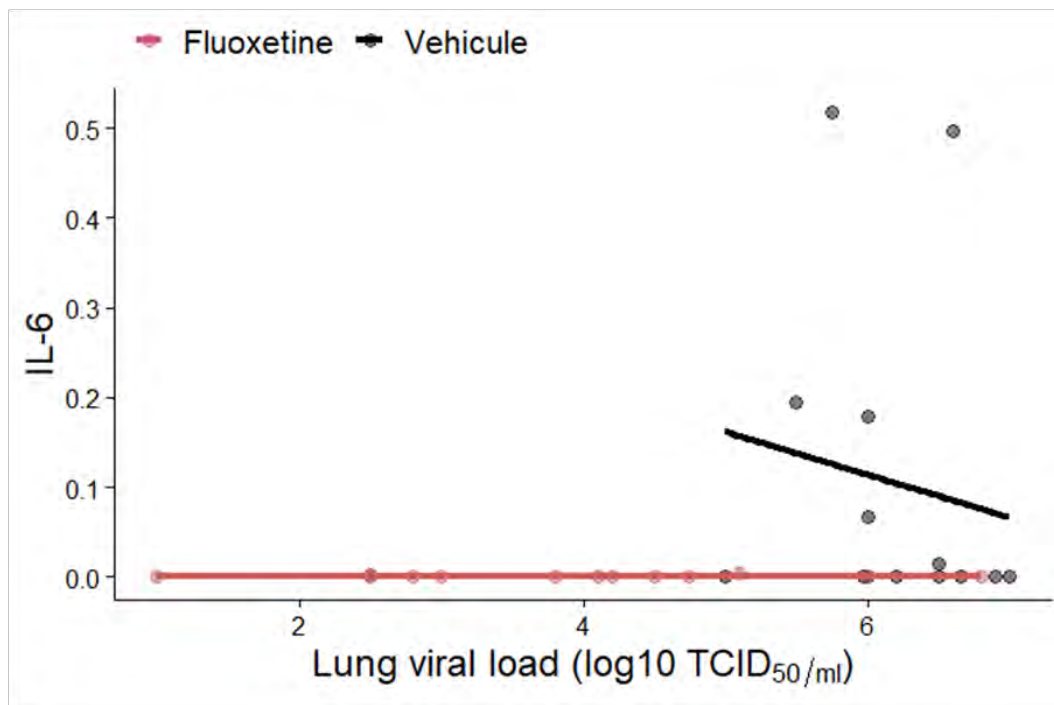
curve of 6 known quantities of plasmids containing the RdRp sequence (107 to 100 copies) and qPCRs were performed in TaqMan Universal PCR Master Mix (Thermo Fisher Scientific). qPCRs for gene expression and viral load were performed in triplicate and assessed with an ABI 7500 real-time PCR system (Applied Biosystems). Primers and probe sequences are provided in Supplemental Table S1.

Supplementary Figures

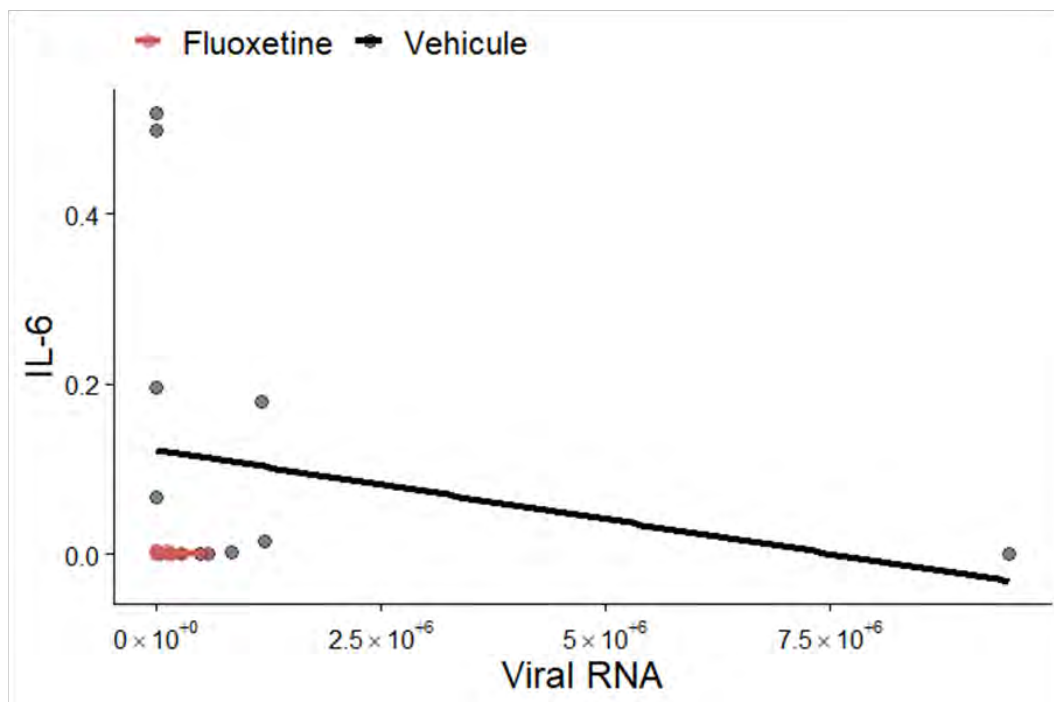


Supplemental Figure S1 (related to Figure 1): Pharmacokinetic studies of fluoxetine in C57BL/6 mice. (A) 5 mg/kg fluoxetine was applied per oral gavage. Serum levels of fluoxetine and its active metabolite desmethylfluoxetine were measured over time, i.e., after 3, 6, 12, 24 and 48 h. (B)(C) Mice were injected intraperitoneally with saline (0.9% NaCl solution) or several doses of fluoxetine (i.e., 10, 20, 30 and 40 mg/kg) in a volume of 10 ml/kg ($n = 4$ mice/group) and blood and lung tissue were collected 6 h later. Fluoxetine and desmethylfluoxetine was measured in serum (B) and ASM activity was measured in the lung tissue (C); ** $p < 0.01$.

A

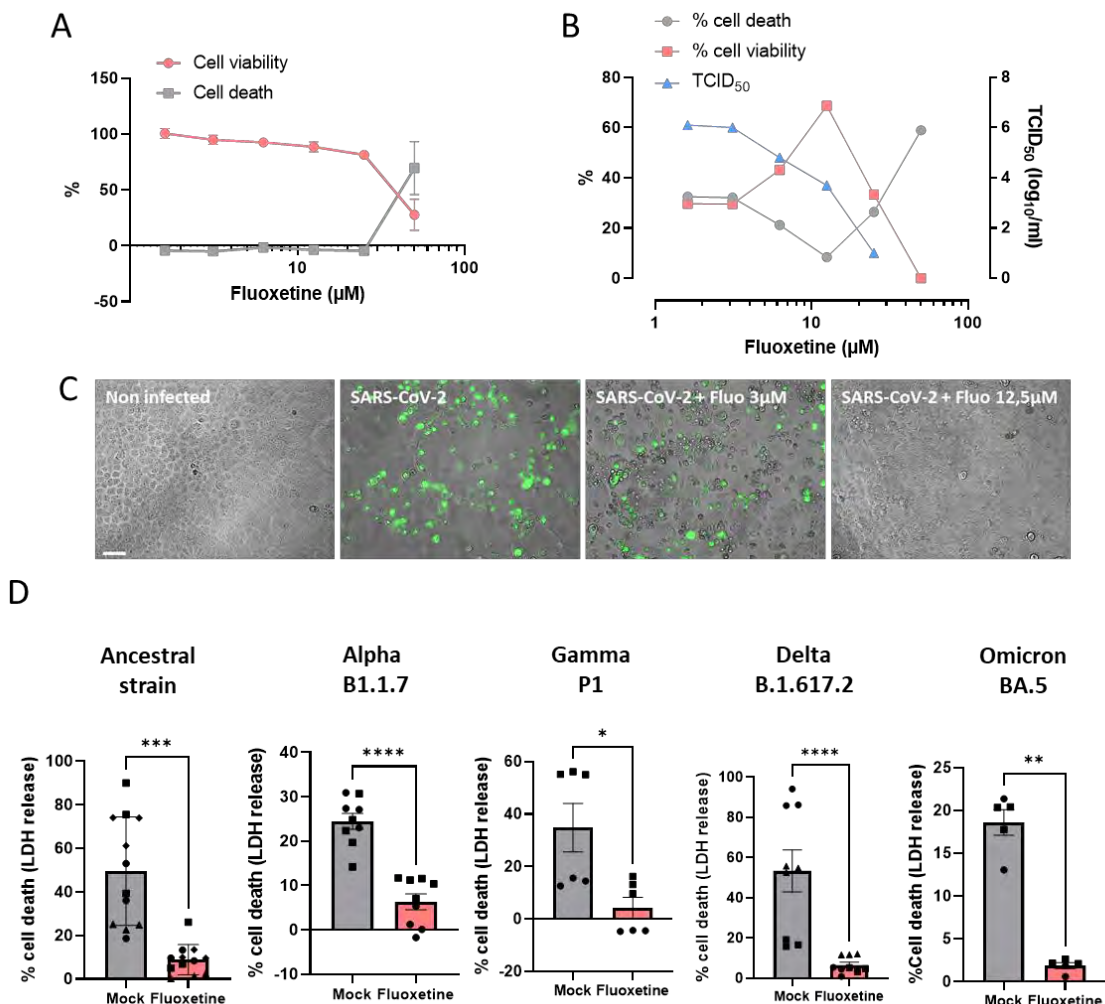


B



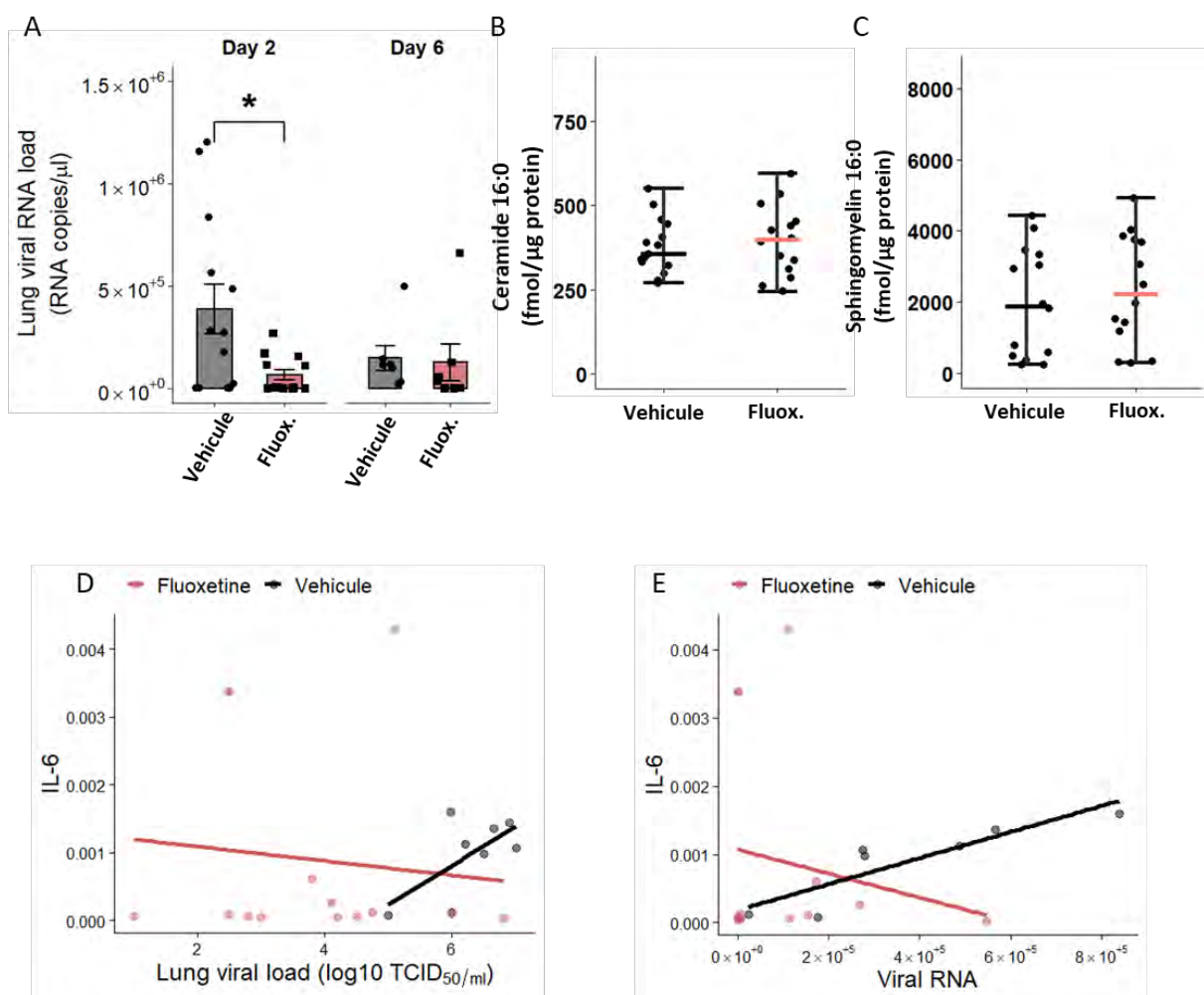
Supplemental Figure S2 (related to Figure 1). Association between viral load and IL-6 expression in mice at day 2 and 6 post-infection combined. (A) association of IL-6 expression level with Lung TCID₅₀ in saline- and fluoxetine-treated mice; (B) association of IL-6 expression level with viral RNA load in saline- and fluoxetine-treated mice.

normalized initial weight was plotted (mean \pm SEM); (C) body temperature recorded at day 6 post-infection. (D-E) A549-dual A549 cells were incubated with fluoxetine (12.5-25 μ M) for 1h prior to be treated with various activators of the NF- κ B and/or IRF pathways including TNF- α (10 ng/mL), IFN- α (10 ng/mL), and poly I:C (10 – 0.1 μ g/mL). fold increase of NF- κ B (D) and IRF (E) pathway activation are shown. Fold increase of NF- κ B, IRF pathways activation and percentage of cell viability were calculated compared to the untreated condition. Data show one experiment representative of two performed independently. *, $p < 0.05$, **, $p < 0.01$; ****, $p < 0.0001$.



Supplemental Figure S4 (related to Figure 3): Fluoxetine activity *in vitro*. Vero E6 cells were treated with fluoxetine at 1, 5 to 50 μ M for 1 hr prior infection and then infected with SARS-CoV-2 for 72 h. (A) Fluoxetine cytotoxicity on Vero E6 cells measured 72 h post-treatment;

(B) Dose-response analysis of SARS-CoV-2 replication, cell viability and cell death with fluoxetine treatment. (C) Representative images 72 h post infection of Vero E6 cells infected or not with mNG-reporter SARS-CoV-2 strain, treated or not with fluoxetine. Scale bar = 100 μ m. (D) Percentage of cell death measured by LDH release assay on Vero E6 cells infected with SARS-CoV-2 variants with or without fluoxetine treatment (12.5 μ M) for 72h. Data represent men \pm SEM from two independent experiments performed in triplicates. *, $p < 0.05$; **, $p < 0.01$; ***, $p < 0.001$; ****, $p < 0.0001$.



Supplemental Figure S5. Data after excluding outliers. (A) Viral RNA levels in the lungs of saline- and fluoxetine-treated mice infected with SARS-CoV-2 at day 2 and 6 post-infection expressed as Log₁₀ SARS-CoV-2 RNA genome copies after excluding outliers; $P < 0.05$ (B) Fluoxetine effect on ceramide 16:0 after excluding outliers; (C) Fluoxetine effect on

sphingomyelin 16:0 after excluding outliers; (D) association of IL-6 expression level with Lung TCID₅₀ in saline- and fluoxetine-treated mice after excluding outliers; (E) association of IL-6 expression level with viral RNA load in saline- and fluoxetine-treated mice after excluding outliers.

Supplemental Table S1 List of qPCR primers

Target	Primers 5'-3'	Reference
Cytokines and chemokines		
IL-6	F- TACCACTTCACAAGTCGGAGGC R- CTGCAAGTGCATCATCGTTGTTC	OriGene
CXCL10	F- ATTGCCACGATGAAAAAGAATGAT R- AGACCAAGGGCAATTAGGACTAGC	Shimizu K, et al. <i>J Immunol.</i> 2011;186(10):5927-5937. doi:10.4049/jimmunol.1003351
TNFα	F- GGTGCCTATGTCTCAGCCTCTT R- GCCATAGAAGTATGAGAGGGAG	OriGene
CCL2	F- GCTACAAGAGGATCACCAGCAG R- GTCTGGACCCATTCTTCTTGG	OriGene
IL-1β	F- TGGACCTCCAGGATGAGGACA R- GTTCATCTCGGAGCCTGTAGTG	OriGene
β-actin	F- GCTGTGCTGTCCCTGTATGCCTCT R- CCTCTCAGCTGTGGTGGTGAAGC	Koblansky AA, et al. <i>Immunity.</i> 2013;38(1):119-130. doi:10.1016/j.immuni.2012.09.016
Viral load		
RdRp	F- GTGARATGGTCATGTGTGGCGG R- CAAATGTTAAAAACACTATTAGCATA Probe- FAM- CAGGTGGAACCTCATCAGGAGATGC – TAMRA	Corman VM, et al. <i>Euro Surveill.</i> 2020;25(3):2000045. doi:10.2807/1560-7917.ES.2020.25.3.2000045 Rebendenne A, et al. <i>J Virol.</i> 2021;95(8):e02415-20. doi:10.1128/JVI.02415-20

Supplemental Table S2. Associations of fluoxetine versus saline exposure with inflammatory markers.

	Day 2		Day 6	
	Fluoxetine vs. Saline	Fluoxetine vs. Saline	Fluoxetine vs. Saline	Fluoxetine vs. Saline
	Viral load	Viral RNA	Viral load	Viral RNA
	OR [95% CI]	OR [95% CI]	OR [95% CI]	OR [95% CI]
IL6				
<i>Crude</i>	0.47 (0.23 - 0.94; 0.042)*	0.47 (0.23 - 0.94; 0.042)*	0.28 (0.12 - 0.65; 0.013)*	0.28 (0.12 - 0.65; 0.013)*
<i>Adjusted</i>	0.43 (0.15 - 1.19; 0.115)	0.42 (0.20 - 0.86; 0.025)*	0.48 (0.15 - 1.59; 0.259)	0.28 (0.11 - 0.67; 0.018)*
TNFα				
<i>Crude</i>	0.32 (0.17 - 0.58; 0.001)*	0.32 (0.17 - 0.58; 0.001)*	0.34 (0.14 - 0.85; 0.040)*	0.34 (0.14 - 0.85; 0.040)*
<i>Adjusted</i>	0.31 (0.12 - 0.76; 0.017)*	0.41 (0.24 - 0.69; 0.003)*	1.08 (0.39 - 3.00; 0.888)	0.35 (0.14 - 0.87; 0.045)*
CXCL10				
<i>Crude</i>	0.44 (0.22 - 0.88; 0.028)*	0.44 (0.22 - 0.88; 0.028)*	0.39 (0.15 - 1.02; 0.080)	0.39 (0.15 - 1.02; 0.080)
<i>Adjusted</i>	0.42 (0.15 - 1.16; 0.107)	0.53 (0.27 - 1.04; 0.076)	0.75 (0.19 - 2.89; 0.681)	0.40 (0.15 - 1.07; 0.095)
CCL2				
<i>Crude</i>	0.26 (0.15 - 0.45; <0.001)*	0.26 (0.15 - 0.45; <0.001)*	0.48 (0.17 - 1.30; 0.174)	0.48 (0.17 - 1.30; 0.174)
<i>Adjusted</i>	0.37 (0.17 - 0.81; 0.020)*	0.29 (0.17 - 0.51; <0.001)*	1.01 (0.25 - 4.12; 0.984)	0.49 (0.18 - 1.35; 0.194)

* Two-sided p-value is significant (p<0.05).

Supplementary Table S3. List of reagents used for ALI staining

Antibody	Cat N°	Supplier	Dilution
Anti acetylated Tubulin	Sc-23950	Santa Cruz	1/300
Goat anti Mouse IgG Dylight 550	GTX MU003D550NHS	Immunoreagent	1/1000
Alexa Fluor 647 Phalloidin	A22287	Invitrogen	1/40

II. Efficacy and Mode of Action of a Direct Inhibitor of *Mycobacterium abscessus* InhA

Authors: Matthéo Alcaraz, Françoise Roquet-Banères, **Stephen Adonai Leon-Icaza**, Jan Abendroth, Yves-Marie Boudehen, Céline Cougoule, Thomas E Edwards, Laurent Kremer.

Contribution: I designed and performed all the experiments for Figure 4 of the article. Briefly, I microinjected CF organoids with Mabs S or R; after infection, I treated or not the organoids with different concentrations of NITD-916, and on day three, I performed live imaging and CFU assay.

This article was published in ACS Infectious Diseases.

Efficacy and Mode of Action of a Direct Inhibitor of *Mycobacterium abscessus* InhA

Matthéo Alcaraz, Françoise Roquet-Banères, Stephen Adonai Leon-Icaza, Jan Abendroth, Yves-Marie Boudehen, Céline Cougoule, Thomas E. Edwards, and Laurent Kremer*



Cite This: <https://doi.org/10.1021/acscinfecdis.2c00314>



Read Online

ACCESS |



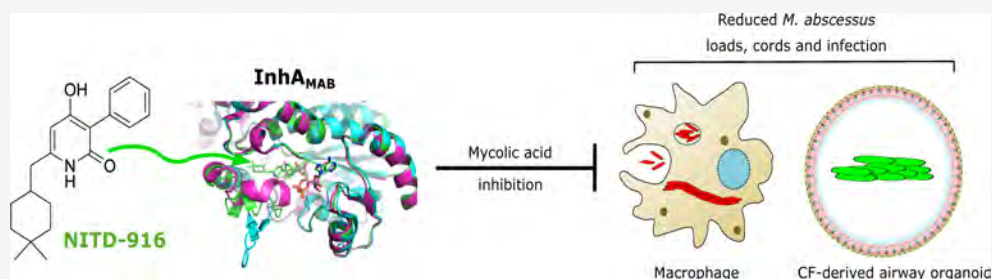
Metrics & More



Article Recommendations



Supporting Information



ABSTRACT: There is an unmet medical need for effective treatments against *Mycobacterium abscessus* pulmonary infections, to which cystic fibrosis (CF) patients are particularly vulnerable. Recent studies showed that the antitubercular drug isoniazid is inactive against *M. abscessus* due to the incapacity of the catalase-peroxidase to convert the pro-drug into a reactive metabolite that inhibits the enoyl-ACP reductase InhA. To validate InhA_{MAB} as a druggable target in *M. abscessus*, we assayed the activity of NITD-916, a 4-hydroxy-2-pyridone lead candidate initially described as a direct inhibitor of InhA that bypasses KatG bioactivation in *Mycobacterium tuberculosis*. The compound displayed low MIC values against rough and smooth clinical isolates in vitro and significantly reduced the bacterial burden inside human macrophages. Moreover, treatment with NITD-916 reduced the number and size of intracellular mycobacterial cords, regarded as markers of the severity of the infection. Importantly, NITD-916 significantly lowered the *M. abscessus* burden in CF-derived lung airway organoids. From a mechanistic perspective, NITD-916 abrogated de novo synthesis of mycolic acids and NITD-916-resistant spontaneous mutants harbored point mutations in InhA_{MAB} at residue 96. That NITD-916 targets InhA_{MAB} directly without activation requirements was confirmed genetically and by resolving the crystal structure of the protein in complex with NADH and NITD-916. These findings collectively indicate that InhA_{MAB} is an attractive target to be exploited for future chemotherapeutic developments against this difficult-to-treat mycobacterium and highlight the potential of NITD-916 derivatives for further evaluation in preclinical settings.

KEYWORDS: *Mycobacterium abscessus*, NITD-916, macrophage, organoid, InhA, mycolic acid

M. abscessus is a rapidly growing nontuberculous mycobacterium (NTM) of rising clinical significance and the cause of difficult-to-cure pulmonary diseases, particularly in patients with cystic fibrosis (CF).¹ In these patients, infection with *M. abscessus* is often associated with a more rapid decline in lung function, and the presence of *M. abscessus* can be deleterious for subsequent lung transplantation.^{2–4} The *M. abscessus* complex comprises three subspecies exhibiting different clinical outcomes and drug susceptible profiles to antibiotics:⁵ *M. abscessus* subsp. *abscessus* (designated hereafter *M. abscessus*), *M. abscessus* subsp. *bolletii* (designated hereafter *M. bolletii*), and *M. abscessus* subsp. *massiliense* (designated hereafter *M. massiliense*).⁶ All three subspecies can display either a smooth (S) or a rough (R) morphotype as a consequence of the presence or absence, respectively, of surface-associated glycopeptidolipids (GPL).^{7–10} These morphological changes are linked to major phenotypic differences, including sliding motility, biofilm formation,^{8,9,11} or produc-

tion of large bacterial cords.^{11,12} S and R variants can be viewed as two representative forms of the same isolate, which can coexist in the patient and evolve differently in response to the host immune pressure. They can also display specific pathophysiological characteristics;¹⁰ S variants are generally less virulent than their corresponding R variants,^{11,13,14} the latter being more frequently associated with severe pulmonary diseases in CF patients.^{2,4} In addition, different susceptibility profiles to drugs have been reported between S and R

Received: June 14, 2022

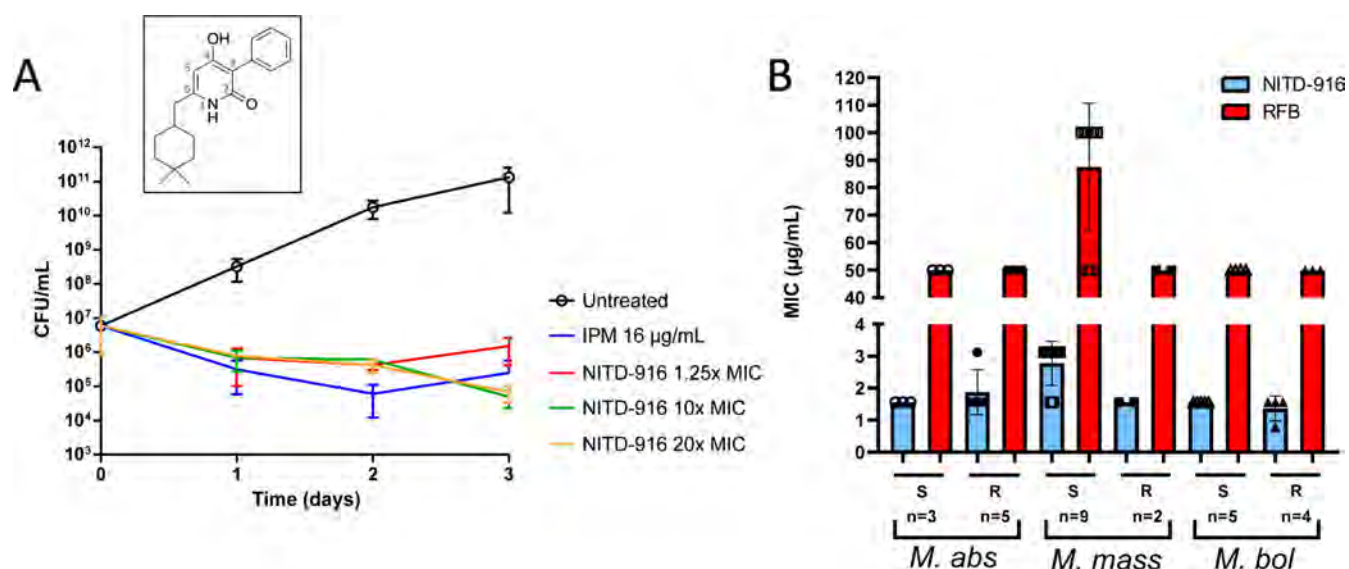


Figure 1. In vitro activity of NITD-916 against *M. abscessus*. (A) Cultures of *M. abscessus* CIP104536^T (S) were exposed to either 1.95, 15.6, 31.2 $\mu\text{g/mL}$ NITD-916 (corresponding to 1.25 \times , 10 \times , and 20 \times MIC) or 16 $\mu\text{g/mL}$ imipenem (IPM) in CaMHB at 30 °C. At various time points, bacteria were plated on LB agar and incubated at 37 °C for 4 days prior to CFU counting. Results are expressed as the mean of 2 independent experiments in triplicates \pm SD. Inset: structure of NITD-916. (B) MIC (in $\mu\text{g/mL}$) of NITD-916 and RFB against *M. abscessus* complex clinical isolates. MIC values were determined in CaMBH for *M. abscessus* subsp. *abscessus* ($n = 8$), *M. abscessus* subsp. *massiliense* ($n = 11$), and *M. abscessus* subsp. *bolletii* ($n = 9$). Data are plotted as mean values \pm SD. S refers to smooth strains; R refers to rough strains.

variants,^{15,16} thus warranting the need for evaluating compounds/drug regimens against both variants.

Due to intrinsic resistance to a wide panel of antimicrobials, including most antitubercular drugs, treatment of *M. abscessus* lung disease remains extremely challenging.^{17–20} Multidrug regimens are administered for months to years, generally comprising an oral macrolide (clarithromycin or azithromycin) and intravenously administered aminoglycosides (amikacin) and β -lactams (imipenem or ceftazidime).^{21–23} Other drugs, such as tigecycline or clofazimine, can be added to strengthen the regimen, mostly in response to toxic side effects or poor clinical response.²⁴ However, despite intensive chemotherapy, treatment success rates typically remain very low in the case of macrolide resistance (25–40%), which occurs in at least 40–60% of clinical isolates.²⁵ Thus, given the unsatisfactory performances of the current regimens, more effective drugs are required. Unfortunately, de novo drug discovery efforts to identify new chemical scaffolds are impeded by low hit rates,^{26,27} explaining why the *M. abscessus* drug pipeline focuses mainly on repurposing and reformulation of approved drugs.

In addition to mutations in genes encoding the drug targets conducting to acquired drug resistance,^{7,26} the widespread resistome of *M. abscessus* results also from the low permeability properties of the cell envelope, the expression of a wide range of drug-modifying enzymes, the induction of efflux pumps and the absence or dysfunctional drug-activating enzymes.^{17,20,28} The latter, for instance, explains why isoniazid (INH) is totally inactive against *M. abscessus*. Indeed, it has been recently shown that the catalase-peroxidase KatG_{MAB} is unable to transform INH into an active metabolite.²⁹ INH, the most efficient first-line anti-TB drug against actively replicating *M. tuberculosis*, remains the first choice for prophylaxis and treatment. Its biotransformation requires the catalase-peroxidase KatG^{30,31} to generate an isonicotinoyl radical that reacts with NAD⁺ to produce an INH-NAD adduct.^{32,33} This adduct blocks the enoyl-ACP reductase (InhA) of the type II fatty acid synthase (FAS-II),^{34–37} leading to the arrest of mycolic acid

biosynthesis. Mycolic acids are essential and unique long-chain (C₇₀–C₉₀) α -alkyl, β -hydroxy fatty acids,^{35,38} and their inhibition ultimately results in mycobacterial cell death.³⁹ However, while being a validated drug target in *M. tuberculosis*, it remains to be established whether InhA represents an attractive target for future drug developments against *M. abscessus*.

To fill this gap, this study was undertaken to test the hypothesis whether NITD-916, a direct inhibitor of InhA that bypasses the KatG bioactivation process,⁴⁰ offers potential for future chemotherapeutic developments against *M. abscessus*. NITD-916 is a 4-hydroxy-2-pyridone lead candidate previously identified in a phenotypic screen against *M. tuberculosis* that exerts bactericidal activity against common INH-resistant TB clinical isolates. Herein, we aimed at assessing the activity of NITD-916 against *M. abscessus* S and R strains in vitro, in macrophages as well as in CF lung airway organoids and report the mechanism of action of the inhibitor in *M. abscessus*.

RESULTS

***M. abscessus* Strains Are Susceptible to NITD-916 Treatment in Vitro.** To address whether InhA inhibitors bypassing KatG bioactivation can offer potential chemotherapeutic options against *M. abscessus*, we first screened the literature for commercially available direct InhA inhibitors, previously validated against *M. tuberculosis* and for which in vitro data and efficacy in mice have been reported. This led to the 4-hydroxy-2-pyridone lead compound NITD-916.⁴⁰ Initial experiments revealed that the *M. abscessus* CIP104536^T S reference strain was particularly susceptible to NITD-916 in CaMHB (MIC = 1.56 $\mu\text{g/mL}$ which is 5 μM). However, as shown previously for other compounds,⁴¹ the MIC was greatly dependent on the medium, with values of 0.195 $\mu\text{g/mL}$ and 6.25 $\mu\text{g/mL}$ in Sauton's medium and Middlebrook 7H9, respectively (Table S1). MICs in an artificial sputum medium

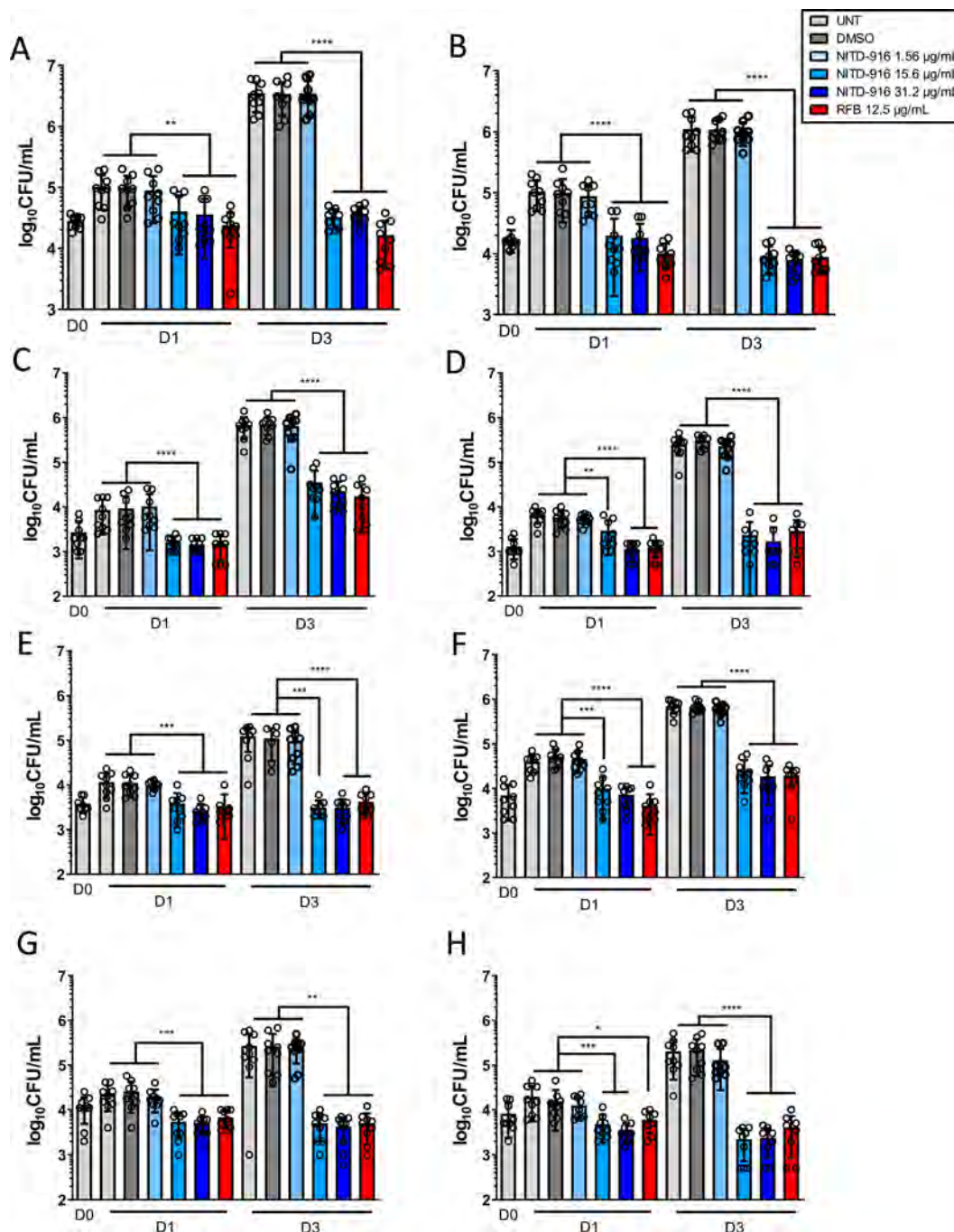


Figure 2. Intracellular activity of NITD-916 on *M. abscessus* complex-infected THP-1 cells. Macrophages were infected with *M. abscessus* reference strains and clinical isolates (MOI of 2:1) for 4 h prior to treatment with 250 µg/mL AMK for 2 h to kill extracellular bacteria. Cells were then exposed to either NITD-916 or to RFB at the indicated concentrations. Untreated (UNT) or DMSO-exposed cells were included as controls. CFU were determined at 0, 1, and 3 days postinfection. The various strains tested and morphotypes are as follows: (A) *M. abscessus* CIP104536^T (S); (B) *M. abscessus* CIP104536^T (R); (C) *M. abscessus* 2069 (S); (D) *M. abscessus* 2524 (R); (E) *M. massiliense* 179 (R); (F) *M. massiliense* 120 (S); (G) *M. bolletii* 112 (R); (H) *M. bolletii* 108 (R). Data of 3 independent experiments in triplicates were analyzed with a Mann–Whitney *t* test. **P* ≤ 0.05; ***P* ≤ 0.01; ****P* ≤ 0.001; *****P* ≤ 0.0001.

(ASM) containing components of the CF sputum⁴² were comparable to those obtained in CaMHB.

To determine the effect of the compound in broth culture, exponentially growing *M. abscessus* was exposed to increasing concentrations of NITD-916, corresponding to 1.25×, 10×, and 20× MIC. This resulted in a noticeable growth inhibition (Figure 1A). However, the number of colony-forming units (CFU) remained relatively stable at the lowest concentration

tested during the 3 days of treatment and comparable to those in the inoculum, suggesting a bacteriostatic effect. In addition, the killing effect was not concentration-dependent, at least during the first 2 days of treatment. An additional 1-Log drop was observed after 3 days with 10× or 20× MIC. At these concentrations, NITD-916 resulted in a growth inhibitory effect comparable to the one of imipenem (IPM) used at the MIC (16 µg/mL), a known β-lactam antibiotic active against

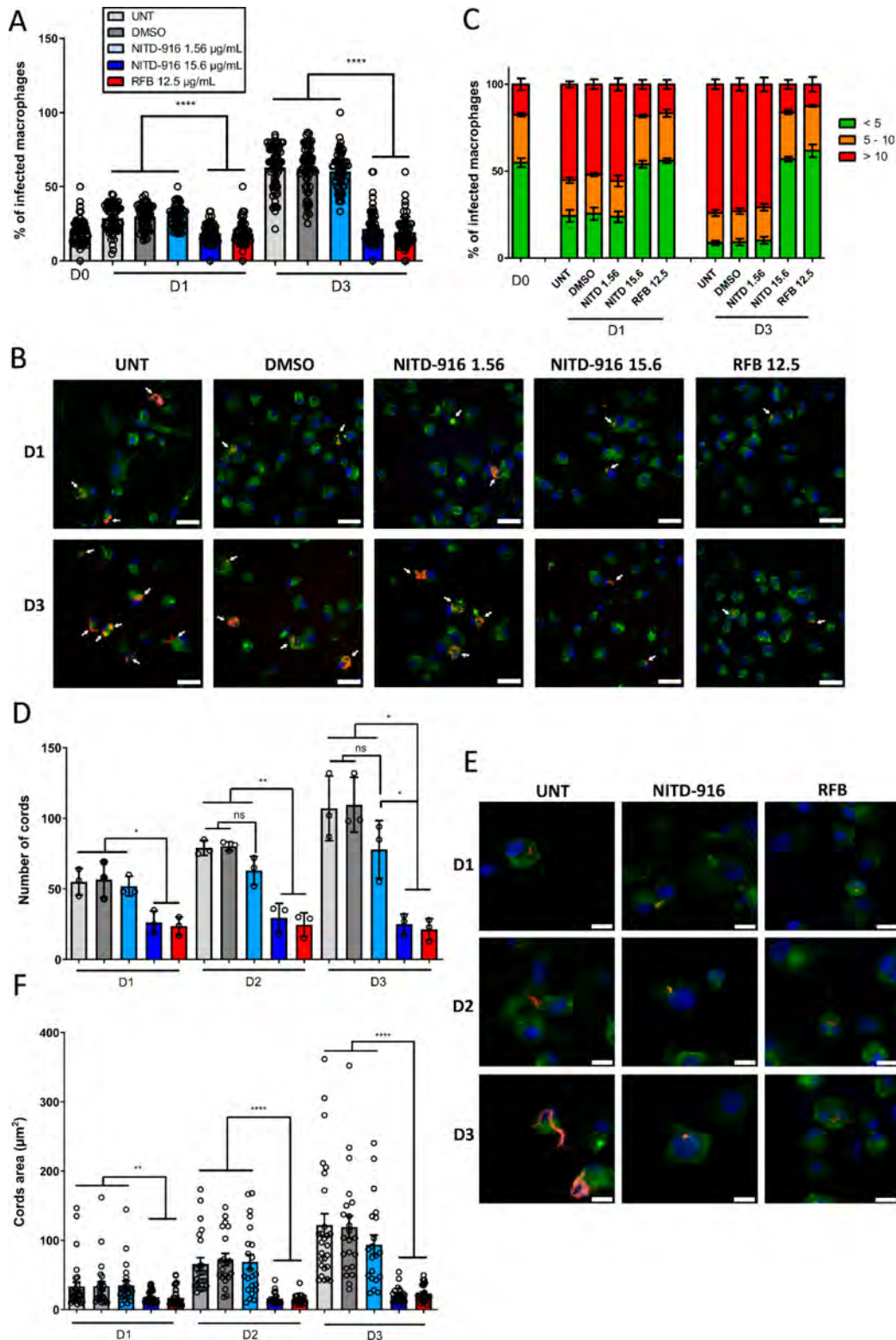


Figure 3. Effect of NITD-916 treatment on intracellular *M. abscessus* loads and cording. (A) Percentage of infected THP-1 macrophages at 0, 1, and 3 days postinfection with *M. abscessus* CIP104536^T (R) (MOI of 2:1) in the absence (UNT) of antibiotics or presence of NITD-916 (1.56 µg/mL and 15.6 µg/mL) or RFB (12.5 µg/mL). DMSO-exposed cells were included as controls. Results are expressed as mean values ± SD for three independent experiments with 30 fields per condition. Data were analyzed using the *t* test. *****P* ≤ 0.0001. (B) Representative immunofluorescent fields were taken at 1 and 3 days postinfection showing macrophages infected with *M. abscessus* CIP104536^T (R) expressing TdTomato (red) in the absence of antibiotics (UNT) or in the presence of NITD-916 (1.56 µg/mL and 15.6 µg/mL) or RFB (12.5 µg/mL). DMSO-exposed cells were included as controls. The surface and the endolysosomal system of the macrophages were detected using anti-CD63 antibodies (green). The nuclei were stained with DAPI (blue). White arrows indicate individual or mycobacterial aggregates. Scale bar, 50 µm. (C) Percentage of macrophages categories infected with different number of bacilli (<5 bacilli/cell, 5–10 bacilli/cell, >10 bacilli/cell). The categories were counted at 0, 1, and 3 days postinfection in the absence of antibiotics or in the presence of NITD-916 (1.56 µg/mL and 15.6 µg/mL) or RFB (12.5 µg/mL). Untreated

Figure 3. continued

(UNT) or DMSO-exposed cells were included as controls. Data are mean values \pm SD for three independent experiments performed in triplicates. (D) Total number of intracellular cords displayed in 30 fields at 1, 2, and 3 days postinfection. Results are expressed as mean values \pm SD for three independent experiments. Data were analyzed using the two-tailed nonpaired *t* test. $*P \leq 0.05$; $**P \leq 0.01$. (E) Representative images of intracellular cords at macrophage 1, 2, and 3 days postinfection. Cords are in red, the macrophage surface is green, and the nucleus in blue as in (B). Scale bar, 20 μ m. (F) Size of the intracellular cords (expressed by the area in μ m²) displayed in 10 fields. Results are expressed as mean values \pm SD for three independent experiments, and each symbol represents the size of a cord ($n = 30$). Data were analyzed using the Mann–Whitney *t* test. $**P \leq 0.01$; $****P \leq 0.0001$.

M. abscessus.⁴³ In addition, while overexpression of KatG from *M. tuberculosis* restored susceptibility to INH in *M. abscessus* carrying pSMT3-*katG*_{MTB}-*tdTomato* as previously reported,²⁹ the MIC of NITD-916 remained unchanged in this strain as compared to its parental progenitor (Table S2). This implies that, in contrast to INH, the activity of NITD-916 is KatG-independent in *M. abscessus*.

The potency of NITD-916 was next assayed using a representative panel of clinical isolates from CF patients or non-CF patients, comprising 8 *M. abscessus*, 11 *M. abscessus*, and 9 *M. abscessus* strains. All these strains were susceptible to NITD-916, similarly to the CIP104536^T reference strains (Figure 1B) and, in general, the MIC of R and S strains were similar, although slight variations were observed between the *M. massiliense* strains. The MIC values of NITD-916 were found to be much lower than those of rifabutin (RFB), included as a control drug.⁴¹ Overall, these results demonstrate that NITD-916 exerts potent activity on the *M. abscessus* complex and is equally active against strains isolated from CF and non-CF patients.

NITD-916 Inhibits Intramacrophage Growth of *M. abscessus*. To assess whether NITD-916 is active against *M. abscessus* in a macrophage infection model, we next compared the intracellular efficacy of the compound in human THP-1 macrophages infected with either CIP104536^T S or R variants after 1 and 3 days of exposure to the compound (Figure 2A and 2B). First, the cytotoxicity of NITD-916 against THP-1 cells was investigated after 1 and 3 days of exposure to the compound. Figure S1 clearly shows that NITD-916 exerts cytotoxicity only at very high concentrations (>100 μ g/mL) at both time points. NITD-916-induced cytotoxicity was intermediate between INH (no cytotoxicity at 100 μ g/mL) and RFB (100% macrophage killing at 100 μ g/mL) after 3 days of exposure to each drug. These results indicate that NITD-916 exhibits very little toxicity at concentrations below 100 μ g/mL and, based on these results, all subsequent macrophage studies were conducted with 1.56, 15.6, and 31.2 μ g/mL NITD-916, corresponding to 1 \times , 10 \times , and 20 \times MIC. RFB was included as a positive control at 12.5 μ g/mL, a concentration at which it significantly reduces the intracellular burden.⁴¹ DMSO-treated macrophages were added as a negative control for intracellular bacterial replication. At 0, 1, and 3 days postinfection (dpi), macrophages were lysed and plated to determine the intracellular bacterial burden after drug treatment. Similarly to the DMSO condition, exposure of macrophages to NITD-916 at 1 \times MIC failed to inhibit intramacrophage growth of *M. abscessus* CIP104536^T S (Figure 2A) and CIP104536^T R (Figure 2B) at 1 and 3 dpi. In contrast, exposure to 10 \times MIC strongly decreased the intracellular bacterial loads at 1 dpi and this effect was further amplified at 3 dpi in both strains. Interestingly, there was no difference between 10 \times and 20 \times MIC of NITD-916, and the CFU counts were comparable to

those in the inoculum (Day 0), similarly to what was observed in liquid cultures (Figure 1A). In addition, the NITD-916 susceptibility profile for the S variant at 1 and 3 dpi was comparable to that of the R variant, with a \sim 2 log reduction in the CFU counts at day 3, reaching the same level of inhibition as RFB (Figure 2A and 2B).

We further explored the activity of NITD-916 against S and R clinical isolates of the *M. abscessus* complex within THP-1 macrophages. Supporting our previous observations with the CIP104536^T reference strains, we found that NITD-916 was very active against all *M. abscessus* subspecies tested within macrophages at 1 and 3 dpi when compared to day 0 and DMSO treatment, irrespective of S and R morphotype: *M. abscessus* 2069 (S) (Figure 2C), *M. abscessus* 2524 (R) (Figure 2D), *M. massiliense* 179 (R) (Figure 2E), *M. massiliense* 120 (S) (Figure 2F), *M. bolletii* 112 (R) (Figure 2G), and *M. bolletii* 108 (R) (Figure 2H). In all cases, the optimal activity was reached in the presence of 10 \times MIC of NITD-916. Overall, these results indicate that NITD-916 is a potent intracellular growth inhibitor of *M. abscessus*.

Intracellular *M. abscessus* Loads and Cording Are Reduced by NITD-916. THP-1 macrophages were infected with red fluorescent *M. abscessus* strains expressing TdTomato and exposed to either DMSO, NITD-916, or RFB, stained with anti-CD63 and DAPI, and observed under the microscope. A quantitative analysis highlighted a marked reduction in the percentage of *M. abscessus* R-infected cells treated with NITD-916 at 10 \times MIC (while no effect was observed at 1 \times MIC), which was comparable to the effect observed with 12.5 μ g/mL RFB at 1 dpi (Figure 3A). This trend was even more pronounced at 3 dpi. Since the proportion of NITD-916-treated infected cells remained similar to the one at day 0, this suggests that the compound is very likely to be bacteriostatic inside the macrophage. Similar results were found when macrophages were infected with *M. abscessus* S (Figure S2A). Representative immunofluorescent fields illustrate the reduced number of macrophages infected with the R (Figure 3B) or S (Figure S2B) variants treated with NITD-916 at 1 and 3 dpi, as compared to the untreated or DMSO-treated control cells.

Macrophages infected with the R variant were then classified into three classes as judged by their bacterial load content: poorly infected (<5 bacilli/cell), moderately infected (5–10 bacilli/cell), and heavily infected (>10 bacilli/cell). Bacteria-containing macrophages were then individually observed under the microscope and scored for their belonging to one of the three categories. The quantitative analysis indicates that treatment with NITD-916 at 10 \times MIC or RFB significantly reduces the percentage of heavily infected THP-1 cells and increases the proportion of the poorly infected category, as compared to the untreated or DMSO-treated cells at 1 and 3 dpi (Figure 3C), with \approx 20% of the infected bacilli belonging to the heavily infected category and \approx 50% associated with the poorly infected category at 3 dpi. Analysis performed on

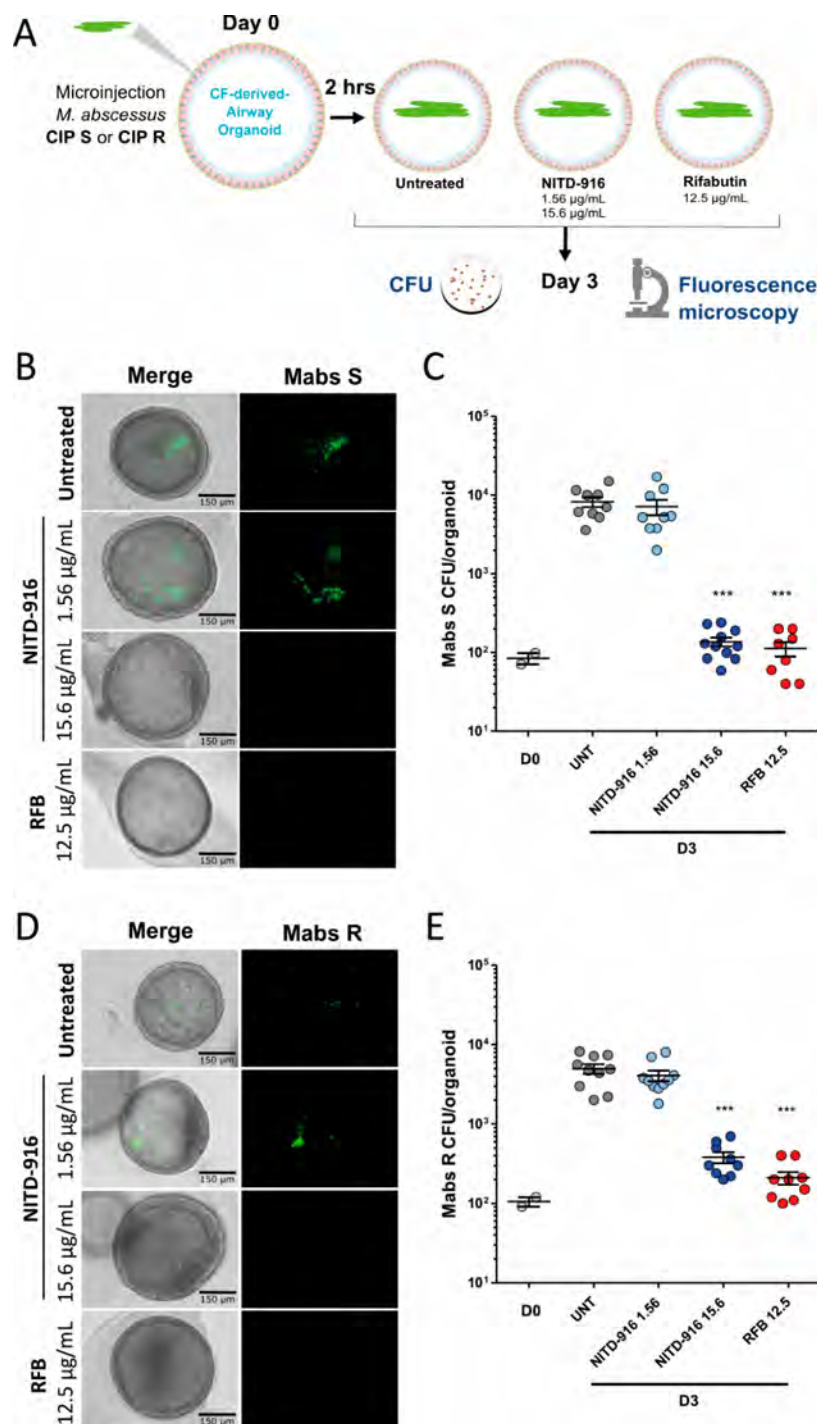


Figure 4. Activity of NITD-916 in *M. abscessus*-infected CF-derived airway organoids. (A) A generalized schematic showing the experimental design. Representative images (B, D) and corresponding bacterial loads determined by CFU counting (C, E) of CF-derived airway organoids at 3 days postinfection with *M. abscessus* S (B, C) or R (D, E) expressing Wasabi in the presence or absence of treatment: untreated groups ($S n = 9$; $R n = 10$), treated with NITD-916 at $1.56 \mu\text{g/mL}$ ($S n = 9$; $R n = 10$), NITD-916 at $15.6 \mu\text{g/mL}$ ($S n = 11$; $R n = 9$), or RFB at $12.5 \mu\text{g/mL}$ ($S n = 8$; $R n = 9$). Graphs show means \pm SD of two independent experiments. Each dot represents one organoid. Data were analyzed using the Mann–Whitney t test. *** $P \leq 0.001$.

macrophages infected with the S variant generated a similar category pattern (Figure S2C). Collectively, these data indicate that NITD-916 enters THP-1 macrophages and impedes bacterial replication of both *M. abscessus* S and R variants.

In contrast to the S variant, strains exhibiting a R morphotype are typified by increased bacterial clumping and R bacilli remain aggregated to generate compact colonies

comprising corded structures on agar, in broth medium, and inside macrophages.^{8,12,14,41} Figure 3D clearly illustrates that, upon infection with TdTomato-expressing *M. abscessus* R, the total number of intracellular cords displayed in 30 fields was significantly reduced in the presence of NITD-916 at 10 \times MIC or $12.5 \mu\text{g/mL}$ RFB when compared to untreated or DMSO-treated cells, and this effect was maintained at 1, 2, and 3 dpi.

Table 1. Characteristics of NITD-916 Spontaneous Resistant Mutants of *M. abscessus*^a

strain	MIC ($\mu\text{g/mL}$)			mutation in <i>inhA</i> _{MAB}		
	NITD-916	RFB	ETH	AA change	frequency of mutation	
CIP104536 ^T (S)	1.56	100	25			
NITD916 ^{R1}	>100	50	12.5	G287T	G96V	2.3×10^{-7}
NITD916 ^{R2}	>100	100	25	G286A	G96S	2.3×10^{-7}
NITD916 ^{R3}	>100	50	50	G286A	G96S	2.3×10^{-7}
NITDR916 ^{R4}	>100	50	25	G287T	G96V	2.3×10^{-7}
CIP104536 ^T (R)	1.56	12.5	25			
NITD916 ^{R5}	>100	12.5	12.5	G287T	G96V	2.4×10^{-6}
NITD916 ^{R6}	>100	12.5	25	G287T	G96V	2.4×10^{-6}
NITD916 ^{R7}	>100	25	25	G287T	G96V	2.4×10^{-6}
NITD916 ^{R8}	>100	12.5	25	G287T	G96V	2.4×10^{-6}

^aMIC ($\mu\text{g/mL}$) were determined in CaMHB. Resistant strains were derived from either the smooth (S) or rough (R) *M. abscessus* CIP104536^T parental strains on LB agar supplemented with 15.6 $\mu\text{g/mL}$ NITD-916 (10 \times MIC). Single-nucleotide polymorphism (SNP) in *inhA*_{MAB} (*MAB_2722c*) and corresponding amino acid (AA) changes as well as frequency of mutation are indicated.

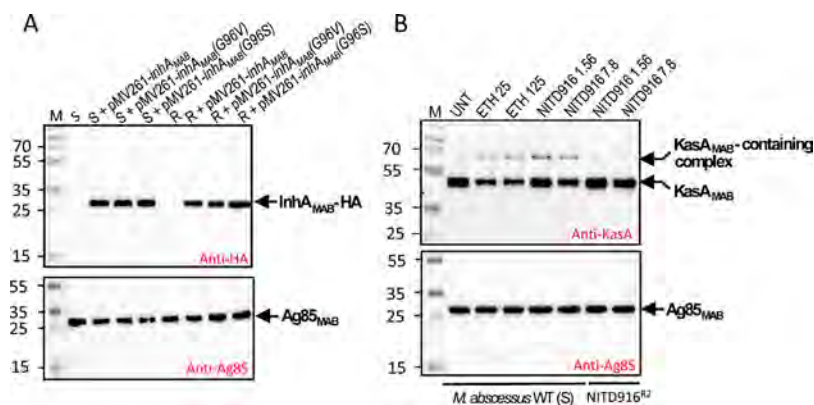


Figure 5. Overexpression of *InhA*_{MAB} variants in *M. abscessus* S and R strains. (A) Western blots using antibodies against the HA-epitope (upper panel) and the Ag85 complex (lower panel) as loading control were done to assess the expression levels of the *InhA*_{MAB} variants in various strains overproducing either *InhA*_{MAB}(WT), *InhA*_{MAB}(G96V), or *InhA*_{MAB}(G96S). Equal amounts of total lysates (10 μg) of each strain were separated on a 12% SDS-PAGE. (B) Wild-type *M. abscessus* CIP104536^T (S) and NITD916^{R2} strains were grown in CaMHB and exposed for 9 h with increasing concentrations of ethionamide (ETH) or NITD-916 at concentrations corresponding to 1 \times and 5 \times MIC. Equal amounts of total lysates (10 μg) of each strain were separated on a 12% SDS-PAGE and probed with anti-KasA (upper panel) anti-Ag85 complex (lower panel) antibodies (used as loading control).

The effect was not significant at 1 \times MIC. Representative images of intracellular cords show the kinetics of cord formation at 1, 2, and 3 dpi (Figure 3E). While very small in size at 1 dpi, cords continue to elongate at 2 dpi and 3 dpi, often leading to a structure capable of extruding out of the cells at 3 dpi, presumably participating in macrophage killing. In the presence of drugs (NITD-916 or RFB), there was a clear reduction in size of the cords as compared to the untreated cells. This effect is supported by a quantitative analysis of the cord surface area (expressed in μm^2). While control cords continue to increase in size over time (reaching a surface area >100 μm^2), their size remained constant ($\approx 20 \mu\text{m}^2$) upon exposure to NITD-916 or RFB (Figure 3F). Together, these results indicate that NITD-916 is highly effective in reducing the number and size of *M. abscessus* cords, which is thought to affect the outcome of the infection.

NITD-916 Reduces *M. abscessus* Loads in Human Airway Organoids. Lung airway organoids (AO) from healthy individuals have recently been developed to study the early steps of interaction between *M. abscessus* and the airway.⁴⁴ In this biological model where mycobacteria are injected in AO, *M. abscessus* was found to actively replicate over 7 days in the lumen, and this was accompanied by

reduced expression of mucin genes, usually participating in the clearance of pulmonary pathogens.⁴⁴ Moreover, AO derived from CF patients were characterized by low CFTR activity and enhanced mucus accumulation, and the subsequent injection of *M. abscessus* in these 3D structures revealed the production of biofilms formed by the S variant and serpentine cords formed by the R variant.⁴⁵ Importantly, both variants replicated more efficiently in CF AO than in AO derived from healthy lungs, thus highlighting the relevance of this model to study the pathogenesis of *M. abscessus* and to test the therapeutic potential of compounds in a system that recapitulates a CF environment.⁴⁵ As illustrated in Figure 4A, CF-derived AO were injected with the *M. abscessus* S and R variants expressing Wasabi, and drug treatment was commenced 2 h later with NITD-916 at 1.56 $\mu\text{g/mL}$ or 15.6 $\mu\text{g/mL}$ and with RFB at 12.5 $\mu\text{g/mL}$, included as a control drug. After 3 days of treatment, fluorescence microscopy showed high bacterial loads in AO left untreated or exposed to 1.56 $\mu\text{g/mL}$ NITD-916, while exposing the AO to the 15.6 $\mu\text{g/mL}$ dose significantly reduced the green fluorescence signal, similarly to the RFB treatment (Figure 4B). AO were then lysed at 3 dpi, and plating the lysates on agar indicated a 2 log increase in the CFU of *M. abscessus* S in the untreated control

or in the presence of 1.56 $\mu\text{g}/\text{mL}$ NITD-916 (Figure 4C). In contrast, treatment with either 15.6 $\mu\text{g}/\text{mL}$ NITD-916 or 12.5 $\mu\text{g}/\text{mL}$ RFB was associated with a striking decrease in the CFU counts, at levels similar to those found in the inoculum (Day 0) (Figure 4C). Very similar results were observed for *M. abscessus* R-containing AO (Figure 4D and 4E). Overall, these results clearly indicate that NITD-916 is active in CF patient-derived AO characterized with severe CF airway dysfunction and susceptibility to *M. abscessus* infection.

Mutations in *inhA_{MAB}* Confer High Resistance Levels to NITD-916. Mutations in *inhA* coding for the enoyl-ACP reductase of the type II fatty acid synthase have been reported previously in *M. tuberculosis* mutants resistant to NITD-916.⁴⁰ To get insights into the mode of action of NITD-916 in *M. abscessus*, a genetic approach was conducted involving the selection of spontaneous NITD-916-resistant mutants derived from either the smooth (S) or rough (R) *M. abscessus* parental strains on agar supplemented with 15.6 $\mu\text{g}/\text{mL}$ NITD-916 (10 \times MIC) at frequencies estimated to 2.3×10^{-7} (S resistant strains) and 2.4×10^{-6} (R resistant strains). MIC determination of four individual colonies for each morphotype confirmed their high resistance levels (MIC > 100 $\mu\text{g}/\text{mL}$) against NITD-916 while remaining susceptible to RFB and ETH (Table 1). Sequencing the *inhA_{MAB}* (*MAB_2722c*) locus identified single nucleotide polymorphisms (SNPs) across the different resistors, leading to amino acid replacements at position 96. In the S resistors, NITD916^{R1} and NITD916^{R4}, Gly96 was replaced by a Val residue, while in NITD916^{R2} and NITD916^{R3}, Gly96 was replaced by a Ser residue. All four mutants derived from the R variant (NITD916^{R5} to NITD916^{R8}) harbored a G96V amino acid exchange (Table 1). As shown for NITD916^{R2}, resistance to NITD-916 was independent of the medium (Table S1).

To validate *inhA_{MAB}* as a specific target of NITD-916, wild-type and mutated *inhA_{MAB}* alleles were cloned in frame with a HA-tag under the control of the constitutive *hsp60* promoter to allow overexpression of the wild-type and mutated versions of the protein. The resulting constructs, pMV261-*inhA_{MAB}*, pMV261-*inhA_{MAB}*(G96V), and pMV261-*inhA_{MAB}*(G96S), were introduced in both S and R variants and expression of the different *InhA_{MAB}* variants was confirmed by Western blotting using anti-HA antibodies, while levels of the Ag85 complex remain constant (Figure 5A). Whereas overproduction of the wild-type proteins did not significantly alter the MIC values as compared to the parental progenitors (2-fold effect), overproduction of *InhA_{MAB}*(G96V) or *InhA_{MAB}*(G96S) resulted in 8- to 32-fold upshift in the MIC level (Table 2). These effects were specific to NITD-916 as the MIC of RFB against the

same recombinant strains were comparable to those of the parental progenitors (Table 2). This indicates that transferring the single point mutations identified in the NITD-916 spontaneous resistant mutants into a susceptible strain is sufficient to confer high resistance levels to NITD-916.

It was previously reported that isoniazid, diazaborine, or ethionamide (ETH) induced the production of a KasA-containing complex in *M. smegmatis* and that formation of this complex is a consequence of *InhA* inhibition while other FAS-II inhibitors such as thiolactomycin or isoxyl, inhibiting KasA and the HadABC dehydratase, respectively, fail to induce this complex.⁴⁶ Thus, we inquired whether NITD-916 induces this complex in *M. abscessus* by probing crude lysates from cultures exposed to 1 \times and 5 \times MIC NITD-916 with anti-KasA antibodies. Figure 5B reveals, in addition to free KasA_{MAB}, the presence of an additional immunoreactive band at both concentrations. This protein comigrated with a protein also present in the ETH-treated lysates (used as a positive control of *InhA_{MAB}* inhibition) while absent in the untreated sample. Importantly, this KasA-containing complex was not induced in strain NITD916^{R2} resistant to NITD-916, presumably because the G96S mutation in *InhA_{MAB}* renders the enzyme insensitive to NITD-916. Overall, these results suggest that *InhA_{MAB}* is the primary target of NITD-916 in *M. abscessus* and that its inhibition leads to the induction of a KasA-containing complex.

NITD-916 Inhibits De Novo Mycolic Acid Biosynthesis in *M. abscessus*. In contrast to *M. tuberculosis*, *M. abscessus* does not synthesize oxygenated mycolic acids but produces exclusively α and α' mycolates, corresponding to long-chain (C₇₇₋₇₉) and short chain (C₆₂₋₆₄) mycolic acid subspecies, respectively.⁴⁷ To interrogate whether NITD-916 inhibits de novo synthesis of mycolic acids, [¹⁴C]-labeled lipids were extracted from wild-type *M. abscessus* cultures treated with increasing concentrations of NITD-916 prior to labeling with 1 $\mu\text{Ci}/\text{mL}$ [2-¹⁴C]acetate. Mycolic acid methyl esters (MAMEs) and fatty acid methyl esters (FAMEs) were then separated by thin-layer chromatography (TLC). Synthesis of both α and α' mycolates was dramatically affected in a dose-dependent manner (Figure 6A). De novo synthesis was almost completely abrogated in the presence of 1.56 $\mu\text{g}/\text{mL}$ (1 \times MIC). ETH, a drug known to target *InhA* and whose biotransformation is dependent on *EthA* instead of *KatG*,⁴⁸ was included as a positive control. However, due to the elevated MIC of ETH against *M. abscessus* (25 $\mu\text{g}/\text{mL}$), only partial inhibition was achieved at the concentrations tested. Importantly, no inhibition was noticed in the production of fatty acid methyl esters (FAMEs) during treatment with NITD-916, which indicates that, like ETH or INH, NITD-916 specifically inhibits FAS-II rather than FAS-I, as expected for *InhA*-dependent inhibition.

We next addressed whether resistance to NITD-916 can be linked to an unaltered mycolic acid profile in strains carrying mutations in *InhA_{MAB}*. Supporting this hypothesis, mycolic acid biosynthesis in strain NITD916^{R2} (carrying G96S point mutation) was much more refractory to inhibition by NITD-916 as compared to the wild-type progenitor (Figure 6B). Collectively, these biochemical data underline a mode of action that results in the abolishment of mycolic acid biosynthesis by targeting *InhA_{MAB}*.

Structural Basis for *InhA_{MAB}* Inhibition by NITD-916. To demonstrate direct target engagement, we obtained a 1.45 Å resolution crystal structure of *InhA_{MAB}* bound to NITD-916 and NAD (Figure 7A and Table S3). As described above,

Table 2. MIC ($\mu\text{g}/\text{mL}$) of NITD-916 and RFB Determined in CaMHB at 30 °C against *M. abscessus* Overexpressing Wild-Type and Mutated *inhA_{MAB}* (*MAB_2722c*) Alleles

strain	NITD-916	RFB
CIP104536 ^T (S)	1.56	50
S + pMV261- <i>inhA_{MAB}</i>	3.12	50
S + pMV261- <i>inhA_{MAB}</i> (G96V)	25	50
S + pMV261- <i>inhA_{MAB}</i> (G96S)	50	50
CIP104536 ^T (R)	1.56	12.5
R + pMV261- <i>inhA_{MAB}</i>	3.12	12.5
R + pMV261- <i>inhA_{MAB}</i> (G96V)	12.5	12.5
R + pMV261- <i>inhA_{MAB}</i> (G96S)	50	12.5

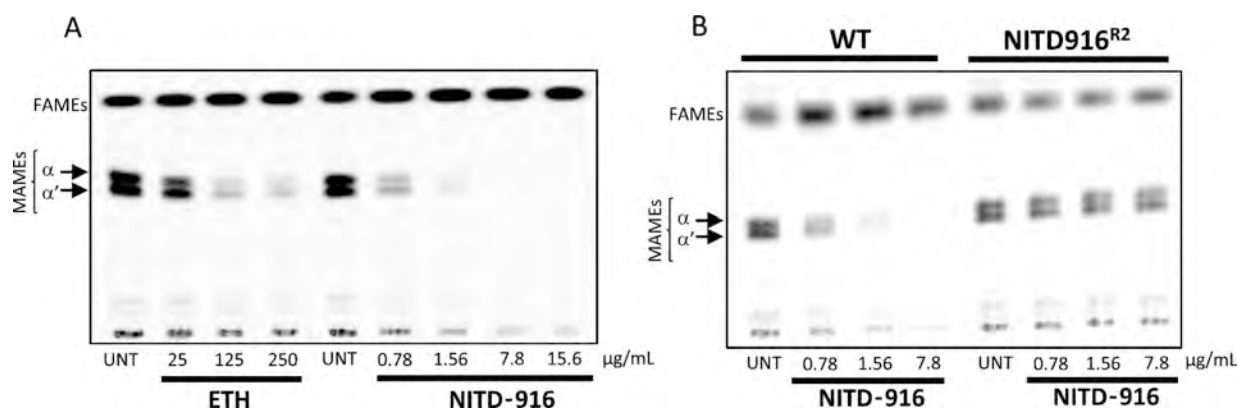


Figure 6. Inhibition of mycolic acid biosynthesis by NITD-916 in *M. abscessus*. (A) Dose–response effects of ETH and NITD-916 in *M. abscessus* CIP104536^T (S). The inhibitory effect on the incorporation of [2-¹⁴C]acetate was assayed by exposing cultures to increasing concentrations of ETH or NITD-916 for 1 h prior to labeling for another 2 h at 37 °C under shaking. The corresponding radiolabeled FAMES and MAMES were extracted. Equal counts (50 000 cpm) were loaded onto a TLC plate and lipids were developed in petroleum ether/acetone (95/5, v/v). (B) Mutant NITD916^{R2} is refractory to mycolic acid inhibition by NITD-916. *M. abscessus* CIP104536^T (S) and its derivative NITD916^{R2} were exposed to concentrations corresponding to 0.5×, 1×, and 5× MIC of NITD-916, labeled and subjected to lipid extraction and analysis as in (A).

resistance mutants arose at residue Gly96. In our structure, the C_α of Gly96 residues is in proximity to the 2'-hydroxyl of the NMN portion of NAD as well as the phenyl moiety of NITD-916 (Figure 7A). Mutation of this residue would cause a steric clash with the phenyl ring of NITD-916, potentially explaining the G96S and G96V resistance mutations. Modifying the phenyl ring of NITD-916 could potentially result in molecules which overcome resistance at G96. However, given the proximity to the 2'-hydroxyl of the NMN portion of NAD, mutation of G96 could also cause loss of InhA specific activity and these resistance mutations may not arise in a clinical setting. Residues interacting with NITD-916 are indicated in Figure 7A.

Overall, our structure is similar to a previously obtained 3.2 Å resolution structure of InhA_{MTB} bound to NITD-916 and NAD⁴⁰ (Figure 7B). The 4-hydroxy-2-pyridin-2-one moiety stacks on top of the nicotinamide ring, presumably where the unsaturated portion of the substrate binds, whereas the 4,4-dimethylcyclohexyl moiety projects into the hydrophobic cavity presumably where the lipid portion of the substrate binds. Thus, NITD-916 appears to be a direct substrate competitor. In addition, there appears to be some induced fit upon NITD-916 binding when compared to our structures of the InhA_{MAB} apoenzyme (1.75 Å resolution) or the holoenzyme (1.85 Å resolution) (Figure 7C). Our structures of InhA_{MAB} in the apoenzyme, holoenzyme, and NITD-916 inhibited state show that the residues spanning Thr196 through Gly212 move considerably in response to the ligand-bound state. In the InhA_{MAB} apoenzyme state these residues form a β-hairpin turn and generate an open catalytic cavity. In the holoenzyme state, these residues change to an α-helix which packs tightly against the cofactor and generate a narrow substrate binding cleft. In the inhibited form, this new α-helix moves away from the cofactor to accommodate the binding of NITD-916. These residues and to a lesser extent α6 (numbering using the apoenzyme state) are the only major conformational changes that occur between the different states. Similar conformational changes have been observed previously for InhA_{MTB} substrates (e.g., PDB ID 1BVR⁴⁹) and other inhibitor-bound structures (e.g., PDB ID 1P44⁵⁰).

To complement the crystallography work and gain some understanding of the effects of the inhibitor NITD-916 on the

thermal stability of InhA_{MAB}, we performed differential scanning fluorimetry (DSF). Apoenzyme InhA_{MAB} had a melting temperature of 39.3 °C (Table S4 and Figure S3). Incubation with the cofactor NAD to generate the holoenzyme resulted in a modest increase in melting temperature to 39.8 °C (ΔT_m = 0.5 °C). Generation of the inhibited complex of InhA_{MAB} with NAD and NITD-916 resulted in a large increase in the melting temperature to 54.0 °C (ΔT_m = 14.7 °C relative to apo or 14.2 °C relative to NAD alone). Although such stability measurements are not directly correlated with affinity, significant stabilization can be indicative of potency in biochemical experiments.

DISCUSSION

The success rate of *M. abscessus* pulmonary disease treatment remains very poor despite prolonged, multidrug antibiotherapy with an important risk of severe secondary effects, emphasizing the rapid need for more effective treatments.²⁶ While mycolic acids represent essential cell wall components in mycobacteria and are the primary target of INH and ETH in *M. tuberculosis*, none of the current drugs used in clinical settings against *M. abscessus* infections are hitting mycolic acid biosynthesis. However, recent studies have emphasized that this metabolic pathway represents an attractive niche for druggable targets in *M. abscessus*. First, thiacetazone has proven to bind to the HadA component of the FAS-II HadABC dehydratase complex, leading to mycolic acid inhibition in *M. tuberculosis*,⁵¹ and thiacetazone derivatives exhibited potent activity against the *M. abscessus* complex.⁵² Second, a large number of hits against *M. abscessus* have recently been shown to inhibit the transport of mycolic acids across the membrane by targeting the MmpL3 transporter.^{27,53,54} In this context, the present study was undertaken to evaluate the potential of inhibiting the FAS-II enoyl-ACP reductase in *M. abscessus*. In agreement with a previous study,²⁹ our results indicate that the lack of activity of INH in *M. abscessus* presumably relies on the incapacity of KatG_{MAB} to convert INH into an active metabolite, while partial susceptibility levels to INH were recovered when overexpressing the *katG* gene from *M. tuberculosis*. This indicates that while KatG-dependent inhibition of InhA is compromised in *M. abscessus*, it opens, however, the possibility of inhibiting mycolic acid biosynthesis via KatG-independent

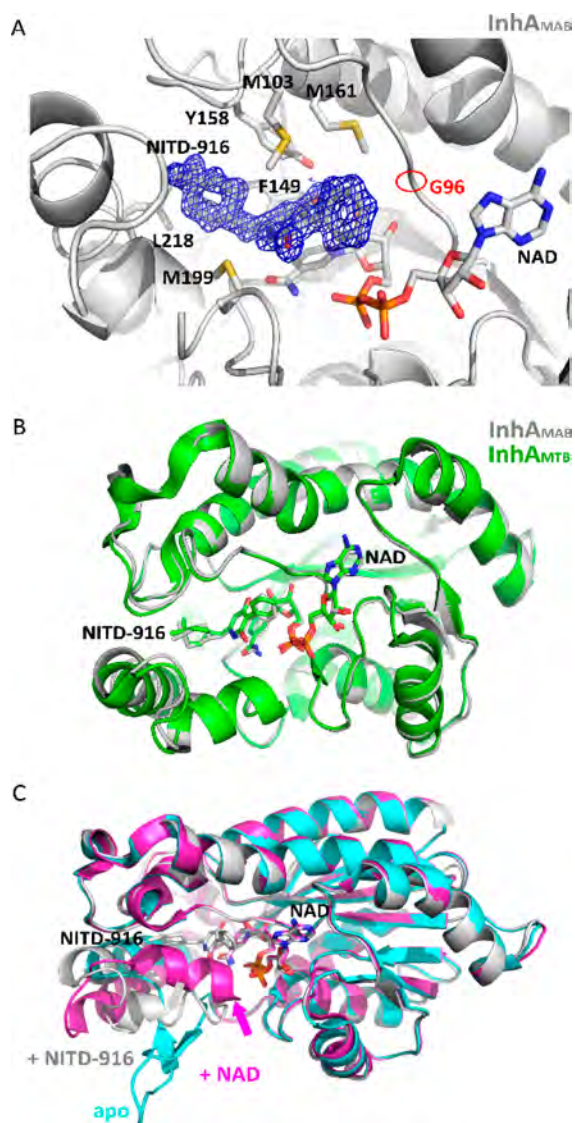


Figure 7. Structural basis of inhibition of *M. abscessus* InhA by NITD-916. (A) Crystal structure of *M. abscessus* InhA bound to NITD-916 and NAD solved at 1.45 Å resolution. For simplicity only one protomer of the tetrameric structure is shown. The protein is depicted as gray ribbons and the inhibitor NITD-916 and cofactor NAD are shown rendered in sticks. The final $2|F_o| - |F_c|$ map for NITD-916 is shown in blue mesh contoured at 1.0 sigma. The site of resistance mutations G96 is circled in red and other residues which interact with NITD-916 are labeled and shown with their side chains rendered in sticks. (B) Overlay of the crystal structures of InhA_{MAB} bound to NITD-916 and NAD depicted as above, and InhA_{MTB} bound to NITD-916 and NAD shown in green ribbons for the protein and green carbon sticks for the inhibitor and cofactor. (C) Overlay of the crystal structure of InhA_{MAB} in the apo state shown in cyan ribbons, the holoenzyme state bound to NAD in magenta with NAD in magenta sticks, and the inhibited state bound to NAD and NITD-916 in gray as in the upper panels. The loop spanning residues Thr196 through Gly212 moves significantly upon cofactor and inhibitor binding.

inhibitors of InhA. This proof-of-concept was verified here through the use and characterization of the mode of action of the 4-hydroxy-2-pyridone lead candidate NITD-916, originally identified in a phenotypic screen against *M. tuberculosis*.⁴⁰

NITD-916 displayed low MIC values against a wide panel of clinical isolates and exerted an in vitro static activity against

M. abscessus at 1× MIC. This higher MIC value of NITD-916 against *M. abscessus* as compared to *M. tuberculosis*⁴⁰ is currently not known but may rely on differences in the composition and/or architecture of the cell wall between the two species, potentially affecting cell wall permeability to this inhibitor. In addition, *M. abscessus* possesses a large number of efflux pumps, which may also contribute to the lower susceptibility of this species to NITD-916. However, at 1× MIC concentration, the compound did not show any activity in *M. abscessus*-infected macrophages. In contrast, at 10× MIC there was a significant reduction in the intracellular bacterial loads at 1 dpi, which remained comparable at 3 dpi, with similar results obtained against various clinical isolates, with no distinctions between S and R morphotypes. In general, at 3 dpi, the CFU levels remained equivalent to those in the inoculum (Day 0), indicating that NITD-916 behaves as a bacteriostatic drug in the macrophage under the conditions tested. NITD-916 not only reduced the intracellular bacterial burden but also the proportion of infected macrophages, similarly to RFB, a drug recently proposed to be included in drug regimens to reduce treatment duration of *M. abscessus* pulmonary diseases.⁵⁵ Furthermore, exposure of macrophages infected with the R variant to NITD-916 was associated with a reduction in the number and size of cords, presumably resulting from bacterial growth inhibition. Therefore, compounds, such as NITD-916 or RFB, inhibiting intracellular cord formation participate also in the prevention of macrophage death caused by the disruptive activity of cords on macrophage integrity. Consistently, we found that NITD-916 was as active as RFB in CF patient-derived AO recapitulating the CF airway dysfunctions, such as thick mucus, and with increased susceptibility to *M. abscessus* infection.⁴⁵ Thus, our data emphasize an unexploited chemical structure class active against *M. abscessus* infections with promising translational development possibilities for the treatment of CF patients.

From a mechanistic perspective, our genetic and biochemical studies unambiguously indicate that NITD-916 does not undergo bioactivation by KatG prior to binding to InhA_{MAB}, but rather inhibits biosynthesis of mycolic acids by directly binding to InhA_{MAB}. These assumptions can be inferred from the following results: (i) A panel of spontaneous mutants resistant to NITD-916 harbored point mutations in InhA_{MAB} at residue 96, and the mycolic acid pattern of these mutants remained unchanged upon exposure to NITD-916. Replacement of Gly96 by a more bulky residue is associated with NITD-916 resistance, suggesting that conservation of Gly96 is requested for susceptibility to this compound. Multiple sequence alignments of InhA proteins from different mycobacterial species indicate that Gly96 is very well conserved (Figure S4), thus suggesting that other NTM may be susceptible to NITD-916 inhibition, although this remains to be investigated in future studies. Interestingly, while replacements occurred only at Gly96 in all *M. abscessus* resistant mutants selected, many more mutations were identified in residues within or near the active site of InhA in *M. tuberculosis* resistant mutants.^{40,56} In addition, strains harboring the InhA_{MAB} G96S or G96V point mutations remained fully sensitive to ETH, as shown previously in *M. tuberculosis*.⁴⁰ (ii) Overexpression of the mutated *inhA* alleles in a susceptible strain conferred resistance to the inhibitor. (iii) NITD-916 treatment induced the formation of a KasA-containing complex, reported previously as a marker of InhA inhibition.⁴⁶ (iv) NITD-916 could be identified in a

ternary NITD-916:NAD:InhA_{MAB} costructure. Collectively, these results indicate that NITD-916 shares the same mode of action in *M. abscessus* and *M. tuberculosis* and confirms that the biosynthetic steps of mycolic acids represent an excellent pathway to be further exploited in drug discovery programs against *M. abscessus*. Previous work indicated that NITD-916 has no mutagenic or cardiotoxicity potential and showed no in vitro safety pharmacological liabilities and did not inhibit the major CYP450 isoenzyme 3A4,⁴⁰ thus stimulating new medicinal chemistry programs for the rational optimization of NITD-916-related analogues targeting InhA_{MAB} with improved efficacy. Changes in the 4-hydroxy 2-pyridone may include substitutions of the R6 lipophilic group and replacement of the R3 phenyl group with other aromatic substituents. In addition, to increase solubility and lipophilicity, phosphate ester prodrugs are typically designed, favoring oral administration and are rapidly hydrolyzed by intestinal alkaline phosphatases. This has been emphasized by synthesizing a 4-hydroxy methyl phosphate ester prodrug of NITD-916, designated NITD-113, displaying improved aqueous solubility by two log orders and with good bioconversion to NITD-916 in mice.⁴⁰ The availability of the InhA_{MAB} crystal structure in complex with NAD and NITD-916 will greatly facilitate and guide the chemistry to generate these analogues. In addition, the very high structural conservation between InhA_{MAB} and InhA_{MTB} is a key factor prompting the future testing of a large panel of validated direct InhA_{MTB} inhibitors against *M. abscessus*. Indeed, such direct InhA_{MTB} inhibitory scaffolds have been identified in high throughout screenings, encoded library technology, or fragment-based screenings and have received considerable attention during these past few years.⁵⁷ Another important feature to consider in future studies relies on the possibility to increase the activity of NITD-916 when given in combination with other drugs. Since any *M. abscessus* antibiotic has to be clinically administered in combination with other drugs,²² the absence of drug–drug interactions is critical for clinical development and needs to be checked. Using the checkerboard assay, we found that the Fractional Inhibitory Concentration Index (FICI) values between NITD-916 and most drugs used in clinics were in the 0.5–1.5 range (Table S5), suggestive of an indifferent interaction between the compounds, and thus highlighting the suitability of including NITD-916 in combination therapy.

CONCLUSIONS

This work reports the potent in vitro and intracellular anti-*M. abscessus* activity of NITD-916 and underscores the strong activity of this unexploited chemical scaffold in CF-derived AO, opening future possibilities for the treatment of CF patients. Subsequent studies should now advance this compound as well as its derivatives into preclinical animal models. Our findings also support the view that targeting mycolic acid biosynthesis has serious translational potential for development into a real tool for treatment and control of *M. abscessus* pulmonary diseases.

METHODS

Mycobacterium abscessus Strains and Culture Conditions. *M. abscessus* subspecies *abscessus* CIP104536^T, *M. abscessus* subspecies *bolletii* CIP108541^T, and *M. abscessus* subspecies *massiliense* CIP108297^T reference strains as well as

clinical strains from CF and non-CF patients were reported earlier.^{52,58} Bacteria were routinely grown and maintained at 37 °C in Middlebrook 7H9 broth (BD Difco) containing 0.025% Tyloxapol (Sigma-Aldrich) and 10% oleic acid, albumin, dextrose, catalase (OADC enrichment; BD Difco) (7H9^{T/OADC}) or on Middlebrook 7H10 agar (BD Difco) containing 10% OADC enrichment (7H10^{OADC}). *M. abscessus* carrying pTEC27 and expressing TdTomato was reported earlier and grown in the presence of 1000 µg/mL hygromycin.¹⁴ *M. abscessus* smooth and rough strains were transformed with pSMT3-*katG*_{MTB}-*tdTomato*⁵⁹ and grown in the presence of 1000 µg/mL hygromycin.

For drug susceptibility testing, bacteria were grown in Cation-Adjusted Mueller–Hinton Broth (CaMHB; Sigma-Aldrich). Rifabutin and NITD-916 were purchased from Selleckchem and Merck, respectively, and dissolved in DMSO.

Drug Susceptibility Testing. The minimal inhibitory concentrations (MIC) were determined according to the CLSI guidelines.⁶⁰ The broth microdilution method was used in CaMHB with an inoculum of 5 × 10⁶ CFU/mL in exponential growth phase. The bacterial suspension was seeded in 100 µL volumes in all of the wells of a 96-well plate, except for the first column, to which 198 µL of the bacterial suspension was added. In the first column, 2 µL of drug at its highest concentration was added to the first well containing 198 µL of bacterial suspension. Two-fold serial dilutions were then carried out, and the plates were incubated for 3–5 days at 30 °C. MICs were recorded by visual inspection. MIC were also determined using Middlebrook 7H9 supplemented with OADC, Sauton's medium, or an artificial sputum medium (ASM) containing components of the CF sputum.⁴²

Growth Kinetics. To monitor growth inhibition of *M. abscessus* CIP104536^T (S), 96-well plates were setup as for MIC determination, and serial dilutions of the bacterial suspensions exposed to increasing concentrations of NITD-916 were plated on LB agar plates after 0, 1, 2, and 3 days. Colony-forming units (CFUs) were counted after 4 days of incubation at 37 °C. Results from each drug concentration are representative of 2 independent experiments in triplicates.

Cytotoxicity Assay. Human THP-1 monocytes were grown in RPMI medium supplemented with 10% Fetal bovine serum (Sigma-Aldrich) (RPMI^{FBS}) and incubated at 37 °C in the presence of 5% CO₂. Cells were differentiated with 20 ng/mL Phorbol Myristate Acetate (PMA) in 96-well flat-bottom tissue culture microplates (2 × 10⁴ cells/well) for 48 h at 37 °C with 5% CO₂ and exposed to decreasing concentrations of NITD-916, RFB, or INH (starting at 100 µg/mL) for 24 or 72 h at 37 °C with 5% CO₂. Following incubation, 10% (v/v) resazurin dye was added to each well and left to incubate for another few hours at 37 °C and 5% CO₂. Data were acquired using a fluorescent plate reader (excitation 540 nm, emission 590 nm).

Intracellular Killing Assay. THP-1 were grown and differentiated into macrophages as reported above but wells were seeded with 10⁵ cells. Infection with *M. abscessus* strains was carried out at 37 °C in the presence of 5% CO₂ for 4 h at a MOI 2:1. After extensive washing with 1× phosphate buffered saline (PBS), macrophages were incubated with RPMI^{FBS} containing 250 µg/mL amikacin for 2 h and washed again with PBS prior to the addition of 500 µL RPMI^{FBS} containing DMSO (negative control) or 500 µL RPMI^{FBS} containing either RFB or NITD-916. Drugs were renewed on a daily basis. Cells were washed with PBS and lysed with 100 µL of 1%

Triton X-100 after 1 day or 3 days postinfection. Serial dilutions of macrophage lysates were plated onto LB agar plates, and colonies were counted to determine intracellular CFU.

Microscopy-Based Infectivity Assays. Differentiated THP-1 macrophages were grown on coverslips in 24-well plates at a density of 10^5 cells/mL for 48 h at 37 °C with 5% CO₂ prior to infection with *M. abscessus* expressing TdTomato for 4 h at a MOI of 2:1. After washing and AMK treatment to remove the extracellular bacilli, cells were exposed to DMSO (negative control), RFB, or NITD-916 and fixed at 0, 1, and 3 days postinfection with 4% paraformaldehyde in 1× PBS for 20 min. Cells were then permeabilized using 0.2% Triton X-100 for 20 min, blocked with 2% BSA in PBS supplemented with 0.2% Triton X-100 for 20 min, incubated with anti-CD63 antibodies (Becton Dickinson; dilution 1:1000) for 1 h and with an Alexa Fluor 488-conjugated antimouse secondary antibody (Molecular Probes, Invitrogen; dilution 1:1000) for 45 min. After 5 min of incubation with DAPI (dilution 1:1000), cells were mounted onto microscope slides using Immu-mount (Calbiochem) and examined with an epifluorescence microscope using a 40× objective. Images were acquired by focusing on combined signals (CD63 in green and *M. abscessus* in red) and captured on a Zeiss Axioimager upright microscope equipped with a 40× and 100× oil objective and processed using ImageJ software. Equal parameters for the capture and scoring of images were consistently applied to all samples. For each condition, approximately 1000 infected macrophages were analyzed. The presence of the intra- or extracellular cords within or among the macrophages infected exclusively with the *M. abscessus* (R) variant were treated in the presence of DMSO, RFB, or NITD-916, counted, and imaged using full-field upright microscopy. Areas of intracellular cords were quantified using ImageJ.

Selection of Resistant *M. abscessus* Mutants and Target Identification. Exponentially growing *M. abscessus* CIP104536^T S and R cultures were plated on LB agar containing 15.6 μg/mL NITD-916, corresponding to 10× MIC. After 1 week of incubation at 37 °C, four individual colonies deriving from the S and R strains were selected, grown in CaMHB and individually assessed for MIC determination and scored for resistance to NITD-916. Identification of SNPs in the NITD-916-resistant strains was completed by PCR amplification using the primers *MAB_2722c s1 (F)* 5'-GTG GCA GGA CTA CTT GAG GGC-3' and *MAB_2722c s2 (R)* 5'-TCA GAG CAG CTG AGT GTG AGC G-3' to produce a 810 bp amplicon for full coverage sequencing of the *inhA_{MAB}* gene.

Cloning and Overexpression of the *inhA_{MAB}* Alleles in *M. abscessus*. Wild-type *inhA_{MAB}* and the corresponding mutated genes harboring the G287T or G286A polymorphisms were amplified by PCR (Q5 polymerase) using genomic DNA prepared from the WT or spontaneous resistant mutants as well the forward 5'-GGG GCA GGA TCC GAG TGG CAG GAC TAC TTG AGG GCA A-3' and reverse 5'-GGG CTA CGA ATT CTG CTA AGC GTA ATC TGG AAC ATC GTA TGG GTA GAG CAG CTG AGT GTG AGC GC-3' primers (restriction sites are underlined and HA tag coding sequence is in bold). PCR-amplified fragments were cloned into the *Bam*HI and *Eco*RI sites of pMV261,⁶¹ and the resulting plasmids were introduced into *M. abscessus* following selection in the presence of 250 μg/mL kanamycin.

Immunoblotting. Bacteria cultures were collected by centrifugation and lysed using 1 mm diameter glass beads and a Mixer Mill MM 301 (Retsch, Germany) at a frequency of 30 Hz for 10 min. Equal amount of total proteins (10 μg) were separated by 12% SDS-PAGE and transferred to a nitrocellulose membrane prior to Western blot analysis. Primary antibodies used were rat anti-HA (1:5000 dilution), rat anti-KasA (1:2000 dilution), or mouse monoclonal antibody 32/15 (1:10 dilution) recognizing the Ag85 complex.⁶² After washing, membranes were incubated for 45 min with an anti-rat or anti-mouse antibody conjugated to HRP (dilution 1:5000), incubated with SuperSignal West Femto (ThermoFisher Scientific) and revealed using a ChemiDoc MP system (Bio-Rad).

Mycolic Acid Analysis. To investigate the drug-induced changes in the mycolic acid profile, *M. abscessus* cultures were exposed to increasing drug concentrations of either ETH included as a positive control or NITD-916 for 1 h prior to metabolic labeling in the presence of 1 μCi/mL of [¹⁴C]-acetate (59 mCi/mmol, PerkinElmer) for an additional 2 h under shaking at 37 °C. Extraction of total mycolic acids was carried out as previously reported.⁴⁸ Briefly, cell pellets were washed and treated with 15% tetrabutylammonium hydroxide (TBAH) at 100 °C overnight. Fatty acids and mycolic acids were methyl-esterified and extracted in diethyl ether. Lipid extracts were dried and resuspended in dichloromethane and separated by thin-layer chromatography (TLC). Fatty acid methyl esters (FAMES) and mycolic acid methyl esters (MAMES) were developed in petroleum ether/acetone (95:5, v/v). The [¹⁴C]-labeled FAME and MAME content was analyzed using an Amersham Typhoon imaging system.

Human Bronchial Organoid Culture. The CHU of Toulouse (CHU 19 244 C) and the CNRS (CNRS 205782) approved the use of materials for this study. Organoids were derived from a lung biopsy of a cystic fibrosis heterozygous patient (G542X/1811 + 1.6kba → G), as previously reported.⁴⁵

Organoid Infections. On the infection day, organoids were infected with *M. abscessus* S and R variants adjusted to OD₆₀₀ = 0.2. Organoids in 25 μL drops of Matrigel (Fisher Scientific) were seeded on Nunclon Delta surface 35 × 10 mm Dish (Thermo Scientific). After Matrigel polymerization, 2 mL of airway organoid complete media⁴⁵ without *N*-acetylcysteine and without antibiotics were added to each plate. Organoids were microinjected using a Femtojet microinjector (Eppendorf), as previously described.⁴⁴ Two hours after infection, organoids were collected, washed in 1× PBS, embedded into a fresh matrix and treated or not for 3 days with 1.56 μg/mL or 15.6 μg/mL NITD-916 or 12.5 μg/mL RFB.

Live Imaging and Colony-Forming Unit Assay. At day 3 post infection, images of the organoids were acquired under an EVOS M7000 Imaging System (20×, at 37 °C with 5% CO₂) (Thermo Scientific). Following image acquisition, infected organoids were individually collected and lysed in 100 μL of 10% Triton X100 in PBS.⁴⁴ Serial dilutions of the lysates were plated on LB agar plates and incubated for 4 days at 37 °C prior to CFU counting.

Crystal Structure Determination. *M. abscessus* *InhA* (*InhA_{MAB}*) was expressed and purified using our standard structural genomics expression and purification protocols reported previously.^{63,64} Briefly, the *MAB_2722c* gene encoding *InhA_{MAB}* was cloned from genomic DNA into the bacterial expression vector BG1861, which encodes a non-

cleavable N-terminal His₆ tag. The protein was expressed in BL21(DE3) cells with autoinduction media followed by cell lysis and purification via nickel affinity then size exclusion chromatography. InhA_{MAB} crystallized at 23.06 mg/mL in the *apo* state in the MCSG1 crystallization screen condition E1 (2 M (NH₄)₂SO₄, 0.1 M Hepes pH 7.5); the crystal was cryoprotected with reservoir supplemented with 20% v/v ethylene glycol. InhA_{MAB} crystallized at 23.06 mg/mL with 4 mM NADH in the JCSG+ crystallization screen condition E1 (0.1 M sodium cacodylate pH 6.27, 1.09 M sodium citrate tribasic); the crystal was cryoprotected with reservoir supplemented with 4 mM NADH and 20% v/v ethylene glycol. InhA_{MAB} crystallized at 23.06 mg/mL with 3.5 mM NADH and 3.5 mM NITD-916 in the Index crystallization screen condition H10 (0.2 M sodium citrate tribasic, 20% PEG 3350); the crystal was cryoprotected with reservoir supplemented with 3.5 mM NADH, 3.5 mM NITD-916, and 20% v/v ethylene glycol. The *apo* and the NADH/NITD-916 bound data sets were collected at the Advanced Photon Source beamLine 21 ID-F with a Rayonix MX-300 CCD detector at 0.97872 Å wavelength. The NADH bound data set was collected in house on a Rigaku FR-E+ SuperBright X-ray generator with a Saturn 944+ detector at 1.5406 Å wavelength. The *apo* structure was solved by molecular replacement using MORDA and the *M. tuberculosis* InhA structure (PDB ID 2H71 superseded by 4U0J) as a search model. The structure was refined with iterative rounds of refinement between Phenix⁶⁵ and Coot.⁶⁶ X-ray diffraction images have been uploaded to the Integrated Resource for Reproducibility in Macromolecular Crystallography (IRRM) database (www.proteindiffraction.org).⁶⁷

Ligand Binding via Differential Scanning Fluorimetry (DSF). Sypro dye based DSF experiments were performed on a Bio-Rad CFX-96 thermal cycler at 0.1 mg/mL InhA_{MAB} in a background buffer of 25 mM Tris pH 8.0, 200 mM NaCl, 1 mM TCEP, and 1% v/v glycerol. DMSO was kept constant at 2% v/v for all measurements. NAD alone or NAD and NITD-916 were added to a final concentration of 1 mM.

Statistical Analyses. Statistical analyses were performed on Prism 9.0 (Graphpad) and detailed for each figure legend. **P* ≤ 0.05, ** *P* ≤ 0.01, *** *P* ≤ 0.001, **** *P* ≤ 0.0001.

■ ASSOCIATED CONTENT

SI Supporting Information

The Supporting Information is available free of charge at <https://pubs.acs.org/doi/10.1021/acsinfecdis.2c00314>.

Table S1: MIC of ethionamide and NITD-916 against *M. abscessus* in different media; Table S2: Activity of INH, NITD-916, and the quinoline-INH hybrid 16g against *M. abscessus* strains overexpressing KatG_{MTB}; Table S3: Crystallographic data collection and refinement statistics; Table S4: Differential scanning fluorimetry (DSF) measurements on InhA_{MAB}; Table S5: Interactions between NITD-916 and other antibiotics using the checkerboard assay; Figure S1: Cytotoxicity assay of NITD-916, isoniazid (INH) and rifabutin (RFB) on THP-1 cells; Figure S2: Percentage of THP-1 macrophages at 0, 1, and 3 days postinfection with *M. abscessus* S in the presence of absence of NITD-916; Figure S3: Differential scanning fluorimetry (DSF) thermal shift analysis of InhA_{MAB}; Figure S4: Multiple sequence alignments of the InhA proteins (PDF)

■ AUTHOR INFORMATION

Corresponding Author

Laurent Kremer – Centre National de la Recherche Scientifique UMR 9004, Institut de Recherche en Infectiologie de Montpellier (IRIM), Université de Montpellier, 34293 Montpellier, France; INSERM, IRIM, 34293 Montpellier, France; orcid.org/0000-0002-6604-4458; Phone: (+33) 4 34 35 94 47; Email: laurent.kremer@irim.cnrs.fr

Authors

Matthéo Alcaraz – Centre National de la Recherche Scientifique UMR 9004, Institut de Recherche en Infectiologie de Montpellier (IRIM), Université de Montpellier, 34293 Montpellier, France

Françoise Roquet-Banères – Centre National de la Recherche Scientifique UMR 9004, Institut de Recherche en Infectiologie de Montpellier (IRIM), Université de Montpellier, 34293 Montpellier, France

Stephen Adonai Leon-Icaza – Institut de Pharmacologie et de Biologie Structurale (IPBS), Université de Toulouse, CNRS, 31400 Toulouse, France; orcid.org/0000-0002-7546-8228

Jan Abendroth – UCB BioSciences, Bainbridge Island, Washington 98109, United States; Seattle Structural Genomics Center for Infectious Disease (SSGICD), Seattle, Washington 98109, United States

Yves-Marie Boudehen – Centre National de la Recherche Scientifique UMR 9004, Institut de Recherche en Infectiologie de Montpellier (IRIM), Université de Montpellier, 34293 Montpellier, France

Céline Cougoule – Institut de Pharmacologie et de Biologie Structurale (IPBS), Université de Toulouse, CNRS, 31400 Toulouse, France

Thomas E. Edwards – UCB BioSciences, Bainbridge Island, Washington 98109, United States; Seattle Structural Genomics Center for Infectious Disease (SSGICD), Seattle, Washington 98109, United States; orcid.org/0000-0002-0474-8003

Complete contact information is available at: <https://pubs.acs.org/doi/10.1021/acsinfecdis.2c00314>

Notes

The authors declare no competing financial interest.

■ ACKNOWLEDGMENTS

This study was supported by the French National Research Agency ANR-19-CE15-0012-01 (SUNLIVE). We acknowledge the Ministère de l'Enseignement Supérieur, de la Recherche et de l'Innovation for funding the PhD of MA. This work was supported by the National Institutes of Health/National Institute of Allergy and Infectious Diseases (Contract No. HHSN272201700059C) to Peter J. Myler (PI for SSGICD). CC and SALI were funded by grants from "Vaincre La Mucoviscidose" and "Grégory Lemarchal" foundations (No. RF20210502852/1/1/48). We would like to thank A. Speer for the generous gift of pSMT3-*katG*_{MTB}-*tdTomato*.

■ REFERENCES

- (1) Cowman, S.; van Ingen, J.; Griffith, D. E.; Loebinger, M. R. Non-Tuberculous Mycobacterial Pulmonary Disease. *Eur. Respir. J.* **2019**, *54* (1), 1900250.
- (2) Jönsson, B. E.; Gilljam, M.; Lindblad, A.; Ridell, M.; Wold, A. E.; Welinder-Olsson, C. Molecular Epidemiology of *Mycobacterium*

- abscessus*, with Focus on Cystic Fibrosis. *J. Clin. Microbiol.* **2007**, *45* (5), 1497–1504.
- (3) Esther, C. R.; Esserman, D. A.; Gilligan, P.; Kerr, A.; Noone, P. G. Chronic *Mycobacterium abscessus* Infection and Lung Function Decline in Cystic Fibrosis. *J. Cyst. Fibros.* **2010**, *9* (2), 117–123.
- (4) Catherinot, E.; Roux, A.-L.; Macheras, E.; Hubert, D.; Matmar, M.; Dannhoffer, L.; Chinet, T.; Morand, P.; Poyart, C.; Heym, B.; Rottman, M.; Gaillard, J.-L.; Herrmann, J.-L. Acute Respiratory Failure Involving an R Variant of *Mycobacterium abscessus*. *J. Clin. Microbiol.* **2009**, *47* (1), 271–274.
- (5) Koh, W.-J.; Jeon, K.; Lee, N. Y.; Kim, B.-J.; Kook, Y.-H.; Lee, S.-H.; Park, Y. K.; Kim, C. K.; Shin, S. J.; Huitt, G. A.; Daley, C. L.; Kwon, O. J. Clinical Significance of Differentiation of *Mycobacterium massiliense* from *Mycobacterium abscessus*. *Am. J. Respir. Crit. Care Med.* **2011**, *183* (3), 405–410.
- (6) Adekambi, T.; Sassi, M.; van Ingen, J.; Drancourt, M. Reinstating *Mycobacterium massiliense* and *Mycobacterium bolletii* as Species of the *Mycobacterium abscessus* Complex. *Int. J. Syst. Evol. Microbiol.* **2017**, *67* (8), 2726–2730.
- (7) Johansen, M. D.; Herrmann, J.-L.; Kremer, L. Non-Tuberculous Mycobacteria and the Rise of *Mycobacterium abscessus*. *Nat. Rev. Microbiol.* **2020**, *18* (7), 392–407.
- (8) Howard, S. T.; Rhoades, E.; Recht, J.; Pang, X.; Alsop, A.; Kolter, R.; Lyons, C. R.; Byrd, T. F. Spontaneous Reversion of *Mycobacterium abscessus* from a Smooth to a Rough Morphotype Is Associated with Reduced Expression of Glycopeptidolipid and Reacquisition of an Invasive Phenotype. *Microbiology (Reading, Engl.)* **2006**, *152* (6), 1581–1590.
- (9) Gutiérrez, A. V.; Viljoen, A.; Ghigo, E.; Herrmann, J.-L.; Kremer, L. Glycopeptidolipids, a Double-Edged Sword of the *Mycobacterium abscessus* Complex. *Front. Microbiol.* **2018**, *9*, 1145.
- (10) Roux, A.-L.; Viljoen, A.; Bah, A.; Simeone, R.; Bernut, A.; Laencina, L.; Deramaut, T.; Rottman, M.; Gaillard, J.-L.; Majlessi, L.; Brosch, R.; Girard-Misguich, F.; Vergne, I.; de Chastellier, C.; Kremer, L.; Herrmann, J.-L. The Distinct Fate of Smooth and Rough *Mycobacterium abscessus* Variants inside Macrophages. *Open Biol.* **2016**, *6* (11), 160185.
- (11) Bernut, A.; Viljoen, A.; Dupont, C.; Sapriel, G.; Blaise, M.; Bouchier, C.; Brosch, R.; de Chastellier, C.; Herrmann, J.-L.; Kremer, L. Insights into the Smooth-to-Rough Transitioning in *Mycobacterium bolletii* Unravels a Functional Tyr Residue Conserved in All Mycobacterial MmpL Family Members. *Mol. Microbiol.* **2016**, *99* (5), 866–883.
- (12) Sánchez-Chardi, A.; Olivares, F.; Byrd, T. F.; Julián, E.; Brambilla, C.; Luquin, M. Demonstration of Cord Formation by Rough *Mycobacterium abscessus* Variants: Implications for the Clinical Microbiology Laboratory. *J. Clin. Microbiol.* **2011**, *49* (6), 2293–2295.
- (13) Nessar, R.; Reyrat, J.-M.; Davidson, L. B.; Byrd, T. F. Deletion of the *MmpL4b* Gene in the *Mycobacterium abscessus* Glycopeptidolipid Biosynthetic Pathway Results in Loss of Surface Colonization Capability, but Enhanced Ability to Replicate in Human Macrophages and Stimulate Their Innate Immune Response. *Microbiology (Reading, Engl.)* **2011**, *157* (4), 1187–1195.
- (14) Bernut, A.; Herrmann, J.-L.; Kissa, K.; Dubremetz, J.-F.; Gaillard, J.-L.; Lutfalla, G.; Kremer, L. *Mycobacterium abscessus* Cording Prevents Phagocytosis and Promotes Abscess Formation. *Proc. Natl. Acad. Sci. U.S.A.* **2014**, *111* (10), E943–952.
- (15) Madani, A.; Ridenour, J. N.; Martin, B. P.; Paudel, R. R.; Abdul Basir, A.; Le Moigne, V.; Herrmann, J.-L.; Audebert, S.; Camoin, L.; Kremer, L.; Spilling, C. D.; Cnaan, S.; Cavalier, J.-F. Cyclosporins and Cyclophostin Analogues as Multitarget Inhibitors That Impair Growth of *Mycobacterium abscessus*. *ACS Infect. Dis.* **2019**, *5* (9), 1597–1608.
- (16) Lavollay, M.; Dubée, V.; Heym, B.; Herrmann, J.-L.; Gaillard, J.-L.; Gutmann, L.; Arthur, M.; Mainardi, J.-L. *In Vitro* Activity of Cefoxitin and Imipenem against *Mycobacterium abscessus* Complex. *Clin. Microbiol. Infect.* **2014**, *20* (5), O297–O300.
- (17) Nessar, R.; Cambau, E.; Reyrat, J. M.; Murray, A.; Gicquel, B. *Mycobacterium abscessus*: A New Antibiotic Nightmare. *J. Antimicrob. Chemother.* **2012**, *67* (4), 810–818.
- (18) van Ingen, J.; Boeree, M. J.; van Soolingen, D.; Mouton, J. W. Resistance Mechanisms and Drug Susceptibility Testing of Nontuberculous Mycobacteria. *Drug Resist. Updat.* **2012**, *15* (3), 149–161.
- (19) Brown-Elliott, B. A.; Nash, K. A.; Wallace, R. J. Antimicrobial Susceptibility Testing, Drug Resistance Mechanisms, and Therapy of Infections with Nontuberculous Mycobacteria. *Clin. Microbiol. Rev.* **2012**, *25* (3), 545–582.
- (20) Lopeman, R.; Harrison, J.; Desai, M.; Cox, J. *Mycobacterium abscessus*: Environmental Bacterium Turned Clinical Nightmare. *Microorganisms* **2019**, *7* (3), 90.
- (21) Griffith, D. E.; Aksamit, T.; Brown-Elliott, B. A.; Catanzaro, A.; Daley, C.; Gordin, F.; Holland, S. M.; Horsburgh, R.; Huitt, G.; Iademarco, M. F.; Iseman, M.; Olivier, K.; Ruoss, S.; von Reyn, C. F.; Wallace, R. J.; Winthrop, K. ATS Mycobacterial Diseases Subcommittee; American Thoracic Society; Infectious Disease Society of America. An Official ATS/IDSA Statement: Diagnosis, Treatment, and Prevention of Nontuberculous Mycobacterial Diseases. *Am. J. Respir. Crit. Care Med.* **2007**, *175* (4), 367–416.
- (22) Floto, R. A.; Olivier, K. N.; Saiman, L.; Daley, C. L.; Herrmann, J.-L.; Nick, J. A.; Noone, P. G.; Bilton, D.; Corris, P.; Gibson, R. L.; Hempstead, S. E.; Koetz, K.; Sadoski, K. A.; Sermet-Gaudelus, I.; Smyth, A. R.; van Ingen, J.; Wallace, R. J.; Winthrop, K. L.; Marshall, B. C.; Haworth, C. S. US Cystic Fibrosis Foundation and European Cystic Fibrosis Society Consensus Recommendations for the Management of Non-Tuberculous Mycobacteria in Individuals with Cystic Fibrosis: Executive Summary. *Thorax* **2016**, *71* (1), 88–90.
- (23) Daley, C. L.; Iaccarino, J. M.; Lange, C.; Cambau, E.; Wallace, R. J.; Andrejak, C.; Böttger, E. C.; Brozek, J.; Griffith, D. E.; Guglielmetti, L.; Huitt, G. A.; Knight, S. L.; Leitman, P.; Marras, T. K.; Olivier, K. N.; Santin, M.; Stout, J. E.; Tortoli, E.; van Ingen, J.; Wagner, D.; Winthrop, K. L. Treatment of Nontuberculous Mycobacterial Pulmonary Disease: An Official ATS/ERS/ESCMID/IDSA Clinical Practice Guideline. *Eur. Respir. J.* **2020**, *56* (1), 2000535.
- (24) Wallace, R. J.; Dukart, G.; Brown-Elliott, B. A.; Griffith, D. E.; Scerpella, E. G.; Marshall, B. Clinical Experience in 52 Patients with Tigecycline-Containing Regimens for Salvage Treatment of *Mycobacterium abscessus* and *Mycobacterium chelonae* Infections. *J. Antimicrob. Chemother.* **2014**, *69* (7), 1945–1953.
- (25) Roux, A.-L.; Catherinot, E.; Soismier, N.; Heym, B.; Bellis, G.; Lemonnier, L.; Chiron, R.; Fauroux, B.; Le Bourgeois, M.; Munck, A.; Pin, I.; Sermet, I.; Gutierrez, C.; Véziris, N.; Jarlier, V.; Cambau, E.; Herrmann, J.-L.; Guillemot, D.; Gaillard, J.-L. OMA group. Comparing *Mycobacterium massiliense* and *Mycobacterium abscessus* Lung Infections in Cystic Fibrosis Patients. *J. Cyst. Fibros.* **2015**, *14* (1), 63–69.
- (26) Wu, M.-L.; Aziz, D. B.; Dartois, V.; Dick, T. NTM Drug Discovery: Status, Gaps and the Way Forward. *Drug Discovery Today* **2018**, *23* (8), 1502–1519.
- (27) Dupont, C.; Viljoen, A.; Dubar, F.; Blaise, M.; Bernut, A.; Pawlik, A.; Bouchier, C.; Brosch, R.; Guérardel, Y.; Lelièvre, J.; Ballé, L.; Herrmann, J.-L.; Biot, C.; Kremer, L. A New Piperidinol Derivative Targeting Mycolic Acid Transport in *Mycobacterium abscessus*. *Mol. Microbiol.* **2016**, *101* (3), 515–529.
- (28) Luthra, S.; Rominski, A.; Sander, P. The Role of Antibiotic-Target-Modifying and Antibiotic-Modifying Enzymes in *Mycobacterium abscessus* Drug Resistance. *Front. Microbiol.* **2018**, DOI: 10.3389/fmicb.2018.02179.
- (29) Gagliardi, A.; Selchow, P.; Luthra, S.; Schäfle, D.; Schulthess, B.; Sander, P. KatG as Counterselection Marker for Nontuberculous Mycobacteria. *Antimicrob. Agents Chemother.* **2020**, *64* (5), No. e02508-19.
- (30) Johnsson, K.; Froland, W. A.; Schultz, P. G. Overexpression, Purification, and Characterization of the Catalase-Peroxidase KatG

- from *Mycobacterium tuberculosis*. *J. Biol. Chem.* **1997**, *272* (5), 2834–2840.
- (31) Zhang, Y.; Heym, B.; Allen, B.; Young, D.; Cole, S. The Catalase-Peroxidase Gene and Isoniazid Resistance of *Mycobacterium tuberculosis*. *Nature* **1992**, *358* (6387), 591–593.
- (32) Rozwarski, D. A.; Grant, G. A.; Barton, D. H.; Jacobs, W. R.; Sacchettini, J. C. Modification of the NADH of the Isoniazid Target (InhA) from *Mycobacterium tuberculosis*. *Science* **1998**, *279* (5347), 98–102.
- (33) Wilming, M.; Johnsson, K. Spontaneous Formation of the Bioactive Form of the Tuberculosis Drug Isoniazid. *Angew. Chem., Int. Ed. Engl.* **1999**, *38* (17), 2588–2590.
- (34) Rawat, R.; Whitty, A.; Tonge, P. J. The Isoniazid-NAD Adduct Is a Slow, Tight-Binding Inhibitor of InhA, the *Mycobacterium tuberculosis* Enoyl Reductase: Adduct Affinity and Drug Resistance. *Proc. Natl. Acad. Sci. U.S.A.* **2003**, *100* (24), 13881–13886.
- (35) Banerjee, A.; Dubnau, E.; Quemard, A.; Balasubramanian, V.; Um, K. S.; Wilson, T.; Collins, D.; de Lisle, G.; Jacobs, W. R. *InhA*, a Gene Encoding a Target for Isoniazid and Ethionamide in *Mycobacterium tuberculosis*. *Science* **1994**, *263* (5144), 227–230.
- (36) Vilchèze, C.; Wang, F.; Arai, M.; Hazbón, M. H.; Colangeli, R.; Kremer, L.; Weisbrod, T. R.; Alland, D.; Sacchettini, J. C.; Jacobs, W. R. Transfer of a Point Mutation in *Mycobacterium tuberculosis inhA* Resolves the Target of Isoniazid. *Nat. Med.* **2006**, *12* (9), 1027–1029.
- (37) Nguyen, M.; Quémard, A.; Broussy, S.; Bernadou, J.; Meunier, B. Mn(III) Pyrophosphate as an Efficient Tool for Studying the Mode of Action of Isoniazid on the InhA Protein of *Mycobacterium tuberculosis*. *Antimicrob. Agents Chemother.* **2002**, *46* (7), 2137–2144.
- (38) Bhatt, A.; Molle, V.; Besra, G. S.; Jacobs, W. R.; Kremer, L. The *Mycobacterium tuberculosis* FAS-II Condensing Enzymes: Their Role in Mycolic Acid Biosynthesis, Acid-Fastness, Pathogenesis and in Future Drug Development. *Mol. Microbiol.* **2007**, *64* (6), 1442–1454.
- (39) Vilchèze, C.; Morbidoni, H. R.; Weisbrod, T. R.; Iwamoto, H.; Kuo, M.; Sacchettini, J. C.; Jacobs, W. R. Inactivation of the *inhA*-Encoded Fatty Acid Synthase II (FASII) Enoyl-Acyl Carrier Protein Reductase Induces Accumulation of the FASI End Products and Cell Lysis of *Mycobacterium smegmatis*. *J. Bacteriol.* **2000**, *182* (14), 4059–4067.
- (40) Manjunatha, U. H. S.; Rao, S. P.; Kondreddi, R. R.; Noble, C. G.; Camacho, L. R.; Tan, B. H.; Ng, S. H.; Ng, P. S.; Ma, N. L.; Lakshminarayana, S. B.; Herve, M.; Barnes, S. W.; Yu, W.; Kuhlen, K.; Blasco, F.; Beer, D.; Walker, J. R.; Tonge, P. J.; Glynn, R.; Smith, P. W.; Diagan, T. T. Direct Inhibitors of InhA Are Active against *Mycobacterium tuberculosis*. *Sci. Transl. Med.* **2015**, *7* (269), 269ra3–269ra3.
- (41) Johansen, M. D.; Daher, W.; Roquet-Banères, F.; Raynaud, C.; Alcaraz, M.; Maurer, F. P.; Kremer, L. Rifabutin Is Bactericidal against Intracellular and Extracellular Forms of *Mycobacterium abscessus*. *Antimicrob. Agents Chemother.* **2020**, *64* (11), No. e00363-20.
- (42) Kirchner, S.; Fothergill, J. L.; Wright, E. A.; James, C. E.; Mowat, E.; Winstanley, C. Use of Artificial Sputum Medium to Test Antibiotic Efficacy Against *Pseudomonas aeruginosa* in Conditions More Relevant to the Cystic Fibrosis Lung. *J. Visualized Exp.* **2012**, No. 64, 3857.
- (43) Lefebvre, A.-L.; Dubée, V.; Cortes, M.; Dorchène, D.; Arthur, M.; Mainardi, J.-L. Bactericidal and Intracellular Activity of β -Lactams against *Mycobacterium abscessus*. *J. Antimicrob. Chemother.* **2016**, *71* (6), 1556–1563.
- (44) Iakobachvili, N.; Leon-Icaza, S. A.; Knoops, K.; Sachs, N.; Mazères, S.; Simeone, R.; Peixoto, A.; Bernard, C.; Murriss-Espin, M.; Mazières, J.; Cam, K.; Chalut, C.; Guilhot, C.; López-Iglesias, C.; Ravelli, R. B. G.; Neyrolles, O.; Meunier, E.; Lugo-Villarino, G.; Clevers, H.; Cougoule, C.; Peters, P. J. Mycobacteria-Host Interactions in Human Bronchiolar Airway Organoids. *Mol. Microbiol.* **2022**, *117* (3), 682–692.
- (45) Leon-Icaza, S. A.; Bagayoko, S.; Iakobachvili, N.; Ferrand, C.; Aydogan, T.; Bernard, C.; Dafun, A. S.; Murriss-Espin, M.; Mazières, J.; Bordignon, P. J.; Mazères, S.; Bernes-Lasserre, P.; Ramé, V.; Lagarde, J.-M.; Marcoux, J.; Bousquet, M. P.; Chalut, C.; Guilhot, C.; Clevers, H.; Peters, P. J.; Molle, V.; Lugo-Villarino, G.; Cam, K.; Berry, L.; Meunier, E.; Cougoule, C. Cystic Fibrosis Patient-Derived Bronchial Organoids Unveil Druggable Pathways against *Mycobacterium abscessus* Infection. *bioRxiv*, January 3, 2022. DOI: 10.1101/2022.01.03.474765.
- (46) Kremer, L.; Dover, L. G.; Morbidoni, H. R.; Vilchèze, C.; Maughan, W. N.; Baulard, A.; Tu, S.-C.; Honoré, N.; Deretic, V.; Sacchettini, J. C.; Loch, C.; Jacobs, W. R.; Besra, G. S. Inhibition of InhA Activity, but Not KasA Activity, Induces Formation of a KasA-Containing Complex in Mycobacteria. *J. Biol. Chem.* **2003**, *278* (23), 20547–20554.
- (47) Halloum, I.; Carrère-Kremer, S.; Blaise, M.; Viljoen, A.; Bernut, A.; Le Moigne, V.; Vilchèze, C.; Guérardel, Y.; Lutfalla, G.; Herrmann, J.-L.; Jacobs, W. R.; Kremer, L. Deletion of a Dehydratase Important for Intracellular Growth and Cording Renders Rough *Mycobacterium abscessus* Avirulent. *Proc. Natl. Acad. Sci. U.S.A.* **2016**, *113* (29), E4228–4237.
- (48) Dover, L. G.; Alahari, A.; Gratraud, P.; Gomes, J. M.; Bhowruth, V.; Reynolds, R. C.; Besra, G. S.; Kremer, L. EthA, a Common Activator of Thiocarbamide-Containing Drugs Acting on Different Mycobacterial Targets. *Antimicrob. Agents Chemother.* **2007**, *51* (3), 1055–1063.
- (49) Rozwarski, D. A.; Vilchèze, C.; Sugantino, M.; Bittman, R.; Sacchettini, J. C. Crystal Structure of the *Mycobacterium tuberculosis* Enoyl-ACP Reductase, InhA, in Complex with NAD⁺ and a C16 Fatty Acyl Substrate. *J. Biol. Chem.* **1999**, *274* (22), 15582–15589.
- (50) Kuo, M. R.; Morbidoni, H. R.; Alland, D.; Sneddon, S. F.; Gourlie, B. B.; Staveski, M. M.; Leonard, M.; Gregory, J. S.; Janjigian, A. D.; Yee, C.; Musser, J. M.; Kreiswirth, B.; Iwamoto, H.; Perozzo, R.; Jacobs, W. R.; Sacchettini, J. C.; Fidock, D. A. Targeting Tuberculosis and Malaria through Inhibition of Enoyl Reductase: Compound Activity and Structural Data. *J. Biol. Chem.* **2003**, *278* (23), 20851–20859.
- (51) Grzegorzewicz, A. E.; Eynard, N.; Quémard, A.; North, E. J.; Margolis, A.; Lindenberger, J. J.; Jones, V.; Korduláková, J.; Brennan, P. J.; Lee, R. E.; Ronning, D. R.; McNeil, M. R.; Jackson, M. Covalent Modification of the *Mycobacterium tuberculosis* FAS-II Dehydratase by Isoxyl and Thiacetazone. *ACS Infect. Dis.* **2015**, *1* (2), 91–97.
- (52) Halloum, I.; Viljoen, A.; Khanna, V.; Craig, D.; Bouchier, C.; Brosch, R.; Coxon, G.; Kremer, L. Resistance to Thiacetazone Derivatives Active against *Mycobacterium abscessus* Involves Mutations in the MmpL5 Transcriptional Repressor MAB_4384. *Antimicrob. Agents Chemother.* **2017**, *61* (4), No. e02509-16.
- (53) Kozikowski, A. P.; Onajole, O. K.; Stec, J.; Dupont, C.; Viljoen, A.; Richard, M.; Chaira, T.; Lun, S.; Bishai, W.; Raj, V. S.; Ordway, D.; Kremer, L. Targeting Mycolic Acid Transport by Indole-2-Carboxamides for the Treatment of *Mycobacterium abscessus* Infections. *J. Med. Chem.* **2017**, *60* (13), 5876–5888.
- (54) Raynaud, C.; Daher, W.; Johansen, M. D.; Roquet-Banères, F.; Blaise, M.; Onajole, O. K.; Kozikowski, A. P.; Herrmann, J.-L.; Dziadek, J.; Gobis, K.; Kremer, L. Active Benzimidazole Derivatives Targeting the MmpL3 Transporter in *Mycobacterium abscessus*. *ACS Infect. Dis.* **2020**, *6* (2), 324–337.
- (55) Dick, T. Rifabutin: A Repurposing Candidate for *Mycobacterium abscessus* Lung Disease. *Front. Microbiol.* **2020**, *11*, 371.
- (56) McNeil, M. B.; Dennison, D.; Shelton, C.; Flint, L.; Korkegian, A.; Parish, T. Mechanisms of Resistance against NITD-916, a Direct Inhibitor of *Mycobacterium tuberculosis* InhA. *Tuberculosis (Edinb)* **2017**, *107*, 133–136.
- (57) Prasad, M. S.; Bhole, R. P.; Khedekar, P. B.; Chikhale, R. V. *Mycobacterium* Enoyl Acyl Carrier Protein Reductase (InhA): A Key Target for Antitubercular Drug Discovery. *Bioorg. Chem.* **2021**, *115*, 105242.
- (58) Singh, S.; Bouzinbi, N.; Chaturvedi, V.; Godreuil, S.; Kremer, L. *In Vitro* Evaluation of a New Drug Combination against Clinical Isolates Belonging to the *Mycobacterium abscessus* Complex. *Clin. Microbiol. Infect.* **2014**, *20* (12), O1124–1127.
- (59) Ho, V. Q. T.; Verboom, T.; Rong, M. K.; Habjan, E.; Bitter, W.; Speer, A. Heterologous Expression of EthA and KatG in

Mycobacterium marinum Enables the Rapid Identification of New Prodrugs Active against *Mycobacterium tuberculosis*. *Antimicrob. Agents Chemother.* **2021**, *65* (4), No. e01445-20.

(60) Woods, G. L.; Brown-Elliott, B. A.; Conville, P. S.; Desmond, E. P.; Hall, G. S.; Lin, G.; Pfyffer, G. E.; Ridderhof, J. C.; Siddiqi, S. H.; Wallace, R. J. *Susceptibility Testing of Mycobacteria, Nocardiae and Other Aerobic Actinomycetes: Approved Standard*, 2nd ed. (M24-A2); Clinical and Laboratory Standards Institute: Wayne, PA, 2011.

(61) Stover, C. K.; de la Cruz, V. F.; Fuerst, T. R.; Burlein, J. E.; Benson, L. A.; Bennett, L. T.; Bansal, G. P.; Young, J. F.; Lee, M. H.; Hatfull, G. F.; et al. New Use of BCG for Recombinant Vaccines. *Nature* **1991**, *351* (6326), 456–460.

(62) Viljoen, A.; Richard, M.; Nguyen, P. C.; Fourquet, P.; Camoin, L.; Paudal, R. R.; Gnawali, G. R.; Spilling, C. D.; Cavalier, J.-F.; Canaan, S.; Blaise, M.; Kremer, L. Cyclopostins and Cyclophostin Analogs Inhibit the Antigen 85C from *Mycobacterium tuberculosis* Both *in Vitro* and *in Vivo*. *J. Biol. Chem.* **2018**, *293* (8), 2755–2769.

(63) Bryan, C. M.; Bhandari, J.; Napuli, A. J.; Leibly, D. J.; Choi, R.; Kelley, A.; Van Voorhis, W. C.; Edwards, T. E.; Stewart, L. J. High-Throughput Protein Production and Purification at the Seattle Structural Genomics Center for Infectious Disease. *Acta Crystallogr. Sect. F Struct. Biol. Cryst. Commun.* **2011**, *67* (9), 1010–1014.

(64) Choi, R.; Kelley, A.; Leibly, D.; Hewitt, S. N.; Napuli, A.; Van Voorhis, W. Immobilized Metal-Affinity Chromatography Protein-Recovery Screening Is Predictive of Crystallographic Structure Success. *Acta Crystallogr. Sect. F Struct. Biol. Cryst. Commun.* **2011**, *67* (9), 998–1005.

(65) Adams, P. D.; Afonine, P. V.; Bunkóczi, G.; Chen, V. B.; Davis, I. W.; Echols, N.; Headd, J. J.; Hung, L.-W.; Kapral, G. J.; Grosse-Kunstleve, R. W.; McCoy, A. J.; Moriarty, N. W.; Oeffner, R.; Read, R. J.; Richardson, D. C.; Richardson, J. S.; Terwilliger, T. C.; Zwart, P. H. PHENIX: A Comprehensive Python-Based System for Macromolecular Structure Solution. *Acta Crystallogr. D Biol. Crystallogr.* **2010**, *66* (2), 213–221.

(66) Emsley, P.; Cowtan, K. Coot: Model-Building Tools for Molecular Graphics. *Acta Crystallogr. D Biol. Crystallogr.* **2004**, *60* (12), 2126–2132.

(67) Grabowski, M.; Cymborowski, M.; Porebski, P. J.; Osinski, T.; Shabalin, I. G.; Cooper, D. R.; Minor, W. The Integrated Resource for Reproducibility in Macromolecular Crystallography: Experiences of the First Four Years. *Struct. Dyn.* **2019**, *6* (6), 064301.

SUPPORTING INFORMATION

Efficacy and mode of action of a direct inhibitor of *Mycobacterium abscessus* InhA

Matthéo Alcaraz¹, Françoise Roquet-Banères¹, Stephen Adonai Leon-Icaza³, Jan Abendroth^{4,5}, Yves-Marie Boudehen¹, Céline Cougoule³, Thomas E. Edwards^{4,5},
and Laurent Kremer^{1,2,#}

¹Centre National de la Recherche Scientifique UMR 9004, Institut de Recherche en Infectiologie de Montpellier (IRIM), Université de Montpellier, 1919 route de Mende, 34293, Montpellier, France.

²INSERM, IRIM, Montpellier, France.

³Institut de Pharmacologie et de Biologie Structurale (IPBS), Université de Toulouse, CNRS, Toulouse, France.

⁴UCB BioSciences, Bainbridge Island, WA 98109 USA

⁵Seattle Structural Genomics Center for Infectious Disease (SSGCID), Seattle, WA 98109 USA

#To whom correspondence should be addressed:

Tel: (+33) 4 34 35 94 47; E-mail: laurent.kremer@irim.cnrs.fr

Running title: Efficacy of NITD-916 against *M. abscessus*

Table S1. MIC of ethionamide and NID-916 against *M. abscessus* in different media.

Table S2. Activity of INH, NITD-916 and the quinoline-INH hybrid **16g** against *M. abscessus* strains overexpressing KatG_{MTB}.

Table S3. Crystallographic data collection and refinement statistics.

Table S4. Differential scanning fluorimetry (DSF) measurements on InhA_{MAB}.

Table S5. Interactions between NITD-916 and other antibiotics using the checkerboard assay.

Figure S1. Cytotoxicity assay of NITD-916, isoniazid (INH) and rifabutin (RFB) on THP-1 cells.

Figure S2. Percentage of THP-1 macrophages at 0, 1 and 3 days post-infection with *M. abscessus* S in the presence or absence of NITD-916.

Figure S3. Differential scanning fluorimetry (DSF) thermal shift analysis of InhA_{MAB}.

Figure S4. Multiple sequence alignments of the InhA proteins.

Table S1. MIC (in $\mu\text{g/mL}$) of ethionamide (ETH) and NID-916 determined in CaMHB, Middlebrook 7H9, Sauton's medium and ASM against wild-type *M. abscessus* CIP104536^T and against strain NITD916^{R2}. Results were completed in triplicate in at least two independent experiments.

Strain	CaMHB		7H9 + OADC		Sauton		ASM	
	ETH	NITD-916	ETH	NITD-916	ETH	NITD-916	ETH	NITD-916
CIP104536 ^T (S)	25	1.56	12.5	6.25	6.25	0.195	25	0.78
NITD916 ^{R2} (S)	25	>200	12.5	>200	6.25	>200	25	>100

Table S2. Activity of INH, NITD-916 and the quinoline-INH hybrid **16g**¹ against *M. abscessus* strains overexpressing KatG_{MTB}. MIC (µg/mL) were determined in CaMHB at 30 °C. Results were confirmed in two separate experiments.

Strain	MIC (µg/mL)		
	INH	NITD-916	16g
CIP104536 ^T (S)	> 1000	1.56	> 200
CIP104536 ^T (S) + pSMT3- <i>katG</i> _{MTB} - <i>tdTomato</i>	62.5	1.56	100
CIP104536 ^T (R)	> 1000	1.56	> 200
CIP104536 ^T (R) + pSMT3- <i>katG</i> _{MTB} - <i>tdTomato</i>	62.5	1.56	100

- (1) Alcaraz, M.; Sharma, B.; Roquet-Banères, F.; Conde, C.; Cochard, T.; Biet, F.; Kumar, V.; Kremer, L. Designing Quinoline-Isoniazid Hybrids as Potent Anti-Tubercular Agents Inhibiting Mycolic Acid Biosynthesis. *Eur J Med Chem* **2022**, *239*, 114531. <https://doi.org/10.1016/j.ejmech.2022.114531>.

Table S3. Crystallographic data collection and refinement statistics.

Data collection and processing	InhA_{MAB} with NITD-916 and NAD
Wavelength (Å)	0.97872
Resolution range (Å)	50 – 1.45
Space group	C2
Unit Cell	78.31, 102.31, 76.82 / 90, 114.65, 90
Total reflections	95,830 (6037)
Multiplicity	3.87 (2.26)
Completeness (%)	98.2 (84.4)
Mean I/sigma(I)	18.13 (4.29)
Wilson B-factor (Å ²)	11.58
R-merge (%)	4.6 (22.8)
Refinement	InhA_{MAB} with NITD-916 and NAD
Number of reflections	93,841
Number of R-free reflections	1989
R-work %	15.05
R-free %	17.87
RMS(bonds)	0.005
RMS(angles)	0.840
Ramachandran plot	
Favored (%)	96.4
Allowed (%)	3.6
Outliers (%)	0
PDB ID	7U0M

Table S4. Differential scanning fluorimetry (DSF) measurements on InhA_{MAB}.

Sample	Melting Temperature T _m (°C)					
	Rep1	Rep2	Rep3	Avg	SD	(ΔT _m)
Apoenzyme	39.5	39.5	39.0	39.3	0.2	--
NAD	40.0	40.0	39.5	39.8	0.2	+0.5
NAD & NITD-916	54.0	54.0	54.0	54.0	0.0	+14.7

Table S5. Interactions between NITD-916 and other antibiotics against *M. abscessus* CIP104536^T (S) and CIP104536^T (R) were determined using the checkerboard assay in CaMHB and MICs evaluated by REMA (resazurin microtiter assay). Plates were incubated for 4 days at 30 °C, after which 10 µL (10%, vol/vol) of resazurin 0.025% was added to the wells and incubated overnight at 30 °C.

CIP 104536 ^T (S)		Interaction with NITD-916	
Compound	MIC (µg/mL)	FICI score (mean ± SD)	Outcome
IPM	16	0.75 ± 0.21	Indifferent
AMK	50	1.25	Indifferent
RFB	50	1.21 ± 0.07	Indifferent
CFX	64	1.17 ± 0.07	Indifferent
BDQ	0.0625	1.125	Indifferent
CFZ	1	0.917 ± 0.26	Indifferent
EJMCh6	0.125	1.052 ± 0.07	Indifferent
CIP 104536 ^T (R)		Interaction with NITD-916	
Compound	MIC (µg/mL)	FICI score (mean ± SD)	Outcome
IPM	16	0.625	Indifferent
AMK	50	1.25	Indifferent
RFB	12.5	1.17 ± 0.07	Indifferent
CFX	64	0.83 ± 0.07	Indifferent
BDQ	0.0625	1.125	Indifferent
CFZ	1	0.833 ± 0.26	Indifferent
EJMCh6	0.125	1.542 ± 0.44	Indifferent

The Fractional Inhibitory Concentration Index (FICI) was calculated as follows: $FICI = (MIC \text{ drug A in combination} / MIC \text{ drug A alone}) + (MIC \text{ drug B in combination} / MIC \text{ drug B alone})$, where drug A was NITD-916 and drug B was imipenem (IPM), amikacin (AMK), rifabutin (RFB), cefoxitin (CFX), bedaquiline (BDQ), clofazimine (CFZ) or EJMCh6 (benzimidazole inhibiting MmpL3). Interaction between the two compounds was defined as synergistic when FICI was ≤ 0.5 , indifferent when $0.5 < FICI \leq 4$, and antagonistic when FICI was > 4 .

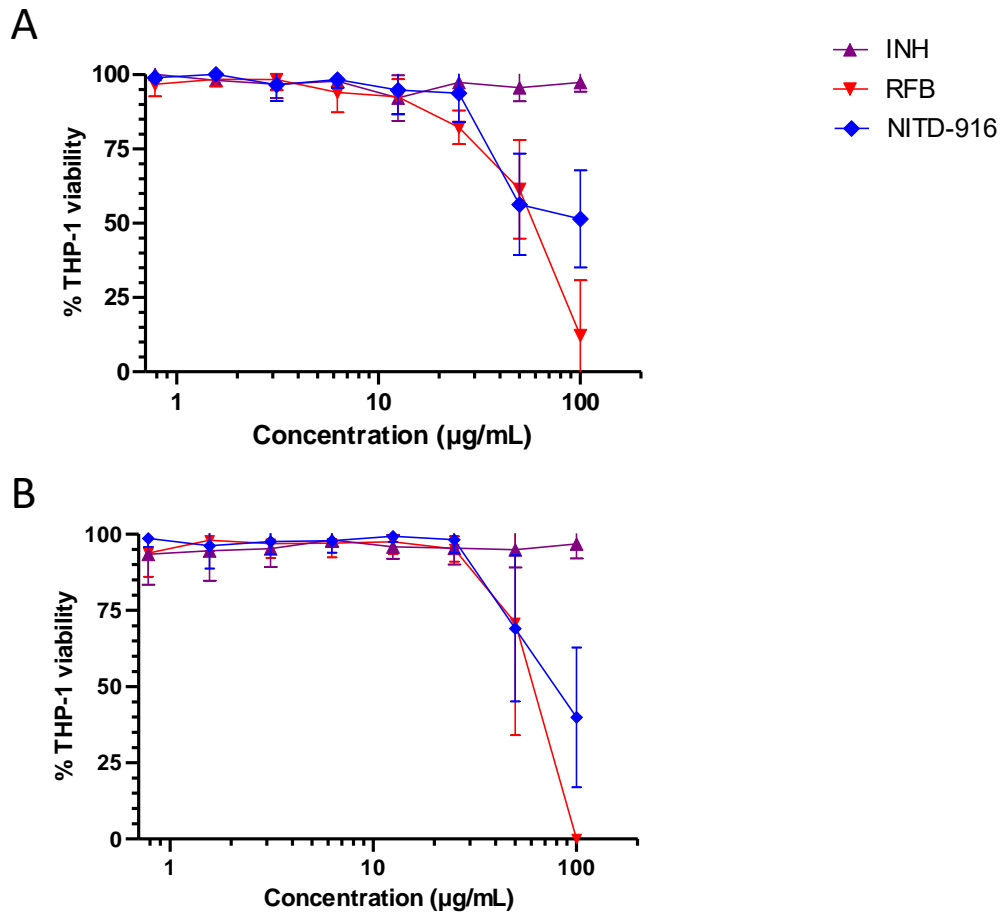


Figure S1. Cytotoxicity assay of NITD-916, isoniazid (INH) and rifabutin (RFB) on THP-1 differentiated macrophages. Cells were differentiated with PMA for 48 hrs and exposed to increasing concentration of either NITD-916, INH or RFB (starting at 100 µg/mL) for an additional 24 hrs (**A**) or 72 hrs (**B**) at 37 °C in the presence of 5% CO₂. Results are the mean of three independent experiments done in duplicates.

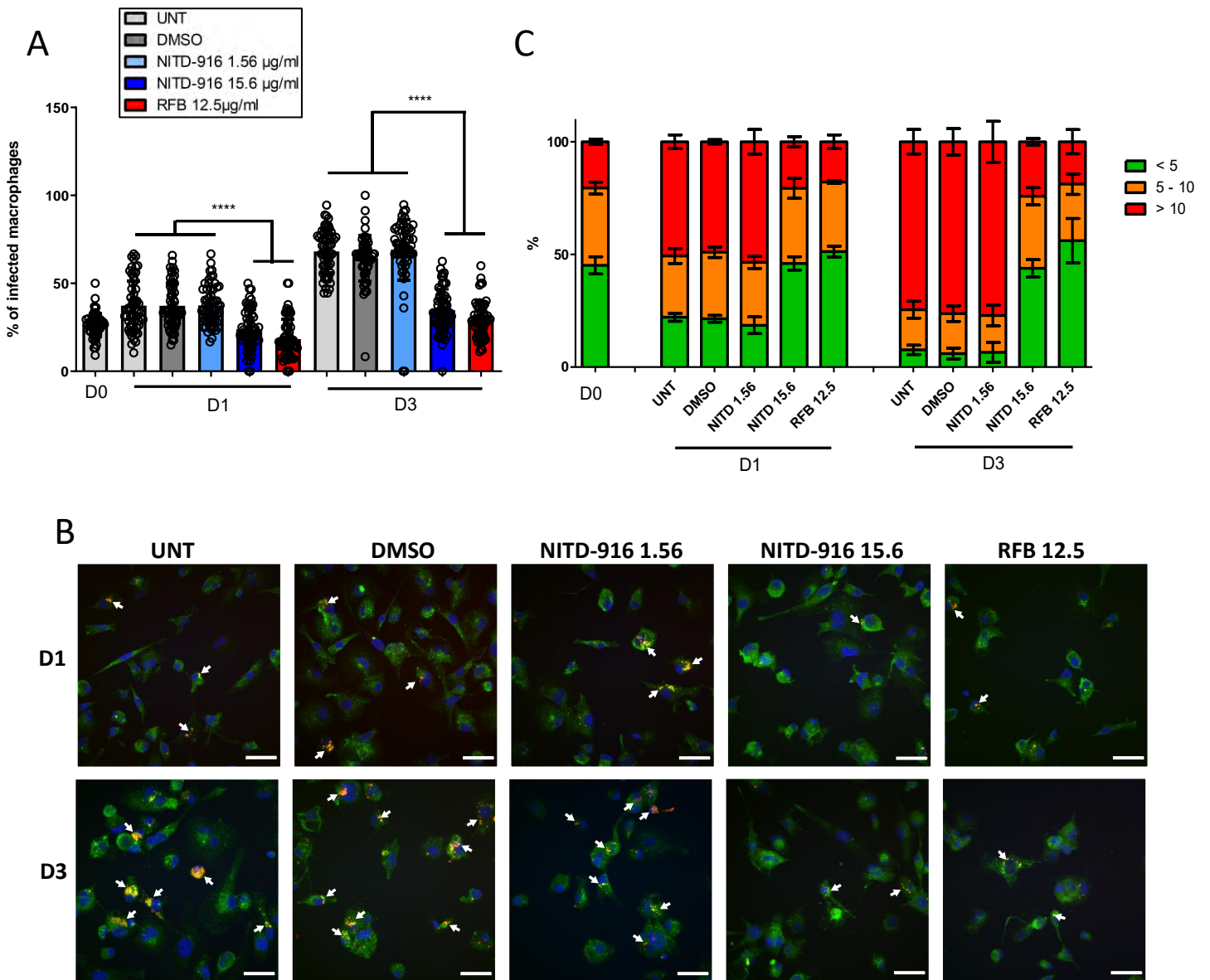


Figure S2. (A) Percentage of THP-1 macrophages at 0, 1 and 3 days post-infection with *M. abscessus* CIP104536^T (S) (MOI of 2:1) in the absence (UNT) of antibiotics or presence of NITD-916 (1.56 µg/mL and 15.6 µg/mL) or RFB (12.5 µg/mL). DMSO-exposed cells were included as controls. Results are expressed as mean values ± SD for three independent experiments with 30 fields per condition. Data were analyzed using the Mann-Whitney *t* test. ****, $P \leq 0.0001$. **(B)** Representative immunofluorescent fields were taken at 1 and 3 days post-infection showing macrophages infected with *M. abscessus* expressing TdTomato (red) in the absence of antibiotics (UNT) or in the presence of NITD-916 (1.56 µg/mL and 15.6 µg/mL) or RFB (12.5 µg/mL). DMSO-exposed cells were included as controls. The surface and the endolysosomal system of the macrophages were detected using anti-CD63 antibodies (green). The nuclei were stained with DAPI (blue). White arrows indicate individual or mycobacterial aggregates. Scale bar, 50 µm. **(C)** Percentage of macrophages categories infected with different number of bacilli (<5 bacilli/cell, 5 to 10 bacilli/cell, >10 bacilli/cell). The categories were counted at 0, 1 and 3 days post-infection in the absence of antibiotics or in the presence of NITD-916 (1.56 µg/mL and 15.6 µg/mL) or RFB (12.5 µg/mL). Untreated (UNT) or DMSO-exposed cells were included as controls. Data are mean values ± SD for three independent experiments.

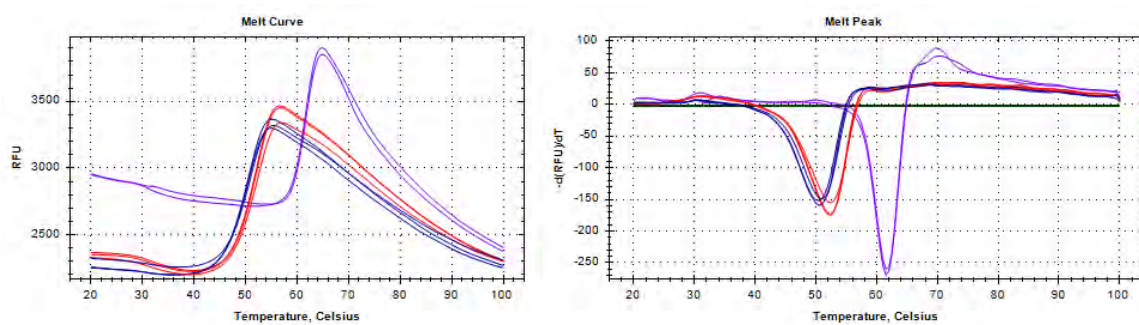


Figure S3. (A) Differential scanning fluorimetry (DSF) thermal shift analysis of InhA_{MAB} in the apo-enzyme state (blue curves in triplicate), in the presence of NAD (red curves) and NAD & NITD-916 (purple curves). **(B)** First derivative profiles of melting curves.

% ID to InhA_MTB		10	20	30	40	50	60	70	80	90
InhA_MTB	100%	MTGLLDGKRILVSGIITDSSIAFHIAARVAQEQAQLVLTGFDRRLRQIRITDRLPAKAPLLELDVQNEEHLASLAGRVTEAIGAGNKLDGVVHSIGFMPQ	100							
InhA_MAB	87.7%	VAGLLEGKRILVGTIITDSSIAFHIAKVAQEQAELVLTGFDRRLRIERITQRLPKAPLLELDVQNEEHLGSLAGRISEVIGEGNKLDGVVHSIGFMPQ	100							
InhA_MLP	90.3%	MAGLLEGKRILVSGIITDSSIAFHIAKVAQEQAQLVLTGFDRRLRQIRIADRLPKAPLIELDVQNEEHLATLAERVTAEIGEGNKLDGVVHSIGFMPQ	100							
InhA_MBOV	100%	MTGLLDGKRILVSGIITDSSIAFHIAARVAQEQAQLVLTGFDRRLRQIRITDRLPAKAPLLELDVQNEEHLASLAGRVTEAIGAGNKLDGVVHSIGFMPQ	100							
InhA_MMAR	92.9%	MAGLLEGKRILVSGIITDSSIAFHIAARVAQEQAQLVLTGFDRMRLQIRIVDRLPKAPLIELDVQNEEHLASLAGRVTEVIGEGNKLDGVVHSIGFMPQ	100							
InhA_MAC	89.6%	MAGLLEGKRILVGTIITDSSIAFHIAKVAQEQAQLVLTGFDRRLRQIRIVDRLPEKAPLIELDVQNEEHLNTLAQRVTAEIGEGNKLDGVVHSIGFMPQ	100							
InhA_MKAN	95.2%	MAGLLEGKRILVSGIITDSSIAFHIAARVAQEQAQLVLTGFDRRLRQIRITDRLPKAPLLELDVQNEEHLATLADRVEAIGAGNKLDGVVHSIGFMPQ	100							

	110	120	130	140	150	160	170	180	190
InhA_MTB	TGMGINPFFDAPYADVSKGIHISAYSYSMAKALLPIMNPGGSIVGMDFDPSRAMPAYNWMTVAKSALESVNRVFVAREAGKYGVRSNLVAAGPIRTLAMS	200							
InhA_MAB	SGMGVNPFFDAPFADVSKGFHISAFYSYSLAKAVLPVMNRGGSIVGMDFDPTTRAMPAYNWMTVAKSALESVNRVFVAREAGKYGVRSNLVAAGPIRTLAMS	200							
InhA_MLP	TGMGTNQFFDAPYEDVSKGIHISTYSYASLAKALLIMNSGGSIVGMDFDPTTRAMPAYNWMTVAKSALESVNRVFVAREAGKYGVRSNLVAAGPIRTLAMS	200							
InhA_MBOV	TGMGINPFFDAPYADVSKGIHISAYSYSMAKALLPIMNPGGSIVGMDFDPSRAMPAYNWMTVAKSALESVNRVFVAREAGKYGVRSNLVAAGPIRTLAMS	200							
InhA_MMAR	SGMGINPFFDAPYEDVSKGIHISAYSYASLAKALLPIMNPGGSIVGMDFDPTTRAMPAYNWMTVAKSALESVNRVFVAREAGKYGVRSNLVAAGPIRTLAMS	200							
InhA_MAC	TGMGINPFFDAPYEDVSKGIHISAYSYASLAKALLPIMNPGGSIVGMDFDPSRAMPAYNWMTVAKSALESVNRVFVAREAGPHGVRSNLVAAGPIRTLAMA	200							
InhA_MKAN	TGMGINPFFDAPYEDVSKGIHISAYSYSMAKALLPIMNRGGSIVGMDFDPSRAMPAYNWMTVAKSALESVNRVFVAREAGKYGVRSNLVAAGPIRTLAMA	200							

	210	220	230	240	250	260	269
InhA_MTB	AIVGGALGEEAGAQIQLLEEGWDQRAPIGWNMKDPTPVAKTVCALLSDWLPATTGDIIFYADGGASTQLL						
InhA_MAB	AIVGGALGDEAGQMQLLLEEGWDQRAPIGWDMKDPTPVAKTVCALLSDWLPATTGDIIFYADGGASTQLL						
InhA_MLP	AIVGGAFGEEAGAQMQLLLEEGWDQRAPIGWNMKDPTPVAKTVCALLSEWLPATTGSIIFYADGGASTQLL						
InhA_MBOV	AIVGGALGEEAGAQIQLLEEGWDQRAPIGWNMKDPTPVAKTVCALLSDWLPATTGDIIFYADGGASTQLL						
InhA_MMAR	AIVGGALGEEAGAQIQLLEDGWDQRAPVGNMKDPTPVAKTVCALLSEWLPATTGDIIFYADGGASTQLL						
InhA_MAC	GIVGGVLGDDAAEQIRLLEEGWDQRAPIGWNMKDPTPVAKTVCALLSDWLPATTGTIIFYADGGASTQLL						
InhA_MKAN	AIVGGALGEEAGAQIQLLEEGWDQRAPIGWNMKDPTPVAKTVCALLSEWLPATTGDIIFYADGGASTQLL						

Figure S4. Multiple sequence alignments using Clustal Omega and the Jalview software of the InhA proteins from *M. tuberculosis* (MTB), *M. abscessus* (MAB), *M. leprae* (MLP), *M. bovis* (MBOV), *M. marinum* (MMAR), *M. avium* (MAC) and *M. kansasii* (MKAN). The percentage of protein identity relative to InhA_{MTB} is indicated in the left margin. The red rectangle indicates the position of the highly conserved Gly96 residue.

III. Human NLRP1 is a sensor of pathogenic coronavirus 3CL proteases in lung epithelial cells

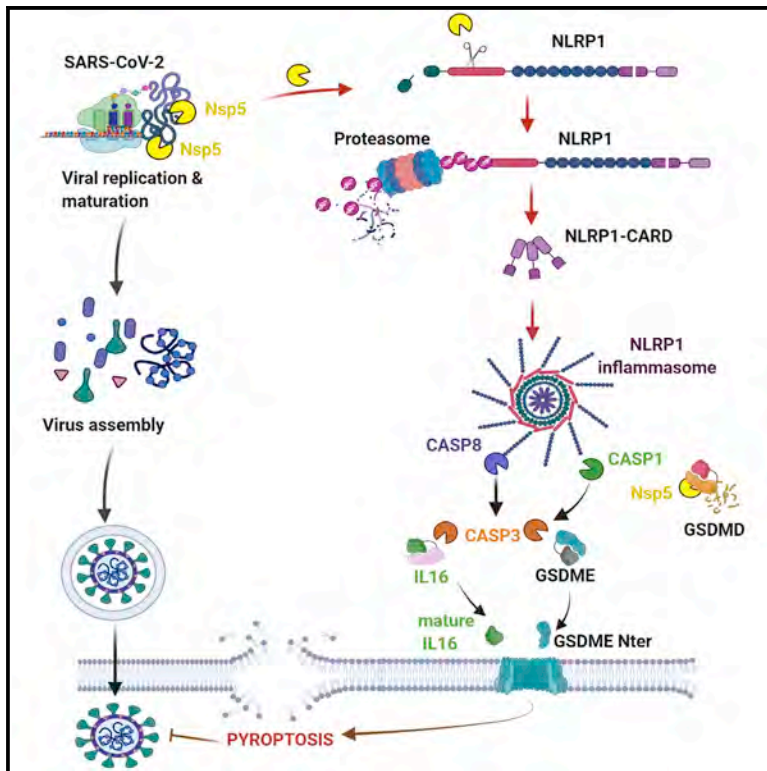
Authors: Rémi Planès, Miriam Pinilla, Karin Santoni, Audrey Hessel, Charlotte Passemar, Kenneth Lay, Perrine Paillette, Ana-Luiza Chaves Valadão, Kim Samirah Robinson, Paul Bastard, Nathaniel Lam, Ricardo Fadrique, Ida Rossi, David Pericat, Salimata Bagayoko, **Stephen Adonai Leon-Icaza**, Yoann Rombouts, Eric Perouzel, Michèle Tiraby, COVID Human Genetic Effort; Qian Zhang, Pietro Cicuta, Emmanuelle Jouanguy, Olivier Neyrolles, Clare E Bryant, Andres R Floto, Caroline Goujon, Franklin Zhong Lei, Guillaume Martin-Blondel, Stein Silva, Jean-Laurent Casanova, Céline Cougoule, Bruno Reversade, Julien Marcoux, Emmanuel Ravet, Etienne Meunier.

Contribution: I standardized and performed the human IL-16 ELISAs for Figure 5 of the article.

This article was published in Molecular Cell.

Human NLRP1 is a sensor of pathogenic coronavirus 3CL proteases in lung epithelial cells

Graphical abstract



Authors

Rémi Planès, Miriam Pinilla, Karin Santoni, ..., Julien Marcoux, Emmanuel Ravet, Etienne Meunier

Correspondence

remi.planes@ipbs.fr (R.P.),
etienne.meunier@ipbs.fr (E.M.)

In brief

Planès et al. identify human NLRP1 as an immune sensor of SARS-CoV2 3CL protease.

Highlights

- SARS-CoV-2 infection activates human NLRP1 inflammasome in epithelial cells
- NSP5 protease cleaves NLRP1 at Glutamine 333 and promotes functional degradation
- NSP5 inactivates GSDMD by cleaving in its pore-forming domain at Glutamine 193
- GSDME triggers alternative epithelial cell death upon GSDMD inactivation



Article

Human NLRP1 is a sensor of pathogenic coronavirus 3CL proteases in lung epithelial cells

Rémi Planès,^{1,2,3,23,24,*} Miriam Pinilla,^{1,2,24} Karin Santoni,^{1,24} Audrey Hessel,^{1,24} Charlotte Passemar,^{4,24} Kenneth Lay,^{5,6} Perrine Paillette,² Ana-Luiza Chaves Valadao,³ Kim Samirah Robinson,⁷ Paul Bastard,^{8,9,10} Nathaniel Lam,^{11,12} Ricardo Fadrique,¹³ Ida Rossi,¹ David Pericat,¹ Salimata Bagayoko,¹ Stephen Adonai Leon-Icaza,¹ Yoann Rombouts,¹ Eric Perouzel,² Michèle Tiraby,² COVID Human Genetic Effort,²⁶ Qian Zhang,⁹ Pietro Cicuta,¹³

(Author list continued on next page)

¹Institute of Pharmacology and Structural Biology (IPBS), University of Toulouse, CNRS, Toulouse, France

²In vivoGen, Toulouse, France

³IRIM, University of Montpellier, CNRS, Montpellier, France

⁴Molecular Immunity Unit, University of Cambridge Department of Medicine, MRC-Laboratory of Molecular Biology, Cambridge, UK

⁵Institute of Medical Biology, Agency of Science, Technology and Research, 8A Biomedical Grove, #06-06 Immunos, 138648 Singapore, Singapore

⁶Laboratory of Human Genetics and Therapeutics, Genome Institute of Singapore (GIS), A*STAR, Singapore, Singapore

⁷A*STAR Skin Research Laboratories, 11 Mandalay Road, 308232 Singapore, Singapore

⁸Laboratory of Human Genetics of Infectious Diseases, Necker Branch, Institut National de la Santé et de la Recherche Médicale U1163, Necker Hospital for Sick Children, Paris, France

⁹University of Paris, Imagine Institute, Paris, France

¹⁰St. Giles Laboratory of Human Genetics of Infectious Diseases, Rockefeller Branch, The Rockefeller University, New York, NY, USA

¹¹University of Cambridge, Department of Veterinary Medicine, Cambridge CB30ES, UK

¹²University of Cambridge, School of Clinical Medicine, Box 111, Cambridge Biomedical Campus, Cambridge CB2 0SP, UK

¹³Biological and Soft Systems, Cavendish Laboratory, University of Cambridge, JJ Thomson Avenue, Cambridge CB3 0HE, UK

(Affiliations continued on next page)

SUMMARY

Inflammation observed in SARS-CoV-2-infected patients suggests that inflammasomes, proinflammatory intracellular complexes, regulate various steps of infection. Lung epithelial cells express inflammasome-forming sensors and constitute the primary entry door of SARS-CoV-2. Here, we describe that the NLRP1 inflammasome detects SARS-CoV-2 infection in human lung epithelial cells. Specifically, human NLRP1 is cleaved at the Q333 site by multiple coronavirus 3CL proteases, which triggers inflammasome assembly and cell death and limits the production of infectious viral particles. Analysis of NLRP1-associated pathways unveils that 3CL proteases also inactivate the pyroptosis executioner Gasdermin D (GSDMD). Subsequently, caspase-3 and GSDME promote alternative cell pyroptosis. Finally, analysis of pyroptosis markers in plasma from COVID-19 patients with characterized severe pneumonia due to autoantibodies against, or inborn errors of, type I interferons (IFNs) highlights GSDME/caspase-3 as potential markers of disease severity. Overall, our findings identify NLRP1 as a sensor of SARS-CoV-2 infection in lung epithelia.

INTRODUCTION

Severe acute respiratory syndrome coronavirus 2 (SARS-CoV-2), responsible for coronavirus disease 2019 (COVID-19), has infected more than 219 million people worldwide. SARS-CoV-2 infection can induce multiorgan failure-associated sepsis with an increased risk in immune-deficient individuals and patients with particular pre-existing comorbidities (Al-Samkari et al., 2020; Cao, 2020; Carvalho et al., 2021; Berlin et al., 2020; Zheng et al., 2020). Given SARS-CoV-2 initially infects nasal, bronchial,

and lung epithelial cells, the host response in these cells can potentially control infection or may result in a response to SARS-CoV-2 that leads to excessive inflammation (Liu et al., 2021; Peng et al., 2021).

Inflammasomes comprise an important response to viral infection. These cytosolic multiprotein complexes are composed of a receptor/sensor, the adaptor protein ASC (at the noticeable exception of the CARD8 inflammasome), and the proinflammatory protease caspase-1 (Broz and Dixit, 2016). Upon inflammasome assembly, caspase-1 autoactivates and processes



Emmanuelle Jouanguy,^{8,9,10} Olivier Neyrolles,¹ Clare E. Bryant,^{11,12} Andres R. Floto,⁴ Caroline Goujon,³ Franklin Zhong Lei,^{7,14,15} Guillaume Martin-Blondel,^{16,17} Stein Silva,¹⁸ Jean-Laurent Casanova,^{8,9,10,19} Céline Cougoule,¹ Bruno Reversade,^{5,6,20,21,22} Julien Marcoux,¹ Emmanuel Ravet,^{2,25} and Etienne Meunier^{1,23,25,27,*}

¹⁴Lee Kong Chian School of Medicine, Nanyang Technological University, 11 Mandalay Road, 308232 Singapore, Singapore

¹⁵Skin Research Institute of Singapore (SRIS), 11 Mandalay Road, 308232 Singapore, Singapore

¹⁶Service des Maladies Infectieuses et Tropicales, CHU de Toulouse, Toulouse, France

¹⁷Institut Toulousain des Maladies Infectieuses et Inflammatoires (Infinity), INSERM UMR1291 - CNRS UMR5051 - Université Toulouse III, Toulouse, France

¹⁸Critical Care Unit, University Hospital of Purpan, Toulouse, France

¹⁹Howard Hughes Medical Institute, New York, NY, USA

²⁰Institute of Molecular and Cell Biology, 61 Biopolis Drive, 138673 Singapore, Singapore

²¹Department of Paediatrics, Yong Loo Lin School of Medicine, National University Health System, National University of Singapore, 10 Medical Drive, 117597 Singapore, Singapore

²²The Medical Genetics Department, Koç University School of Medicine, 34010 Istanbul, Turkey

²³Present address: Institute of Pharmacology and Structural Biology (IPBS), University of Toulouse, CNRS, Toulouse, France

²⁴These authors contributed equally

²⁵These authors contributed equally

²⁶Further details can be found in the supplemental information

²⁷Lead contact

*Correspondence: remi.planes@ipbs.fr (R.P.), etienne.meunier@ipbs.fr (E.M.)

<https://doi.org/10.1016/j.molcel.2022.04.033>

proinflammatory cytokines of the interleukin (IL)-1 family, IL-1 β and IL-18, as well as Gasdermin D (GSDMD) (Broz and Dixit, 2016). GSDMD cleavage activates a type of lytic cell death, pyroptosis, that also triggers the release of the cellular content (Broz and Dixit, 2016; Kayagaki et al., 2021). Although pyroptosis and IL-1-related cytokines are important defenses against a range of microbial infections, dysregulation of the inflammasome promotes excessive inflammation (Kayagaki et al., 2015; Shi et al., 2015; Yu et al., 2021). Specifically, IL-1-related cytokines are detected in SARS-CoV-2-infected patients and are suspected to directly and indirectly contribute to severe COVID-19-linked sepsis (Cauchois et al., 2020; Cavalli and Dagna, 2021; Junqueira et al., 2021; Lucas et al., 2020; Pan et al., 2021; Rodrigues et al., 2021; Yap et al., 2020).

As previously described, immunoblotting analysis of the expression of inflammasome-forming sensors in human primary epithelial and cell lines highlights that primary bronchial and alveolar epithelial cells specifically express the inflammasome-forming sensor NLRP1 (Figures 1A and S1A) (Bauernfried et al., 2021; Lee et al., 2019; Robinson et al., 2020).

NLRP1, a NOD-like receptor (NLR), exhibits a domain FIIND (function-to-find domain) that autocleaves NLRP1 into two proteins noncovalently connected (Chavarría-Smith et al., 2016; Chui et al., 2019; Johnson et al., 2018; Mitchell et al., 2019; Okondo et al., 2018; Sandstrom et al., 2019; Zhong et al., 2018). In this process, the proteases DPP8/DPP9 keep the C-Term CARD in an inactive conformation.

Pathogen-driven activation of the NLRP1 inflammasome can occur in the following different ways. First, cleavage of NLRP1 close to the N-terminal PYRIN domain can send N-terminal NLRP1 to the proteasome, thus allowing the C-terminal CARD domain to oligomerize and activate caspase-1 (Mitchell et al., 2019). This mechanism occurs when murine NLRP1B is exposed to the anthrax lethal factor (LF) protease (Chavarría-Smith et al., 2016; Chui et al., 2019; Sandstrom et al., 2019) and also in humans in response to enterovirus 3C cysteine proteases (Robinson et al., 2020; Tsu et al., 2021). Another mech-

anism that activates NLRP1 is binding of long double-stranded RNA detection to its NACHT- (NAIP [neuronal apoptosis inhibitor protein], C2TA [MHC class 2 transcription activator], HET-E [incompatibility locus protein from *Podospora anserina*] and TP1 [telomerase-associated protein]) LRR (Leucine-Rich Repeats) domain. This mechanism also promotes inflammasome signaling in keratinocytes and bronchial epithelial cells infected with the RNA-positive (+RNA) strand Semliki Forest Virus (Bauernfried et al., 2021). SARS-CoV-2 is a +strand RNA virus that expresses two proteases, a 3CL-(3C-like) protease, namely NSP5, and a chymotrypsin protease, NSP3. Thus, here, we evaluate the ability of NLRP1 to detect SARS-CoV-2 infection.

RESULTS

NLRP1 triggers an inflammasome response upon SARS-CoV-2 infection of epithelial cells

NLRP1 is expressed in primary airway epithelial cells, but its expression is lost in various human tumor cell lines (Figures 1A, S1A, and S1B), limiting the ability to use these cells to analyze the innate immune response to viral infection. Therefore, we expressed hNLRP1 in the alveolar epithelial cell line A549^{ACE2}. This cell line expresses endogenous ASC, caspase-1, and GSDMD (Figure S1A). Fluorescent (GFP)-tagged ASC was coexpressed in some experiments, allowing us to monitor inflammasome assembly upon NLRP1 activation and ASC polymerization (Figure S1B; Dick et al., 2016; Franklin et al., 2014; Lu et al., 2014). We activated NLRP1 using poly(I:C) or the pharmacological agent Val-boroPro (Val-boro) to evaluate the efficacy of our cell lines (Figures S1C–S1F; Johnson et al., 2018; Okondo et al., 2018). Transfection of poly(I:C) or treatment with various doses of Val-boro only triggered cell lysis in NLRP1-expressing cells (Figures S1C–S1E). In addition, only NLRP1-expressing cells contained ASC-GFP specks upon Val-boro treatment, indicating that this fusion protein can be used to monitor inflammasome assembly (Figure S1F).

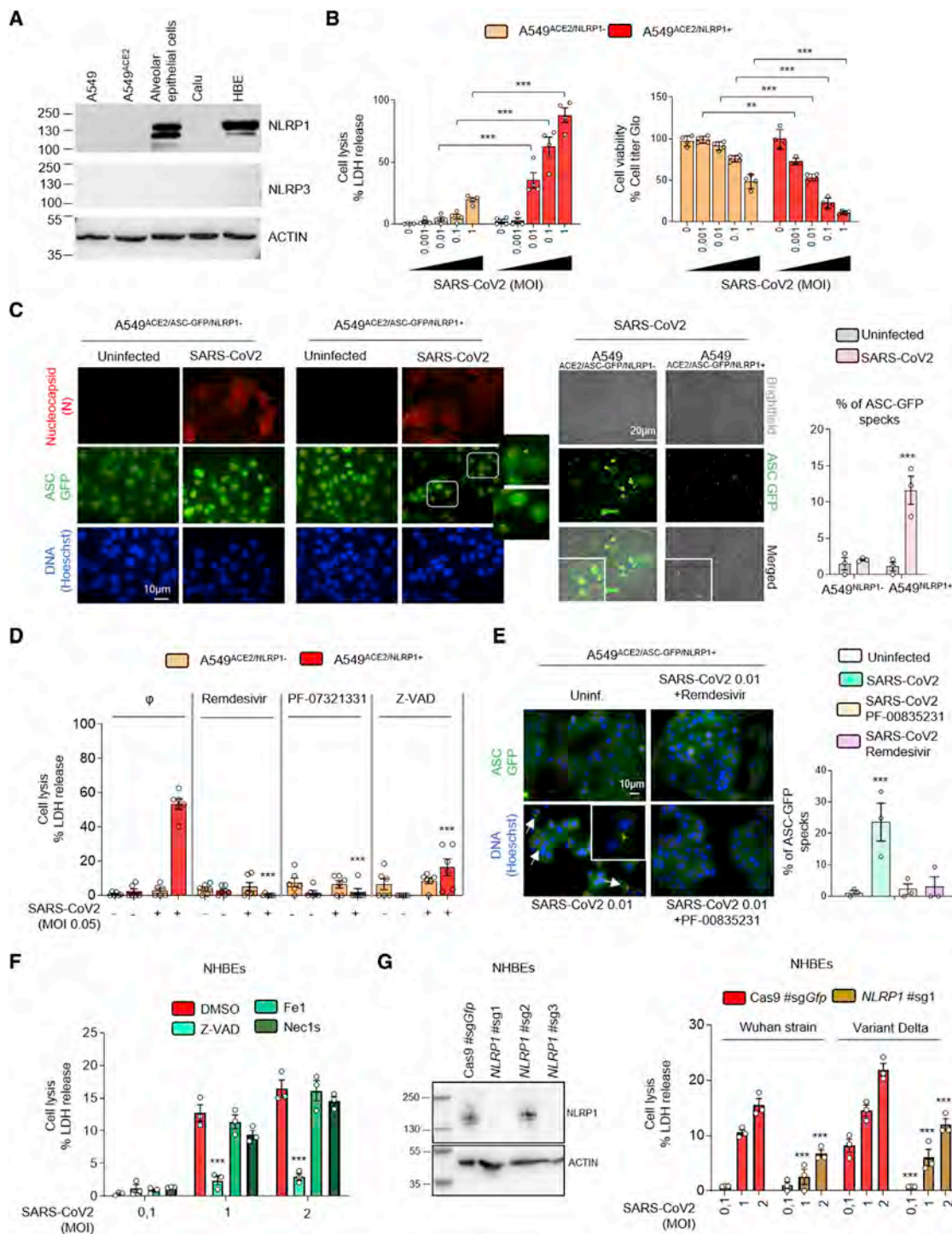


Figure 1. NLRP1 is an innate immune sensor of SARS-CoV-2 infection

(A) Western blot examination of NLRP1, NLRP3, and ACTIN in various human epithelial cells and cell lines.

(B) Cell death (LDH) and viability (ATP Glo) evaluation in A549^{ACE2/NLRP1+} and A549^{ACE2/NLRP1-} airway epithelial cell lines infected with various multiplicity of infection (MOI) of SARS-CoV-2 for 24 h.

(C) Fluorescence microscopy and associated quantifications of ASC-GFP specks in A549^{ACE2/NLRP1+/ASC-GFP} and A549^{ACE2/NLRP1-/ASC-GFP} airway epithelial cell lines infected with SARS-CoV-2 (MOI 0.05) for 24 h. Nucleus was stained with Hoechst (blue), and nucleocapsid (N) was stained in red after fixation. Brightfield/ASC-GFP pictures were taken in dish during cell infection. Images shown are from one experiment and are representative of n = 3 independent

(legend continued on next page)

Next, we infected A549^{ACE2/NLRP1+} or A549^{ACE2/NLRP1-} cells with various multiplicity of infection (MOI) of SARS-CoV-2 and monitored for cell lysis (LDH release), cell viability (ATP levels), and inflammasome activation (ASC-speck formation) over time (Figures 1B–1D). We observed that SARS-CoV-2 infection triggered a dose-dependent cell death of epithelial cells, a process that was dependent on the NLRP1 expression (Figures 1B and 1C). In addition, only cells expressing NLRP1 exhibited active inflammasome complexes upon SARS-CoV-2 infection, hence suggesting that NLRP1 is an innate immune sensor of SARS-CoV-2 infection (Figure 1C). In addition, we observed that such process occurred in the presence of various SARS-CoV-2 variants, suggesting that NLRP1-driven response is not directly impacted by the appearance of those viral mutations (Figure S1G). Although primary bronchial epithelial cells and A549^{ACE2/NLRP1+} cells do not express detectable levels of NLRP3, we controlled that NLRP3 was not involved in triggering this process by treating NHBEs and A549^{ACE2/NLRP1+} cells with an inhibitor of the NLRP3 inflammasome, namely MCC950 (Figures S1H and S1I). We observed no impact of MCC950 in the ability of SARS-CoV-2 to promote cell death or ASC-speck formation in either NLRP1⁺ or NLRP1⁻ cells (Figure S1H). The efficacy of MCC950 was also tested in THP1 human monocyte cell line, which express detectable levels of NLRP3 and inhibited the activation of NLRP3 inflammasome upon exposure with the well-known toxin nigericin (Figure S1I).

Next, we explored the viral steps that were required for efficient NLRP1 inflammasome activation upon SARS-CoV-2 infection. We used two inhibitors of SARS-CoV-2 replication, namely remdesivir that targets SARS-CoV-2 RNA polymerase and PF-00835231 that inhibits the activity of the 3CL NSP5 protease. Both inhibitors efficiently inhibited SARS-CoV-2 replication in A549^{ACE2/NLRP1+} cells as measured by the lack of appearance of the nucleocapsid (N) protein (Figure S1J). When we addressed the ability of both compounds to modulate SARS-CoV-2-dependent NLRP1 activation, we found that cell lysis (LDH release) levels as well as ASC-specks did not appear in presence of those inhibitors (Figures 1D and 1E). As control, those inhibitors did not show any effect in inhibiting NLRP1 inflammasome activation when cells were exposed to Val-boro (Figure S1K). Furthermore, the use of the pan-caspase inhibitor Z-VAD potently inhibited

SARS-CoV-2-induced NLRP1-dependent cell death both in primary and in A549^{ACE2/NLRP1+} cells, suggesting that caspases are important regulators of this process (Figures 1D and S1J).

Finally, we aimed at determining the reproducibility of our observations in primary human epithelial cells. Hence, we used normal human bronchial epithelial cells (NHBEs) and evaluated the importance of NLRP1 in SARS-CoV-2-driven epithelial cell death. Infection of NHBE with various SARS-CoV-2 strains led to the induction of cell death, a process that was strongly impaired in presence of the pan-caspase inhibitor Z-VAD but not in presence of Necroptosis inhibitor Nec1s or the ferroptosis inhibitor Fe1 (Figures 1F and S1L), suggesting a critical function of caspases in SARS-CoV-2-driven epithelial cell death. Next, we generated genetic inactivation of *NLRP1* gene expression using CRISPR-Cas9 in NHBE cells (Figure 1G). Infection of NHBE^{WT} and NHBE^{NLRP1-/-} epithelial cells with SARS-CoV-2 showed a significant involvement of NLRP1 expression in NHBE cell lysis after 36 h of infection (Figure 1G), hence confirming that NLRP1-dependent cell death occurs both in cell lines and in primary epithelial cells.

Altogether, our results suggest that in airway epithelial cells, NLRP1 behaves as a sensor of SARS-CoV-2, a process that requires viral replication.

SARS-CoV-2 3CL protease-cleaved NLRP1 triggers inflammasome assembly

Next, we wondered about the viral effectors able to drive NLRP1 activation. Both dsRNA and HRV 3C proteases promote NLRP1 degradation by the proteasome system that induces an efficient inflammasome response, a process we also observed upon SARS-CoV-2 infection (Figure S2A) (Bauernfried et al., 2021; Hollingsworth et al., 2021; Robinson et al., 2020; Sandstrom et al., 2019). However, 3C protease cleaves NLRP1 between Glutamine Q¹³⁰ and Glycine G¹³¹ sites, which generates a free Nter¹³¹ Glycine. This allows the recruitment of the Ubiquitin-processing complex Cullin ZER1/ZYG11B and the targeting of ubiquitinated-NLRP1 for proteasome degradation and subsequent release and activation of the Cter UPA-CARD domain (Robinson et al., 2020). Consequently, we infected A549^{ACE2/NLRP1+} cells with SARS-CoV-2 in the presence or absence of MLN4924, an inhibitor of the Cullin ZER1/ZYG11B complex, and evaluated the ability of cells to undergo cell lysis (Figure 2A; Eldeeb et al.,

experiments. For quantifications, the percentage of cells with ASC complexes was determined by determining the ratios of cells positives for ASC speckles on the total nuclei. At least 10 fields from $n = 3$ independent experiments were analyzed. Values are expressed as mean \pm SEM.

(D) Cell death (LDH) evaluation in A549^{NLRP1+} and A549^{NLRP1-} airway epithelial cell lines infected with SARS-CoV-2 (MOI 0.05) for 24 h in the presence/absence of the pan-caspase inhibitor Z-VAD (25 μ M), NSP5 protease inhibitor PF-00835231 (10 μ M), or the RNA-dependent RNA polymerase (RdRp) inhibitor remdesivir (5 μ M).

(E) Fluorescence microscopy and associated quantifications of ASC-GFP specks in A549^{ACE2/NLRP1+/ASC-GFP} and A549^{ACE2/NLRP1-/ASC-GFP} airway epithelial cell lines infected with SARS-CoV-2 (MOI 0.05) for 24 h. Nucleus was stained with Hoechst (blue). Brightfield/ASC-GFP pictures were taken in dish during cell infection. Images shown are from one experiment and are representative of $n = 3$ independent experiments; scale bars, 10 μ m. For quantifications, the percentage of cells with ASC complexes was determined by determining the ratios of cells positives for ASC speckles on the total nuclei. At least 10 fields from $n = 3$ independent experiments were analyzed. Values are expressed as mean \pm SEM.

(F) Cell death (LDH) evaluation in NHBE airway epithelial cells infected with various multiplicity of infection (MOI) of SARS-CoV-2 for 36 h in the presence/absence of the pan-caspase inhibitor Z-VAD (25 μ M), Necroptosis inhibitor Necrostatin-1s (Nec1s, 30 μ M), or the Ferroptosis inhibitor Ferrostatin-1 (Fe1, 10 μ M).

(G) Western blot characterization of genetic inactivation of *NLRP1* in NHBE population using CRISPR-Cas9 and measure of cell lysis (LDH release) in NHBE^{WT} and NHBE^{NLRP1-/-} airway epithelial cells infected with various multiplicity of infection (MOI) of Wuhan or Delta variant SARS-CoV-2 for 36 h. Efficiency of genetic inactivation by single-guide RNAs (sgRNAs) were evaluated at the whole cell population.

Data information: western blot (A and G) images are from one experiment performed 3 times. Graphs (B), (D), (F), and (G) show data presented as means \pm SEM from $n = 3$ (F and G), $n = 4$ (B) and $n = 6$ (D) independent pooled experiments; *** $p \leq 0.001$ for the indicated comparisons with t test. Images (C and E) are representative of one experiment performed 3 times.

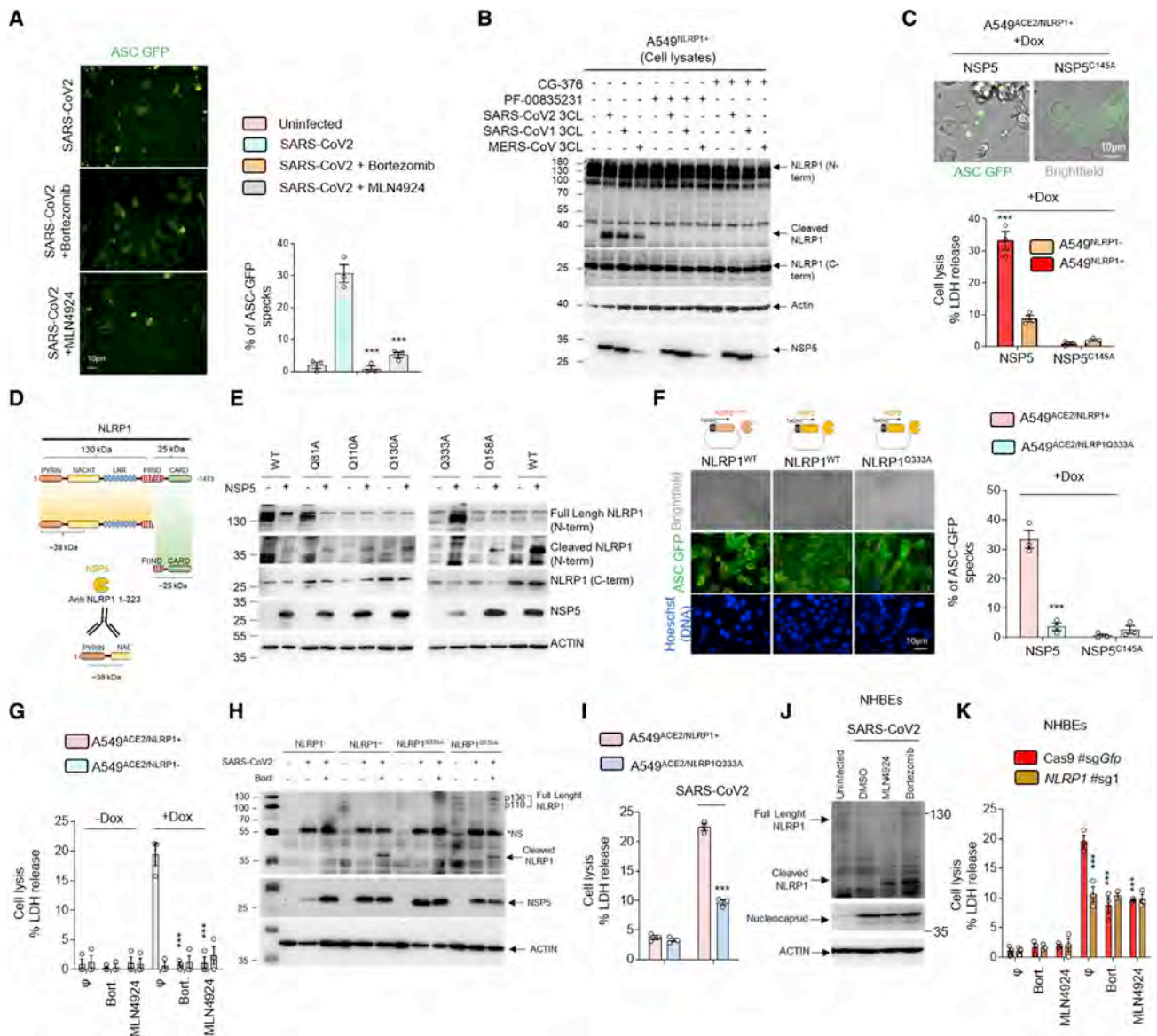


Figure 2. SARS-CoV-2 NSP5 protease-cleaved NLRP1 at the Q333 site nucleates NLRP1 inflammasome

(A) Fluorescence microscopy and associated quantifications of ASC-GFP specks in A549^{NLRP1+/ASC-GFP} and A549^{NLRP1-/ASC-GFP} airway epithelial cell lines infected with SARS-CoV-2 (MOI 0.05) for 24 h in the presence or absence of proteasome inhibitor bortezomib (0.1 μM) or inhibitor of the glycine N-degron pathway MLN4924 (1 μM). Images shown are from one experiment and are representative of n = 3 independent experiments; scale bars 10 μm. For quantifications, the percentage of cells with ASC complexes was determined by determining the ratios of cells positives for ASC speckles on the total cells presents in the wells. At least 10 fields from n = 3 independent experiments were analyzed. Values are expressed as mean ± SEM.

(B) Western blot examination of NLRP1 cleavage using an anti-NLRP1 N-terminal antibody (aa 1–323) upon coincubation of SARS-CoV-2, SARS-CoV-1, or MERS-CoV 3CL (NSP5) proteases (5 μM) with A549^{NLRP1+} airway epithelial cell lysates in presence or absence of the 3CL inhibitors GC-376 (10 μM) or PF-00835231 (10 μM). NLRP1 N-terminal, NLRP1 C-terminal, NSP5, and ACTIN were immunoblotted.

(C) Fluorescence microscopy and associated quantifications of ASC-GFP specks in A549^{NLRP1+/ASC-GFP} airway epithelial cell lines transduced with a doxycycline (dox)-inducible plasmid encoding NSP5 or its catalytically inactive mutant NSP5^{C145A}. Images shown are from one experiment and are representative of n = 3 independent experiments; scale bars, 10 μm. For quantifications, the percentage of cells with ASC complexes was determined by determining the ratios of cells positives for ASC speckles on the total cells presents in the wells. At least 10 fields from n = 3 independent experiments were analyzed. Values are expressed as mean ± SEM.

(D) Schematic representation of the approximate NLRP1 N-terminal fragment generated by NSP5 protease cut.

(E) Western blot examinations of the ability of NSP5 to cleave various NLRP1 constructs mutated in glutamine (Q) at various sites. Immunoblots show anti-N-terminal NLRP1, ACTIN, and NSP5.

(F) Fluorescence microscopy and associated quantifications of ASC-GFP specks in A549^{NLRP1+/ASC-GFP} or A549^{NLRP1Q333A/ASC-GFP} airway epithelial cell lines transduced with a doxycycline (dox)-inducible plasmid encoding NSP5 or its catalytically inactive mutant NSP5^{C145A}. Images shown are from one experiment

(legend continued on next page)

2019). The use of MLN4924 markedly inhibited SARS-CoV-2-induced NLRP1-dependent ASC-speck formation (Figure 2A). This suggested us that a SARS-CoV-2-dependent proteolytic cleavage of NLRP1 might be of importance in triggering inflammasome response in epithelial cells. As SARS-CoV-2 expresses both a 3CL protease NSP5 and a chymotrypsin protease NSP3, we hypothesized that one of those two proteases might cleave NLRP1 and generates a Glycine fragment accessible for Ubiquitination-driven NLRP1 degradation. Hence, we incubated NLRP1⁺ and NLRP1⁻ cell lysates with recombinant NSP3 or NSP5 proteases and analyzed by immunoblotting their ability to process NLRP1 by using an anti-NLRP1 N-terminal antibody (generated with the NLRP1 N-term peptide 1–323 aa) (Figures 2B and S2B–S2E). We observed that NSP5 protease cleaved NLRP1 and generated a 38 kDa Nterm-sized peptide, a process that was inhibited by the 3CL protease inhibitor PF-00835231 (Figures 2B, and S2B–S2D). As other coronaviruses also express 3CL proteases, we also incubated lysates of NLRP1-expressing cells with the MERS-CoV and SARS-CoV-1 3CL proteases. As for NSP5, both proteases also cleaved NLRP1 and generated an Nter fragment of similar sizes, suggesting a conserved ability of coronaviruses 3CL proteases to cleave NLRP1 (Figure 2B). Such process was also seen using recombinant NLRP1 protein in the presence of recombinant NSP5 proteases from pathogenic coronaviruses, hence suggesting that NSP5 alone is sufficient to mediate this process (Figures S2B and S2C). To further determine if NSP5 catalytic activity accounts at activating the NLRP1 inflammasome, we expressed doxycycline-inducible NSP5 or its catalytically inactive mutant (NSP5^{C145A}) in NLRP1⁺ and NLRP1⁻ cells. Monitoring for cell death and ASC-speck formation, we observed a strong ability of the WT NSP5 protease, but not its catalytically dead mutant, to promote both NLRP1-dependent cell death (LDH release) and GFP-ASC-speck formation, suggesting that NSP5 protease activity is required to nucleate an active NLRP1 inflammasome complex (Figure 2C).

Next, we determined where NSP5 cleaves NLRP1. The 3CL protease NSP5 is predicted to cleave after Glutamine (Q) in the amino acid triad LQA, LQS, LQN, or LQG (Anand et al., 2003; Kiemer et al., 2004). In addition, our observation that the anti-NLRP1 Nter antibody (aa 1–323) detected a fragment of approximately 38 kDa allowed us to map cleavage to a region in the

NLRP1 NACHT domain that contains the sequence ³³²LQG³³⁴ (Figures 2B–2D and S2D). Interestingly, protein alignments showed that this sequence is not conserved in murine Nlrp1B isoforms, suggesting that the NSP5-cleavage site in NLRP1 might be species specific (Figure S2D).

Therefore, we generated NLRP1-expressing constructs where Q333 is mutated to an Alanine (NLRP1^{Q333A}). We also used previously generated NLRP1 constructs that carry various mutations in Glutamine (Q) at different positions in the Nter domain (Robinson et al., 2020). Lysates from cells expressing the different NLRP1 mutants were incubated with NSP5. The SARS-CoV-2 protease cleaved NLRP1 and generated 38 kDa fragments from all constructs with the exception of NLRP1^{Q333A} (Figure 2E). To determine if the NLRP1^{Q333} site is important for NSP5-mediated NLRP1 inflammasome nucleation, we transduced ASC-GFP expressing cells with the NLRP1^{WT} or the NLRP1^{Q333A} construct and monitored for NSP5-induced ASC-speck formation and cell death. Cells expressing NLRP1^{WT} exhibited ASC-GFP specks, cell death induction, and proteasome/Cullin ligase-dependency upon NSP5 expression (Figures 2F and 2G). In contrast, NLRP1^{Q333A}-expressing cells did not show ASC-GFP specks or robust cell death upon NSP5 induction. We verified that the NLRP1^{Q333A} construct was still functional using nonprotease activators of NLRP1. Hence, Val-boro treatment induced NLRP1^{WT}- and NLRP1^{Q333A}-dependent cell lysis, suggesting that the NLRP1^{Q333} site is specifically required for efficient NLRP1-dependent cell death upon NSP5 exposure (Figure S2E).

Then, we aimed at determining if SARS-CoV-2-infected epithelial cells also engage NSP5-dependent NLRP1 cleavage. We infected A549^{ACE2/NLRP1+} cells with SARS-CoV-2 in the presence of bortezomib. Indeed, as NLRP1 cleavage leads to proteasomal degradation of the cleaved fragments, the used proteasome or Cullin ligase inhibitors allows cleaved fragment of NLRP1 accumulation and their putative observation by immunoblotting approaches. Thus, immunoblotting experiments against NLRP1 showed that SARS-CoV-2 infection in the absence of bortezomib did not allow detecting NLRP1 cleaved fragments (Figure 2H). However, treatment with bortezomib led to the detection of a cleaved NLRP1 fragment in A549^{ACE2/NLRP1+} and A549^{ACE2/NLRP1Q130A} cells, which was not seen in A549^{ACE2/NLRP1Q333A} cells, hence suggesting that the

and are representative of $n = 3$ independent experiments; scale bars, 10 μm . For quantifications, the percentage of cells with ASC complexes was determined by determining the ratios of cells positives for ASC speckles on the total nuclei (Blue). At least 10 fields from $n = 3$ independent experiments were analyzed. Values are expressed as mean \pm SEM.

(G) Cell death (LDH) evaluation in A549^{NLRP1+} and A549^{NLRP1-} airway epithelial cell lines expressing a doxycycline (dox)-inducible plasmid encoding NSP5 in the presence or absence of the proteasome inhibitor bortezomib (0.1 μM) or inhibitor of the glycine N-degron pathway MLN4924 (1 μM).

(H) Western blot examination of NLRP1 cleavage using an anti-NLRP1 N-terminal antibody (aa 1–323) after infection of A549^{NLRP1-}, A549^{NLRP1+}, A549^{NLRP1Q333A}, or A549^{NLRP1Q130A} airway epithelial cells with SARS-CoV-2 (MOI 0.05) for 24 h in the presence/absence of the proteasome inhibitor bortezomib (0.1 μM , Bort.). NLRP1 N-terminal, NSP5, and ACTIN were immunoblotted. *NS: prominent nonspecific bands, not specific.

(I) Cell death (LDH) evaluation in A549^{NLRP1+} and A549^{NLRP1Q333A} airway epithelial cell lines infected with SARS-CoV-2 (MOI 0.05) for 24 h.

(J) Western blot examination of NLRP1 cleavage using an anti-NLRP1 N-terminal antibody (aa 1–323) after infection of NHBE^{WT} airway epithelial cells with SARS-CoV-2 (MOI 1) for 36 h in the presence/absence of the proteasome inhibitor bortezomib (0.1 μM) or inhibitor of the glycine N-degron pathway MLN4924 (1 μM). NLRP1 N-terminal, nucleocapsid, and ACTIN were immunoblotted.

(K) Measure of cell lysis (LDH release) in NHBE^{WT} and NHBE^{NLRP1-/-} airway epithelial cells infected with SARS-CoV-2 (MOI 1) for 36 h in the presence/absence of the proteasome inhibitor bortezomib (0.1 μM) or inhibitor of the glycine N-degron pathway MLN4924 (1 μM).

Data information: images (A, C, and F) show one experiment performed 3 times. Western blot (B, E, H, and J) images are from one experiment performed 3 times. Graphs (C, G, I, and K) show data presented as means \pm SEM from $n = 3$ independent pooled experiments; *** $p \leq 0.001$ for the indicated comparisons with t test.

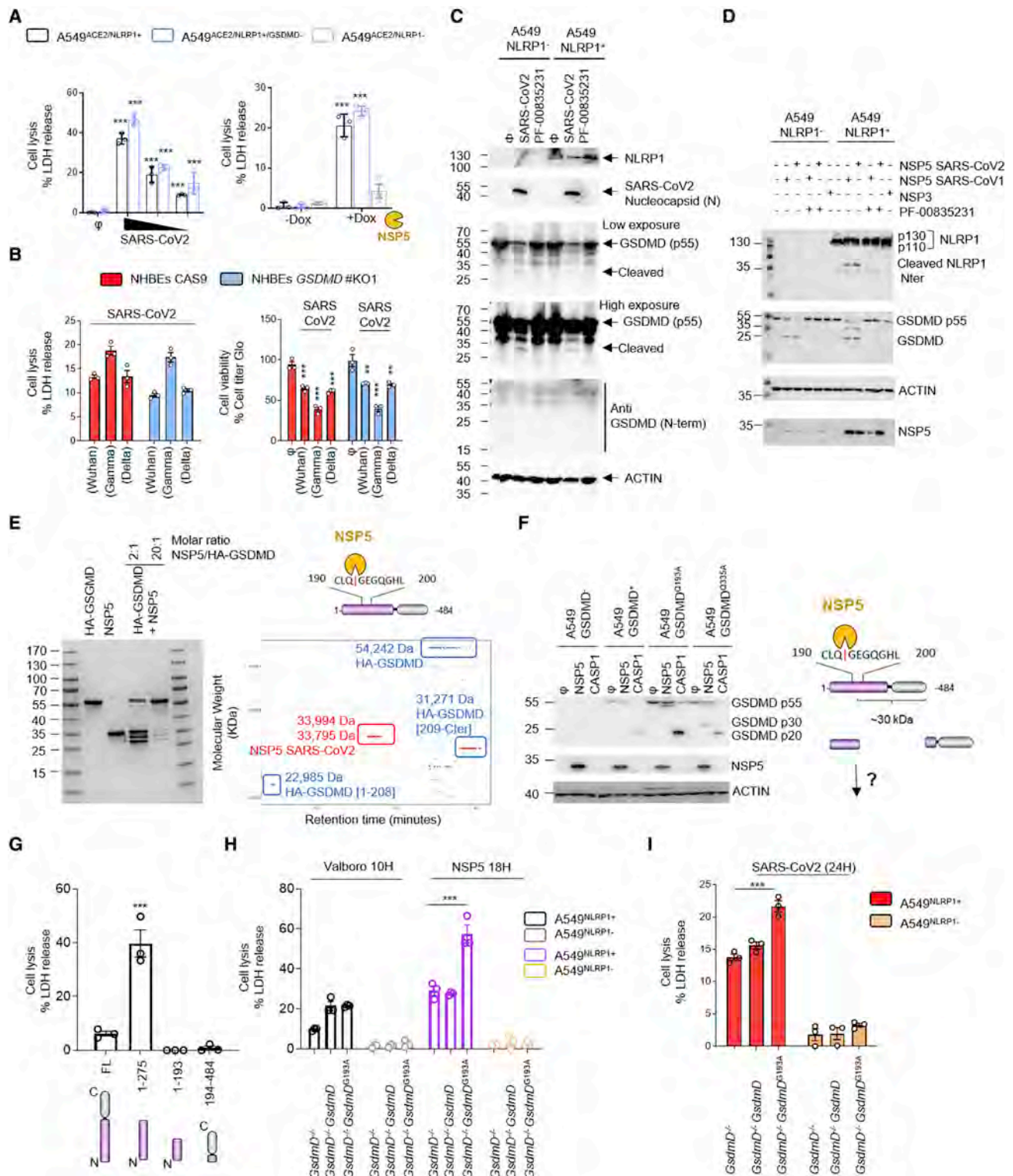


Figure 3. NSP5 protease cleaves Gasdermin D in its pore-forming domain

(A) Cell death (LDH) evaluation in A549^{NLRP1+}, A549^{NLRP1-}, or A549^{NLRP1+/GSDMD-} airway epithelial cell lines infected for 24 h with SARS-CoV-2 (MOIs 0.1, 0.01, and 0.001) or stimulated with doxycycline (dox)-induced NSP5 expression.

(B) Measure of cell lysis (LDH release) and cell viability (Cell titer Glo) in NHBE^{WT} and NHBE^{GSDMD-/-} airway epithelial cells infected with various SARS-CoV-2 viral strains (MOI 1) for 36 h.

(legend continued on next page)

NLRP1^{Q333} site is important for cleavage upon SARS-CoV-2 infection and can be significantly revealed when inhibiting proteasome-driven degradation (Figure 2H). Furthermore, A549^{ACE2/NLRP1Q333A} cells showed greater resistance to cell death than A549^{ACE2/NLRP1+} cells upon SARS-CoV2 infection, arguing that the Q333 site is important for efficient NLRP1 activation during viral infection (Figure 2I).

Finally, we performed NLRP1 immunoblotting in NHBE-infected cells with SARS-CoV-2 and also observed the accumulation of cleaved NLRP1 fragments in the presence of bortezomib or MLN4924 inhibitors (Figure 2J). Both bortezomib and MLN4924 inhibited SARS-CoV-2-dependent cell death in NHBE^{WT} (Figure 2K). Altogether, our results suggest that the SARS-CoV-2 protease NSP5 activates the NLRP1 inflammasome by cleavage at the NLRP1^{Q333} site, a process that depends on a functional degradation pathway (Figure S2F).

SARS-CoV-2 3CL protease dampens inflammasome signaling by inactivating Gasdermin D

In order to further understand the mechanism by which SARS-CoV-2 infection impacts cells, we next examined NLRP1 downstream effectors that promote cell death. Once an inflammasome is nucleated, it licenses caspase-1 autoactivation. Subsequent cleavage of the pyroptosis executioner GSDMD activates this pathway. Using CRISPR-Cas9 editing, we generated GSDMD KO lines in NHBE and A549^{ACE2/NLRP1+} cells and infected them with SARS-CoV-2 (Figures 3A, 3B, and S3A). However, we failed to detect a reliable involvement of GSDMD at regulating NLRP1-dependent cell death upon SARS-CoV-2 infection or NSP5 induction (Figures 3A and 3B). Similarly, immunoblots of infected cell samples (combined supernatants and cell extracts) showed a decrease in the proform of GSDMD (antibody anti-GSDMD-Cter) but also intermediate cleavage bands of GSDMD (25–30 kDa) that do not correspond to the size of active GSDMD (N.B. When using the anti-GSDMD Cter antibody, the expected size of caspase-1-processed GSDMD is around 20 kDa) (Figure 3C). In addition, the use of an antibody that specifically recognizes the active Nter GSDMD fragment failed to detect any active GSDMD (Figure 3B). This result was consistent in A549^{ACE2/NLRP1+} and A549^{ACE2/NLRP1-} cells, suggesting that

some protease-based, but inflammasome-independent, mechanism mediates this distinct processing of GSDMD (Figure 3B).

In order to determine whether SARS-CoV-2-encoded enzymes influence GSDMD activation independently of NLRP1, we tested the hypothesis that the GSDMD intermediate bands are generated by a viral protease. Therefore, we checked whether NSP3 and NSP5 directly or indirectly cleave GSDMD. Coincubation of NSP3 and NSP5 proteases with cell lysates led to GSDMD cleavage at distinct sites from caspase-1, suggesting that the SARS-CoV-2 NSP5 protease can cleave GSDMD (Figures 3D and S3B). We also analyzed the ability of NSP5 to cleave other Gasdermins, including GSDME and GSDMB, both expressed in epithelial cells. However, although NSP5 can cleave GSDMD, the viral protease was unable to cleave GSDMB or GSDME (Figure S3B). Next, we checked whether NSP5-cleaved GSDMD is active. GSDMD was incubated with NSP5, and the resulting mixture was subjected to proteomic analysis. This approach detected GSDMD fragments corresponding to the Nter of GSDMD 1-Q¹⁹³ (Figure 3E). In order to determine if NSP5 effectively cleaves at the Q¹⁹³ site of GSDMD, we expressed GSDMD^{WT}, GSDMD^{193A}, or GSDMD^{335A} encoding constructs in A549^{GSDMD} cells. This approach was previously used to detect enterovirus EV71 3C protease-mediated cleavage at this site (Lei et al., 2017). Incubation of cell lysates with either NSP5 or recombinant human caspase-1 (CASP1) showed that CASP1 efficiently cleaved all GSDMD constructs (Figures 3F and S3C). However, we observed that NSP5 was unable to process GSDMD^{Q193A}, suggesting that NSP5 cleaves GSDMD at the Q¹⁹³ site (Figures 3F and S3C).

Next, we transfected plasmids encoding for NSP5-generated GSDMD fragments (1–193, 194–484) in A549 cells and monitored for their pore-forming activity by measuring cell lysis induction. Although caspase-1-generated GSDMD^{1–275} fragment showed strong lytic activity in A549 cells, none of the NSP5-generated fragments showed pore-forming activity, suggesting that NSP5-cleaved Nterm GSDMD inhibits GSDMD-mediated pyroptosis (Figure 3G). To test our hypothesis, we generated cell expressing GSDMD mutated in the NSP5 cleavage site. Expression of NSP5 protease in cells expressing

(C) Western blot examination of Gasdermin D (GSDMD) processing in A549^{NLRP1+} cells infected with SARS-CoV-2 at MOI of 0.1 for 24 h. GSDMD was immunoblotted using an anti-C-terminal antibody (recognizes full-length and C-terminal cleaved forms of GSDMD) or with an anti-GSDMD active N-terminal fragment (30 kDa) specific antibody. NLRP1, ACTIN, and SARS-CoV-2 nucleocapsid were also evaluated.

(D) Western blot examination of GSDMD and NLRP1 cleavages upon coincubation of SARS-CoV-2 NSP3 protease or SARS-CoV-2/SARS-CoV1 3CL (NSP5) proteases (5 μM) with A549^{NLRP1+} or A549^{NLRP1-} cell lysates in the presence or absence of the 3CL inhibitor PF-00835231 (10 μM). GSDMD (anti C-terminal), NLRP1 N-terminal, NSP5, and ACTIN were immunoblotted.

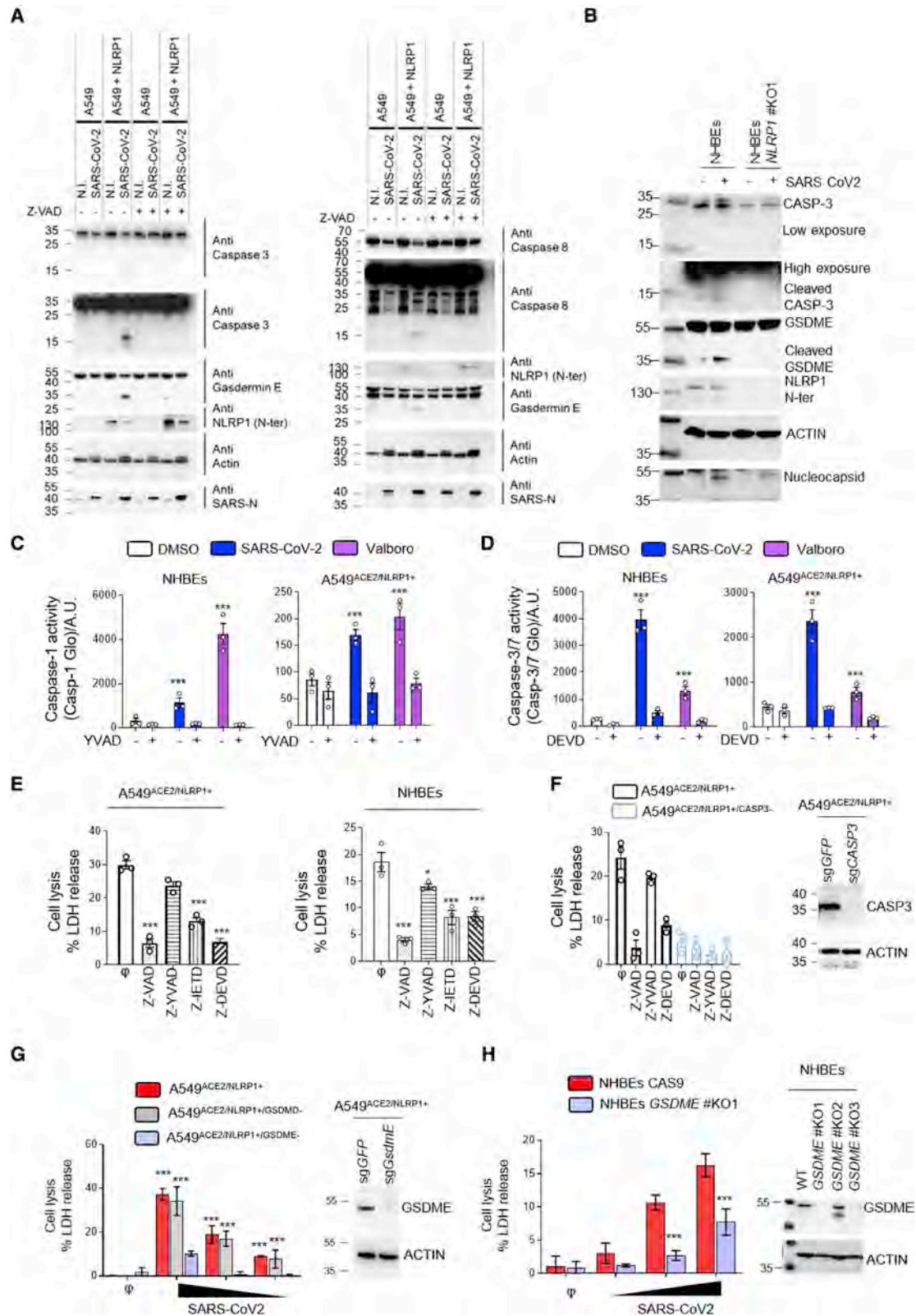
(E) Coomassie observation of recombinant GSDMD cleavage by various amounts of SARS-CoV-2 NSP5 protease and top-down mass-spectrometry identification of GSDMD-cleaved fragments. In blue are represented the various GSDMD fragments identified upon NSP5 coincubation. In red is the NSP5 protease detected by mass spectrometry.

(F) Western blot examination and schematic representation of GSDMD cleavage by SARS-CoV-2 3CL (NSP5) or recombinant human caspase-1 (CASP1) proteases in cell lysates from A549 expressing WT GSDMD or GSDMD^{193A} constructs. GSDMD (anti-C-terminal), NSP5, and ACTIN were immunoblotted.

(G) Cell death (LDH) evaluation in A549 cells expressing doxycycline-inducible GSDMD fragments, including GSDMD full-length (FL), caspase-1-generated active GSDMD (1–275), or NSP5-generated 1–193 and 194–484 GSDMD fragments. Cell lysis was determined 18 h after doxycycline (dox) addition in the culture medium.

(H and I) Cell death (LDH) evaluation in A549^{NLRP1+/GSDMD-} cells complemented or not with constructs coding for WT GSDMD or GSDMD^{193A}. Cells were transfected with dox-inducible NSP5 plasmids, treated with the NLRP1 activator Val-boro (10 μM) or infected (I) with SARS-CoV-2 (MOI 0.01). Cell lysis was determined 18 h after doxycycline (dox) addition, 10 h after Val-boro addition in the culture medium, or 24 h after infection.

Data information: graphs (A, B, G, H, and I) show data presented as means ± SEM from n = 3 independent pooled experiments; ***p ≤ 0.001 for the indicated comparisons with t test. Western blot (C, D, and F) images are from one experiment performed 3 times. Images (E) show one experiment performed 3 times.



(legend on next page)

NSP5-uncleavable GSDMD (GSDMD^{193A}) exhibited enhanced cell death, a process that was lowered in cells expressing WT GSDMD (Figure 3H). To the contrary, Val-boro-induced cell lysis was not altered by the presence of GSDMD^{193A} (Figure 3H). Finally, SARS-CoV-2 infection also induced higher cell death levels in GSDMD^{193A}-expressing cells than that in parental cells, suggesting that GSDMD cleavage by NSP5 might lower the efficiency of GSDMD-dependent pyroptosis upon inflammasome activation in epithelial cells (Figure 3I). Those results suggest that NSP5 can also counteract the inflammasome signaling by directly targeting and inactivating GSDMD.

NLRP1-driven caspase-3 activation promotes Gasdermin E-dependent pyroptosis of airway epithelial cells

The ability of epithelial cells to undergo NLRP1-dependent cell death, even in the absence of GSDMD activation, suggests that additional cell death effectors might be activated by SARS-CoV-2 infection. Previous studies revealed that caspase-1 and/or caspase-8 are important for activating caspase-3 (CASP3)/Gasdermin E (GSDME)-dependent cell death in the absence of GSDMD expression (Heilig et al., 2020; Orzalli et al., 2021; Taabazuig et al., 2017; Tsuchiya et al., 2019; Zhou and Abbott, 2021). Depending on the cell type, CASP3/GSDME activation can trigger apoptosis, lytic apoptosis, or pyroptosis. We hypothesized that NLRP1 uses a distinct pathway involving caspase-3 and GSDMD to promote cell death upon SARS-CoV-2 infection. We tested for the presence of active caspase-8, active caspase-3, and cleaved GSDME in SARS-CoV-2-infected cells using immunoblotting. We observed the appearance of caspase-8 and caspase-3 active fragments as well as processed GSDME fragment in A549^{ACE2/NLRP1+} and HBE^{WT} but not in A549^{ACE2/NLRP1-} or HBE^{NLRP1-/-} cells (Figures 4A and 4B). In addition, the pan-caspase inhibitor Z-VAD strongly impaired GSDME cleavage, suggesting that

NLRP1-dependent caspase-8 and caspase-3 activation licenses GSDME cleavage (Figure 4A). Furthermore, quantitation of caspase-1 or caspase-3/7 activities in SARS-CoV-2-infected A549^{ACE2/NLRP1+} and HBE^{WT} cells revealed that the activity of both caspases is increased (Figures 4C and 4D). However, we noticed that the levels of caspase-1 activity in A549^{ACE2/NLRP1+} cells were extremely low (10 times lower) compared with those observed in HBE^{WT} cells (Figures 4C and 4D). Thus, to definitively determine if caspase-1 plays a role in SARS-CoV-2-driven epithelial cell death, we used specific inhibitors of caspase-8, caspase-1, and caspase-3 and monitored their ability to block NLRP1-dependent cell death upon SARS-CoV-2 infection both in A549^{ACE2/NLRP1+} and in HBE^{WT} cells. Although caspase-1 inhibition showed a negligible reduction in cell death both in A549^{ACE2/NLRP1+} and in HBE^{WT} cells, the most striking inhibition was observed in the presence of Z-VAD as well as the caspases-8 (Z-IETD)-specific and caspases-3 (Z-DEVD)-specific inhibitors (Figures 4E and 4F). These data suggest that in the absence of efficient GSDMD activation, NLRP1 triggers a compensatory pathway involving caspase-8 and caspase-3 in epithelial cells. As caspase-3 can cleave and activate GSDME, which generates pyroptosis in human keratinocytes (Orzalli et al., 2021), but not in macrophages or monocytes (Taabazuig et al., 2017), we explored whether the cell death we observed was caspase-3 and/or GSDME dependent. Hence, we generated A549^{ACE2/NLRP1+} cells deficient for either caspase-3 or GSDME and infected them with SARS-CoV-2 (Figure 4G). Analysis of cell death levels (LDH release) showed that both genetic removal caspase-3 and GSDME improved cell survival upon SARS-CoV-2 infection (Figures 4G and 4H). Finally, SARS-CoV-2 infection of primary NHBE cells in which GSDME was knocked out supported the hypothesis that GSDME is involved in NHBE lysis upon SARS-CoV-2 infection. In short, our data argue that both caspase-3 and GSDME initiate lytic

Figure 4. NLRP1 engages a caspase-3/Gasdermin E-dependent pyroptosis pathway upon SARS-CoV-2 infection

(A) Western blot examination of Gasdermin E, caspases-3, and caspases-8 processing in A549^{NLRP1+} and A549^{NLRP1-} cells after 24 h of infection with SARS-CoV-2 (MOI 0.05) in the presence or absence of the pan-caspase inhibitor Z-VAD (25 μ M). Immunoblots were performed against full-length and processed forms of Gasdermin E (p55 and p30), caspase-8 (p54 and p15), caspase-3 (p35 and p17/19), SARS-CoV-2 nucleocapsid (p40), NLRP1 N-terminal (p130/110), and ACTIN (p40).

(B) Western blot examination of Gasdermin E and caspases-3 processing in HBE^{WT} and HBE^{NLRP1-/-} cells after 36 h of infection with SARS-CoV-2 (MOI 1). Immunoblots were performed against full-length and processed forms of Gasdermin E (p55 and p30), caspase-3 (p35 and p17/19), SARS-CoV-2 nucleocapsid (p40), NLRP1 N-terminal (p130/110), and ACTIN (p40).

(C and D) Measure of caspase-1 (C) and caspase-3/-7 (D) activities in SARS-CoV-2-infected (MOI 0.5) HBE^{WT} or A549^{NLRP1+} cells for 36 h in the presence or absence of inhibitors of caspase-1 (Z-YVAD, 40 μ M) or caspase-3/-7 (Z-DEVD, 30 μ M). Val-boro (5 μ M) was used a positive control of NLRP1-driven caspase activity for 10 h.

(E) Measure of cell lysis (LDH release) in A549^{NLRP1+} or HBE-infected cells with SARS-CoV-2 (MOI 0.05 and 1, respectively) for 24 h in the presence/absence of the pan-caspase inhibitor Z-VAD (25 μ M), the caspase-1 inhibitor Z-YVAD (40 μ M), the caspase-8 inhibitor Z-IETD (40 μ M), or the caspase-3 inhibitor Z-DEVD (30 μ M).

(F) Western blot characterization of genetic invalidation of CASP3 in A549 population cells using CRISPR-Cas9 approaches and measure of cell lysis (LDH release) in A549^{NLRP1+} or A549^{NLRP1+/CASP3-}-infected cells with SARS-CoV-2 (MOI 0.05) for 24 h in the presence/absence of the pan-caspase inhibitor Z-VAD (25 μ M), the caspase-1 inhibitor Z-YVAD (40 μ M), or the caspase-3 inhibitor Z-DEVD (30 μ M). Efficiency of genetic invalidation by single-guide RNAs (sgRNAs) targeting GFP or caspase-3 was evaluated at the whole cell population.

(G) Western blot characterization of genetic invalidation of GSDME in A549 population cells using CRISPR-Cas9 approaches and measure of cell lysis (LDH release) in A549^{NLRP1+}, A549^{NLRP1+/GSDMD-}, or A549^{NLRP1+/GSDME-}-infected cells with SARS-CoV-2 (MOIs 0.001, 0.01, and 0.1) for 24 h. Efficiency of genetic invalidation by single-guide RNAs (sgRNAs) targeting GFP or GSDME was evaluated at the whole cell population.

(H) Western blot characterization of genetic invalidation of GSDME in NHBE population cells using CRISPR-Cas9 approaches and measure of cell lysis (LDH release) in HBE^{WT} or HBE^{GSDME-/-}-infected cells with SARS-CoV-2 (MOIs 0.1, 0.5, and 1) for 36 h. Efficiency of genetic invalidation by single-guide RNAs (sgRNAs) targeting GFP or GSDME was evaluated at the whole cell population.

Data information: western blot (A, B, and E–G) images are from one experiment performed 3 times. Graphs (C–G) show data presented as means \pm SEM from $n = 3$ independent pooled experiments; *** $p \leq 0.001$ for the indicated comparisons with t test.

cell death in airway epithelial cells upon SARS-CoV-2 infection (Figure 4I).

Altogether, our results underline the crucial function of apoptotic caspase-3 and pyroptotic GSDME as sentinels that trigger efficient epithelial cell death induction during SARS-CoV-2 infection if the canonical pyroptosis executioner GSDMD is inactive.

NLRP1-dependent pyroptosis restricts the generation of viral infectious particles and promotes the release of alarmins/DAMPs

Next, we wondered about the immunological and microbicidal importance of SARS-CoV-2-induced NLRP1 inflammasome activation in epithelial cells. We monitored the viral titers in A549^{ACE2/NLRP1+}, A549^{ACE2/NLRP1-}, or NHBE^{WT}/NHBE^{NLRP1-/-} cells. Measuring the production of infectious particles by the TCID50 method, we observed that NLRP1-deficient cells were significantly more prone at generating SARS-CoV-2 viral particles (Figures S4A and S4B). However, we failed to see a robust involvement of NLRP1 at controlling SARS-CoV-2 replication as measured by the appearance of genes encoding SARS-CoV-2 RNA polymerase (Figure S4C). This suggested to us that pyroptosis might be a good mean to restrict the generation of mature and infectious viral particles but does not account as a direct replication inhibitory mechanism.

As pyroptosis is a very well-known process able to promote the release of specific caspase-associated inflammatory cytokines (e.g., IL-1B/IL-18) but also various alarmins and DAMPs (damage-associated molecular patterns), we next aimed at determining the importance of NLRP1 at regulating alarmins/DAMPs release upon SARS-CoV-2 infection. We specifically dedicated our analysis on already known alarmins and pyroptosis markers such as HMGB1, IL-18, and IL-1B, but also the caspase-3-derived alarmin interleukin-16 (IL-16). IL-16 is not an inflammasome-derived alarmin; however, its cleavage by caspase-3 allows its maturation and release. Hence, given the strong involvement of the caspase-3/GSDME axis in SARS-CoV2-dependent cell death, we also included IL-16 in our analysis as a read out of caspase-3-driven cytokine maturation and release. At the exception of IL-1B, all other alarmins/cytokines tested showed an NLRP1-dependent enrichment in the supernatant of infected A549^{ACE2/NLRP1+} and NHBE^{WT} cells, hence confirming that NLRP1-dependent pyroptosis in epithelial cells generates robust alarmin and DAMP responses (Figures S4D and S4E).

Plasmatic levels of caspase-3/IL-16 and Gasdermin E are associated with COVID-19 severity

Intriguingly, a recent report unveiled that IL-18 and IL-16 are enriched in plasma from severe COVID-19 pneumonia patients, suggesting that the inflammasome route might contribute to the development of the pathology in sensitive patients (Lucas et al., 2020). However, our results suggest that at least in 2D epithelial cell cultures, NLRP1 exhibits some protective function against SARS-CoV-2 infection (Figure S4A). Regarding this, about 20% of patients with critical COVID-19 pneumonia exhibit strong defect either in IFN response or in IFN production, suggesting that the IFN/inflammasome balance might be key in the regulation of COVID-19 severity (Asano

et al., 2021; Bastard et al., 2020, 2021a, 2021b; Koning et al., 2021; Zhang et al., 2020). Therefore, to test this hypothesis, we expressed NLRP1 in A549^{ACE2} cells deficient for the expression of MAVS, a central modulator of interferon production upon SARS-CoV-2 infection (Figures S5A–S5C). We next infected A549^{ACE2/NLRP1-/MAVS+}, A549^{ACE2/NLRP1+/MAVS+}, A549^{ACE2/NLRP1-/MAVS-}, and A549^{ACE2/NLRP1+/MAVS-} cells with SARS-CoV-2 and monitored for cell death. We observed a very strong induction of NLRP1-dependent cell lysis in MAVS-deficient cells, when compared with MAVS-expressing cells after 24 h of infection, suggesting that in absence of a proper IFN response, SARS-CoV-2 hyper replication triggers NLRP1 over activation (Figure S5A). As consequence, the release of the caspase-3-derived alarmin IL-16 as well as IL-18 in the supernatant of MAVS-deficient cells was strongly increased in response to SARS-CoV-2 (Figure S5B). Relying on those observations, we hypothesized that in healthy patients, where the IFN and inflammasome responses are well balanced, NLRP1 might actually be protective, a process completely lost in absence of a proper IFN response.

We obtained plasma samples from SARS-CoV-2 patients admitted at the hospital who exhibited three different profiles (WHO Working Group on the Clinical Characterization and Management of COVID-19, 2020). First, patients with moderate (non-hypoxemic) COVID-19 pneumonia on admission and throughout their stay at the hospital (group “Moderate” with a WHO score of 5); second, patients with moderate COVID-19 on admission with subsequent clinical worsening and severe COVID-19 (WHO score >5) requiring intensive care unit (ICU) admission (group “Moderate → Severe”); and third, patients with severe disease requiring ICU already on admission (group “Severe”) (Figures 5A and S5D).

We sampled 10–15 patients from each category, and already in this small cohort, we were able to distinguish significant trends in the levels of various pyroptosis markers, including a strong correlation between increased levels of plasma caspase-3 (CASP3), cleaved caspase-3, IL-18, IL-16, GSDMD, and GSDME with the severity status of patients (Figure 5A). IL-6 also showed deep correlation with COVID-19 severity as previously described; however, we failed to detect significant differences in IL-1B levels among the different type of patients we assayed (Figure 5A). As genetic or acquired alterations in IFN signaling pathways account for patient sensitivity to SARS-CoV-2 infection, we also analyzed plasma from patients with critical disease due to either genetic inactivating mutations of type I IFN signaling (TBK1, IFNAR1, and IRF7) or developing high titers of autoantibodies against type IFNs (Bastard et al., 2020; Zhang et al., 2020). As control, plasma from low/mid/severe patients were used to determine the relative differences of pyroptosis markers between those patients. All patients with IFN alterations showed a strong enrichment of IL-16, IL-18, CASP3, cleaved CASP3, GSDMD, and GSDME as previously seen with patients exhibiting severe COVID-19 (Figure 5A; Lopez et al., 2021; Wijst et al., 2021). Should NLRP1 specifically be involved will however require the development of more complex models such as humanized mouse for NLRP1. Nevertheless, our findings support a model between pyroptosis-associated markers and COVID-19 severity either in severe COVID-19 or in IFN-altered patients.

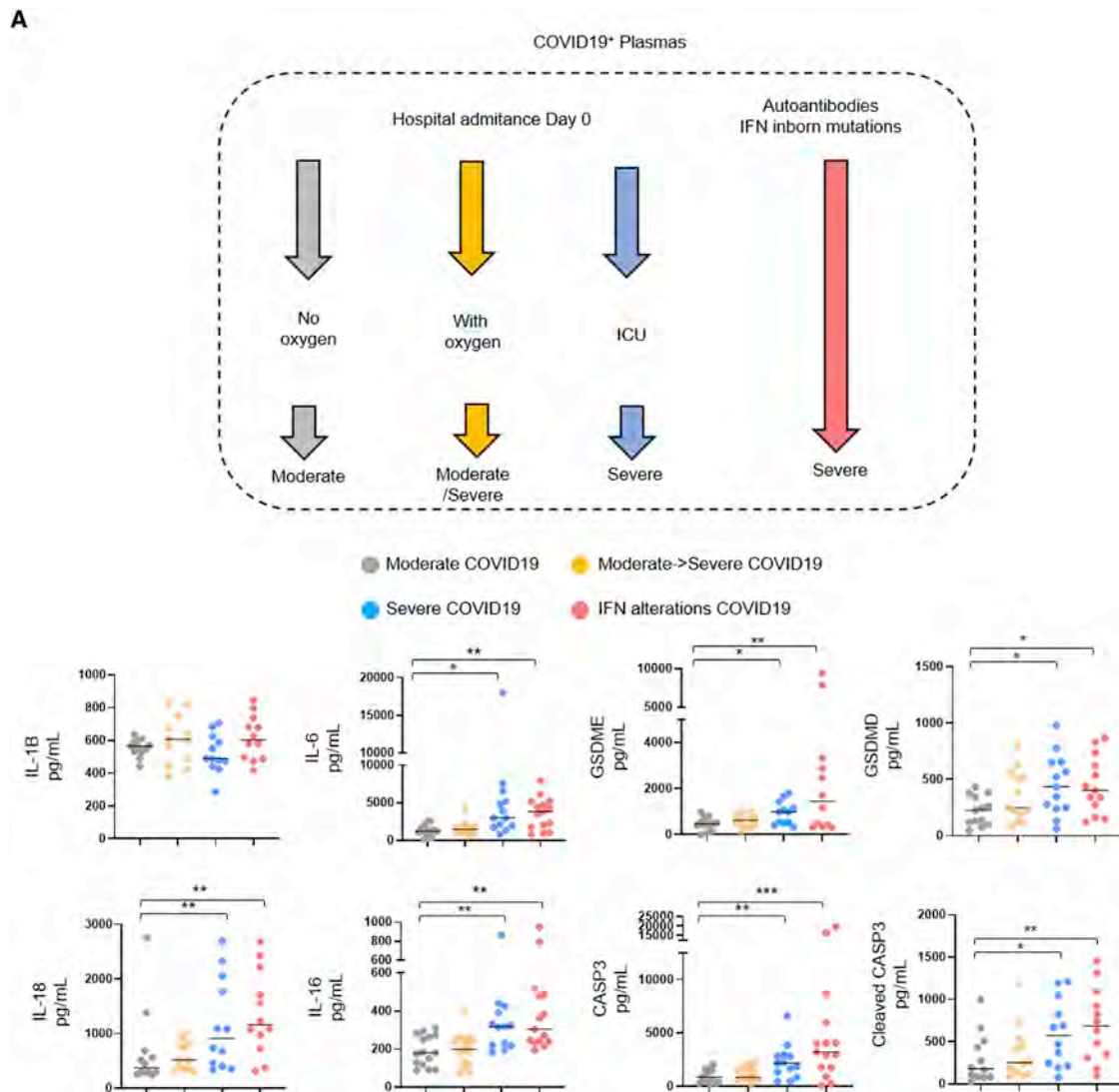


Figure 5. Caspase-3/IL-16 and GSDME as potential markers of COVID-19 severity

(A) Measure of the presence of various inflammatory mediators in plasmas from hospitalized patients presenting COVID-19 disease and analyzed according to their disease severity degree ($n = 60$ patients, including 15 with moderate COVID-19, 15 with moderate COVID-19 on admission, 15 with severe COVID-19 on admission, and 15 IFN alterations with severe COVID-19). Samples were prepared at day 0 posthospitalization.

Data information: data shown as means from $n = 12$ different donors per category (moderate/moderate \rightarrow severe/severe/IFN alterations); each category is represented with a colored circle; * $p \leq 0.05$, ** $p \leq 0.01$, *** $p \leq 0.001$ for the indicated comparisons using t test with Bonferroni correction.

DISCUSSION

Our study identifies NLRP1 as a central sensor of SARS-CoV-2 3CL protease NSP5 but also highlights NSP5 as a virulence factor against GSDMD-mediated pyroptosis. In line with pioneering studies on the ability of picornavirus 3C proteases to cleave human NLRP1 at a different site (Q¹³⁰-G¹³¹) and promote its activation, our study suggests that human NLRP1 is a broad protease sensor that carries evolutionary conserved decoy capabilities (Robinson et al., 2020; Tsu et al., 2021). Since human exposure to pathogenic coronavirus is relatively recent, how NLRP1 and GSDMD are so specifically targeted by viral proteases remains puzzling. Answers may come from future studies that test

whether NLRP1 and GSDMD are targets of viral proteases from nonpathogenic coronaviruses. Regarding this, the 3C protease from EV71 enterovirus was shown to cleave and inactivate GSDMD at the 193Q site (Lei et al., 2017). It is tempting to speculate that 3C and the closely related 3CL proteases might share conserved targets. Beyond this, two recent studies showed a particular ability of the bacterial pathogen *Shigella flexneri* to ubiquitinate both GSDMD and GSDMB and target them for proteasomal degradation, thereby allowing *Shigella* to establish a replicative niche in human cells (Hansen et al., 2021; Luchetti et al., 2021).

Beyond epithelial detection of pathogenic coronavirus proteases by NLRP1, the cytokine storm observed in SARS-CoV-2

associates with a NLRP3 inflammasome signature mostly driven by myeloid cells. Whether exaggerated NLRP1 inflammasome activation or a lack of NLRP1 response directly or indirectly promotes an NLRP3-dependent response in patient myeloid cells is an important future question to pursue. Similarly, recent findings from Bhaduri-McIntosh lab identified SARS-CoV-2 Orf3a as a trigger of the NLRP3 inflammasome in epithelial cells (Xu et al., 2022). In our epithelial cell models, we failed to detect robust NLRP3 expression; however, we always worked in the absence of priming. Whether, priming with various PRR ligands might promote NLRP3 expression in epithelial cells warrants further investigations.

Induction of a well-balanced innate immune response is central to controlling microbial infections, including those triggered by pathogenic coronaviruses (Broggi et al., 2019; Schultze and Aschenbrenner, 2021; Tay et al., 2020; Zheng et al., 2020). Consequently, any delay in a robust type I interferon production/response exposes the host to robust viral replication and exacerbated inflammation, leading to heavy organ damage (Asano et al., 2021; Bastard et al., 2020, 2021a, 2021b, 2021c; Galani et al., 2020; Hadjadj et al., 2020; Koning et al., 2021; Zannoni, 2021; Zhang et al., 2020). Our insights into NLRP1 inflammasome activation upon SARS-CoV-2 infection of epithelial cells *in vitro* suggest that NLRP1-driven inflammation might be both beneficial and detrimental in COVID-19 patients.

Overall, our results place the NLRP1 inflammasome as an innate immune sensor of the SARS-CoV-2 3CL protease but also highlight the virulence mechanisms by which this devastating virus counteracts cell intrinsic immunity.

Limitations of the study

The lack of conservation of the NLRP1 proteins between mice and humans strongly limits the physiopathological translation of our results into a broader and more complex model such as mice. The generation of humanized models in the future should help to determine the importance of the NLRP1 inflammasome in pathogenic coronavirus infections. Finally, although NLRP1 might be of importance to generate proinflammatory mediators at the epithelial barrier level, its role in the development of a cytokine storm observed in patients exhibiting severe COVID-19 has not been formally demonstrated in our study, which will require further investigations.

STAR★METHODS

Detailed methods are provided in the online version of this paper and include the following:

- KEY RESOURCES TABLE
- RESOURCE AVAILABILITY
 - Lead contact
 - Materials availability
 - Data and code availability
- EXPERIMENTAL MODEL AND SUBJECT DETAILS
 - Safety procedures
 - Ethical approvals of human studies
 - Cell culture
- METHOD DETAILS

- Cell engineering
- Generation of mutations in Gasdermin D gene
- Generation of mutations in NLRP1 gene
- Generation of doxycycline-inducible plasmids
- Cell transfection/transduction
- SARS-CoV-2 production and infection
- Virus titration by TCID₅₀ calculation
- Viral replication determination by qRT-PCR
- Cell death
- Cell viability
- Cytokines/Alarmins quantification
- Caspase activities
- Top-down LC-MSMS
- Human recombinant Gasdermin D production and purification
- Immunoblot
- *In vitro* cleavage assays
- Cell imaging
- Sample preparation for immunoblot
- Generation of knock-out cells by CRISPR/Cas9
- QUANTIFICATION AND STATISTICAL ANALYSIS

SUPPLEMENTAL INFORMATION

Supplemental information can be found online at <https://doi.org/10.1016/j.molcel.2022.04.033>.

CONSORTIA

The members of the COVID Human Genetic Effort are Tayfun Ozcelik, Nevin Hapitoglu, Filomeen Haerynck, Sevgi Keles, Ahmed A. Bousfiha, and Rafael Leon Lopez. For affiliation information, see the supplemental information.

ACKNOWLEDGMENTS

This project was funded by grants from the Fondation pour la Recherche Médicale (F.R.M.) and the ERC StG (INFLAME) to E.M., the ERC StG (ANTIVIR) to C.G., and the French Ministry of Health with the participation of the Groupement Interrégional de Recherche Clinique et d'Innovation Sud-Ouest Outre-Mer (PHRCI 2020 IMMUNOMARK-COV) to G.-M.B. The ASB3 structure is supported by LABEX, Investissement d'Avenir and foundation Bettencourt grants to O.N. M.P. and R.P. were, respectively, funded by a CIFRE PhD fellowship and a research grant from InvivoGen. S.B. is supported by a PhD fellowship from Mali Ministry of Education and from the FRM (FDT 12794). S.A.L.-I. is supported by a Vaincre La Mucoviscidose (VLM) PhD fellowship. We thank the following organizations for the highly valuable contribution of the COVID-BioToul biobank: the CRB TBR, the Clinical Research Center 1436, and the Delegation for clinical research and innovation of the Toulouse University Hospital. The authors acknowledge Celine Beronne and Flavie Moreau of the IPBS Institute Animal Facility Level 3 (ASB3) members for their help regarding the operating and technical procedures. The authors acknowledge BEI for SARS-CoV-2 material transfer, including SARS-CoV-2 variants, NSP5- and NSP5^{C145A}-expressing plasmids, and antibodies.

The authors deeply acknowledge all patients for their willingness and support in contributing and sharing samples for academic research. [Biorender.com](https://biorender.com) was used to generate some graphical figures. Life Science Editors performed language editing. Funders had no influence on how the project was conducted.

AUTHOR CONTRIBUTIONS

E.M. and R.P. conceptualized the study. E.M., R.P., E.R., M.P., K.S., A.H., and C.P. designed the methodology. R.P., M.P., K.S., A.H., C.P., P.P., A.-L.C.V., I.R., N.L., R.F., D.P., S.-A.L.-I., Y.R., C.G., C.C., and J.M. performed the

experiments. E.M., R.P., C.C., G.M.-B., and E.R. conducted the analysis. K.L., K.S.R., E.P., M.T., O.N., F.Z.L., G.M.-B., C.E.B., A.R.F., P.C., J.-L.C., B.R., E.R., E.P., C.G., and M.T. provided critical reagents and essential medical, technological, and infrastructure access and support. E.M., R.P., and E.R. wrote the manuscript with input from all authors. E.M., O.N., E.P., and M.T. acquired and provided funding.

DECLARATION OF INTERESTS

The authors declare no competing interests.

Received: October 19, 2021

Revised: February 16, 2022

Accepted: April 25, 2022

Published: May 16, 2022

REFERENCES

- Akama-Garren, E.H., Joshi, N.S., Tammela, T., Chang, G.P., Wagner, B.L., Lee, D.Y., Rideout, W.M., Papagiannakopoulos, T., Xue, W., and Jacks, T. (2016). A modular assembly platform for rapid generation of DNA constructs. *Sci. Rep.* **6**, 16836.
- Al-Samkari, H., Karp Leaf, R.S.K., Dzik, W.H., Carlson, J.C.T., Fogerty, A.E., Waheed, A., Goodarzi, K., Bendapudi, P.K., Bornikova, L., Gupta, S., et al. (2020). COVID-19 and coagulation: bleeding and thrombotic manifestations of SARS-CoV-2 infection. *Blood* **136**, 489–500.
- Anand, K., Ziebuhr, J., Wadhvani, P., Mesters, J.R., and Hilgenfeld, R. (2003). Coronavirus main proteinase (3CLpro) structure: basis for design of anti-SARS drugs. *Science* **300**, 1763–1767.
- Asano, T., Boisson, B., Onodi, F., Matuozzo, D., Moncada-Velez, M., Maglorius Renkilaraj, M.R.L.M., Zhang, P., Meertens, L., Bolze, A., Materna, M., et al. (2021). X-linked recessive TLR7 deficiency in ~1% of men under 60 years old with life-threatening COVID-19. *Sci. Immunol.* **6**, 65.
- Barger, C.J., Chee, L., Albahrani, M., Munoz-Trujillo, C., Boghean, L., Branick, C., Odunsi, K., Drapkin, R., Zou, L., and Karpf, A.R. (2021). Coregulation and function of FOXM1/ RHNO1 bidirectional genes in cancer. *eLife* **10**, e55070.
- Bastard, P., Gervais, A., Le Voyer, T., Rosain, J., Philippot, Q., Manry, J., Michailidis, E., Hoffmann, H.H., Eto, S., Garcia-Prat, M., et al. (2021a). Autoantibodies neutralizing type I IFNs are present in ~4% of uninfected individuals over 70 years old and account for ~20% of COVID-19 deaths. *Sci. Immunol.* **6**, eabl4340.
- Bastard, P., Orlova, E., Sozaeva, L., Lévy, R., James, A., Schmitt, M.M., Ochoa, S., Kareva, M., Rodina, Y., Gervais, A., et al. (2021b). Preexisting autoantibodies to type I IFNs underlie critical COVID-19 pneumonia in patients with APS-1. *J. Exp. Med.* **218**, 29.
- Bastard, P., Rosen, L.B., Zhang, Q., Michailidis, E., Hoffmann, H.H., Zhang, Y., Dorgham, K., Philippot, Q., Rosain, J., Béziat, V., et al. (2020). Autoantibodies against type I IFNs in patients with life-threatening COVID-19. *Science* **370**, eabd4585.
- Bastard, P., Zhang, Q., Cobat, A., Jouanguy, E., Zhang, S.Y., Abel, L., and Casanova, J.L. (2021c). Insufficient type I IFN immunity underlies life-threatening COVID-19 pneumonia. *C. R. Biol.* **344**, 19–25.
- Bauernfried, S., Scherr, M.J., Pichlmair, A., Duderstadt, K.E., and Hornung, V. (2021). Human NLRP1 is a sensor for double-stranded RNA. *Science* **371**, eabd0811.
- Berlin, D.A., Gulick, R.M., and Martinez, F.J. (2020). Severe Covid-19. *N. Engl. J. Med.* **383**, 2451–2460.
- Broggi, A., Granucci, F., and Zanoni, I. (2019). Cytokines Focus Type III interferons: balancing tissue tolerance and resistance to pathogen invasion. *J. Exp. Med.* **217**, e20190295.
- Broz, P., and Dixit, V.M. (2016). Inflammasomes: mechanism of assembly, regulation and signalling. *Nat. Rev. Immunol.* **16**, 407–420.
- Cao, X. (2020). COVID-19: immunopathology and its implications for therapy. *Nat. Rev. Immunol.* **20**, 269–270.
- Carvalho, T., Krammer, F., and Iwasaki, A. (2021). The first 12 months of COVID-19: a timeline of immunological insights. *Nat. Rev. Immunol.* **21**, 245–256.
- Cauchois, R., Koubi, M., Delarbre, D., Manet, C., Carvelli, J., Blasco, V.B., Jean, R., Fouche, L., Bornet, C., Pauly, V., et al. (2020). Early IL-1 receptor blockade in severe inflammatory respiratory failure complicating COVID-19. *Proc. Natl. Acad. Sci. USA* **117**, 18951–18953.
- Cavalli, G., and Dagna, L. (2021). The right place for IL-1 inhibition in COVID-19. *Lancet Respir. Med.* **9**, 223–224.
- Chavarría-Smith, J., Mitchell, P.S., Ho, A.M., Daugherty, M.D., and Vance, R.E. (2016). Functional and evolutionary analyses identify proteolysis as a general mechanism for NLRP1 inflammasome activation. *PLoS Pathog.* **12**, e1006052.
- Chui, A.J., Okondo, M.C., Rao, S.D., Gai, K., Griswold, A.R., Johnson, D.C., Ball, D.P., Taabazuig, C.Y., Orth, E.L., Vittimberga, B.A., et al. (2019). N-terminal degradation activates the NLRP1B inflammasome. *Science* **364**, 82–85.
- Corman, V.M., Landt, O., Kaiser, M., Molenkamp, R., Meijer, A., Chu, D.K., Bleicker, T., Brünink, S., Schneider, J., Schmidt, M.L., et al. (2020). Detection of 2019 novel coronavirus (2019-nCoV) by real-time RT-PCR. *Eurosurveillance* **25**, 2000045.
- Dick, M.S., Sborgi, L., Rühl, S., Hiller, S., and Broz, P. (2016). ASC filament formation serves as a signal amplification mechanism for inflammasomes. *Nat. Commun.* **7**, 1–13.
- Eldeeb, M., Esmaili, M., and Fahlman, R. (2019). Degradation of proteins with N-terminal glycine. *Nat. Struct. Mol. Biol.* **26**, 761–763.
- Eren, E., Planès, R., Bagayoko, S., Bordignon, P.J., Chaoui, K., Hessel, A., Santoni, K., Pinilla, M., Lagrange, B., Burlet-Schiltz, O., et al. (2020). Irgm2 and Gate-16 cooperatively dampen Gram-negative bacteria-induced caspase-11 response. *EMBO Rep.* **21**, e50829.
- Everman, J.L., Rios, C., and Seibold, M.A. (2018). Primary airway epithelial cell gene editing using CRISPR-Cas9. *Methods Mol. Biol.* **1706**, 267–292.
- Franklin, B.S., Bossaller, L., Nardo, D. De, Ratter, J.M., Stutz, A., Engels, G., Brenker, C., Nordhoff, M., Mirandola, S.R., Al-Amoudi, A., et al. (2014). ASC has extracellular and prionoid activities that propagate inflammation. *Nat. Immunol.* **15**, 727–737.
- Galani, I.-E., Rovina, N., Lampropoulou, V., Triantafyllia, V., Manioudaki, M., Pavlos, E., Koukaki, E., Fragkou, P.C., Panou, V., Rapti, V., et al. (2020). Untuned antiviral immunity in COVID-19 revealed by temporal type I/III interferon patterns and flu comparison. *Nat. Immunol.* **22**, 32–40.
- Hadjadj, J., Yatim, N., Barnabei, L., Corneau, A., Boussier, J., Smith, N., Péré, H., Charbit, B., Bondet, V., Chenevier-Gobeaux, C., et al. (2020). Impaired type I interferon activity and inflammatory responses in severe COVID-19 patients. *Science* **369**, 718–724.
- Hansen, J.M., de Jong, M.F., Wu, Q., Zhang, L.S., Heisler, D.B., Alto, L.T., and Alto, N.M. (2021). Pathogenic ubiquitination of GSDMB inhibits NK cell bactericidal functions. *Cell* **184**, 3178–3191.e18.
- Heilig, R., Dilucca, M., Boucher, D., Chen, K.W., Hancz, D., Demarco, B., Shkarina, K., and Broz, P. (2020). Caspase-1 cleaves Bid to release mitochondrial SMAC and drive secondary necrosis in the absence of GSDMD. *Life Sci. Alliance* **3**, e202000735.
- Hollingsworth, L.R., Sharif, H., Griswold, A.R., Fontana, P., Mintseris, J., Dagbay, K.B., Paulo, J.A., Gygi, S.P., Bachovchin, D.A., and Wu, H. (2021). DPP9 sequesters the C terminus of NLRP1 to repress inflammasome activation. *Nature* **592**, 778–783.
- Johnson, D.C., Taabazuig, C.Y., Okondo, M.C., Chui, A.J., Rao, S.D., Brown, F.C., Reed, C., Peguero, E., de Stanchina, E., Kentsis, A., et al. (2018). DPP8/DPP9 inhibitor-induced pyroptosis for treatment of acute myeloid leukemia. *Nat. Med.* **24**, 1151–1156.
- Junqueira, C., Crespo, A., Ranjbar, S., Ingber, J., Parry, B., Ravid, S., de Lacerda, L.B., Lewandrowski, M., Clark, S., Ho, F., et al. (2021).

SARS-CoV-2 infects blood monocytes to activate NLRP3 and AIM2 inflammasomes, pyroptosis and cytokine release. *Res. Sq.* <https://doi.org/10.21203/rs.3.rs-153628/v1>.

Kayagaki, N., Kornfeld, O.S., Lee, B.L., Stowe, I.B., O'Rourke, K., Li, Q., Sandoval, W., Yan, D., Kang, J., Xu, M., et al. (2021). NINJ1 mediates plasma membrane rupture during lytic cell death. *Nature* 591, 131–136.

Kayagaki, N., Stowe, I.B., Lee, B.L., O'Rourke, K., Anderson, K., Warming, S., Cuellar, T., Haley, B., Roose-Girma, M., Phung, Q.T., et al. (2015). Caspase-1 cleaves gasdermin D for non-canonical inflammasome signalling. *Nature* 526, 666–671.

Kiemer, L., Lund, O., Brunak, S., and Blom, N. (2004). Coronavirus 3CLpro protease cleavage sites: possible relevance to SARS virus pathology. *BMC Bioinformatics* 5, 72.

Koning, R., Bastard, P., Casanova, J.L., Brouwer, M.C., van de Beek, D., van Agtmael, M., Algera, A.G., Appelman, B., van Baarle, F., and Bax, D. (2021). Autoantibodies against type I interferons are associated with multi-organ failure in COVID-19 patients. *Intensive Care Med.* 47, 704–706.

Lee, S., Ishitsuka, A., Noguchi, M., Hirohama, M., Fujiyasu, Y., Petric, P.P., Schwemmler, M., Staeheli, P., Nagata, K., and Kawaguchi, A. (2019). Influenza restriction factor MxA functions as inflammasome sensor in the respiratory epithelium. *Sci. Immunol.* 4, eaau4643.

Lei, X., Zhang, Z., Xiao, X., Qi, J., He, B., and Wang, J. (2017). Enterovirus 71 inhibits pyroptosis through cleavage of gasdermin D. *J. Virol.* 91. e01069–e01017.

Liu, J., Li, Y., Liu, Q., Yao, Q., Wang, X., Zhang, H., Chen, R., Ren, L., Min, J., Deng, F., et al. (2021). SARS-CoV-2 cell tropism and multiorgan infection. *Cell Discov.* 7, 1–4.

Lopez, J., Mommert, M., Mouton, W., Pizzorno, A., Brengel-Pesce, K., Mezidi, M., Villard, M., Lina, B., Richard, J.C., Fassier, J.B., et al. (2021). Early nasal type I IFN immunity against SARS-CoV-2 is compromised in patients with autoantibodies against type I IFNs. *J. Exp. Med.* 218. jem.2021121108132021c.

Lu, A., Magupalli, V.G., Ruan, J., Yin, Q., Atianand, M.K., Vos, M.R., Schröder, G.F., Fitzgerald, K.A., Wu, H., and Egelman, E.H. (2014). Unified polymerization mechanism for the assembly of ASC-dependent Inflammasomes. *Cell* 156, 1193–1206.

Lucas, C., Wong, P., Klein, J., Castro, T.B.R., Silva, J., Sundaram, M., Ellingson, M.K., Mao, T., Oh, J.E., Israelow, B., et al. (2020). Longitudinal analyses reveal immunological misfiring in severe COVID-19. *Nature* 584, 463–469.

Luchetti, G., Roncaioli, J.L., Chavez, R.A., Schubert, A.F., Kofoed, E.M., Reja, R., Cheung, T.K., Liang, Y., Webster, J.D., Lehoux, I., et al. (2021). Shigella ubiquitin ligase IpaH7.8 targets gasdermin D for degradation to prevent pyroptosis and enable infection. *Cell Host Microbe* 29, 1521–1530.e10.

Mitchell, P.S., Sandstrom, A., and Vance, R.E. (2019). The NLRP1 inflammasome: new mechanistic insights and unresolved mysteries. *Curr. Opin. Immunol.* 60, 37–45.

Okondo, M.C., Rao, S.D., Taabazuing, C.Y., Chui, A.J., Poplawski, S.E., Johnson, D.C., and Bachovchin, D.A. (2018). Inhibition of Dpp8/9 activates the Nlrp1b inflammasome. *Cell Chem. Biol.* 25, 262–267.e5.

Orzalli, M.H., Prochera, A., Payne, L., Smith, A., Garlick, J.A., and Kagan, J.C. (2021). Virus-mediated inactivation of anti-apoptotic Bcl-2 family members promotes gasdermin-E-dependent pyroptosis in barrier epithelial cells. *Immunity* 54, 1447–1462.e5.

Pan, P., Shen, M., Yu, Z., Ge, W., Chen, K., Tian, M., Xiao, F., Wang, Z., Wang, J., Jia, Y., et al. (2021). SARS-CoV-2 N protein promotes NLRP3 inflammasome activation to induce hyperinflammation. *Nat. Commun.* 12, 1–17.

Peng, R., Wu, L.A., Wang, Q., Qi, J., and Gao, G.F. (2021). Cell entry by SARS-CoV-2. *Trends Biochem. Sci.* 46, 848–860.

Rebendenne, A., Valadão, A.L.C., Tauziet, M., Maarifi, G., Bonaventure, B., McKellar, J., Planès, R., Nisole, S., Arnaud-Arnould, M., Moncorgé, O., et al. (2021). SARS-CoV-2 triggers an MDA-5-Dependent interferon response which

is unable to control replication in lung epithelial cells. *J. Virol.* 95, e02415–e02420.

Reed, L.J., and Muench, H. (1938). A simple method of estimating fifty per cent endpoints. *Am. J. Epidemiol.* 27, 493–497.

Resnick, S.J., Iketani, S., Hong, S.J., Zask, A., Liu, H., Kim, S., Melore, S., Lin, F.Y., Nair, M.S., Huang, Y., et al. (2021). Inhibitors of coronavirus 3CL proteases protect cells from protease-mediated cytotoxicity. *J. Virol.* 95, e0237420.

Robinson, K.S., Teo, D.E.T., Tan, K.S., Toh, G.A., Ong, H.H., Lim, C.K., Lay, K., Au, B.V., Lew, T.S., Chu, J.J.H., et al. (2020). Enteroviral 3C protease activates the human NLRP1 inflammasome in airway epithelia. *Science* 370, eaay2002.

Rodrigues, T.S., de Sá, K.S.G., Ishimoto, A.Y., Becerra, A., Oliveira, S., Almeida, L., Gonçalves, A.V., Perucello, D.B., Andrade, W.A., Castro, R., et al. (2021). Inflammasomes are activated in response to SARS-CoV-2 infection and are associated with COVID-19 severity in patients. *J. Exp. Med.* 218, e20201707.

Sandstrom, A., Mitchell, P.S., Goers, L., Mu, E.W., Lesser, C.F., and Vance, R.E. (2019). Functional degradation: A mechanism of NLRP1 inflammasome activation by diverse pathogen enzymes. *Science* 364, eaau1330.

Sanjana, N.E., Shalem, O., and Zhang, F. (2014). Improved vectors and genome-wide libraries for CRISPR screening. *Nat. Methods* 11, 783–784.

Schultze, J.L., and Aschenbrenner, A.C. (2021). COVID-19 and the human innate immune system. *Cell* 184, 1671–1692.

Shi, J., Zhao, Y., Wang, K., Shi, X., Wang, Y., Huang, H., Zhuang, Y., Cai, T., Wang, F., and Shao, F. (2015). Cleavage of GSDMD by inflammatory caspases determines pyroptotic cell death. *Nature* 526, 660–665.

Taabazuing, C.Y., Okondo, M.C., and Bachovchin, D.A. (2017). Pyroptosis and apoptosis pathways engage in bidirectional crosstalk in monocytes and macrophages. *Cell Chem. Biol.* 24, 507–514.e4.

Tay, M.Z., Poh, C.M., Rénia, L., MacAry, P.A., and Ng, L.F.P. (2020). The trinity of COVID-19: immunity, inflammation and intervention. *Nat. Rev. Immunol.* 20, 363–374.

Tsu, B.V., Beierschmitt, C., Ryan, A.P., Agarwal, R., Mitchell, P.S., and Daugherty, M.D. (2021). Diverse viral proteases activate the nlrp1 inflammasome. *eLife* 10, 1–76.

Tsuchiya, K., Nakajima, S., Hosojima, S., Thi Nguyen, D., Hattori, T., Manh Le, T., Hori, O., Mahib, M.R., Yamaguchi, Y., Miura, M., et al. (2019). Caspase-1 initiates apoptosis in the absence of gasdermin D. *Nat. Commun.* 10, 1–19.

WHO Working Group on the Clinical Characterisation and Management of COVID-19 Infection (2020). A minimal common outcome measure set for COVID-19 clinical research. *Lancet Infect. Dis.* 20, e192–e197.

Wijst, M.G.P. van der, Vazquez, S.E., Hartoularos, G.C., Bastard, P., Grant, T., Bueno, R., Lee, D.S., Greenland, J.R., Sun, Y., Perez, R., et al. (2021). Type I interferon autoantibodies are associated with systemic immune alterations in patients with COVID-19. *Sci. Transl. Med.* 13, eab2624.

Xie, X., Muruato, A., Lokugamage, K.G., Narayanan, K., Zhang, X., Zou, J., Liu, J., Schindewolf, C., Bopp, N.E., Aguilar, P.V., et al. (2020). An infectious cDNA clone of SARS-CoV-2. *Cell Host Microbe* 27, 841–848.e3.

Xu, H., Akinyemi, I.A., Chitre, S.A., Loeb, J.C., Lednický, J.A., McIntosh, M.T., and Bhaduri-McIntosh, S. (2022). SARS-CoV-2 viroporin encoded by ORF3a triggers the NLRP3 inflammatory pathway. *Virology* 568, 13–22.

Yap, J.K.Y., Moriyama, M., and Iwasaki, A. (2020). Inflammasomes and pyroptosis as therapeutic targets for COVID-19. *J. Immunol.* 205, 307–312.

Yu, P., Zhang, X., Liu, N., Tang, L., Peng, C., and Chen, X. (2021). Pyroptosis: mechanisms and diseases. *Signal Transduct. Target. Ther.* 6, 1–21.

Zanoni, I. (2021). Interfering with SARS-CoV-2: are interferons friends or foes in COVID-19? *Curr. Opin. Virol.* 50, 119–127.

Zhang, Q., Bastard, P., Liu, Z., Le Pen, J., Moncada-Velez, M., Chen, J., Ogishi, M., Sabli, I.K.D., Hodeib, S., Korol, C., et al. (2020). Inborn errors of type I IFN immunity in patients with life-threatening COVID-19. *Science* 370, eabd4570.

Zheng, Z., Peng, F., Xu, X., Zhao, J., Liu, H., Peng, J., Li, Q., Jiang, Q., Zhou, Y., Liu, S., et al. (2020). Risk factors of critical & mortal COVID-19 cases: A systematic literature review and meta-analysis. *J. Infectol.* *81*, e16–e25.

Zhong, F.L., Robinson, K.S., Teo, D.E.T., Tan, K.Y., Lim, C., Harapas, C.R., Yu, C.H., Xie, W.H., Sobota, R.M., Au, V.B., et al. (2018). Human DPP9 represses

NLRP1 inflammasome and protects against autoinflammatory diseases via both peptidase activity and FIIND domain binding. *J. Biol. Chem.* *293*, 18864–18878.

Zhou, B., and Abbott, D.W. (2021). Gasdermin E permits interleukin-1beta release in distinct sublytic and pyroptotic phases. *Cell Rep.* *35*, 108998.

STAR★METHODS

KEY RESOURCES TABLE

REAGENT or RESOURCE	SOURCE	IDENTIFIER
Antibodies		
Anti- Gasdermin D (N-terminal), 1: 1000	ab215203;RRID: AB_2916166	Abcam
Anti- Gasdermin D (C-terminal), 1: 1000	ab210070;RRID: AB_2893325	Abcam
Anti- NLRP1 (N-terminal), 1: 1000	AF6788-SP;RRID: AB_2916167	R&D system
Anti- NLRP1 (C-terminal), 1: 1000	ab36852;RRID: AB_776633	Abcam
Anti -ACE2, 1: 1000	ab108252;RRID: AB_10864415	Abcam
Anti -TMPRSS2, 1: 1000	ab92323;RRID: AB_10585592	Abcam
Anti-actin 1: 5000	A1978;RRID: AB_476692	Sigma-Aldrich
anti-Sheep igG HRP (1/4000)	HAF016;RRID: AB_562591	R&D
Goat anti-mouse HRP (1/4000)	1034-05;RRID: AB_2794340	SouthernBiotech
Goat-anti-rabbit IgG (H+L), HRP conjugate (1/4000)	R-05072-500;RRID: AB_10719218	Advansta
Rabbit anti-Goat IgG (H+L) Secondary Antibody, HRP (1/4000)	81-1620;RRID: AB_2534006	Invitrogen
Donkey anti-Rabbit IgG (H&L) - Affinity Pure, DyLight®550 Conjugate (1/1000 IF)	DkxRb-003-D550NHSX;RRID: AB_2916168	ImmunoReagents
Anti Caspase 8 (1: 1000)	ALX-804-242-C100;RRID: AB_2050949	Enzo Life
Anti Caspase 1 (1: 1000)	AG-20B-0048-C100;RRID: AB_2916169	Adipogen
Anti Caspase 3 (1: 1000)	9662S;RRID: AB_331439	Cell Signaling
Anti gasdermin E (1: 1000)	Ab215191;RRID: AB_2737000	Abcam
Anti SARS NSP5 (1: 1000)	NBP3-07061;RRID: AB_2916170	Novusbio
Anti SARS Nucleocapsid (1: 1000)	NB100 56683;RRID: AB_838841	Novusbio
Bacterial and virus strains		
BetaCoV/France/IDF0372/2020	Sylvie van der Werf and the National Reference Centre for Respiratory Viruses	Institut Pasteur (Paris, France)
hCoV-19/USA/MD-HP05647/2021 (Delta Variant)		BEI
hCoV-19/USA/OR-OHSU-PHL00037/2021 (Alpha Variant)		BEI
hCoV-19/Japan/TY7-503/2021 (Gamma Variant)		BEI
Biological samples		
Plasma from Covid patients	Covid Biotoul cohort/Toulouse, France	Hospital of Toulouse
Plasma from patients with inborn mutations or autoantibodies	Institut Imagine/Covid genetic effort	Institut Imagine, Paris/France
Chemicals, peptides, and recombinant proteins		
Z-VAD: 40 μ M	tIrl-vad	Invivogen
Y-VAD: 40 μ M	inh-yvad	Invivogen
Z-DEVD: 40 μ M	S7312	Selleck Chemicals
Z-IETD: 40 μ M	inh-ietd	Invivogen
MCC950: 10 μ M	inh-mcc	Invivogen
VX765: 10 μ M	inh-vx765i-1	Invivogen
DMF: 10 μ M	S2586	Selleck Chemicals
MLN4924: 1 μ M	6499	Tocris
Remdesivir: 5 μ M	282T7766	Tebubio
Bortezomib: 0,1 μ M	S1013	Selleck Chemicals
PF-00835231: 10 μ M	S9731	Selleck Chemicals

(Continued on next page)

Continued

REAGENT or RESOURCE	SOURCE	IDENTIFIER
CG-376	SE-S0475	Euromedex
Nigericin	tlr-nig-5	Invivogen
Hoescht	62249	Invitrogen
Poly(I:C) HMW	tlr-pic	Invivogen
Nate	lyec-nate	Invivogen
Lipofectamine 2000	11668030	Invitrogen
Lipofectamine LTX	15338030	Invitrogen
Doxycycline	S5159	Selleck chemicals
Recombinant human IL-18	(rcyec-hil18)	Invivogen
Critical commercial assays		
IL-1B	88-7261-77	Fisher Scientific
IL-6	555220	BD
IL-16	DY316	R&D
Caspase 3	BMS2012INST	Invitrogen
Gasdermin E	AG-45B-0024-KI01	Adipogen
HMGB1	NBP2-62766	Novusbio
Deposited data		
Original blots and microscopy images	https://doi.org/10.17632/nwhd3w9w5x.1	Mendeley dataset
Experimental models: Cell lines		
THP1 KO NLRP3	Thp-konlrp3z	Invivogen
THP1	Thp-null	Invivogen
A549	A549d-nfis	Invivogen
A549-Dual™ ACE2 & TMPRSS2	a549d-cov2r	Invivogen
A549-Dual™ KO-MAVS Cells	a549d-komavs	Invivogen
A549 ACE2 & TMPRSS2 Cells	a549-hace2tpsa	Invivogen
IL-18 Reporter HEK 293 Cells	(hkb-hmil18)	Invivogen
Lonza, B-ALI kit 00193514	00193514	Lonza
Corning HTS Transwell-24 well permeable supports	CLS3379	Corning
Recombinant DNA		
LentiCas9-Blast	addgen ref 52962	(Sanjana et al., 2014)
p8.91	Didier Trono lab	Didier Trono lab
pMD.2G	addgene ref 12259	Didier Trono lab
LentiGuide-Puro	addgen ref 52963	(Sanjana et al., 2014)
Vector pLVX-EF1 α -IRES-Puro Containing the SARS-CoV-2, USA-WA1/2020 3C-Like Protease Gene, C145A Mutant	BEI NR-52953	BEI
pLEX307-SARS-CoV-2-3CL (NSP5)	addgene #160278	(Resnick et al., 2021)
pSC2+ NLRP1 constructs		(Robinson et al., 2020)
pLV-72-Cas9-GFP	N/A	Invivogen
pLVB-Tet ON	N/A	Invivogen
pLVB-TetR	N/A	Invivogen
pBRGEN	N/A	Invivogen
pMSCV-puro	Addgene plasmid # 68469	(Akama-Garren et al., 2016)
pMSCV-GsdmB	GeneScript	N/A

(Continued on next page)

<i>Continued</i>		
REAGENT or RESOURCE	SOURCE	IDENTIFIER
pMSCV-GsdmE	GeneScript	N/A
pMSCV-GsdmD	GeneScript	N/A
pCW57-RFP- P2A-MCS	Addgene #89182	(Barger et al., 2021)
LENTI V2 plasmid	Addgene 52961	N/A
Oligonucleotides		
sgRNA targeting Gasdermin E (Exon 2)	CAGTTTTTATCCCTCACCT	Sigma-Aldrich
sgRNA targeting Gasdermin E (Exon 2)	TAAGTTACAGCTTCTAAGTC	Sigma-Aldrich
sgRNA targeting Gasdermin E (Exon 3)	GTCGGACTTTGTGAAATACG	Sigma-Aldrich
sgRNA targeting Casp1 (Exon 2)	TTGTGAAGAAGACAGTTACC	Sigma-Aldrich
sgRNA targeting Casp1 (Exon 4)	AAGGATATGGAAACAAAAGT	Sigma-Aldrich
sgRNA targeting Gasdermin D (Exon 5)	TTAGGAAGCCCTCAAGCTCA	Sigma-Aldrich
sgRNA targeting Gasdermin D (Exon 6)	GAATGTGTACTCGCTGAGTG	Sigma-Aldrich
sgRNA targeting Gasdermin D (Exon 5)	AGGTTGACACACTTATAACG	Sigma-Aldrich
sgRNA targeting Caspase 3 (Exon 4)	CATACATGGAAGCGAATCAA	Sigma-Aldrich
sgRNA targeting Caspase 3 (Exon 5)	TGTCGATGCAGCAAACCTCA	Sigma-Aldrich
sgRNA targeting MAVS	ACCTCAGCAGATGATAGGCTCGGCC	Sigma-Aldrich
sgRNA targeting MAVS	ACCTCGCCCATCAACTCAACCCGTGC	Sigma-Aldrich
sgRNA targeting NLRP1 (Exon 2)	GCTCAGCCAGAGAAGACGAG	Sigma-Aldrich
sgRNA targeting NLRP1	GATAGCCCGAGTGACATCGG	Sigma-Aldrich
sgRNA targeting NLRP1	AGCCCGAGTGACATCGGTGG	Sigma-Aldrich
sgRNA targeting GFP	GGAGCGCACCATCTTCTCA	Sigma-Aldrich
Fwd Q333A	GAACCTCGCATAGTCATACT GGCGGGGGCTGCTGGAATTGGGAAG	Sigma-Aldrich
Rev Q333A	CTTCCCAATTCCAGCAGCCCCGCCA GTATGACTATGCGAGGTTC	Sigma-Aldrich
HA-GsdmD Q335A fwd2	GGCGCTGGAGgccGGCCAGAGCCTT GGGCC	Sigma-Aldrich
HA-GsdmD Q335 rev2	cgcaacccaacccccggatccCTAGTGGGG CTCCTGGCTC	Sigma-Aldrich
HA-GsdmD Q193 fwd	cagatcgctggagaattggctagcATGTACCCA TACGATGTTCCA	Sigma-Aldrich
HA-GsdmD Q193 rev	cgcaacccaacccccggatccctcaCTGCAAGC ACGTGGCTC	Sigma-Aldrich
HA-GsdmD N-ter fwd	cagatcgctggagaattggctagcATGTACCC ATACGATGTTCC	Sigma-Aldrich
HA-GsdmD N-ter rev	cgcaacccaacccccggatccctcaATCTGTCA GGAAGTTGTGG	Sigma-Aldrich
GsdmD Q193 fwd1	aggcgccggaattagatctctcgagatggactaca aagacgatgacgacaagGGTGGAGGTGGA GGTGA	Sigma-Aldrich
GsdmD Q193A rev1	GGCCCTCACCGgccCAAGCACGTGGC TCCGG	Sigma-Aldrich
HA-GsdmD Q193A fwd2	CACGTGCTTGgccGGTGGAGGGCCAG GGCCAT	Sigma-Aldrich
GsdmD Q193 rev2 pMSCV	ctcccctaccgtagaattcCTAGTGGGGC TCCTGGCTC	Sigma-Aldrich
GsdmD Q335 fwd1	aggcgccggaattagatctctcgagatggacta caaagacgatgacgacaagGGTGGAGG TGGAGGTGGAG	Sigma-Aldrich
GsdmD Q335A rev1	GGCTCTGGCCgccCTCCAGCGCC TCCTCCAA	Sigma-Aldrich

(Continued on next page)

Continued

REAGENT or RESOURCE	SOURCE	IDENTIFIER
HA-GsdmD Q335A fwd2	GGCGCTGGAGgccGGCCAGAGC CTTGGGCC	Sigma-Aldrich
GsdmD Q335 rev2 pMSCV	ctcccctaccggtagaattcCTAGT GGGGCTCCTGGCTC	Sigma-Aldrich
Recombinant proteins		
Recombinant SARS-COV 3CL	E-718-050	Novusbio
Recombinant SARS-CoV-2 3CL	E-720-050	Novusbio
Recombinant MERS-CoV 3CL	E-719-050	Novusbio
Recombinant human caspase-1 protein (active)	Ab39901	Abcam
Nsp3, peptidase C16 of PLpro	PX-COV-P004	proteogenix
HRV3C Protease	SAE0045	Sigma-Aldrich
Software and algorithms		
Snappgene	GSL Biotech LLC, Chicago, U.S.A.	N/A
Fiji (Image J)		N/A
Benchling Software		N/A
Image Lab 6.1 (Biorad)		N/A
Biorender.com		N/A
Graphpad 8.0a		N/A
Uniprot database		N/A

RESOURCE AVAILABILITY**Lead contact**

Further information and requests for resources and reagents listed in [method details](#) and [key resources table](#) sections should be directed to and will be fulfilled by the lead contact, Etienne Meunier, Etienne.meunier@ipbs or Emmanuel Ravet, e.ravet@invivogen.com

Regarding the [experimental model and subject details](#) that relate to medical aspects of this study, request of information must be sent to jean-laurent.casanova@inserm.fr and Guillaume-martin.blondel@chu-tlse.fr

Materials availability

Plasmids generated in this study are freely accessible upon request.

Cell lines generated in this study are freely accessible upon request and a completed Material Transfer Agreement (MTA).

Data and code availability

All data reported in this paper will be shared by the [lead contact](#) upon request.

Original blots and microscopy images are freely accessible in the following Mendeley data set: <https://doi.org/10.17632/nwhd3w9w5x.1>

Any additional information required to reanalyze the data reported in this paper is available from the [lead contact](#) upon request.

EXPERIMENTAL MODEL AND SUBJECT DETAILS**Safety procedures**

All described experiments involving SARS-CoV-2 infections (Microscopy of infected cells, Cell death assays, ELISA, sample preparation for Immunoblotting, virus production, TCDI50, RNA extraction) have been entirely performed and processed in a Biosafety Level 3 facility.

Ethical approvals of human studies**COVID-BioToul**

Clinical data and blood samples for plasma isolation and cryopreservation were collected at the Toulouse University Hospital, France, in the frame of the COVID-BioToul biobank (ClinicalTrials.gov Identifier: NCT04385108). All donors had given written informed consent and the study was approved by the ethical review board "Comité de Protection des Personnes Est-III" (ID-RCB 2020-A01292-37). Plasma samples were collected on admission to the hospital for COVID-19 proven by a positive PCR performed

on respiratory samples. COVID-19 patients were graded according to the severity on admission and on maximum severity during their hospitalization based on The World Health Organization's (WHO) ordinal scale (WHO Working Group on the Clinical Characterisation and Management of COVID-19, 2020). Patients were considered as having moderate disease when they required oxygen by mask or nasal prongs (WHO grade 5), and severe disease when they required high flow oxygen therapy, non-invasive ventilation, invasive ventilation, or extra-corporeal membrane oxygenation (WHO grade >5). Three groups of non-immunocompromised patients were identified for the purpose of this study: patients with moderate COVID-19 on admission and throughout their stay at the hospital (group "Moderate"); patients with moderate COVID-19 on admission with subsequent clinical worsening and severe COVID-19 requiring ICU admission (group "Moderate/Severe"); and patients with severe disease requiring ICU already on admission (group "Severe"). Mean age of COVID-19 patients was 60.8 ± 12 years, the percentage of females was 24.4.

Plasma from patients with interferon alterations

15 plasmas from patients with life-threatening COVID-19 pneumonia who developed critical disease (Bastard et al., 2020; Zhang et al., 2020) were obtained. Specifically, 3 patients exhibited inborn autosomic recessive (AR) or autosomic dominant (AD) mutation in genes encoding for interferon production/response, including AD TBK1 (MB019430), AR IRF7 (MB019096) and AR IFNAR1 (MB019091) (Zhang et al., 2020). The 12 other plasma samples came from COVID-19 patients with proven auto-antibodies to IFN α 2/IFN ω (Figure S5D; Bastard et al., 2020).

All donors had given written informed consent and the study was approved by local Institutional Review Boards (IRBs).

COVID-19 disease severity was assessed in accordance with the Diagnosis and Treatment Protocol for Novel Coronavirus Pneumonia. The term life-threatening COVID-19 pneumonia describes pneumonia in patients with critical disease, whether pulmonary, with mechanical ventilation [continuous positive airway pressure (CPAP), bilevel positive airway pressure (BIPAP), intubation, or high-flow oxygen], septic shock, or damage to any other organ requiring admission in the intensive care unit (ICU) (Bastard et al., 2020; Zhang et al., 2020).

Plasma and serum samples from the patients were frozen at -20°C immediately after collection.

Cell culture

Vero E6, Calu, THP1, HEK 293FT, THP1^{Nlrp3^{-/-}} and A549 cells were maintained in Dulbecco's modified Eagle's medium (DMEM, Gibco) supplemented with 10% heat-inactivated fetal bovine serum (FBS), 1% penicillin-streptomycin, and 1% L-glutamine.

Primary airway epithelial cells were from Epithelix and NHBE cells were from Lonza (CC-2540 and CC-2541).

Normal Human Bronchial Epithelial (NHBE) cell Air-Liquid interface (ALI) culture

NHBE cell culture was performed as suggested by the manufacturer (Lonza, B-ALI kit 00193514). Briefly, cells were seeded onto collagen-coated (0.03mg/mL) HTS Transwell-24 well permeable supports (Corning, CLS3379) at a density of $5 \cdot 10^4$ cells per insert for three days in B-ALI Growth Medium (Lonza, B-ALI kit 00193514). Cells were then cultured at the air-liquid interface in B-ALI Differentiating Medium (Lonza, B-ALI kit 00193514) at $37^{\circ}\text{C}/5\%\text{CO}_2$ for 20 days, with a medium change every two days.

For SARS infections, $100\mu\text{L}$ of $5 \cdot 10^4$ (MOI 0.5), $1 \cdot 10^5$ (MOI 1) or $2 \cdot 10^5$ (MOI 2) viral inoculum were added on cells for 3 hours. After washing two times the cells, medium was then replaced by B-ALI Differentiating Medium and cells were incubated for 24-36 hours before cell processing for further experiments.

For histological experiments, primary NHBEs were fixed for 30 minutes then processed using a Tissue-Tek VIP 6 and embedded using a Tissue-Tek TEC 5 (Sakura). Transwells were bisected and embedded vertically before sectioning. Serial paraffin sections ($4\mu\text{m}$) were prepared using a RM2135 rotary microtome (Leica), then deparaffinised with xylene and rehydrated with graded ethanols and water. For immunohistochemical staining, sections were heated for 15 minutes at 98°C in a citrate acid-based antigen unmasking solution (Vector Laboratories), then endogenous peroxidase activity blocked with 3% hydrogen peroxide for 15 minutes. Slides were stained in goat serum (1:5; G9023, Sigma) containing mouse monoclonal anti-SARS-CoV-2 spike (1:1000; GTX632604, GeneTex) for 90 minutes at 37°C . Following washing with TBS, sections were incubated with goat anti-mouse immunoglobulins/HRP (1:100; Dako) for 30 minutes at room temperature. Staining was visualised by application of diaminobenzidine for five minutes. For Alcian blue/periodic acid – Schiff (AB-PAS) staining, slides were stained in 1% Alcian blue in 3% acetic acid (Pioneer Research Chemicals) for five minutes, washed with water, then oxidised in 1% aqueous periodic acid (Acros Organics) for five minutes. Following another washing step, sections were stained in Schiff reagent (Thermo Fisher) for 10 minutes. All slides were counterstained with haematoxylin to stain the nuclei and mounted in DPX Mountant (Sigma-Aldrich) using a CV5030 fully automated glass coverslipper (Leica), then digitally scanned using a Nanozoomer 2.0HT at 40x objective (Hamamatsu).

METHOD DETAILS

Cell engineering

To reconstitute the NLRP1 inflammasome pathway in A549, cells were transduced with VSV-G pseudotyped lentiviral vector carrying the *NLRP1* gene (NCBI accession NP001028225.1) and/or *asc* (NCBI accession NP037390.2) fused to *gfp*. To render cells permissive to SARS-CoV-2 infections cells were transduced with VSV-G pseudotyped lentiviral vector carrying the *ace2* (NCBI accession NP068576.1) and *tmprss2* (NCBI accession NP001128571.1) genes. Engineered A549 cell lines were characterized for NLRP1, ASC-GFP, ACE-2 and TMPRSS2 expression by q-RT-PCR, immunoblot and flow cytometry.

To generate cells stably expressing *GSDMD* gene mutated for protease cleavage sites (*GSDMD*^{Q193A} and *GSDMD*^{Q335A}) we reconstituted *GSDMD* deficient cells with full length or mutated *GSDMD* constructs (*GSDMD*^{Q193A} and *GSDMD*^{Q335A}). Cells were transduced with VSV-G pseudotyped lentiviral vector carrying different *GSDMD* constructs in presence of 8 μg/ml polybrene and centrifugated for 2h at 2900 rpm at 32°C. 48 h later, medium was replaced and Puromycin selection (1 μg/mL) was applied to select positive clones for two weeks.

Generation of mutations in Gasdermin D gene

To express the N-terminal and C-terminal fragments of *GSDMD* generated following cleavage by Sars-CoV-2 3CL protease we used the following strategy: 1) nucleotide sequence coding for the N-terminal and C-terminal domains of *GSDMD* peptides were generated following proteases cleavage by using SnapGene software; 2) N-terminal and C-terminal *GSDMD* coding sequence were generated by PCR with the addition of a 5' Start codon ATG and 3' Stop codon TGA; 3) Amplified PCR fragments were cloned into pCW57-RFP-P2A-MCS lentiviral vector plasmid between BamHI and EcoRI restriction sites. This system allows ectopic expression of the N-terminal and C-terminal domains of *GSDMD* in order to study their activity.

To generate cells stably expressing *Gsdmd* gene mutated for protease cleavage sites (mutations *GSDMD*^{Q193A} and *GSDMD*^{Q335A}) we introduced point mutations in the *GSDMD* coding sequence by overlapping PCR and cloned mutated *GSDMD* in pMSCV-puro vector between BamHI and NotI restriction sites. Restriction enzymes were all from New England BioLabs. All the construct generated were verified by DNA sequencing (Eurofins genomics). Primers of the different constructions are listed in [key resources table](#).

Generation of mutations in NLRP1 gene

The transient expression plasmid of NLRP1Q333A was cloned into the pCS2+ vector using standard restriction cloning using ClaI and XhoI flanking the open reading frames. Site-directed mutagenesis was carried out with QuickChangeXL II (Agilent #200522) according to the manufacturer's instructions. Primers:

Rev Q333A: CTTCCCAATTCCAGCAGCCCCCGCCAGTATGACTATGCGAGGTTC

Fwd Q333A: GAACCTCGCATAGTCATACTGGCGGGGGCTGCTGGAATTGGGAAG

Generation of doxycycline-inducible plasmids

To generate doxycycline-inducible SARS-CoV-2 3-CL protease (NSP5) constructs, WT NSP5 or NSP5C145A were amplified by PCR from pLEX307-SARS-CoV-2-3-CL and pLVX-EF1α-IRES-Puro 3CL^{C145A} template respectively. PCR products were digested with AgeI and NheI restriction enzymes and digested insert were ligated in pLVB-TetON vector between AgeI and NheI restriction sites. To generate cell lines nsp5-inducible A549 cell lines, cells were transduced with both pLVB-nlr-TetR and pLVB-TetON-NSP5.

Primer1 (44-mer): ATTTATATTAACCGGTATGAGTGGTTTTAGAAAAATGGCATTCC

Primer2(45-mer): AATTATAATGCTAGCTTATTGGAAAGTAACACCTGAGCATTGTC

Cell transfection/transduction

A549 transfected with NLRP1 mutated plasmids

The day prior to the transfection, 2 x 10⁵ A549 cells were plated in 6 well plate in 10% FBS DMEM (Gibco) supplemented with 1% penicillin-streptomycin (Gibco). The day after, cells were treated with Nate 1X (Invivogen) for 30 min. DNA-lipids complexes were prepared with 1 μg of pCS2+ NLRP1 mutated plasmids ([Robinson et al., 2020](#)) or pCS2+ NLRP1^{Q333A}, lipofectamine LTX and PLUS reagent diluted in Opti-MEM and incubated for 30 min at room temperature according to the manufacturer's instructions (Invitrogen). DNA-lipid complexes were added to cells and incubated O/N at 37°C in 10% FBS DMEM.

A549 transfected with Gasdermin d plasmids

The day prior to the transfection, 2 x 10⁵ A549 dual cells were plated in 6 well plate in 10% FBS DMEM (Gibco) supplemented with 1% penicillin-streptomycin (Gibco). The day after, DNA-lipids complexes were prepared with 1 μg of *GSDMD*NT pcW57 plasmids and polyethylenimine (PEI) diluted in Opti-MEM. DNA-lipid complexes were added to cells and incubated for 48h at 37°C in Opti-MEM (Fischer Scientific).

SARS-CoV-2 production and infection

Experiments using SARS-CoV-2 virus were performed in BSL-3 environment. The BetaCoV/France/IDF0372/2020 isolate was supplied by Sylvie van der Werf and the National Reference Centre for Respiratory Viruses hosted by Institut Pasteur (Paris, France). The patient sample from which strain BetaCoV/France/IDF0372/2020 was isolated was provided by X. Lescure and PY. Yazdanpanah from the Bichat Hospital, Paris, France. The mNeonGreen (mNG) ([Xie et al., 2020](#)) reporter SARS-CoV-2 were based on 2019-nCoV/USA_WA1/2020 isolated from the first reported SARS-CoV-2 case in the USA, and provided through World Reference Center for Emerging Viruses and Arboviruses (WRCEVA), and UTMB investigator, Dr. Pei Yong Shi. SARS-CoV-2. Isolate hCoV-19/USA/MD-HP05647/2021 (Delta Variant), SARS-CoV-2, Isolate hCoV-19/USA/OR-OHSU-PHL00037/2021 (Alpha Variant) and SARS-CoV-2, Isolate hCoV-19/Japan/TY7-503/2021 (Gamma Variant) were obtained from BEI.

SARS-CoV-2 isolates were amplified by infecting Vero E6 cells (MOI 0.005) in DMEM (Gibco) supplemented with 10mM HEPES and 1% penicillin-streptomycin (Gibco). The supernatant was harvested at 48 h post-infection when cytopathic effects were observed,

cell debris were removed by centrifugation, and aliquots were frozen at -80°C . Viral stocks were titrated by plaque assays in Vero E6 cells. Typical titers were 5 to 10×10^6 PFU/ml.

The day prior to infection, 50,000 or 250,000 A549-ACE2-TMPRSS2, expressing or not NLRP1, cells were seeded in 96-well or 24-well tissue culture plates respectively in 10% FBS DMEM supplemented with 10mM HEPES (Gibco) and 1% penicillin-streptomycin (Gibco), and then incubated overnight at 37°C in a humidified, 5% CO_2 atmosphere-enriched chamber. The day after, cells were infected with mNeonGreen SARS-CoV-2 or the BetaCoV/France/IDF0372/2020 strains at indicated MOI in 50 μL DMEM supplemented with 10mM Hepes, 1% penicillin-streptomycin and 1% L-Glutamine for 1h at 37°C . Then, culture medium was completed up to 200 μL with DMEM or Opti-MEM.

Virus titration by TCID₅₀ calculation

The day prior to infection, 50,000 VeroE6 cells per well were seeded in 96-well tissue culture plates using 10% FBS DMEM, and then incubated overnight at 37°C in a humidified, 5% CO_2 atmosphere-enriched chamber. On the day of infection, serial 2.5-fold dilutions (from 10^{-1} to $10^{-6.5}$) of the A549 cell culture supernatant were prepared in DMEM and used to infect Vero E6 cells; each dilution was tested in four replicates. The plates were incubated for at least 96 h and observed to monitor the development of cytopathic effect (CPE) using an EVOS Fluid microscope (Invitrogen). Viral titers, expressed as TCID₅₀/mL, were calculated according to both Reed and Muench and Karber methods based on three or four replicates for dilution (Reed and Muench, 1938).

Viral replication determination by qRT-PCR

The day prior to infection, 100,000 NHBE, A549-ACE2-NLRP1- or A549-ACE2-NLRP1+ cells per well were seeded in 48-well plates. As previously described (Rebendenne et al., 2021), cells were infected or not with SARS-CoV-2 at the indicated MOI and harvested 24 h and 48 h later, and total RNA was extracted using the RNeasy kit (Qiagen) employing on-column DNase treatment, according to the manufacturer's instructions. 125 ng of total RNAs were used to generate cDNAs. To quantify SARS-CoV-2 RNAs, the cDNAs were analyzed by qPCR using published RdRp primers and probe (Corman et al., 2020), as follow: RdRp_for 5'-GTGARATGGT CATGTGTGGCGG-3', RdRp_rev 5'-CAAATGTAAAACTATTAGCATA-3', and RdRp_probe 5'-FAM-CAGGTGGAACCTCAT CAGGAGATGC-TAMRA-3'. A standard curve was used in parallel to calculate relative cDNA copy numbers and confirm the assay linearity. qPCR reactions were performed in triplicate, in universal PCR master mix using 900 nM of each primer and 250 nM probe or the indicated Taqmans. After 10 min at 95°C , reactions were cycled through 15 s at 95°C followed by 1 min at 60°C for 40 repeats. Triplicate reactions were run according to the manufacturer's instructions using a ViiA7 Real Time PCR system (ThermoFisher Scientific).

Cell death

Cell death was measured by quantification of the lactate dehydrogenase (LDH) release into the cell supernatant using LDH Cytotoxicity Detection Kit (Takara). Briefly, 50 μL cell supernatant were incubated with 50 μL LDH substrate and incubated for 15 min. The enzymatic reaction was stopped by adding 50 μL of stop solution. Maximal cell death was determined with whole cell lysates from unstimulated cells incubated with 1% Triton X-100.

Cell viability

Cell viability was measured by quantification of intracellular ATP using CellTiter-Glo® One Solution Assay (Promega) according to manufacturer's instructions.

Cytokines/Alarmins quantification

Human cytokines secretion were quantified by ELISA kits, according to the manufacturer's instructions, IL-1B (Thermo Fisher Scientific, (88-7261-77), IL-6 (BD, 555220), IL-16 (R&D, DY316), Caspase 3 (Invitrogen, BMS2012INST), Gasdermin E (AG-45B-0024-KI01), Gasdermin D (Abcam, ab272463), Cleaved Caspase-3/caspase-3 (Abcam, ab220655). Before use, the samples were diluted 1/3 to 1/5 with their respective assay diluents. IL-18 was quantified using IL-18 Reporter HEK 293 Cells according to the manufacturer's instructions (InvivoGen). HMGB1 was quantified by ELISA according to the manufacturer's instructions (Novus Biologicals).

Caspase activities

Caspase (G8090, G9951, Promega) activity were addressed in cells after 24 hours treatment or infection according to the manufacturer instructions.

Top-down LC-MSMS

Nano-LC-MSMS analyses of Gasdermin-D were performed on a nanoRS UHPLC system (Dionex) coupled to an LTQ-Orbitrap Fusion Tribrid mass spectrometer (Thermo Fisher Scientific). Briefly, a total of 5 μL of sample at ~ 1 -5 μM was loaded onto a reverse-phase C4-precolum (300 μm i.d. \times 5 mm; Thermo Fisher Scientific) at 20 $\mu\text{L}/\text{min}$ in 2% acetonitrile (ACN) and 0.2% formic acid (FA). After 5 minutes of desalting, the precolum was switched online with an analytical C4 nanocolum (75 μm i.d. \times 15 cm; in-house packed with C4 Reprosil) equilibrated in 95% solvent A (5% ACN, 0.2% FA) and 5% solvent B (0.2% FA in ACN). Proteins were eluted using a binary gradient ranging from 5% to 40% (5 minutes) and then 40% to 99% (33 minutes) of solvent B at a flow rate of 300 nL/min.

The Fusion Tribrid (Thermo Fisher Scientific) was operated in positive mode with the Xcalibur software (Thermo Fisher Scientific). The spray voltage was set to 1900 V, the ion transfer tube temperature to 350°C, the RF lens to 60%, and no in-source dissociation was applied.

MS scans were acquired in the 1000–2000 m/z range, in the Orbitrap at 7500 resolution with the following parameters: 10 μ scans for averaging, AGC target set to 3e5 and maximum injection time to 50 ms. 3 second MSMS cycles were used, with the following parameters: HCD activation was done with 25% activation energy, MSMS spectra were acquired in the Orbitrap at 60000 resolution. The AGC target was set to 1e6 and the maximum injection time to 400 ms. Dynamic exclusion for 60 s was used within 30 s to prevent repetitive selection of the same precursor (selection tolerance: \pm 20ppm) and improve the number of identified proteins. LC-MSMS.raw files were automatically deconvoluted with the rolling window deconvolution software RoWinPro and the proteoform footprints were visualized with VisioProt-MS v2.0. Spectra identification was done in Proteome Discoverer (Thermo Fisher Scientific) v.2.3, using a three Tier search including an Absolute Mass Search (precursor mass tolerance - 100 Da, fragment mass tolerance - 10ppm) followed by a Biomarker Search (no enzyme precursor tolerance - 100 ppm, fragment mass tolerance - 50 ppm) and a last Absolute Mass Search (precursor mass tolerance - 1000 Da, fragment mass tolerance - 10 ppm). The identified truncated proteoforms were then manually validated. The search database was generated using a custom made.fasta file containing the sequences of GSDMD and the 3CL protease.

Human recombinant Gasdermin D production and purification

Human recombinant Gasdermin D fused with an N-terminus hexahistidine-MBP-tag was expressed in BL21 (DE3) E coli strain and purified according to Shiyu Xia et al. (Monitoring Gasdermin pore formation in vitro, *Methods Enzymol.* 2019; 625: 95–107.) with slight modifications. Briefly, after cell harvest, bacteria were lysed by sonication under ice and recombinant human Gasdermin D was purified by a first nickel metal affinity chromatography (Takara). The 6His-MBP tag was removed by O/N TEV digestion at 4°C and a second nickel metal affinity chromatography was performed to separate the Gasdermin D (unbound fraction) from the 6His-MBP tag. After sample concentration, a Superdex 200 size exclusion column (GE Healthcare) was done as a final purification step.

Immunoblot

Cells lysates were homogenized by pipetting up and down ten times and supplemented with laemli buffer (1X final) before boiling sample for 10 min at 95°C. Cell lysates were then separated by denaturing SDS-PAGE and transferred on PVDF membrane. After transfer, the membrane is saturated 1h at room temperature in TBS-T (Tris 10 mM pH 8, NaCl 150 mM, Tween 20 0.05%) containing 5% nonfat milk. Then, the membrane is incubated overnight at 4°C with the different primary antibodies, under agitation. After 3 washes with TBS-T, the membrane is further incubated with the secondary antibodies coupled with the peroxidase enzyme HRP (horseradish peroxidase) for 1 hour at room temperature and under agitation. Then membranes are washed 3 times with TBS-T. The blots are revealed with the ECL revelation kit (Advansta) and images are acquired using ChemiDoc Imaging System (BioRad). The primary antibodies and secondary antibody used are listed in Reagent [key resources table](#).

In vitro cleavage assays

Recombinant proteins

The human purified recombinant gasdermin D (6 μ M final concentration), produced and purified in the lab or the human recombinant NLRP1 (0.7 μ M final concentration), from Origen (CAT#: TP316481) was incubated in 20 mM Tris at pH7,5 150 mM NaCl 1 mM DTT with recombinant SARS-CoV-2 3CL protease (Sigma-Aldrich SAE0172, R&D Systems, Novus Biologicals), recombinant SARS-CoV-2 PL^{pro} recombinant (Sigma-Aldrich) SARS-CoV-1 or MERS-CoV 3CL (Novus Biologicals) at molar ratio of 3:1 otherwise as indicated in figure legends, for O/N at 4°C, in presence or absence of protease inhibitor (PF-00835231, 10 μ M - Selleck Chemicals S9731). Human recombinant caspase 1 (Abcam 39901) was used as a positive control of the gasdermin D cleavage. Then, to detect gasdermin and NLRP1 cleavage(s), samples were analyzed on a SDS-PAGE follow by Coomassie blue staining or by immunoblot following transfer to PVDF membrane. When a cleavage occurred, fragments identification was done by IPBS mass spectrometry platform.

Cell lysate

Cell lysate of A549 and A549-NLRP1 cells was prepared as following: one day before lysis, 2,5 x 10⁵ cells were plated in 24 well plate. The day of lysis, medium was removed and cells were washed once with ice cold PBS 1X (Phosphate Buffered Saline) and incubated for 30 min on ice in 60 μ L of protease assay lysis buffer (20 mM Tris-HCl pH 7.4, 135 mM NaCl, 1% Triton X-100, 10% glycerol). Cell lysate was then collected, and clarified from insoluble fraction by centrifugation at 14,000 rpm for 30 min at 4°C before being stored at -80°C for further assays.

Cell imaging

Cells were imaged in BSL-3 facility under EVOS Floid (Invitrogen) fluorescent microscope with 20 X objective.

Sample preparation for immunoblot

At the end of the experiment, cell' supernatant was collected and soluble proteins from cell supernatant fraction were precipitated using trichloroacetic acid (TCA) as described previously (Eren et al., 2020). Precipitated pellet was then resuspended in 50 μ L of RIPA buffer plus laemli supplemented with protease inhibitor cocktail (Roche). Adherent cells were lysed in 50 μ L of RIPA buffer (150 mM

NaCl, 50 mM Tris-HCl, 1% Triton X-100, 0.5% Na-deoxycholate) supplemented with protease inhibitor cocktail (Roche). Collected cell lysate was homogenized by pipetting up and down ten times and supplemented with laemli buffer (1X final). Cells and supernatant fractions were heat for 20 min at 80°C in BSL-3 facility. Sample were then taken out of BSL-3, and boiled for 15 min at 95°C. Cell lysate and cell supernatant fraction were then analyzed by immunoblot either individually or in pooled sample of lysate plus supernatant (equal vol/vol).

Generation of knock-out cells by CRISPR/Cas9

A549 cells were transfected using lipofectamine LTX transfection reagent, in presence of NATE 1X (Invivogen) with (pCas9-GFP) to allow transient expression of Cas9-GFP and sgRNA targeting Gasdermin D (TTAGGAAGCCCTCAAGCTCA and GAATGTGTAAGTCTCGCTGAGTG), Gasdermin E (CAGTTTTTATCCCTCACCT and TAAGTTACAGCTTCTAAGTC), MAVS (ACCTC GCCCATCAACTCAACCCGTGC and ACCTCAGCAGATGATAGGCTCGGCC) and Caspase 3 (CATACATGGAAGCGAATCAA and TGTCGATGCAGCAAACCTCA). 48h after transfection, GFP-expressing cells were isolated by fluorescence associated cell sorting, diluted in single clones and knock-out clones were screened by PCR, and western blot. Alternatively, A549 cells were transduced with lentiviral vectors coding for Cas9 and blasticidin resistance cassette, and lentiviral vectors coding for sgRNA and puromycin resistance cassette. 48h after transduction, cells were selected during 2 weeks and blasticidin/puromycin double resistant cells were used in functional assays.

NHBE deficient cells were obtained by using Ribonucleoprotein (RNP) technic (Everman et al., 2018). Briefly, RNP mixes containing Cas9 protein (90pmoles, 1081059, IDT), gRNA (450pmoles) and electroporation enhancer (1μL/Mix, 1075916, IDT) were electroporated using the Neon transfection system (Life Technologies) in T Buffer (Life Technologies). Settings were the following: 1900 V Voltage, 10 Width, 1 Pulse, 20ms.

The following sgRNA targeting *NLRP1* (GCTCAGCCAGAGAAGACGAG/**KO1**, GATAGCCCGAGTGACATCGG/**KO2**, AGCCC GAGTGACATCGGTGG/**KO3**) *GSDMD* (TTAGGAAGCCCTCAAGCTCA/**KO1/2**, GAATGTGTAAGTCTCGCTGAGTG**KO3/4**, AGGTTGA CACACTTATAACG/**KO5**) or *GSDME* (GTCGGACTTTGTGAAATACG/**KO1**, CAGTTTTTATCCCTCACCT/**KO2** and TAAGTTA CAGCTTCTAAGTC/**KO3**) were used for the purpose of this study. Genetic invalidation efficiency was tested by immunoblotting after 21-28 days of cell differentiation onto Transwell.

QUANTIFICATION AND STATISTICAL ANALYSIS

Statistical data analysis was performed using Prism 8.0a (GraphPad Software, Inc.). Comparison of two groups was performed using T-test with Bonferroni correction. Otherwise specified, data are plotted as mean with SEM. P values are given in figures. Significance is defined as * $p \leq 0.05$; ** $p \leq 0.01$, *** $p \leq 0.001$.

Supplemental information

**Human NLRP1 is a sensor of pathogenic
coronavirus 3CL proteases in lung
epithelial cells**

Rémi Planès, Miriam Pinilla, Karin Santoni, Audrey Hessel, Charlotte Passemar, Kenneth Lay, Perrine Paillette, Ana-Luiza Chaves Valadão, Kim Samirah Robinson, Paul Bastard, Nathaniel Lam, Ricardo Fadrique, Ida Rossi, David Pericat, Salimata Bagayoko, Stephen Adonai Leon-Icaza, Yoann Rombouts, Eric Perouzel, Michèle Tiraby, COVID Human Genetic Effort, Qian Zhang, Pietro Cicuti, Emmanuelle Jouanguy, Olivier Neyrolles, Clare E. Bryant, Andres R. Floto, Caroline Goujon, Franklin Zhong Lei, Guillaume Martin-Blondel, Stein Silva, Jean-Laurent Casanova, Céline Cougoule, Bruno Reversade, Julien Marcoux, Emmanuel Ravet, and Etienne Meunier

SUPPLEMENTAL INFORMATIONS

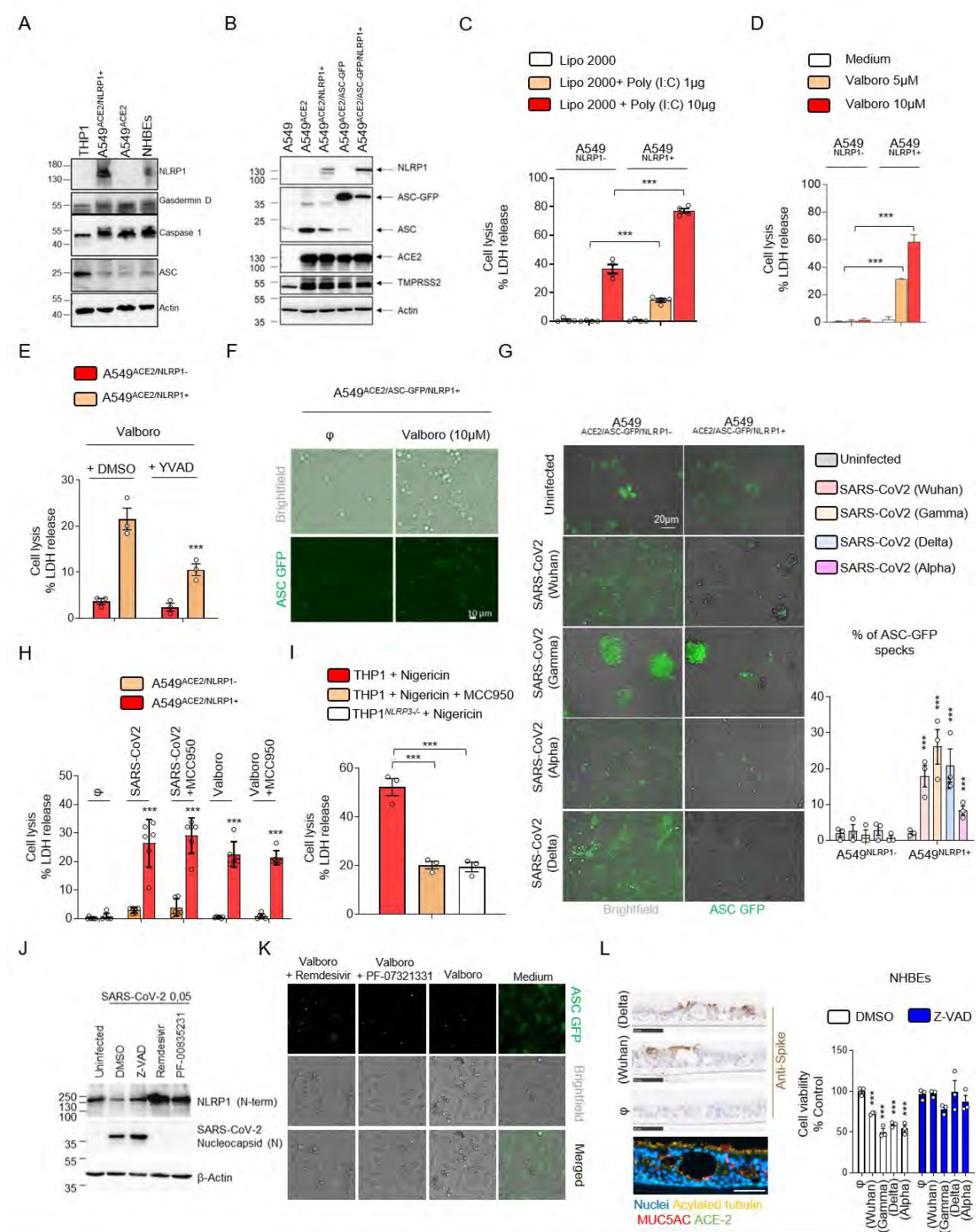


Figure S1 (Related to Figure 1). NLRP1 detects SARS-CoV-2 infection in epithelial cells

(A) Western Blot examination of the expression of NLRP1, ASC, Gasdermin-D (GSDMD), Caspase-1 (CASP1) and ACTIN in THP-1 (monocytes), NHBE (bronchial epithelial cells) or A549 cells engineered for the purpose of this study. Immunoblots

were performed against full-length NLRP1 Nter (p130/110), ASC (p22), GSDMD (p55), CASP1 (p50) and ACTIN (p40).

(B) Western Blot examination of the expression of NLRP1, ASC, ASC-GFP, ACE2, TMRSS2 and ACTIN in A549 cells engineered for the purpose of this study. Immunoblots were performed against full-length NLRP1 Nter (p130/110), ASC (p22), ASC-GFP (p50), TMRSS2 (p54), ACE2 (p130) and ACTIN (p40).

(C-E) Measure of cell lysis (LDH release) in A549^{NLRP1+} or A549^{NLRP1-} transfected with polyI:C (0.1µg or 1µg) (B) or treated with Valboro (5 and 10µM) (C) in presence/absence of the Caspase-1 inhibitor Z-YVAD (25µM) for 10 hours.

(F) Florescence microscopy of ASC-GFP specks in A549^{ACE2/NLRP1+/ASC-GFP} and A549^{ACE2/NLRP1-/ASC-GFP} airway epithelial cell lines treated with 5µM of Valboro for 10 hours. Images shown are from one experiment and are representative of n=3 independent experiments; scale bars 10 µm.

(G) Florescence microscopy and associated quantifications of ASC-GFP specks in A549^{ACE2/NLRP1+/ASC-GFP} airway epithelial cell lines infected for 24 hours with various strains of SARS-CoV-2 (MOI 0.01).

(H) Measure of cell lysis (LDH release) in A549^{NLRP1+} or A549^{NLRP1-} treated with Valboro (5 µM) for 10 hours or infected with SARS-CoV-2 (MOI 0.05) for 24 hours in presence/absence of the NLRP3 inhibitor MCC950 (10µM).

(I) Measure of cell lysis (LDH release) in PMA (100ng/mL)-primed THP1 myeloid cells treated with Nigericin (20µM) for 2 hours in presence/absence of the NLRP3 inhibitor MCC950 (10µM).

(J) Western blot examination of NLRP1 and SARS-CoV-2 Nucleocapsid (N) in A549^{ACE2/NLRP1+} and A549^{ACE2/NLRP1-} airway epithelial cell lines infected with SARS-CoV-2 for 24 hours multiplicity of infection (MOI) of 0.05 in presence /absence of the NSP5 protease inhibitor PF-00835231 (10µM), Remdesivir (5µM), or Z-VAD (25 µM).

(K) Florescence microscopy of ASC-GFP specks in A549^{ACE2/NLRP1+/ASC-GFP} airway epithelial cell lines treated with 5µM of Valboro for 10 hours in presence/absence of the 3CL inhibitor PF-00835231 (10µM) or Remdesivir (5 µM). Images shown are from one experiment and are representative of n=3 independent experiments; scale bars 10 µm.

(L) Microscopy characterization of Air-Liquid Interface-differentiated and infected epithelial cells (ACE2, Mucin 5AC, Acylated tubulin, Nuclei, SARS-CoV-2) and measure of cell lysis (LDH release) in NHBE epithelial cells infected for 36 hours with various strains of SARS-CoV-2 (MOI 1) in presence/absence of the pan Caspase inhibitor Z-VAD (40 μ M). Images shown are from one experiment and are representative of n=2 independent experiments; scale bars 50 μ m.

Data information:

Western Blot (A, B, J) images are from one experiment performed three times. Graphs C, D, E, H, I, L show data presented as means \pm SEM from n=6 (G) or n=3 independent pooled experiments; ***p \leq 0.001 for the indicated comparisons with t-test. Images (F, G, K) show one experiment performed three times.

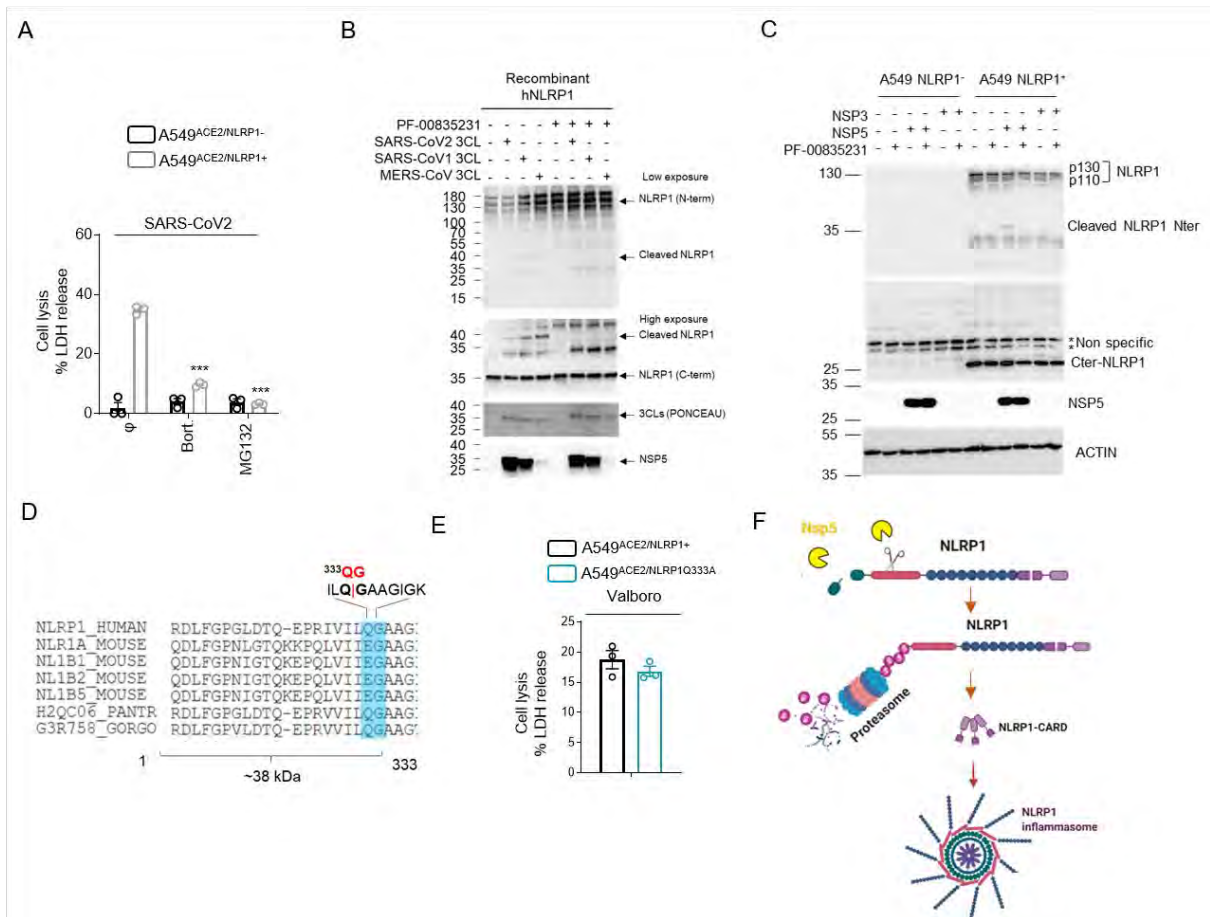


Figure S2 (Related to Figure 2). NSP5-cleaved NLRP1 nucleates inflammasome activation

(A) Measure of cell lysis (LDH release) in A549^{NLRP1+} or A549^{NLRP1-} infected with SARS-CoV-2 (MOI 0.05) for 24 hours in presence/absence of the proteasome inhibitors bortezomib (0.1 μ M) or MG-132 (0.1 μ M).

(B) Western blot examination of NLRP1 cleavage using an anti NLRP1 Nter antibody (aa1-323) upon co incubation of SARS-CoV-2, SARS-CoV1 or MERS-CoV 3CL (NSP5) proteases with recombinant human NLRP1 in presence or absence of the 3CL inhibitor PF-00835231 (10 μ M). NLRP1 N-terminal, NLRP1 C-terminal, NSP5 and ACTIN were immunoblotted.

(C) Western blot examination of NLRP1 cleavage using an anti NLRP1 N-terminal antibody (aa1-323) upon co incubation of SARS-CoV-2 NSP5 or SARS-CoV-2 NSP3 proteases with A549^{NLRP1+} cell lysates in presence or absence of the 3CL inhibitor PF-00835231 (10 μ M). NLRP1 Nter, NLRP1Cetr, NSP5 and ACTIN were immunoblotted.

(D) Sequence alignment of the NSP5-targeted human NLRP1^{Q333} site with mouse and primate NLRP1.

(E) Measure of cell lysis (LDH release) in A549^{NLRP1+} or A549^{NLRP1Q33A} treated with Valboro (10 μ M) for 10 hours.

(F) Proposed mechanism of human NLRP1 activation by NSP5 protease.

Data informations:

Western Blot (A-C) images are from one experiment performed three times. Graph E show data presented as means \pm SEM from n=3 independent pooled experiments; ***p \leq 0.001 for the indicated comparisons with t-test. G was created using biorender.com

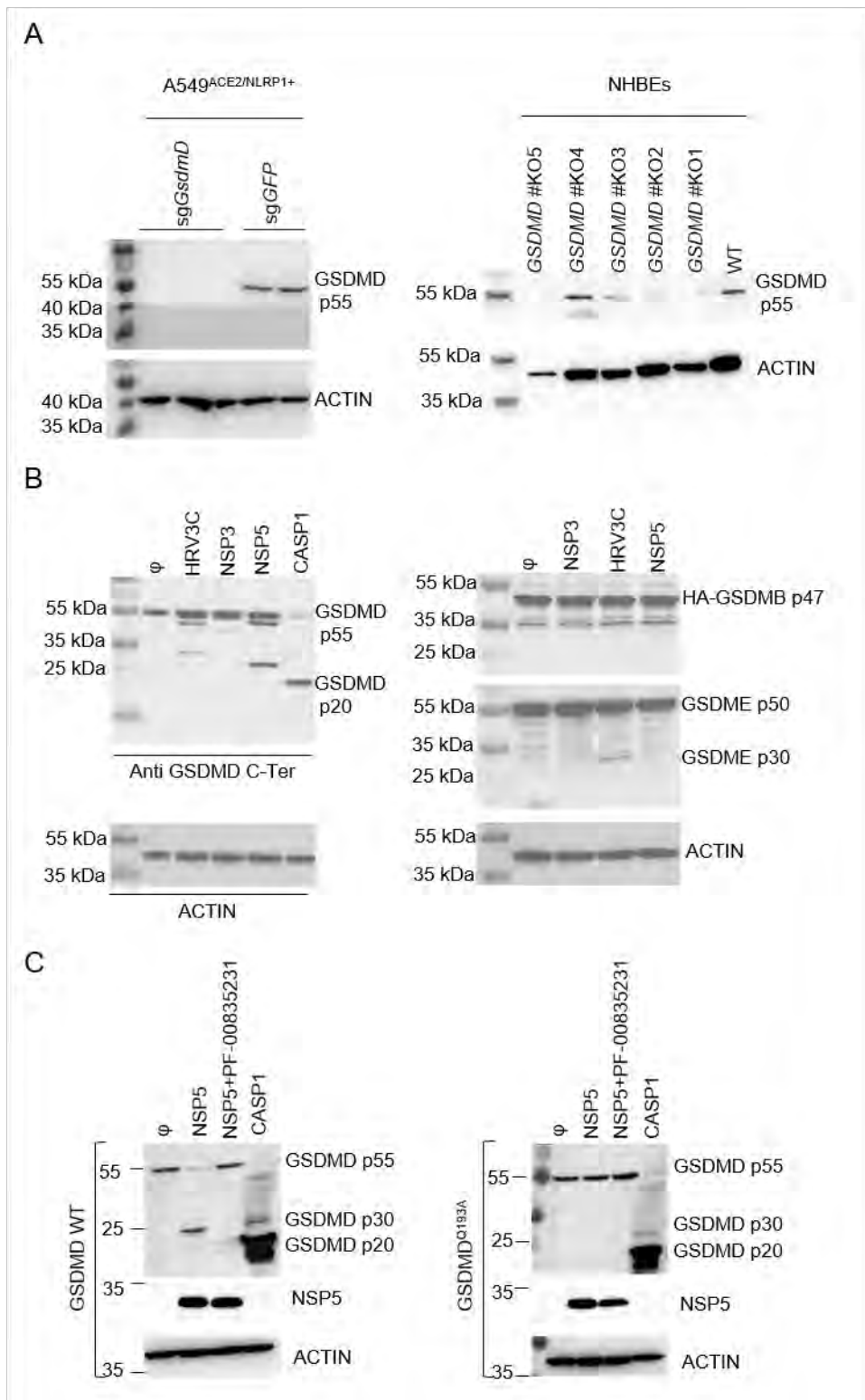


Figure S3 (Related to Figure 3). NSP5 cleaves and inactivates GSDMD

(A) Western Blot examination of genetic invalidation of GSDMD in A549^{NLRP1+} or NHBE cells using CRISPR Cas9 technic.

(B) Western blot examination of Gasdermin cleavages by SARS-CoV-2 NSP5 or NSP3, HRV3C or recombinant human Caspase-1 (CASP1) proteases in cell lysates from A549 expressing GSDMD, GSDMB or GSDME. GSDMD (anti Cter), GSDME, GSDMB, NSP5 and ACTIN were immunoblotted.

(C) Western blot examination of GSDMD cleavage by SARS-CoV-2 3CL (NSP5) or recombinant human Caspase-1 (CASP1) proteases in cell lysates from A549 expressing WT GSDMD or GSDMD^{193A} constructs in presence/absence of the 3CL inhibitor PF-00835231 (10 μ M). GSDMD (anti Cter), NSP5 and ACTIN were immunoblotted.

Data information:

Western Blot (A-C) images are from one experiment performed three times.

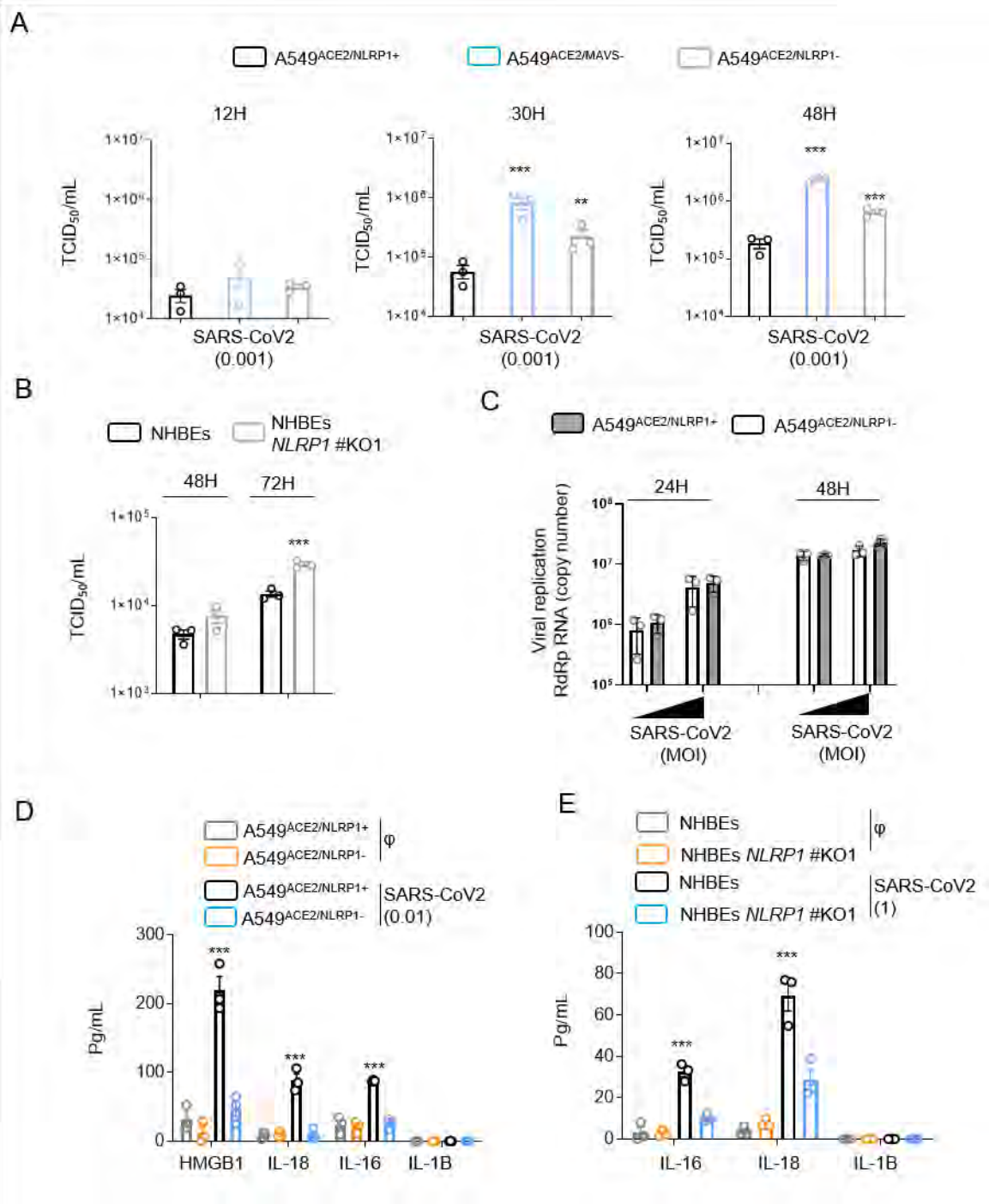


Figure S4 (Related to Figures 1-4). NLRP1-dependent pyroptosis both limits the production of infectious particles and promotes alarmin/DAMP release

(A) TCID₅₀ measure of production of infectious viral particles in A549^{ACE2/NLRP1+}, A549^{ACE2/NLRP1-} and A549^{ACE2/MAVS-} cells infected for various times with SARS-CoV-2.

(B) TCID₅₀ measure of production of infectious viral particles in NHBE^{WT} and NHBE^{NLRP1-/-} cells infected for various times with SARS-CoV-2 (MOI 0.5).

(C) Q-RT PCR evaluation of SARS-CoV-2 RdRp mRNA levels in A549^{ACE2/NLRP1+} or A549^{ACE2/NLRP1-} cells after 24 and 48 hours of SARS-CoV-2 infection (MOIs 0.05 and 0.005).

(D, E) Measure of the release of various Alarmins/Cytokines after 24 (D) or 36 (E) hours of infection with SARS-CoV-2 (MOI 0.05 and 1 respectively) by A549^{ACE2/NLRP1+}, A549^{ACE2/NLRP1-}, NHBE^{WT} and NHBE^{NLRP1-/-} cells.

Data informations:

Graphs A-E show data presented as means \pm SEM from n=3 independent pooled experiments; **p \leq 0.01, ***p \leq 0.001 for the indicated comparisons with t-test.

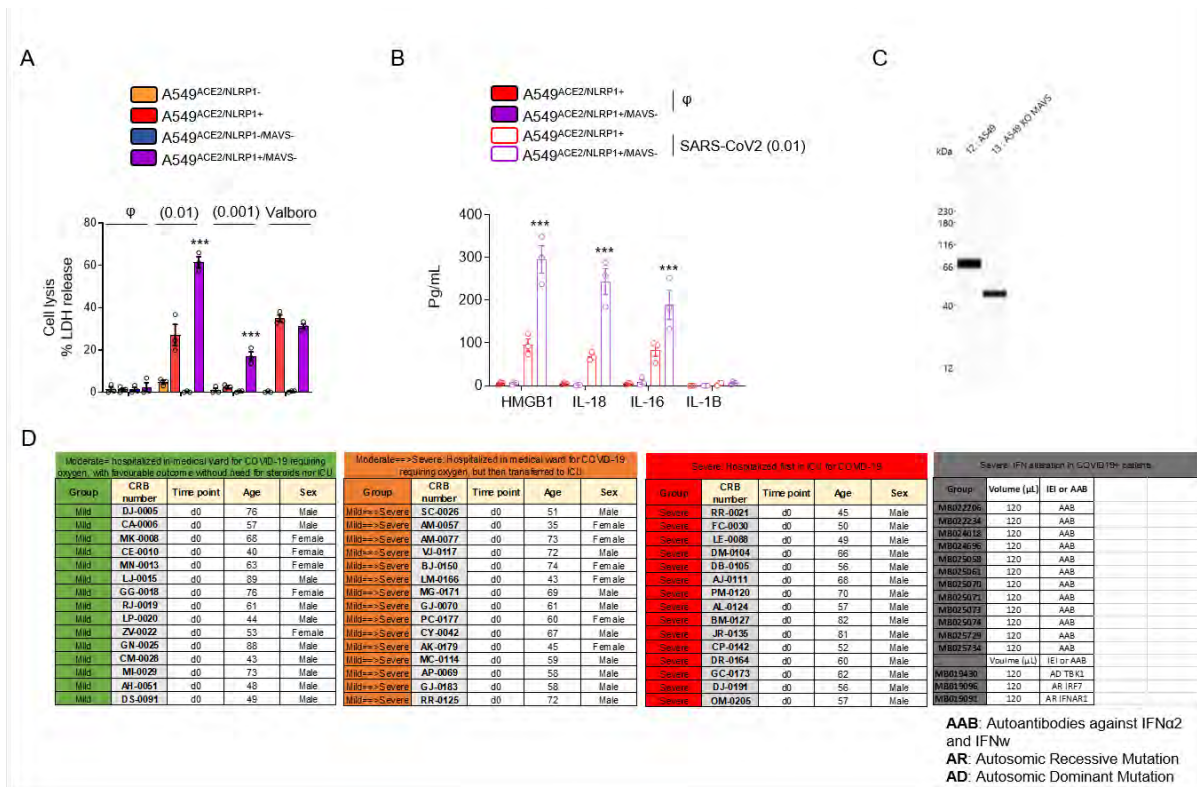


Figure S5 (Related to Figure 4). Plasmas from COVID19 patients show enrichments in (IL)-16/-18/GSDME and CASP3.

(A) Measure of cell lysis (LDH release) in A549^{NLRP1+}, A549^{NLRP1-}, A549^{NLRP1+/MAVS-} and A549^{NLRP1-/MAVS-} upon SARS-CoV-2 infection or Valboro (5 μM) treatment for 24 hours.

(B) Measure of cytokine/alarmin release in A549^{NLRP1+} or A549^{NLRP1+/MAVS-} upon SARS-CoV-2 infection for 24 hours.

(C) Western Blot examination of genetic invalidation of MAVS in A549 cells. MAVS appears at the 66kDa.

(D) Information on COVID-19⁺ patients hospitalized and COVID-19⁺ patients exhibiting Interferon alterations used in this study

Data information:

Graphs A, B show data presented as means ± SEM from n=3 independent pooled experiments; ***p ≤ 0.001 for the indicated comparisons with t-test. Western Blot (C) image is from one experiment.

COVID Human Genetic Effort members and affiliations

The affiliations of the members of the COVID Human Genetic Effort are as follows.

Tayfun Ozcelik: Department of Molecular Biology and Genetics, Bilkent University, Bilkent - Ankara, Turkey

Nevin Hapitoglu: Pediatric Infectious Diseases Unit, Bakirkoy Dr. Sadi Konuk Training and Research Hospital, University of Health Sciences, Istanbul, Turkey

Filomeen Haerynck: Department of Pediatric Immunology and Pulmonology, Center for Primary Immunodeficiency Ghent, Jeffrey Model Diagnosis and Research Center, PID research lab, Ghent University Hospital, Ghent, Belgium

Sevgi Keles: Meram Medical Faculty, Necmettin Erbakan University, Meram Medical Faculty, Konya, Turkey

Ahmed A. Bousfiha: Clinical Immunology Unit, Department of Pediatric Infectious Disease, CHU Ibn Rushd and LICIA, Laboratoire d'Immunologie Clinique, Inflammation et Allergie, Faculty of Medicine and Pharmacy, Hassan II University, Casablanca, Morocco

Rafael Leon Lopez: Hospital Universitario Reina Sofía, Cordoba, Spain

IV. Nigratine as dual inhibitor of necroptosis and ferroptosis regulated cell death

Authors: Claire Delehouzé, Arnaud Comte, **Stephen Adonai Leon-Icaza**, Céline Cougoule, Marcelle Hauteville, Peter Goekjian, Jeannette Chloë Bulinski, Marie-Thérèse Dimanche-Boitrel, Etienne Meunier, Morgane Rousselot, Stéphane Bach.

Contribution: I designed and performed all the experiments for Figure 6 of the article. Briefly, I performed time-lapse microscopy and their associated quantifications of the measure of plasma membrane permeabilization using propidium iodide to determine if the nigratine molecule can be considered a dual inhibitor of cell death by necroptosis and ferroptosis.

This article was published in Scientific Reports.



OPEN

Nigratine as dual inhibitor of necroptosis and ferroptosis regulated cell death

Claire Delehouzé^{1,2}, Arnaud Comte³, Stephen Adonai Leon-Icaza⁴, Céline Cougoule⁴, Marcelle Hauteville⁵, Peter Goekjian⁶, Jeannette Chloë Bulinski^{2,7}, Marie-Thérèse Dimanche-Boitrel⁸, Etienne Meunier⁴, Morgane Rousselot¹✉ & Stéphane Bach^{2,9,10}✉

Nigratine (also known as 6E11), a flavanone derivative of a plant natural product, was characterized as highly specific non-ATP competitive inhibitor of RIPK1 kinase, one of the key components of necroptotic cell death signaling. We show here that nigratine inhibited both necroptosis (induced by Tumor Necrosis Factor- α) and ferroptosis (induced by the small molecules glutamate, erastin, RSL3 or cumene hydroperoxide) with EC_{50} in the μM range. Taken together, our data showed that nigratine is a dual inhibitor of necroptosis and ferroptosis cell death pathways. These findings open potential new therapeutic avenues for treating complex necrosis-related diseases.

Advances in systems biology have revealed that single-target compounds are less efficient in preventing or curing complex diseases such as neurodegenerative diseases^{1,2}. Drug discovery failures in complex cases, including Alzheimer's disease (AD), suggest that the definition of a "magic bullet" (i.e., drug selective for a single molecular target), the scientific concept developed by Paul Ehrlich more than a century ago³, may need to be revised. The development of multi-target-directed ligands (MTDLs) for AD treatment is a notable example of promising therapeutic strategies². Moreover, the central nervous system (CNS) drugs most effective clinically, such as clozapine for treatment of schizophrenia, act as "magic shotguns": non-selective drugs with pleiotypic actions⁴. These compounds are effective in treating complex human disorders because they are able to modulate multiple targets involved in the pathophysiological processes, a strategy called polypharmacology. Synergistic effects are also among the main advantages of this combined therapeutic approach⁵. This strategy is now widely used in drug development as evidenced by the fact that, from 2015 to 2017, 21% of the new molecular entities (NMEs) approved by the food and drug administration (FDA) are multi-target drugs (by contrast, 34% were single-target small molecules)⁶.

The systemic breakdown of physiological networks in disease is not restricted to brain tissue; it is observed in numerous other tissues, including kidneys and liver. Functional redundancy has been described for numerous cellular pathways and is well-described for regulated cell death (RCD) signaling⁷. Indeed, in RCD signaling, redundancy may reflect the evolutionary history of cell suicide pathways, wherein autophagic, apoptotic or necrotic elements might have arisen from an ancestral cell death mechanism. Ancestral cell death routes probably include ferroptosis, a non-apoptotic cell death that is catalyzed by iron⁸, as ferroptosis-like pathway exists in cyanobacteria, phytoplankton that evolved over 2.7 billion years ago⁹. There are at least 12 distinct types of RCD including various forms of regulated necrosis⁷. Since the term "regulated" indicates a reliance on fine-tuned

¹SeaBeLife Biotech, Place Georges Teissier, 29680 Roscoff, France. ²Sorbonne Université, CNRS, UMR 8227, Integrative Biology of Marine Models Laboratory (LBI2M), Station Biologique de Roscoff, 29680 Roscoff, France. ³Université de Lyon, CNRS UMR 5246, ICBMS, Chimiothèque, Université Claude Bernard Lyon 1, 69622 Villeurbanne, France. ⁴Institut de Pharmacologie et Biologie Structurale (IPBS), Université de Toulouse, CNRS, UPS, Toulouse, France. ⁵Laboratoire de Biochimie Analytique et Synthèse Bioorganique, Université de Lyon, Université Claude Bernard Lyon 1, 69622 Villeurbanne, France. ⁶Université de Lyon, CNRS UMR 5246, ICBMS, Laboratoire Chimie Organique 2-Glycosciences, Université Claude Bernard Lyon 1, 69622 Villeurbanne, France. ⁷Department of Biological Sciences, Columbia University, New York, NY 10027, USA. ⁸Univ Rennes, Inserm, EHESP, Irset (Institut de Recherche en Santé, Environnement et Travail) - UMR_S 1085, 35000 Rennes, France. ⁹Sorbonne Université, CNRS, FR 2424, Plateforme de Criblage KISSf (Kinase Inhibitor Specialized Screening Facility), Station Biologique de Roscoff, 29680 Roscoff Cedex, France. ¹⁰Centre of Excellence for Pharmaceutical Sciences, North-West University, Private Bag X6001, Potchefstroom 2520, South Africa. ✉email: morgane.rousselot@seabelife.com; bach@sb-roscoff.fr

molecular signaling machinery, it is possible to screen for small chemical compounds that can modulate the signaling cascades and effectors in RCD pathways (such as necrostatins that block necroptosis¹⁰).

Small molecule inhibitors of RCD pathways are potential new therapeutic approaches to pathologies such as inflammatory and neurodegenerative diseases¹¹. Necroptosis is a regulated cell necrosis route that can be activated under apoptosis-deficient conditions. Necroptosis depends notably on the serine/threonine kinase activity of RIPK1 (Receptor-Interacting Protein Kinase 1) and RIPK3 and on the trafficking and accumulation at the plasma membrane of the pseudokinase MLKL (Mixed lineage kinase domain-like)^{11,12}. As of March, 2021, four RIPK1 inhibitors had reached clinical trials (GSK2982772 and GSK3145095 developed by GSK, DNL747 (SAR 443060) and DNL758 (SAR443122) developed by Sanofi and Denali Therapeutics, respectively), and GFH312 developed by GenFleet Therapeutics, for treatments of psoriasis (phase II), ulcerative colitis (phase II), rheumatoid arthritis (phase II), or pancreatic cancer (phase II), for the molecules developed by GSK; Alzheimer's disease (phase I), cutaneous lupus erythematosus (phase II, *not yet recruiting*), amyotrophic lateral sclerosis and multiple sclerosis (phase I), and severe coronavirus caused by SARS-Co-V-2 (COVID-19) for the molecules developed by Sanofi and Denali Therapeutics; and for evaluation of the safety/tolerability and pharmacokinetics in healthy subjects (phase I, *not yet recruiting*) for the molecule developed by GenFleet Therapeutics (data from clinicaltrials.gov and¹³). Numerous other compounds (40+) also have demonstrated binding affinity for RIPK1¹³. Recently, Tonnus et al. generated a combined small molecule inhibitor (Nec-1f) that simultaneously targets RIPK1 and ferroptosis. Nec-1f was shown to improve survival in models of ischemia–reperfusion injury¹⁴.

Our research group has contributed to the characterization of synthetic and natural product derivatives that are potent inhibitors of RIPK1, including the 7-azaindole derivative Sibiriline¹⁵, the marine-derivative 2-aminobenzothiazole MBM105¹⁶ and the flavanone nigratine (also known as 6E11)¹⁷. Nigratine (2-(4-(benzyloxy)phenyl)-2,5-dihydroxy-7-methoxychroman-4-one) is a synthetic derivative of the naturally occurring 2,5-dihydroxy-2-phenylchroman-4-ones isolated from *Populus nigra* buds. We previously showed that nigratine is a non-ATP competitive inhibitor with a remarkable selectivity toward RIPK1 and is able to protect human aortic endothelial cells (HAEC) from cold hypoxia/reoxygenation-induced cell death¹⁷.

We now report the characterization of nigratine as new inhibitor of the ferroptosis RCD pathway (with EC₅₀ in the μM range). Nigratine is thus considered as a new dual inhibitor (or “magic shotgun”) of both necroptosis and ferroptosis RCD death that can be used in polypharmacological approaches for treatments of regulated-necrosis related disorders.

Results

Effect of nigratine on necroptotic cell-death induced by TNF-α. Nigratine was characterized by Delehouzé et al. as new necroptosis inhibitor using a TNF-induced FADD-deficient human Jurkat necroptosis assay¹⁷. TNF-α can induce necroptosis in Jurkat cells when FADD is deleted. We used an MTS assay to measure the viability of lymphocytes and we determined nigratine effects on RIPK1-kinase activity, in order to elucidate the mechanism of necroptosis inhibition. In this study, we compared the bioactivity of nigratine to that of necrostatin-1 (Nec-1), a known inhibitor of necroptosis¹⁰. Both compounds were tested at concentrations of 10 and 50 μM. The results obtained and the chemical structures of these compounds are depicted in Fig. 1. In this assay, nigratine inhibited both necroptosis cell death and RIPK1 kinase activity with an activity similar to that of Nec-1 (with both EC₅₀ and IC₅₀ in the μM range). The value of the protection index (dubbed ProtecΔ) for nigratine at 10 μM (45.0) compared to the value at 50 μM (26.0) suggested that in Jurkat FADD-deficient cells the higher concentration produced a lesser effect.

Nigratine protects neuronal cells against ferroptotic cell death. In Delehouzé et al., we previously showed that treatment of human aortic endothelial cells (HAEC) with nigratine during cold hypoxia or during reoxygenation following cold hypoxia conferred measurable benefits on cell survival. Nigratine was significantly more potent than the specific RIPK1 necroptosis inhibitor, Nec-1s¹⁷. This result suggested that the observed effect of nigratine was not fully attributable to its inhibition of RIPK1 kinase. Indeed, when compared to nigratine, Nec-1s is a more potent inhibitor of RIPK1¹⁷.

We next analyzed the effect of nigratine treatment on ferroptotic cell-based models. Ferroptosis was first characterized in *NRAS*-mutant HT-1080 fibrosarcoma cells treated with erastin⁸. Erastin, like excess L-glutamate (5 mM), is a class I ferroptosis inducer. Both compounds inhibit cystine uptake by the heterodimeric cystine/glutamate antiporter (system xc⁻), thus inducing oxidative toxicity. This antiporter is a key component essential for protection of cells from oxidative stress and lethal lipid peroxidation, both of which are major hallmarks of ferroptosis. Glutathione peroxidase (GPX4) is also a key player of ferroptosis. The execution of ferroptosis depends on massive lipid peroxidation, which can be reduced by the lipid repair enzyme, GPX4. RSL3 belongs to class II of the ferroptosis-inducing agents by virtue of its inhibition of GPX4¹⁸. Accordingly, we tested the protective effect of nigratine against class I (glutamate and erastin) and II (RSL3) ferroptosis inducers in two neuronal cell lines, mouse HT22 (hippocampal neuronal cell line) and in human SH-SY5Y (neuroblastoma cell line). These cell lines have been widely used as models of neurodegeneration, neurotoxicity, and neuroprotection^{19,20}. As shown on Figs. 2 and 3, 50 μM nigratine was able to strongly inhibit the ferroptotic cell death induced by excess of glutamate, erastin, and RSL3, in both murine HT22 and human SH-SY5Y cell lines.

The dose-dependent effect of nigratine on cell viability was analyzed using an MTS assay. In order to validate the effect of nigratine on neuroprotection and necrosis, the extracellular lactate dehydrogenase (LDH) detection assay was also used as an independent cell death assay²¹. This assay measures LDH that is released into the extracellular space when the plasma membrane is damaged; this release is characteristic of necrotic cell death²². As shown in Fig. 3b, the treatment of SH-SY5Y cells with nigratine protected cells against cell-death in a dose-dependent manner, correlated with the dose-dependent increase in cell survival. Our data also showed that

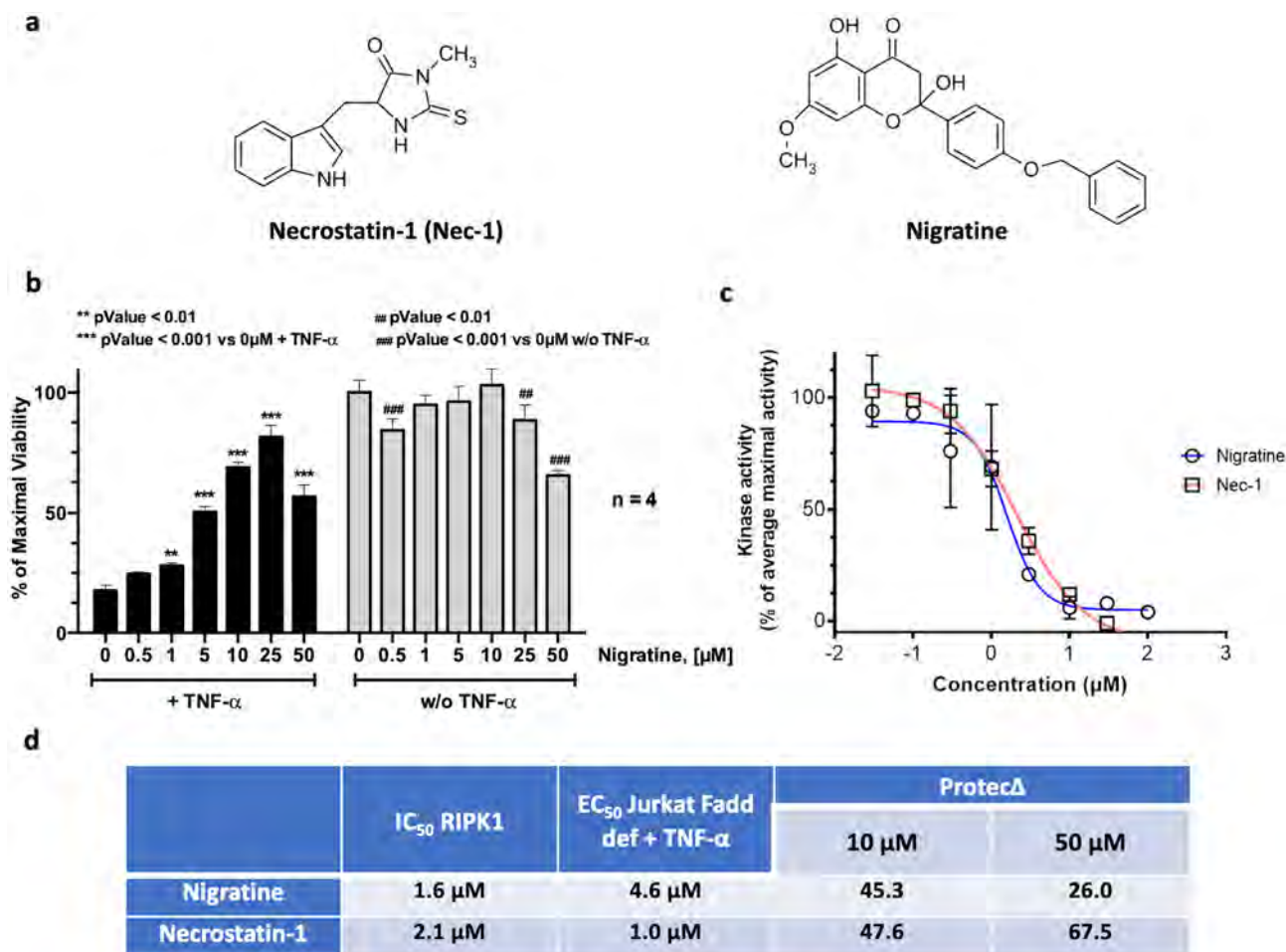


Figure 1. Nigritine inhibits necroptosis by targeting RIPK1 kinase. (a) Nigritine and necrostatin-1 (Nec-1), as control inhibitor of necroptosis, are structurally non related molecules. (b) Jurkat-Fadd def cells were treated 24 h with increasing concentrations of nigritine alone or co-treated with 10 ng/ml of TNF- α . Cell viability was estimated by MTS assay. Data are shown as the mean \pm SD of four replicates. (c) The RIPK1 catalytic activity was monitored using myelin basic protein, MBP, as a substrate. RIPK1 was assayed in the presence of increasing concentrations of both nigritine and Nec-1. The kinase activities are expressed in % of average maximal activity, i.e. measured in the presence of DMSO ($n=2$, mean \pm SEM). (d) The IC₅₀ (on kinase) and EC₅₀ and “protection delta” (Protec Δ) (on cells) values were determined from the dose–response curves using Graphpad PRISM software and reported in the table. The level of protection against the TNF- α -induced cell death is estimated using the Protec Δ values (first described and used in¹⁶). These data are determined by subtracting the value obtained for cells only treated with TNF- α from the value obtained for co-treatment with TNF- α and with the tested compound.

nigritine had a negligible cytotoxic effect on SH-SY5Y neuroblastoma cells when applied at ≤ 10 μ M (Fig. 3b). Interestingly, nigritine is active against ferroptosis on SH-SY5Y cells with an EC₅₀ of ~ 6.5 μ M (EC_{50(LDH)} = 6.0 μ M and EC_{50(MTS)} = 6.9 μ M) similar to its activity in preventing necroptosis (EC_{50(MTS)} = 4.6 μ M).

Nigritine inhibits phospholipid peroxidation. We next characterized the effect of nigritine on the peroxidation of phospholipids induced by the inhibition of GPX4 with RSL3; for this study we selected the well-characterized porcine renal epithelial proximal tubule cell line (LLC-PK1). As shown in Fig. 4, our results showed that: (i) nigritine significantly protects renal epithelial cells against ferroptotic cell death induced by RSL3 (Fig. 4a) and (ii) nigritine inhibits phospholipid peroxide formation detected in cells using BODIPY 581/591 C11 probe (Fig. 4b,c). The BODIPY dye was used as a sensitive indicator of free radical processes that have the potential to oxidize lipids within membranes. Taken together, these results suggested that nigritine has a marked effect on lipid peroxidation, a major hallmark of ferroptosis.

Nigritine is a weak antioxidant compound. Ferroptosis, catalyzed by iron, comprises a failure of the glutathione-dependent antioxidant defenses that result from a loss of activity of the lipid repair enzyme, glutathione peroxidase 4 (GPX4)²³. This in turn leads to an accumulation of lipid-based reactive oxygen species (ROS), and lipid peroxidation. Antioxidant compounds such as α -tocopherol (vitamin E), a potent radical-trap-

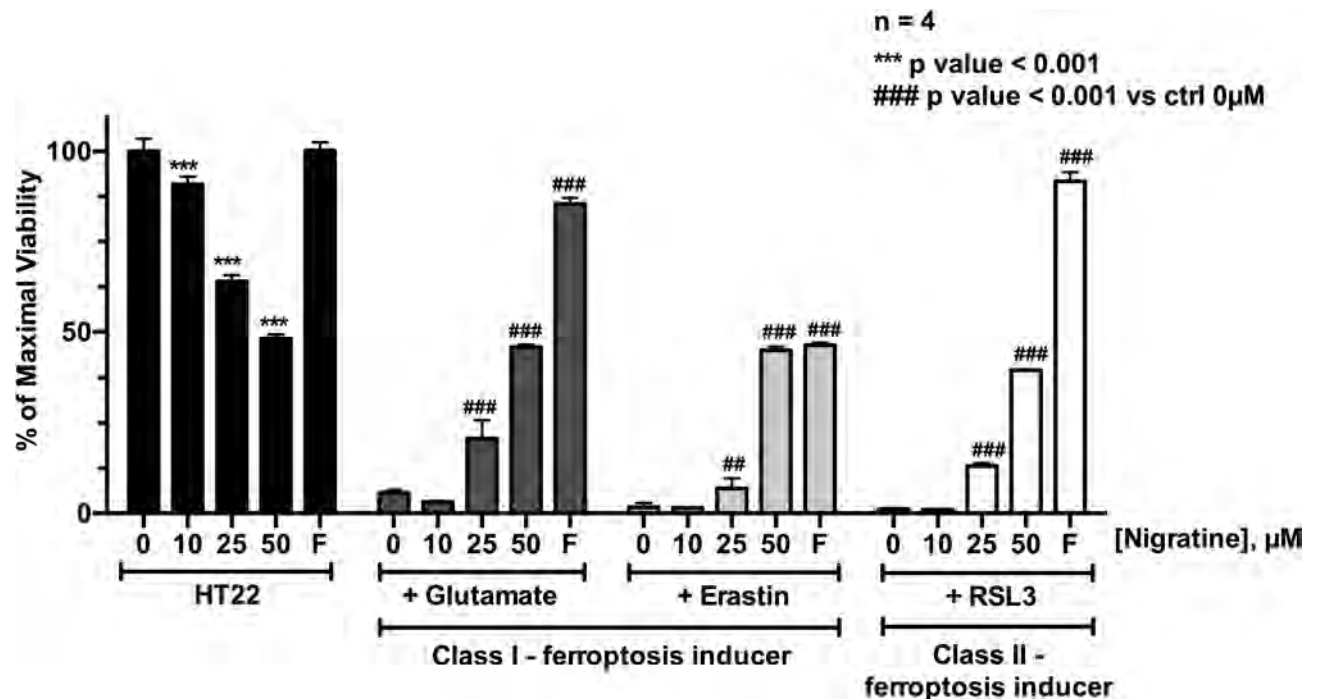


Figure 2. Nigritine protects HT-22 mouse hippocampal neuronal cell line from cell death triggered by both class I and II-inducers of ferroptosis. HT22 cells were treated 24 h with increasing concentrations (0–50 μM) of the tested chemical compounds alone (“HT22”) or co-treated with 5 mM glutamate, 0.5 μM erastin or 1 μM of RSL3. Ferrostatin-1 (“F”) was used as a positive control for ferroptosis inhibition. Cell viability was estimated by MTS assay. Data are shown as the mean \pm SD of four replicates.

ping antioxidant that blocks the auto-oxidation of chain-propagating peroxy radicals and protects hydrocarbon biological systems from oxidation and membrane damage in ferroptosis, have been shown to inhibit ferroptotic RCD (see²⁴ for review). Our results (Fig. 5) suggest that nigritine is only a weak antioxidant compound compared to α -tocopherol and the lipophilic antioxidant ferrostatin-1.

Nigritine protects human bronchial organoids against both ferroptotic and necroptotic cell death. To determine in a more complex system the dual ability of nigritine to inhibit both necroptosis and ferroptosis, we exploited human bronchial organoids from healthy patients and exposed them to activators of necroptosis (Z-VAD/TNF- α /BV-6) or ferroptosis (Cumene Hydroperoxide, CuOOH). We monitored propidium iodide (PI) incorporation as a marker of plasma membrane destabilization over time. Our results showed a strong inhibitory effect of nigritine and necrostatin-1 against Z-VAD/TNF- α /BV-6-induced PI incorporation in lung organoids (Fig. 6). The study of CuOOH-induced ferroptosis of bronchial human organoids showed that ferrostatin-1 and nigritine inhibited and delayed PI incorporation, suggesting that nigritine exhibits some anti-ferroptotic properties. Taken together, our results suggest that nigritine has a dual effect against ferroptosis and necroptosis in primary human organoids.

Discussion

Nigritine was previously described as a putative non-ATP competitive type III RIPK1 kinase inhibitor that can block the necroptosis RCD pathway in various cellular models, including Jurkat lymphocytes, with an EC_{50} in the μM range¹⁷. Necroptosis is clearly distinct from apoptosis as it does not involve the key apoptosis regulators, such as caspases or cytochrome c release from mitochondria. In the present study, we showed that nigritine also inhibits ferroptosis. For example, nigritine suppressed cell death induced by class I, II and IV ferroptosis inducers; namely, the presence of excess glutamate, erastin, RSL3 and cumene hydroperoxide, respectively. We also showed that nigritine inhibits phospholipid peroxidation induced by RSL3 in epithelial LLC-PK1 porcine renal cells, an inhibition that was also observed for the known ferroptosis inhibitor, ferrostatin-1. The dual protective effect of nigritine against both necroptosis and ferroptosis was also observed in human bronchial organoids.

Polypharmacological approaches, that is, use of drugs that act on multiple targets, appears well-suited to improving the outcome of complex diseases. Thus, nigritine would seem to be very attractive as a therapy for preventing and/or treating disorders associated with the induction of necroptosis and/or ferroptosis. As an example, the therapeutic benefit of nigritine could be evaluated in animal models of cisplatin-induced nephrotoxic acute kidney injury (AKI), in which both regulated RCD pathways are known to be involved in proximal tubular cell death^{25–27}. Ischemia/reperfusion injuries (IRI), which have been attributed to cell necrosis for decades²⁸, should also be explored with nigritine.

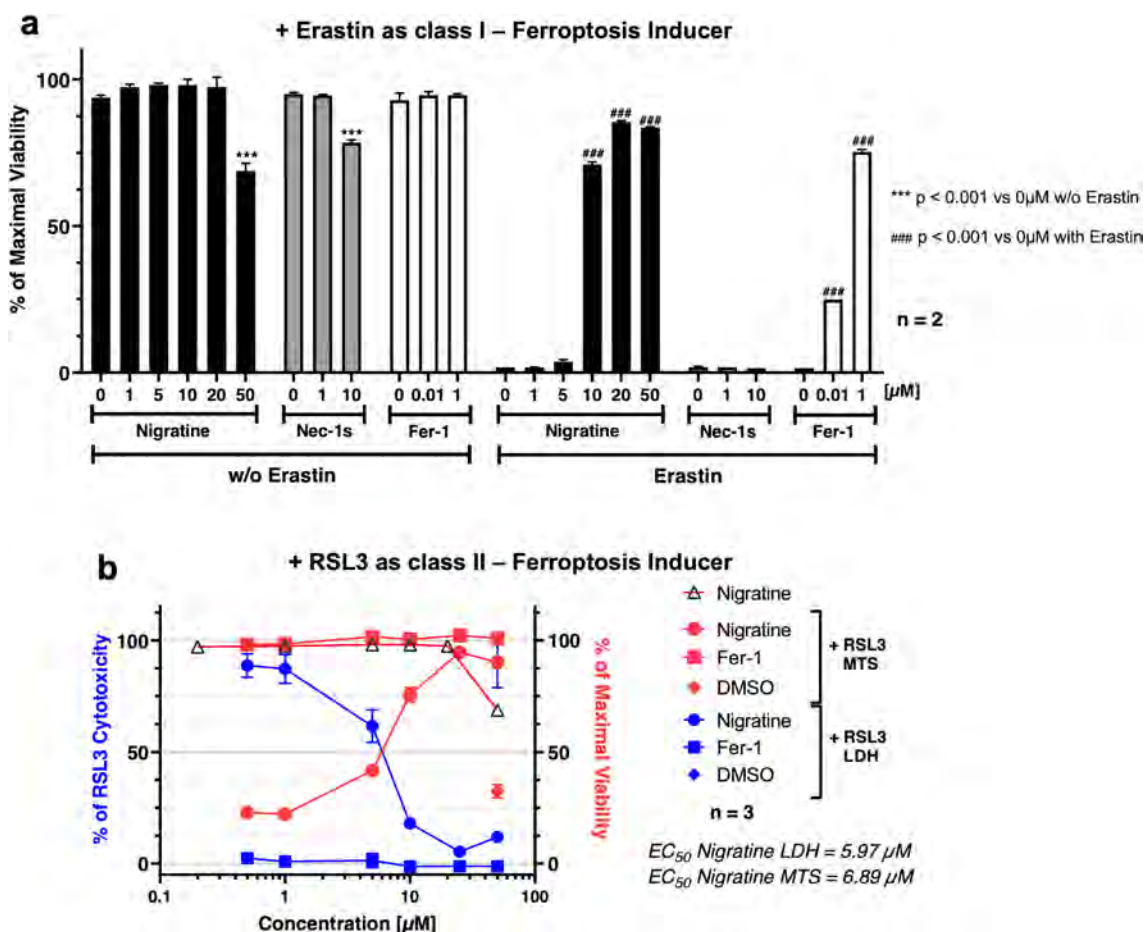


Figure 3. Nigratine protects SH-SY5Y human neuroblastoma cell line from cell death triggered by both class I and II-inducers of ferroptosis. **(a)** SH-SY5Y cells were co-treated 24 h with various concentrations of the tested chemical compounds alone and 10 µM of erastin. Ferrostatin-1 (Fer-1) was used as a positive control for ferroptosis inhibition. Cell viability was estimated by MTS assay. Data are shown as the mean ± SEM of two replicates. **(b)** SH-SY5Y cells were treated 24 h with 5 µM of RSL3 and increasing concentrations of nigratine or ferrostatin-1 (Fer-1). Cell death was evaluated by lactate dehydrogenase (LDH) release assay. Results are plotted in % of LDH release measured when cells are treated with RSL3 (left axis, colored blue). Cell viability was measured by MTS reduction assay. The results obtained (colored red) were plotted in % of maximal viability (detected in DMSO-treated cells, right axis). Data are shown as the mean ± SD of three replicates.

Canonical ferroptosis inhibitors like the lipophilic antioxidant, ferrostatin-1, prevent the accumulation of toxic lipid and cytosolic ROS, inhibiting ferroptotic cell death. As observed here using the DPPH assay, nigratine is comparatively less potent as an antioxidant than the two aromatic amines, ferrostatin-1 and α -tocopherol. We consequently hypothesize that nigratine does not use a mechanism linked to peroxy radical scavenging for inhibiting ferroptosis. Alternatively, nigratine may inhibit another cellular target that concomitantly contributes to the overall protection from RCD. Future work will be carried out to identify the molecular target(s) of nigratine in ferroptosis, using various approaches such as target fishing (see²⁹ for review). Identification of nigratine's molecular target(s) is a prerequisite for improving the efficacy of multi-target inhibitors on ferroptosis-related phenotypes, without affecting the activity of its primary target, the receptor-interacting protein kinase 1 (RIPK1). Numerous approaches are available to increase the efficacy of this class of drugs via rational drug design. These approaches include the combination of medicinal chemistry and computational strategies that has been successfully applied to dual-target kinase inhibitors³⁰.

Taken together, our results on nigratine indicate that pharmaceutical agents acting on both necroptosis and ferroptosis RCD pathways can be engineered for use in treating complex diseases that involve the activation of multiple RCD pathways. Our study sheds light on the emergence of polypharmacological approaches for treating multiple disorders in which necrosis is of central pathophysiological relevance, such as: ischemia–reperfusion injury in brain, heart and kidney, inflammatory diseases, sepsis, retinal disorders and neurodegenerative diseases.

Methods

Cell lines and culture. SH-SY5Y and HT22 cell lines were obtained from American Type Culture Collection (ATCC, Manassas, VA, USA) and were maintained in Dulbecco's modified eagle's medium (DMEM) containing 10% fetal bovine serum (FBS) in a humidified atmosphere of 5% CO₂ at 37 °C. LLC-PK1 was obtained

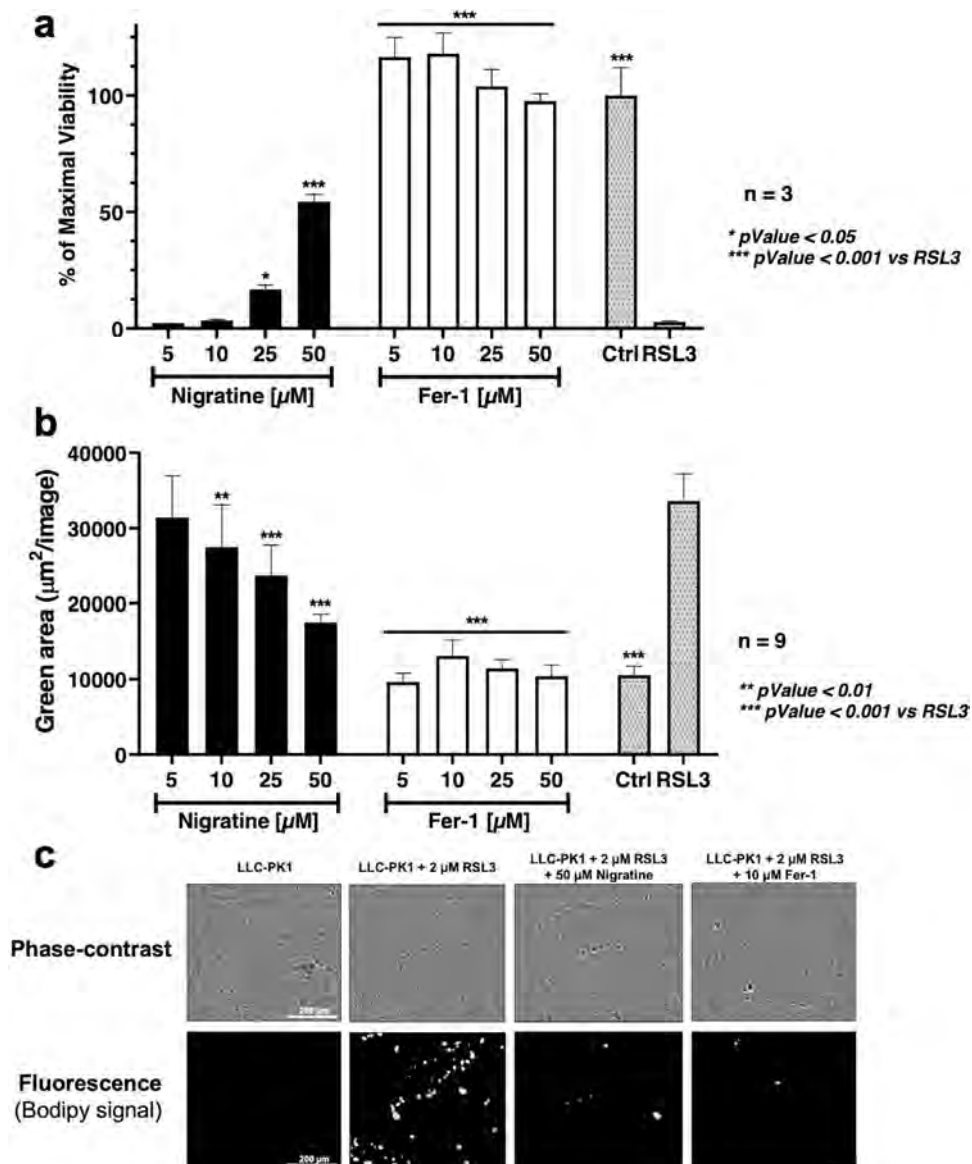


Figure 4. Nigratine protects porcine kidney epithelial LLC-PK1 cell line from lipid peroxidation and cell death triggered by RSL3. LLC-PK1 cell line was treated with 2 µM of RSL3 and increasing concentration of nigratine or ferrostatin-1 (Fer-1). **(a)** Cell viability was estimated by MTS assay. Data are shown as the mean ± SD of three replicates. **(b)** Lipid peroxidation was detected by cellular BODIPY 581/591 C11 staining. Fluorescence was recorded with the IncuCyte S3 live cell imaging apparatus. Data are shown as the mean ± SD of three replicates of nine replicates. **(c)** Representative phase-contrast and fluorescence images of cells stained with BODIPY 581/591 C11 probe are visualized using the IncuCyte S3 live cell imaging apparatus.

from the European Collection of Authenticated Cell Cultures (ECACC, Porton Down, Salisbury, UK) and maintained in M199 medium supplemented with 10% FBS and cultured in humidified atmosphere at 37 °C under 5% CO₂. Medium and serum were purchased from Thermo Fisher Scientific (Gibco, Waltham, MA, USA).

Reagents. Necrostatin-1 (Nec-1) and necrostatin-1s (Nec-1s) were from Calbiochem (VWR International, Fontenay-sous-Bois, France), Z-VAD was from Invivogen (Toulouse, France), Ferrostatin-1 (Fer-1), BV-6, Ras-selective lethal small molecule (RSL3) were from Selleckchem (Houston, TX, USA), 2,2-Diphenyl-1-picrylhydrazyl (DPPH), cumene hydroperoxide and α-tocopherol (vitamin E) were from Sigma Aldrich (St. Louis, MO, USA). Human TNF-α was obtained from Invitrogen (Carlsbad, CA, USA). This cytokine was used in the cell-based assay for the characterization of necroptosis inhibitors. Nigratine was obtained from SeaBeLife Biotech (Roscoff, France). The chemical synthesis of nigratine was described by Hauteville et al.³¹

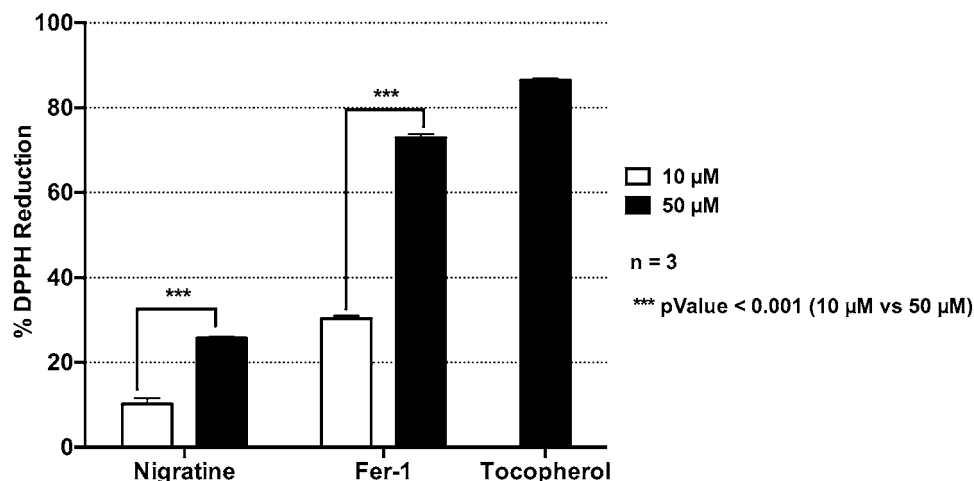


Figure 5. Antioxidant activity of nigratine. DPPH reduction assay was conducted for 30 min at room temperature after the addition of a DPPH solution at 15.85 μM (in 90/10, vol/vol, methanol/water) in 96-well plate. Reduction of DPPH was determined by absorbance measurement at 517 nm. Tocopherol (vitamin E), a well-known antioxidant, and Fer-1, as lipophylic antioxidant, were used as a positive controls. Data are shown as the mean ± SD of three replicates.

Cell death and cell viability assays. SH-SY5Y and HT22 cells were seeded in 96-well plates at a density of 10 000 or 5000 cells per well respectively, following overnight incubation. Cells were treated with 5 μM (SH-SY5Y cells) or 1 μM (HT22 cells) of RSL3; 10 μM (SH-SY5Y cells) or 0.5 μM (HT22 cells) of erastin or 5 mM (HT22 cells) of glutamate and increasing concentrations of compounds for 24 h (100 μl per well).

Cell death was determined by measurement of lactate dehydrogenase (LDH) leakage using the LDH Cytotoxicity assay kit (Invitrogen, Carlsbad, CA, USA) following manufacturer's recommendations. LDH is a cytosolic enzyme that is rapidly released into the supernatant after cell damage. After 24 h of treatment 50 μl of supernatants were transferred into a clean 96-well plates, reagents were added and LDH activity was measured using a microplate reader. Calculation of cytotoxicity was determined by dividing the LDH activity of each compounds with RSL3 by that of DMSO with RSL3, then multiplying the result by 100.

Cell viability was assessed by MTS assay (CellTiter 96[®] Aqueous Non-Radioactive Cell Proliferation Assay; Promega, Fitchburg, WI, USA) according to the manufacturer's instructions. This assay is based in the reduction of the 3-(4,5-dimethylthiazol-2-yl)-5-(3-carboxymethoxyphenyl)-2-(4-sulfophenyl)-2H-tetrazolium (MTS) by viable cells to form a colored formazan product. After treatment, cells were incubated 3 h at 37 °C, 5% CO₂ with MTS. The absorbance was measured using a microplate reader at 490 and 630 nm and the percentage of viability was calculated by dividing the absorbance of testing compound by the absorbance of DMSO treated cells (control).

Human bronchial organoid production and maintenance. Airway organoids were derived from healthy lung tissue of donors receiving surgical treatment for non-small cell lung carcinoma (NSCLC) as described^{32,33}. Human lung tissue was provided by the university hospital (CHU of Toulouse, France), according to the CNRS-approved protocol, CHU 19 244 C and Ref CNRS 205,782. An "informed consent to scientific use of their material" was obtained from all patients (or, if participants are under 18, from a parent and/or legal guardian) participating in this study. All methods were performed in accordance with the relevant guidelines and regulations. The organoids were passaged every 4 weeks.

Airway organoids stimulation. Before stimulation, 40 μl drops of Cultrex growth factor reduced BME type 2 (R & D Systems) containing airway organoids were seeded on Nunclon Delta surface 24-well plates (Thermo Scientific) and 500 μl of Advanced DMEM/F12 (Invitrogen) supplemented with 1 × L-Glutamine (Fisher Scientific) and 10 mM Hepes (Fisher Scientific) was added to each plate. Depending on the indicated conditions, organoids were pretreated or no with 25 μM nigratine (SeaBeLife Biotech, Roscoff, France), 40 μM necrostatin-1 or 40 μM Ferrostatin-1 for 1 h before stimulation. All the inhibitors were maintained throughout the experiment. After pretreatment, the organoids were stimulated to induce necroptosis with the mix of 40 μM Z-VAD, 100 ng/ml Human TNF-α and 5 μM BV-6 or to trigger ferroptosis with 800 μM of cumene hydroperoxide. For time-lapse imaging, stimulated organoids were stained with 50 μg/ml Propidium Iodide (Thermo Scientific). Images were acquired every 15 min for the duration of experiments under an EVOS M7000 (Thermo Scientific) Imaging System (10 × objective, organoids were incubated at 37 °C with 5% CO₂). Data was analyzed using the open source image processing program Fiji/ImageJ (<https://imagej.nih.gov/ij/index.html>).

RIPK1 kinase assay. Human RIPK1 full length GST-tagged was purchased from SignalChem (Richmond, CA, USA). The protocol used to detect the enzymatic activity was described in Delehouzé et al.¹⁷. Briefly, RIPK1

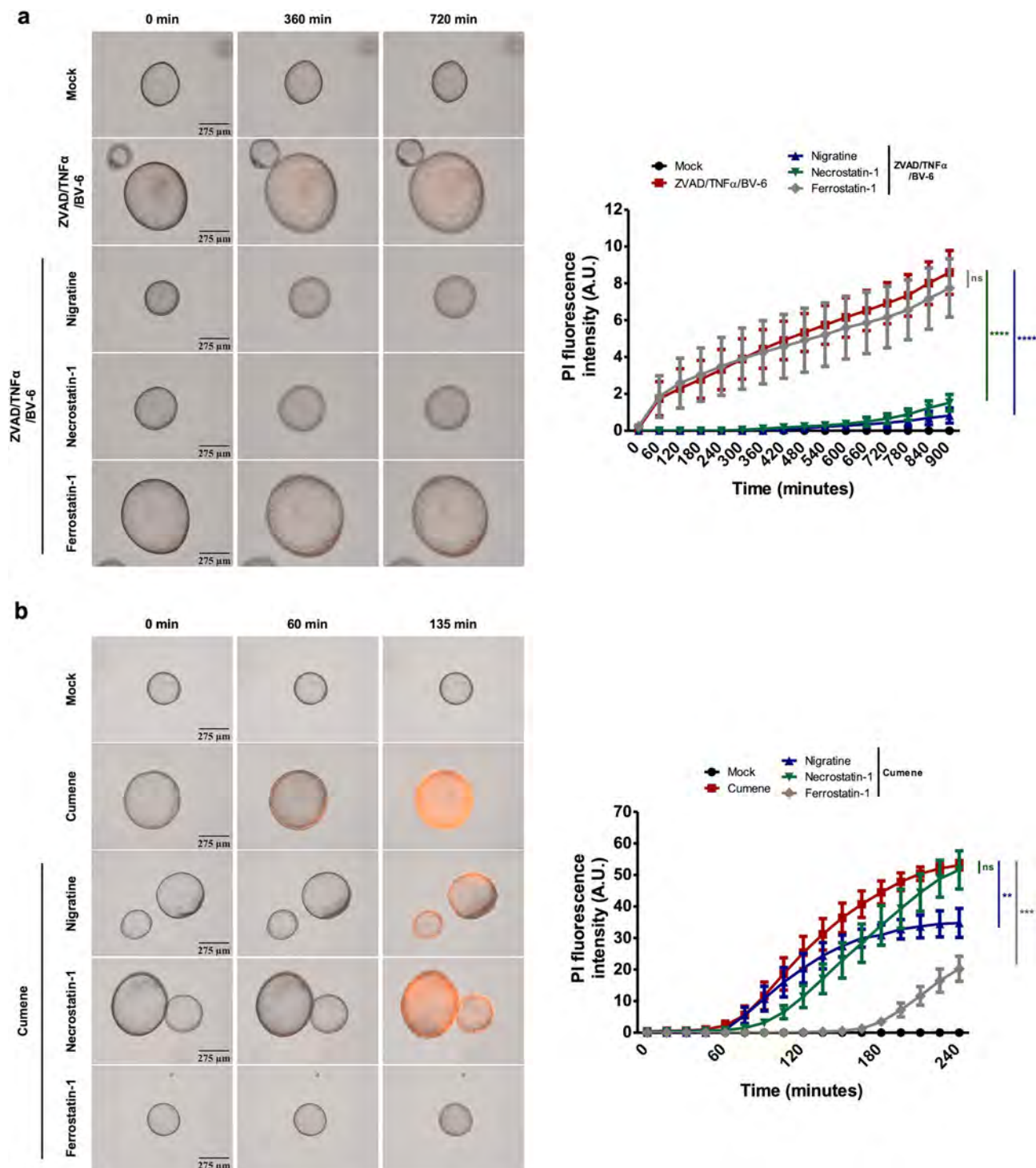


Figure 6. Nigraline protects human bronchial organoids from necroptosis and ferroptosis. **(a)** Time-lapse microscopy and the associated quantifications of the measure of plasma membrane permeabilization using propidium iodide incorporation in human primary bronchial organoids stimulated with the mix of 40 μM Z-VAD, 100 ng/ml Human TNF- α and 5 μM BV-6 in presence or absence of 25 μM nigraline, 40 μM necrostatin-1 or 40 μM ferrostatin-1 for 15 h. Data are plotted as means \pm SEM. pValue calculated by *t*-test. **(b)** Time-lapse microscopy and the associated quantifications of the measure of plasma membrane permeabilization using propidium iodide incorporation in human primary bronchial organoids stimulated with 800 μM of cumene hydroperoxide in presence or absence of 25 μM nigraline, 40 μM necrostatin-1 or 40 μM ferrostatin-1 for 4 h. Data are plotted as means \pm SEM. pValues were calculated by *t*-test (**pValue < 0.01, ***pValue < 0.001, ****pValue < 0.0001).

kinase was performed on KISSf Screening Facility (IBISA, Biogenouest, Station Biologique, Roscoff, France) with myelin basic protein (MBP, Sigma, #M1891) as substrate and in the presence of 15 μ M ATP.

Cell-based lipid peroxidation assay. Ferroptosis was induced by treatment of porcine LLC-PK1 cells (derived from the renal epithelial cells of Hampshire pigs PK1) with 2 μ M of RSL3. For lipid peroxidation assay, cells were seeded in 96-well black plates with clear bottom at a density of 10,000 cells per well. The assay was performed as previously described by Kahn-Kirby et al.³⁴. Briefly, after overnight incubation, cells were pre-labeled with 10 μ M of BODIPY 581/591 C11 dye (Invitrogen, Carlsbad, CA, USA) for 30 min at 37 °C; 5% CO₂. Cells were washed 3 times with PBS before adding treatment. Cells were then treated with RSL3 (2 μ M) and increasing concentrations of nigratine or ferrostatin-1 (Fer-1) and incubated at 37 °C with 5% CO₂ during 24 h in the IncuCyte S3 live-cell imaging and analysis system (Essen BioScience, Sartorius, Göttingen, Germany). Images were acquired using a 10X objective and 440–480 nm Excitation / 504–544 nm Emission filters, once hourly for up to 24 h.

DPPH reduction assay. Antioxidant activity of compounds was determined by a DPPH (2,2-Diphenyl-1-picrylhydrazyl) reduction assay. DPPH was prepared at 15.85 μ M in 90% methanol and added to several concentrations of compounds in 96-well plate (200 μ L per well). Tocopherol, a well-known antioxidant, was used as control. The reaction was conducted at room temperature for 30 min and absorbance was measured at 517 nm using the EnVision microplate reader (PerkinElmer, Waltham, MA, USA). The percentage of DPPH reduction was calculated by dividing the difference between the absorbance of DPPH and those of compounds by the absorbance of DPPH, and multiplying by 100.

Statistical analyses. Data from a minimum of two experiments were expressed as means \pm range; \pm SD or \pm SEM. Statistical analyses were done by ANOVA, Tukey's Multiple Comparison Test and Student's *t*-test for two groups of data, and significance levels used are **P* < 0.05, ***P* < 0.01, ****P* < 0.001, *****P* < 0.0001 by using GraphPad Prism6 software (GraphPad Software, San Diego, CA, USA).

Received: 23 March 2021; Accepted: 14 March 2022

Published online: 24 March 2022

References

- Gandini, A. *et al.* Tau-centric multitarget approach for Alzheimer's disease: Development of first-in-class dual glycogen synthase kinase 3beta and tau-aggregation inhibitors. *J. Med. Chem.* **61**, 7640–7656. <https://doi.org/10.1021/acs.jmedchem.8b00610> (2018).
- Albertini, C., Salerno, A., SenaMurteira Pinheiro, P. & Bolognesi, M. L. From combinations to multitarget-directed ligands: A continuum in Alzheimer's disease polypharmacology. *Med. Res. Rev.* <https://doi.org/10.1002/med.21699> (2020).
- Ehrlich, P. Beiträge zur Theorie und Praxis der histologischen Färbung. *The Collected Papers of Paul Ehrlich, London Pergamon*, 29–64 (2013).
- Roth, B. L., Sheffler, D. J. & Kroeze, W. K. Magic shotguns versus magic bullets: Selectively non-selective drugs for mood disorders and schizophrenia. *Nat. Rev. Drug Discov.* **3**, 353–359. <https://doi.org/10.1038/nrd1346> (2004).
- Rosini, M. Polypharmacology: The rise of multitarget drugs over combination therapies. *Future Med. Chem.* **6**, 485–487. <https://doi.org/10.4155/fmc.14.25> (2014).
- Ramsay, R. R., Popovic-Nikolic, M. R., Nikolic, K., Uliassi, E. & Bolognesi, M. L. A perspective on multi-target drug discovery and design for complex diseases. *Clin. Transl. Med.* <https://doi.org/10.1186/s40169-017-0181-2> (2018).
- Galluzzi, L. *et al.* Molecular mechanisms of cell death: Recommendations of the nomenclature committee on cell death 2018. *Cell Death Differ.* **25**, 486–541. <https://doi.org/10.1038/s41418-017-0012-4> (2018).
- Dixon, S. J. *et al.* Ferroptosis: An iron-dependent form of nonapoptotic cell death. *Cell* **149**, 1060–1072. <https://doi.org/10.1016/j.cell.2012.03.042> (2012).
- Aguilera, A. *et al.* Cell Death in cyanobacteria: Current understanding and recommendations for a consensus on its nomenclature. *Front. Microbiol.* <https://doi.org/10.3389/fmicb.2021.631654> (2021).
- Degterev, A. *et al.* Chemical inhibitor of nonapoptotic cell death with therapeutic potential for ischemic brain injury. *Nat. Chem. Biol.* **1**, 112–119. <https://doi.org/10.1038/nchembio711> (2005).
- Degterev, A., Ofengeim, D. & Yuan, J. Targeting RIPK1 for the treatment of human diseases. *Proc. Natl. Acad. Sci.* **116**, 9714–9722. <https://doi.org/10.1073/pnas.1901179116> (2019).
- Samson, A. L. *et al.* MLKL trafficking and accumulation at the plasma membrane control the kinetics and threshold for necroptosis. *Nat. Commun.* <https://doi.org/10.1038/s41467-020-16887-1> (2020).
- Martens, S., Hofmans, S., Declercq, W., Augustyns, K. & Vandenebeele, P. Inhibitors targeting RIPK1/RIPK3: old and new drugs. *Trends Pharmacol. Sci.* **41**, 209–224. <https://doi.org/10.1016/j.tips.2020.01.002> (2020).
- Tonnus, W. *et al.* Dysfunction of the key ferroptosis-surveillance systems hypersensitizes mice to tubular necrosis during acute kidney injury. *Nat. Commun.* **12**, 4402. <https://doi.org/10.1038/s41467-021-24712-6> (2021).
- Le Cann, F. *et al.* Sibiriline, a new small chemical inhibitor of receptor-interacting protein kinase 1, prevents immune-dependent hepatitis. *FEBS J.* **284**, 3050–3068. <https://doi.org/10.1111/febs.14176> (2017).
- Benchekroun, M. *et al.* Discovery of simplified benzazole fragments derived from the marine benzoscoperin B as necroptosis inhibitors involving the receptor interacting protein Kinase-1. *Eur. J. Med. Chem.* <https://doi.org/10.1016/j.ejmech.2020.112337> (2020).
- Delehouze, C. *et al.* 6E11, a highly selective inhibitor of receptor-interacting protein kinase 1, protects cells against cold hypoxia-reoxygenation injury. *Sci. Rep.* **7**, 12931. <https://doi.org/10.1038/s41598-017-12788-4> (2017).
- Conrad, M., Angeli, J. P., Vandenebeele, P. & Stockwell, B. R. Regulated necrosis: Disease relevance and therapeutic opportunities. *Nat. Rev. Drug Discov.* **15**, 348–366. <https://doi.org/10.1038/nrd.2015.6> (2016).
- Lewerenz, J., Ates, G., Methner, A., Conrad, M. & Maher, P. Oxytosis/ferroptosis—(re-) emerging roles for oxidative stress-dependent non-apoptotic cell death in diseases of the central nervous system. *Front. Neurosci.* <https://doi.org/10.3389/fnins.2018.00214> (2018).
- Ito, K. *et al.* MPP+ induces necrostatin-1- and ferrostatin-1-sensitive necrotic death of neuronal SH-SY5Y cells. *Cell Death Discov.* **3**, 17013. <https://doi.org/10.1038/cddiscovery.2017.13> (2017).
- Chan, F. K.-M., Moriwaki, K. & De Rosa, M. J. In *Immune Homeostasis Methods in Molecular Biology* Ch. Chapter 7, 65–70 (2013).

22. Grootjans, S., Vanden Berghe, T. & Vandenabeele, P. Initiation and execution mechanisms of necroptosis: An overview. *Cell Death Differ.* **24**, 1184–1195. <https://doi.org/10.1038/cdd.2017.65> (2017).
23. Yang, W. S. & Stockwell, B. R. Ferroptosis: Death by lipid peroxidation. *Trends Cell Biol.* **26**, 165–176. <https://doi.org/10.1016/j.tcb.2015.10.014> (2016).
24. Kajarabille, D. & Latunde, D. Programmed cell-death by ferroptosis: Antioxidants as mitigators. *Int. J. Mol. Sci.* <https://doi.org/10.3390/ijms20194968> (2019).
25. Hu, Z. X. *et al.* VDR activation attenuate cisplatin induced AKI by inhibiting ferroptosis. *Cell Death Dis.* **11**, 2 (2020).
26. Deng, F., Sharma, I., Dai, Y. B., Yang, M. & Kanwar, Y. S. Myo-inositol oxygenase expression profile modulates pathogenic ferroptosis in the renal proximal tubule. *J. Clin. Investig.* **129**, 5033–5049. <https://doi.org/10.1172/Jci129903> (2019).
27. Xu, Y. F. *et al.* A role for tubular necroptosis in cisplatin-induced AKI. *J. Am. Soc. Nephrol.* **26**, 2647–2658. <https://doi.org/10.1681/Asn.2014080741> (2015).
28. Brady, H. R. & Singer, G. G. Acute renal failure. *Lancet* **346**, 1533–1540. [https://doi.org/10.1016/s0140-6736\(95\)92057-9](https://doi.org/10.1016/s0140-6736(95)92057-9) (1995).
29. Guiffant, D. *et al.* Identification of intracellular targets of small molecular weight chemical compounds using affinity chromatography. *Biotechnol. J.* **2**, 68–75 (2007).
30. Sun, D. *et al.* Dual-target kinase drug design: Current strategies and future directions in cancer therapy. *Eur. J. Med. Chem.* <https://doi.org/10.1016/j.ejmech.2019.112025> (2020).
31. Hauteville, M., Chopin, J., Geiger, H. & Schuler, L. Protogenkwanin, a new flavonoid from equisetum-arvense L. *Tetrahedron* **37**, 377–381. [https://doi.org/10.1016/S0040-4020\(01\)92024-1](https://doi.org/10.1016/S0040-4020(01)92024-1) (1981).
32. Iakobachvili, N. *et al.* Mycobacteria-host interactions in human bronchiolar airway organoids. *Mol. Microbiol.* <https://doi.org/10.1111/mmi.14824> (2021).
33. Sachs, N. *et al.* Long-term expanding human airway organoids for disease modeling. *EMBO J.* <https://doi.org/10.15252/embj.2018100300> (2019).
34. Kahn-Kirby, A. H. *et al.* Targeting ferroptosis: A novel therapeutic strategy for the treatment of mitochondrial disease-related epilepsy. *PLoS ONE* <https://doi.org/10.1371/journal.pone.0214250> (2019).

Acknowledgements

We thank Amandine Bescond for advice on the DPPH assay and Blandine Baratte for RIPK1 inhibition assays. The authors also thank the Cancéropôle Grand Ouest ("Marines molécules, métabolisme et cancer" network), IBSA (French Infrastructures en sciences du vivant: biologie, santé et agronomie), Biogenouest (Western France life science and environment core facility network supported by the Conseil Régional de Bretagne) for supporting the KISSf screening facility (FR2424, CNRS and Sorbonne Université), Roscoff, France. Claire Delehouzé is recipient of a CIFRE PhD fellowship. Stéphane Bach and Marie-Thérèse Dimanche-Boitrel were supported by SATT Ouest Valorisation ("Gref-Pres" maturation program). Stéphane Bach is supported by the Fondation d'Entreprise Grand Ouest ("Houarnine" program). SeaBeLife is supported by the Technopole Brest Iroise, BPI, Biotech Santé Bretagne and Région Bretagne.

Author contributions

C.D. performed and analyzed in vitro data and co-wrote the manuscript. S.L.I., C.C. and E.M. performed and analyzed the results on human bronchial organoids. A.C. and M.H. synthesized and characterized nigratine chemical compound. P.G. and M.T.D.B. analyzed results of chemical synthesis and biological evaluation, respectively, and revised the manuscript. M.R. and S.B. supervised the study (design and coordination) and were the co-promoters of the PhD of CD. J.C.B. co-wrote and revised the manuscript. S.B. wrote the manuscript. All the authors read and approved the final manuscript submitted for publication.

Competing interests

Claire Delehouzé, Marie-Thérèse Dimanche-Boitrel, Morgane Rousselot and Stéphane Bach are the founders and members of the scientific advisory board of SeaBeLife Biotech, which is developing novel therapies for treating liver and kidney acute disorders. Peter Goekjian is member of the scientific advisory board of SeaBeLife Biotech. The other authors declare that they have no competing interests.

Additional information

Correspondence and requests for materials should be addressed to M.R. or S.B.

Reprints and permissions information is available at www.nature.com/reprints.

Publisher's note Springer Nature remains neutral with regard to jurisdictional claims in published maps and institutional affiliations.



Open Access This article is licensed under a Creative Commons Attribution 4.0 International License, which permits use, sharing, adaptation, distribution and reproduction in any medium or format, as long as you give appropriate credit to the original author(s) and the source, provide a link to the Creative Commons licence, and indicate if changes were made. The images or other third party material in this article are included in the article's Creative Commons licence, unless indicated otherwise in a credit line to the material. If material is not included in the article's Creative Commons licence and your intended use is not permitted by statutory regulation or exceeds the permitted use, you will need to obtain permission directly from the copyright holder. To view a copy of this licence, visit <http://creativecommons.org/licenses/by/4.0/>.

© The Author(s) 2022

V. Host phospholipid peroxidation fuels ExoU-dependent cell necrosis and supports *Pseudomonas aeruginosa*-driven pathology

Authors: Salimata Bagayoko, **Stephen Adonai Leon-Icaza***, Miriam Pinilla*, Audrey Hessel*, Karin Santoni, David Péricat, Pierre-Jean Bordignon, Flavie Moreau, Elif Eren, Aurélien Boyancé, Emmanuelle Naser, Lise Lefèvre, Céline Berrone, Nino Iakobachvili, Arnaud Metais, Yoann Rombouts, Geanncarlo Lugo-Villarino, Agnès Coste, Ina Attrée, Dara W. Frank, Hans Clevers, Peter J. Peters, Céline Cougoule, Rémi Planès, Etienne Meunier.

*These authors contributed equally.

Contribution: I quantified the peroxidized lipids in figure 3E. For Figure 4G, I designed, standardized, and performed the microinjection process of *Pseudomonas aeruginosa* in healthy airway organoids, as well as I performed time-lapse microscopy and the associated quantifications of the measure of plasma membrane permeabilization using propidium iodide incorporation in human airway organoids infected (microinjection) with *P. aeruginosa* expressing exoU+ or its isogenic mutant (exoU-) in presence or absence of ferrostatin-1 (a lipid peroxidation inhibitor). I also participated in the writing of the article.

This article was published in PLOS Pathogens.

RESEARCH ARTICLE

Host phospholipid peroxidation fuels ExoU-dependent cell necrosis and supports *Pseudomonas aeruginosa*-driven pathology

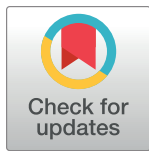
Salimata Bagayoko¹, Stephen Adonai Leon-Icaza^{1☯}, Miriam Pinilla^{1☯}, Audrey Hessel^{1☯}, Karin Santoni¹, David Péricat¹, Pierre-Jean Bordignon¹, Flavie Moreau^{1,2}, Elif Eren¹, Aurélien Boyancé¹, Emmanuelle Naser^{1,3}, Lise Lefèvre⁴, Céline Berrone^{1,2}, Nino Iakobachvili⁵, Arnaud Metais¹, Yoann Rombouts¹, Geancarlo Lugo-Villarino¹, Agnès Coste⁴, Ina Attrée⁶, Dara W. Frank⁷, Hans Clevers⁸, Peter J. Peters⁵, Céline Cougoule¹, Rémi Planès^{1✉*}, Etienne Meunier^{1✉*}

1 Institute of Pharmacology and Structural Biology (IPBS), University of Toulouse, CNRS, Toulouse, France, **2** Level 3 Biosafety Animal Core facility, Anexplo platform, Institute of Pharmacology and Structural Biology (IPBS), University of Toulouse, CNRS, Toulouse, France, **3** Cytometry & Imaging Core facility, Institute of Pharmacology and Structural Biology (IPBS), University of Toulouse, CNRS, Toulouse, France, **4** RESTORE institute, University of Toulouse, CNRS, Toulouse, France, **5** Division of Nanoscopy, Maastricht Multimodal Molecular Imaging Institute, Maastricht University, Maastricht, The Netherlands, **6** Univ. Grenoble Alpes, CNRS, CEA, IBS, Bacterial Pathogenesis and Cellular Responses, Grenoble, France, **7** Department of Microbiology and Immunology, Medical College of Wisconsin, Milwaukee, Wisconsin, United States of America, **8** Oncode Institute, Hubrecht Institute, Royal Netherlands Academy of Arts and Sciences and University Medical Center, Utrecht, Netherlands

☯ These authors contributed equally to this work.

✉ Current Address: Institute of Pharmacology and Structural Biology (IPBS), CNRS, Toulouse; France

* remi.planes@ipbs.fr (RP); etienne.meunier@ipbs.fr (EM)



OPEN ACCESS

Citation: Bagayoko S, Leon-Icaza SA, Pinilla M, Hessel A, Santoni K, Péricat D, et al. (2021) Host phospholipid peroxidation fuels ExoU-dependent cell necrosis and supports *Pseudomonas aeruginosa*-driven pathology. PLoS Pathog 17(9): e1009927. <https://doi.org/10.1371/journal.ppat.1009927>

Editor: Gregory P. Priebe, Children's Hospital Boston, UNITED STATES

Received: February 19, 2021

Accepted: August 29, 2021

Published: September 13, 2021

Peer Review History: PLOS recognizes the benefits of transparency in the peer review process; therefore, we enable the publication of all of the content of peer review and author responses alongside final, published articles. The editorial history of this article is available here: <https://doi.org/10.1371/journal.ppat.1009927>

Copyright: © 2021 Bagayoko et al. This is an open access article distributed under the terms of the [Creative Commons Attribution License](https://creativecommons.org/licenses/by/4.0/), which permits unrestricted use, distribution, and reproduction in any medium, provided the original author and source are credited.

Data Availability Statement: All relevant data are within the manuscript and its [Supporting Information](#) files [S1](#) and [S2](#) Datas.

Abstract

Regulated cell necrosis supports immune and anti-infectious strategies of the body; however, dysregulation of these processes drives pathological organ damage. *Pseudomonas aeruginosa* expresses a phospholipase, ExoU that triggers pathological host cell necrosis through a poorly characterized pathway. Here, we investigated the molecular and cellular mechanisms of ExoU-mediated necrosis. We show that cellular peroxidised phospholipids enhance ExoU phospholipase activity, which drives necrosis of immune and non-immune cells. Conversely, both the endogenous lipid peroxidation regulator GPX4 and the pharmacological inhibition of lipid peroxidation delay ExoU-dependent cell necrosis and improve bacterial elimination *in vitro* and *in vivo*. Our findings also pertain to the ExoU-related phospholipase from the bacterial pathogen *Burkholderia thailandensis*, suggesting that exploitation of peroxidised phospholipids might be a conserved virulence mechanism among various microbial phospholipases. Overall, our results identify an original lipid peroxidation-based virulence mechanism as a strong contributor of microbial phospholipase-driven pathology.

Funding: This project was funded by grants from the National Research Agency (ANR, Endiabac), FRM “Amorçage Jeunes Equipes” (AJE20151034460), ERC StG (INFLAME 804249) and ATIP-Avenir program to EM, from National Research Agency (ANR, MacGlycoTB) to YR, from the European Society of Clinical Microbiology and Infectious Diseases (ESCMID, 2020) to RP, from the Van Gogh Programme to IPBS-M4i institutes, from Invivogen-CIFRE collaborative PhD fellowship to MP and from the FRM (FDT202106012794), Mali and Campus France cooperative agencies to SB. The funders had no role in study design, data collection and analysis, decision to publish, or preparation of the manuscript.

Competing interests: The authors have declared that no competing interests exist.

Author summary

Although a proper activation of various regulated cell necrosis confer a significant advantage against various infectious agents, their dysregulation drives host tissue damages that can end up with fatal sepsis. Specifically, 30% of the bacterial strains of *Pseudomonas aeruginosa* (*P. aeruginosa*) express the phospholipase A2-like toxin ExoU that is injected into host target cells through the Type-3 Secretion System. This toxin induces, through a yet unknown mechanism, a strong and fast necrotic cell death that supports fatal respiratory infections. Therefore, in this study, we sought to determine the cellular mechanisms by which ExoU triggers host cell necrosis. In this context, we found that ExoU exploits basal cellular phospholipid peroxidation to promote cell necrosis. Mechanistically, host cell lipid peroxidation stimulates ExoU phospholipase activity, which then triggers a pathological cell necrosis both *in vitro* and *in vivo*. Altogether, our results unveil that targeting host cell lipid peroxidation constitutes a virulence mechanism developed by microbial phospholipases, a process that contributes to *P. aeruginosa*-mediated pathology.

Introduction

Regulated cell necrosis (RCNs) drives physiological and immune processes, yet dysregulation of this process promotes pathological responses such as organ-failure and sepsis [1–4]. Mechanistically, oxygen-dependent cell death is an evolutionary conserved process that involves the production of reactive oxygen species (ROS), transition metals (e.g. iron) and peroxidised lipid accumulation [5–8]. In addition to cell necrosis, lipid peroxidation broadly involves cellular processes essential to mediate optimal efferocytosis of dead cells, cellular communication resulting from the formation of lipids derived from peroxidised phospholipids (e.g. isoprostanes, platelet activating factor) or the production of bioactive lipids (eicosanoids) from arachidonic acid [9,10]. In addition, the peroxidation of the mitochondrial phospholipid cardiolipin initiates apoptosis while the accumulation of peroxidised phosphatidyl ethanolamines (PE) promote the cellular necrosis, ferroptosis [11–17]. Specifically, the dysregulation of lipid peroxidation processes is associated with various human pathologies such as cancer chemoresistance, brain and ischemia injuries, neurological alterations, metabolic diseases as well as tuberculosis susceptibility [18–23]. In this context, the enzymes glutathione peroxidase 4 (GPX4) and ferroptosis-suppressor protein-1 (FSP1) that belongs to the CoQ antioxidant system, detoxify phospholipid hydroperoxide accumulation, hence allowing lipid peroxide amounts to be balanced in cells [5,11,12,14,24]. On the contrary, iron excess, lipoxygenase activity or cytochrome P450 oxidoreductase (CYPOR) all promote phospholipid peroxidation, which can end with ferroptosis induction in the absence of proper regulation [5,14–16,25,26].

In this regard, the bacterial pathogen *Pseudomonas aeruginosa* (*P. aeruginosa*) expresses ExoU, an A2 phospholipase from the patatin family, that triggers a necrosis-dependent pathology through a poorly understood pathway [27–36]. In presence of cellular co-factors such as ubiquitin [31] or the trafficking chaperone DNAJC5 [37], ExoU activity rapidly cleaves at the sn-2 position of host membrane phospholipids, liberating large amounts of arachidonic acid that are then metabolized into eicosanoids by cellular enzymes cyclooxygenases, cytochrome P450 or lipoxygenases [32,38–40]. Importantly, *in vivo*, ExoU expression by *P. aeruginosa* is associated with a robust production of oxidized lipids such the platelet activating factor (PAF) or isoprostanes [38,41]. In this context, we explored the possibility that *P. aeruginosa* ExoU mediates a necrosis-dependent host pathology involving lipid peroxidation.

Results

P. aeruginosa infection triggers ExoU-dependent alarmin and peroxidised lipid production in mice

P. aeruginosa ExoU is injected into cells by the Type-3 Secretion System (T3SS) [28,36], which triggers a fast and violent cellular necrosis. Therefore, we first monitored the profile of ExoU-dependent pathology in mice infected with the clinical isolate PP34 *exoU*⁺ or its isogenic mutant (*exoU*⁻). Similar to previous studies [27,29,42,43], intranasal instillation with either *exoU*⁺ or *exoU*⁻ strains highlighted a *P. aeruginosa*-induced acute pathology mainly due to ExoU, as mice infected with *exoU*⁻ bacteria showed improved survival to infection (Fig 1A). This observation was paralleled with lower bacterial loads of *P. aeruginosa* *exoU*⁻ than *exoU*⁺ in the bronchoalveolar lavage fluids (BALFs), the lungs, the blood and the spleen, suggesting that ExoU also promotes bacterial dissemination (Fig 1B). As *P. aeruginosa* triggers NLR4-, NLRP3- and Caspase-11-dependent inflammasome response [42,44,45–52,53], we infected inflammasome-deficient mice (*Casp1/Casp11*^{-/-}, *Nlrc4*^{-/-} and *GasderminD*^{-/-}) and observed that those mice were not protected against *P. aeruginosa* *exoU*⁺, hence suggesting that ExoU-promoted mouse pathology occurs independently from the inflammasome machineries (S1A and S1B Fig). A hallmark of host cell necrosis is the release of intracellular mediators such as alarmins that contribute to the initiation and the development of an inflammatory reaction, which occurs upon *P. aeruginosa* infection [42,54]. Therefore, we primarily focused our analysis on alarmin release. We observed a strong ExoU-dependent alarmin production in BALFs 6

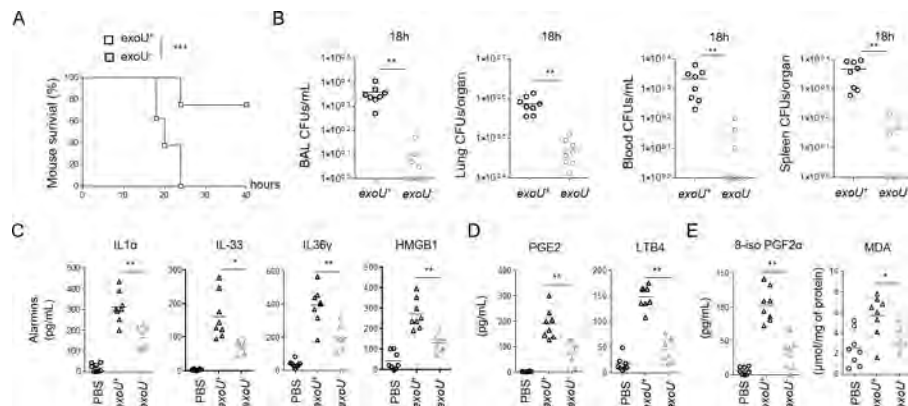


Fig 1. ExoU-dependent lung pathology in mice associates to an alarmin and peroxidized lipid signature. (A) Survival of WT mice intranasally infected ($n = 7$ animals per condition) with 5.10^5 CFUs of *P. aeruginosa* PP34 or its isogenic mutant PP34^{*exoU*⁻}. Graphs represent one experiment (8 mice/group) out of three independent *in vivo* experiments. Log-rank Cox-Mantel test was used for survival comparisons. *** $p \leq 0.001$. (B) Bronchoalveolar (BAL), lung, blood and spleen bacterial loads from WT mice ($n = 8$) 18 hours after intranasal infection with 5.10^5 CFUs of *P. aeruginosa* PP34 or its isogenic mutant PP34^{*exoU*⁻}. Graphs represent one experiment (8 mice/group) out of three independent *in vivo* experiments. ** $p \leq 0.01$, Mann-Whitney analysis test. (C) Alarmin levels in bronchoalveolar fluids (BALFs) from WT mice ($n = 8$) 6 hours after intranasal infection with 5.10^5 CFUs of *P. aeruginosa* PP34 or its isogenic mutant PP34^{*exoU*⁻}. Graphs represent one experiment (8 mice/group) out of three independent *in vivo* experiments; * $p \leq 0.05$; ** $p \leq 0.01$, Mann-Whitney analysis test. (D) Prostaglandin E2 (PGE2) and Leukotriene B4 (LTB4) levels in bronchoalveolar fluids (BALFs) from WT mice ($n = 8$) 6 hours after intranasal infection with 5.10^5 CFUs of *P. aeruginosa* PP34 or its isogenic mutant PP34^{*exoU*⁻}. Graphs represent one experiment (8 mice/group) out of three independent *in vivo* experiments; ** $p \leq 0.01$, Mann-Whitney analysis test. (E) Peroxidized lipid product (isoprostanes and MDA) levels in bronchoalveolar fluids (BALFs) from WT mice ($n = 8$) 6 hours after intranasal infection with 5.10^5 CFUs of *P. aeruginosa* PP34 or its isogenic mutant PP34^{*exoU*⁻}. Graphs represent one experiment (8 mice/group) out of three independent *in vivo* experiments; * $p \leq 0.05$; ** $p \leq 0.01$, Mann-Whitney analysis test. Data information: Data shown as means (Graphs B-E) and are representative of one experiment performed three times; * $p \leq 0.05$; ** $p \leq 0.01$, *** $p \leq 0.001$, Mann-Whitney analysis test (B-E) and log-rank Cox-Mantel test for survival comparisons (A).

<https://doi.org/10.1371/journal.ppat.1009927.g001>

h after infection, such as IL-1 family alarmins IL1 α , IL-33 or IL-36 γ [55] (Fig 1C). In addition, we also detected that *exoU*-expressing *P. aeruginosa* triggered a strong production of phospholipid- and arachidonic acid (aa)-derived mediators such as prostaglandin E2 and leukotriene B4, which correlates with the robust phospholipase activity of ExoU (Fig 1D) [38–40]. Importantly, BALFs of mice infected with *exoU*-expressing *P. aeruginosa* also exhibited a marked presence of oxidized lipid (by)-products such as isoprostanes (8-iso PGF2 α) or Malondialdehyde (MDA), which suggests that *exoU*-expressing *P. aeruginosa* also drives an exacerbated lipid oxidation response in mice (Fig 1E) [41,56].

Lipid peroxidation contributes to ExoU-induced cell necrosis and *P. aeruginosa* escape from phagocyte-mediated killing

The observation that *exoU*-expressing *P. aeruginosa* infection associates to a lipid peroxidation signature *in vivo*, encouraged us to determine the importance of lipid peroxidation on ExoU-induced cellular necrosis. As *P. aeruginosa* strains that do not express ExoU can promote an NLRC4 inflammasome response in macrophages [50], we used mouse Bone-Marrow-Derived Macrophages (BMDMs) that lack *Nlr4* expression to specifically address the importance of lipid peroxidation on ExoU-dependent cell necrosis. We infected *Nlr4*^{-/-} primary murine BMDMs with *P. aeruginosa* strains expressing or not expressing ExoU. The pharmacological inhibition of various regulated necrosis pathways (e.g. pyroptosis, necroptosis, apoptosis, parthanatos) showed that only ferrostatin-1, a potent and well characterized inhibitor of phospholipid peroxidation [57], repressed ExoU-dependent cell necrosis (Figs 2A and 2B and S2A and S1–S6 Movies). Ferrostatin-1 action was specific to lipid peroxidation-dependent cell necrosis as it also inhibited Cumene hydroperoxide-induced ferroptosis (CuOOH, 400 μ M) but not Flagellin-/LPS-induced pyroptosis or TCPA-1/Z-VAD/TNF α -dependent necroptosis (Fig 2B). In addition, ExoU-induced IL-1 α and HMGB1 alarmin release in macrophages was reduced in presence of ferrostatin-1 whereas TNF α levels remained similar (Fig 2C), suggesting that lipid peroxidation contributes to alarmin release in response to ExoU. We noticed that ExoU-triggered ferrostatin-1-sensitive necrosis was not restricted to murine BMDMs as primary human macrophages, the human U937 monocytic cell line, human and murine neutrophils and eosinophils, the human bronchial epithelial (HBEs), A549 or HeLa epithelial cells were all sensitive to lipid peroxidation inhibition upon infection with *exoU*-expressing *P. aeruginosa* (S2A and S2B Fig). ExoU exhibits a calcium-independent phospholipase A2-like activity [33]. Hence, we transfected recombinant ExoU protein (rExoU) or its enzymatically inactive mutant ExoU^{S142A} [58] in WT BMDMs and monitored for cell necrosis. Only macrophages transfected with active ExoU underwent to cell death, a process that was inhibited by the use of ferrostatin-1 or the phospholipase inhibitor MAFP (S2C Fig). In line, we found that ferrostatin-1 itself did not alter bacterial growth or ExoU secretion (S2D and S2E Fig), suggesting that ferrostatin-1 does not directly alter bacterial physiology nor expression/secretion of ExoU. Upon phospholipase activation arachidonic acid release can be metabolized and oxidized by various cellular enzymes, including cyclooxygenases 1 and 2 (COX1, COX2), lipoxygenases (ALOX5 and ALOX12/15 in mice) or cytochrome p450 (CYPs) enzymes. Therefore, we transfected recombinant ExoU in WT, *Alox5*^{-/-} or *Alox12/15*^{-/-} BMDMs in presence or absence of various COX, CYP or different lipid peroxidation inhibitors (a-tocopherol, liprostatin-1, Resveratrol, ferrostatin-1). Although we observed that all lipid peroxidation inhibitors have a strong inhibitory impact on cell death, cyclooxygenase, cytochrome P450 or lipoxygenase targeting did not interfere with ExoU-dependent cell necrosis, hence suggesting that those enzymes do not regulate lipid-peroxidation-dependent cell necrosis upon ExoU exposure (Fig 2D). Importantly, we also observed that ferrostatin-1 delayed ExoU-induced cell necrosis,

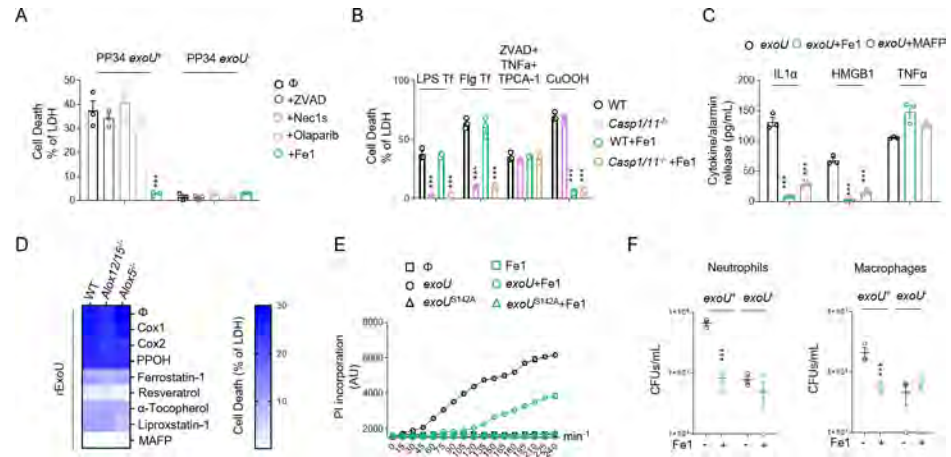


Fig 2. Lipid peroxidation inhibition delays ExoU-induced cell necrosis. Otherwise specified, cells were infected with an MOI of 0.5 of *P. aeruginosa* PP34, PP34^{exoU} or PP34^{exoUS142A} for various times. ***p ≤ 0.001, t-test with Bonferroni correction. (A) Measure of LDH release in *Nlr4*^{-/-} BMDMs infected with PP34 or PP34^{exoU} in presence of Z-VAD (40μM), olaparab (10μM), Necrostatin-1s (Ne1s, 40μM) or Ferrostatin-1 (Fe1, 10μM) for 2 hours. ***p ≤ 0.001, t-test with Bonferroni correction. (B) Measure of LDH release in WT or *Casp1*^{-/-}/*Casp11*^{-/-} BMDMs transfected (Lipofectamin 2000) with 1μg of LPS or Flagellin (Flg) to induce pyroptosis, treated with Z-VAD (40μM)/TNFα (500UI/mL)/TPCA-1 (5 μM) to induce necroptosis or with Cumene hydroperoxide (CuOOH, 400μM) to induce ferroptosis in presence or absence of Ferrostatin-1 (Fe1, 10μM) for 6 hours. ***p ≤ 0.001, t-test with Bonferroni correction. (C) Measure of alarmin/cytokine release in *Nlr4*^{-/-} BMDMs infected with PP34 or PP34^{exoU} in presence of Z-VAD (40μM), olaparab (10μM), Necrostatin-1s (Ne1s, 40μM) or Ferrostatin-1 (Fe1, 10μM) for 2 hours. ***p ≤ 0.001, t-test with Bonferroni correction. (D) Heat map representing measure of LDH release in WT, *ALOX5*^{-/-} and *ALOX12/15* BMDMs transfected with recombinant ExoU in presence/absence of Cox1 inhibitor (Ketorolac Tromethamine, 10μM), Cox2 inhibitor (NS 398, 25μM), Cyp450 epoxygenase activity inhibitor (PPOH, 10μM), phospholipase inhibitor MAFP (50μM) or lipid peroxidation inhibitors Ferrostatin-1 (Fe1, 20μM), Resveratrol (5μM), Liproxstatin-1 (30μM), a-Tocopherol (20μM) for 2 hours. The heat map shows the mean of three combined independent experiments, each performed in triplicate. (E) Time course measure of plasma membrane permeabilization using propidium iodide incorporation in *Nlr4*^{-/-} BMDMs infected with PP34 or PP34^{exoUS142A} in presence/absence of Ferrostatin-1 (Fe1, 20μM). ***p ≤ 0.001, t-test with Bonferroni correction. (F) Microbicidal activity of macrophages (5h) and neutrophils (3h) after infection with *P. aeruginosa* *exoU*⁺ and *exoU*⁻ (MOI 0.5) in presence/absence of ferrostatin-1 (10μM). ***p ≤ 0.001, t-test with Bonferroni correction. Data information: Data are represented as means +/- SEM (graphs A - F) from n = 3 independent pooled experiments; ***p ≤ 0.001 for the indicated comparisons using t-test with Bonferroni correction.

<https://doi.org/10.1371/journal.ppat.1009927.g002>

suggesting either that the phospholipase activity of ExoU promotes lipid peroxidation-independent cell death or that the inhibitory effect of ferrostatin-1 is unstable over time (Fig 2E). Regarding this, the replenishment of *P. aeruginosa*-infected cells with fresh ferrostatin-1 each hour strongly improved cell viability, suggesting that the instability of Fe1 might also account in the delayed ExoU-induced cell necrosis we observed (S2F Fig). Finally, we evaluated if the inhibition of lipid peroxidation would modulate macrophage and neutrophil microbicidal response upon *exoU*-expressing *P. aeruginosa* infection. We observed that ferrostatin-1 strongly improved both macrophage and neutrophil microbicidal activities to a level close to those observed in response to *exoU*-deficient *P. aeruginosa* (Fig 2F), hence suggesting that *P. aeruginosa* ExoU relies on lipid peroxidation-dependent cell necrosis to escape from phagocyte attack. Together, our results suggest that host cell lipid peroxidation is important for ExoU-induced host cell necrosis and release of alarmins.

Lipid peroxidation fuels ExoU phospholipase activity

Lipid-peroxidation requires reactive oxygen species (ROS), such as H₂O₂, that can oxidize various phospholipids [5]. Therefore, we evaluated the ability of ExoU to induce ROS-dependent lipid peroxidation in macrophages. Although we observed that, 30 minutes after transfection,

ExoU but not its catalytically inactivated mutant ExoU^{S142A}, triggered an acute ROS production in BMDMs, we surprisingly failed to detect a robust lipid peroxidation accumulation as measured by the C11 Bodipy probe (Figs 3A and S3A and S3B). As control, the well-known lipid peroxidation inducer Cumene hydroperoxide (CuOOH) promoted cellular lipid peroxidation (Fig 3A) [59]. In contrast, we observed that basal lipid peroxidation in cells was reduced upon ExoU transfection or PP34 infection, a process that was further strengthened in presence of ferrostatin-1 (Figs 3A and S3B).

These results suggest that, instead of promoting pathological lipid peroxidation, ExoU might actually use cellular lipid peroxidation to promote cell necrosis. To this regard, various host phospholipase A2 enzymes have been described to specifically cleave and remove peroxidised phospholipids from membranes [60–62]. To address this hypothesis, we performed a redox phospholipidomic approach to determine if ExoU could interfere with the endogenous levels of peroxidised phospholipids (Figs 3B and S3C). We used a 45 min time-point to perform our experiments, as a point where plasma membrane permeabilization (propidium uptake monitoring) is not observed. This design excludes the possibility that a decrease in peroxidised phospholipids is due to cell necrosis induced by ExoU (S3D Fig). We observed that ExoU-treated macrophages had a decrease in peroxidised phospholipids as measured by the reduction in hydroperoxyl (-OOH)- and hydroxyl (-OH)-phosphoinositols (PIs)/- phosphoserines (PSs) and—phosphocholines (PCs) with arachidonic acid (C20:4/C22:4) acid side chains (Figs 3B and S3C).

In cells, peroxidised phospholipids are detoxified by various factors, one of the most important being the ferroptosis regulator glutathione peroxidase 4 (GPX4) [5]. Consequently, the use of pro oxidant molecules or *Gpx4* genetic inactivation both induce a strong accumulation of various peroxidised phospholipids in cell membranes [5]. Therefore, we hypothesized that prestimulation of macrophages with non-cytotoxic doses of the lipid peroxidation and ferroptosis inducer Cumene hydroperoxide (20μM, 1h) might sensitize cells to ExoU-induced cell necrosis. We transfected recombinant (r)ExoU in WT BMDMs in presence or absence of non-toxic doses of the pro-oxidant Cumene hydroperoxide (CuOOH, 20μM, 1h) [59]. Although CuOOH promoted lipid peroxidation but not BMDM cell death, rExoU transfection specifically induced an increased cell necrosis in CuOOH-primed BMDMs, a process that was inhibited by the use of ferrostatin-1 (Fig 3C and 3D). In agreement with this result, we measured a strong decrease in lipid peroxidation in CuOOH-primed cells transfected with rExoU (Fig 3C and 3D), confirming that ExoU efficiently targeted lipid peroxides induced by CuOOH. In addition, microscopy observations of CuOOH-primed cells highlighted a decrease of peroxidized lipids at the plasma membrane upon infection by ExoU-expressing strain of *P. aeruginosa* (PP34), suggesting that ExoU mostly target plasma membrane peroxidized phospholipids to promote cell necrosis (Fig 3E). The enzyme cytochrome p450 oxidoreductase (CYPOR) has recently been found to be an important provider of peroxidized phospholipids upon ferroptosis induction; we hypothesized that ExoU function might be regulated by CYPOR-regulated phospholipid peroxidation. We acquired *Cypor*-deficient HeLa cells but also generated *Cypor*^{-/-} immortalized (i)BMDMs using CRISPR (S3E Fig) and evaluated the importance of CYPOR on ExoU-driven cell necrosis. PP34 infection of WT and *Cypor*^{-/-} immortalized BMDMs triggered similar cell deaths, suggesting that in resting cells, CYPOR does not promote the basal lipid peroxidation involved in ExoU-dependent cell necrosis (Fig 3G and 3H). However, in CuOOH-primed macrophages, where phospholipid peroxidation is induced, we observed that CYPOR was a major contributor of phospholipid peroxidation (S3F Fig). This was associated to enhanced ability of PP34 to trigger cell necrosis in CuOOH-primed WT but not in *Cypor*^{-/-} iBMDMs and HeLa cells (Fig 3G and 3H), which suggests that CYPOR-induced lipid peroxidation heightens ExoU-dependent toxicity. However, in resting cells,

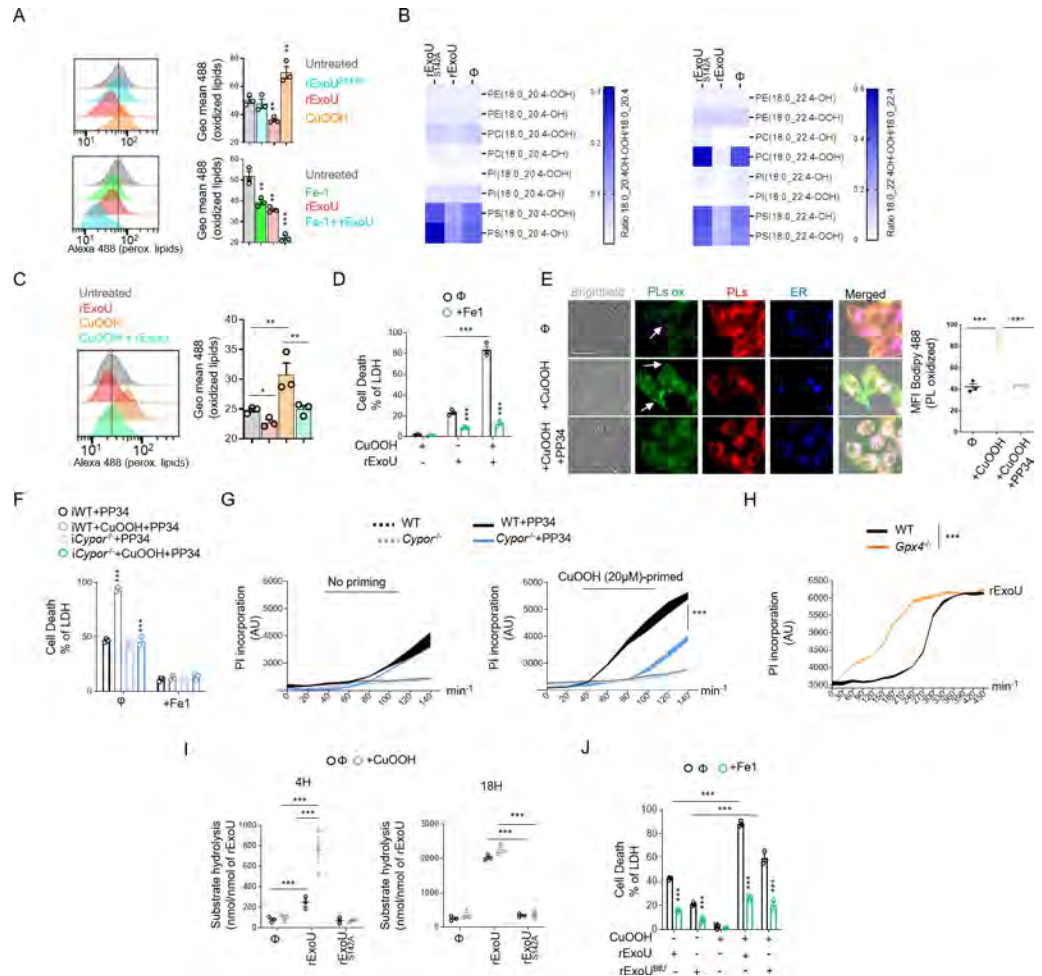


Fig 3. ExoU-induced cell death involves ROS-induced lipid peroxidation but proceeds in a ferroptosis independent manner. (A) Cytometry detection and quantification of (phospho)lipid peroxidation using the probe C11-bodipy in WT BMDMs treated with CuOOH (20µM) or transfected with rExoU (500ng) or its catalytically dead mutant rExoU^{S142A} (500ng) for 1 hour in presence or absence of Ferrostatin-1 (20µM). Sample were acquired using FACSCalibur (BD). The graphs shows the mean±/SEM of one experiment performed in triplicate out of three independent experiments. **P≤0.001, ***P≤0.001 for the indicated comparisons using t-test with Bonferroni correction. (B) (Redox) lipidomic analysis of phospholipid peroxidation in BMDMs transfected with recombinant ExoU or its catalytically dead mutant ExoU^{S142A} for 45 minutes. Each value is standardized to the corresponding phospholipid content shown in (S3B Fig). The heat map shows the mean of one experiment performed in triplicate. (C) Cytometry detection and quantification of (phospho)lipid peroxidation using the probe C11-bodipy in WT BMDMs pre-treated or not for 1 hour with CuOOH (20µM) in presence or absence of Ferrostatin-1 (20µM) and then transfected with rExoU (500ng) for 1 hour. Sample were acquired using FACSCalibur (BD). The graphs shows the mean±/SEM of one experiment performed in triplicate out of three independent experiments. *P≤0.05, **P≤0.001, for the indicated comparisons using t-test with Bonferroni correction. (D) Measure of LDH release in WT BMDMs pre-treated or not for 1 hour with CuOOH (20µM) in presence or absence of Ferrostatin-1 (20µM) and then transfected with rExoU (500ng) for 3 hours. ***p≤0.001, T-test with Bonferroni correction. (E) Representative microscopy images (phospho)lipid peroxidation and quantifications using the probe C11-bodipy in CuOOH-primed (20µM) HELA cells infected with PP34 (MOI5) for 2 hours. Images show two independent experiments, each performed three times at 2 hours post infection. Scale bar 20µm; Green, oxidized bodipy (oxidized phospholipids, PLs ox); Red, bodipy (phospholipids, PLs); Blue (Endoplasmic Reticulum, ER tracker probe, 1µM). Arrows show enriched peroxidised phospholipids in the plasma membrane area. Quantifications show the Mean Fluorescence Intensity (MFI) quantification of Peroxidized lipids from one experiment performed three times (50–60 cells counted). ***P<0.001 by T-test. (F) Measure of LDH release in immortalized (i) WT or *Cypor*^{-/-} BMDMs primed or not with CuOOH (20µM, 1hour) in presence or absence of ferrostatin-1 (20µM) and infected for 2 hours with PP34. ***p≤0.001, T-test with Bonferroni correction. (G) Time course measure of plasma membrane permeabilization using propidium iodide incorporation in WT and *Cypor*^{-/-} HELA cells primed or not with CuOOH (20µM, 1hour) and infected with PP34 (MOI5) for 2 hours. ***p≤0.001, T-test with Bonferroni correction. (H) Time course measure of plasma membrane permeabilization using propidium iodide incorporation in immortalised WT and *Gpx4*^{-/-} BMDMs transfected with rExoU (500ng) for 7 hours. ***p≤0.001, T-test with Bonferroni correction. (I) ExoU phospholipase

activity determination in WT BMDM lysates pre-treated or not with CuOOH (20 μ M, 1hour). 100 pmols of ExoU were used and phospholipase hydrolysis rate (nmoles of substrate hydrolysed/nmole of ExoU) was measured after 4 h and 16 hours. *** $p \leq 0.001$, T-test with Bonferroni correction. (J) Measure of LDH release in WT BMDMs primed or not with CuOOH (20 μ M, 1hour) in presence or absence of ferrostatin-1 (20 μ M) and transfected for 3 hours with 5 μ g of rExoU^{BtU} or 500ng rExoU. *** $p \leq 0.001$, T-test with Bonferroni correction. Data information: Data are plotted as means \pm SEM (D, F-J) from $n = 3$ independent pooled experiments; *** $P \leq 0.001$ for the indicated comparisons using t-test with Bonferroni correction.

<https://doi.org/10.1371/journal.ppat.1009927.g003>

basal lipid peroxidation appears to be regulated by other processes/enzymes. Finally, using Crispr-Cas9, we generated *Gpx4*^{-/-} immortalized BMDMs (S3G Fig). As previously observed by others in other cell lines [16,24], *Gpx4*^{-/-} immortalized BMDMs exhibited increased basal levels of peroxidised lipids (S3H Fig). Therefore, rExoU transfection triggered faster cell death of *Gpx4*^{-/-} macrophages than their WT counterpart, suggesting that lipid peroxidation of cells enhances ExoU-dependent toxicity (Figs 3H and S3G and S3H).

Upon phospholipid peroxidation, arachidonic acid-containing phospholipids form isoprostanes that are potent intra- and extra-cellular inflammatory mediators [9,10]. Once formed, these isoprostanes are released from phospholipids by the action of phospholipases [9,10]. Therefore, we reasoned that if ExoU targets peroxidised phospholipids, this would promote ExoU phospholipase-dependent release of endogenous pre-formed isoprostanes. Accordingly, the release of the 8-PGF2 α isoprostane was specifically induced by ExoU in WT macrophages, a process that was further amplified by the co treatment of cells with non-toxic concentrations of Cumene hydroperoxide (CuOOH 20 μ M, 1 h) and ExoU (S3I Fig). Of importance, ferrostatin-1 strongly inhibited ExoU- and ExoU/CuOOH-induced 8-PGF2 α release (S3I Fig). In addition, we also detected that in CuOOH-primed macrophages, the amount of arachidonic acid-derived eicosanoids leukotriene B4 and prostaglandin E2, which are an indirect indication of the phospholipase activity of ExoU, were also strongly increased after the exposure to ExoU, hence suggesting that ExoU-targeted peroxidised phospholipids might increase its phospholipase activity toward all phospholipids (peroxidized or not) (S3J Fig). Consequently, we measured the phospholipase activity of ExoU in cell lysates where we chemically induced non-lethal lipid peroxidation with Cumene hydroperoxide (CuOOH, 20 μ M) for 1 h or not. We observed that in CuOOH-primed cell lysates, ExoU exhibited a stronger activity than in unprimed samples after 4 h of incubation (Fig 3I). Importantly, after 18 h incubation, we observed the same accumulation of hydrolysed substrate in CuOOH-primed and unprimed samples, which suggests that lipid peroxidation exacerbates the early activation of ExoU (Fig 3I). As control, ExoU^{S142A}- treated cell lysates did not show a significant phospholipase activity induction, suggesting that we mostly measured the PLA2 activity from ExoU, but not from cellular phospholipases (Fig 3I). Finally, we aimed at challenging our findings by determining if other toxic phospholipases also had a similar activation pattern to ExoU. Hence, we transfected macrophages with the closely related patatin-like phospholipase A2 from *Burkholderia thailandensis* (ExoU^{BtU}) [31]. We observed that recombinant ExoU^{BtU} transfection induced BMDMs necrosis, a process that was exacerbated by CuOOH priming and inhibited by the use of ferrostatin-1, suggesting that ExoU^{BtU} also follows a pattern involving host cell lipid peroxidation (Fig 3J). Altogether, our results suggest a surprising mechanism by which ExoU exploits cellular lipid peroxidation to trigger necrosis, a process that can be extended to the action of *B. thailandensis* ExoU^{BtU}-related phospholipase.

Ferrostatin-1 improves mouse resistance to infection by *exoU*-expressing *P. aeruginosa*

ExoU-induced necrosis promotes host lung pathology, which leads to a sepsis like response as well as respiratory failure syndrome. Therefore, we hypothesized that ferrostatin-1 use could

protect mice against *exoU*-expressing *P. aeruginosa*. Intranasal infection of mice using *P. aeruginosa* *exoU*⁺ showed that mice intraperitoneally pre-treated with ferrostatin-1 (6 h before infection, 6mg.k⁻¹) had diminished bacterial loads in BALFs, lungs and spleen. Ferrostatin-1 pre-treatment did not significantly modify bacterial loads of *exoU*-deficient bacteria, suggesting that ferrostatin-1 mainly modulates ExoU-dependent processes in mice (Fig 4A). Similarly, ferrostatin-1 also attenuated ExoU-dependent alarmin release (e.g. IL-36γ, IL33, IL1α) and the level of oxidized lipids (isoprostanes, MDA) in the BALs (Fig 4B and 4C). Additionally, evaluation of the cellular contents in BALFs showed that ferrostatin-1 significantly protected a pool of alveolar macrophage upon *P. aeruginosa* challenge simultaneously decreasing the number of recruited neutrophils, eosinophils and monocytes (Figs 4D and S4A). Although a pathological function of recruited immune cells such as neutrophils is probable, we hypothesize that ferrostatin-1-inhibited resident alveolar macrophage death in response to *exoU*-expressing *P. aeruginosa* might confer an improved immune protection characterized by lower immune cell recruitment and lower tissue damages. Regarding this, lung histological observations showed that the inflammatory status of mice infected with non-lethal doses of ExoU-expressing *P. aeruginosa* (1.10⁵ CFUs) was improved in presence of ferrostatin-1 (Fig 4E). Next, we addressed survival upon ExoU-expressing *P. aeruginosa* challenge. We observed that ferrostatin-1-treated mice (4–6 h before infection, 6mg.k⁻¹) had an improved survival rate than those treated with PBS after 40 h after infection (Fig 4F). We validated that ferrostatin-1 specifically protected mice against ExoU-induced pathology as ferrostatin-1-treated mice did not show enhanced protection (survival) against ExoU-deficient *P. aeruginosa* (Fig 4F).

Finally, we aimed to evaluate if *P. aeruginosa* ExoU would trigger pathological lipid peroxidation-dependent cell necrosis in human bronchial organoids. Organoids were derived from normal lung tissue adjacent to tumors obtained from patients undergoing lung resection due to non-small cell lung carcinoma (NSCLC). Live cell imaging of organoids microinjected with *P. aeruginosa* showed that ExoU triggered complete organoid collapse (Fig 4G and S7–S12 Movies). Importantly, ferrostatin-1 strongly attenuated *P. aeruginosa*-dependent organoid damages (Fig 4G and S7–S12 Movies). Altogether, our results identified that *P. aeruginosa* ExoU phospholipase benefits from lipid peroxidation to trigger pathology both in mice and in human bronchial organoids.

Discussion

As a preferential extracellular pathogen, *P. aeruginosa* uses its Type 3-Secretion System (T3SS) to inject virulence factors (Exo S, T, Y and U), allowing bacterial escape from phagocytic uptake and killing. Although *exoS*-expressing *P. aeruginosa* strains associate to the development of chronic infections, *exoU*-expressing *P. aeruginosa* triggers acute deadly infections that associate with a strong oxidative imbalance. In this study, we describe that endogenous basal lipid peroxidation contributes to ExoU-dependent cellular toxicity and mouse pathology. Though we do not exclude that *in vivo*, lipid peroxidation might play various pathological roles that go beyond the sole regulation of cell necrosis, such processes appear to be linked to ExoU expression. In this context, previous studies showed that ExoU promotes production of the platelet-activating factor or the 8-PGF2α isoprostane, two oxidized lipids [41]. In addition, ExoU directly promotes a strong release of arachidonic acid from phospholipids. Enzymes such as cytochrome P450/COXs/LOXs can enzymatically produce oxygenated arachidonic products such as prostaglandin E2/leukotriene B4 involved in pathological signalling pathways upon *P. aeruginosa* infection [38,40,63]. However, results from others and ours mostly suggest that, taken individually, those enzymes only play a negligible role in ExoU-induced cell necrosis [38,40,63]. Regarding the central cell types involved in ExoU-induced pathology, previous studies identified macrophages and

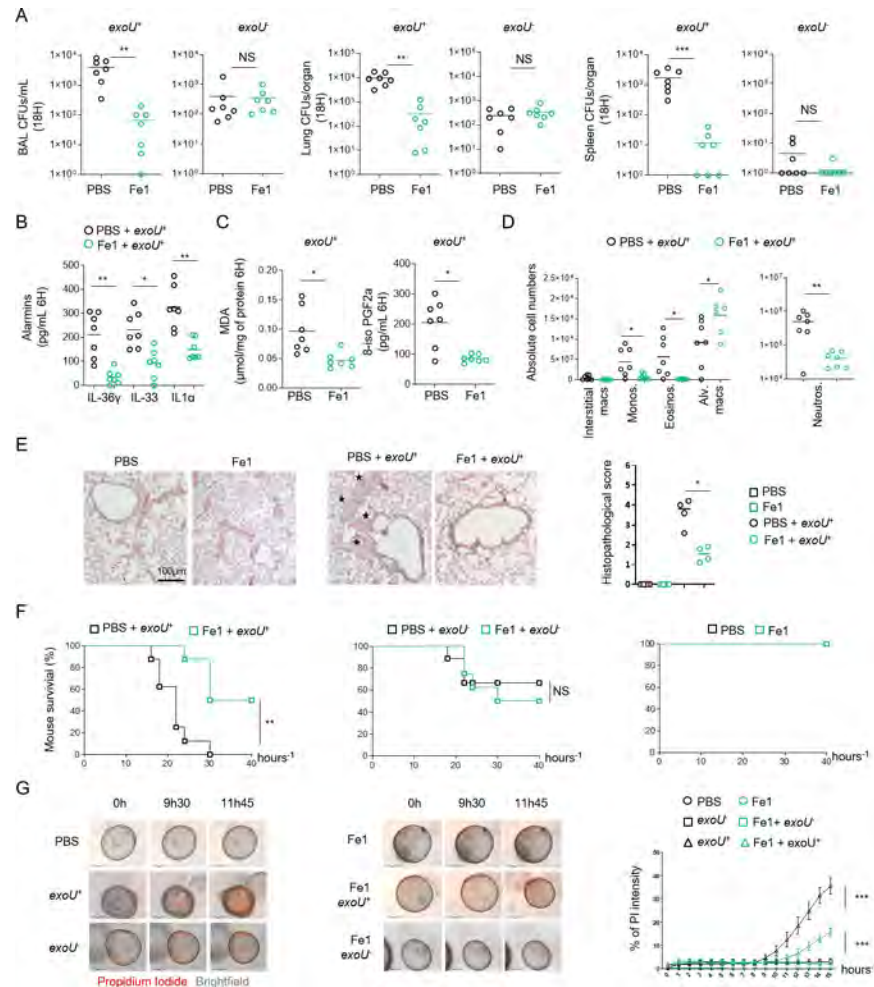


Fig 4. Ferrostatin-1 protects mice against ExoU-induced lung pathology. (A) Bronchoalveolar (BAL), lung and spleen bacterial loads from WT mice (n = 7/group) 18 hours after intranasal infection with 5.10^5 CFUs of *P. aeruginosa* PP34 or its isogenic mutant PP34^{exoU-}. When specified, mice were intraperitoneally pretreated with ferrostatin-1 (6mg.k⁻¹ or PBS) 4 hours before intranasal infection. Graphs represent one experiment (7 mice/group) out of three independent *in vivo* experiments. **p ≤ 0.01, Mann-Whitney analysis test. NS: Not significant. (B, C) Alarmin and lipid peroxide products levels in bronchoalveolar fluids (BALFs) from WT mice (n = 7 mice/group) 6 hours after intranasal infection with 5.10^5 CFUs of *P. aeruginosa* PP34 or its isogenic mutant PP34^{exoU-}. When specified, mice were intraperitoneally pretreated with ferrostatin-1 (6mg.k⁻¹ or PBS) 4 hours before intranasal infection. Graphs represent one experiment (7 mice/group) out of three independent *in vivo* experiments; *p ≤ 0.05; **p ≤ 0.01, Mann-Whitney analysis test. (D) Immune cell (CD45+) populations in bronchoalveolar fluids (BALFs) from WT mice (n = 7 mice/group) 6 hours after intranasal infection with 5.10^5 CFUs of *P. aeruginosa* PP34 or its isogenic mutant PP34^{exoU-}. When specified, mice were intraperitoneally treated with ferrostatin-1 (6mg.k⁻¹ or PBS) 4–6 hours before intranasal infection. Graphs represent one experiment (7 mice/group) out of three independent *in vivo* experiments; *p ≤ 0.05; **p ≤ 0.01, Mann-Whitney analysis test. (E) Histological observation and scoring of bronchial and lung cellular infiltrations upon *exoU*-expressing *P. aeruginosa* intranasal infection. When specified, mice were intraperitoneally pretreated with ferrostatin-1 (6mg.k⁻¹ or PBS) 4–6 hours before intranasal infection. Stars show the cellular infiltrates. *p ≤ 0.05; Mann-Whitney analysis test. (F) Mice survival (n = 7 mice/group) 40 hours after intranasal infection with 5.10^5 CFUs of *P. aeruginosa* PP34 or its isogenic mutant PP34^{exoU-}. Mice were intraperitoneally pretreated with ferrostatin-1 (6mg.k⁻¹ or PBS) 4 hours before intranasal infection. Graphs represent one experiment (7 mice/group) out of three independent *in vivo* experiments; **p ≤ 0.01, Log-rank Cox-Mantel test was used for survival comparisons. (G, H) Time-lapse microscopy and the associated quantifications of the measure of membrane permeabilization using propidium iodide incorporation in human primary bronchial organoids infected (microinjection) with *P. aeruginosa* expressing *exoU*⁺ or its isogenic mutant (*exoU*) in presence or absence of ferrostatin-1 (40μM) for 15 hours. Data are plotted as means± SEM. ***p ≤ 0.001, T-test with Bonferroni correction. Data information: Data shown as means (Graphs A–E) and are representative of one experiment performed three times; *p ≤ 0.05; **p ≤ 0.01, Mann-Whitney analysis test (A–E) and log-rank Cox-Mantel test for survival comparisons (F).

<https://doi.org/10.1371/journal.ppat.1009927.g004>

neutrophils as central targets of ExoU injection by *P. aeruginosa*. Therefore, future studies will be of importance to determine if the respective contribution of each cell type in pathology induced by ExoU-exploited lipid peroxidation. Regarding this, our *in vivo* observations that targeting lipid peroxidation confers some protection of mice against ExoU-dependent pathology is to put in the light of a decrease in some eicosanoid production such as LTB4 and PGE2, two important modulators of ExoU-driven pathology [38,40,63]. Therefore, the use of *Alox5^{-/-}* or *Cox^{-/-}* mice, unable to generate LTB4 or various prostaglandins respectively, will also help to determine the respective importance of eicosanoid burst or cell necrosis upon lipid peroxidation-driven ExoU activity.

Although controlled phospholipid peroxidation is of importance for the cells to perform various processes such as efferocytosis through the engagement of peroxidised-PS, mitochondria-dependent apoptosis through cardiolipin peroxidation, signal transduction through peroxidised PC-derived lipids, unrestricted accumulation of peroxidised PEs drives ferroptosis [9,10,64]. A question in both basal lipid peroxidation and ferroptosis-induced lipid peroxidation lies on the compartment phospholipid peroxidation occurs. Peroxisomes are key at providing ether-phospholipids that will be peroxidised upon ferroptosis induction, the Endoplasmic reticulum is also a central regulator of phospholipid turn over and plasma membrane constitutes the probable location of lipid peroxidation-driven cell lysis upon ferroptosis induction [16,65,66]. Our observations also suggest that although lipid peroxidation can occur in various cellular compartments, ExoU-induced cell necrosis mostly arises from plasma membrane cleaved peroxidized phospholipids. Yet, this does not exclude at all that phospholipid peroxidation could occur in other intracellular organelles, including the endoplasmic reticulum.

Ferroptosis is thought to be a constitutively activated form of cell death that is kept under control through the activity of endogenous regulators of lipid peroxidation such as GPX4, FSP1-mediated coQ10 production, α -tocopherol (vitamin E). In addition, the host cellular calcium (Ca^{2+})-independent PLA2 γ , the peroxiredoxin Prdx6 PLA2 or the PLA2G6 (Ca^{2+} -independent PLA2 β) can cleave and remove preferentially peroxidised phospholipids, hence contributing to phospholipid peroxide detoxification [61,62,67–71]. It is important to notice that both the iPLA2 β and iPLA2 γ belong to the patatin-like phospholipase family, as ExoU, which suggests that this family of phospholipases might have some conserved affinities to peroxidized phospholipids [72]. The activity of those phospholipases is tightly regulated by various cellular systems (e.g. ROS levels, calcium fluxes, phospholipid composition) that ensure an optimal but not dysregulated phospholipid cleavage [71]. To this regard, our findings that cellular phospholipid peroxidation is a strong enhancer of ExoU-induced pathological necrosis appears in first view counter intuitive. In this context, we envision that, as a virulence factor, ExoU activity does not follow host regulation and uses host peroxidized phospholipids to boost its patatin-like A2 phospholipase activity allowing to aberrantly target and cleave host (peroxidized) phospholipids. Consequently, the use of lipid peroxidation inhibitors such as resveratrol, lipoxstatin-1 or ferrostatin-1 attenuates the potency and the speed of ExoU-induced cell necrosis. This offers a key time window for macrophage and neutrophil-mediated bacterial uptake and killing. Although, the identification of cellular enzymatic systems that promote basal lipid peroxidation remains to be explored and characterized, lipid peroxidation accumulation upon *Gpx4* removal or oxidant stress enhances ExoU-induced cellular necrosis. It is intriguing that endogenous peroxidised phospholipids favour ExoU-induced cell necrosis, suggesting that ExoU-expressing strains of *P. aeruginosa* take advantage of the host ferroptosis pathways to maximally damage host tissues. Hence, oxidant-activated cytochrome P450 oxidoreductase CYPOR, a crucial regulator of ferroptosis, strongly enhanced ExoU-dependent cell necrosis, which suggests a important link between ferroptosis-regulated pathways and ExoU activity. Should other regulators of ferroptosis such as ACSL and LPCAT acyl transferases on ExoU-dependent toxicity warrants further investigations [15].

Phospholipases are also present in venoms or various microbial pathogens (e.g. *M. tuberculosis*, *L. monocytogenes*, *S. pyogenes*) and can also promote fast cell necrosis [73–75]. Conversely, we extended our findings to the ExoU closely related ExoU^{BtU} phospholipase from *B. thailandensis*. Remarkably, snake, scorpion or spider venoms are a complex mixture of various components, including the L-amino acid oxidase, able to generate H₂O₂-driven lipid peroxidation, and secreted phospholipases able to cleave phospholipids [73]. In this context, it is tempting to speculate that venoms have all components necessary to mediate cell damage in a complex single-injection mixture. L-amino acid oxidase-induced lipid peroxidation might work with venom PLA2 to optimize phospholipid cleavage and subsequent cell necrosis. Related to this, Sevanian and colleagues made pioneer observations that the PLA2 activity from the snake *Crotalus adamanteus* is exacerbated in contact of liposomes constituted of peroxidised phospholipids, a process that is thought to be due to the better accessibility of the sn2-peroxidized fatty acid to phospholipase [70]. Whether ExoU and its relatives follow a similar pathway of activation will be studied in future studies.

In a broader point of view, it is interesting to note that phospholipases can promote allergic shock associated with a strong release of the allergic alarmin interleukin-33 [76], a signature we also observed in mice infected with ExoU-expressing *P. aeruginosa*. Should lipid peroxidation be involved in IL33-driven allergy or asthma in response to phospholipases or other allergens (e.g. proteases) [77] will require additional study.

Understanding the mechanisms of regulated cell necrosis and their physio-pathological consequences is currently driving intensive research and debates. While the importance of lipid peroxidation in antigen presentation, anti-cancer treatments or in exacerbating neurodegenerative diseases becomes more and more clear, its function in infectious diseases remains less studied. Regarding this, Dar et al., recently described that, upon chronic infection, secreted *P. aeruginosa* lipoxygenase (loxA) could sensitize cells to lipid peroxidation-induced ferroptosis [22]. In addition, Kain and colleagues recently linked regulation of host lipid peroxidation and ferroptosis to restriction of liver-stage malaria, which suggests that host peroxidised phospholipids might play yet unsuspected functions in immunity or susceptibility to various pathogens [78]. Thus, our findings that the bacterial patatin-like phospholipase A2 ExoU contributes to pathology by exploiting target cell lipid peroxidation adds an additional piece of significance for the role of lipid peroxidation in infectious diseases but also offers novel insights to target host lipid peroxidation pathways in the frame of infectious diseases ([S1 Graphical Abstract](#)).

Material and method

Ethics statements

The use of human cells was performed under the agreement of the Research Ethical Committee, Haute-Garonne, France. Buffy coats came anonymously by the EFS (établissement français du sang, Toulouse, France). For each donor, a written informed consent was obtained according to the EFS contract agreement n° 21PLER2017-0035AV02, according, to “Decret N° 2007–1220 (articles L1243-4, R1243-61)”.

Animal experiments were approved by local (CE01 committee) and national ethic committees (License APAFIS#8521–2017041008135771, Minister of Research, France) and performed according to local guidelines (French ethical laws) and the European Union animal protection directive (Directive 2010/63/EU).

Mice

Nlr4^{-/-}, *Casp1*^{-/-}*Casp11*^{-/-}, *GsdmD*^{-/-}, *ALOX12/15*^{-/-} and *ALOX5*^{-/-} mice were generated and described in previous studies [79–82]. Mice were bred at the IPBS (Toulouse, France) animal

facilities in agreement to the EU and French directives on animal welfare (Directive 2010/63/EU). Charles Rivers provided WT C57BL/6 mice.

Animal infection models

6–10 mice/group were intranasally infected with 5.10^5 Colony Forming Units (CFUs) of *P. aeruginosa* PP34 strain (*ExoU*⁺) or its isogenic mutant (*ExoU*⁻) and animal survival was followed over 40–50 hours after infection. When specified, mice were intraperitoneally treated with 100 μ L of PBS or ferrostatin-1 (6mg.k^{-1}) 4–6 hours before intranasal infections with bacterial strains.

Regarding bacterial loads assays, 6–10 mice/group were intranasally infected with 2.10^5 bacteria for 24 hours, and Bronchoalveolar (BALs), lung spleen and blood bacterial numbers were evaluated using CFU plating. BAL fluids (BALFs) were also used to address cytokine, alarmin and lipid levels using ELISA, EIA and colorimetric kits. There were no randomization or blinding performed.

Histological experiments and scoring

Mice were intraperitoneally treated with 100 μ L of PBS or ferrostatin-1 (6mg.k^{-1}) 4–6 hours before intranasal infections with sub-lethal doses (2.10^5 CFUs) of *exoU*-expressing *P. aeruginosa*. 6 hours later, lung tissues were fixed for 48 h in 10% buffered formalin, washed 3 times in ethanol 70% and embedded in paraffin. 5 μ m sections were stained with hematoxylin and eosin (HE). Histopathological scoring from 0 to 3 were attributed based on the severity of peri-bronchial, perivascular, and interstitial cell infiltration, resulting in a maximum score of 9.

Bacterial cultures

P. aeruginosa (PP34, PA103, CHA, PAO1, PA14) bacteria and their isogenic mutants were grown overnight in Luria Broth (LB) medium at 37°C with aeration and constant agitation in the presence or absence of EGTA (10mM) to ensure T3SS expression. Bacteria were sub-cultured the next day by dilution overnight culture 1/50 and grew until reaching an optical density (OD) O.D600 of 0.6–1. Bacterial strains and their mutants are listed in [Table 1](#).

Bone Marrow-derived Macrophage (BMDMs), Eosinophil (BMDEs) or Neutrophil (BMDNs) isolation and culture

Murine Bone Marrow-Derived Macrophages (BMDMs) from bone marrow progenitors were differentiated in DMEM (Invitrogen) supplemented with 10% v/v FCS (Thermo Fisher Scientific), 10% v/v MCSF (L929 cell supernatant), 10 mM HEPES (Invitrogen), and nonessential amino acids (Invitrogen) for 7 days as previously described [85].

Murine Bone Marrow-Derived Eosinophils were differentiated *in-vitro* from bone marrow as previously described [86]. cells were resuspended and cultured at 10^6 /mL in RPMI glutamax medium with HEPES containing 20% FBS, 100 IU/ml penicillin and 10 μ g/ml streptomycin, 1 mM sodium pyruvate (Life Technologies), and 50 μ M 2-ME (Sigma-Aldrich) supplemented with 100 ng/ml stem cell factor (SCF; PeproTech) and 100 ng/ml FLT3 ligand (FLT3-L; PeproTech) from days 0 to 4. On day 4, the medium containing SCF and FLT3-L was replaced with medium containing 10 ng/ml recombinant mouse (rm) IL-5 (R&D Systems) only. Medium was replaced every 4 days and the concentration of the cells was adjusted each time to 10^6 /ml. After 10 to 14 days of culture, cells were recovered by gentle pipetting and used as Eosinophils in our experiments. Over 95% of cells had the standard phenotype of Eosinophils: CD11b⁺ Siglec F⁺ after FACS analysis.

Table 1. Resource of reagents used in this study. Information and reagents are available upon request to Etienne.meunier@ipbs.fr.

REAGENT or RESOURCE	SOURCE	IDENTIFIER
Antibodies		
GPX4, 1/1000	abcam	ab125066
ExoU, 1/1000	Ina Attree/CNRS, France.	[37]
CYPOR 1/1000	abcam	ab180597
Gapdh 1/10000	Gentex	GTX100118
Goat anti-Rabbit HRP (1/10000)	Advansta	R-05072-500
Bacterial and Virus Strains		
PAO1	J. Buyck/Univ of Poitiers/France	N.A.
PP34	Ina Attree/CNRS, France.	[37]
PP34 $exoU$	Ina Attree/CNRS, France.	[37]
PP34 $exoU^{\delta 142A}$	Ina Attree/CNRS, France.	[37]
CHA	Ina Attree/CNRS, France.	[37]
CHAdST	Ina Attree/CNRS, France.	[37]
CHAdST $exoU^+$	Ina Attree/CNRS, France.	[37]
PA103	J. Buyck/Univ of Poitiers/France	N.A.
PA103 $exoU$	J. Buyck/Univ of Poitiers/France	N.A.
PA14	J. Buyck/Univ of Poitiers/France	N.A.
PA14 $exoU$	J. Buyck/Univ of Poitiers/France	N.A.
Biological Samples		
Human lung biopsy	Hospital of Toulouse	CHU 19 244 C CNRS 205782
Human blood	EFS	21PLER2017-0035AV02
Chemicals, Peptides, and Recombinant Proteins		
Recombinant ExoU	This study	[31]
Recombinant ExoUS142A	This study	[31]
FCS	Fisher Scientific	16010–159
mMCSF	L929 cell supernatant	NA
HEPES	Fisher Scientific	SH30237.01
Non-essential amino acids	Invitrogen	
ECL Clarity Max Substrate	BioRad	1705060
ECL Clarity Max Substrate	BioRad	1705062
Western Blot Strip Buffer	Diagomics	R-03722-D50
Tris base	euromedex	200923-A
SDS ultra-pure (4x)	Euromedex	1012
Acrylamide / Bisacrylamide 37.5/1 30%	Euromedex	EU0088-B
Temed	Sigma	T9281-25ML
Ammonium persulfate	Sigma	248614-100g
Page Ruler 10–180 kDa	Fisher Scientific	15744052
Triton X-100	Euromedex	2000
DMEM	Fisher Scientific	41965–039
LB	Fisher Scientific	BP1426-2
LB Agar	INVITROGEN	22700025
Roche protease inhibitor cocktail	Sigma	000000011697498001
BSA	SIGMA	A9647-100G
Propidium iodide	Invitrogen	P3566
Beads Neutrophils human	Miltenyi biotec	130-104-434
Beads Neutrophils murine	Miltenyi biotec	130-120-337
Kit de coloration bleue et fixable des cellules mortes LIVE/DEAD pour excitation UV	ThermoFisher Scientifique	L34961

(Continued)

Table 1. (Continued)

REAGENT or RESOURCE	SOURCE	IDENTIFIER
APC/Cyanine7 anti-mouse CD45 Antibody	BioLegend	103116
PE/Dazzle 594 anti-human CD64 Antibody	BioLegend	305032
FITC anti-mouse MERTK (Mer) Antibody	BioLegend	151504
CD170 (Siglec F) Monoclonal Antibody (1RNM44N), Super Bright 780,	eBioscience	78-1702-82
Ly-6G Monoclonal Antibody (1A8-Ly6g), APC	eBioscience	17-9668-82
Brilliant Violet 650 anti-mouse/human CD11b Antibody	BioLegend	101259
Brilliant Violet 421 anti-mouse Ly-6C Antibody	BioLegend	128032
PE/Cyanine7 anti-mouse CD11c Antibody	BioLegend	117318
Eosinophil differentiation cocktail (IL-5)	R&D Systems	405-ML-005
Eosinophil differentiation cocktail (SCF)	Biolegend	579706
Eosinophil differentiation cocktail (Flt-3)	Biolegend	550706
Puromycin	ThermoFisher Scientifique	A1113803
G418 (Geneticin)	invivoGen	ant-gn-1
Blasticidin	nvivoGen	ant-bl-1
Cumene hydroperoxide	Sigma-Aldrich	247502-5G
RSL3	Sigma-Aldrich	SML2234
Ferrostatin-1	Sigma-Aldrich	SML0583
Liproxstatin-1	Sigma-Aldrich	SML1414
DFO	Sigma-Aldrich	D9533
a-tocopherol	Sigma-Aldrich	258024
MAFP	Sigma-Aldrich	M2689
PPOH	CaymanChem	75770
Cox1 inhibitor	Ab142904 (Abcam)	Ab142904
Cox2 inhibitor	NS 398 (Abcam)	Ab120295
cPLA2 assay kit	Cayman Chemical	765021
CD14+ beads	Miltenyi biotec	130-050-201
RPMI	Fisher Scientific	72400-021
OPTIMEM	Fisher Scientific	31985-04
Z-VAD	Invivogen	tlrl-vad
TPCA-1	Tocris	2559
mTNFa	abcam	ab259411
Olaparib	CaymanChem	10621
Necrostatin-1s	Sigma-Aldrich	N9037 10MG
hMCSF	Miltenyi biotec	170-076-171
Fisher BioReagents Lymphocyte Separation Medium-LSM	Fisher Scientific	BP2663500
ExoU	This study	N.A.
ExoUS142A	This study	N.A.
Human bronchial organoid culture reagents		
Advanced DMEM/F12	Invitrogen	12634028
Gibco L-Glutamine (200 mM)	Fisher	11500626
Hepes 1 M	Fisher	11560496
Penicillin/Streptomycin	Fisher	11548876
Primocin	Invivogen	ant-pm-1
Basic Media	In house	NA
Rspo1	In house	NA
Noggin	In house	NA
B27	Gibco/Invitrogen	17504044

(Continued)

Table 1. (Continued)

REAGENT or RESOURCE	SOURCE	IDENTIFIER
N-Acetylcysteine	Sigma	A9165-5g
Nicotinamide	Sigma	N0636
Y-27632	Cayman	10005583
A83-01	Tocris	2939
SB 202190	Sigma	S7067
FGF-7	Peprtech	100-19
FGF-10	Peprtech	100-26
Critical Commercial Assays		
mIL-1alpha ELISA kit	Fisher Scientific	88-5019-88
mIL-36g ELISA kit	Ray Biotech	ELM-IL36G
LDH Cytotoxicity Detection Kit	Takara	MK401
mTNFalpha ELISA kit	Fisher Scientific	88-7324-22
mIL-33 ELISA kit	Fisher Scientific	88-7333-88
mHMGB1 ELISA kit	Clinisciences	LS-F4040-1
TBAR MDA colorimetric kit	Cayman	10009055
PGE2 EIA Kit	Cayman	514010
LTB4 EIA kit	Cayman	520111
8-PGF2 EIA kit	Cayman	516351
H2DCFDA ROS detecting probe	Invitrogen	D399
C11 bodipy phospholipid peroxide detection probe	Invitrogen	D3861
ER-Tracker Blue-White DPX, for live-cell imaging	Invitrogen	E12353
Experimental Models: Cell Lines		
WT Mouse Bone marrow derived macrophages	This study	
Alox5 ^{-/-} Mouse Bone marrow derived macrophages	This study	
Alox12/15 ^{-/-} Mouse Bone marrow derived macrophages	This study	
Nlrc4 ^{-/-} Mouse Bone marrow derived macrophages	This study	
Casp1 ^{-/-} /Casp11 ^{-/-} Mouse Bone marrow derived macrophages	This study	
GsdmD ^{-/-} Mouse Bone marrow derived macrophages	This study	
WT Mouse bone marrow derived eosinophils	This study	
WT Mouse bone marrow derived neutrophils	This study	
Human blood monocyte derived macrophages	This study	
Human blood neutrophils	This study	
Immortalized WT murine bone marrow derived macrophages	This study	
Immortalized Gpx4 ^{-/-} murine bone marrow derived macrophages	This study	
Human Bronchial epithelial cells	This study	
Human Alveolar epithelial A549 cell line	This study	
Human intestinal epithelial HELA cell line	This study	
Experimental Models: Organisms/Strains		
WT C57Bl6J mice	C. Rivers	
WT C57Bl6N mice	C. Rivers	
Alox5 ^{-/-} C57Bl6 mice	A.Coste	[79]
Alox12/15 ^{-/-} C57Bl6 mice	A.Coste	[79]
Nlrc4 ^{-/-} C57Bl6 mice	C.Bryant	[80]
Casp1 ^{-/-} /Casp11 ^{-/-} C57Bl6 mice	B.Py/ Junying Yuan	[81]
GsdmD ^{-/-} C57Bl6 mice	P.Broz	[82]
Human Bronchial organoids	This study	[83,84]
Oligonucleotides		

(Continued)

Table 1. (Continued)

REAGENT or RESOURCE	SOURCE	IDENTIFIER
Guide Crispr mGpx4- Exon1 Forward	Sigma-Aldrich	GGACGCTGCAGACAGCGCGG
Guide Crispr mCypor- Exon1 Forward	Sigma-Aldrich	
Recombinant DNA		
Plasmid: ExoU	[31]	[31]
Plasmid: ExoUS142A	[31]	[31]
Plasmid: ExoU ^{BtU}	[31]	[31]
LentiGuide-Puro	Feng Zhang lab	Addgene #52963
Lenti-multi-Guide	From Qin Yan	Addgene #85401
pMD.2G	Didier Trono lab	Addgene #12259
p8.91	Didier Trono lab	N.A.
LentiCas9-Blast	Feng Zhang lab	Addgene #52962
Software and Algorithms		
Graph Pad Prism 8.0		
Image J		
Snapgene	GSL Biotech LLC, Chicago, U.S.A	
FlowJo	FlowJo LLC	
Benchling Software		
Other		

<https://doi.org/10.1371/journal.ppat.1009927.t001>

Murine Bone Marrow-derived Neutrophils were isolated and purified from fresh bone marrows using Anti-Ly-6G micro bead kit (Miltenyi Biotec). Analysis of cell purity by FACS show that over 95% of cells had the standard phenotype of Neutrophils Ly6G⁺/Ly6C⁺.

2.5×10^5 BMDMs or 1.1×10^6 BMDEs/BMDNs were seeded in 24 well-plates and infected or exposed to various treatments. Regarding ferroptosis experiments, BMDMs were infected with various bacterial strains of *P. aeruginosa* expressing or not *exoU* at an MOI 0.1–1 for various times. When specified, recombinant microbial phospholipases (10ng–1 μ g) were transfected in BMDMs using Fugene (3 μ l per 1 μ g of transfected protein) for 2–4 hours. Compound-induced ferroptosis was achieved using RSL-3 (10 μ M, 8H) or Cumene hydroperoxide (CuOOH, 500 μ M, 3H).

When required, BMDMs were pretreated for 2 hours with pharmacological inhibitors necrostatin-1s (40 μ M), Z-VAD (40 μ M), olaparib (10 μ M), ferrostatin-1 (1–40 μ M), MAFP (50 μ M), liproxstatin (30 μ M), α -tocopherol (20 μ M).

For all stimulations, cell culture medium was replaced by serum-free and antibiotic-free Opti-MEM medium and triggers were added to the cells for various times.

Cell line culture

Immortalized murine bone-marrow derived macrophages have been described previously [85]. U937 cells were cultured in RPMI glutamax medium containing 10% FBS, 100 IU/ml penicillin and 10 μ g/ml streptomycin, 1 mM sodium pyruvate (Life Technologies), and 50 μ M 2-ME (Sigma-Aldrich). Medium was renewed every 3 days and the concentration of the cells was adjusted each time to 5×10^5 /ml. A549, HeLa and HBE cells were cultured in DMEM glutamax medium with HEPES containing 10% FBS, 100 IU/ml penicillin and 10 μ g/ml streptomycin, 1 mM sodium pyruvate (Life Technologies). When the cells reach approximately 90% confluency, cells are detached with Trypsin 0.05% (Gibco), cell suspension is diluted 1/10 in fresh medium, and placed back in the incubator for culture.

Purification and generation of human blood neutrophils and monocyte-derived Macrophages

Monocytes were isolated from Peripheral Blood Mononuclear Cells (PBMCs) from the buffy coat of healthy donors obtained from the EFS Toulouse Purpan (France) as described previously [87]. Briefly, PBMCs were isolated by centrifugation using standard Ficoll-Paque density (GE Healthcare) [85]. The blood was diluted 1:1 in phosphate-buffered saline (PBS) pre-warmed to 37°C and carefully layered over the Ficoll-Paque gradient. The tubes were centrifuged for 25 min at 2000 rpm, at 20°C. The cell interface layer was harvested carefully, and the cells were washed twice in PBS (for 10 min at 1200 rpm followed by 10 min at 800 rpm) and re-suspended in RPMI-1640 supplemented with 10% of foetal calf serum (FCS), 1% penicillin (100 IU/mL) and streptomycin (100 µg/ml). Monocytes were separated from lymphocytes by positive selection using CD14+ isolation kit (Myltenyi biotec). To allow differentiation into monocyte-derived macrophages, cells were cultured in RPMI medium (GIBCO) supplemented with 10% FCS (Invitrogen), 100 IU/ml penicillin, 100µg/ml streptomycin, 10 ng/ml M-CSF for 7 days.

Human blood neutrophils were isolated from whole blood of healthy donors obtained from the EFS Toulouse Purpan (France). Neutrophils were enriched using MACSxpress Whole Blood Neutrophil Isolation Kit whole blood neutrophil isolation kit (Myltenyi biotec) according to manufacturer instructions. Red blood cells (RBC) were removed by 10 min incubation in RBC Lysis Buffer (BioLegend).

Genetic invalidation of *Gpx4* and *Cypor* genes in immortalized BMDMs

Targeted genes were knocked-out using the crispr/cas9 system in immortalized BMDMs. Single guide RNAs (sgRNA) specifically targeting *Gpx4* exon1 (for 5' GGACGCTGCAGA-CAGCGCGG 3' *Cypor* exon2 (for 5' AGTGTCTCTATTCAGCACAA 3' were designed using Benchling tool (Benchling.com), and oligonucleotides were synthesized by Sigma-Aldrich. Crispr guide RNA oligonucleotides were hybridized and subsequently cloned into the vector Lenti-gRNA-Puromycin using BsmBI restriction enzyme (Addgene 52963, Feng Zhang lab). Generated constructs were then transfected in lipofectamine 2000 into HEK293T for 48 hours together with the lentiviral packaging vector p8.91 (Didier Trono lab, EPFL, Switzerland) and the envelop coding VSVg plasmid (pMD.2G, Addgene 12259, Didier Trono lab). Viral supernatants were harvested, filtered on 0.45 µm filter and used to infect cells expressing Cas9 (1,000,000 cells/well in 6-well plates. Efficient infection viral particles was ensured by centrifuging cells for 2 h at 2900 rpm at 32°C in presence of 8µg/ml polybrene. 48 h later, medium was replaced and Puromycin selection (10µg/mL) was applied to select positive clones for two weeks. Puromycin-resistant cells were sorted at the single cell level by FACS (Aria cell sorter). Individual clones were subjected to western blotting to confirm the absence of targeted proteins.

Human bronchial organoid production and maintenance

Airway organoids were derived from lung biopsies as described [83,84]. Briefly, Human lung tissue was provided by the CHU of Toulouse under the CNRS approved protocols CHU 19 244 C and CNRS 205782. All patients participating in this study consented to scientific use of their material. Biopsies (1 mm³) of normal lung tissue adjacent to the tumor obtained from patients who underwent lung resection due to Non-small cell lung carcinoma (NSCLC) were minced and digested with 2 mg ml⁻¹ collagenase (Sigma) on an orbital shaker at 37°C for 1h. The digested tissue suspension was sheared using flamed glass Pasteur pipettes and strained

over a 100- μm cell strainer (Falcon). The resultant single cell suspensions were embedded in 10 mg ml⁻¹ of Cultrex growth factor reduced BME type 2 (R & D Systems) and 40 μl drops were seeded on Nunclon Delta surface 24-well plates (Thermo Scientific). Following polymerization, 500 μl of Advanced DMEM/F12 (Invitrogen) supplemented with 1x L-Glutamine (Fisher Scientific), 10mM Hepes (Fisher Scientific), 100 U ml⁻¹ / 100 μg ml⁻¹ Penicillin / Streptomycin (Fisher Scientific), 50 μg ml⁻¹ Primocin (InvivoGen), 10% Noggin (homemade), 10% Rspo1 (homemade), 1x B27 (Gibco), 1.25mM N-Acetylcysteine (Sigma-Aldrich), 10mM Nicotinamide (Sigma-Aldrich), 5 μM Y-27632 (Cayman Chemical), 500nM A83-01 (Tocris Bioscience), 1 μM SB 202190 (Sigma-Aldrich), 25 ng ml⁻¹ FGF-7 (PeproTech), 100 ng ml⁻¹ FGF-10 (PeproTech) was added to each well and plates transferred to humidified incubator at 37°C with 5% CO₂. The organoids were passaged every 4 weeks.

Organoid infections

Before infection, 35 μl drops of Matrigel (Fisher Scientific) containing organoids were seeded on Nunclon Delta surface 35x10mm Dish (Thermo Scientific) and 2ml of Advanced DMEM/F12 supplemented with 1x L-Glutamine and 10mM Hepes was added to each plate. Depending on the indicated conditions, organoids were pretreated or no with 40 μM Ferrostatin-1 for 1hr before infection. Ferrostatin-1 was maintained throughout the experiment. PP34 *exoU* or *exoU*^{S142A} were grown as previously described until reach OD600 = 1. Bacterial density was adjusted to OD600 = 0.0005, and phenol red added at 0.005% to visualize successful microinjection (2). Injected organoids were individually collected and re-seeded into fresh matrix for subsequent analysis. For time-lapse imaging, injected and stimulated organoids were stained with 50 μg ml⁻¹ Propidium Iodide (Thermo Scientific). Images were acquired every 15 minutes for the duration of experiments under an EVOS M7000 (Thermo Scientific) Imaging System (10x, at 37°C with 5% CO₂). Data was analyzed using Fiji/ImageJ.

Cell necrosis, alarmin/cytokine and lipid release assays

LDH Cytotoxicity Detection Kit (Takara) was used to determine the percentage of cell lysis. Normalization of spontaneous lysis was calculated as follows: (LDH infected-LDH uninfected)/(LDH total lysis-LDH uninfected)*100.

Murine IL-1 α , IL-33, IL-36 α , IL-36 γ , HMGB1, TNF α , cytokine levels in cell supernatants or in BALFs were measured by ELISA listed in resource [Table 1](#).

Oxidized lipids isoprostanes, eicosanoids PGE2 and LTB4 were detected in cellular supernatants or BALFs using EIA kits listed in resource [Table 1](#).

Plasma membrane permeabilization assays

Cells are plated at density of 1 x 10⁵ per well in 96-well Plates or at 2x10⁵/well in 24-well plates (Corning 356640) in complete culture medium. The following day, medium is replaced by Opti-MEM supplemented with Propidium iodide (100 ng/ml) or SYTOX green (100ng/mL). Pharmacological inhibitors are added 1h before infection. Red (Propidium Iodide) or green (SYTOX) fluorescence are measured in real-time using Clariostar plate reader or an EVOS7000 microscope, both equipped with a 37°C cell incubator.

Malondialdehyde (MDA) assays

Malondialdehyde production was addressed using the MDA lipid peroxidation kit according to the manufacturer's instructions (Abcam, ab118970). Cells were lysed using 500 μl of lysis buffer supplemented with butylated hydroxytoluene. Cell lysates were centrifuged for 10 min

at 13,000 g (RCF) and the supernatants were used for MDA assay. TBA solution was added to each replicate, and samples were then incubated at 95°C for 1 hour. 100µL of each sample was then processed for fluorometric assay at Ex/Em = 532/553 nm. BAL levels of MDA were normalized to the total protein concentration.

Recombinant protein production

Plasmids coding for *exoU*^{BtU}, *exoU* or *exoU*^{S142A} were a kind gift from Dara W. Frank's lab. All recombinant proteins were expressed in BL21(DE3) pLysS strain in LB medium, according to Anderson DM et al. [31]. Proteins fused with an N-terminus hexahistidine-tag were purified as previously described with slight modifications. Briefly, after cell harvest, bacteria were lysed by sonication under ice and recombinant proteins were purified by nickel metal affinity chromatography (Takara). After sample concentration, Superose 6 was exchanged for a Superdex 200 size exclusion column (GE Healthcare) as a final purification step. Samples were either used fresh or kept at -80°C for long-term storage. ExoU and ExoUS142A activities were validated on cellular lysates (Fig 3I) based on the advices and experience of our collaborator [37].

Cytometry quantification of immune cells in mice BAL fluids (BALFs)

C57BL/6 mice received an injection of Ferrostatine (6mg/kg) or PBS as control intraperitoneally. 4-6h after, mice were infected by intranasal instillation of 50 µL of PBS containing or not 5x10⁶ bacteria (PP34) in presence or absence of Ferrostatin-1 (6mg /kg). 18h after infection, BALFs were collected and quality/quantity of immune cells content was assayed by flow cytometry. Briefly, cells were pelleted (1000 rpm, 5 minutes), Red blood cells (RBC) were removed by 10 min incubation in RBC Lysis Buffer (BioLegend), monocytes, macrophages, neutrophils, and eosinophils were subsequently stained with a cocktail of fluorochrome-conjugated antibodies detailed in the "Material and Method" section. Cells were then fixed in 4% PFA before fluorescence associated cell sorting (FACS) analysis using a LSRII instrument. AccuCheck Counting Beads (ThermoFisher) were used to determine absolute cell number. Data analysis and processing were performed using FlowJO software.

Lipid peroxidation or ROS production

To measure lipid peroxidation or ROS production, cells were first washed with PBS 1X, and then incubated with either C11-BODIPY(581/591) (ThermoFisher) at 2 µM, or H2DCFDA (ThermoFisher) at 10 µM in Opti-MEM medium for 30 min at 37°C. After three washes with PBS 1X cells are resuspended in Opti-MEM medium and infected/treated in presence or absence of pharmacological inhibitors. After 1-3h of infection, cells are washed with PBS, detached in MACS buffer (PBS-BSA 0.5%-EDTA 2mM) and samples were acquired within one hour using a flow cytometer (BD FORTESSA LSR II or a FACS Calibur). Data were analysed with FlowJO software (version 10). When specified, adherent cells loaded with Bodipy probes where infected at indicated MOIs of *P. aeruginosa* and lipid peroxidation is observed using an EVOS7000 microscope. For live imaging, the GFP brightness threshold was kept equal for all the independent experiments. Mean fluorescence intensity (MFI) was analyzed using Fiji/ImageJ.

Immunoblotting

Cell lysate generation has been described previously [85]. Briefly, proteins were loaded in 12% SDS-PAGE gels and then transferred on PVDF membranes. After saturation for 1 hour in Tris-buffered saline (TBS) supplemented with 0.05% Tween 20 containing 5% non-fat milk (pH8), membranes were exposed with antibodies at 4°C overnight (Table 1). Next day,

membranes were washed 3 times in TBS 0.1% Tween 20 and incubated with the corresponding secondary antibodies conjugated to horseradish peroxidase (HRP) (Table 1) for 1h at room temperature. Immunoblottings were revealed using a chemiluminescent substrate ECL substrate (Biorad) and images were acquired on a ChemiDoc Imaging System (Biorad). All antibodies and their working concentrations are listed in Table 1.

(Redox) lipidomic

1 million bone-marrow-derived macrophages were seeded into 6-well plates. Next day, BMDMs were transfected with recombinant ExoU or ExoU^{S142A} proteins (500ng/well) for one hour. Then, supernatant was removed, cells were washed two times in PBS. Finally, 500μL of a cold solution of 50% PBS/50% Methanol was added to cells and samples were transferred to -80°C for storage and subsequent analyses.

After thawing, lipids were extracted using a methyl-tert-butyl ether (MTBE)-based liquid-liquid extraction method. Cell suspensions (500 μL in PBS/methanol 1:1, v/v) were thawed on ice before adding 100 μL methanol MeOH containing 50 ng each of the internal standards PC (15:0/18:1-d7), PE(15:0/18:1-d7), PG(15:0/18:1-d7), PI(15:0/18:1-d7) and PS(15:0/18:1-d7) (EquiSPLASH, Avanti Polar Lipids). Samples were then transferred into 8-mL screw-cap tubes, and then 1.125 methanol and 5 mL MTBE were added. After vigorous mixing, samples were incubated at room temperature on a tabletop shaker for 45 min. For phase separation, 1.25 mL water was added, and samples were vortexed and centrifuged for 15 min at 2000 x g. The upper organic phase of each sample was carefully removed using a Pasteur pipette, transferred into an empty glass round-bottom tube, and dried under vacuum in a SpeedVac concentrator. The dried lipid extracts were resuspended in 200 μL HPLC mobile phase A/mobile phase B 3:1 (v/v) for targeted lipidomic analysis of oxidized phospholipids. For LC-MS/MS, using a Sciex ExionLC Integrated System, 20 μL of each lipid extract was injected using Column Kinetex 2.6 μm HILIC 100 Å 100x2.1 mm, Phenomenex and a Flow Rate of 200 μL/min. Then, the analyte-specific m/z transition profile was determined and the area under the peak (ion intensity vs. elution time) was calculated using MultiQuant, Sciex software.

Data calculation was performed by doing ratio between the values of “area ratio analyte/internal standard” of each oxidized phospholipid and its non-oxidized phospholipid. The fold induction in oxidized phospholipid was then calculated by doing a ratio between each oxidized ratio and the non-stimulated condition. Accordingly, the unstimulated condition oxidized ratios were 1 or 0 when no peroxidation was detected in any condition.

Phospholipase activity measurement

Evaluation of ExoU phospholipase activity was performed using the Cayman Chemical cPLA2 kit and performed as previously described with minor modifications [37]. Briefly, 10 μL of a 1mg/mL (160pmols) solution of recombinant ExoU or ExoU^{S142} proteins were mixed in 96-well plates with 10μL of lysed cell samples and 10μL of Assay Buffer. Then, samples were incubated for 1 hour at room temperature with 250μL of substrate solution (1.5 mM arachidonyl thiophosphatidylcholine) and then for additional 4 or 16 hours in dark. Reaction was stopped using 25mM solution of DTNB according to manufacturer instructions and absorbance was detected at 405nm using a Clariostar plate reader. Phospholipase activity of ExoU or ExoU^{S142} was calculated as the hydrolysis rate accordingly to the manufacturer instructions.

Statistical analysis

Statistical data analysis was performed using Prism 8.0a (GraphPad Software, Inc.). We used t-test with Bonferroni correction for comparison of two groups. Data are reported as mean with

SEM. Regarding animal experiments, we used Mann-Whitney tests and mouse survival analysis were done using log-rank Cox-Mantel test. P values in figures have the following meaning; NS non-significant and Significance is specified as * $p \leq 0.05$; ** $p \leq 0.01$, *** $p \leq 0.001$.

Supporting information

S1 Data. Original immunoblotting membranes.

(TIF)

S2 Data. Numerical values obtained in the current study.

(XLSX)

S1 Fig. ExoU-dependent lung pathology in mice occurs in an inflammasome-independent manner. (A) Survival of WT, *Casp1*^{-/-}/*Casp11*^{-/-}, *Nlrc4*^{-/-} and *GsdmD*^{-/-} mice intranasally infected (n = 6 animals per condition) with 5.10⁵ CFUs of *P. aeruginosa* PP34. Graphs represent one experiment (6 mice/group) out of three independent *in vivo* experiments. NS: Not significant using Log-rank Cox-Mantel test for survival comparisons. (B) Bronchoalveolar (BAL) and lung bacterial loads from WT, *Casp1*^{-/-}/*Casp11*^{-/-}, *Nlrc4*^{-/-} and *GsdmD*^{-/-} mice (n = 6) 18 hours after intranasal infection with 5.10⁵ CFUs of *P. aeruginosa* PP34. Graphs represent one experiment (6 mice/group) out of three independent *in vivo* experiments. NS: Not significant using Mann-Whitney analysis test.

(TIF)

S2 Fig. Lipid peroxidation contributes to ExoU-induced necrosis in various cell types. (A, B) Measure of LDH release in various human and murine cell types infected with various *P. aeruginosa* strains expressing or not *exoU* in presence of Ferrostatin-1 (Fe1, 10 μ M) for 2 hours. (C) LDH release in BMDMs transfected with recombinant ExoU (100ng) or its catalytically inactive mutant ExoU^{S142A}, in presence of MAFP (50 μ M) or Ferrostatin-1 (Fe1, 10 μ M) for 3 hours. *** $p \leq 0.001$, T-test with Bonferroni correction. (D) Immunoblotting of ExoU secretion by *P. aeruginosa* in presence of ferrostatin-1 (20 μ M). Star (*) show non-specific bands. (E) Measure of bacterial growth (O.D 600) in presence or absence of ferrostatin-1 (10, 20 μ M) for 14 hours. (F) Measure of LDH release in *Nlrc4*^{-/-} BMDMs infected with PP34 (MOI5) in presence of Ferrostatin-1 (Fe1, 10 μ M) for 3 hours. Each hour, fresh Ferrostatin-1 (10 μ M) was added to cells (+) or not (ϕ). “pi” refers to post-infection.

(TIF)

S3 Fig. Lipid peroxidation fuels ExoU-dependent necrosis. (A) ROS production in WT BMDMs transfected with ExoU or its catalytically dead mutant ExoU^{S142A} for 45 minutes using H2DCFDA (1 μ M) probe. (B) Cytometry detection and quantification of (phospho)lipid peroxidation using the probe C11-bodipy in WT BMDMs infected with PP34^{ExoU+} or PP34^{ExoU-} (MOI 5) for 1 hour. Sample were acquired using FACSCalibur (BD). The graph shows the mean \pm SEM of one experiment performed in triplicate out of three independent experiments. * $P \leq 0.05$, for the indicated comparisons using t-test with Bonferroni correction. (C) Lipidomic analysis of the relative amount of each phospholipid upon rExoU transfection analysed in Fig 3B. (D) Representative microscopy images and time course experiment of propidium iodide uptake in WT BMDMs transfected with rExoU or its catalytically inactive mutant ExoU^{S142A} (500ng) in presence or not of ferrostatin-1 (Fe1, 10 μ M). Images show two independent experiments, each performed three times at 45 minutes or 3 hours post transfection. (E) Immunoblotting of Crispr Cas9-mediated *Cypor* gene deletion in immortalized (i)BMDMs or of *Cypor*-deficient HELA cells. The *Cypor*#2 (red) was selected for further analysis. GFP means that cells were transduced with sgRNA targeting *Gfp* and used as control. (F) Cytometry detection and

quantification of (phospho)lipid peroxidation using the probe C11-bodipy in WT or *Cypor*^{-/-} immortalized (i)BMDMs pre-treated or not for 1 hour with CuOOH (20μM) in presence or absence of Ferrostatin-1 (20μM) and then infected with PP34^{ExoU+} or PP34^{ExoU-} (MOI 5) for 1 hour. Sample were acquired using FACSCalibur (BD). The graphs shows the mean±/SEM of one experiment performed in triplicate out of three independent experiments. *P ≤ 0.05, **P ≤ 0.001, for the indicated comparisons using t-test with Bonferroni correction. (G) Immunoblotting of Crispr Cas9-mediated *Gpx4* gene deletion in immortalized BMDMs. The Gpx4#1 (red) was selected for further analysis. CD8 and GFP means that cells were transduced with sgRNA targeting *Gfp* or *Cd8* genes and used as controls. (H) Cytometry detection and quantification of phospholipid peroxidation using the probe C11-bodipy in immortalized WT or *Gpx4*^{-/-} BMDMs using a fortessa cytometer. (I) Measure of 8-iso PGF2α isprostane in cell supernatant in WT BMDMs pre-treated or not for 1 hour with CuOOH (20μM) in presence or absence of Ferrostatin-1 (20μM) and then transfected with rExoU (500ng) for 3 hours. ***p ≤ 0.001, T-test with Bonferroni correction. (J) PGE2 and LTB4 eicosanoid release in WT BMDMs pre-treated or not for 1 hour with CuOOH (20μM) and then transfected with 100ng of ExoU or its catalytically dead mutant ExoU^{S142A} for 3 hours. (TIF)

S4 Fig. Ferrostatin-1 protects mice against ExoU-induced lung pathology. (A) Gating strategy to analyse Immune cell populations in bronchoalveolar fluids (BALFs). Immune cells were identified as CD45+ cells. Among CD45+ cells, different subset of immune cells including Interstitial/Alveolar Macrophages, Eosinophils and Neutrophils are identified based on specific cell surface marker expression. (TIF)

S1 Graphical Abstract. Host lipid peroxidation fuels ExoU-induced cell necrosis-dependent pathology. In resting cells or in cells with induced lipid peroxidation (e.g. ferroptosis pathway), ExoU (purple) becomes hyper-activated by host cell peroxidised phospholipids, which drives an exacerbated cell necrosis, alarmin and lipid release and contributes to the subsequent pathology. Consequently, targeting lipid peroxidation (ferrostatin-1) inhibits ExoU-dependent cell necrosis and attenuates the host deleterious consequences. EM and SB used Biorender.com to create this figure. (TIF)

S1 Movie. Live cell imaging of uninfected immortalized murine *Nlrc4*^{-/-} BMDMs cell death using SYTOX green. 1 “time point” corresponds to 150s. (AVI)

S2 Movie. Live cell imaging of uninfected immortalized murine *Nlrc4*^{-/-} BMDMs cell death in presence of 20μM of ferrostatin-1 using SYTOX green. 1 “time point” corresponds to 150s. (AVI)

S3 Movie. Live cell imaging of immortalized murine *Nlrc4*^{-/-} BMDMs cell death infected with *exoU*-expressing *P. aeruginosa* (MOI1) using SYTOX green. 1 “time point” corresponds to 150s. (AVI)

S4 Movie. Live cell imaging of immortalized murine *Nlrc4*^{-/-} BMDMs cell death infected with *exoU*-expressing *P. aeruginosa* (MOI1) in presence of ferrostatin-1 (20μM) using SYTOX green. 1 “time point” corresponds to 150s. (AVI)

S5 Movie. Live cell imaging of immortalized murine *Nlrc4*^{-/-} BMDMs cell death infected with *exoU*-deficient *P. aeruginosa* (MOI1) using SYTOX green. 1 “time point” corresponds to 150s.

(AVI)

S6 Movie. Live cell imaging of immortalized murine *Nlrc4*^{-/-} BMDMs cell death infected with *exoU*-deficient *P. aeruginosa* (MOI1) in presence of ferrostatin-1 (20μM) using SYTOX green. 1 “time point” corresponds to 150s.

(AVI)

S7 Movie. Live cell imaging of uninfected human bronchial organoids using Propidium Iodide up to 12 hours.

(AVI)

S8 Movie. Live cell imaging of uninfected human bronchial organoids in presence of ferrostatin-1 (40μM) using Propidium Iodide up to 12 hours.

(AVI)

S9 Movie. Live cell imaging of human bronchial organoids microinjected with *exoU*-expressing *P. aeruginosa* using Propidium Iodide up to 12 hours.

(AVI)

S10 Movie. Live cell imaging of human bronchial organoids microinjected with *exoU*-expressing *P. aeruginosa* in presence of ferrostatin-1 (40μM) using Propidium Iodide up to 12 hours.

(AVI)

S11 Movie. Live cell imaging of human bronchial organoids microinjected with *exoU*-deficient *P. aeruginosa* using Propidium Iodide up to 12 hours.

(AVI)

S12 Movie. Live cell imaging of human bronchial organoids microinjected with *exoU*-deficient *P. aeruginosa* in presence of ferrostatin-1 (40μM) using Propidium Iodide up to 12 hours.

(AVI)

Acknowledgments

Alox5^{-/-} and *Alox12/15*^{-/-} mice came from Jaxson Laboratory. *Nlrc4*^{-/-} mice were provided by Clare E. Bryant and generated by Millenium, *GsdmD*^{-/-} mice came from P. Broz (Univ of Lausanne), and *Casp1*^{-/-}/*Casp11*^{-/-} came from B. Py (ENS Lyon, France) and were generated by Junying Yuan (Harvard Med School, Boston, USA). Phospholipid redox lipidomic experiments were performed by Cayman Chemical Company (Ann Arbor, USA). Authors also acknowledge the animal facility and Cytometry/microscopy platforms of the IPBS institute. The graphical abstract was generated using Biorender.com.

Author Contributions

Conceptualization: Rémi Planès, Etienne Meunier.

Data curation: Salimata Bagayoko, Rémi Planès, Etienne Meunier.

Formal analysis: Salimata Bagayoko, Céline Cougoule, Rémi Planès, Etienne Meunier.

Funding acquisition: Yoann Rombouts, Céline Cougoule, Rémi Planès, Etienne Meunier.

Investigation: Stephen Adonai Leon-Icaza, Miriam Pinilla, Audrey Hessel, Karin Santoni, David Péricat, Pierre-Jean Bordignon, Flavie Moreau, Elif Eren, Aurélien Boyancé, Céline Berrone, Yoann Rombouts, Céline Cougoule.

Methodology: Emmanuelle Naser, Nino Iakobachvili, Arnaud Metais.

Project administration: Salimata Bagayoko, Rémi Planès, Etienne Meunier.

Resources: Lise Lefèvre, Geanncarlo Lugo-Villarino, Agnès Coste, Ina Attrée, Dara W. Frank, Hans Clevers, Peter J. Peters.

Supervision: Rémi Planès, Etienne Meunier.

Validation: Salimata Bagayoko, Rémi Planès, Etienne Meunier.

Visualization: Salimata Bagayoko, Céline Cougoule, Rémi Planès, Etienne Meunier.

Writing – original draft: Salimata Bagayoko, Rémi Planès, Etienne Meunier.

Writing – review & editing: Salimata Bagayoko, Rémi Planès, Etienne Meunier.

References

1. Galluzzi L, Vitale I, Aaronson SA, Abrams JM, Adam D, Agostinis P, et al. Molecular mechanisms of cell death: Recommendations of the Nomenclature Committee on Cell Death 2018. *Cell Death and Differentiation*. Nature Publishing Group; 2018. pp. 486–541. <https://doi.org/10.1038/s41418-017-0012-4> PMID: 29362479
2. Tang L, Lu C, Zheng G, Burgering BMT. Emerging insights on the role of gasdermins in infection and inflammatory diseases. *Clinical and Translational Immunology*. John Wiley and Sons Inc; 2020. <https://doi.org/10.1002/cti2.1186> PMID: 33033617
3. Bedoui S, Herold MJ, Strasser A. Emerging connectivity of programmed cell death pathways and its physiological implications. *Nature Reviews Molecular Cell Biology*. Nature Research; 2020. pp. 678–695. <https://doi.org/10.1038/s41580-020-0270-8> PMID: 32873928
4. Place DE, Lee SJ, Kanneganti TD. PANoptosis in microbial infection. *Current Opinion in Microbiology*. Elsevier Ltd; 2021. pp. 42–49. <https://doi.org/10.1016/j.mib.2020.07.012> PMID: 32829024
5. Dixon SJ, Lemberg KM, Lamprecht MR, Skouta R, Zaitsev EM, Gleason CE, et al. Ferroptosis: An iron-dependent form of nonapoptotic cell death. *Cell*. 2012; 149: 1060–1072. <https://doi.org/10.1016/j.cell.2012.03.042> PMID: 22632970
6. Conrad M, Kagan VE, Bayir H, Pagnussat GC, Head B, Traber MG, et al. Regulation of lipid peroxidation and ferroptosis in diverse species. *Genes and Development*. Cold Spring Harbor Laboratory Press; 2018. pp. 602–619. <https://doi.org/10.1101/gad.314674.118> PMID: 29802123
7. Jenkins NL, James SA, Salim A, Sumardy F, Speed TP, Conrad M, et al. Changes in ferrous iron and glutathione promote ferroptosis and frailty in aging *Caenorhabditis elegans*. *Elife*. 2020; 9: 1–28. <https://doi.org/10.7554/eLife.56580> PMID: 32690135
8. Bogacz M, Krauth-Siegel RL. Tryparedoxin peroxidase-deficiency commits trypanosomes to ferroptosis-type cell death. *Elife*. 2018; 7. <https://doi.org/10.7554/eLife.37503> PMID: 30047863
9. Bochkov VN, Oskolkova O V., Birukov KG, Levonen AL, Binder CJ, Stöckl J. Generation and biological activities of oxidized phospholipids. *Antioxidants and Redox Signaling*. Mary Ann Liebert, Inc.; 2010. pp. 1009–1059. <https://doi.org/10.1089/ars.2009.2597> PMID: 19686040
10. Tyurina YY, Tyurin VA, Anthonymuthu T, Amoscato AA, Sparvero LJ, Nesterova AM, et al. “Redox lipidomics technology: Looking for a needle in a haystack.” *Chemistry and Physics of Lipids*. Elsevier Ireland Ltd; 2019. pp. 93–107. <https://doi.org/10.1016/j.chemphyslip.2019.03.012> PMID: 30928338
11. Bersuker K, Hendricks JM, Li Z, Magtanong L, Ford B, Tang PH, et al. The CoQ oxidoreductase FSP1 acts parallel to GPX4 to inhibit ferroptosis. *Nature*. 2019; 575: 688–692. <https://doi.org/10.1038/s41586-019-1705-2> PMID: 31634900
12. Doll S, Freitas FP, Shah R, Aldrovandi M, da Silva MC, Ingold I, et al. FSP1 is a glutathione-independent ferroptosis suppressor. *Nature*. 2019; 575: 693–698. <https://doi.org/10.1038/s41586-019-1707-0> PMID: 31634899

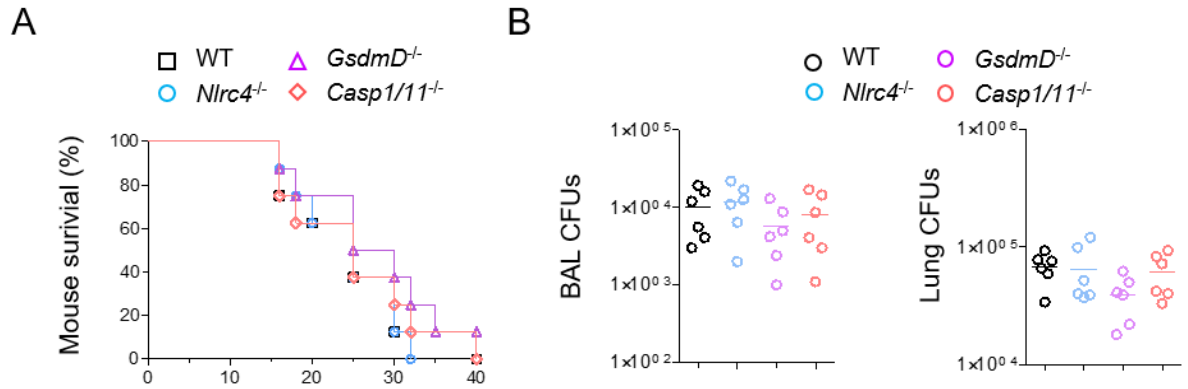
13. Conrad M, Pratt DA. The chemical basis of ferroptosis. *Nat Chem Biol*. 2019; 15: 1137–1147. <https://doi.org/10.1038/s41589-019-0408-1> PMID: 31740834
14. Yang WS, Kim KJ, Gaschler MM, Patel M, Shchepinov MS, Stockwell BR. Peroxidation of polyunsaturated fatty acids by lipoxygenases drives ferroptosis. *Proc Natl Acad Sci U S A*. 2016; 113: E4966–E4975. <https://doi.org/10.1073/pnas.1603244113> PMID: 27506793
15. Doll S, Proneth B, Tyurina YY, Panzilius E, Kobayashi S, Ingold I, et al. ACSL4 dictates ferroptosis sensitivity by shaping cellular lipid composition. *Nat Chem Biol*. 2017; 13: 91–98. <https://doi.org/10.1038/nchembio.2239> PMID: 27842070
16. Kagan VE, Mao G, Qu F, Angeli JPF, Doll S, Croix CS, et al. Oxidized arachidonic and adrenic PEs navigate cells to ferroptosis. *Nat Chem Biol*. 2017; 13: 81–90. <https://doi.org/10.1038/nchembio.2238> PMID: 27842066
17. Wiernicki B, Dubois H, Tyurina YY, Hassannia B, Bayir H, Kagan VE, et al. Excessive phospholipid peroxidation distinguishes ferroptosis from other cell death modes including pyroptosis. *Cell Death Dis*. 2020; 11: 922. <https://doi.org/10.1038/s41419-020-03118-0> PMID: 33110056
18. Stockwell BR, Jiang X, Gu W. Emerging Mechanisms and Disease Relevance of Ferroptosis. 2020 [cited 13 Nov 2020]. <https://doi.org/10.1016/j.tcb.2020.02.009> PMID: 32413317
19. Amaral EP, Costa DL, Namasivayam S, Riteau N, Kamenyeva O, Mittereder L, et al. A major role for ferroptosis in *Mycobacterium tuberculosis*-induced cell death and tissue necrosis. *J Exp Med*. 2019; 216: 556–570. <https://doi.org/10.1084/jem.20181776> PMID: 30787033
20. Li N, Wang W, Zhou H, Wu Q, Duan M, Liu C, et al. Ferritinophagy-mediated ferroptosis is involved in sepsis-induced cardiac injury. *Free Radic Biol Med*. 2020; 160: 303–318. <https://doi.org/10.1016/j.freeradbiomed.2020.08.009> PMID: 32846217
21. Zhu H, Santo A, Jia Z, Li Y. GPx4 in Bacterial Infection and Polymicrobial Sepsis: Involvement of Ferroptosis and Pyroptosis. *React Oxyg Species*. 2019; 7: 154. <https://doi.org/10.20455/ros.2019.835> PMID: 31106276
22. Dar HH, Tyurina YY, Mikulska-Ruminska K, Shrivastava I, Ting HC, Tyurin VA, et al. *Pseudomonas aeruginosa* utilizes host polyunsaturated phosphatidylethanolamines to trigger theft-ferroptosis in bronchial epithelium. *J Clin Invest*. 2018; 128: 4639–4653. <https://doi.org/10.1172/JCI99490> PMID: 30198910
23. Meunier E, Neyrolles O. Die another way: Ferroptosis drives tuberculosis pathology. *J Exp Med*. 2019; 216: 471–473. <https://doi.org/10.1084/jem.20190038> PMID: 30787032
24. Friedmann Angeli JP, Schneider M, Proneth B, Tyurina YY, Tyurin VA, Hammond VJ, et al. Inactivation of the ferroptosis regulator Gpx4 triggers acute renal failure in mice. *Nat Cell Biol*. 2014; 16: 1180–1191. <https://doi.org/10.1038/ncb3064> PMID: 25402683
25. Yan1 B, Ai1 Y, Zhang1 Z, Sun1 Q, Ma1 Y, Zhang1 Z, et al. Oxidoreductases generate hydrogen peroxide that drives iron-dependent lipid peroxidation during ferroptosis 2 The inhibition of antioxidant systems of glutathione peroxidase 4 (GPX4) or ferroptosis suppressor protein 1 (FSP1) causes iron-dependent peroxid. *bioRxiv*. 2020; 2020.08.01.231993. <https://doi.org/10.1101/2020.08.01.231993>
26. Zou Y, Li H, Graham ET, Deik AA, Eaton JK, Wang W, et al. Cytochrome P450 oxidoreductase contributes to phospholipid peroxidation in ferroptosis. *Nat Chem Biol*. 2020; 16: 302–309. <https://doi.org/10.1038/s41589-020-0472-6> PMID: 32080622
27. Howell HA, Logan LK, Hauser AR. Type III secretion of ExoU is critical during early *Pseudomonas aeruginosa* Pneumonia. *MBio*. 2013;4. <https://doi.org/10.1128/mBio.00032-13> PMID: 23481600
28. Gendrin C, Contreras-Martel C, Bouillot S, Elsen S, Lemaire D, Skoufias DA, et al. Structural Basis of Cytotoxicity Mediated by the Type III Secretion Toxin ExoU from *Pseudomonas aeruginosa*. Saper MA, editor. *PLoS Pathog*. 2012; 8: e1002637. <https://doi.org/10.1371/journal.ppat.1002637> PMID: 22496657
29. Phillips RM, Six DA, Dennis EA, Ghosh P. In Vivo Phospholipase Activity of the *Pseudomonas aeruginosa* Cytotoxin ExoU and Protection of Mammalian Cells with Phospholipase A2 Inhibitors. *J Biol Chem*. 2003; 278: 41326–41332. <https://doi.org/10.1074/jbc.M302472200> PMID: 12915403
30. Sato H, Frank DW. ExoU is a potent intracellular phospholipase. *Molecular Microbiology*. *Mol Microbiol*; 2004. pp. 1279–1290. <https://doi.org/10.1111/j.1365-2958.2004.04194.x> PMID: 15387809
31. Anderson DM, Sato H, Dirck AT, Feix JB, Frank DW. Ubiquitin activates patatin-like phospholipases from multiple bacterial species. *J Bacteriol*. 2015; 197: 529–541. <https://doi.org/10.1128/JB.02402-14> PMID: 25404699
32. Wilson SK, Knoll LJ. Patatin-like phospholipases in microbial infections with emerging roles in fatty acid metabolism and immune regulation by Apicomplexa. *Molecular Microbiology*. Blackwell Publishing Ltd; 2018. pp. 34–46. <https://doi.org/10.1111/mmi.13871> PMID: 29090840
33. Dessen A. Phospholipase A2 enzymes: Structural diversity in lipid messenger metabolism. *Structure*. Current Biology Ltd; 2000. pp. R15–R22. [https://doi.org/10.1016/s0969-2126\(00\)00097-6](https://doi.org/10.1016/s0969-2126(00)00097-6) PMID: 10673441

34. Sitkiewicz I, Nagiec MJ, Sumbly P, Butler SD, Cywes-Bentley C, Musser JM. Emergence of a bacterial clone with enhanced virulence by acquisition of a phage encoding a secreted phospholipase A2. *Proc Natl Acad Sci U S A*. 2006; 103: 16009–16014. <https://doi.org/10.1073/pnas.0607669103> PMID: 17043230
35. Diaz MH, Hauser AR. *Pseudomonas aeruginosa* cytotoxin ExoU is injected into phagocytic cells during acute pneumonia. *Infect Immun*. 2010; 78: 1447–1456. <https://doi.org/10.1128/IAI.01134-09> PMID: 20100855
36. Rabin SDP, Hauser AR. *Pseudomonas aeruginosa* ExoU, a toxin transported by the type III secretion system, kills *Saccharomyces cerevisiae*. *Infect Immun*. 2003; 71: 4144–4150. <https://doi.org/10.1128/IAI.71.7.4144-4150.2003> PMID: 12819106
37. Deruelle V, Bouillot S, Job V, Taillebourg E, Fauvarque M-O, Attrée I, et al. The bacterial toxin ExoU requires a host trafficking chaperone for transportation and to induce necrosis. *bioRxiv*. 2020; 2020.11.04.367706. <https://doi.org/10.1101/2020.11.04.367706>
38. Machado GB, de Oliveira A V., Saliba AM, de Lima CDM, Suassuna JHR, Plotkowski MC. *Pseudomonas aeruginosa* toxin ExoU induces a PAF-dependent impairment of alveolar fibrin turnover secondary to enhanced activation of coagulation and increased expression of plasminogen activator inhibitor-1 in the course of mice pneumosepsis. *Respir Res*. 2011; 12: 104. <https://doi.org/10.1186/1465-9921-12-104> PMID: 21819560
39. Pazos MA, Lanter BB, Yonker LM, Eaton AD, Pirzai W, Gronert K, et al. *Pseudomonas aeruginosa* ExoU augments neutrophil transepithelial migration. *PLoS Pathog*. 2017; 13. <https://doi.org/10.1371/journal.ppat.1006548> PMID: 28771621
40. Saliba AM, Nascimento DO, Silva MCA, Assis MC, Gayer CRM, Raymond B, et al. Eicosanoid-mediated proinflammatory activity of *Pseudomonas aeruginosa* ExoU. *Cell Microbiol*. 2005; 7: 1811–1822. <https://doi.org/10.1111/j.1462-5822.2005.00635.x> PMID: 16309466
41. da Cunha LG, Ferreira MF, de Moraes JA, Reis PA, Castro-Faria-Neto HC, Barja-Fidalgo C, et al. ExoU-induced redox imbalance and oxidative stress in airway epithelial cells during *Pseudomonas aeruginosa* pneumosepsis. *Med Microbiol Immunol*. 2015; 204: 673–680. <https://doi.org/10.1007/s00430-015-0418-x> PMID: 25904542
42. Al Moussawi K, Kazmierczak BI. Distinct contributions of interleukin-1 α (IL-1 α) and IL-1 β to innate immune recognition of *Pseudomonas aeruginosa* in the lung. *Infect Immun*. 2014; 82: 4204–4211. <https://doi.org/10.1128/IAI.02218-14> PMID: 25069982
43. Shaver CM, Hauser AR. Relative contributions of *Pseudomonas aeruginosa* ExoU, ExoS, and ExoT to virulence in the lung. *Infect Immun*. 2004; 72: 6969–6977. <https://doi.org/10.1128/IAI.72.12.6969-6977.2004> PMID: 15557619
44. Miao EA, Ernst RK, Dors M, Mao DP, Aderem A. *Pseudomonas aeruginosa* activates caspase 1 through Ipaf. *Proc Natl Acad Sci U S A*. 2008; 105: 2562–2567. <https://doi.org/10.1073/pnas.0712183105> PMID: 18256184
45. Eren E, Planès R, Buyck J, Bordignon P-J, Colom A, Cunrath O, et al. Type-3 Secretion System–induced pyroptosis protects *Pseudomonas* against cell-autonomous immunity. *bioRxiv*. 2019; 650333. <https://doi.org/10.1101/650333>
46. Santos JC, Dick MS, Lagrange B, Degrandi D, Pfeffer K, Yamamoto M, et al. LPS targets host guanylate-binding proteins to the bacterial outer membrane for non-canonical inflammasome activation. *EMBO J*. 2018; 37. <https://doi.org/10.15252/embj.201798089> PMID: 29459437
47. Bitto NJ, Baker PJ, Dowling JK, Wray-McCann G, De Paoli A, Tran LS, et al. Membrane vesicles from *Pseudomonas aeruginosa* activate the noncanonical inflammasome through caspase-5 in human monocytes. *Immunol Cell Biol*. 2018; 96: 1120–1130. <https://doi.org/10.1111/imcb.12190> PMID: 30003588
48. Franchi L, Stoolman J, Kanneganti TD, Verma A, Ramphal R, Núñez G. Critical role for Ipaf in *Pseudomonas aeruginosa*-induced caspase-1 activation. *Eur J Immunol*. 2007; 37: 3030–3039. <https://doi.org/10.1002/eji.200737532> PMID: 17935074
49. Balakrishnan A, Karki R, Berwin B, Yamamoto M, Kanneganti T-D. Guanylate binding proteins facilitate caspase-11-dependent pyroptosis in response to type 3 secretion system-negative *Pseudomonas aeruginosa*. *Cell Death Discov*. 2018; 4: 66. <https://doi.org/10.1038/s41420-018-0068-z> PMID: 30062052
50. Sutterwala FS, Mijares LA, Li L, Ogura Y, Kazmierczak BI, Flavell RA. Immune recognition of *Pseudomonas aeruginosa* mediated by the IPAF/NLRC4 inflammasome. *J Exp Med*. 2007; 204: 3235–3245. <https://doi.org/10.1084/jem.20071239> PMID: 18070936
51. Cohen TS, Prince AS. Activation of inflammasome signaling mediates pathology of acute *P. aeruginosa* pneumonia. *J Clin Invest*. 2013; 123: 1630–1637. <https://doi.org/10.1172/JCI66142> PMID: 23478406
52. Faure E, Mear JB, Faure K, Normand S, Couturier-Maillard A, Grandjean T, et al. *Pseudomonas aeruginosa* type-3 secretion system dampens host defense by exploiting the NLRC4-coupled inflammasome. *Am J Respir Crit Care Med*. 2014; 189: 799–811. <https://doi.org/10.1164/rccm.201307-1358OC> PMID: 24555512

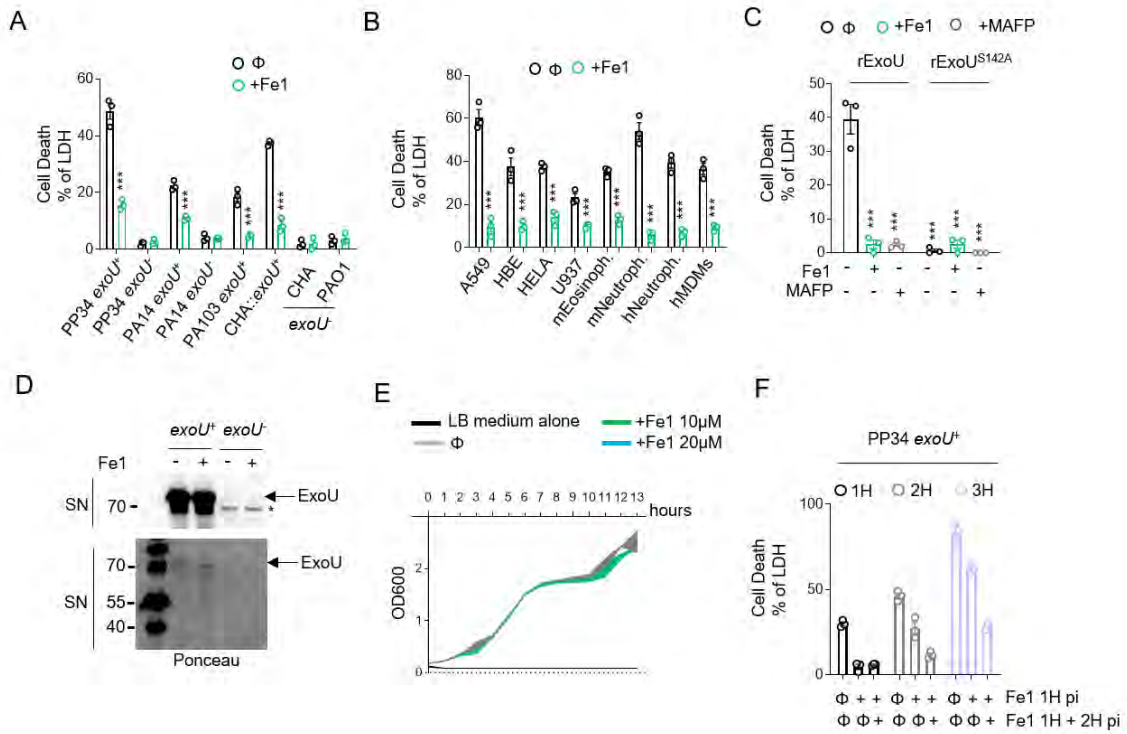
53. Iannitti RG, Napolioni V, Oikonomou V, De Luca A, Galosi C, Pariano M, et al. IL-1 receptor antagonist ameliorates inflammasome-dependent inflammation in murine and human cystic fibrosis. *Nat Commun*. 2016; 7: 1–16. <https://doi.org/10.1038/ncomms10791> PMID: 26972847
54. Aoyagi T, Newstead MW, Zeng X, Nanjo Y, Peters-Golden M, Kaku M, et al. Interleukin-36γ and IL-36 receptor signaling mediate impaired host immunity and lung injury in cytotoxic *Pseudomonas aeruginosa* pulmonary infection: Role of prostaglandin E2. *PLoS Pathog*. 2017; 13. <https://doi.org/10.1371/journal.ppat.1006737> PMID: 29166668
55. Yang D, Han Z, Oppenheim JJ. Alarmins and immunity. *Immunological Reviews*. Blackwell Publishing Ltd; 2017. pp. 41–56. <https://doi.org/10.1111/immr.12577> PMID: 29027222
56. Saliba AM, De Assis MC, Nishi R, Raymond B, Marques EDA, Lopes UG, et al. Implications of oxidative stress in the cytotoxicity of *Pseudomonas aeruginosa* ExoU. *Microbes Infect*. 2006; 8: 450–459. <https://doi.org/10.1016/j.micinf.2005.07.011> PMID: 16293434
57. Skouta R, Dixon SJ, Wang J, Dunn DE, Orman M, Shimada K, et al. Ferrostatis inhibit oxidative lipid damage and cell death in diverse disease models. *J Am Chem Soc*. 2014; 136: 4551–4556. <https://doi.org/10.1021/ja411006a> PMID: 24592866
58. Tamura M, Ajayi T, Allmond LR, Moriyama K, Wiener-Kronish JP, Sawa T. Lysophospholipase A activity of *Pseudomonas aeruginosa* type III secretory toxin ExoU. *Biochem Biophys Res Commun*. 2004; 316: 323–331. <https://doi.org/10.1016/j.bbrc.2004.02.050> PMID: 15020221
59. Lovatt M, Adnan K, Kocaba V, Dirisamer M, Peh GSL, Mehta JS. Peroxiredoxin-1 regulates lipid peroxidation in corneal endothelial cells. *Redox Biol*. 2020; 30: 101417. <https://doi.org/10.1016/j.redox.2019.101417> PMID: 31901729
60. Beatty A, Singh T, Tyurina YY, Nicolas E, Maslar K, Zhou Y, et al. Conjugated linolenic fatty acids trigger ferroptosis in triple-negative breast cancer. [cited 11 Jan 2021]. <https://doi.org/10.1101/556084>
61. Lu B, Chen X, Hong Y, Cai Z, Zhu H, He Q, Jun, Yang B, et al. Identification of PRDX6 as a regulator of ferroptosis. *Acta Pharmacol Sin*. 2019; 40: 1334–1342. <https://doi.org/10.1038/s41401-019-0233-9> PMID: 31036877
62. Beharier O, Tyurin VA, Goff JP, Guerrero-Santoro J, Kajiwarra K, Chu T, et al. PLA2G6 guards placental trophoblasts against ferroptotic injury. *Proc Natl Acad Sci U S A*. 2020; 117: 27319–27328. <https://doi.org/10.1073/pnas.2009201117> PMID: 33087576
63. Sadikot RT, Zeng H, Azim AC, Joo M, Dey SK, Beyer RM, et al. Bacterial clearance of *Pseudomonas aeruginosa* is enhanced by the inhibition of COX-2. *Eur J Immunol*. 2007; 37: 1001–1009. <https://doi.org/10.1002/eji.200636636> PMID: 17330822
64. Tyurin VA, Balasubramanian K, Winnica D, Tyurina YY, Vikulina AS, He RR, et al. Oxidatively modified phosphatidylserines on the surface of apoptotic cells are essential phagocytic “eat-me” signals: Cleavage and inhibition of phagocytosis by Lp-PLA2. *Cell Death Differ*. 2014; 21: 825–835. <https://doi.org/10.1038/cdd.2014.1> PMID: 24464221
65. Magtanong L, Ko PJ, To M, Cao JY, Forcina GC, Tarangelo A, et al. Exogenous Monounsaturated Fatty Acids Promote a Ferroptosis-Resistant Cell State. *Cell Chem Biol*. 2019; 26: 420–432.e9. <https://doi.org/10.1016/j.chembiol.2018.11.016> PMID: 30686757
66. Zou Y, Henry WS, Ricq EL, Graham ET, Phadnis V V., Maretich P, et al. Plasticity of ether lipids promotes ferroptosis susceptibility and evasion. *Nature*. 2020; 585: 603–608. <https://doi.org/10.1038/s41586-020-2732-8> PMID: 32939090
67. Kinsey GR, Blum JL, Covington MD, Cummings BS, McHowat J, Schnellmann RG. Decreased iPLA2γ expression induces lipid peroxidation and cell death and sensitizes cells to oxidant-induced apoptosis. *J Lipid Res*. 2008; 49: 1477–1487. <https://doi.org/10.1194/jlr.M800030-JLR200> PMID: 18398221
68. Miyamoto S, Dupas C, Murota K, Terao J. Phospholipid hydroperoxides are detoxified by phospholipase A2 and GSH peroxidase in rat gastric mucosa. *Lipids*. 2003; 38: 641–649. <https://doi.org/10.1007/s11745-003-1109-6> PMID: 12934674
69. van Kuijk FJGM, Sevanian A, Handelman GJ, Dratz EA. A new role for phospholipase A2: protection of membranes from lipid peroxidation damage. *Trends Biochem Sci*. 1987; 12: 31–34. [https://doi.org/10.1016/0968-0004\(87\)90014-4](https://doi.org/10.1016/0968-0004(87)90014-4)
70. Sevanian A, Wratten M, Lou, McLeod LL, Kim E. Lipid peroxidation and phospholipase A2 activity in liposomes composed of unsaturated phospholipids: a structural basis for enzyme activation. *Biochim Biophys Acta (BBA)/Lipids Lipid Metab*. 1988; 961: 316–327. [https://doi.org/10.1016/0005-2760\(88\)90079-3](https://doi.org/10.1016/0005-2760(88)90079-3) PMID: 3401498
71. Yedgar S, Cohen Y, Shoseyov D. Control of phospholipase A2 activities for the treatment of inflammatory conditions. *Biochimica et Biophysica Acta—Molecular and Cell Biology of Lipids*. Elsevier; 2006. pp. 1373–1382. <https://doi.org/10.1016/j.bbalip.2006.08.003> PMID: 16978919

72. Kienesberger PC, Oberer M, Lass A, Zechner R. Mammalian patatin domain containing proteins: A family with diverse lipolytic activities involved in multiple biological functions. *Journal of Lipid Research*. American Society for Biochemistry and Molecular Biology; 2009. p. S63. <https://doi.org/10.1194/jlr.R800082-JLR200> PMID: 19029121
73. Hiu JJ, Yap MKK. Cytotoxicity of snake venom enzymatic toxins: Phospholipase A2 and L-amino acid oxidase. *Biochemical Society Transactions*. Portland Press Ltd; 2020. pp. 719–731. <https://doi.org/10.1042/BST20200110> PMID: 32267491
74. Flores-Díaz M, Monturiol-Gross L, Naylor C, Alape-Girón A, Flieger A. Bacterial Sphingomyelinases and Phospholipases as Virulence Factors. *Microbiol Mol Biol Rev*. 2016; 80: 597–628. <https://doi.org/10.1128/MMBR.00082-15> PMID: 27307578
75. Sitkiewicz I, Stockbauer KE, Musser JM. Secreted bacterial phospholipase A2 enzymes: better living through phospholipolysis. *Trends Microbiol*. 2007; 15: 63–69. <https://doi.org/10.1016/j.tim.2006.12.003> PMID: 17194592
76. Palm NW, Rosenstein RK, Yu S, Schenten DD, Florsheim E, Medzhitov R. Bee venom phospholipase A2 induces a primary type 2 response that is dependent on the receptor ST2 and confers protective immunity. *Immunity*. 2013; 39: 976–985. <https://doi.org/10.1016/j.immuni.2013.10.006> PMID: 24210353
77. Cayrol C, Duval A, Schmitt P, Roga S, Camus M, Stella A, et al. Environmental allergens induce allergic inflammation through proteolytic maturation of IL-33. *Nat Immunol*. 2018; 19: 375–385. <https://doi.org/10.1038/s41590-018-0067-5> PMID: 29556000
78. Kain HS, Glennon EKK, Vijayan K, Arang N, Douglass AN, Fortin CL, et al. Liver stage malaria infection is controlled by host regulators of lipid peroxidation. *Cell Death Differ*. 2020; 27: 44–54. <https://doi.org/10.1038/s41418-019-0338-1> PMID: 31065106
79. Lefèvre L, Authier H, Stein S, Majorel C, Couderc B, Dardenne C, et al. LRH-1 mediates anti-inflammatory and antifungal phenotype of IL-13-activated macrophages through the PPAR γ ligand synthesis. *Nat Commun*. 2015; 6: 1–13. <https://doi.org/10.1038/ncomms7801> PMID: 25873311
80. Man SM, Hopkins LJ, Nugent E, Cox S, Glück IM, Tourlomousis P, et al. Inflammasome activation causes dual recruitment of NLRC4 and NLRP3 to the same macromolecular complex. *Proc Natl Acad Sci U S A*. 2014; 111: 7403–7408. <https://doi.org/10.1073/pnas.1402911111> PMID: 24803432
81. Li P, Allen H, Banerjee S, Franklin S, Herzog L, Johnston C, et al. Mice deficient in IL-1 β -converting enzyme are defective in production of mature IL-1 β and resistant to endotoxic shock. *Cell*. 1995; 80: 401–411. [https://doi.org/10.1016/0092-8674\(95\)90490-5](https://doi.org/10.1016/0092-8674(95)90490-5) PMID: 7859282
82. Demarco B, Grayczyk JP, Bjanec E, Roy D Le, Tonnus W, Assenmacher CA, et al. Caspase-8-dependent gasdermin D cleavage promotes antimicrobial defense but confers susceptibility to TNF-induced lethality. *Sci Adv*. 2020; 6: 3465–3483. <https://doi.org/10.1126/sciadv.abc3465> PMID: 33208362
83. Bartfeld S, Clevers H. Organoids as model for infectious diseases: Culture of human and murine stomach organoids and microinjection of helicobacter pylori. *J Vis Exp*. 2015;2015. <https://doi.org/10.3791/53359> PMID: 26650279
84. Sachs N, Papaspyropoulos A, Zomer-van Ommen DD, Heo I, Böttinger L, Klay D, et al. Long-term expanding human airway organoids for disease modeling. *EMBO J*. 2019;38. <https://doi.org/10.15252/emj.2018100300> PMID: 30643021
85. Eren E, Planès R, Bagayoko S, Bordignon P, Chaoui K, Hessel A, et al. Irgm2 and Gate-16 cooperatively dampen Gram-negative bacteria-induced caspase-11 response. *EMBO Rep*. 2020; 21. <https://doi.org/10.15252/embr.202050829> PMID: 33124769
86. Dyer KD, Moser JM, Czapiga M, Siegel SJ, Percopo CM, Rosenberg HF. Functionally Competent Eosinophils Differentiated Ex Vivo in High Purity from Normal Mouse Bone Marrow. *J Immunol*. 2008; 181: 4004–4009. <https://doi.org/10.4049/jimmunol.181.6.4004> PMID: 18768855
87. Troegeler A, Lastrucci C, Duval C, Tanne A, Cougoule C, Maridonneau-Parini I, et al. An efficient siRNA-mediated gene silencing in primary human monocytes, dendritic cells and macrophages. *Immunol Cell Biol*. 2014; 92: 699–708. <https://doi.org/10.1038/icb.2014.39> PMID: 24890643

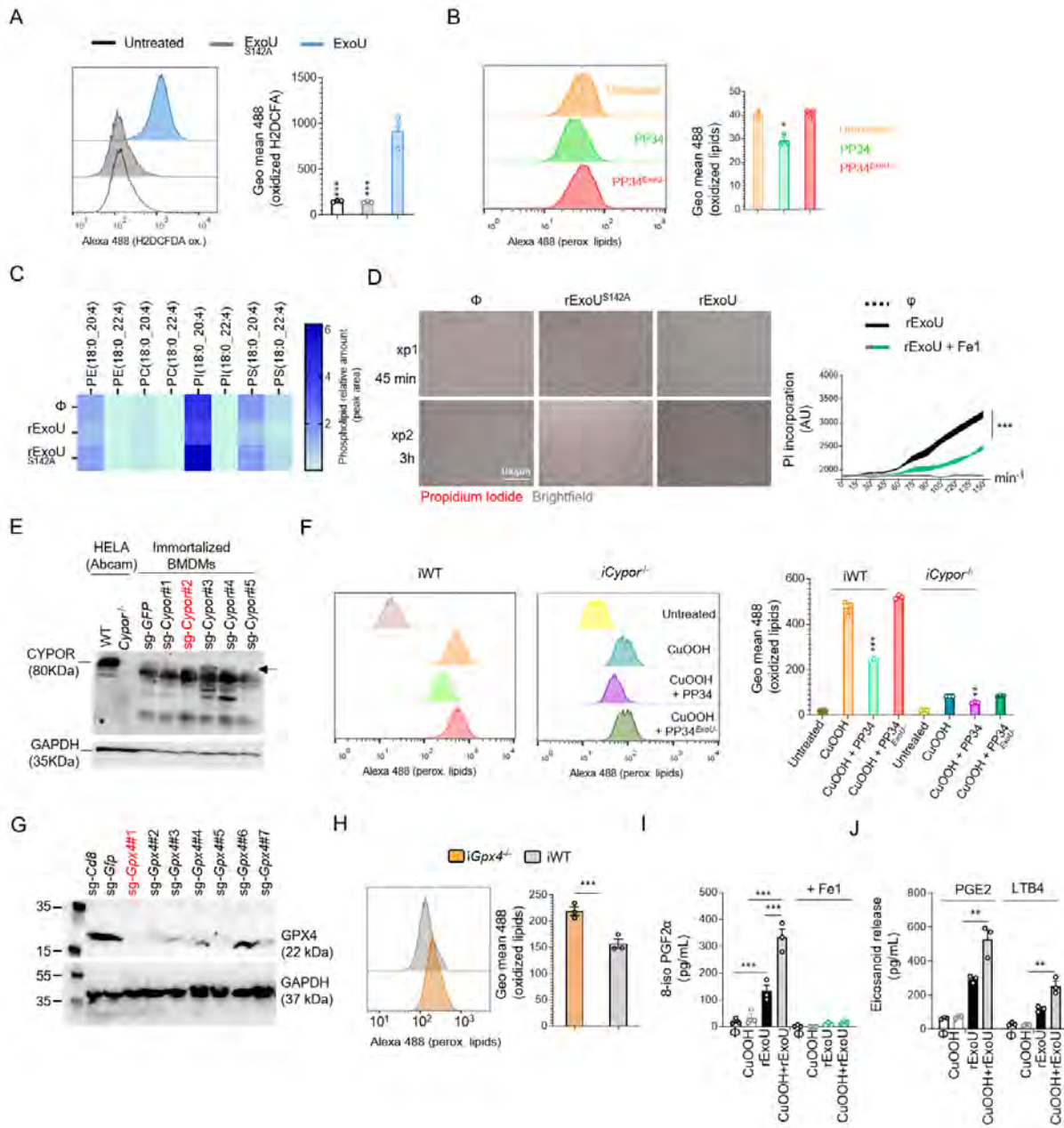
Supp fig 1



Supp Fig 2

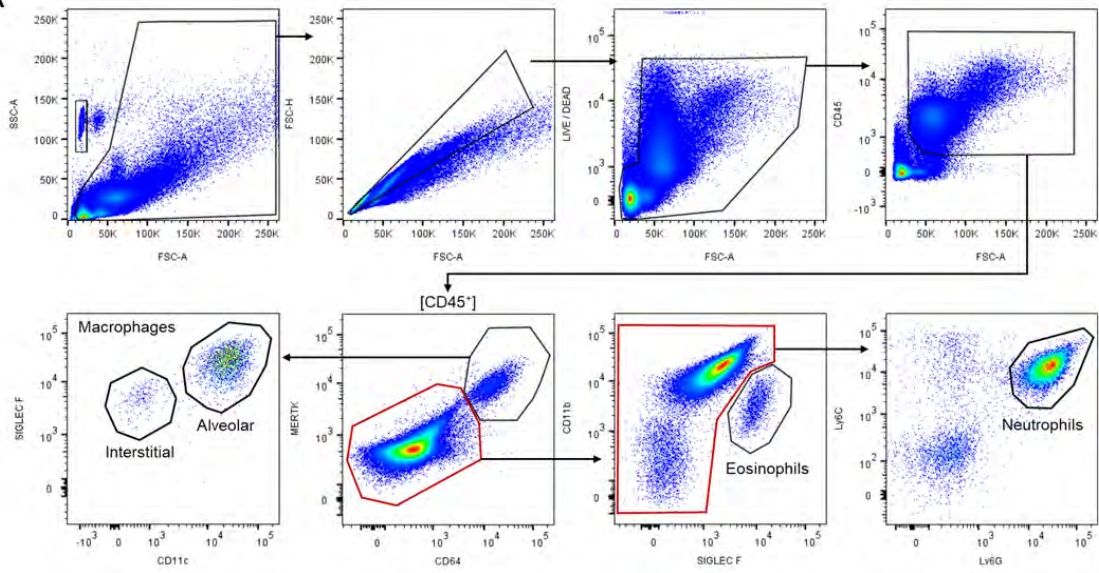


Supp Fig 3



Sup fig 4

A



VI. A Pulmonary *Lactobacillus murinus* Strain Induces Th17 and ROR γ t + Regulatory T Cells and Reduces Lung Inflammation in Tuberculosis

Authors: Lucie Bernard-Raichon, André Colom, Sarah C Monard, Amine Namouchi, Margaux Cescato, Hugo Garnier, **Stephen A Leon-Icaza**, Arnaud Métais, Alexia Dumas, Dan Corral, Natsinet Ghebrendrias, Pauline Guilloton, Christel Vérollet, Denis Hudrisier, Aude Remot, Philippe Langella, Muriel Thomas, Céline Cougoule, Olivier Neyrolles, Geanncarlo Lugo-Villarino.

Contribution: I trained Hugo Garnier to standardize, design, and perform qPCRs. Together, we performed and analyzed all the qPCR in Figure 4C. During this project, I got access to the BSL-3 facilities for work with Mtb.

This article was published in The Journal of Immunology.



Vaccine Adjuvants

Take your vaccine to the next level

InVivoGen



A Pulmonary *Lactobacillus murinus* Strain Induces Th17 and ROR γ ⁺ Regulatory T Cells and Reduces Lung Inflammation in Tuberculosis

This information is current as of September 3, 2021.

Lucie Bernard-Raichon, André Colom, Sarah C. Monard, Amine Namouchi, Margaux Cescato, Hugo Garnier, Stephen A. Leon-Icaza, Arnaud Métais, Alexia Dumas, Dan Corral, Natsinet Ghebrendrias, Pauline Guilloton, Christel Vérolet, Denis Hudrisier, Aude Remot, Philippe Langella, Muriel Thomas, Céline Cougoule, Olivier Neyrolles and Geanncarlo Lugo-Villarino

J Immunol published online 3 September 2021
<http://www.jimmunol.org/content/early/2021/09/03/jimmunol.2001044>

Supplementary Material <http://www.jimmunol.org/content/suppl/2021/09/03/jimmunol.2001044.DCSupplemental>

Why *The JI*? [Submit online.](#)

- **Rapid Reviews! 30 days*** from submission to initial decision
- **No Triage!** Every submission reviewed by practicing scientists
- **Fast Publication!** 4 weeks from acceptance to publication

**average*

Subscription Information about subscribing to *The Journal of Immunology* is online at: <http://jimmunol.org/subscription>

Permissions Submit copyright permission requests at: <http://www.aai.org/About/Publications/JI/copyright.html>

Email Alerts Receive free email-alerts when new articles cite this article. Sign up at: <http://jimmunol.org/alerts>



A Pulmonary *Lactobacillus murinus* Strain Induces Th17 and ROR γ ⁺ Regulatory T Cells and Reduces Lung Inflammation in Tuberculosis

Lucie Bernard-Raichon,^{*1} André Colom,^{*2} Sarah C. Monard,^{*3} Amine Namouchi,[†] Margaux Cescato,^{**2} Hugo Garnier,^{*4} Stephen A. Leon-Icaza,^{*5} Arnaud Métais,^{*6} Alexia Dumas,^{**3} Dan Corral,^{**4} Natsinet Ghebrendrias,^{**5} Pauline Guilloton,^{*7} Christel Vérollet,^{*8} Denis Hudrisier,^{*9} Aude Remot,^{‡,6} Philippe Langella,[‡] Muriel Thomas,[‡] Céline Cougoule,^{**7} Olivier Neyrolles,^{**7} and Geanncarlo Lugo-Villarino^{**7}

The lungs harbor multiple resident microbial communities, otherwise known as the microbiota. There is an emerging interest in deciphering whether the pulmonary microbiota modulate local immunity, and whether this knowledge could shed light on mechanisms operating in the response to respiratory pathogens. In this study, we investigate the capacity of a pulmonary *Lactobacillus* strain to modulate the lung T cell compartment and assess its prophylactic potential upon infection with *Mycobacterium tuberculosis*, the etiological agent of tuberculosis. In naive mice, we report that a *Lactobacillus murinus* (*Lagilactobacillus murinus*) strain (CNCM I-5314) increases the presence of lung Th17 cells and of a regulatory T cell (Treg) subset known as ROR γ ⁺ Tregs. In particular, intranasal but not intragastric administration of CNCM I-5314 increases the expansion of these lung leukocytes, suggesting a local rather than systemic effect. Resident Th17 and ROR γ ⁺ Tregs display an immunosuppressive phenotype that is accentuated by CNCM I-5314. Despite the well-known ability of *M. tuberculosis* to modulate lung immunity, the immunomodulatory effect by CNCM I-5314 is dominant, as Th17 and ROR γ ⁺ Tregs are still highly increased in the lung at 42-d postinfection. Importantly, CNCM I-5314 administration in *M. tuberculosis*-infected mice results in reduction of pulmonary inflammation, without increasing *M. tuberculosis* burden. Collectively, our findings provide evidence for an immunomodulatory capacity of CNCM I-5314 at steady state and in a model of chronic inflammation in which it can display a protective role, suggesting that *L. murinus* strains found in the lung may shape local T cells in mice and, perhaps, in humans. *The Journal of Immunology*, 2021, 207: 1–14.

The lung has been considered as a sterile organ until recently (1, 2). Technological improvements (e.g., high-throughput 16S rRNA sequencing) provided direct evidence for the presence of transient microorganism niches along the respiratory

tract; these range from the oral cavity to the lung, and they are limited by environmental parameters and immune defense mechanisms (1, 3–6). Despite the low biomass, there is a core of lung-resident bacteria among humans, dominated by *Streptococcus*, *Prevotella*,

^{*}Institut de Pharmacologie et Biologie Structurale, Université de Toulouse, CNRS, UPS, Toulouse, France; [†]Centre for Integrative Genetics, Norwegian University of Life Sciences, As, Norway; and [‡]Micalis Institute, INRAE, AgroParisTech, Université Paris-Saclay, Jouy-en-Josas, France

¹Current address: Kimmel Center for Biology and Medicine at the Skirball Institute, New York University School of Medicine, New York, NY

²Current address: Department of Bioengineering, College of Engineering, Hanyang University, Seoul, Republic of Korea

³Current address: Conway Institute, University College Dublin, Dublin, Ireland

⁴Current address: Metaorganism Immunity Section, Laboratory of Immune System Biology, National Institute of Allergy and Infectious Diseases, National Institutes of Health, Bethesda, MD

⁵Current address: New York University College of Global Public Health, New York University, New York, NY

⁶Current address: INRAE, Université de Tours, UMR1282 ISP, Nouzilly, France

⁷C.C., O.N., and G.L.-V. are senior authors and contributed equally to this work.

ORCID: 0000-0001-8482-280X (L.B.-R.); 0000-0001-7149-312X (S.C.M.); 0000-0002-3480-3341 (H.G.); 0000-0002-7546-8228 (S.A.L.-I.); 0000-0001-8307-8644 (N.G.); 0000-0002-1507-4243 (P.G.); 0000-0001-9896-3216 (A.R.); 0000-0002-7608-3274 (M.T.); 0000-0003-0047-5885 (O.N.); 0000-0003-4620-8491 (G.L.-V.).

Received for publication September 14, 2020. Accepted for publication July 24, 2021.

Conceptualization and methodology: L.B.-R., A.C., S.C.M., A.N., S.A.L.-I., A.M., A.D., D.C., C.V., D.H., C.C., A.R., P.L., M.T., O.N., and G.L.-V. Investigation: L.B.-R., A.C., S.C.M., M.C., H.G., S.A.L.-I., A.M., A.D., D.C., N.G., P.G., C.V., C.C., and G.L.-V. Resources: A.N., D.H., A.R., P.L., M.T., O.N., and G.L.-V. Visualization:

L.B.-R. and C.C. Funding acquisition: D.H., O.N., and G.L.-V. Corresponding authors G.L.-V. and L.B.-R. are responsible for ownership and responsibility that are inherent to aspects of this study.

This work was supported by the CNRS, Université Paul Sabatier in Toulouse, the Agence Nationale de la Recherche (ANR-15-CE15-0012 (MMI-TB) to G.L.-V. and ANR-18-CE15-0004-01 to D.H.), the Fondation pour la Recherche Médicale (DEQ2016 0334894 to O.N.), and the Fondation Bettencourt Schueller. A.R. was supported by the European Union framework of the Marie-Curie FP7 COFUND People Program (Agreenskills fellowship, Grant Agreement 267196). A.R., M.T., and P.L. were funded by Université Paris-Saclay: Applied Lung Bacteria for Health (2014-2015) with an IDEX Prematuration Grant. L.B.-R. was supported by MMI-TB (ANR-15-CE15-0012) and by Fondation pour la Recherche Médicale (FDT201805005210), and N.G. was supported by the National Science Foundation-funded International Research Experiences for Undergraduates.

Address correspondence and reprint requests to Dr. Geanncarlo Lugo-Villarino and Dr. Lucie Bernard-Raichon, Institut de Pharmacologie et de Biologie Structurale, 205 Route de Narbonne, CNRS UMR5089, Toulouse, Haute-Garonne 31000, France. E-mail addresses: lugo@ipbs.fr (G.L.-V.) and lucie.bernard03@gmail.com (L.B.-R.).

The online version of this article contains supplemental material.

Abbreviations used in this article: CNCM, French National Collection of Microorganism Cultures; CSB, Cell Staining Buffer; cTreg, conventional Treg; Foxp3, forkhead box P3; Fw, forward primer; HK, heat-inactivated; i.g., intragastric administration (gavage); IHC, immunohistochemistry; i.n., intranasal; INOS, inducible NO synthase; MPO, myeloperoxidase; ROR γ t, retinoic acid receptor-related orphan nuclear receptor γ ; RT-qPCR, quantitative RT-PCR; Rv, reverse primer; SPF, specific pathogen-free; TB, tuberculosis; T-bet, T-box expressed in T cells; Treg, regulatory T cell.

Copyright © 2021 by The American Association of Immunologists, Inc. 0022-1767/21/\$37.50

and *Veillonella* genera, and they can be altered by environmental factors and respiratory diseases often leading to an increase in Proteobacteria (7–11). The airway bacterial community, distinct from those of the gut, seems to play an essential role in respiratory health, as the acquisition of specific bacterial classes after birth is key for lung architecture development and immune tolerance against respiratory inflammatory pathologies later in life (12–15). It is well established that the gut microbiota shape lung immunity via the gut–lung axis (16, 17, 18) and that oral administration of gut probiotics improves immune responses during respiratory infections (19–21). Similarly, approaches using aerosolized antibiotic administration or intranasal (i.n.) delivery of bacterial strains indicate that the lung microbiota can also modulate lung immunity (15, 22–24). In line with this notion, recent studies show that administration of bacteria, either directly isolated from the airways or closely related to resident bacteria but from other sources, confers a potent probiotic effect to prevent and treat respiratory diseases (2, 25, 26). Therefore, the identification of pulmonary bacterial strains capable of modulating lung immunity and their use as probiotics holds promise but still remains in its infancy.

Multiple studies established that microbiota at mucosal sites, such as the gastrointestinal tract, are associated with the abundance of Th17 and regulatory T cells (Tregs) (27, 28). Not unexpectedly, germ-free mice exhibit a diminished number of Th17 and Tregs along with an altered intestinal barrier and defects in the establishment of peripheral tolerance (29–32). Intestinal recolonization of germ-free mice with segmented filamentous bacteria or Clostridia bacteria (clusters IV and XIVa) induces local induction of Th17 or Tregs, respectively (29–32). In general, Th17 cells express the transcription factor retinoic acid receptor–related orphan nuclear receptor γ (ROR γ t), and contribute to type 3 immunity (33). Most of what we know about Th17 cells is within the context of inflammation. Although they often confer protection against extracellular pathogens, particularly through neutrophil recruitment to mucosal tissue, Th17 cells are also implicated in autoimmune and inflammatory disorders when uncontrolled (33). However, seminal studies point out toward a dichotomous nature of Th17 cells, as they also engage in homeostatic functions (34, 35). For example, the presence of these nonpathogenic resident Th17 cells, depending on defined components of the gut microbiota (e.g., segmented filamentous bacteria), improves intestinal epithelial damage repair via the production of IL-22 in a model of *Citrobacter rodentium* infection (29, 36). In the case of Tregs, the role of microbiota is much clearer. By controlling effector T cells, Tregs are key actors of immune tolerance that ensure the protection of the host against tissue immunopathology. When dysregulated, however, Tregs are involved in pathogen susceptibility (37). These cells are found at mucosal sites, express the transcription factor forkhead box P3 (Foxp3) and originate either from the thymus or are induced at peripheral sites (38, 39). Thymic Tregs, or conventional Tregs (cTregs), express the transcription factor Helios, and they are specific for self-antigens and migrate to peripheral tissues to reduce autoimmunity (39). Induced Tregs at mucosal peripheral sites display a degree of plasticity to adapt to a given environment. In particular, one subset known for its coexpression of Foxp3 and ROR γ t, referred hereafter as to “ROR γ ⁺ Tregs,” is essential to limit immune activation toward resident microorganisms. Indeed, the presence of ROR γ ⁺ Tregs at mucosal sites highly depends on microbiota (31, 32). Analyses of their TCR repertoire reveal their specificity for commensal bacteria (28, 38), and multiple studies suggest that these cells have protective functions in intestinal homeostasis (41).

Both Th17 and ROR γ ⁺ Tregs are present in the lung in low numbers at steady-state conditions, but the impact of local microbiota on these cells is unknown (41). In the case of lung Th17 cells,

most studies have been performed in the context of inflammation (42). Although airway Th17 cells are protective against both extracellular (e.g., *Candida albicans*) and intracellular (e.g., *Mycoplasma pneumoniae*) pathogens, they can also contribute, if not properly controlled, to inflammatory lung diseases, such as autoimmunity, fibrosis, asthma, and chronic obstructive pulmonary disease (42). It remains unclear how these different contexts of action for Th17 and lung microbiota are interconnected beyond the correlation between their abundance and physiopathological situations. For instance, the abundance of Proteobacteria in the lower airways correlates with Th17-mediated asthma (43) as well as the enrichment of the lung microbiome with oral taxa and Th17-driven inflammation (44), suggesting that certain airway microbiota communities regulate these lymphocytes. With regards to ROR γ ⁺ Tregs, the only report that describes their presence in the lung was done by Lochner et al. (45) in 2008. Yet the authors did not investigate how these cells are influenced by the lung microbiota. Other than this, the induction of ROR γ ⁺ Tregs along with that of Th17 cells was observed during dysbiosis of oral mucosa microbiota upon *Candida* infections (46). In mice, antibiotic-mediated depletion of oropharyngeal microbiota not only reduces the abundance of both resident Th17 and ROR γ ⁺ Tregs, but also increases the incidence of tissue damage and high fungal burden in oropharyngeal mucosa, arguing that the interrelationship between resident bacteria and these leukocytes is key against periodontal inflammation generated during infection (46–48). The primordial evidence for a role of pulmonary microbiota in the induction of lung Tregs comes from studies in neonate mice. Although specific pathogen–free (SPF) neonates are as sensitive to allergic asthma as germ-free mice, postbirth microbiota acquisition in the lung transiently modulates the dendritic cell phenotype, which foments the differentiation of Tregs to establish long-term tolerance, resulting in adult SPF mice resistance against asthma (2, 13, 14). In line with these studies, Le Noci et al. (22) recently demonstrated that the use of aerosolized antibiotics induces dysbiosis specifically of the lung microbiota, resulting in a decrease of local Tregs and better immune control of lung cancer (22, 23). Therefore, although direct evidence is lacking about the capacity of specific pulmonary bacterial strains to modulate the abundance and phenotype of Th17 and ROR γ ⁺ Tregs, these studies make it plausible that airway microbiota may exert host protective functions via the regulation of these leukocytes.

In this study, we investigate the capacity of a recently isolated pulmonary bacterial strain, *Lactobacillus murinus* CNCM I-5314, to regulate the abundance and phenotype of lung Th17 and ROR γ ⁺ Tregs, and whether this modulation correlates with any potential beneficial effect in the context of a respiratory chronic infection.

Materials and Methods

Bacteria

The microbiota bacterial strain used in this study was previously isolated from neonatal mouse lung homogenates (2). This strain was deposited at the French National Collection of Microorganism Cultures (CNCM) under the name CNCM I-5314 (associated with patent file PCT N° WO2020201145A1). Based on its 16S and genomic sequence, CNCM I-5314 was identified as *Lactobacillus murinus*. CNCM I-5314 was cultivated in Man, Rogosa, Sharpe liquid medium (BD Difco; Thermo Fisher Scientific) without shaking at 30°C (for overnight preculture) or 37°C (for shorter cultures) or grown in 15% agar containing Man, Rogosa, Sharpe medium at 37°C for CFU assays.

Mycobacterium tuberculosis (H37Rv) was grown in 7H9 liquid medium (BD Difco) supplemented with 10% albumin–dextrose–catalase (BD Difco), 0.5% glycerol (Promega), and 0.05% Tween 80 (EUROMEDEX) or in 7H10 Agar medium (BD Difco) supplemented with 0.1% peptone (Thermo Fisher Scientific), 10% oleic acid–albumin–dextrose–catalase (BD Difco) and 0.5% glycerol (49).

Fresh cultures in exponential growth (3–4 h for CNCM I-5314 and 24 h for *M. tuberculosis*) were used for all inoculum preparation. Bacterial concentration was determined based on OD at 600 nm and previously

determined correspondence between OD and bacterial concentration using CFU assays; for CNCM I-5314, in exponential growth, 1uDO is equivalent to 2×10^8 CFU/ml. Pellets were harvested by centrifugation at $3,000 \times g$ at 4°C, washed twice in PBS (MgCl₂, CaCl₂ free; Life Technologies) and resuspended in PBS at 5×10^8 CFU/ml (for i.n. administration) or 5×10^9 CFU/ml (for intragastric administration [gavage] [i.g.]) for CNCM I-5314 or at 5×10^4 CFU/ml for *M. tuberculosis*.

In some experiments, heat-inactivated CNCM I-5314 was obtained by incubation of a part of the inoculum for 30 min at 70°C, a pasteurization process conserving bacterial component integrity (50). Other experiments were performed with labeled bacteria. Accordingly, CFSE-stained bacteria were obtained after incubation of the inoculum in 100 µg/ml CFSE (Cell-Trace CFSE Cell Proliferation Kit; Invitrogen) for 10 min at 37°C, three washes in PBS 10% FCS (PAN-Biotech), and resuspension in PBS for administration (51).

Mice

Animal care and experimentations were consistent with the French guidelines, and were approved by the Ministry of Higher Education and Research (agreement APAFIS 5704). Six- to eight-week-old female SPF C57BL/6 mice were purchased from Charles River Laboratories. Five to thirteen mice per group were used per experiment. To perform *M. tuberculosis* infection, mice were i.n. inoculated with H37Rv (1×10^3 CFU per mouse in 20 µl PBS) under 4% isoflurane anesthesia (Vetflurane; Virbac). CNCM I-5314 (1×10^7 CFU in 20 µl of PBS) or mock (PBS) were administered i.n. three times a week during a 2-wk period before sacrifice (naive mice) or infection under 4% isoflurane anesthesia. During *M. tuberculosis* infection, CNCM I-5314 administration was continued twice per week until sacrifice. When indicated, CNCM I-5314 was administered i.g. (1×10^9 CFU in 200 µl of PBS) every day during a 10-d period before sacrifice.

Histology

Mice (three to six per group) were sacrificed at 42 d postinfection by i.p. administration of pentobarbital (Doléthol; Vétoquinol) at lethal dose. The lungs were inflated and fixed with 10% neutral buffered formalin (Sigma-Aldrich, Merck), and embedded in paraffin. Lung sections (5 µm) were stained with H&E or immunostaining by immunohistochemistry (IHC). For the IHC characterization of mouse leukocytes in tissues, rabbit polyclonal anti-inducible NO synthase (iNOS) (clone 54, 1/100; BD Transduction Laboratories) or rabbit polyclonal anti-mouse myeloperoxidase (MPO) (RB-373, 1/100; Thermo Fisher Scientific) were incubated overnight at 4°C after heat-induced epitope retrieval with 10 mM Tris–1 mM EDTA (pH 9) or 10 mM citrate (pH 6), respectively. The sections were incubated at room temperature with goat anti-rabbit HRP (P0448, 1/400; Dako) for 2 h, streptavidin–HRP (GT85912, 1/200; GeneTex) for 1 h, revealed with DAB (C09-12; GBI Labs), and counterstained with hematoxylin (HEMML-OT-100; BioGnost). All sections were digitized using a Panoramic 250 scanner (3DHISTECH). Histopathological scoring was determined by dividing the area of infiltrated lung tissue by the total area of lung tissue from the H&E staining or IHC immunostaining using the CaseViewer software (3DHISTECH).

Tissue homogenate preparation

Mice (five to eight per group) were sacrificed by cervical dislocation under 4% isoflurane anesthesia 21 or 42 d postinfection or 15 d after first CNCM I-5314 administration (naive mice). In some experiments presented in Supplemental Fig. 1A, bronchoalveolar lavages were performed by gentle intratracheal injection of 1 ml of PBS. Alternatively, lung and spleen were prepared individually into cell suspensions (49). To discriminate by flow cytometry lung-resident leukocytes from those in blood, when indicated, mice were injected i.v. with 2 µg of anti-CD45.2 Ab (BD Biosciences) 5 min prior to sacrifice (52). Lung and spleen were collected in C Tubes (Miltenyi Biotec), homogenized with a gentleMACS Dissociator (Miltenyi Biotec), incubated with 2 mg/ml collagenase D (Roche, Merck), and 0.1 mg/ml DNase I (Roche) for 30 min at 37°C under 5% CO₂. For *M. tuberculosis*-infected mice, a part of the lung and spleen cell suspension was serially diluted in PBS and spread on Agar medium for CFU scoring to assess *M. tuberculosis* bacterial load. The remaining homogenates were filtered on 70-µm cell strainers (ClearLine; Dominique Dutscher). Alternatively, spleen collected from noninfected mice and used specifically for flow cytometry were directly crushed on 70-µm cell strainers. After centrifugation of lung and spleen cell suspensions at $330 \times g$ for 5 min, supernatants were 0.22-µm filtered (Millex-GP Sterile Syringe Filters with PES, Millipore Express Plus polyethersulfone; Merck) to exclude *M. tuberculosis* and stored at –80°C. Cytokine concentration in supernatants was later assessed by ELISA using BD OptEIA Sets (BD Biosciences) following the manufacturer's instructions. Cell pellets were resuspended in 1 ml of PBS. RBCs were lysed in 150 mM NH₄Cl, 10 mM KHCO₃, and 0.1 mM EDTA

(pH 7.2) buffer for 5 min; RBC lysis was stopped by the addition of 10% FCS-containing medium (RPMI 1640, GlutaMAX Supplement, HEPES; Thermo Fisher Scientific) (53). After centrifugation, cell pellets were 40-µm filtered (ClearLine). A portion of the cell pellet was conserved in TRIzol reagent (Invitrogen) at –80°C for RNA quantification and the rest was used for flow cytometry.

Flow cytometry

For a fraction of the lung cell suspension, cytokine production was stimulated in RPMI supplemented with 10% FCS, 50 ng/ml PMA (Sigma-Aldrich) and 500 ng/ml ionomycin (Sigma-Aldrich) and blocked with brefeldin A (Golgi-Plug, 1/1000; BD Biosciences) and monensin (GolgiStop, 1/2000; BD Biosciences) for 4 h at 37°C with 5% CO₂. The remaining cell suspension was stored in Cell Staining Buffer (CSB; BioLegend) at 4°C for the assessment of extracellular marker and transcription factor staining. Cell staining was performed in V-bottom, 96-well plates, and centrifugations were performed at $600 \times g$ (or $700 \times g$ after cell fixation) for 2 min. Cell suspensions were first incubated 20–30 min at 4°C with a mixture containing blocking anti-CD16/32 Ab (TruStain FcX; BioLegend), a viability marker (LIVE/DEAD Fixable Blue Dead Cell Stain Kit; Invitrogen), and the indicated extracellular Abs were diluted in CSB. The following Abs (clone) were used: anti-CD45.2 (104), anti-Siglec F (E50-2440), anti-Ly-6G (1A8), anti-CD4 (SK3), anti-PD-1 (J43) (from BD Biosciences); anti-CD86 (GL1) from eBioscience; anti-CD11b (M1/70), anti-CD11c (N418), anti-MerTK (2B10C42), anti-CD64 (X54-5/7.1), anti-MHCII (M5/114.15.2), anti-CD24 (M1/69), anti-CD103 (2E7), anti-Ly-6C (HK1.4), anti-TCR-β (H57-597), anti-CD3 (17A2), anti-CD8a (53-6.7), anti-CD4 (RM4-5 and GK1.5), anti-ICOS (C3998.4A), anti-CCR6 (29-2L17), anti-CD80 (16-10A1), anti-CD206 (C068C2), and anti-CD16/32 (93) from BioLegend. Cells were washed in CSB, fixed 30 min at room temperature, and permeabilized for 15 min at room temperature using reagents from the Foxp3/Transcription Factor Staining Buffer Set (eBioscience and Thermo Fisher Scientific). Cells were stained with an Ab set to detect intracellular factors diluted in the permeabilization buffer for 45 min at room temperature. Abs (clone) used included anti-RORγt (Q31 378), anti-LAP (TW7-16B4), and anti-TNF (MP6-XT22) from BD Biosciences; anti-T-bet (4B10), anti-FOXP3 (FJK-16s), anti-Ki67 (SolA15), anti-Helios (22F6), and anti-IL-17 (17B7) from eBioscience; and anti-CTLA-4 (UC10-4B9) and anti-IFN-γ (XMG1.2) from BioLegend. In the context of *M. tuberculosis*-infected mice, the stained cell preparation was fixed for 2 h with 4% paraformaldehyde (Pierce, Thermo Fisher Scientific) at room temperature to ensure *M. tuberculosis* killing. Just before acquisition, 10–20 µl of counting beads (CountBright; Molecular Probes and Thermo Fisher Scientific) were added to cell suspensions to determine absolute cell numbers. Staining was acquired with an LSR II or LSRFortessa flow cytometer (BD Biosciences) and analyzed with the FlowJo V10 software (Tree Star). Of note, cells were first gated on singlets (forward scatter height versus forward scatter width and side scatter height versus side scatter width) and live cells before further analysis, as shown in (Supplemental Fig. 2).

Gene expression by quantitative RT-PCR

RNeasy spin columns (RNeasy Mini Kit; QIAGEN) were used to extract RNA from frozen TRIzol samples, according to the manufacturer's instructions. RNA was then reverse-transcribed into cDNA using M-MLV Reverse Transcriptase (Invitrogen). Quantitative RT-PCR (RT-qPCR) was performed using a 7500 Real-Time PCR System, and data were analyzed using the 7500 Software version v2.3 (Applied Biosystems and Thermo Fisher Scientific). Values were normalized using the housekeeping β-actin gene and expressed as a fold change between experimental (CNCM I-5314-treated mice) relative to control samples. The gene-targeted primer sets used in this study were as follows: β-actin, forward primer (Fw) 5'-GCTGTCTGCTCCCTGTATGCTCT-3' and reverse primer (Rv) 5'-CCTCTCAGCTGTGGTGGTGAAGC-3'; *Tnf*, Fw 5'-CAAATTCGAGTGACAAGCCTGT-3' and Rv 5'-CCA CTGGTGGTTTGTACGA-3'; *Ifng*, Fw 5'-CAGCAACAGCAAGGCG AA-3' and Rv 5'-GGACCTGTGGTGTGGTACT-3'; *Il-6*, Fw 5'-ATG TTCTCTGGGAAATCGTGA-3' and Rv 5'-AGAATTGCCATTGCACA ACTCT-3'; *Il-1b*, Fw 5'-GCCCATCTCTGTGACTCAT-3' and Rv 5'-AGGCCACAGGTATTTTGTGCG-3'; *Mpo*, Fw 5'-GCACAATATGGCAGC CCAA-3' and Rv 5'-CCAAGGCCTGCTCTGCTGT-3'; *Inos*, Fw 5'-TCCTCACGCTTGGTCTTGTTC-3' and Rv 5'-TCCAACGTTCTCCGTT CTCTTG-3'; and *Il-10*, Mm_III10_1_SG (GT00106169, QuantiTect Primer Assay; QIAGEN).

Statistics

Statistical analyses were performed using the software Prism 7 (GraphPad Software, San Diego, CA). A minimum of four mice per group was used in each experiment. Pooled results obtained from two to five experiments are presented in most figures as indicated in figure legends. For

M. tuberculosis-infected mice, *M. tuberculosis* infection was verified for all mice, and uninfected mice were not included in the analyses. When samples followed a normal distribution, the mean value for each group was represented, and a Student *t* test (comparison between two groups) or one-way ANOVA followed by a Holm-Sidak posttest (to compare more than two groups) were applied to establish significance relative to controls. In the absence of a normal distribution, the bar in the graphs represents the median of each group, and a Mann-Whitney *U* test or a Kruskal-Wallis followed by Dunn posttest was applied to compare each experimental group with controls. When indicated, a two-way ANOVA followed by a Sidak multiple comparisons test was performed to compare PBS- to CNCM I-5314-treated mice among different cell types. A significant statistical difference was represented by **p* < 0.05, ***p* < 0.01, ****p* < 0.001, and *****p* < 0.0001; NS results were indicated when the *p* value was greater than 0.05.

Results

Intranasal but not intragastric delivery of CNCM I-5314 induces both lung Th17 and ROR γ t⁺ Tregs in naive mice

We previously isolated 20 bacterial strains from lung homogenates of neonatal SPF mice (2). Importantly, i.n. administration of one of these strains (i.e., *Enterococcus faecalis*, CNCM I-4969) in neonates dramatically reduced type 2 immunity and the incidence of allergic asthma in mouse lungs, suggesting that these pulmonary bacteria have the potential to modulate lung immunity (2). To expedite the search for prospective probiotics, our main approach was to first test those strains closely related to generally recognized as safe bacteria, which are mainly composed of *Lactobacillus* species (21, 54). Among our collection of pulmonary bacteria, we identified *L. murinus* (CNCM I-5314; *Lagilactobacillus murinus* under new taxonomic reclassification) (2, 55), a common resident of the murine gastrointestinal tract associated with the regulation of gut Th17 and Tregs (56, 57). Different studies reported a decrease in *Lactobacillus* species, particularly *L. murinus*, in different pathological conditions in the gastrointestinal tract (56–60). In some of these models, administration of *L. murinus* recapitulated the protective effect by transplantation of gut microbiota, and this was associated with a strong induction of Tregs via the local production of TGF- β and IL-10 (56). More recently, overcolonization of the gastrointestinal tract by *L. murinus* was shown to result in the particular expansion of Tregs in the lungs, leading to protection against allergic airway inflammation (61). Therefore, the CNCM I-5314 strain seemed like an obvious candidate to be tested as a prospective probiotic. To this end, we first verified that the i.n. delivery of CFSE-labeled CNCM I-5314 reached the lungs and bronchoalveolar space as free bacteria as well as internalized by resident leukocytes, as illustrated in supplementary Supplemental Fig. 1. Having confirmed this, we then assessed the capacity of CNCM I-5314 to induce lung Th17 and ROR γ t⁺ Tregs by flow cytometry after i.n. or i.g. delivery in naive mice to probe the local versus systemic effects, respectively (Fig. 1A, Supplemental Fig. 2A). The i.n. delivery of CNCM I-5314 resulted in an increase in the proportion and cell number of lung Th17 and ROR γ t⁺ Tregs but not lung cTregs when compared with those levels observed in mock-treated mice (Fig. 1B–D). By contrast, i.g. administration of CNCM I-5314 resulted in a slight increase in the proportion and cell number of ROR γ t⁺ Tregs as well as in the total number of cTregs but had no effect on Th17 cells in the lungs (Fig. 1B–D). Importantly, with the exception of a slight (but statistically significant) increase in splenic ROR γ t⁺ Tregs, the proportion of Th17 and cTregs in the spleen remained intact after i.n. administration of CNCM I-5314 as compared with that in mock-treated mice, suggesting that this bacterial strain mostly exerts a local effect in the lung rather than a systemic one reflected in secondary lymphoid organs (Supplemental Fig. 2B). Our data also indicated that CNCM I-5314 modulates Th17 and ROR γ t⁺ Tregs in the lung tissue and airway because the exclusion of

circulating leukocytes in the lung vasculature yielded the same proportion and cell number (Supplemental Fig. 2C, 2D). Interestingly, the proportion of lung Th17 cells relative to ROR γ t⁺ Tregs at steady state decreased upon i.n. delivery of CNCM I-5314, indicating that this pulmonary bacterial strain favors ROR γ t⁺ Tregs over Th17 cells (Fig. 1E). In fact, among total lung Foxp3⁺ CD4⁺ T cells, the proportion of ROR γ t⁺ Tregs increased from 15% up to 45% after delivery of CNCM I-5314 (Fig. 1E). Furthermore, i.n. administration of heat-inactivated (HK) CNCM I-5314 induced a similar increase in the proportion and cell number of Th17 and ROR γ t⁺ Tregs as live bacteria when compared with mock-treated mice (Fig. 1B–E), suggesting that a structural component rather than a secreted metabolite, for example, is responsible for this effect. Notably, the different variations of CNCM I-5314 delivery had no impact on the total number of lung CD4⁺ T cells (Fig. 1D), a selective effect which was previously observed for probiotic strains with beneficial effects in disease context (62). Altogether, these findings indicate an important and local rather than systemic (i.e., through the gut–lung axis) effect of CNCM I-5314 in the regulation of lung Th17 and ROR γ t⁺ Tregs.

Formal characterization of lung Th17 and ROR γ t⁺ Tregs before and after CNCM I-5314 administration

Although ROR γ t⁺ Tregs were previously identified in the lung (45), their characteristics and modulation by the microbiota have not yet been assessed. Because ROR γ t⁺ Tregs and Th17 cells induced by the microbiota may play a key role in respiratory health and disease (31, 32, 36, 63), we performed a formal characterization of these lung T cell populations at steady state and after i.n. delivery of CNCM I-5314. As described for ROR γ t⁺ Tregs of gut origin (31, 32, 63), lung ROR γ t⁺ Tregs expressed Foxp3 and ROR γ t at a similar level to cTregs and Th17, respectively (Fig. 2A). In addition, a smaller proportion of lung ROR γ t⁺ Tregs (12%) expressed Helios when compared with cTregs (50%), suggesting a peripheral rather than thymic origin (Fig. 2A, 2B) as previously proposed for these leukocytes in the gut (32, 31, 64). In terms of their activation status, we noticed that, like Th17 cells, there was a high proportion of lung ROR γ t⁺ Tregs expressing the ICOS receptor (68%), which was further increased across all CD4⁺ T cells by CNCM I-5314 in comparison with the PBS control group (Fig. 2A, 2B). Likewise, 96% of lung ROR γ t⁺ Tregs expressed the immune-suppressive receptor CTLA-4, which was higher than in cTregs (71%). In addition, 47% of lung Th17 cells were positive for CTLA-4, which was further increased (67%) in CNCM I-5314-treated mice when compared with PBS-treated mice (Fig. 2A, 2B). Moreover, 52% of lung ROR γ t⁺ Tregs displayed the suppressive receptor PD-1, which was higher than in cTregs (19%) and Th17 (29%) cells; CNCM I-5314 only affected the PD-1 expression in Th17 cells (50%) relative to that found in PBS-treated mice (Fig. 2A, 2B). As previously described (30), we confirmed that lung Th17 (12%) and ROR γ t⁺ Tregs (23%) expressed the CCR6 chemokine receptor; CNCM I-5314 enhanced CCR6 expression only in Th17 cells (23%) when compared with those from PBS-treated mice (Fig. 2A, 2B). Moreover, when we assessed the proliferation status of the lung CD4⁺ T cells by measuring the Ki67 nuclear marker, we noticed that lung Th17 and ROR γ t⁺ Tregs had a higher proliferation index compared with cTregs, which was further enhanced in both leukocytes by CNCM I-5314 treatment (Fig. 2A, 2B). In terms of cytokine production, lung Th17 (44%), cTregs (33%), and ROR γ t⁺ Tregs (15%) exhibited a lower proportion of TNF expression compared with other CD4⁺ T cells (61%), and administration of CNCM I-5314 decreased TNF production across all lung CD4⁺ T cells when compared with the PBS treatment (Fig. 2C). By contrast, the percentage of leukocytes producing IL-17A was uniquely higher in Th17 cells

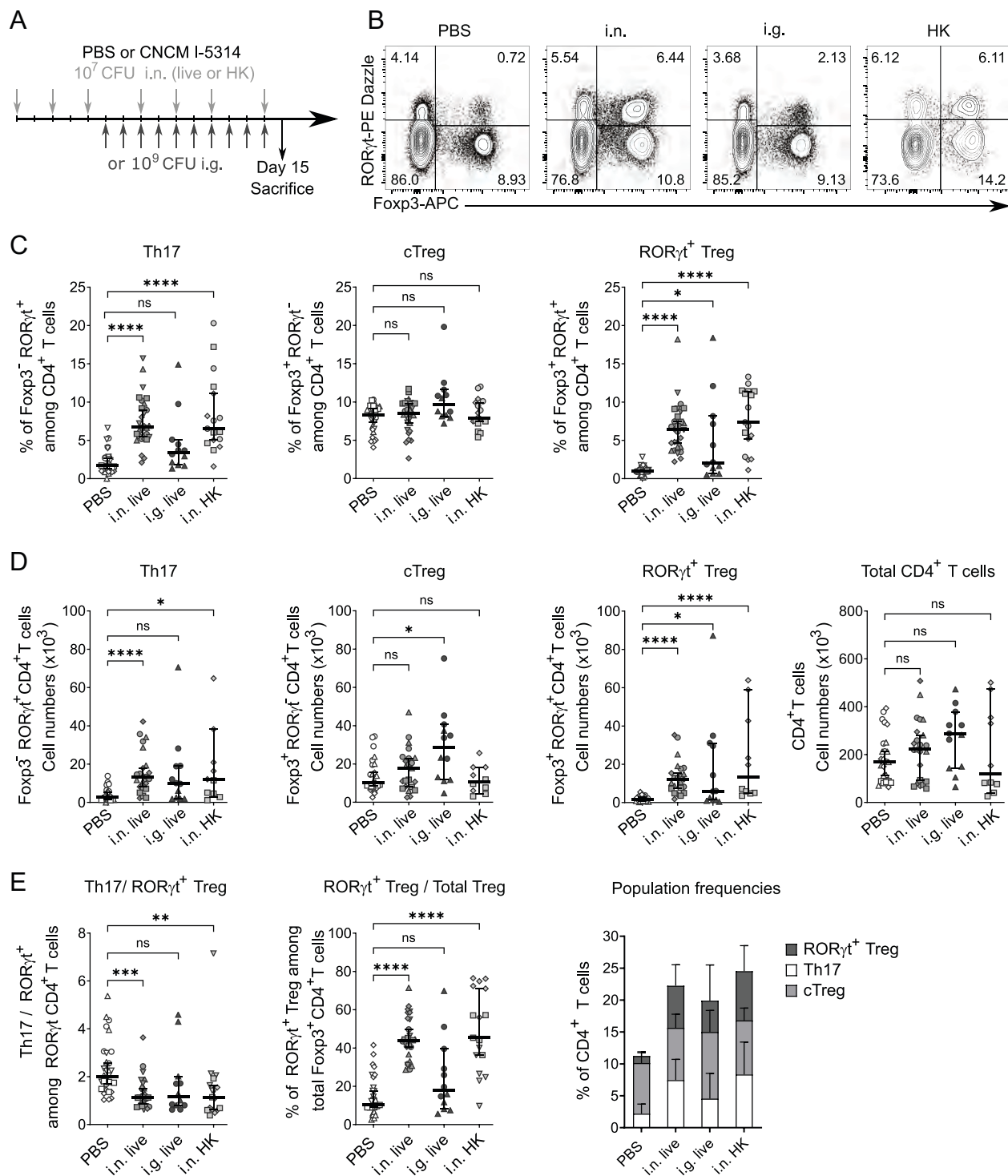


FIGURE 1. Intranasal but not intragastric delivery of live or HK CNCM I-5314 induces both lung Th17 and ROR γ t⁺ Tregs in naive mice. **(A)** Experimental protocol. C57BL/6 naive mice were inoculated i.n. with 1×10^7 CFU of live or HK *L. murinus* CNCM I-5314 in 20 μ l of PBS (or PBS alone) three times per week during 2 wk before the sacrifice point. Another mouse group received i.g. administration of 1×10^9 CFU of live *L. murinus* CNCM I-5314 in 200 μ l of PBS (or PBS alone) every day during a 10-d period before being sacrificed. Mice treated with PBS i.n. or i.g. are displayed together as the PBS group. Thereafter, a single-cell suspension was prepared from lung homogenates, and the CD4⁺ T cell compartment was analyzed by flow cytometry, as illustrated in Supplemental Fig. 2A; cells from the blood circulation were not excluded. **(B)** Dot plots showing the frequencies of Th17 (Foxp3⁻ROR γ t⁺), cTregs (Foxp3⁺ROR γ t⁻), and ROR γ t⁺ Tregs (Foxp3⁺ROR γ t⁺) among lung CD4⁺ T cells from a representative mouse belonging to each experimental group. **(C and D)** Vertical scatter plots show CD4⁺ T cell subpopulation frequencies among CD4⁺ T cells (C) or total cell number (D) in lung homogenates according to the indicated experimental group. **(E)** Vertical scatter plots represent ratio of Th17 (Foxp3⁻ROR γ t⁺) to ROR γ t⁺ Tregs (Foxp3⁺ROR γ t⁺) among all ROR γ t⁺ CD4⁺ T cells (left), proportion of ROR γ t⁺ Tregs (Foxp3⁺ROR γ t⁺) among all Foxp3⁺ cells (middle), and summary of frequencies of Th17, ROR γ t⁺ Tregs, and cTregs among CD4⁺ T cells (right) as indicated for each experimental group. Three to five independent experiments ($n = 5-8$ mice per experiment) are pooled in the graphs and indicated by different symbols; each symbol represents an individual mouse. The median [or mean for cTreg frequencies (C) and cell number (D) that follow a normal distribution] and 95% CIs are represented by the black bars. A Kruskal–Wallis test and Dunn posttest [or ordinary one-way ANOVA followed by Tukey posttest for cTreg frequencies (C) and cell number (D)] were performed to compare the mean rank of each group to the PBS control group (as the groups did not follow a normal distribution). * $p < 0.05$, ** $p < 0.01$, *** $p < 0.001$, **** $p < 0.0001$. NS values, $p > 0.05$.

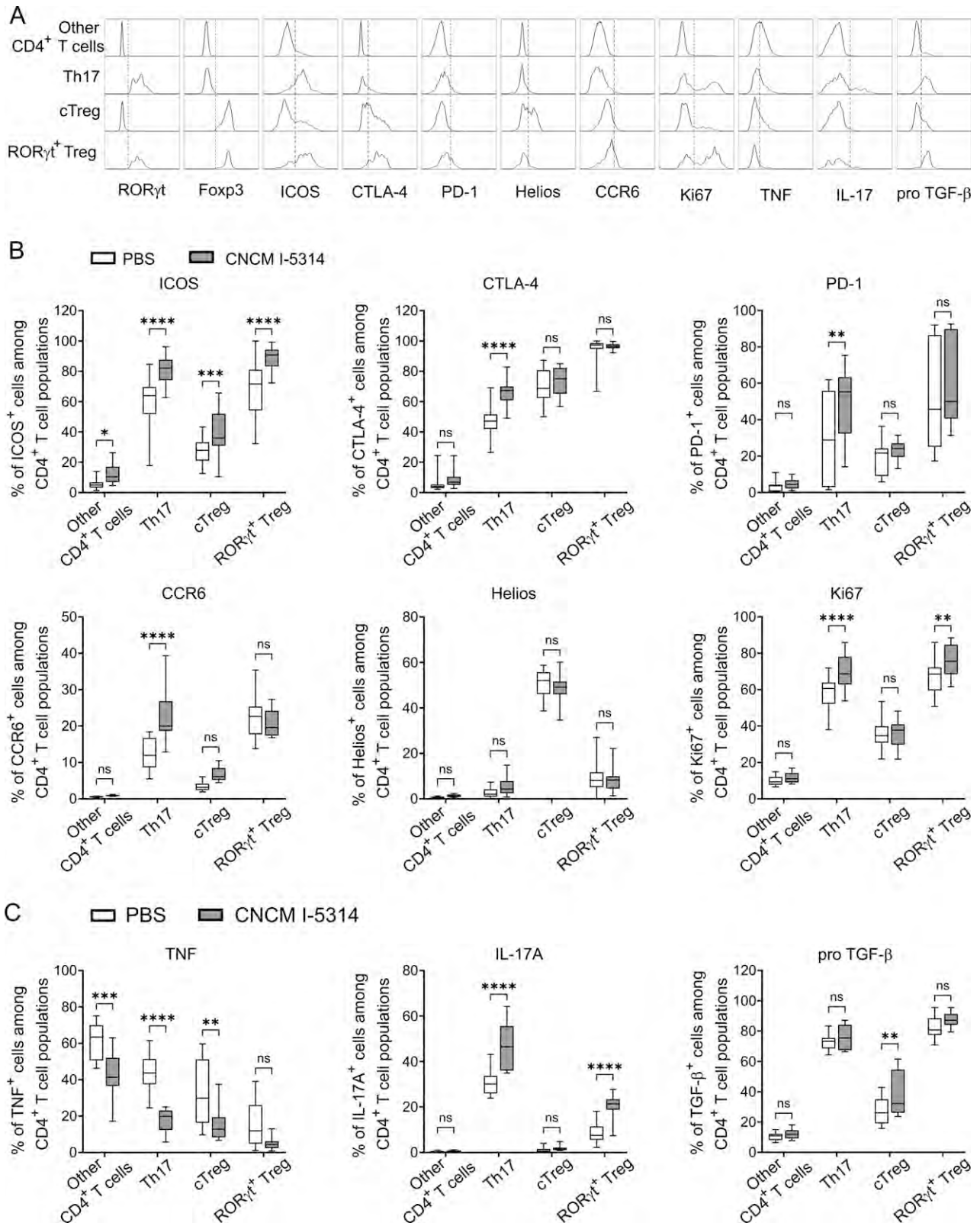


FIGURE 2. Formal characterization of lung Th17 and ROR γ ⁺ Tregs before and after administration of CNCM I-5314. C57BL/6 naive mice were inoculated i.n. with 1×10^7 CFU of live *L. murinus* (CNCM I-5314, gray) in 20 μ l of PBS or PBS alone (white) three times per week during a 2-wk period before being sacrificed. A single-cell suspension was prepared from lung homogenates, and the CD4⁺ T cell compartment was analyzed by flow cytometry, as illustrated in Supplemental Fig. 2A; cells from the blood circulation were not excluded. A fraction of the lung homogenates was stimulated for 4 h with PMA and ionomycin in the presence of brefeldin A and monensin to quantify intracellular cytokine production by flow cytometry. Pro-TGF- β ⁺ cells were quantified using an antilactency-associated protein Ab. **(A)** Histograms showing cell count (y -axis) of indicated markers and cytokines (x -axis) among the following lung CD4⁺ T cells populations: Th17 (Foxp3⁻ROR γ ⁺), cTregs (Foxp3⁺ROR γ ⁻), ROR γ ⁺ Tregs (Foxp3⁺ROR γ ⁺), and other CD4⁺ T cells (Foxp3⁻ROR γ ⁻) after i.n. administration of PBS or CNCM I-5314. **(B and C)** Box plots show the corresponding frequencies of CD4⁺ T cell populations expressing ICOS, CTLA-4, PD-1, CCR6, Helios, and Ki67 in unstimulated cells (B) or the intracellular cytokine (*Figure legend continues*)

(31%) and increased by CNCM I-5314 treatment specifically in Th17 (48%) and ROR γ t⁺ Tregs (20%) (Fig. 2C). In the case of immunosuppressive cytokines, we failed to detect lung CD4⁺ T cells expressing IL-10 by our intracellular cell staining approach, independent of the CNCM I-5314 administration. However, the proportion of leukocytes expressing the proform of TGF- β 1 was higher in both Th17 (72%) and ROR γ t⁺ Tregs (82%) compared with cTregs (28%); the CNCM I-5314 treatment only had an increasing effect in cTregs (45%) when compared with PBS control group (Fig. 2C).

Collectively, this characterization indicates that lung ROR γ t⁺ Tregs share phenotypic characteristics reminiscent of immunosuppressive leukocytes at steady state, which is maintained after administration of CNCM I-5314. This is mirrored by the expansion of Th17 cells with an anti-inflammatory phenotype that may indicate potential lung homeostatic functions rather than proinflammatory responses.

Intranasal administration of CNCM I-5314 increases lung Th17 and ROR γ t⁺ Tregs during M. tuberculosis infection

To better understand the immunomodulatory effect enacted by CNCM I-5314 in the context of pulmonary disease, we assessed its potential prophylactic effect in the context of one of the most historical and deadly respiratory pathogens to afflict humans, *M. tuberculosis*, the etiological agent of tuberculosis (TB). In fact, both Th17 and cTregs play protective and pathogenic roles in TB, depending on the stage and severity of the disease (65–71). As illustrated in Fig. 3A, mice were inoculated i.n. with CNCM I-5314, or vehicle control (PBS alone) three times per week during a 2-wk period prior to i.n. infection with *M. tuberculosis*, or mock infection (PBS alone). Thereafter, mice were inoculated twice per week postinfection with CNCM I-5314 (or PBS alone) until the indicated sacrifice time points postinfection. We assessed lung T cells by flow cytometry at 42 d postinfection, which is a standard reference time point to observe the dedicated adaptive immune response against *M. tuberculosis* (Fig. 3B, Supplemental Fig. 2A). Unlike Th1 cells, which are characterized by the lineage T-box expressed in T cells (T-bet) transcription factor, and are the crucial effector T cells in the control of *M. tuberculosis*, the administration of CNCM I-5314 increased the proportion and number of lung Th17 cells compared with those obtained in mock-treated mice (Fig. 3B–D). In addition, whereas the proportion of cTregs was slightly diminished, CNCM I-5314 administration strongly increased the proportion and cell number of ROR γ t⁺ Tregs (Fig. 3B–D). CNCM I-5314 also modulated Th17 and ROR γ t⁺ Tregs locally in the lung tissue and airway because the exclusion of circulating leukocytes in the lung vasculature yielded the same proportion and cell number (Fig. 3C, 3D). Unlike in steady-state conditions, in which the proportion of Th17 cells relative to ROR γ t⁺ Tregs decreases upon delivery of CNCM I-5314 (Fig. 1E), this ratio remained constant during *M. tuberculosis* infection, indicating that the higher abundance of Th17 cells over ROR γ t⁺ Tregs might be favored in an inflammatory context (Fig. 3E). When considering all lung Foxp3⁺ CD4⁺ T cells in infected mice, however, the proportion of the ROR γ t⁺ Tregs among total Tregs increased from 14% up to 50% after CNCM I-5314 delivery (Fig. 3E). Notably, compared with the minute proportion of these cells obtained in the PBS-treated *M. tuberculosis*-infected animals, the CNCM I-5314 appeared responsible for the higher proportion of Th17 and ROR γ t⁺ Tregs (11% and 8%, respectively) in the lung

CD4⁺ T cell compartment in *M. tuberculosis*-infected mice (Fig. 3E). Because the probiotic use of *Lactobacillus* strains modulates the levels and phenotype of CD4⁺ T cells (62), we also examined their cytokine production in the presence of CNCM I-5314 at day 42 postinfection with *M. tuberculosis* (Fig. 4A, 4B). Although most cytokines (TNF, IFN- γ , pro-TGF- β) were not modified by CNCM I-5314 administration, there was an increase in IL-17 production by lung CD4⁺ T cells in CNCM I-5314-treated *M. tuberculosis*-infected mice (Fig. 4A, 4B) that correlated with the *Il17a* mRNA expression detected in whole lung tissue from these animals (Fig. 4C). Interestingly, whereas the CNCM I-5314 treatment did not alter the cytokine mRNA gene expression (*Tnf*, *Ifng*, *Il6*, *Il10*, or *Il1b*) in lung tissue (Fig. 4C), it decreased significantly the TNF and IFN- γ (but not IL-6 or IL-10) protein production found in lung exudate from *M. tuberculosis*-infected mice (Fig. 4D).

Altogether, these findings establish that the immunomodulatory effect of exogenous administration of CNCM I-5314 on lung CD4⁺ T cells, distinguished by an increase in Th17 and ROR γ t⁺ Tregs, overcomes the well-known capacity of *M. tuberculosis* to modulate lung immunity (72).

CNCM I-5314 decreases lung inflammation associated with M. tuberculosis infection

To evaluate whether the immunomodulatory effect exerted by CNCM I-5314 influences TB infection outcome, we first verified that the CNCM I-5314 treatment did not result in unwanted inflammation in the lung. As measured by histology at day 42 after mock infection, we confirmed that CNCM I-5314 delivery during mock infection (PBS only) did not result in leukocyte infiltration indicative of lung lesions during *M. tuberculosis* infection (Fig. 5A). Next, in a 2 × 2 experimental design, in which we compared PBS-treated mock-infected mice with PBS-treated *M. tuberculosis*-infected mice and CNCM I-5314-treated mock-infected mice with CNCM I-5314-treated *M. tuberculosis*-infected mice (Supplemental Fig. 3A), we noticed that CNCM I-5314 treatment did not increase the mRNA profiles of proinflammatory genes, such *Il1b*, *Mpo*, and *Inos* in lung tissue at day 42 postinfection with *M. tuberculosis* (or mock) (Supplemental Fig. 3B). Of note, unlike PBS-treated *M. tuberculosis*-infected mice, in which there is an expected induction in *Inos* mRNA expression in lung tissue compared with that obtained in PBS-treated mock-infected mice, we observed a decreasing trend in the expression of this gene in lung tissue from both CNCM I-5314-treated mock-infected mice and CNCM I-5314-treated *M. tuberculosis*-infected mice (Supplemental Fig. 3B). At the protein level, the CNCM I-5314 treatment did not provoke the release of proinflammatory (TNF, IFN- γ , and IL-6) or anti-inflammatory (IL-10) cytokines in the lung exudate as expected for day 42 postinfection with *M. tuberculosis* (Supplemental Fig. 3C). Moreover, flow cytometry analyses of intracellular staining for hallmark Th1 markers, such as T-bet and IFN- γ , revealed that the rise of Th1 cells is specific to *M. tuberculosis* infection, as they become abundant in the lungs of PBS-treated *M. tuberculosis*-infected mice compared with PBS-treated mock-infected mice (Supplemental Fig. 3D, 3E). Similar to PBS-treated mock-infected mice, Th1 cells are nonexistent in CNCM I-5314-treated mock-infected mice (Supplemental Fig. 3D, 3E). By contrast, we confirmed that the rise of Tregs and IL-17A-producing cells is specific to the CNCM I-5314 treatment, as these cells are only significantly augmented in the lungs of CNCM I-5314-treated mock-infected mice in comparison with

content for TNF, IL-17, and pro-TGF- β in PMA-ionomycin-stimulated cells (C). The box plots represent the interquartile range, where the middle line is the median and the whiskers show the maximum and minimum values. Three to five independent experiments were pooled together ($n = 5–8$ mice per experiment). An ordinary two-way ANOVA followed by Sidak multiple comparison posttest was performed to compare the mean of the CNCM I-5314-treated mice to the PBS control group for each cell population. * $p < 0.05$, ** $p < 0.01$, *** $p < 0.001$, **** $p < 0.0001$. NS, $p \geq 0.05$.

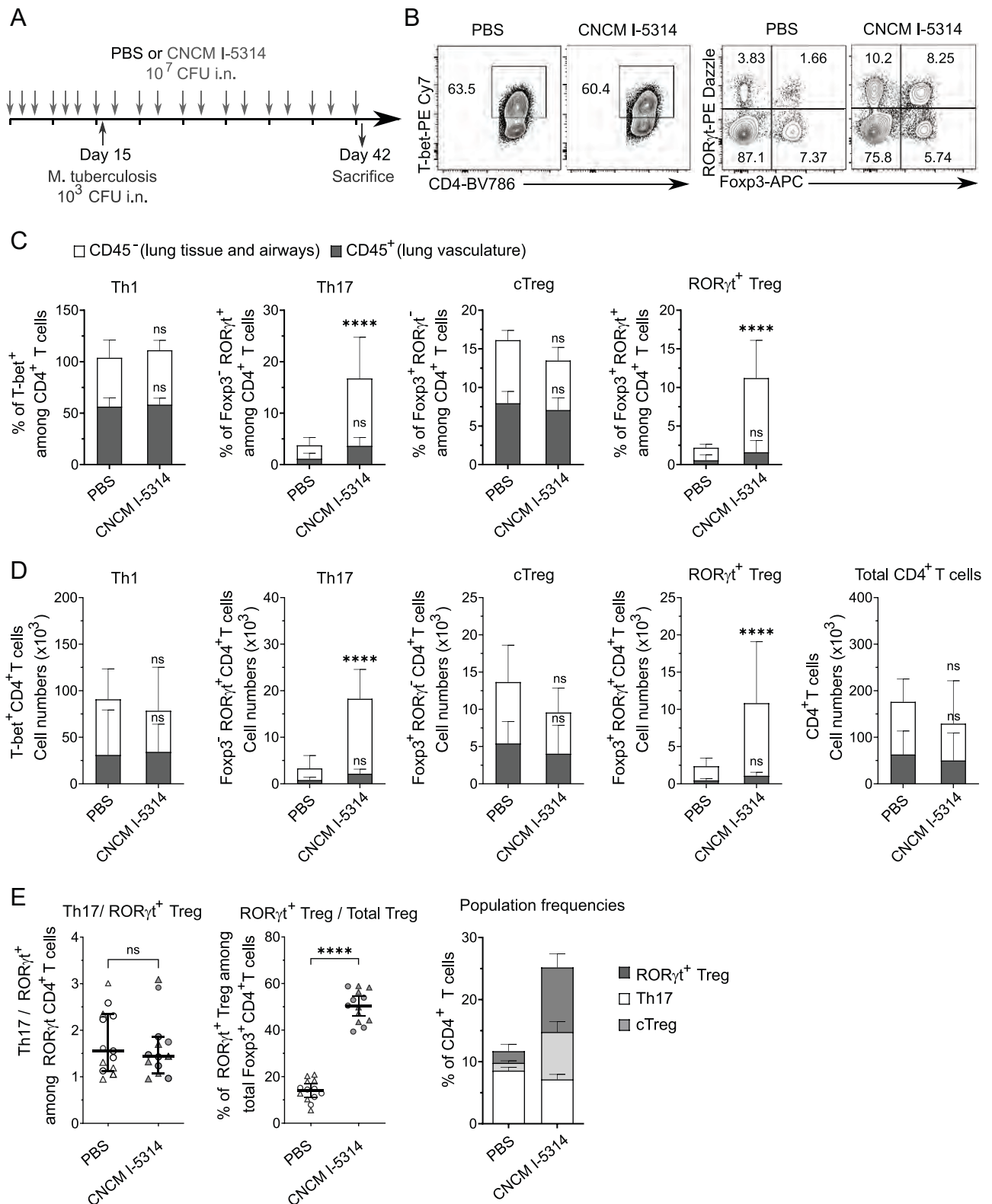
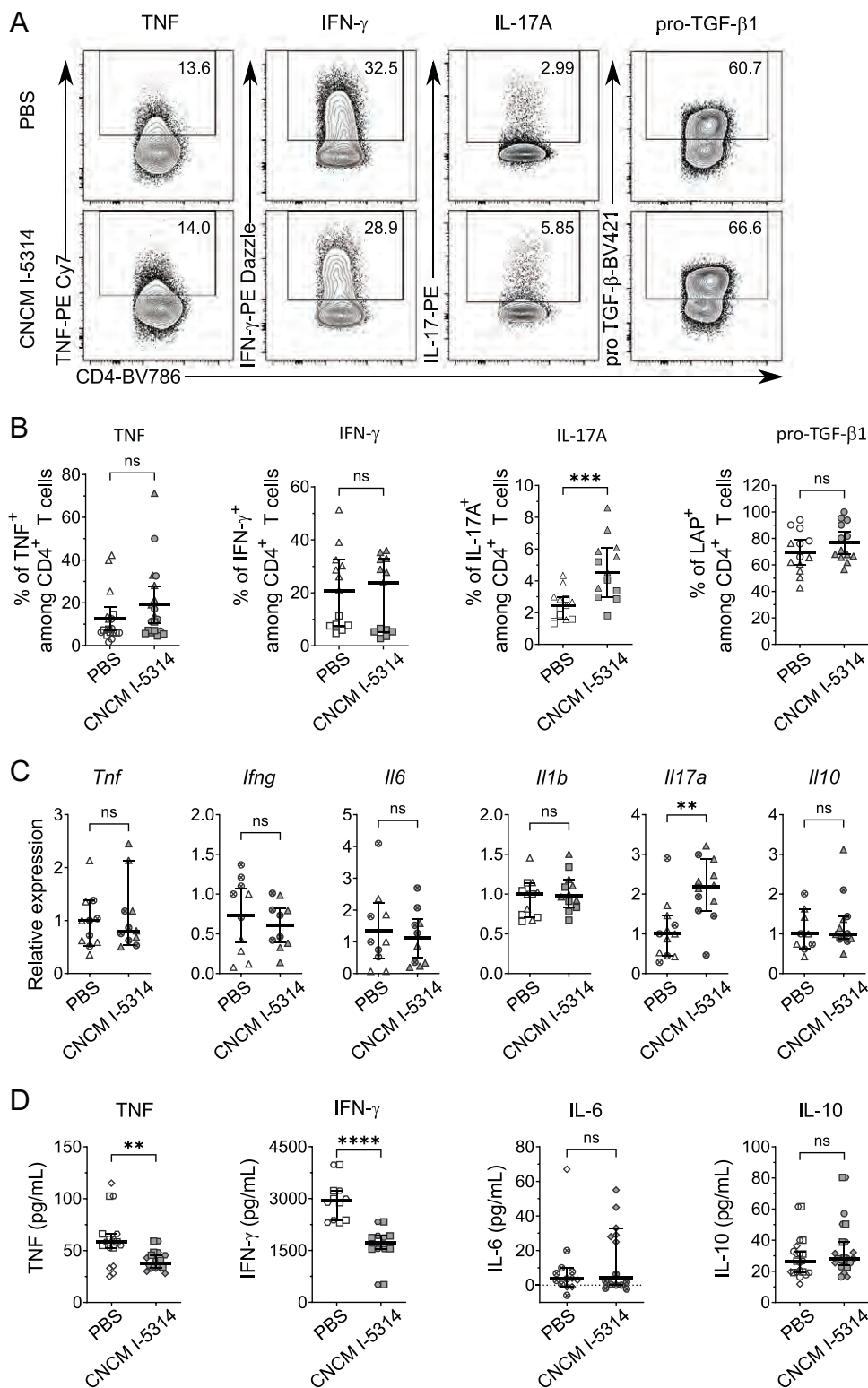


FIGURE 3. CNCM I-5314 increases lung Th17 and ROR γ t⁺ Tregs during *M. tuberculosis* infection. **(A)** Experimental design. C57BL/6 mice were inoculated i.n. with 1×10^7 CFU of live *L. murinus* (CNCM I-5314) in 20 μ l of PBS or mock (PBS alone) three times per week during a 2-wk period prior to i.n. infection with 1×10^3 CFU of *M. tuberculosis* H37Rv. Thereafter, mice were inoculated twice per week postinfection with CNCM I-5314 until the sacrifice time point at 42 d postinfection. At this time point, a single-cell suspension was prepared from lung homogenates, and the CD4⁺ T cell compartment was analyzed by flow cytometry, as illustrated in Supplemental Fig. 1A. **(B)** Dot plot displaying the expression of T-bet (left) and ROR γ t and Foxp3 (right) among lung CD4⁺ T cells from a representative mouse belonging to each experimental group. **(C and D)** Five minutes prior to sacrifice, mice received an anti-CD45.2 Ab i.v., allowing staining of cells present in the blood circulation. Vertical scatter plots show the percentage frequencies (C) and absolute numbers (D) of the indicated lung CD4⁺ T cells present in the lung vasculature (CD45⁺, dark gray) or in the lung tissue and airways (CD45⁻, white) as quantified by flow cytometry. Two independent experiments ($n = 6-7$ mice per experiment) were pooled together. **(E)** Vertical scatter plots represent ratio of Th17 (Foxp3⁻ROR γ t⁺) to ROR γ t⁺ Tregs (Foxp3⁺ROR γ t⁺) among all ROR γ t⁺ CD4⁺ T cells (left), proportion of ROR γ t⁺ Tregs (Foxp3⁺ROR γ t⁺) among all Foxp3⁺ cells (middle), and summary of the frequencies of Th17 (Foxp3⁻ROR γ t⁺), ROR γ t⁺ Tregs (Foxp3⁺ROR γ t⁺) and cTregs (Figure legend continues)

FIGURE 4. Characterization of inflammatory cytokines in lungs of CNCM I-5314–treated mice infected with *M. tuberculosis*. C57BL/6 mice were inoculated i.n. with 1×10^7 CFU of *L. murinus* (CNCM I-5314, gray) in 20 μ l of PBS or mock (PBS alone, white) three times a week during a 2-wk period prior to i.n. infection with 1×10^3 CFU of *M. tuberculosis* H37Rv. Thereafter, mice were inoculated twice per week postinfection with CNCM I-5314 until the sacrifice point at 42 d postinfection. A single-cell suspension was prepared from lung homogenates to analyze, in part, the intracellular cytokine production within the CD4⁺ T cell compartment by flow cytometry (**A** and **B**), the cytokine gene expression in total lung cells (**C**), and the cytokine protein secretion in lung exudate (**D**). (**A** and **B**) Part of the lung homogenates was stimulated for 4 h with PMA and ionomycin in the presence of brefeldin A and monensin to determine cytokine production by flow cytometry. Pro-TGF- β 1⁺ cells were quantified using an antilatency-associated protein Ab. Representative dot plots (**A**) and vertical scatter plots showing the frequencies (**B**) of each cytokine-producing cell population among CD4⁺ T cells for each experimental group. (**C**) Relative expression of *Tnf*, *Ifng*, *Il6*, *Il1b*, *Il17*, and *Il10* to that of β -actin in unstimulated lung single-cell suspension was measured by RT-qPCR. Values are expressed as a fold change between CNCM I-5314–treated mice relative to PBS-treated mice. (**D**) Vertical scatter plots illustrate the indicated cytokine concentration detected in lung homogenate supernatants as measured by ELISA. Two independent experiments ($n = 5$ –8 mice per experiment) were pooled together and are distinguished by different symbols; each symbol represents an individual mouse. The median (or mean for TNF, pro-TGF- β 1 frequencies, as well as for the *Ifng* and *Il6* relative expression, which display normal distributions) and 95% CIs are represented by the black bars. A Mann-Whitney *U* test (or an unpaired *t* test for TNF, pro-TGF- β 1 frequencies, as well as for *Ifng* and *Il6* expression) was performed to compare the median (or mean) of the CNCM I-5314– and mock-treated mice. ** $p < 0.01$, *** $p < 0.001$, **** $p < 0.0001$. NS, $p \geq 0.05$.

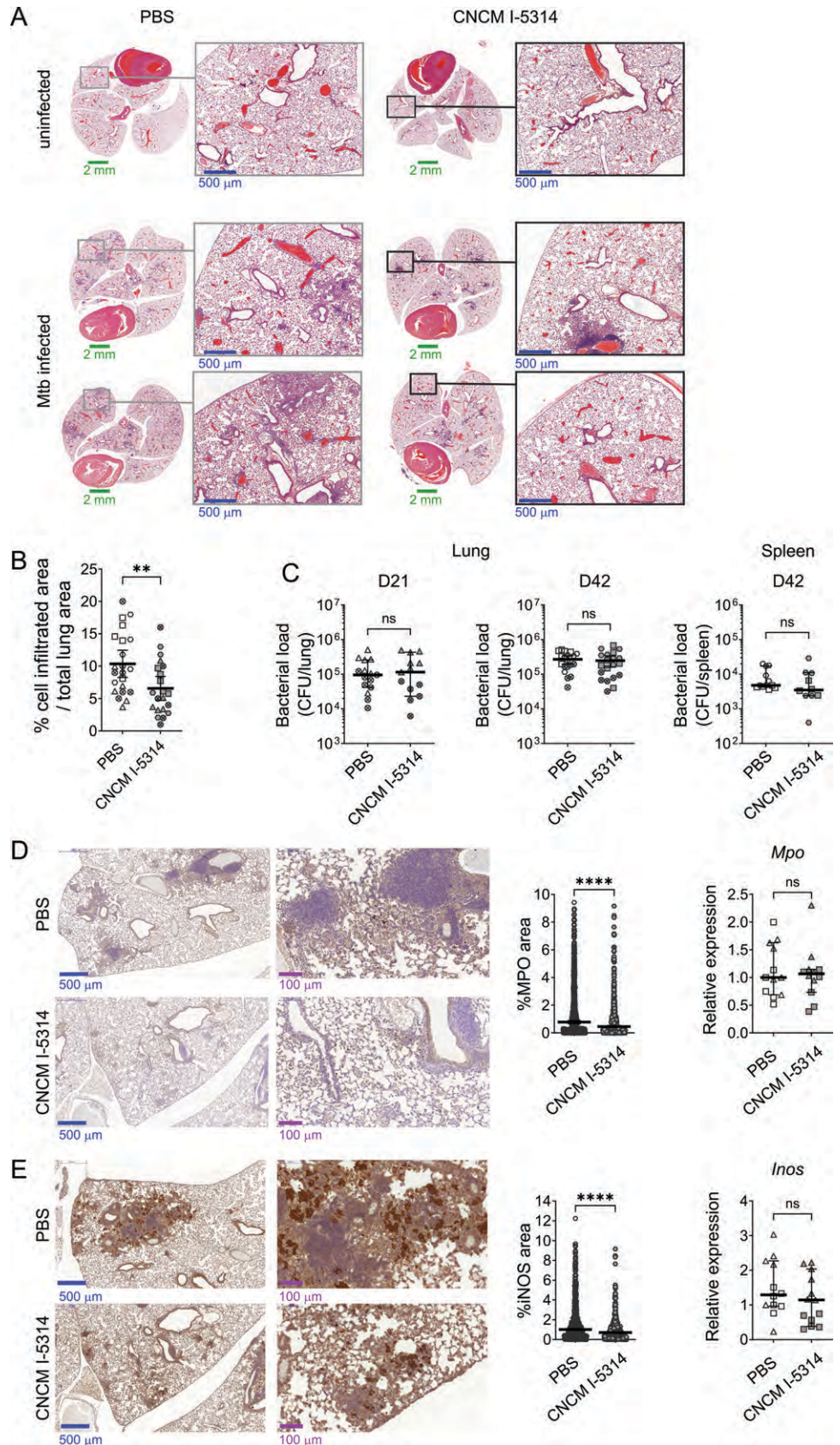


PBS-treated mock-infected mice (Supplemental Fig. 3D, 3E). Collectively, these data clearly eliminate the possibility that treatment with CNCM I-5314 causes unwanted inflammation in the lungs of mock- and *M. tuberculosis*–infected animals.

Next, we measured the *M. tuberculosis* burden and lung inflammation in infected mock- and CNCM I-5314–treated mice (Fig. 3A). Histological analyses at 42 d postinfection revealed that administration of CNCM I-5314 reduces lung leukocyte infiltration

(Foxp3⁺ROR γ t⁻) among all CD4⁺ T cells (right) as indicated for each experimental group. Five independent experiments ($n = 5$ –8 mice per experiment) were pooled together. For all panels, the black bar lines or bars represent the median of each group and 95% CIs. A two-way ordinary ANOVA followed by Sidak posttest was used in (C) and (D) to compare the mean of the CNCM I-5314– and mock-treated mice among CD45⁻ or CD45⁺ cells; a Mann-Whitney *U* test was performed to compare the medians of the CNCM I-5314– and mock-treated mice in (E). **** $p < 0.0001$. NS, $p \geq 0.05$.

FIGURE 5. The pulmonary bacterial strain CNCM I-5314 decreases lung inflammation associated with *M. tuberculosis* infection. C57BL/6 mice were inoculated i.n. with 1×10^7 CFU of live *L. murinus* (CNCM I-5314, gray) in 20 μ l of PBS or mock (PBS alone, white) three times per week during a 2-wk period prior to i.n. infection with 1×10^5 CFU of *M. tuberculosis* H37Rv (or mock, uninfected mice). Thereafter, mice were inoculated twice per week postinfection with CNCM I-5314 until the sacrifice time points at 21 or 42 d postinfection. **(A and B)** Leukocyte infiltration detected **(A)** and quantified **(B)** by histological H&E staining in pulmonary tissue. No leukocyte infiltration was detected in uninfected mice. Green scale bars, mm; blue scale bars (6.2 \times zoom insets), 0.5 mm. In **(A)**, one noninfected mouse and two *M. tuberculosis*-infected mice are shown for each condition (PBS or CNCM I-5314 administration) as example. In **(B)**, each dot represents the sum of areas infiltrated by leukocyte in one whole lung slide for one mouse. **(C)** Vertical scatter plots show the load of *M. tuberculosis* in lung homogenates at 21 or 42 d postinfection (left and middle) or spleen homogenates at 42 d postinfection (right). **(D and E)** MPO **(D)** and INOS **(E)** expression detected and quantified (left and middle) by IHC or RT-qPCR (right) analyses. Pulmonary tissue images from PBS-treated mice are shown on the top row and those from CNCM I-5314-treated animals are on the bottom row (two mice are shown as example). Blue scale bars, 500 μ m; purple scale bars, 100 μ m. The RT-qPCR panels depict relative expression to β -actin in unstimulated lung single-cell suspension at 42 d postinfection and are expressed as a fold change between CNCM I-5314-treated mice relative to PBS-treated mice. Two to four independent experiments ($n = 5$ –6 mice per experiment) were pooled together and indicated by different symbols; each symbol represents an individual mouse. The black bar lines within the vertical graphs represent the median (or mean for bacterial load in the lung at day 42 and leukocyte infiltration, which displays a normal distribution) of each group and 95% CIs. A Mann-Whitney *U* test (or an unpaired *t* test for bacterial load in the lung at 42 d postinfection and leukocyte infiltration) was performed to compare the median (or mean) in the CNCM I-5314- and control mock-treated groups. ** $p < 0.01$, **** $p < 0.0001$. NS, $p \geq 0.05$.



associated with *M. tuberculosis* infection (Fig. 5A, 5B). However, administration of CNCM I-5314 did not modify the pathogen burden in the lungs nor dissemination to the spleen at 21 or 42 d postinfection (Fig. 5C). IHC staining for lung inflammation markers associated with *M. tuberculosis* infection, such as MPO and induced

INOS, revealed that the CNCM I-5314 treatment decreased significantly the abundance of lung leukocytes positive for these markers at 42 d postinfection (Fig. 5D, 5E). In the case of MPO, quantitative RT-PCR analyses indicated the total mRNA level of the *Mpo* gene in lung tissue was not affected by CNCM I-5314 treatment at 42 d

postinfection (Fig. 5D). Moreover, flow cytometry analyses revealed that neutrophils (Ly-6G^{hi}CD11b^{hi}), one of the main leukocytes known to express MPO (73), were not altered by CNCM I-5314 delivery in *M. tuberculosis*-infected mice (Supplemental Fig. 4A). With regards to INOS, whereas the total mRNA level of the *Inos* gene was not affected by CNCM I-5314 (Fig. 5E), we identified Ly-6C⁺ inflammatory monocytes as the only leukocyte population being diminished in the lung, as measured by flow cytometry at 42 d postinfection (Supplemental Fig. 4A, 4B). Inflammatory monocytes are known to express both MPO and INOS proteins (73–75). Interestingly, in contrast to interstitial macrophages, dendritic cells, and eosinophils, the total number of alveolar macrophages was augmented in the lungs of CNCM I-5314-treated mice (Supplemental Fig. 4A, 4B). Further analyses of these macrophages seem to indicate that CNCM I-5314 administration established a wound-healing/tissue-repair phenotype characterized by upregulation of the mannose receptor (CD206) and of the FcγRIIIa/FcγRIIIb receptors (CD16/CD32) (76) that was mirrored by the downregulation of proinflammatory markers, such as CD80, ultimately correlating with the overall drop of MPO⁺ and INOS⁺ cells upon CNCM I-5314 treatment (Supplemental Fig. 4B). Indeed, both MPO and INOS are considered markers for proinflammatory (M1) macrophages (76, 77). These data argue that the CNCM I-5314 administration modulates the number of inflammatory monocytes/macrophages infiltrating the lung and the abundance and phenotype of resident macrophages during *M. tuberculosis* infection.

Altogether, these findings indicate that CNCM I-5314 reduces TB-associated lung inflammation without affecting *M. tuberculosis* lung colonization or extrapulmonary dissemination or generating unwanted pulmonary inflammation.

Discussion

Respiratory diseases, such as chronic obstructive pulmonary disease, asthma, acute lower respiratory tract infections, and TB, are among the most common causes of death and severe illness (78). Dysbiosis of the lung microbiota is one of the shared features among these diseases, often associated with deleterious consequences to the host, suggesting that resident microorganisms contribute to respiratory health and disease (8, 9, 79, 80). There is an emerging interest in deciphering whether pulmonary microbiota modulate local immunity. This knowledge could shed light on mechanisms operating in lung homeostasis and response to respiratory pathogens. In this study, we addressed these issues and propose the following contributions to the field.

Pulmonary CNCM I-5314 can regulate the levels of local Th17 cells distinguished by a nonpathogenic phenotype. Recent studies in the intestine have shed light on the dichotomous nature of Th17 cells, which allows them to support the intestinal barrier integrity (34). At steady state, Th17 cells are mainly found in the intestine, but they are also located in small quantities in other barrier organs, such as the skin, the oral cavity, and the lungs (34). These cells are characterized by the core expression of RORγt, CCR6, ICOS, IL-17A and IL-17F, which is a common feature of all RORγt⁺ leukocytes (42). We observe that resident Th17 cells are present, albeit scarcely, in the lung at steady state, confirming previous studies (34, 42, 45). They display a phenotype distinguished by a CCR6^{lo} ICOS^{int}CTLA-4^{int}PD-1^{int}IL-17A^{int}pro-TGF-β1^{hi}TNF^{int}Ki67^{hi} profile. Interestingly, a high proportion of lung Th17 cells is positive for immunosuppressive markers, such as CTLA-4, PD-1, and, particularly, pro-TGF-β1, suggesting these cells are nonpathogenic. Moreover, the high percentage of Ki67⁺ Th17 cells indicates a proliferation capacity in situ. Upon CNCM I-5314 i.n. administration, the proportion and number of Th17 cells are increased by a factor of four in the lungs, and their immunosuppressive-oriented phenotype is enhanced, as reflected

by the higher expression of CTLA-4 and PD-1 for instance. This effect seems independent of the gut–lung axis because an oral delivery failed to reproduce the induction of lung Th17 cells. These are important findings, given the emerging interest about the role of airway microbiota in Th17-mediated respiratory immunity and inflammatory disorders (44).

Pulmonary CNCM I-5314 can control the homeostasis of lung RORγt⁺ Tregs. As reported in the literature (45), we confirm the low presence of these lymphocytes in the lung, which constitutes ~15% of the total Treg population at steady-state conditions. Like Th17 cells, RORγt⁺ Tregs are specifically increased in the lungs by i.n. administration of CNCM I-5314, comprising 50% of all Tregs. In fact, this effect is reproduced by the HK version of CNCM I-5314, suggesting that soluble molecules produced by live bacteria are not responsible. Unlike Th17 cells, i.g. administration of CNCM I-5314 also increases (albeit to a lower extent than i.n. delivery) the proportion and numbers of lung cTregs and RORγt⁺ Tregs, alluding to a partial contribution by the gut–lung axis. This is in line with a recent study reporting that overcolonization of the gastrointestinal tract by *L. murinus* results in an expansion of lung Tregs, leading to protection against allergic airway inflammation (61). Likewise, Sefik et al. (32), who used monoassociation of germ-free mice with 22 bacterial species from the human gastrointestinal tract, including those from the Firmicutes phylum (e.g., *Lactobacillus* species), demonstrated that multiple but not all strains induce intestinal RORγt⁺ Tregs. We also provide the characterization of lung RORγt⁺ Tregs as Helios^{lo}CD25^{lo}ICOS^{int}CTLA-4^{hi}PD-1^{int}CCR6^{int}IL-17^{lo}pro-TGF-β1^{hi}TNF^{lo}Ki67^{hi}, which resembles an immunosuppressive phenotype that is slightly enhanced after CNCM I-5314 administration. As in the gut, lung RORγt⁺ Tregs expressed ICOS, which is considered a mucosal Treg marker that is essential for their development and production of IL-10 (81). Lung RORγt⁺ Tregs highly express CTLA-4 and PD-1 compared with cTregs, indicating a potential immunosuppressive capacity (31). This is supported by a study demonstrating that the setup of a tolerogenic lung environment during colonization by the microbiota was dependent on the generation of PD-1⁺Helios[−] Tregs (13). Like Th17 cells, there is a high proportion of lung RORγt⁺ Tregs positive for Ki67, which is further augmented by CNCM I-5314 administration, arguing for the capacity of these cells to proliferate in situ. Regarding the cytokine profile, lung RORγt⁺ Tregs produce IL-17A, accompanied by contrasting levels of pro-TGF-β1 (81%) and TNF (12%), which becomes accentuated upon administration of CNCM I-5314. IL-17 production by these cells was described to be pathogenic in other contexts and linked with aggravated inflammation (82–86). However, it is worth noting that a TGF-β-rich environment supports an anti-inflammatory role for cells producing IL-17 in the regulation of an immune response (87). Thus, the CNCM I-5314-induced RORγt⁺ Treg-driven production of IL-17A, in combination with a high ratio of pro-TGF-β1:TNF, may play a homeostatic role that contributes to tissue integrity.

CNCM I-5314 increases Th17 and RORγt⁺ Tregs during *M. tuberculosis* infection. In the TB context, Th17 cells mainly play a proinflammatory role, resulting in either protection or pathology as typically reflected by the recruitment of neutrophils into the lungs (88, 89). In our mouse model of *M. tuberculosis* infection, the presence of the Th1 cells dwarfs that of Th17 cells in the lung, which is expected because of the crucial importance of Th1 cells in TB. In CNCM I-5314-treated mice infected with *M. tuberculosis*, lung Th17 cells augment considerably without affecting the abundance of Th1 cells, but this is not accompanied by neutrophil recruitment in the lungs, suggesting that these cells do not provoke an inflammatory effect during infection. A recent study demonstrated that intestinal Th17 cells (characterized by IL-22 and IL-17 production)

induced by local commensals are not involved in models of systemic pathological inflammation or in *C. rodentium* clearance (36). Instead, they decrease the barrier permeability and favor epithelium damage repair during *C. rodentium* infection. By contrast, pathogen-elicited Th17 cells exhibit high plasticity toward proinflammatory cytokine (e.g., IFN- γ) production and a better engagement in *C. rodentium* clearance but also contributed to systematic pathological inflammation (36). Concerning ROR γ ⁺ Tregs, we observed similar trends as Th17 cells in our infection model, despite the well-known capacity of *M. tuberculosis* to shape the lung immune response. Whereas this Treg subset represents a minor cell population compared with cTregs in mock-treated animals, it augments considerably in infected animals treated with CNCM I-5314. These observations are interesting, considering that the role of Tregs in TB is also controversial (71). On the one hand, early presence of Tregs in the lung is thought to allow bacterial escape from immune control. On the other hand, Tregs are critical to avoid overinflammation, leading to necrosis and lung tissue damage at later stages of *M. tuberculosis* infection (71). However, whether these cells belong to the ROR γ ⁺ Treg subtype and whether the ROR γ ⁺ Tregs induced by lung microbiota could alter the specific response to *M. tuberculosis* is unknown. Like Th17 cells, the physiological function for ROR γ ⁺ Tregs is complex and highly dependent on the microenvironment (41). Most of the reports allude a protective role for intestinal ROR γ ⁺ Tregs against inflammatory disorders such as allergy and colitis (12, 31, 32, 41). Alternatively, there are reports about ROR γ ⁺ Tregs acquiring Th17-like pathogenic features to promote inflammation in, for example, autoimmunity. Likewise, their presence can also be dysregulated to promote immunosuppression to aggravate cancer and chronic inflammation or to play a deleterious role in the context of helminth infection (82–86). All things considered, we propose that part of the biological role for the pulmonary CNCM I-5314 strain is to regulate the dichotomy of ROR γ ⁺ Tregs toward a possible protective role during the inflammation generated by respiratory infection such as TB.

CNCM I-5314 decreases lung inflammation associated with *M. tuberculosis* infection without altering pathogen load. We and others have recently reported an increased susceptibility to *M. tuberculosis* infection in mice in which the microbiota composition was altered by administration of broad-spectrum antibiotics (21, 49, 80, 90). However, the contribution of lung microbiota to shape the immune response against *M. tuberculosis* is still poorly understood. In the current study, we demonstrate that CNCM I-5314 reduces lung leukocyte infiltration and IFN- γ /TNF production when administered i.n. to *M. tuberculosis*-infected mice. Not only do we show a lower abundance of lung MPO- and iNOS-positive leukocytes, but also, we describe a lower abundance of inflammatory monocytes mirrored by a significant increase of alveolar macrophages with an inflammatory phenotype. Future studies will assess the direct impact of CNCM I-5314 in the activation of inflammatory monocytes/macrophages and their capacity to generate inflammation and engage in lung homeostatic functions such as wound healing and tissue repair. Notably, our data indicate that CNCM I-5314 has anti-inflammatory properties without affecting *M. tuberculosis* load in the lung and spleen, nor does it interfere with the generation of Th1 cells and the CD4⁺ T cell-mediated production of IFN- γ and TNF during infection. Although leukocyte infiltration following *M. tuberculosis* infection is associated with immunopathology leading to lung tissue damage (91), it is difficult to conclude whether the reduction of leukocyte infiltration and inflammatory signals observed in the lungs of CNCM I-5314-treated mice ultimately yield a net health benefit to the host. One factor influencing these results is the choice of SPF mice with an intact microbiota in the lungs. We predict that CNCM I-5314 administration will have different effects in lung immunity in mouse

models lacking microbiota (e.g., germ free) or in which dysbiosis is induced specifically in the lungs (e.g., aerosolized antibiotics).

Collectively, our findings provide evidence for a potential role of the pulmonary microbiota in respiratory health and disease. In a model of chronic lung inflammation, our data highlight the importance of Th17 and ROR γ ⁺ Tregs as probable mediators for the immunomodulatory effect enacted by a lung *L. murinus* strain. Whether additional pulmonary bacterial strains replicate the same effect remains to be investigated. Yet, as we predict that this may be a general feature of resident lung bacteria, we propose that a better characterization of the mechanisms leading to the regulation of these cell populations and their role in lung immunity will deeply improve our understanding of the microbe–host interactions at this mucosal site. Likewise, the identification of new beneficial pulmonary bacterial strains, especially from the human lung, will represent an essential microbial source of therapeutic molecules for multiple respiratory diseases.

Acknowledgments

We greatly acknowledge F. Capilla, A. Alloy, and T. Al Saati (US006/ CREFRE) for histological analyses; P. Constant, F. Levillain, F. Moreau, C. Berrone, and B. Raynaud-Messina (Institut de Pharmacologie et de Biologie Structurale [IPBS] and Genotoul Anexplo-IPBS platform), for accessing the BSL3 facilities; A. Tridon and G. Marsal (IPBS) for access to zootechnics facilities; and E. Näser and the Genotoul TRI-IPBS facilities for imaging and flow cytometry. We thank A. Charton (IPBS) for her key assistance with in vivo experiments, M. Dupont (IPBS) for RT-qPCR analyses, L. Bermudez (Micalis Institute) for advice on handling of commensal bacterial strains, and Y.-M. Boudehen (IPBS) for technical expertise provided in molecular biology. We are grateful to C. A. Spinner, B. Raymond, C. Gutierrez (IPBS), and V. Saint-Criq (Micalis Institute) for critical reading of the manuscript and helpful comments.

Disclosures

The authors have no financial conflicts of interest.

References

- Dickson, R. P., and G. B. Huffnagle. 2015. The lung microbiome: new principles for respiratory bacteriology in health and disease. *PLoS Pathog.* 11: e1004923.
- Remot, A., D. Descamps, M. L. Noordine, A. Boukadiri, E. Mathieu, V. Robert, S. Riffault, B. Lambrecht, P. Langella, H. Hammad, and M. Thomas. 2017. Bacteria isolated from lung modulate asthma susceptibility in mice. *ISME J.* 11: 1061–1074.
- Bassis, C. M., J. R. Erb-Downward, R. P. Dickson, C. M. Freeman, T. M. Schmidt, V. B. Young, J. M. Beck, J. L. Curtis, and G. B. Huffnagle. 2015. Analysis of the upper respiratory tract microbiotas as the source of the lung and gastric microbiotas in healthy individuals. *MBio* 6: e00037.
- Man, W. H., W. A. de Steenhuijsen PETERS, and D. Bogaert. 2017. The microbiota of the respiratory tract: gatekeeper to respiratory health. *Nat. Rev. Microbiol.* 15: 259–270.
- Morris, A., J. M. Beck, P. D. Schloss, T. B. Campbell, K. Crothers, J. L. Curtis, S. C. Flores, A. P. Fontenot, E. Ghedin, L. Huang, et al; Lung HIV Microbiome Project. 2013. Comparison of the respiratory microbiome in healthy nonsmokers and smokers. *Am. J. Respir. Crit. Care Med.* 187: 1067–1075.
- Venkataraman, A., C. M. Bassis, J. M. Beck, V. B. Young, J. L. Curtis, G. B. Huffnagle, and T. M. Schmidt. 2015. Application of a neutral community model to assess structuring of the human lung microbiome. *mBio* 6: e02284-14.
- Cuthbertson, L., A. W. Walker, A. E. Oliver, G. B. Rogers, D. W. Rivett, T. H. Hampton, A. Ashare, J. S. Elborn, A. De Soysa, M. P. Carroll, et al. 2020. Lung function and microbiota diversity in cystic fibrosis. *Microbiome* 8: 45.
- Erb-Downward, J. R., D. L. Thompson, M. K. Han, C. M. Freeman, L. McCloskey, L. A. Schmidt, V. B. Young, G. B. Toews, J. L. Curtis, B. Sundaram, et al. 2011. Analysis of the lung microbiome in the “healthy” smoker and in COPD. *PLoS One* 6: e16384.
- Hilty, M., C. Burke, H. Pedro, P. Cardenas, A. Bush, C. Bossley, J. Davies, A. Ervine, L. Poulter, L. Pachter, et al. 2010. Disordered microbial communities in asthmatic airways. *PLoS One* 5: e8578.
- Pettigrew, M. M., A. S. Laufer, J. F. Gent, Y. Kong, K. P. Fennie, and J. P. Metlay. 2012. Upper respiratory tract microbial communities, acute otitis media pathogens, and antibiotic use in healthy and sick children. *Appl. Environ. Microbiol.* 78: 6262–6270.

11. Rylance, J., A. Kankwatira, D. E. Nelson, E. Toh, R. B. Day, H. Lin, X. Gao, Q. Dong, E. Sodergren, G. M. Weinstock, et al. 2016. Household air pollution and the lung microbiome of healthy adults in Malawi: a cross-sectional study. *BMC Microbiol.* 16: 182–189.
12. Al Nabhani, Z., S. Dulauroy, R. Marques, C. Cousu, S. Al Bounny, F. Déjardin, T. Sparwasser, M. Bérand, N. Cerf-Bennussan, and G. Eberl. 2019. A weaning reaction to microbiota is required for resistance to immunopathologies in the adult. *Immunity* 50: 1276–1288.e5.
13. Gollwitzer, E. S., S. Saglani, A. Trompette, K. Yadava, R. Sherburn, K. D. McCoy, L. P. Nicod, C. M. Lloyd, and B. J. Marsland. 2014. Lung microbiota promotes tolerance to allergens in neonates via PD-L1. *Nat. Med.* 20: 642–647.
14. Olszak, T., D. An, S. Zeissig, M. P. Vera, J. Richter, A. Franke, J. N. Glickman, R. Siebert, R. M. Baron, D. L. Kasper, and R. S. Blumberg. 2012. Microbial exposure during early life has persistent effects on natural killer T cell function. *Science* 336: 489–493.
15. Yun, Y., G. Srinivas, S. Kuenzel, M. Linnenbrink, S. Alnahas, K. D. Bruce, U. Steinhoff, J. F. Baines, and U. E. Schaible. 2014. Environmentally determined differences in the murine lung microbiota and their relation to alveolar architecture. *PLoS One* 9: e113466.
16. Galvão, I., L. P. Tavares, R. O. Corrêa, J. L. Fachi, V. M. Rocha, M. Rungue, C. C. Garcia, G. Cassali, C. M. Ferreira, F. S. Martins, et al. 2018. The metabolic sensor GPR43 receptor plays a role in the control of *Klebsiella pneumoniae* infection in the lung. *Front. Immunol.* 9: 142.
17. Marsland, B. J., A. Trompette, and E. S. Gollwitzer. 2015. The gut-lung axis in respiratory disease. *Ann. Am. Thorac. Soc.* 12(Suppl. 2): S150–S156.
18. den Besten, G., K. van Eunen, A. K. Groen, K. Venema, D. J. Reijngoud, and B. M. Bakker. 2013. The role of short-chain fatty acids in the interplay between diet, gut microbiota, and host energy metabolism. *J. Lipid Res.* 54: 2325–2340.
19. Damjanovic, D., R. Lai, M. Jeyanathan, C. M. Hogaboam, and Z. Xing. 2013. Marked improvement of severe lung immunopathology by influenza-associated pneumococcal superinfection requires the control of both bacterial replication and host immune responses. *Am. J. Pathol.* 183: 868–880.
20. Vieira, A. T., V. M. Rocha, L. Tavares, C. C. Garcia, M. M. Teixeira, S. C. Oliveira, G. D. Cassali, C. Gamba, F. S. Martins, and J. R. Nicoli. 2016. Control of *Klebsiella pneumoniae* pulmonary infection and immunomodulation by oral treatment with the commensal probiotic *Bifidobacterium longum* 5(1A). *Microbes Infect.* 18: 180–189.
21. Dumas, A., L. Bernard, Y. Poquet, G. Lugo-Villarino, and O. Neyrolles. 2018. The role of the lung microbiota and the gut-lung axis in respiratory infectious diseases. *Cell. Microbiol.* 20: e12966.
22. Le Noci, V., S. Guglielmetti, S. Arioli, C. Camisaschi, F. Bianchi, M. Sommariva, C. Storti, T. Triulzi, C. Castellani, A. Balsari, et al. 2018. Modulation of pulmonary microbiota by antibiotic or probiotic aerosol therapy: a strategy to promote immunosurveillance against lung metastases. *Cell Rep.* 24: 3528–3538.
23. Pellaton, C., S. Nutton, A. C. Thierry, C. Boudousquié, N. Barbier, C. Blanchard, B. Corthésy, A. Mercenier, and F. Spertini. 2012. Intra-gastric and intranasal administration of *Lactobacillus paracasei* NCC2461 modulates allergic airway inflammation in mice. *Int. J. Inflamm.* 2012: 686739.
24. Youn, H. N., D. H. Lee, Y. N. Lee, J. K. Park, S. S. Yuk, S. Y. Yang, H. J. Lee, S. H. Woo, H. M. Kim, J. B. Lee, et al. 2012. Intranasal administration of live *Lactobacillus* species facilitates protection against influenza virus infection in mice. *Antiviral Res.* 93: 138–143.
25. Brown, R. L., R. P. Sequeira, and T. B. Clarke. 2017. The microbiota protects against respiratory infection via GM-CSF signaling. *Nat. Commun.* 8: 1512.
26. Kanmani, P., P. Clua, M. G. Vizoso-Pinto, C. Rodriguez, S. Alvarez, V. Melnikov, H. Takahashi, H. Kitazawa, and J. Villena. 2017. Respiratory commensal bacteria *Corynebacterium pseudodiphtheriticum* improves resistance of infant mice to respiratory syncytial virus and *Streptococcus pneumoniae* superinfection. *Front. Microbiol.* 8: 1613.
27. Ivanov, I. I., R. L. Frutos, N. Manel, K. Yoshinaga, D. B. Rifkin, R. B. Sartor, B. B. Finlay, and D. R. Littman. 2008. Specific microbiota direct the differentiation of IL-17-producing T-helper cells in the mucosa of the small intestine. *Cell Host Microbe* 4: 337–349.
28. Atarashi, K., T. Tanoue, T. Shima, A. Imaoka, T. Kuwahara, Y. Momose, G. Cheng, S. Yamasaki, T. Saito, Y. Ohba, et al. 2011. Induction of colonic regulatory T cells by indigenous *Clostridium* species. *Science* 331: 337–341.
29. Ivanov, I. I., K. Atarashi, N. Manel, E. L. Brodie, T. Shima, U. Karaoz, D. Wei, K. C. Goldfarb, C. A. Santee, S. V. Lynch, et al. 2009. Induction of intestinal Th17 cells by segmented filamentous bacteria. *Cell* 139: 485–498.
30. Kim, K. S., S. W. Hong, D. Han, J. Yi, J. Jung, B. G. Yang, J. Y. Lee, M. Lee, and C. D. Surh. 2016. Dietary antigens limit mucosal immunity by inducing regulatory T cells in the small intestine. *Science* 351: 858–863.
31. Ohnmacht, C., J. H. Park, S. Cording, J. B. Wing, K. Atarashi, Y. Obata, V. Gaboriau-Routhiau, R. Marques, S. Dulauroy, M. Fedoseeva, et al. 2015. Mucosal Immunology. The microbiota regulates type 2 immunity through ROR γ ⁺ T cells. *Science* 349: 989–993.
32. Sefik, E., N. Geva-Zatorsky, S. Oh, L. Konnikova, D. Zemmour, A. M. McGuire, D. Burzyn, A. Ortiz-Lopez, M. Lobera, J. Yang, et al. 2015. Mucosal immunology. Individual intestinal symbionts induce a distinct population of ROR γ ⁺ regulatory T cells. *Science* 349: 993–997.
33. Hirahara, K., and T. Nakayama. 2016. CD4⁺ T-cell subsets in inflammatory diseases: beyond the Th1/Th2 paradigm. *Int. Immunol.* 28: 163–171.
34. Stockinger, B., and S. Omenetti. 2017. The dichotomous nature of T helper 17 cells. *Nat. Rev. Immunol.* 17: 535–544.
35. Peters, A., Y. Lee, and V. K. Kuchroo. 2011. The many faces of Th17 cells. *Curr. Opin. Immunol.* 23: 702–706.
36. Omenetti, S., C. Bussi, A. Metidji, A. Iseppon, S. Lee, M. Tolaini, Y. Li, G. Kelly, P. Chakravarty, S. Shoaie, et al. 2019. The intestine harbors functionally distinct homeostatic tissue-resident and inflammatory Th17 cells. *Immunity* 51: 77–89.e6.
37. Eberl, G. 2016. Immunity by equilibrium. *Nat. Rev. Immunol.* 16: 524–532.
38. Haribhai, D., J. B. Williams, S. Jia, D. Nickerson, E. G. Schmitt, B. Edwards, J. Ziegelbauer, M. Yassai, S. H. Li, L. M. Relland, et al. 2011. A requisite role for induced regulatory T cells in tolerance based on expanding antigen receptor diversity. *Immunity* 35: 109–122.
39. Cebula, A., M. Seweryn, G. A. Rempala, S. S. Pabla, R. A. McIndoe, T. L. Denning, L. Bry, P. Kraj, P. Kisielow, and L. Ignatowicz. 2013. Thymus-derived regulatory T cells contribute to tolerance to commensal microbiota. *Nature* 497: 258–262.
40. Solomon, B. D., and C. S. Hsieh. 2016. Antigen-specific development of mucosal Foxp3⁺ROR γ ⁺ T cells from regulatory T cell precursors. *J. Immunol.* 197: 3512–3519.
41. Park, J. H., and G. Eberl. 2018. Type 3 regulatory T cells at the interface of symbiosis. *J. Microbiol.* 56: 163–171.
42. Weaver, C. T., C. O. Elson, L. A. Fouser, and J. K. Kolls. 2013. The Th17 pathway and inflammatory diseases of the intestines, lungs, and skin. *Annu. Rev. Pathol.* 8: 477–512.
43. Huang, Y. J., S. Nariya, J. M. Harris, S. V. Lynch, D. F. Choy, J. R. Arron, and H. Boushey. 2015. The airway microbiome in patients with severe asthma: associations with disease features and severity. *J. Allergy Clin. Immunol.* 136: 874–884.
44. Segal, L. N., J. C. Clemente, J. C. Tsay, S. B. Koralov, B. C. Keller, B. G. Wu, Y. Li, N. Shen, E. Ghedin, A. Morris, et al. 2016. Enrichment of the lung microbiome with oral taxa is associated with lung inflammation of a Th17 phenotype. *Nat. Microbiol.* 1: 16031.
45. Lochner, M., L. Peduto, M. Cherrier, S. Sawa, F. Langa, R. Varona, D. Riethmacher, M. Si-Tahar, J. P. Di Santo, and G. Eberl. 2008. In vivo equilibrium of proinflammatory IL-17⁺ and regulatory IL-10⁺ Foxp3⁺ ROR γ ⁺ T cells. *J. Exp. Med.* 205: 1381–1393.
46. Pandiyan, P., N. Bhaskaran, M. Zou, E. Schneider, S. Jayaraman, and J. Huehn. 2019. Microbiome dependent regulation of T_{regs} and Th17 cells in mucosa. *Front. Immunol.* 10: 426.
47. Bhaskaran, N., S. Cohen, Y. Zhang, A. Weinberg, and P. Pandiyan. 2015. TLR-2 signaling promotes IL-17A production in CD4⁺CD25⁺Foxp3⁺ regulatory cells during oropharyngeal candidiasis. *Pathogens* 4: 90–110.
48. Darveau, R. P. 2010. Periodontitis: a polymicrobial disruption of host homeostasis. *Nat. Rev. Microbiol.* 8: 481–490.
49. Dumas, A., D. Corral, A. Colom, F. Levillain, A. Peixoto, D. Hudrisier, Y. Poquet, and O. Neyrolles. 2018. The host microbiota contributes to early protection against lung colonization by *Mycobacterium tuberculosis*. *Front. Immunol.* 9: 2656.
50. Plovier, H., A. Everard, C. Druart, C. Depommier, M. Van Hul, L. Geurts, J. Chilloux, N. Ottman, T. Duparc, L. Lichtenstein, et al. 2017. A purified membrane protein from *Akkermansia muciniphila* or the pasteurized bacterium improves metabolism in obese and diabetic mice. *Nat. Med.* 23: 107–113.
51. Ueckert, J. E., G. Nebe von-Caron, A. P. Bos, and P. F. ter Steeg. 1997. Flow cytometric analysis of *Lactobacillus plantarum* to monitor lag times, cell division and injury. *Let. Appl. Microbiol.* 25: 295–299.
52. Patel, B. V., K. C. Tatham, M. R. Wilson, K. P. O’Dea, and M. Takata. 2015. In vivo compartmental analysis of leukocytes in mouse lungs. *Am. J. Physiol. Lung Cell. Mol. Physiol.* 309: L639–L652.
53. Spinner, C. A., I. Lamsoul, A. Métais, C. Febrissy, C. Moog-Lutz, and P. G. Lutz. 2019. The E3 ubiquitin ligase Asb2 α in T helper 2 Cells negatively regulates antitumor immunity in colorectal cancer. *Cancer Immunol. Res.* 7: 1332–1344.
54. Pandey, K. R., S. R. Naik, and B. V. Vakil. 2015. Probiotics, prebiotics and synbiotics: a review. *J. Food Sci. Technol.* 52: 7577–7587.
55. Zheng, J., S. Wittouck, E. Salvetti, C. M. A. P. Franz, H. M. B. Harris, P. Mattarelli, P. W. O’Toole, B. Pot, P. Vandamme, J. Walter, et al. 2020. A taxonomic note on the genus *Lactobacillus*: description of 23 novel genera, emended description of the genus *Lactobacillus* Beijerinck 1901, and union of *Lactobacillaceae* and *Leuconostocaceae*. *Int. J. Syst. Evol. Microbiol.* 70: 2782–2858.
56. Tang, C., T. Kamiya, Y. Liu, M. Kadoki, S. Kakuta, K. Oshima, M. Hattori, K. Takeshita, T. Kanai, S. Saijo, et al. 2015. Inhibition of dectin-1 signaling ameliorates colitis by inducing *Lactobacillus*-mediated regulatory T cell expansion in the intestine. *Cell Host Microbe* 18: 183–197.
57. Wilck, N., M. G. Matus, S. M. Kearney, S. W. Olesen, K. Forslund, H. Bartolomaeus, S. Haase, A. Mähler, A. Balogh, L. Markó, et al. 2017. Salt-responsive gut commensal modulates Th17 axis and disease. *Nature* 551: 585–589.
58. Tang, C., S. Kakuta, K. Shimizu, M. Kadoki, T. Kamiya, T. Shimazu, S. Kubo, S. Saijo, H. Ishigame, S. Nakae, and Y. Iwakura. 2018. Suppression of IL-17F, but not of IL-17A, provides protection against colitis by inducing T_{reg} cells through modification of the intestinal microbiota. *Nat. Immunol.* 19: 755–765.
59. Kamiya, T., C. Tang, M. Kadoki, K. Oshima, M. Hattori, S. Saijo, Y. Adachi, N. Ohno, and Y. Iwakura. 2018. β -Glucans in food modify colonic microflora by inducing antimicrobial protein, calprotectin, in a dectin-1-induced-IL-17F-dependent manner. *Mucosal Immunol.* 11: 763–773.
60. Singer, J. R., E. G. Blosser, C. L. Zindl, D. J. Silberger, S. Conlan, V. A. Laufer, D. DiToro, C. Deming, R. Kumar, C. D. Morrow, et al. 2019. Preventing dysbiosis of the neonatal mouse intestinal microbiome protects against late-onset sepsis. *Nat. Med.* 25: 1772–1782.
61. Han, W., C. Tang, S. Baba, T. Hamada, T. Shimazu, and Y. Iwakura. 2021. Ovalbumin-induced airway inflammation is ameliorated in dectin-1-deficient mice, in which pulmonary regulatory T cells are expanded through modification of intestinal commensal bacteria. *J. Immunol.* 206: 1991–2000.

62. Kim, H. W., R. Hong, E. Y. Choi, K. Yu, N. Kim, J. Y. Hyeon, K. K. Cho, I. S. Choi, and C. H. Yun. 2018. A Probiotic Mixture Regulates T cell balance and reduces atopic dermatitis symptoms in mice. *Front. Microbiol.* 9: 2414.
63. Yang, B. H., S. Hagemann, P. Mamarelli, U. Lauer, U. Hoffmann, M. Beckstette, L. Föhse, I. Prinz, J. Pezoldt, S. Suerbaum, et al. 2016. Foxp3(+) T cells expressing ROR γ t represent a stable regulatory T-cell effector lineage with enhanced suppressive capacity during intestinal inflammation. *Mucosal Immunol.* 9: 444–457.
64. Getnet, D., J. F. Grosso, M. V. Goldberg, T. J. Harris, H. R. Yen, T. C. Bruno, N. M. Durham, E. L. Hipkiss, K. J. Pyle, S. Wada, et al. 2010. A role for the transcription factor Helios in human CD4(+)CD25(+) regulatory T cells. *Mol. Immunol.* 47: 1595–1600.
65. O'Garra, A., P. S. Redford, F. W. McNab, C. I. Bloom, R. J. Wilkinson, and M. P. Berry. 2013. The immune response in tuberculosis. *Annu. Rev. Immunol.* 31: 475–527.
66. Lyadova, I. V., and A. V. Pantelev. 2015. Th1 and Th17 cells in tuberculosis: protection, pathology, and biomarkers. *Mediators Inflamm.* 2015: 854507.
67. Nandi, B., and S. M. Behar. 2011. Regulation of neutrophils by interferon- γ limits lung inflammation during tuberculosis infection. *J. Exp. Med.* 208: 2251–2262.
68. Boer, M. C., S. A. Joosten, and T. H. Ottenhoff. 2015. Regulatory T-cells at the interface between human host and pathogens in infectious diseases and vaccination. *Front. Immunol.* 6: 217.
69. Shafiani, S., C. Dinh, J. M. Ertelt, A. O. Mogueche, I. Siddiqui, K. S. Smigiel, P. Sharma, D. J. Campbell, S. S. Way, and K. B. Urdahl. 2013. Pathogen-specific Treg cells expand early during mycobacterium tuberculosis infection but are later eliminated in response to interleukin-12. *Immunity* 38: 1261–1270.
70. Larson, R. P., S. Shafiani, and K. B. Urdahl. 2013. Foxp3(+) regulatory T cells in tuberculosis. *Adv. Exp. Med. Biol.* 783: 165–180.
71. Windish, H. P., P. L. Lin, J. T. Mattila, A. M. Green, E. O. Onuoha, L. P. Kane, and J. L. Flynn. 2009. Aberrant TGF- β signaling reduces T regulatory cells in ICAM-1-deficient mice, increasing the inflammatory response to Mycobacterium tuberculosis. *J. Leukoc. Biol.* 86: 713–725.
72. Young, D., and A. O'Garra. 2007. Mycobacterium tuberculosis and its ability to resist immunity. *Novartis Found. Symp.* 281: 169–177; discussion 177–180, 208–169.
73. van der Veen, B. S., M. P. de Winther, and P. Heeringa. 2009. Myeloperoxidase: molecular mechanisms of action and their relevance to human health and disease. [Published erratum appears in 2010 Antioxid. Redox. Signal. 12: 322.] *Antioxid. Redox Signal.* 11: 2899–2937.
74. Dijkstra, G., A. J. Zandvoort, A. C. Kobold, A. de Jager-Krikken, P. Heeringa, H. van Goor, H. M. van Dullemen, J. W. Tervaert, A. van de Loosdrecht, H. Moshage, and P. L. Jansen. 2002. Increased expression of inducible nitric oxide synthase in circulating monocytes from patients with active inflammatory bowel disease. *Scand. J. Gastroenterol.* 37: 546–554.
75. Terrazas, C., S. Varikuti, S. Oghumu, H. M. Steinkamp, N. Ardic, J. Kimble, H. Nakhasi, and A. R. Satoskar. 2017. Ly6C(hi) inflammatory monocytes promote susceptibility to Leishmania donovani infection. *Sci. Rep.* 7: 14693.
76. Murray, P. J., J. E. Allen, S. K. Biswas, E. A. Fisher, D. W. Gilroy, S. Goerdts, S. Gordon, J. A. Hamilton, L. B. Ivashkiv, T. Lawrence, et al. 2014. Macrophage activation and polarization: nomenclature and experimental guidelines. *Immunity* 41: 14–20.
77. Italiani, P., and D. Boraschi. 2014. From monocytes to M1/M2 macrophages: phenotypical vs. functional differentiation. *Front. Immunol.* 5: 514.
78. GBD 2015 Mortality and Causes of Death Collaborators. 2016. Global, regional, and national life expectancy, all-cause mortality, and cause-specific mortality for 249 causes of death, 1980–2015: a systematic analysis for the Global Burden of Disease Study 2015. *Lancet* 388: 1459–1544.
79. van der Gast, C. J., A. W. Walker, F. A. Stressmann, G. B. Rogers, P. Scott, T. W. Daniels, M. P. Carroll, J. Parkhill, and K. D. Bruce. 2011. Partitioning core and satellite taxa from within cystic fibrosis lung bacterial communities. *ISME J.* 5: 780–791.
80. Osei Sekyere, J., N. E. Maningi, and P. B. Fourie. 2020. Mycobacterium tuberculosis, antimicrobials, immunity, and lung-gut microbiota crosstalk: current updates and emerging advances. *Ann. N. Y. Acad. Sci.* 1467: 21–47.
81. Redpath, S. A., N. van der Werf, A. M. Cervera, A. S. MacDonald, D. Gray, R. M. Maizels, and M. D. Taylor. 2013. ICOS controls Foxp3(+) regulatory T-cell expansion, maintenance and IL-10 production during helminth infection. *Eur. J. Immunol.* 43: 705–715.
82. Esposito, M., F. Ruffini, A. Bergami, L. Garzetti, G. Borsellino, L. Battistini, G. Martino, and R. Furlan. 2010. IL-17- and IFN- γ -secreting Foxp3+ T cells infiltrate the target tissue in experimental autoimmunity. *J. Immunol.* 185: 7467–7473.
83. Kryczek, I., K. Wu, E. Zhao, S. Wei, L. Vatan, W. Szeliga, E. Huang, J. Greenson, A. Chang, J. Roliński, et al. 2011. IL-17+ regulatory T cells in the microenvironments of chronic inflammation and cancer. *J. Immunol.* 186: 4388–4395.
84. Blatner, N. R., M. F. Mulcahy, K. L. Dennis, D. Scholtens, D. J. Bentrem, J. D. Phillips, S. Ham, B. P. Sandall, M. W. Khan, D. M. Mahvi, et al. 2012. Expression of ROR γ t marks a pathogenic regulatory T cell subset in human colon cancer. *Sci. Transl. Med.* 4: 164ra159.
85. Chellappa, S., H. Hugenschmidt, M. Hagness, P. D. Line, K. J. Latori, G. Wiedswang, K. Taskén, and E. M. Aandahl. 2015. Regulatory T cells that co-express ROR γ t and FOXP3 are pro-inflammatory and immunosuppressive and expand in human pancreatic cancer. *OncolImmunology* 5: e1102828.
86. Kluger, M. A., M. C. Meyer, A. Nosko, B. Goerke, M. Luig, C. Wegscheid, G. Tiegs, R. A. Stahl, U. Panzer, and O. M. Steinmetz. 2016. ROR γ t(+)FOXP3(+) cells are an independent bifunctional regulatory T cell lineage and mediate crescentic GN. *J. Am. Soc. Nephrol.* 27: 454–465.
87. Ghoreschi, K., A. Laurence, X. P. Yang, C. M. Tato, M. J. McGeachy, J. E. Konkel, H. L. Ramos, L. Wei, T. S. Davidson, N. Bouladoux, et al. 2010. Generation of pathogenic T(H)17 cells in the absence of TGF- β signalling. *Nature* 467: 967–971.
88. Gallegos, A. M., J. W. van Heijst, M. Samstein, X. Su, E. G. Pamer, and M. S. Glickman. 2011. A gamma interferon independent mechanism of CD4 T cell mediated control of M. tuberculosis infection in vivo. *PLoS Pathog.* 7 (5, e1002052): e1002052.
89. Torrado, E., and A. M. Cooper. 2010. IL-17 and Th17 cells in tuberculosis. *Cytokine Growth Factor Rev.* 21: 455–462.
90. Khan, N., A. Vidyarthi, S. Nadeem, S. Negi, G. Nair, and J. N. Agrewala. 2016. Alteration in the gut microbiota provokes susceptibility to tuberculosis. *Front. Immunol.* 7: 529.
91. Hawn, T. R., A. I. Matheson, S. N. Maley, and O. Vandal. 2013. Host-directed therapeutics for tuberculosis: can we harness the host? *Microbiol. Mol. Biol. Rev.* 77: 608–627.